



**Università degli Studi di Pavia**

European School for Advanced Studies in Reduction of Seismic Risk

**ROSE SCHOOL**

**Behaviour of Deep Reinforced Concrete Beams under  
Monotonic and Reversed Cyclic Load**

A Thesis Submitted in Partial Fulfilment of the Requirements  
for the Degree of Doctor of Philosophy in

**EARTHQUAKE ENGINEERING**

by

**Boyan Mihaylov**

October, 2008







**Università degli Studi di Pavia**

European School for Advanced Studies in Reduction of Seismic Risk

**ROSE SCHOOL**

**Behaviour of Deep Reinforced Concrete Beams under  
Monotonic and Reversed Cyclic Load**

A Thesis Submitted in Partial Fulfilment of the Requirements  
for the Degree of Doctor of Philosophy in

**EARTHQUAKE ENGINEERING**

by

**Boyan Mihaylov**

Supervisors: Prof. Michael P. Collins and Prof. Evan C. Bentz, University of Toronto

October, 2008



## ABSTRACT

Deep reinforced concrete beams find extensive application in cases where heavy loads need to be transferred over a given span. The safety of this kind of structural element is often critical for the safety of the structure as a whole. The research described in this thesis is devoted to studying the behaviour of lightly-reinforced deep beams under monotonic and reversed cyclic loads, with particular consideration given to the load-bearing mechanisms which occur in moderately-deep beams. The choice of this topic was motivated in part by verification studies which show that the current code procedures for shear design of members without web reinforcement are least accurate in the range of transition from deep to slender beams. Furthermore, the issue of cyclic response of deep beams with small amounts of transverse reinforcement is of great importance for seismic assessment of existing structures, especially if the similarity between the load-bearing mechanisms in deep beams and those in other non-slender components such as coupling beams, squat shear walls, and frame joints is recognized.

An experimental program consisting of ten tests of deep reinforced concrete beams has been performed. All specimens failed in shear after transition from beam load-bearing mechanism to arch action (specimens without stirrups) or truss action (specimens with stirrups). A kinematic model was developed and successfully used to interpret the various deformation measurements. The results showed that a portion of the ultimate shear was carried by mechanisms involving tensile stresses being transferred through cracked concrete. It was observed that for these types of members load reversals had little effect on the overall response. A test of a deep beam provided with a single bar #18 demonstrated that anchorage by anchor heads is effective even when the largest ASTM reinforcing bar is used. Comparison between the experimentally-obtained and calculated shear strengths showed that the CSA code produced reasonably conservative predictions compared to the mostly unconservative results of the ACI and EC2 codes.

Theoretical work resulted in a derivation of an improved strut-and-tie model (ISTM) which is based on the CSA shear provisions but accounts for shear carried under the critical diagonal cracks of non-slender beams without web reinforcement. Verification against a large number of tests showed that the new model is consistent with physical observations and explains well the transition from deep to slender beams. Furthermore, it was shown that the ISTM can be used in combination with the above-mentioned kinematic model for estimation of the ultimate mid-span displacement and ultimate deformed shape of non-slender beams.



## **ACKNOWLEDGEMENTS**

I would like to express my sincere gratitude to my supervisors, Prof. Michael P. Collins and Prof. Evan C. Bentz, for making me part of their excellent research team and for sharing with me their impressive knowledge of concrete structures.

Thanks also to the staff of ROSE School and the Civil Engineering Department at the University of Toronto for the academic and financial support. The help of Headed Reinforcement Corp. who provided the headed reinforcing bars used in the experimental program of this study is greatly acknowledged.

Many thanks to Kristel, Marcos, Rajeev, Kushan, Amjad, Eleni, Ihsan, Konstantinos, Liping, Juan Pablo and to all other wonderful people I met in Pavia and Toronto. Their friendship is the best thing that has happened to me away from my home. Special thanks to Jimmy Susetyo for being the friend who I could always rely on for help or advice.

Thanks also go to Renzo Basset, Joel Babbín, Giovanni Buzzeo, and Alan McClenaghan from the Structural Laboratory at the University of Toronto as well as to all students who helped me to accomplish the experimental part of this research project. Many thanks to John MacDonald from whom I learnt so much and with whom I had such a great time working on the tests.

Finally, I am thankful to my family for being so close to me regardless of the thousands of kilometres which have been separating us for the last four years.



## TABLE OF CONTENTS

ABSTRACT.....	v
ACKNOWLEDGEMENTS .....	vii
TABLE OF CONTENTS .....	ix
LIST OF FIGURES.....	xiii
LIST OF TABLES .....	xix
LIST OF SYMBOLS.....	xxi
1. INTRODUCTION.....	1
1.1 GENERAL .....	1
1.2 B- AND D- REGIONS IN REINFORCED CONCRETE STRUCTURES.....	2
1.3 BEAM ACTION AND ARCH ACTION IN BEAMS WITHOUT WEB REINFORCEMENT .....	4
1.4 MOTIVATION FOR RESEARCH AND OBJECTIVES.....	6
1.5 THESIS OUTLINE.....	8
2. BACKGROUND.....	11
2.1 TESTS OF DEEP BEAMS, COUPLING BEAMS, AND SHEAR WALLS.....	11
2.1.1 Monotonic tests .....	11
2.1.2 Cyclic tests .....	22
2.2 MODELS FOR SHEAR STRENGTH .....	27
2.2.1 Models for B-regions .....	27
2.2.2 Models for D-regions .....	28

3. EXPERIMENTAL PROGRAM.....	39
3.1 INTRODUCTION .....	39
3.2 SPECIMENS .....	41
3.2.1 Dimensions and Reinforcement.....	41
3.2.2 Construction.....	44
3.2.3 Materials.....	45
3.3 TEST SETUP .....	48
3.4 INSTRUMENTATION .....	51
3.5 LOADING HISTORY.....	56
4. TEST RESULTS AND DISCUSSION.....	59
4.1 DATA PROCESSING .....	59
4.1.1 General .....	59
4.1.2 Data from load cells and pressure gauges .....	59
4.1.3 Zürich data.....	60
4.1.4 LVDT data.....	61
4.1.5 Strain gauges .....	61
4.1.6 Sign convention for loads and displacements .....	61
4.2 TEST L0M.....	62
4.2.1 Global behaviour.....	62
4.2.2 Kinematic model .....	69
4.2.3 Chord strains .....	73
4.2.4 Web strains .....	76
4.2.5 Support zone strains.....	83



4.2.6	Shear strength .....	84
4.3	SPECIMENS S0M/C, S1M/C, L0M/C, AND L1M/C.....	88
4.3.1	Effect of transverse reinforcement – specimens L1M and L0M.....	88
4.3.2	Effect of beam slenderness - specimens S0M and L0M.....	96
4.3.3	Effect of loading history – specimens L0C and L0M.....	104
4.3.4	Load-displacement response and failure .....	116
4.3.5	Shear Strengths .....	123
4.4	SPECIMENS MB AND SB.....	127
4.5	SUMMARY OF EXPERIMENTAL RESULTS .....	139
5.	IMPROVED STRUT-AND-TIE MODEL FOR DEEP BEAMS WITHOUT WEB REINFORCEMENT.....	141
5.1	FORMULATION AND SOLUTION PROCEDURE .....	141
5.2	COMPARISON WITH EXPERIMENTS.....	148
5.2.1	Specimens S0M/C and L0M/C.....	148
5.2.2	Shear database.....	156
5.3	DEFORMATIONS.....	158
6.	COMPARISON BETWEEN EXPERIMENTAL RESULTS AND VecTor2 ANALYSES .	161
6.1	INTRODUCTION.....	161
6.2	MODELING.....	162
6.3	RESULTS .....	165
7.	SUMMARY AND CONCLUSIONS.....	179
	REFERENCES.....	185
	Appendix A: Concrete Tests	
	Appendix B: Experimental Data	

Appendix C: Calculation of Angle  $\theta$

Appendix D: Verification of the Improved Strut-and-Tie Model

Appendix E: VecTor2 Input Files

## LIST OF FIGURES

Figure 1.1 Transfer girder in a 15-storey building.....	1
Figure 1.2 Cap beam in the substructure of a bridge.....	2
Figure 1.3 Examples for D- regions (adapted from Schlaich, Schäfer, and Jennewein, 1987) .....	3
Figure 1.4 Effect of beam slenderness on the shear strength – tests results of Kani (1979) (adapted from Collins and Mitchell, 1991).....	5
Figure 1.5 Beam action and arch action in beams without web reinforcement.....	5
Figure 1.6 Prediction-to-experiment ratios for members without web reinforcement acc. to ACI 318-08, EN 1992-1-1:2004 (EC2), CSA A23.3-04, and BS8110 (Collins, Mitchell, and Bentz, 2008).....	6
Figure 1.7 Load-bearing mechanisms of deep beams, coupling beams, squat shear walls, frame joints.....	7
Figure 2.1 Results from tests of Leonhardt and Walther (1961).....	12
Figure 2.2 Scatter of strength in tests of Leonhardt and Walther (1961).....	13
Figure 2.3 Kani’s “valley of diagonal failure”.....	15
Figure 2.4 Failure of beams tested by Duncan Lee (1982).....	16
Figure 2.5 Scatter of strength in tests of Rogowsky, MacGregor, and Ong (1986a).....	18
Figure 2.6 Results from tests of Yang et al. (2003) .....	19
Figure 2.7 Crack patterns under $V/bdf_c'=0.1$ – tests of Zhang and Tan (2007).....	20
Figure 2.8 Results from the shear database by Collins, Bentz, and Sherwood (2008).....	21
Figure 2.9 Load-rotation relationship for beams with $a/h=1.29$ tested by Paulay (1971a) .....	23

---

Figure 2.10 Load-displacement response of shear walls tested by Lefas, Kotsovos, and Ambraseys (1990).....	24
Figure 2.11 Failure of beams tested by Alcocer and Uribe (2008).....	26
Figure 2.12 Hysteretic response of beams tested by Alcocer and Uribe (2008).....	26
Figure 2.13 Models for shear strength of B- regions .....	27
Figure 2.14 Models for strength of D- regions .....	28
Figure 2.15 Strut-and-tie model of deep beams using the CSA code .....	31
Figure 2.16 Crushing strength of compressive strut versus orientation of tension tie passing through strut (Collins and Mitchell, 1986) .....	33
Figure 2.17 Splitting of bottle-shaped struts acc. to ACI 318-08.....	36
Figure 3.1 Loading and support conditions .....	40
Figure 3.2 Specimens S0M/C, S1M/C, L0M/C, and L1M/C- dimensions and reinforcement.....	42
Figure 3.3 Specimens SB and MB- dimensions and reinforcement.....	43
Figure 3.5 Construction process.....	44
Figure 3.6 Cylinder compressive test – specimens SB and MB.....	45
Figure 3.7 Concrete in compression – specimens SB and MB.....	46
Figure 3.8 Modulus of rupture test – specimens SB and MB.....	46
Figure 3.9 Tensile coupon test - #3 bars .....	47
Figure 3.10 Test setup for cyclic tests – scale drawing .....	49
Figure 3.11 Test setup for cyclic tests – general view .....	50
Figure 3.12 Test setup for specimen SB and MB.....	51
Figure 3.13 Zürich targets on the south face .....	53
Figure 3.14 LVDI's on the north face .....	54
Figure 3.15 Strain gauges.....	55

Figure 3.16 Loading histories .....	57
Figure 4.1 Load – displacement response - specimen L0M.....	62
Figure 4.2 Cracks and deformed shapes - specimen L0M .....	63
Figure 4.3 Crushing of concrete near loading plate – specimen L0M .....	67
Figure 4.4 Kinematic model.....	70
Figure 4.5 Displacements – west side of specimen L0M, Load Stage 7 .....	73
Figure 4.6 Flexural strains – specimen L0M .....	74
Figure 4.7 Bottom-chord strains – specimen L0M.....	75
Figure 4.8 Top-chord strains – specimen L0M.....	76
Figure 4.9 Strains in the web at mid shear span – specimen L0M.....	78
Figure 4.10 Linearly-varying versus real web displacements – west side of specimen L0M at Load Stage 7.....	80
Figure 4.11 Diagonal web strains – specimen L0M at Load Stage 7 .....	81
Figure 4.12 Local web strains – specimen L0M at Load Stage 7 .....	82
Figure 4.13 Transverse web strains – specimen L0M.....	83
Figure 4.14 Support zone strains – specimen L0M.....	84
Figure 4.15 Experimental Strength vs. CSA code prediction– specimen L0M .....	87
Figure 4.16 Load – displacement response - specimens L1M and L0M.....	88
Figure 4.17 Cracks – specimens L1M and L0M.....	89
Figure 4.18 Distribution of internal forces – specimens L1M and L0M at failure.....	91
Figure 4.19 Flexural strains – specimens L1M and L0M .....	92
Figure 4.20 Longitudinal reinforcement strains – specimens L1M and L0M.....	92
Figure 4.21 Transverse strains – specimens L1M and L0M.....	93
Figure 4.22 Load – displacement response - specimens S0M and L0M.....	96

---

Figure 4.23 Cracks – specimens S0M and L0M.....	97
Figure 4.24 Critical loading zones at failure– specimens S0M and L0M.....	98
Figure 4.25 Effect of beam slenderness on the crack pattern.....	99
Figure 4.26 Crack roughness– specimens S0M and L0M.....	99
Figure 4.27 Deformed shapes – specimens S0M and L0M.....	100
Figure 4.28 Flexural strains– specimens S0M and L0M.....	101
Figure 4.29 Longitudinal reinforcement strains – specimens S0M and L0M.....	102
Figure 4.30 Transverse web strains– specimens S0M and L0M.....	103
Figure 4.31 Support zone strains– specimens S0M and L0M.....	103
Figure 4.32 Load – displacement response- specimens L0C and L0M.....	104
Figure 4.33 Cracks – specimens L0C and L0M.....	106
Figure 4.34 Specimens L0M and L0C after failure.....	108
Figure 4.35 Idealized hysteretic behaviour – specimen L0C.....	110
Figure 4.36 Envelope curves - specimens L0C and L0M.....	111
Figure 4.37 Critical loading zones at failure– specimens L0C and L0M.....	111
Figure 4.38 Deformed shapes – specimens L0C and L0M.....	113
Figure 4.39 Bottom flexural strains – specimens L0C and L0M.....	113
Figure 4.40 Bottom reinforcement strains – specimens L0C and L0M.....	114
Figure 4.41 Strains in the web at mid shear span – specimens L0C and L0M.....	115
Figure 4.42 Support zone strains – specimens L0C and L0M.....	116
Figure 4.43 Full load-displacement response – specimens S0M and S0C.....	117
Figure 4.44 Full load-displacement response – specimens S1M and S1C.....	117
Figure 4.45 Full load-displacement response – specimens L0M and L0C.....	118

---

Figure 4.46 Full load-displacement response – specimens L1M and L1C.....	118
Figure 4.47 Envelope curves – specimens S0M/C, S1M/C, L0M/C, L1M/C.....	120
Figure 4.48 Specimens S0M/C, S1M/C, L0M/C, and L1M/C after failure.....	121
Figure 4.49 Critical loading zones after failure – specimens S0M (on the left) and S0C (on the right).....	123
Figure 4.50 Experimental shear strength vs. CSA code prediction – specimens S0M/C, S1M/C, L0M/C, and L1M/C.....	125
Figure 4.51 Experimental shear strength vs. ACI and EC2 code predictions – specimens S0M/C, S1M/C, L0M/C, and L1M/C.....	126
Figure 4.52 Load – displacement response- specimens MB and SB.....	127
Figure 4.53 Cracks – specimens MB and SB.....	129
Figure 4.53 - cont.....	130
Figure 4.54 Failure – specimens MB and SB.....	131
Figure 4.55 Deformed shapes – specimens MB and SB.....	134
Figure 4.56 Flexural strains – specimens MB and SB.....	134
Figure 4.57 Bottom-chord strains – specimen SB.....	135
Figure 4.58 Damage around anchor heads – specimen SB.....	136
Figure 4.59 Head bearing and bond – specimen SB.....	137
Figure 5.1 Specimen L0M and improved strut-and-tie model.....	142
Figure 5.2 Panel tests (Vecchio and Collins, 1986).....	143
Figure 5.3 Behaviour of CTT node region– specimen L0M.....	146
Figure 5.4 Experimental shear strength, CSA model, and Improved strut-and-tie model – specimens S0M/C and L0M/C.....	152
Figure 5.5 Failure of specimen 01T0 tested by Higgins et al. (2004).....	152
Figure 5.6 Effect of residual beam action on the shear strength – specimens S0M/C and L0M/C.....	154

---

Figure 5.7 Chord strains acc. to the ISTM – comparison with specimens S0M and L0M.....	155
Figure 5.8 Crack widths acc. to the ISTM – comparison with specimens S0M and L0M .....	155
Figure 5.9 Shear strains acc. to the ISTM – comparison with specimens S0M and L0M.....	156
Figure 5.10 Experiment-to-prediction ratios – shear database - 534 test results.....	158
Figure 5.11 Predicted residual beam action and its effect on the shear strength – shear database	158
Figure 5.12 Improved strut-and-tie model and kinematic model .....	159
Figure 5.13 Ultimate displacement according to the improved STM used together with the kinematic model – comparison with specimens S0M/C and L0M/C .....	160
Figure 6.1 Finite element models - mesh and support conditions.....	164
Figure 6.2 Finite element models – loading conditions .....	165
Figure 6.3 Experimentally-obtained load-displacement response vs. predictions from monotonic VecTor2 analysis– specimens S0M/C, S1M/C, L0M/C, and L1M/C .....	166
Figure 6.4 Crack patterns from VecTor2 analysis – specimens S0M/C, S1M/C, L0M/C, and L1M/C .....	170
Figure 6.5 Deformed shapes from VecTor2 analysis – specimens S0M/C, S1M/C, L0M/C, and L1M/C .....	172
Figure 6.6 Failure modes predicted by VecTor2.....	174
Figure 6.7 Experimentally-obtained load-displacement response vs. VecTor2 predictions – specimens S0M and S0C.....	175
Figure 6.8 Experimentally-obtained load-displacement response vs. VecTor2 predictions – specimens S1M and S1C.....	175
Figure 6.9 Experimentally-obtained load-displacement response vs. VecTor2 predictions – specimens L0M and L0C .....	176
Figure 6.10 Experimentally-obtained load-displacement response vs. VecTor2 predictions – specimens L1M and L1C .....	176
Figure 7.1 Improved strut-and-tie model and kinematic model.....	183

---



## LIST OF TABLES

Table 2.1 Limits on stresses in node regions and struts - ACI 318-08, EN 1992-1-1:2004 (EC2), CSA A23.3-04.....	35
Table 3.1 Tests summary.....	39
Table 3.2 Concrete tests results.....	47
Table 4.1 Web strains and kinematic model – specimen L0M.....	79
Table 4.2 Experimental shear strength vs. CSA code prediction – specimens S0M/C, S1M/C, L0M/C, and L1M/C.....	124
Table 4.3 Experimental shear strength vs. CSA, ACI and EC2 code predictions – specimens S0M/C, S1M/C, L0M/C, and L1M/C.....	125
Table 4.4 Summary of experimental results and CSA code predictions .....	140
Table 5.1 Comparison between the CTT and CCT node regions .....	146
Table 5.2 Predictions of the CSA code supplemented by the ISTM vs. predictions of the CSA code alone – specimens S0M/C, S1M/C, L0M/C, L1M/C, SB, and MB.....	153



## LIST OF SYMBOLS

$A_s$	= Area of longitudinal reinforcement on the flexural tension side of the section
$A_A$	= Area of a leg of a stirrup
$A_{si}$	= Total area of surface reinforcement at spacing $s_i$ in the $i$ -th layer of reinforcement crossing the strut at an angle $\alpha_i$ to the axis of the strut
$C$	= Flexural compressive force at the mid-span section
$COV$	= Coefficient of variation
$D$	= Force in support strut
$D_u$	= Strength of support strut
$E_s$	= Modulus of elasticity of the steel
$F$	= Applied concentrated load
$dF$	= Load increment
$F_{BL}$	= Bottom applied load
$F_{LC}$	= Total tensile force in the four load cells from the test setup
$F_{TL}$	= Top applied load
$F_{TL,u,exp}$	= Experimentally-obtained ultimate top load
$F_u$	= Ultimate applied load
$F_v$	= Force in the vertical ties which model the stirrups
$G$	= Weight of the specimen
$H$	= Depth of “no-bending” beam within the shear span
$H_w$	= Shear wall height
$M$	= Mid-span bending moment
$M_{\beta}$	= Flexural strength of the section

$M_u$	= Mid-span bending moment at ultimate load
$R_{roller}$	= Reaction force in each of the two bottom rollers from the test setup
$T$	= Tensile force in the bottom chord of beams or in the bottom tie of a strut-and-tie model near the supports
$T_b$	= Bond force
$T_f$	= Flexural tensile force
$T_{hb}$	= Force acting upon the anchor heads (head bearing)
$V$	= Shear force
$V_a$	= Vertical component of the force acting in the top strut of the arch mechanism of the ISTM
$V_b$	= Vertical component of the force acting in the strut of the beam mechanism of the ISTM
$V_c$	= Concrete contribution term in the ACI expression for shear strength
$V_s$	= Term in the ACI expressions for shear strength accounting for the contribution of transverse reinforcement
$V_u$	= Ultimate shear force
$V_{u,CSA}$	= Shear-strength prediction according to the CSA code
$V_{u,exp}$	= Experimentally-obtained ultimate shear
$V_{u,ISTM}$	= Shear-strength prediction of the ISTM used in combination with the sectional model of the CSA code
$V_{u,pred}$	= Predicted ultimate shear
$V_{u,STM}$	= Shear-strength prediction based on the strut-and-tie model of the CSA code
$a$	= Shear span
$a_d$	= Clear shear span
$a_g$	= Maximum aggregate size
$b$	= Width of rectangular cross section
$b_w$	= Width of the web
$d$	= Effective depth of the cross section
$d_a$	= Depth of the TTC node region of the ISTM

$d_b$	= Bar diameter
$d_r$	= Effective shear depth
$f_c'$	= Concrete cylinder strength
$f_{ct}$	= Average principal tensile stress in cracked concrete
$f_{\sigma}$	= Effective concrete strength in models of the Theory of Plasticity
$f_{ck}$	= Characteristic concrete cylinder strength according to EC2
$f_{2max} \equiv f_{cu}$	= Ultimate stress in struts
$f_y$	= Yield strength of flexural reinforcement
$f_t$	= Concrete tensile strength
$f_{ty}$	= Yield strength of transverse reinforcement
$f_{\tau}$	= Vertical stress in the TTC node region of the ISTM
$f_{c2}$	= Average principal compressive stress in cracked concrete
$h$	= Depth of the cross section
$h_a$	= Two times the distance from the axis of the bottom reinforcement to the bottom edge of the cross section
$k_n$	= Secant stiffness under negative load
$k_p$	= Secant stiffness under positive load
$l$	= Span length
$l_b$	= Length of the horizontal projection of the TTC node region of the ISTM
$l_{b1}$	= One-half the width of the loading element
$l_{b2}$	= Support width
$l_w$	= Depth of the cross section of shear walls
$s_i$	= Distance between the bars of the $i$ -th layer of surface reinforcement
$s_{max}$	= Average spacing of cracks perpendicular to the flexural reinforcement
$s_{m\tau}$	= Average spacing of cracks parallel to the flexural reinforcement
$u$	= Horizontal displacement
$u_{bot}$	= Horizontal displacements along the bottom chord

---

$u_{top}$	= Horizontal displacements along the top chord
$v$	= Vertical displacement
$v_b$	= Average shear stress acting on vertical and horizontal planes in the TTC node region of the ISTM
$v_{bot}$	= Vertical displacements along the bottom chord
$v_i$	= Shear stress acting on crack faces
$v_{i,u}$	= Shear capacity of crack faces
$v_{top}$	= Vertical displacements along the top chord
$w$	= Crack width
$w_b$	= Width of the support strut
$x$	= Horizontal coordinate or one-half the width of the top node region
$x_d$	= One-half the width of the top node region corresponding to strut crushing
$x_b$	= One-half the width of the top node region corresponding to limit on the horizontal principal stress in the support node region
$x_u$	= One-half the width of the top node region corresponding to ultimate load on the strut-and-tie model
$x_v$	= One-half the width of the top node region corresponding to limit on the vertical principal stress in the support node region
$x_y$	= One-half the width of the top node region corresponding to tie yielding
$\xi$	= Vertical coordinate
$y$	= One-half the depth of the top node region
$y_b$	= One-half the depth of the top node region corresponding to limit on the horizontal principal stress in the support node region of deep beam without stirrups
$y_b'$	= One-half the depth of the top node region corresponding to limit on the horizontal principal stress in the support node region of deep beam with stirrups
$y_y$	= One-half the depth of the top node region corresponding to tie yielding
$\Delta$	= Vertical mid-span displacement
$d\Delta$	= Displacement increment
$\Delta_c$	= Mid-span displacement associated with deformations in the critical loading zone
$\Delta_{c,u}$	= Ultimate mid-span displacement associated with deformations in the critical

---

	loading zone
$\Delta_l$	= Mid-span displacement associated with elongation of the bottom longitudinal reinforcement
$\Delta_u$	= Mid-span displacement at ultimate load
$\Delta_{u,exp}$	= Experimentally-obtained mid-span displacement at ultimate load
$\Delta_{u,prd}$	= Predicted mid-span displacement at ultimate load
$\alpha_i$	= Angle between the bars of the $i$ -th layer of surface reinforcement and the direction of the strut
$\delta_G$	= Mid-span displacement of the uncracked specimens under self-weight
$\epsilon$	= Strain
$\epsilon_l$	= Average strain in the bottom longitudinal reinforcement over the shear span
$\epsilon_1$	= Average principal tensile strain at the bottom end of the support struts or in the web of the test specimens
$\epsilon_2$	= Average principal compressive strain in the web of the test specimens
$\epsilon_{135}$	= Average strain along the LVDTs installed in the middle of the shear spans and “fanning” away from the bottom loading point
$\epsilon_{45}$	= Average strain along the LVDTs installed in the middle of the shear spans and “fanning” away from the top loading point
$\epsilon_{90}$	= Average strain along the vertical LVDTs installed in the middle of the shear spans
$\epsilon_{9-56}$	= Average strain between Zürich targets 9 and 56
$\epsilon_{t1}$	= Average principal tensile strain in cracked concrete
$\epsilon_{c2}$	= Average principal compressive strain in cracked concrete
$\epsilon_f$	= Average flexural strain in the bottom reinforcement
$\epsilon_s$	= Average strain in the bottom reinforcement near the supports
$\epsilon_{s,u}$	= Ultimate average strain in the bottom longitudinal reinforcement over the shear span
$\epsilon_v$	= Average transverse strain over the effective shear depth
$\epsilon_x$	= Average horizontal strain in the TTC node region of the ISTM
$\epsilon_{x,cr}$	= Steel strain at the cracks located in the TTC node region of the ISTM
$\phi$	= Angle between the axis of the LVDT and the longitudinal axis of the specimens

- $\phi_2$  = Angle between the direction of the principal compressive strains in the web and the longitudinal axis of the specimens
- $\gamma_{xz}$  = Average shear strain in the TTC node region of the ISTM
- $\varphi$  = Strength reduction factor
- $v_n$  = Efficiency factor for node regions
- $v_s$  = Efficiency factor for struts
- $\theta$  = Angle between the bottom tie and the strut which represents the residual beam action in the ISTM
- $\theta_k$  = Value of the angle  $\theta$  at which a distinct change in the response of the TTC node region takes place
- $\alpha_s \equiv \theta_s$  = Angle between the bottom tie and the support struts
- $\theta_{s1}$  = Angle between the bottom tie and the strut which represents the truss action in beams with stirrups
- $\rho_{eff}$  = Effective reinforcement ratio of the TTC node region of the ISTM
- $\rho_l$  = Ratio of flexural reinforcement
- $\rho_r$  = Ratio of transverse reinforcement



# 1.INTRODUCTION

## 1.1 GENERAL

Deep reinforced concrete beams are characterized by relatively small span-to-depth ratios. This results in stiff members with high shear capacity which makes them very effective in situations in which heavy loads need to be carried over a given span. Typical examples include transfer girders which carry the loading from multi-story columns in high rise buildings (see Figure 1.1) and cap beams which support bridge girders (see Figure 1.2). These common examples are demonstration that the safety of deep beams is often critical for the safety of the structure as a whole.



Figure 1.1 Transfer girder in a 15-storey building



Figure 1.2 Cap beam in the substructure of a bridge

## 1.2 B- AND D- REGIONS IN REINFORCED CONCRETE STRUCTURES

For the purpose of design, reinforced concrete structures can be viewed as consisting of B-regions (where B stands for beam, bending or Bernoulli) and D-regions (disturbed, discontinuity or detail) (Schlaich, Schäfer, and Jennewein, 1987). Beam regions are those parts of the structure in which the hypothesis of linear strain distribution (or plane sections remain plane) is assumed valid and in which the normal stresses perpendicular to the longitudinal axis of the member (clamping stresses) can be neglected. This type of strain and stress state occurs in particular zones of relatively slender beams, columns, shear walls, and slabs. The disturbed regions, on the other hand, are characterized by complex and irregular strain/stress distribution. They are located at the vicinity of abrupt changes of cross-sectional dimensions (geometric discontinuities) and near concentrated loads and reactions (statical discontinuities). Examples of D- regions are illustrated in Figure 1.3 with shaded areas. The position of the division lines between the B- and D- regions can be determined approximately through the principle of Saint-Venant which

states that discontinuities affect the strain pattern over a distance comparable with the dimensions of the cross section. Beams with overlapping disturbed regions (see the bottom sketch in Figure 1.3b) are defined as deep while those with relatively long beam regions (see the top sketch in Figure 1.3b) – as slender.

As a conservative design simplification, slender members are usually treated as B-regions over their entire clear length including the zones adjacent to applied loads and supports. This approach is adopted for the purpose of the following discussion.

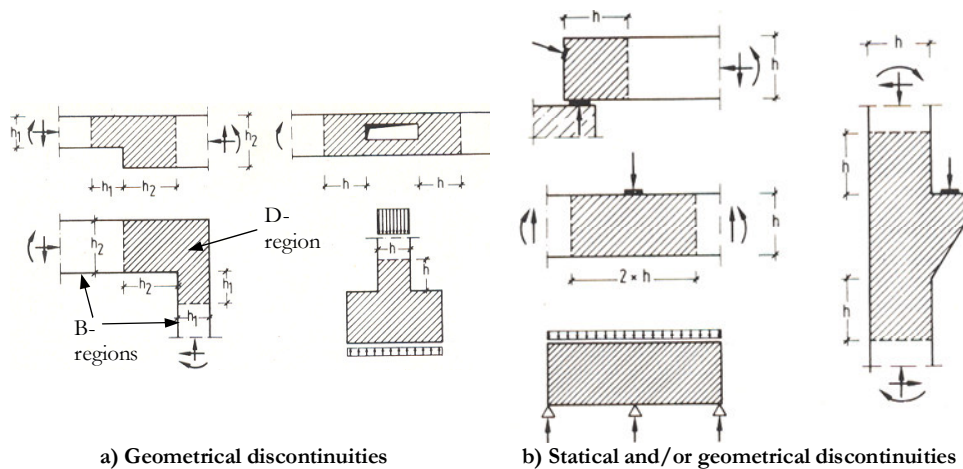


Figure 1.3 Examples for D-regions (adapted from Schlaich, Schäfer, and Jennewein, 1987)

B-regions can behave in a very ductile manner if controlled by yielding of the longitudinal reinforcement (flexural yielding). This is the preferred mode of failure since it allows for redistribution of forces in statically indeterminate systems and gives ample warning prior to collapse. Furthermore, a ductile response in flexure is the main goal of modern seismic design of reinforced concrete structures (Paulay and Priestley, 1992). Accurate prediction of the flexural response is a relatively simple task when the “plane sections remain plane” hypothesis is used together with proper constitutive relations for the concrete and the steel. Unlike flexural failures, diagonal tension and diagonal compression failures (shear failures) are relatively brittle and should be suppressed. However, the shear capacity of beam regions is influenced by a large number of variables (Leonhardt, 1970, suggested “more than twenty parameters”) which makes it very difficult to be predicted. One of these variables is the type of loading. There is experimental evidence that load reversals beyond flexural yielding may cause significant reduction in ductility by triggering premature shear failures. The most common approaches for predicting the shear strength of B-regions include empirical and semi-empirical solutions, lower- and upper-bound

solutions of the Theory of Plasticity, and compression-field models. All of them take advantage of the relatively smooth variation of strains in the web of slender elements by assuming uniform distribution of shear stresses over the depth of the cross section.

Many D-regions are inherently brittle and, in general, need to be designed to remain essentially elastic. Exceptions are, for example, squat walls and coupling beams which are often relied on for limited energy dissipation under strong earthquake excitations. Tests of some types of disturbed regions with reinforcement in two orthogonal directions have indicated that their load-bearing capacity is not significantly affected by load reversals (see for example Alcocer and Uribe, 2008). The tools for design of D-regions include strut-and-tie models, solutions of the Theory of Plasticity, and empirical expressions.

### 1.3 BEAM ACTION AND ARCH ACTION IN BEAMS WITHOUT WEB REINFORCEMENT

Figure 1.4 shows results from a series of tests of reinforced concrete beams without web reinforcement. The specimens had almost identical cross sections and material properties but different shear span  $a$ . The size of the loading and support plates was varied as well. On the abscissa of the graph is the shear-span-to-effective-depth ratio ( $a/d$  ratio) which can be seen as a measure of the slenderness of the zones subjected to shear. The ordinates of the experimental points represent the normalized ultimate shears. All beams failed prior to yielding of the bottom longitudinal reinforcement. Note that the shortest specimen in the series was about six times stronger than the longest. The plot illustrates that the shear strength of deep beams ( $a/d$  smaller than about 2) decreases rapidly with increasing slenderness while the strength of slender beams ( $a/d$  larger than about 2.5) changes relatively little. These two clearly different trends have been associated with two very different load-bearing mechanisms: arch action in deep beams and beam action in slender beams (Fenwick and Paulay, 1968).

As illustrated in Figure 1.5a), the beam action relies on diagonal tensile stresses in the web of the member. The tension in the cracked part of the beam is explained by the ability of the cracks to transfer shear through aggregate interlock. The stresses in the web reduce the tension force  $T$  in the bottom chord from its maximum value at mid-span to almost zero near the supports. The member fails when the interlocking of the cracks breaks down and catastrophic diagonal crack propagates towards the loading point. Deep beams are able to make transition from beam mechanism to arch mechanism which consists of direct compression between the loading and support points, and constant tension in the bottom chord (see Figure 1.5b). The combination of broken and solid lines, describing the flow of internal compressive and tensile forces, respectively, represents in fact a strut-and-tie model of the beam. Failure of the member occurs due to concrete crushing at either the loading or support region.

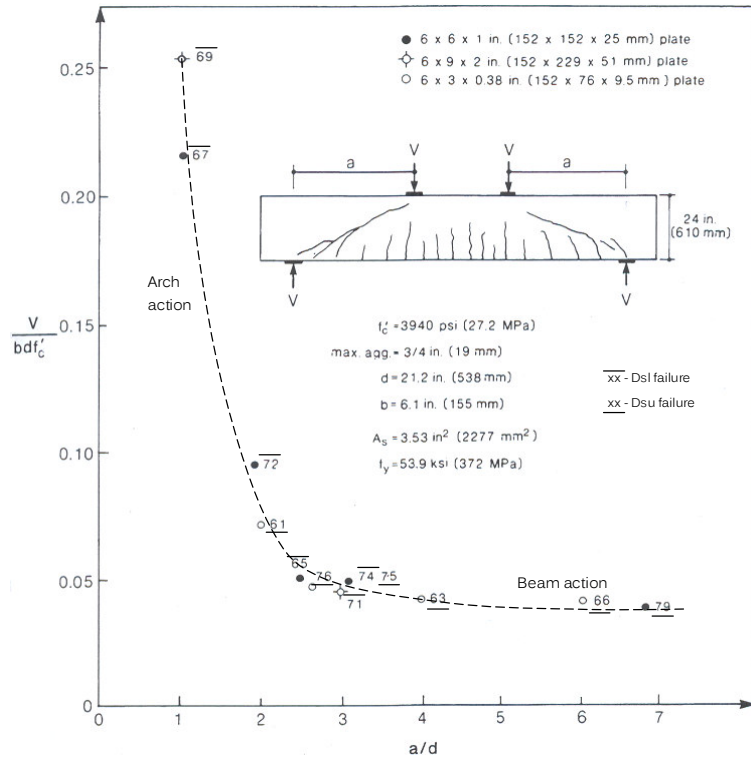
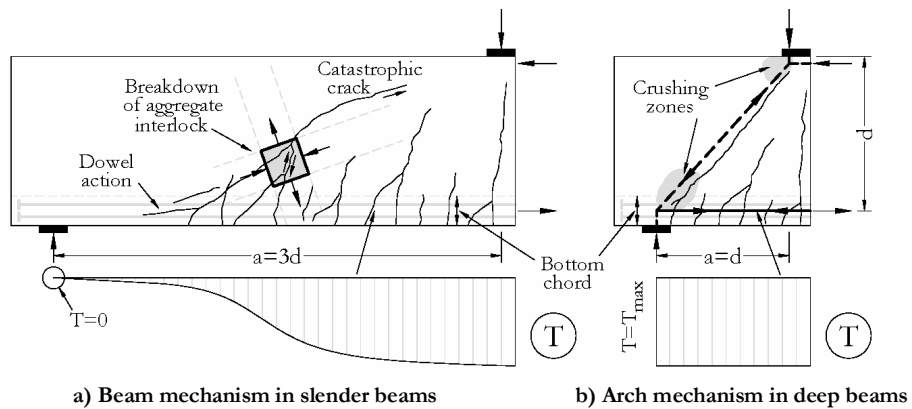


Figure 1.4 Effect of beam slenderness on the shear strength – tests results of Kani (1979) (adapted from Collins and Mitchell, 1991)



a) Beam mechanism in slender beams      b) Arch mechanism in deep beams

Figure 1.5 Beam action and arch action in beams without web reinforcement

#### 1.4 MOTIVATION FOR RESEARCH AND OBJECTIVES

Collins, Mitchell, and Bentz (2008) used a large collection of results from tests of members without web reinforcement to evaluate the overall accuracy of the Canadian (CSA A23.3-04), American (ACI 318-08), European (EN 1992-1-1:2004, EC2), and British (BS8110) code provisions for shear design. As shown in Figure 1.6, the calculated prediction-to-experiment ratios were plotted versus the  $a/d$  ratios of the specimens. It was concluded that the CSA code provides the least scattered predictions and the most uniform safety. In many cases the ACI and EC2 codes gave very unconservative estimates of the experimentally-obtained ultimate shears, while the BS8110 code was very conservative for members with  $a/d$  smaller than about 2.5.

In addition to the above conclusions, Figure 1.6 demonstrates that code procedures for members without web reinforcement are least accurate in the range of  $a/d$  from about 1.5 to about 3. This is the range of moderately-deep beams where the load-bearing capacity is controlled by either arch action or beam action. The CSA, ACI, and EC2 codes treat these two mechanisms with separate models. It is assumed that breakdown of beam action happens instantaneously and that the whole load associated with it is immediately “transferred” to the arch mechanism. Further load increase is possible only if the arch mechanism is stronger than the beam mechanism. In reality, the transition from beam action (zero tension in the reinforcement at the supports) to arch action (uniform tension in the reinforcement over the entire shear span) is likely to take place over a certain load increment during which failure may occur. Therefore, it is of great interest to study the mechanics of moderately-deep beams using proper large-scale tests and applying the knowledge about behaviour of deep and slender beams. Such an investigation may also assist for better understanding the sources of the significant scatter in shear strength observed between seemingly identical tests of members with small slenderness.

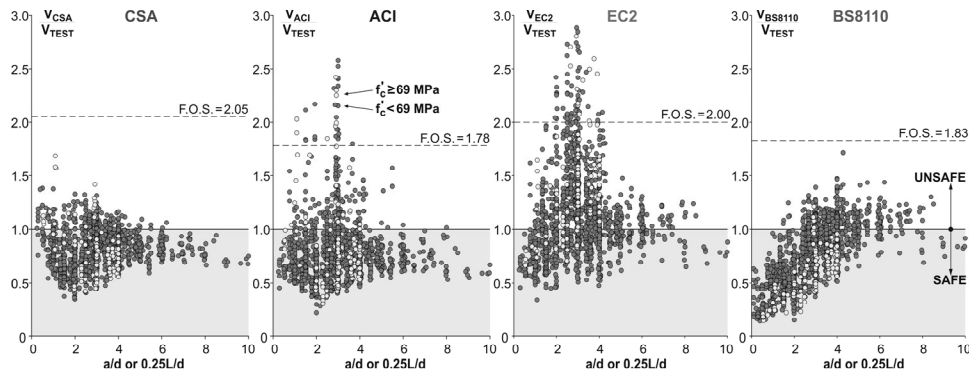


Figure 1.6 Prediction-to-experiment ratios for members without web reinforcement acc. to ACI 318-08, EN 1992-1-1:2004 (EC2), CSA A23.3-04, and BS8110 (Collins, Mitchell, and Bentz, 2008)

One further step is to examine how deep beams with no or small amounts of web reinforcement resist reversed cyclic load. This issue is relevant, for instance, to evaluation and retrofit of existing structures built in seismic zones according to traditional construction practices. Figure 1.7 demonstrates that the load-bearing mechanisms of deep beams, coupling beams, squat shear walls, and frame joints are very similar. In all these cases part of the shear is resisted through direct diagonal compression while the rest is carried by a truss mechanism involving tension in the transverse reinforcement. Codes for seismic assessment of buildings such as ATC-40, FEMA 356, and EC8 Part 3 (see also Mihaylov, 2006) prescribe reduced shear strength when the longitudinal reinforcement is expected to undergo inelastic cyclic deformations.

Lastly, it is well known that the strength of deep beams is strongly influenced by the detailing of their support zones. Of particular importance is the anchorage of the longitudinal bars because, as shown in Figure 1.5a), they work with high tension over the entire shear span. One possible solution, preferred mainly because of its compactness, is anchorage by anchor heads. Even though this approach has been studied by many researches (see for example Thompson et al., 2005, 2006), tests with large bars are relatively rare. This gives motivation for performing a test of a deep beam reinforced with a single headed bar #18 ( $d_b=57$  mm), which is the largest reinforcing bar according to the ASTM standard.

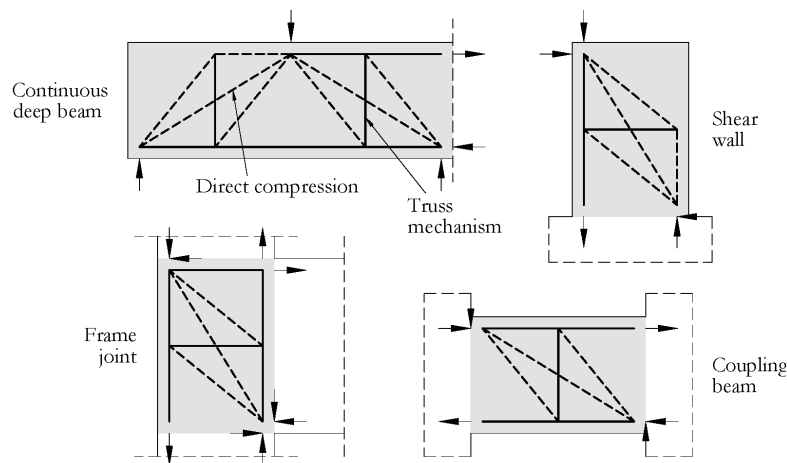


Figure 1.7 Load-bearing mechanisms of deep beams, coupling beams, squat shear walls, frame joints



## 1.5 THESIS OUTLINE

This thesis consists of 7 chapters and 5 appendixes.

Chapter 2 is a brief literature review which comprises tests and models relevant to the topic of this work. The selected experimental studies provide information on how parameters such as  $a/d$  ratio, amount of longitudinal and transverse reinforcement, concrete strength, member size, detailing, and type of loading history influence the response of deep beams, coupling beams, and shear walls. Included are important plots, interesting test observations, and conclusions made by the authors of the publications. The modelling part of the chapter discusses existing approaches for design of B- and D-regions with emphasis put on the current code procedures for disturbed regions.

Chapter 3 describes an experimental program which was planned and performed as part of this study. The program consists of ten monotonic and cyclic tests of deep beams. Additional experimental variables include the amount of transverse reinforcement and the detailing of the longitudinal reinforcement. Given in the chapter are the geometrical properties of the specimens, results from material tests, the test setup, instrumentation, and loading histories.

Chapter 4 presents the results from the experimental program together with a detailed discussion on the behaviour of the tested beams. A kinematic model is proposed and used for better interpretation of the various deformation measurements. The tests results are compared and the influence of the experimental variables is assessed. The shear strength of the specimens is compared to the predictions of the CSA, ACI, and EC2 codes.

Chapter 5 is devoted to the derivation of an improved strut-and-tie model for predicting the shear strength of non-slender beams without web reinforcement. The assumptions of the model are discussed in the context of experimental observations. The model is verified against a large number of experimental results from the literature. A combination of the improved strut-and-tie model and the kinematic model from Chapter 4 is presented as a tool for predicting the ultimate deformed shape of beams with small slenderness.

Chapter 6 contains comparisons between experimental results and VecTor2 analysis. In order to simulate a common situation from the engineering practice, it is assumed that the only information available prior to the analysis is geometry, boundary conditions, and basic material properties. The comparisons are done in terms of load-displacement response, deformed shapes, crack patterns, and failure modes.



Chapter 7 presents a summary and conclusions from this study as well as suggestions for further research.

Appendix A contains the full set of experimentally-obtained properties of the concrete used in the experimental program.

Appendix B contains detailed experimental data from the ten tests of large non-slender beams.

Appendix C presents the derivation of an analytical expression for the angle  $\theta$  which is an important parameter of the improved strut-and-tie model.

Appendix D contains results from the verification of the improved strut-and-tie model against data from 534 shear tests.

Finally, Appendix E shows VecTor2 input files used for the analyses of specimens S1C and L0M.



## 2. BACKGROUND

### 2.1 TESTS OF DEEP BEAMS, COUPLING BEAMS, AND SHEAR WALLS

Numerous test programs have been devoted to studying the behaviour of deep beams, coupling beams, and shear walls. For the sake of brevity, this section presents summaries of only 12 well-documented experimental studies which are considered particularly relevant to this work.

#### 2.1.1 Monotonic tests

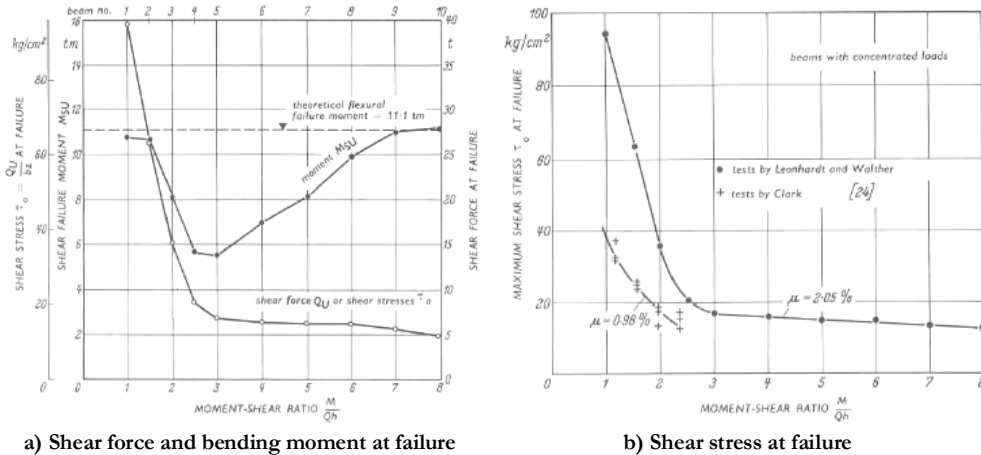
*Leonhardt and Walther (1961)* conducted an extensive experimental program to study the shear behaviour of beams and slab strips. In a systematic way they covered a large number of experimental variables such as shear-span-to-depth ratio, bond, beam depth, shear reinforcement, web width. Of particular interest for the current study are 14 beam tests devoted solely to the effect of the shear-span-to-depth ratio ( $a/d$  ratio). The beams were simply supported and subjected to two symmetric forces. The load-spreading plates were unsymmetric in order to ascertain if their length would have any effect on the global response. The cross section was rectangular with effective depth  $d=270$  mm. The  $a/d$  ratio was varied from 1 to 8 by changing the length of the shear span  $a$ . Beams with  $a/d \geq 6$  were duplicated while other were retested after strengthening the shear span which failed first. All the specimens were provided with longitudinal reinforcement with ratio of 2.07% ( $A_s/bd$ ) and had no web reinforcement. Normal-strength concrete was used.

It was reported that beams with shear-span-to-depth ratio between 1 and 6 failed in shear, while those between 7 and 8 – in flexure. More specifically, specimens with  $a/d=1-4$  exhibited gradual development of cracks until their compressive zone was destroyed. Interestingly, the crushing in the case of  $a/d=2-2.5$  took place between the applied forces. According to the authors, this failure mode should still be classified as related to shear because the depth of the crushed compression zone was determined by the diagonal cracks which propagated from the shear span, under the load-spreading plate, into the zone of pure flexure. The crushing did not take place under the loading plate because the concrete there was well confined by the pressure exerted by the load. Specimens with  $a/d=5-6$  failed suddenly and violently as a result of sudden occurrence of a flat shear crack. The flexural failures were characterized by crushing at the top of the mid-span section prior to yielding of the bottom reinforcement. No consistent effect of the

difference in length between the two load-spreading plates was detected in any of the tests.

Based on the test observations, Leonhardt and Walther concluded that the behaviour of the slender beams failing in shear was the most unfavorable because there was very little warning prior to failure. On the other hand, they stated that slender beams require smaller amounts of shear reinforcement to suppress shear failures than deep beams do.

Figure 2.1a) shows how the ultimate shear force and mid-span bending moment varied with increasing  $a/d$  ratio. Two ranges were distinguished: a range where there was considerable effect of the shear-span-to-depth ratio ( $a/d=1-3$ ) with shear capacity decreasing quickly with increasing beam slenderness; and a range where there was only a small effect of the shear-span-to-depth ratio ( $a/d=3-8$ ) with almost constant maximum shear provided that the reinforcement is sufficient to insure that flexural failure does not occur first. The authors stated that the strength increase for small values of the moment-shear ratio was definitely a result of “arch and tie-rod” or “truss” action. The smaller the  $a/d$  ratio is, the steeper the slope of the thrust resultants, the larger the load-bearing capacity. In addition to the results from the tests of Leonhardt and Walther, Figure 2.1b) contains data points from tests performed by Clark. The main difference between the two sets of tests was the amount of bottom reinforcement. As evident from the plot, the tests of Clark had less steel which led to smaller load-bearing capacity.



a) Shear force and bending moment at failure

b) Shear stress at failure

Figure 2.1 Results from tests of Leonhardt and Walther (1961)

Figure 2.2 shows the results from duplicated and retested specimens. It can be seen that on average the scatter of the load-bearing capacity increases with decreasing  $a/d$  ratio.

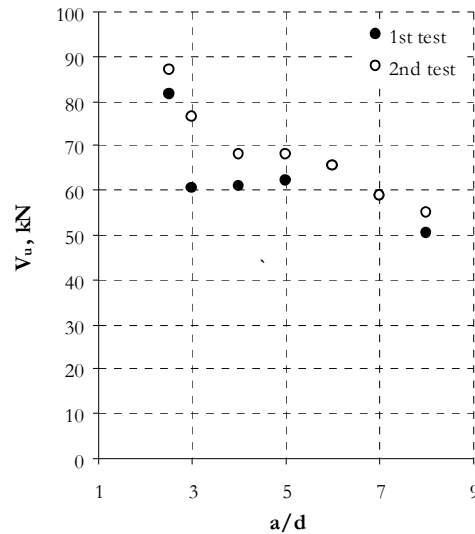


Figure 2.2 Scatter of strength in tests of Leonhardt and Walther (1961)

*ACI-ASCE Committee 326 "Shear and Diagonal Tension" (1962)* after 10 years of work presented a "... review of scientific knowledge, construction experiences regarding shear and diagonal tension in reinforced concrete beams, frames, slabs, and footings. Recommendations for new design procedures are substantiated by extensive tests data". The experimental database included results from a large number and variety of tests performed mostly during the 1950's. Some of the interesting findings and recommendations regarding deep beams are quoted below.

"In relatively short beams, diagonal tension cracking also forms as described above, but at a much slower rate. The propagation of the diagonal cracks is gradual as loading is continued, and one beam may sustain without collapse several cracks whose upper ends are only a few inches below the compression surface of the beam near the section of maximum moment. Barring yielding of the reinforcement, further loading of a beam in such a cracked condition is possible with little apparent extension of the cracks. Eventually, however, the concrete in the region at the end of the cracks or above them fails, and the beam collapses. Such failures are generally referred to as shear-compression failures."

"The ability of the beam to reach force equilibrium seems to depend primarily on the stability of the compression zone and may be influenced by several factors other than the

length of shear span and the percentage of reinforcement. Certainly the depth of the compression zone above the diagonal crack is important. Experimental data indicate that this depth can be affected by random variations in the location and path of the critical diagonal crack. The location of the point load application with respect to the location of the compression zone appears to be important. If the load is applied to the compression surface adjacent to the compression zone, the strength of the zone will be higher than if the load is applied beneath the compression surface as, for example, through secondary beams framing into sides of a girder.”

“Although most of the short specimens tested have failed in shear compression at loads as much as 100 percent greater than causing the critical diagonal tension crack, enough of them have failed in diagonal tension to indicate that detailed knowledge is lacking regarding the ability of a beam to reach force equilibrium after redistribution. Furthermore, little is known about the long-time behaviour of a diagonally cracked beam. Accordingly, the load causing formation of a critical diagonal tension crack must ordinarily be considered in design as the usable ultimate load-carrying capacity of a reinforced concrete member without web reinforcement.”

“... the web reinforcement contains the diagonal crack, thus preventing deep penetration of the diagonal crack into the compression zone. In general, the presence of web reinforcement assures a gradual development of shear-compression failure, usually following large increases in diagonal crack width as the web reinforcement reaches its yield.”

*Mario Kani, Huggins, and Wittkopp (1979)* published a summary of the most important theoretical and experimental work done by Prof. Gasper Kani on shear at the University of Toronto in the 1960's. Included were results from more than seven hundred tests devoted to a systematic examination of the influence of parameters such as concrete strength, amount of longitudinal reinforcement, shear-span-to-effective-depth ratio, member size, type of cross section, type and amount of web reinforcement, and bond on the shear behavior of reinforced concrete elements. The effect of the first three parameters was studied through a series of 133 simply supported beams subjected to two symmetric forces. The specimens had cross section of 152 mm x 305 mm and no web reinforcement. Three concrete strengths ( $f'_c = 17.2$  MPa, 26.2 MPa, and 34.5 MPa) and four reinforcement percentages ( $\rho = 0.80\%$ , 1.88%, and 2.80%) were considered. The shear-span-to-effective-depth ( $a/d$ ) ratio varied between 1 and 7. The reinforcing bars were anchored with external anchor plates. Some specimens were duplicated.

The failure modes were categorized as  $F$  (flexural),  $D_{su}$  (sudden diagonal failure immediately upon the development of diagonal crack), and  $D_{sl}$  (slow diagonal failure, where the ultimate capacity of the beam exceeded the diagonal cracking capacity of the

beam). The summarized test results show that the  $D_{su}$  and  $D_{sl}$  failures were typical for relatively long and relatively short specimens, respectively (see Figure 1.4). Kani preferred to present the results in terms of relative beam strength  $M_u/M_{fl}$ , where  $M_u$  is the ultimate mid-span bending moment at failure of the test beam and  $M_{fl}$  is the calculated pure flexural strength of the section. Thus a value of  $M_u/M_{fl}=70\%$ , for example, implies that the member failed in shear at 70% of flexural capacity. It was concluded that the shear strength expressed this way was rather insensitive to the concrete strength and hence the final results were plotted without recognition of the  $f'_c$  values (see Figure 2.3). The relative strength was however considerably influenced by the  $\rho_l$  and  $a/d$  ratios.

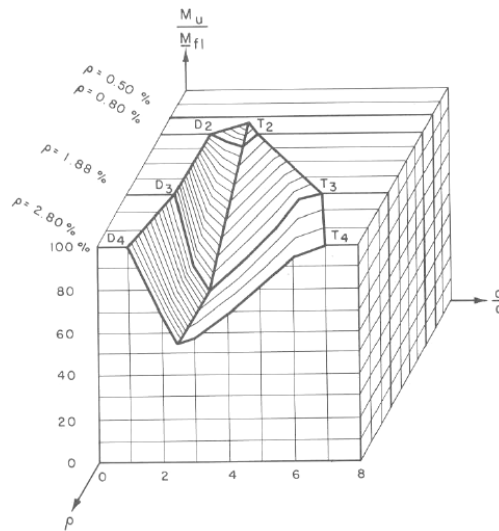
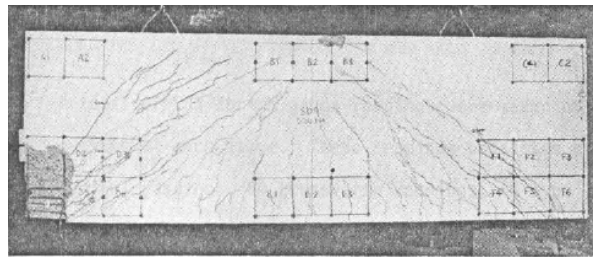


Figure 2.3 Kani's "valley of diagonal failure"

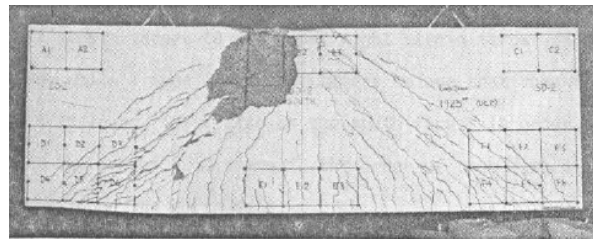
*Duncan Lee (1982)* tested 4 normal-strength concrete deep beams under three-point bending at the University of Toronto. The only experimental variable was the depth of distribution of the main longitudinal reinforcement with values ranging from  $0.16b$  to  $0.31b$ . As the depth over which the main longitudinal steel was distributed increased, the effective depth,  $d$ , decreased. The specimens were all 1000 mm deep and had shear-span-to-effective-depth ratios between 1.56 and 1.78. The percentage of chord reinforcement and transverse web reinforcement was  $\sim 1\%$  and  $0.5\%$ , respectively. The stirrups had a yield strength of 529 MPa. The main longitudinal bars were developed just 200 mm beyond the inner edges of the support plates.

The specimen with shallowest depth of distribution failed with abrupt concrete crushing at one of the support zones while the rest of the beams exhibited gradual crushing at the

region adjacent to the loading plate (see Figure 2.4). Strain measurements at the bottom ends of the beams showed that the stirrups yielded. Despite the short development length, no anchorage failure was observed. The shear strength decreased with increasing depth of distribution of the main longitudinal reinforcement due to the reduction in the effective depth of the reinforcement.



a) Support-zone crushing



b) Loading-zone crushing

Figure 2.4 Failure of beams tested by Duncan Lee (1982)

*Rogovsky, MacGregor, and Ong (1986a)* reported tests of 7 simply supported and 17 two-span continuous deep beams subjected to concentrated loads at the middle of the clear spans. The specimens had varying shear-span-to-effective-depth ( $a/d$ ) ratios and different combinations of vertical and horizontal web reinforcement. The length of the outer shear span was fixed to 1000 mm. The most stout beam had  $a/d=1.05$  while for the most slender it was 2.82. The ratio of bottom longitudinal reinforcement was of the order of 1%. The bars were anchored with hooks. An exception was a simply supported beam which had straight bars extended 150 mm into the supporting columns. The simply supported beams had four arrangements of web reinforcement: no reinforcement; vertical reinforcement (stirrups) of 0.15%; horizontal reinforcement of 0.15%; and reinforcement of 0.15% in both directions. The stirrups had a yield strength of 570 MPa. The two shear spans were reinforced differently and after failure of one of them the failed span was repaired and the beam was then retested to fail the other shear span. The continuous beams had a large variety of symmetric reinforcement solutions as some of



the specimens had web reinforcement ratios as large as 0.6%. Normal-strength concrete was used.

It was found that beams with no stirrups or small amount of stirrups behaved very differently than those with a large amount of transverse reinforcement. In the former case arch action was well developed and the failure was sudden with little or no plastic deformation. In the later case the compression struts between the cracks tended to be less well defined and the beams failed in a ductile manner.

The paper contains detailed description of four of the tests. Of particular relevance for the current study is a test of a simply supported beam with  $a/d=1.05$  and minimum amount of stirrups in one of the shear spans. It was observed that major shear cracks developed almost instantaneously on both sides of the mid-span section at load levels much smaller than the load-bearing capacity. This resulted in full development of arch action associated with constant strains along the bottom reinforcement. Interestingly, the first failure took place on the side of the beam which contained stirrups. Explicit description of the failure mode was not given. Strain measurements at the critical shear crack showed that the stirrups had all yielded when maximum load was reached. The last yielded stirrup was the one closest to the loading column. The unreinforced shear span failed with strut crushing at the support zone.

The beam with poorly anchored longitudinal reinforcement failed with slip of the bars at one of the support zones. It was calculated that the bond stress along the development length reached 7.6 MPa. The authors explained this extremely high value as being due to the favorable effect of clamping stresses exerted by the support reaction. Another reason suggested was that the bars were anchored within the reinforcing cages of the supporting columns.

The shear strengths, expressed in terms of non-dimensional shear stress ( $V_u/bd\sqrt{f_c}$ ) at maximum load, were very variable but still showed some trends. Beams with no or minimum (0.15%) vertical web reinforcement exhibited decreasing strength with increasing shear-span-to-effective-depth ratio. In contrast, beams with maximum (0.6%) vertical web reinforcement had almost constant shear capacity. The addition of a minimum amount of stirrups resulted in only a small strength increase. Beams with the maximum amount of stirrups were much stronger than those without web reinforcement especially in the cases of large  $a/d$  ratios. The horizontal web reinforcement had very little effect on the strength.

Figure 2.5 shows results from the tests of continuous beams. A pair of data points with same abscissa and colour represents ultimate shears sustained by the two internal shear spans of a given specimen. The plot demonstrates that the scatter of load-bearing

capacity increases with decreasing  $a/d$  ratio and with decreasing percentage of transverse reinforcement. The maximum ratio of high to low failure load for the to shear spans of the same beam equals 1.66. This outcome can be partly attributed to the different distributions of internal forces in the original beam prior to failure of the first shear span and in the repaired beam prior to failure of the second shear span (Asin, 1999).

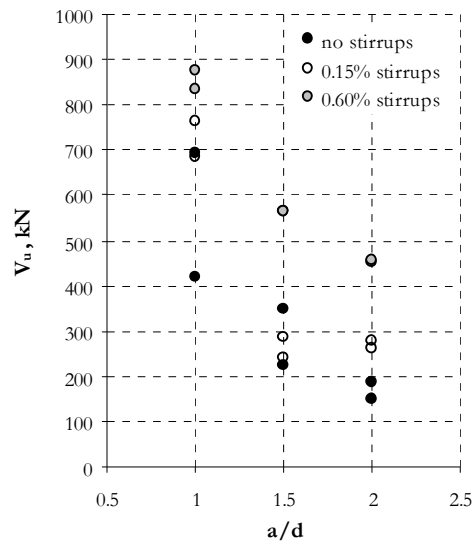


Figure 2.5 Scatter of strength in tests of Rogowsky, MacGregor, and Ong (1986a)

Lefas, Kotsivos, and Ambraseys (1990) reported 13 large scale tests of shear walls with rectangular cross section. The specimens were cast with large heavily reinforced concrete blocks at both ends. The bottom block was fixed to the strong floor while the top block functioned as an element through which axial and lateral loads were applied. The main experimental variables were the magnitude of vertical load (0%, 10%, or 20% of the axial strength of the concrete section), the clear-height-to-depth ratio ( $H_w/l_w=1$  or 2), and the percentage of horizontal web reinforcement ( $\rho_w=1.10\%$  or  $0.4\%$ ). Of interest for the current study are 3 tests of squat walls and 3 tests of slender walls subjected to lateral load only. The depth of the cross section of the specimens was 750 mm and 650 mm in the case of  $H_w/l_w=1$  and  $H_w/l_w=2$ , respectively. The area of the main flexural reinforcement represented about 3.2% of the gross concrete area of the edge elements. The horizontal bars had yield strength of 520 MPa. The vertical web reinforcement had a ratio of approximately 2.4%. Normal strength concrete was used.

All six walls failed with crushing of the concrete at the flexural-compression side of the base section. According to the authors, the resistance of the specimens was associated with development of triaxial compressive stress conditions in that region. The in-plane stresses were the result of shear and flexural compression, while the stirrups of the edge elements and the massive base block provided confinement stresses. Despite the significant differences in terms of horizontal web reinforcement ( $\rho_{v,max} : \rho_{v,min} = 2.75$ ) and in terms of concrete strength ( $f'_{c,max} : f'_{c,min} = 1.6$ ), the load-bearing capacity was affected primarily by the  $H_w/l_w$  ratio. The squat walls were about 2.2 times stronger than the slender ones.

Yang, Chung, Lee, and Eun (2003) published results from 21 tests of simply supported deep beams subjected to two symmetric concentrated loads. The experimental variables were the shear-span-to-total-depth ratio ( $a/b = 0.5$  or  $1$ ), the total depth of the cross section ( $b = 400$  mm –  $1000$  mm), and the compressive strength of the concrete ( $f'_c = 31.4$  MPa or  $78.5$  MPa). The specimens had a flexural reinforcement ratio of 1% and no web steel. The loading and support plates had widths of  $100$  mm.

It was reported that the propagation of flexure-shear cracks was sudden and accompanied by an increase in mid-span displacement. All beams failed in a brittle manner with crushing above the critical diagonal cracks near the loading plates. The brittleness of the specimens increased with decreasing  $a/b$  ratio and increasing depth of the section. Figure 2.6 shows the ultimate shear stress of the beams plotted as a function of  $b$ . Some of the data points represent the average shear strengths of identical specimens. It can be seen that increasing the strength of the concrete by a factor of 2.5 resulted in a significant increase in shear capacity. Even though the depth of the section was a primary experimental variable, the test results can not be used to draw firm conclusions on size effect since the size of the loading and support plates was not scaled with the depth of the beam.

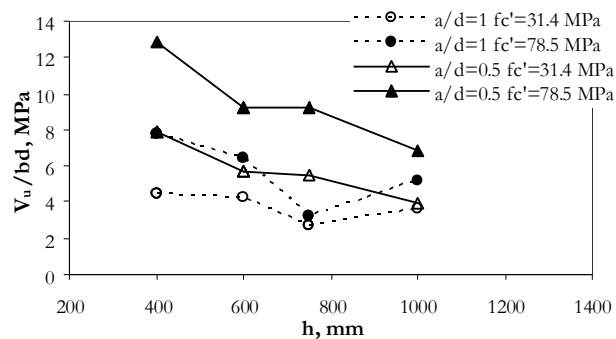


Figure 2.6 Results from tests of Yang et al. (2003)

Zhang and Tan (2007) reported 11 tests of simply supported deep beams subjected to two symmetric concentrated loads. The experimental variables were the size of the specimens, the slenderness of the cross section  $b/b$ , and the percentage of transverse reinforcement  $\rho_v$ . The beams were designed in three groups of four, as one of the tests was used for two of the groups. All groups consisted of specimens with variable size ( $b=350, 500, 700,$  or  $1000$  mm), constant in-plane geometrical proportions (including properly scaled width of the loading and support plates), and ratio of flexural reinforcement  $\rho_f=1.2\%$ . The shear-span-to-effective-depth ratio was equal to 1.1. The beams from Groups 1 and 3 had  $b/b$  ratio of 4.38 while those from Group 2 had cross-sectional width of 80 mm ( $b/b$  ratios varied from 4.38 to 12.5). Transverse reinforcement was provided only in the specimens from the first group. The stirrups had ratio of 0.4% and yield strength of about 420 MPa. Normal strength concrete was used.

All specimens failed with crushing at either the loading or support zones (shear-compression failure) well after development of the critical flexure-shear cracks. Figure 2.7 shows the state of cracking of the beams under normalized shear stress of 0.1. Based on these diagrams, the authors concluded that the size of the member had almost no effect on the rate of development of diagonal cracks (compare the crack patterns within each of the groups) and that the propagation of diagonal cracks was restrained by the stirrups (compare the crack patterns of Group 1 to those of Groups 2 and 3). It was shown that the normalized shear stress corresponding to maximum crack width of 0.3 mm decreased with increasing specimen size as this effect was less pronounced in the beams with transverse reinforcement. On the contrary, almost no size effect was observed in terms of shear stress at diagonal cracking and at failure. The stirrups enhanced the shear strength, while the aspect ratio of the cross section had almost no effect on the behaviour of the specimens.

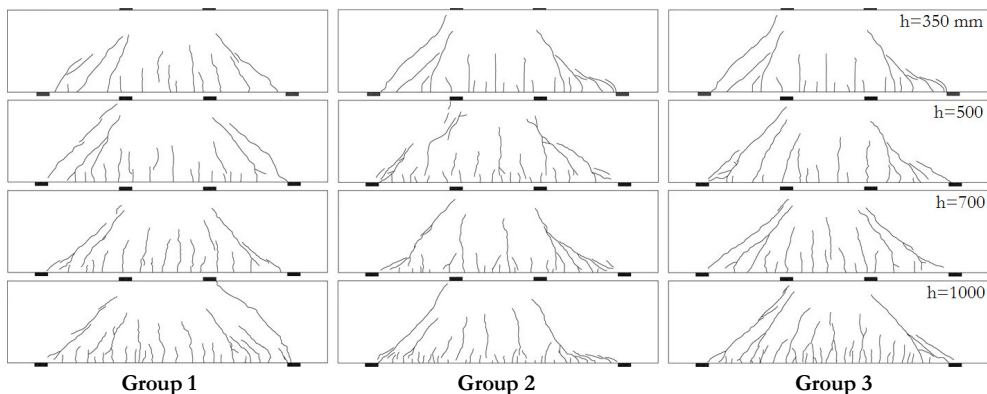


Figure 2.7 Crack patterns under  $V/bdf_c^0.1=0.1$  – tests of Zhang and Tan (2007)

Collins, Bentz, and Sherwood (2008) assembled a database of 1849 shear tests of reinforced concrete members without web reinforcement performed over the last 60 years and published predominantly by the American Concrete Institute. The following are some of the rules used for selecting members: no limits on concrete strength, rectangular or Tee beam sections, no axial load, no prestressing, point loads or uniform loads, simply supported or continuous, no geometrical limits on member size, no anchorage or bond failures. In total 1601 of the failures were classified as shear failures while the remaining 248 were determined to be flexural failures.

The authors divided the specimens failing in shear into two groups: slender ( $a/d \geq 2.5$ ) and short ( $a/d < 2.5$ ). Each of these groups was further subdivided into nine groups depending on the depth of the member  $d$  and on the values of the parameter  $(M/Vd+1)/\rho$ , where  $M/Vd$  is the moment-shear ratio for the critical section and  $\rho$  is the ratio of flexural reinforcement. This parameter represents a measure of the stress in the longitudinal steel at the critical section.

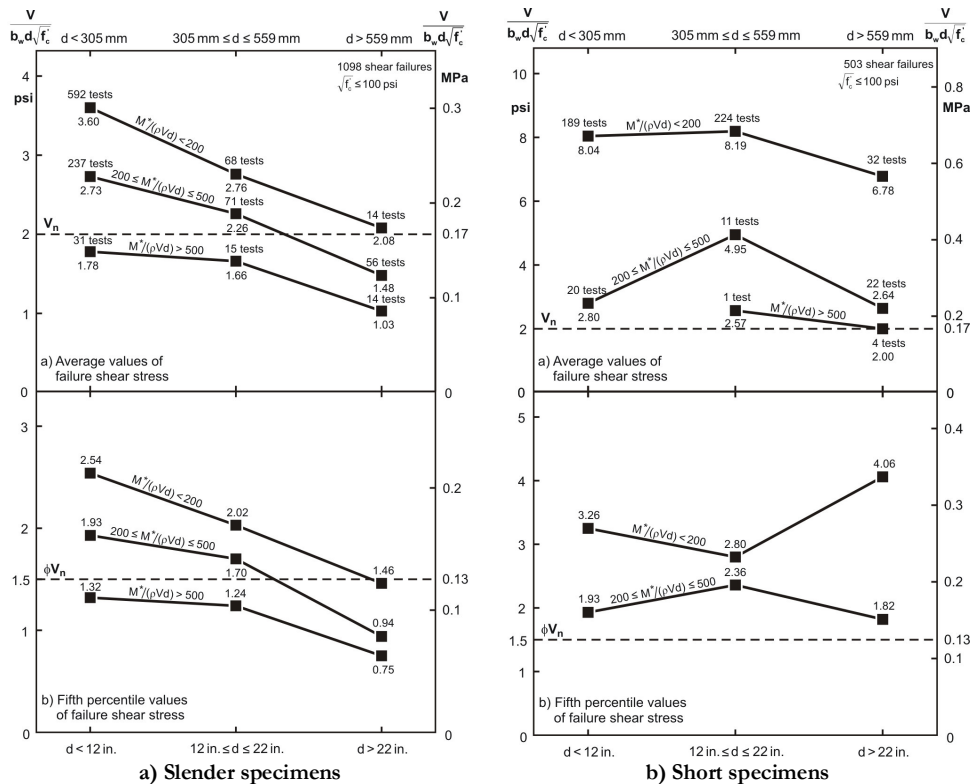


Figure 2.8 Results from the shear database by Collins, Bentz, and Sherwood (2008)

Figure 2.8 shows the results from the total of 18 groups of tests expressed in terms of  $\beta = V_u / b_w d \sqrt{f'_c}$ , where  $V_u$  is the ultimate shear at the critical section and  $b_w$  is the width of the web of the member. The plots for slender specimens reveal two clear patterns:  $\beta$  decreases with increasing member depth (size effect) and increasing stress in the steel (strain effect). The  $\beta$  values for short specimens are much higher and do not indicate the presence of a size effect.

### 2.1.2 Cyclic tests

*Panlay (1971a, 1971b)* published results from 9 tests of deep beams subjected to double curvature bending (spandrel/coupling beams) with equal end moments. The tests were part of the first large research program devoted to studying the non-linear behaviour of coupled shear walls exposed to seismic disturbances. The study was motivated in part by the severe damage which some structures of this type suffered during the 1964 Alaska earthquake. The load on the specimens was applied through large heavily-reinforced end concrete blocks. The main experimental variables were the clear-span-to-total-depth ratio ( $l/b=1.05$  or  $1.29$ ) and the percentage of transverse web reinforcement ( $\rho_t=0.88\%$  -  $2.52\%$ ). The longitudinal web reinforcement was varied slightly as well. The clear span was set to 1016 mm. The ratio of the symmetric flexural reinforcement was of the order of 1.3%. The yield strength of the stirrups varied slightly from beam to beam but the average value was about 340 MPa. Two specimens (one deep and one shallow) with  $\rho_t=0.88\%$  were tested under monotonic load while the rest of the beams – under fully reversed cyclic load simulating seismic action. Normal strength concrete was used.

It was found that at higher loads the longitudinal bars were subjected to tension over the entire span length even though the bending moment diagram changes its sign at the middle of the beams. Consecutive cycles with constant load amplitude caused a growth of strains with a diminishing rate. Yielding took place at the flexural tension side of the end sections of all beams. The load repetitions resulted in an accumulation of plastic deformations in these zones. The author analyzed the variation of tension along the flexural reinforcement by considering equilibrium along the relatively straight cracks radiating from the corners of the specimens. It was concluded that no matter how much transverse reinforcement is provided, the longitudinal bars would always be subjected to tension in the compression zone of a coupling beam with cracks along its diagonals.

Measurements along the transverse reinforcement showed that it was strained the most near the mid-span mid-depth of the specimens. These measurements were used together with experimentally-obtained stress-strain curves to obtain the magnitude of shear carried by stirrups (truss action) across the major diagonal cracks. The results showed that the transverse steel became active after diagonal cracking and its contribution to the shear resistance increased with increasing load. In specimens with “insufficient” web

reinforcement this trend was maintained up to yielding of the stirrups. Further loading was possible due to presence of arch action, dowel action, and aggregate interlock. In the cases of “sufficient” web reinforcement the stirrups remained elastic and eventually resisted the whole applied shear. It was shown that load-bearing mechanisms other than truss action gradually deteriorated under cyclic loading.

The failure modes were categorized as DT (diagonal tension) and SC (shear compression). Diagonal tension failures were characterized by yielding of the transverse reinforcement and separation along the major diagonal. Specimens that failed in this way exhibited low stiffness upon load reversal (pinching effect) and very little ductility (see Figure 2.9a)). Shear compression failures took place with yielding of the longitudinal reinforcement and destruction of the concrete at the end sections (see Figure 2.9b). The beams attained about 85% of the moment capacity derived from sectional analysis. Since the compression steel was in tension, all the flexural compression had to be carried by the concrete. The combination of flexural and shear compression brought about the failure of the critical section where significant sliding deformations took place. The ductility factor had values of the order of 3. According to the author, the contribution of the dowel forces across the flexural reinforcement was very small in comparison to the total shear capacity.

A comparison between the only two identical specimens ( $a/d=1.02$  and  $\rho_r=0.88\%$ ) showed that the beam tested monotonically was just 4% stronger than the one subjected to reversed cyclic load.

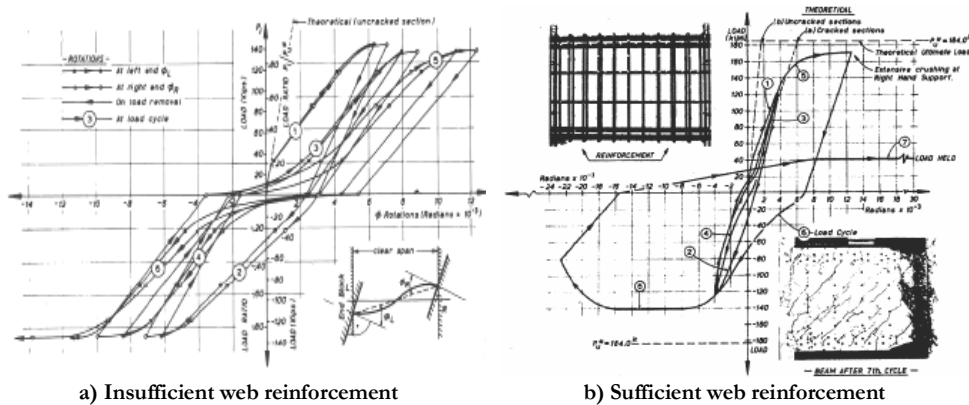


Figure 2.9 Load-rotation relationship for beams with  $a/h=1.29$  tested by Paulay (1971a)

Lefas, Kotsovos, and Ambraseys (1990) tested 4 identical shear walls under different loading histories. The specimens had the same geometry, main flexural reinforcement, and

boundary conditions as those of the slender walls tested by the authors in a companion study (see 2.1.1). The percentage of horizontal and vertical web reinforcement was 0.39% and 1.52%, respectively. The yield strength of the stirrups was 520 MPa. Normal strength concrete was used. One of the walls was subjected to monotonically increasing lateral load, while the other three were tested under different reversed cyclic loads named *A*, *B*, and *C* (see Figure 2.10). Loading history *A* consisted of several symmetric cycles at load level corresponding to yielding of the outer flexural bars, followed by monotonic push to failure. History *B* was similar to *A*, but the cycling was performed at higher load level. Loading type *C* represented a combination of types *A* and *B*. In addition, the push to failure was performed through several cycles of controlled lateral displacement.

All four walls failed with concrete crushing at the compression zone of the base section. The strength and deformational response of the specimens were found to be independent of the cyclic loading regime.

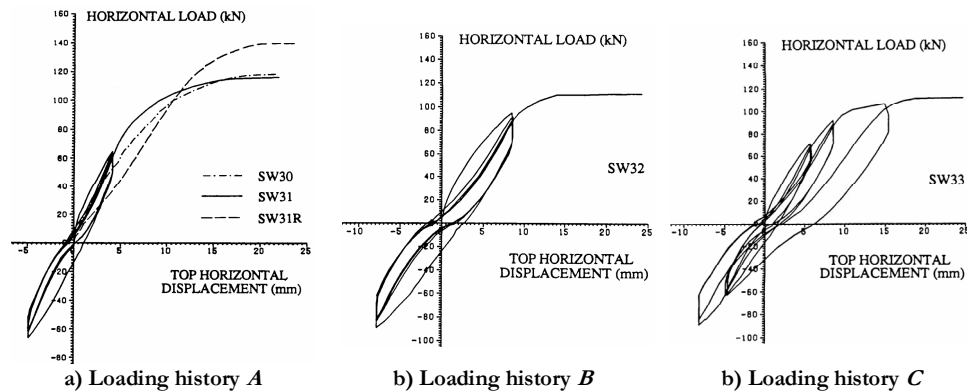


Figure 2.10 Load-displacement response of shear walls tested by Lefas, Kotsovos, and Ambraseys (1990)

*Alcoer and Uribe (2008)* compared two simply supported deep beams subjected to monotonic loading with two similar beams subjected to reversed cyclic loading (see Figure 2.11). All the specimens were made of normal-strength concrete. Besides the type of loading, the other two experimental variables were the development length of the bottom longitudinal reinforcement and the amount of stirrups in the zone of the supports. The specimens had total depth  $h=1200$  mm and shear-span-to-effective-depth ( $a/d$ ) ratio of 1.17. They were designed according to the 1996 FIP recommendations for the chosen positive and negative load. Part of the chord reinforcement was cut off in agreement with a strut-and-tie model involving a direct strut mechanism and truss mechanism. In order to suppress flexural failure, extra bars were provided at the region of pure bending. The anchor hooks at the ends of the beams were designed according to the



ACI 318-99 provisions. Two of the specimens (one tested monotonically and one cyclically) had insufficient bottom hooks (30% shorter than required by the code). The web reinforcement consisted of longitudinal bars and stirrups with ratio of 0.29% and 0.53%, respectively. The transverse reinforcement had yield strength of 429 MPa. The cyclic loading history was intended to represent seismic action and consisted of cycles of increasing imposed displacements. The negative load had amplitude of approximately one-half of the corresponding amplitude of the positive load.

The shape of the positive envelopes of the four “shear force vs. deflection” curves was very similar. The hysteresis loops from the cyclic tests showed considerable pinching and severe stiffness degradation (Figure 2.12). It was noticed that relative displacements along the major diagonal cracks activated dowel action of the longitudinal reinforcement near the support plates. The transverse reinforcement yielded almost over the entire shear spans while the longitudinal reinforcement yielded at the zones of bar cut off. According to the authors, the yielding of the longitudinal bars had a pronounced effect on the stiffness degradation. It was found that prior to failure the main resisting strut was reacting against the bottom longitudinal reinforcement in the zone of dowel action. The beams failed with crushing of the concrete in regions adjacent to the loading and support plates. The four specimens had almost identical strengths. The authors attributed the minor differences to variations in materials and dimensions as well as differences in loading conditions. The displacement ductility was of the order of 2.

The authors concluded that the load reversals had little effect on the behaviour of the beams. It was suggested that models for deep beams under monotonic loads can be used for seismic design/assessment if the shear demands do not exceed  $0.73\sqrt{f_c}$  and rotational demands are smaller than 2.3%. The rotations were computed by dividing the displacement at the loading point by the length of the shear span. It was found that the difference in development lengths and amount of stirrups above the supports did not affect the response of the specimens.

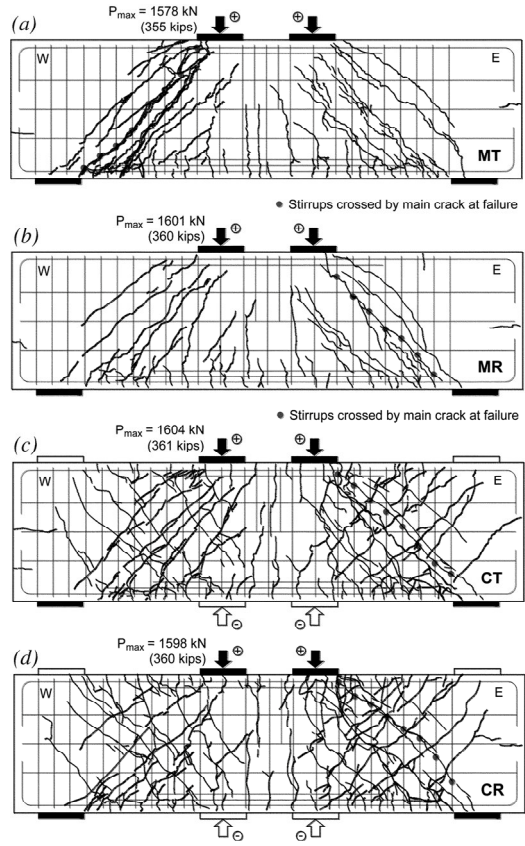


Figure 2.11 Failure of beams tested by Alcocer and Uribe (2008)

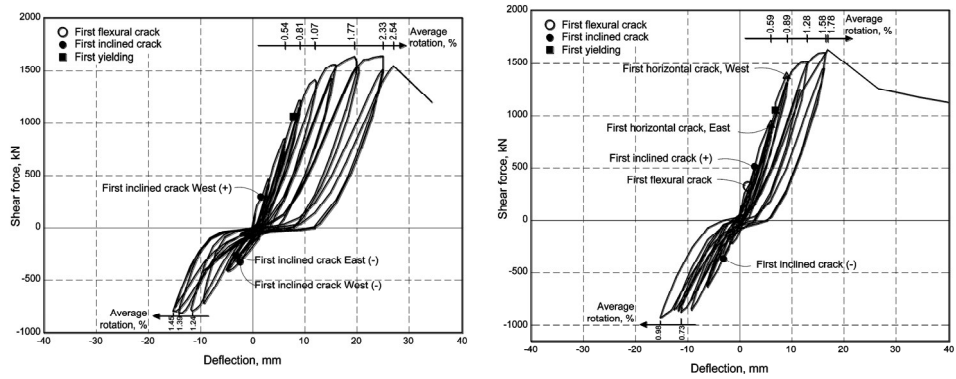


Figure 2.12 Hysteretic response of beams tested by Alcocer and Uribe (2008)

2.2 MODELS FOR SHEAR STRENGTH

2.2.1 Models for B-regions

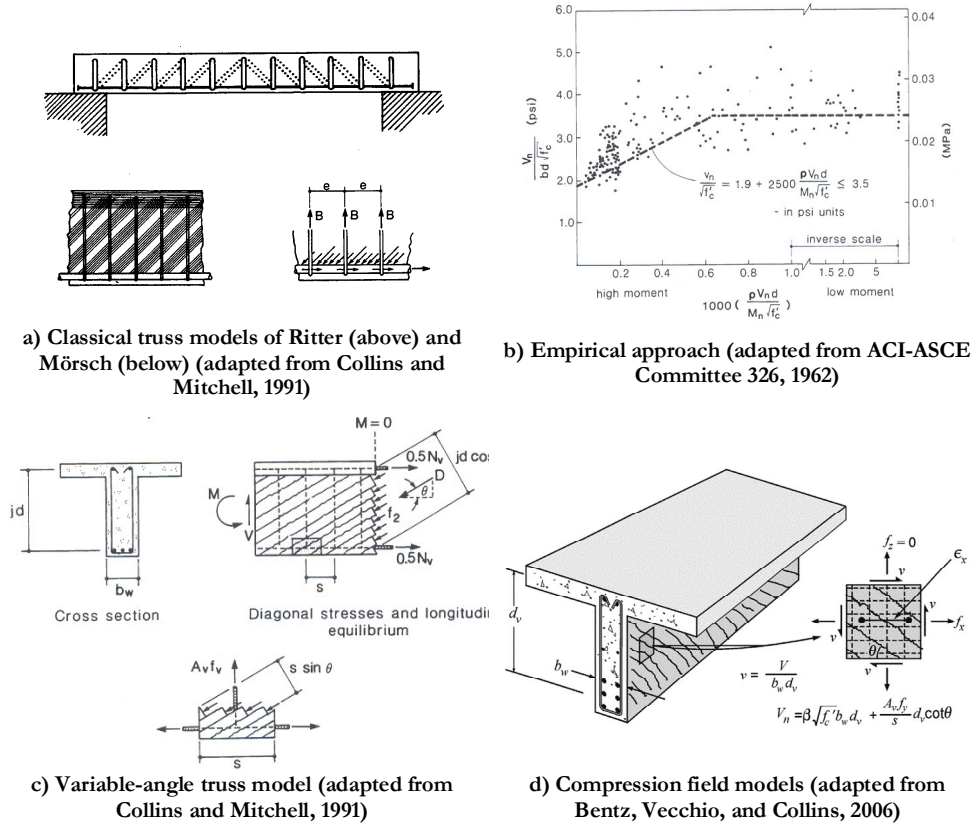


Figure 2.13 Models for shear strength of B- regions

Figure 2.13 summarizes some of the currently-used approaches for predicting the shear strength of B-regions. The classical models of Ritter and Mörch (see plot a) date back to the beginning of the 20<sup>th</sup> century. They represent the flow of forces in members with stirrups in terms of a truss with diagonals at 45°. The empirical approaches (plot b), on the other hand, offer expressions for shear strength obtained in two steps. First, the main variables affecting the shear strength and the structure of the equations are derived from first principles combined with reasonable hypotheses, and second, the coefficients in the equations are obtained through fitting to experimental results. Such an approach has been used, for example, in the development of the concrete contribution term  $V_c$  in the shear provisions of the American code (ACI 318-08, Chapter 11). The full shear strength is

expressed as sum of  $V_c$  and  $V_s$ , where the term  $V_s$  comes from the classical truss model and accounts for the effect of transverse reinforcement. The variable-angle truss model, shown in plot c), is based on the lower-bound approach of the Theory of Plasticity and is implemented in the European design code (EN 1992-1-1:2004, EC2, Section 6.2). Unlike the classical truss model, the angle of inclination of the compression diagonals can be varied over a certain range of admissible values. The capacity of the truss is governed by either diagonal crushing or yielding of the transverse links. For members without stirrups EC2 gives purely empirical expressions. Finally, the compression field models (plot d) include conditions for strain compatibility and material stress-strain relations, which allow for explicit calculation of the inclination of the principal compression in the web of the member. In addition, the Modified Compression Field Theory (MCFT - Vecchio and Collins, 1986) accounts for diagonal tension in the cracked concrete. This tension is related to the ability of the inclined cracks to transfer shear through aggregate interlock. The MCFT forms the basis of the Canadian shear provisions (CSA A.23.3-04, Clause 11.3) for B- regions with and without web reinforcement.

## 2.2.2 Models for D-regions

### 2.2.2.1 General

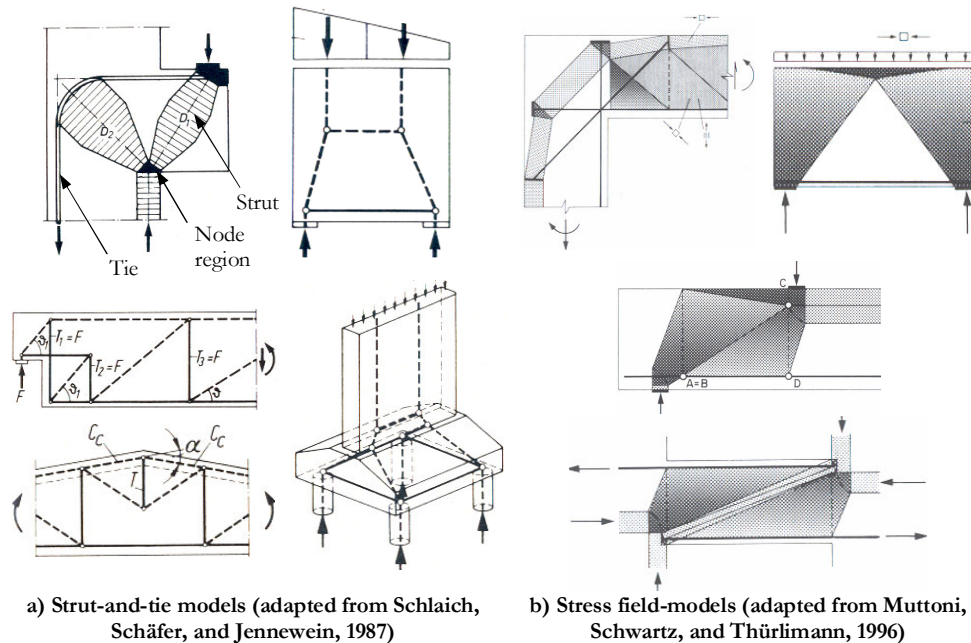


Figure 2.14a) illustrates the most commonly-used approach for modeling of D-regions at ultimate limit state. The so-called strut-and-tie models can be viewed as a generalized version of the classical truss models of Ritter and Mörch (Schlaich, Schäfer, and Jennewein, 1987, see also Reineck, 2002). The struts represent relatively smooth compression fields in the concrete, the ties model the tensile reinforcement, while nodal regions account for the zones with turbulent states of stresses where the struts and the ties meet. The orientation of the strut-and-tie model can vary but should not deviate drastically from the principal-stress trajectories obtained by linear elastic analysis. Load paths which do not comply with this principle can require significant redistribution of internal forces accompanied by opening of wide cracks and high ductility demands. Similarly to a real truss, a D-region is expected to fail when the capacity of a tie, a strut, or a node region is exhausted. Exceptions are statically indeterminate strut-and-tie models since they can tolerate yielding of more than one tie. As stated by Rogowsky and MacGregor (1986b), “An appropriate truss model is one which correctly identifies the reinforcement which is at yield at failure of the beam and discounts the remaining reinforcement”. While it is clear that the strength of the ties equals the cross-sectional area of the reinforcement times the yield stress of the steel, consensus is still lacking on how to calculate the geometry of struts and nodes and how to define the stress limits for them. As far as the geometry is concerned, there exist two principally different approaches for 2D models. The first approach uses node regions in which the two principle stresses are equal to the nodal stress limit. These regions are called “hydrostatic” even though the out-of-plane stress is implicitly zero. The size of the nodes and the struts is increased until a geometrical limit, such as support width for example, is reached. The second approach uses non-hydrostatic node regions with fixed dimensions which depend on the width of the supporting and loading elements, on the detailing of the reinforcement, and on other geometrical features of the member. The load on the model is increased until a stress limit is reached. A third possibility is to use combination of the above two approaches.

The stress limits for struts and node regions are usually expressed as:

- Struts:

$$v_s f_c', \quad (2.1)$$

- Node regions:

$$v_n f_c', \quad (2.2)$$

where  $v_s$  – strut efficiency factor,  $v_n$  – nodal efficiency factor, and  $f_c'$  is the compressive strength of the concrete. Different researchers have suggested numerous expressions for

the efficiency factors involving quantities such as concrete strength, slenderness ratios, reinforcement ratios, etc. Comprehensive summary and evaluation of these expressions can be found, for example, in a publication by Foster and Malik (2002). In addition to the efficiency factors, design codes apply strength reduction factors to provide appropriate safety margin. The solutions adopted in the CSA, ACI, and EC2 codes are discussed in the following two subsections.

Figure 2.14b) shows examples of D-regions modeled with stress fields. This approach is based on the lower-bound theorem of the Theory of Plasticity which states that “A load system, based on a statically admissible stress field which nowhere violates the yield condition is a lower bound of the collapse load” (Muttoni, Schwartz, Thürlimann, 1996). The yield condition for concrete is expressed in terms of effective strength  $f_e$  which takes into account that concrete is not rigid-plastic material. The strut-and-tie models are often categorized as simple stress-field models and equations (2.1) and (2.2) are seen as simplified yield conditions.

In addition to the lower-bound approaches shown in Figure 2.13c) and Figure 2.14b), the Theory of Plasticity offers upper-bound solutions (failure-mechanism models) for both B- and D- regions (see for example Nielsen, 1999).

#### **2.2.2.2 Canadian Code (CSA A.23.3-04, Clause 11.4)**

The CSA code was the first to include strut-and-tie models for design of disturbed regions (CSA 1984, Collins and Mitchell, 1986). The code provisions will be demonstrated through the symmetric simply supported deep beam shown in Figure 2.15. It is assumed that the characteristics of the beam (geometry, reinforcement, and material properties) are known and its load-bearing capacity needs to be assessed. For this reason the strength reduction factors are given a value of unity.

If the beam has no web reinforcement, the flow of internal forces can be represented by an arch which consists of one horizontal and two diagonal struts tied by a bottom tie (see the left shear span in Figure 2.15). The diagonal struts and the tie meet at bottom node regions defined by the width of the support plate  $l_{b2}$  and by the concrete “cover” of the tie  $b_a/2=b-d$ . Parameters  $x$  and  $y$ , on the other hand, determine the geometry of the top node regions. If  $y$  is known,  $x$  can be selected such that the top nodes are under hydrostatic pressure. This condition requires the diagonal strut to be perpendicular to the hypotenuse of the node region, and can be expressed as:

$$x = \frac{-(a_{cl} + l_{b2}/2) + \sqrt{(a_{cl} + l_{b2}/2)^2 + 4y(d - y)}}{2} \quad (2.3)$$

Values of  $x$  smaller than  $l_{b1}/2$  may seem unrealistic if we assume that the loading plate applies uniform pressure on the top surface of the beam. A reduced node width leads to steeper diagonal struts and, as it will be shown later, to higher strength predictions. This solution can be justified if we recall that the strut-and-tie models are generally expected to give a lower bound to the true strength.

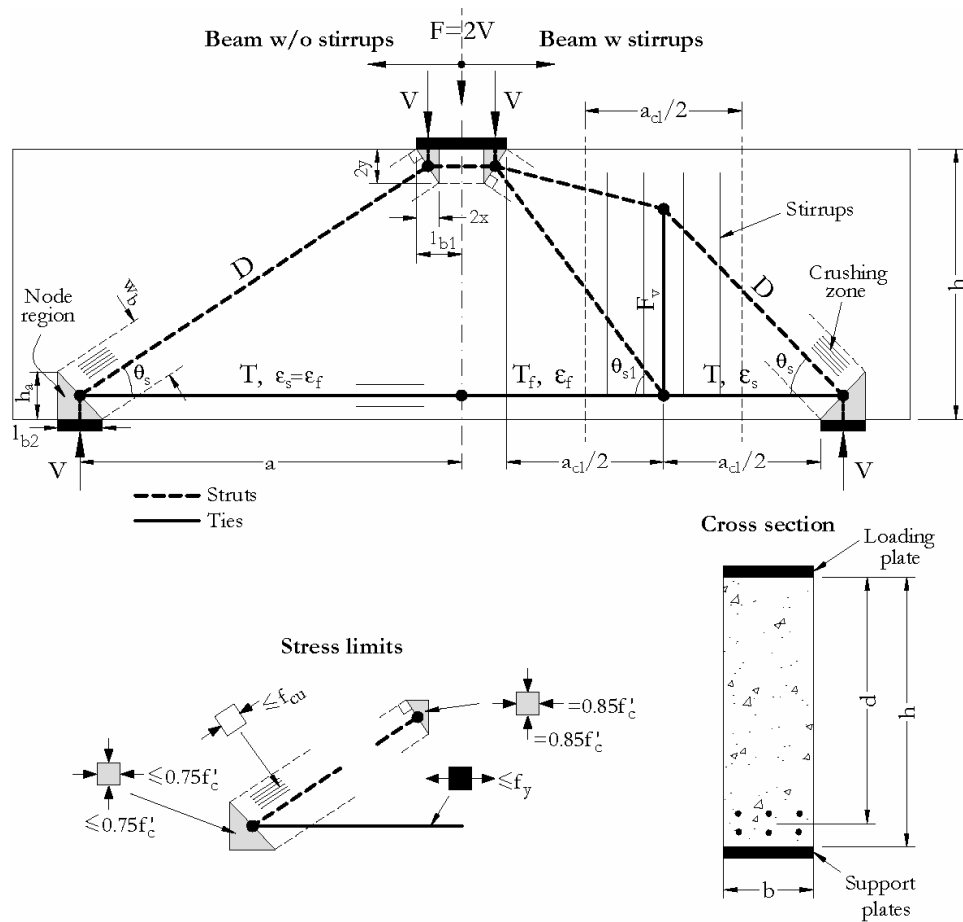


Figure 2.15 Strut-and-tie model of deep beams using the CSA code

When  $x$  is known,  $y$  can be calculated from:

$$y = \frac{d - \sqrt{d^2 - 4x(a_d + l_{b2} / 2 + x)}}{2}. \quad (2.4)$$

The CSA code limits the stresses in node regions bounded by struts and bearing areas (compression – compression – compression nodes or CCC nodes) to  $0.85f'_c$ . The load-bearing capacity of the beam can be therefore written as:

$$F_u = 2V_u = 2 \times 0.85f'_c(2x_u b) \leq 2 \times 0.85f'_c(l_{b1} b). \quad (2.5)$$

The critical width of the top node regions  $2x_u$  is obtained by gradually increasing  $x$  until one the following code limits is reached: 1) horizontal compressive stress of  $0.75f'_c$  in the bottom node zones; 2) vertical compressive stress of  $0.75f'_c$  in the bottom node zones; 3) stress of  $f_{cu}$  in the bottom ends of the diagonal struts; or 4) tension force of  $A_{jt}$  in the tie (see Figure 2.15). Note that the load magnitude as well as the geometry and the statics of the strut-and-tie model are uniquely defined for a given value of  $x$ . The stress limit of  $0.75f'_c$  applies to nodes anchoring a tie in only one direction (compression – compression – tension nodes or CCT nodes). If the ties are in more than one direction (CIT and TIT nodes), the limit decreases to  $0.65f'_c$ . These efficiency factors account for long term action of the loads as well as for disruption of the node regions related to incompatibility between the tensile strains in the ties and the compressive strains in the struts.

The horizontal compressive stress in the bottom node zones reaches value of  $0.75f'_c$  when  $y$  reaches value of  $y_b$  expressed as:

$$y = y_b = \frac{0.75}{2 \times 0.85} b_a = 0.441 b_a, \quad (2.6)$$

while vertical stress of same magnitude leads to:

$$x = x_v = \frac{0.75}{2 \times 0.85} l_{b2} = 0.441 l_{b2}. \quad (2.7)$$

The stress  $f_{cu}$  causing strut crushing near the bottom node regions decreases with increasing tensile strain  $\epsilon_1$  perpendicular to the direction of the strut:

$$f_{cu} = \frac{f'_c}{0.8 + 170\epsilon_1} \leq 0.85f'_c. \quad (2.8)$$

This relation reflects the so-called compression softening effect from the Modified Compression Field Theory (Vecchio and Collins, 1986). The principle tensile strain  $\epsilon_1$



arises from compatibility between the strain in the reinforcement  $\epsilon_s$  and the strain in the surrounding concrete at the vicinity of the support plates. Assuming that the principle compressive strain in the concrete at crushing of the strut equals 0.002,  $\epsilon_1$  is expressed as:

$$\epsilon_1 = \epsilon_s + (\epsilon_s + 0.002) \cot^2 \theta_s. \quad (2.9)$$

The strain  $\epsilon_s$  can be obtained from the tie tension force  $T$  by neglecting the stiffening effect of the concrete between the cracks. Figure 2.16 shows how the strength of the strut  $f_{2max} \equiv f_{cu}$  varies with the angle  $\alpha_s \equiv \theta_s$  for  $\epsilon_s = 0.002$ . The smaller the angle  $\theta_s$ , the larger the strain  $\epsilon_1$ , and the smaller the strength  $f_{cu}$ . The limit case of  $\theta_s = 0$  corresponds to overlapping of the strut and the tie which violates compatibility and logically results in zero crushing strength.

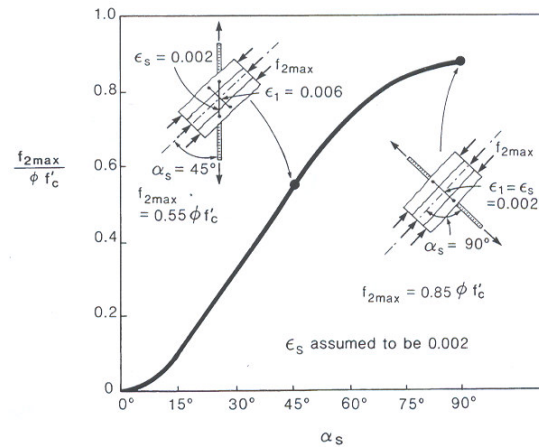


Figure 2.16 Crushing strength of compressive strut versus orientation of tension tie passing through strut (Collins and Mitchell, 1986)

The width of the top node regions which corresponds to diagonal strut crushing can be calculated from:

$$x = x_d = \frac{f_{cu} w_b \sin \theta_s}{2(0.85 f'_c)}. \quad (2.10)$$

This equation needs to be solved iteratively since  $f_{cu}$ ,  $w_b$ , and  $\theta_s$  all depend on  $x_d$ .

Yielding of the bottom reinforcement corresponds to:

$$y = y_y = \frac{A_s f_y}{2(0.85 f_c') b}. \quad (2.11)$$

Finally, the load-bearing capacity of the beam without web reinforcement is calculated from (2.5) using  $x_u = \min(x_b, x_y, x_d, x_j)$ . The values of  $x_b$  and  $x_y$  are obtained from (2.3) by substituting  $y = y_b$  and  $y = y_y$ , respectively. If  $F_u = 2 \times 0.85 f_c' (l_b b)$ , the beam is expected to fail with crushing of the top node regions. Usually, the limit on the stress in the strut controls the strength prediction. Crushing of the bottom nodal regions may govern if one of the ratios  $w_b / l_b$  or  $w_b / h_a$  is unusually large.

If the beam has transverse reinforcement, the flow of internal forces can be represented by the truss depicted in the right shear span in Figure 2.15. The vertical ties model stirrups which are effective in resisting shear and yield prior to failure. It is assumed that the forces  $F_v$  carried by those ties equal  $\rho_v a_d b f_y / 2$ , where  $\rho_v$  is the percentage of transverse reinforcement. Note that the strut-and-tie model in Figure 2.15 differs from the commonly used model shown in Figure 1.7. The model used here has two main advantages. First, it gives a better understanding of how the beam carries the load since the top two inclined struts represent the line of thrust in the concrete above the diagonal cracks. In this way it becomes clear, for example, that the transverse reinforcement can be effective even if it does not extend all the way to the top of the beam. Second, the solution with one diagonal strut at the supports makes the stress checks in these zones straightforward.

Similarly to the case of beam without web reinforcement,  $x$  is gradually increased until one of the four code limits is reached. Expression (2.6), which comes from limit on the horizontal nodal stress, needs to be modified to:

$$y_b' = \frac{0.75 f_c' b_d b - F_v \cot \theta_{s1}}{2 \times 0.85 f_c' b}. \quad (2.12)$$

In addition to the stress limits, the CSA code requires orthogonal web reinforcement with a ratio not smaller than 0.2% in each direction. This reinforcement is aimed to control the cracks and improve the ductility. Exceptions are non-slender slabs and footings which can be designed without this “crack control” reinforcement.

It is important to note that the CSA code does not limit the applicability of the two models discussed above. The designer is allowed to use the maximum of the load-bearing capacities obtained from a strut-and-tie-model (intended for D-regions) and from a sectional model (developed for B-regions). The strength of a beam without web reinforcement, calculated from a strut-and-tie model, decreases quickly with increasing shear-span-to-effective-depth ( $a/d$ ) ratio because of two reasons. First, the larger the  $a/d$

ratio is, the flatter the diagonal struts (see Figure 2.15), and hence the smaller the vertical component of the force they can resist. Second, the flatter the diagonals, the more pronounced the compression softening effect (see Figure 2.16), and hence the smaller the strength of the struts. As a result, the strength prediction for slender beams is naturally governed by the sectional model.

### 2.2.2.3 American Code (ACI 318-08, Appendix A) and European Code (EN 1992-1-1:2004, EC2 Section 6.5)

Similarly to the CSA code, ACI and EC2 codes contain strut-and-tie provisions for the design of disturbed regions. Table 2.1 summarizes the efficiency factors adopted in the three codes as well as the strength reduction factors  $\phi$ . It should be noted that the values recommended in EC2 can be adjusted by the national annexes of the countries which apply the code.

Table 2.1 Limits on stresses in node regions and struts - ACI 318-08, EN 1992-1-1:2004 (EC2), CSA A23.3-04

	Conditions	$\nu$ - factors		
		ACI	EC2	CSA
Node regions	CCC nodes	0.85	$1 \times (1 - f'_c / 250)$	0.85
	CCT nodes	0.68	$0.85(1 - f'_c / 250)$	0.75
	CTT and TTT nodes	0.51	$0.75(1 - f'_c / 250)$	0.65
Struts	Prismatic struts	0.85	1*	$\frac{1}{0.8 + 170\epsilon_1} \leq 0.85$
	Bottle-shaped struts with sufficient reinforcement	0.64	$0.60(1 - f'_c / 250)$	
	Bottle-shaped struts with insufficient reinforcement	0.51		
	Struts in tension members	0.34		
	All other cases	0.51		

Note: For the sake of simple comparison, the nominal strength  $f'_c$  used in ACI and CSA codes is assumed to be equivalent to the characteristic strength  $f_{ck}$  in EC2

\* EC2 specifies factor of 1 for struts “with transverse compressive or no transverse stress”.

$\phi = 0.75, 0.67,$  and  $0.65$  for ACI, EC2, and CSA code, respectively.

According to the ACI code, bottle-shaped struts are susceptible to splitting caused by tensile stresses perpendicular to the strut axis (see Figure 2.17). The splitting governs the failure of plain-concrete struts and struts with small amounts of reinforcement. Surface reinforcement placed to resist the splitting force restrains the width of the cracks and

allows the strut to resist larger axial load. The amount of this reinforcement can be obtained through the strut-and-tie model shown in Figure 2.17. For concrete with  $f'_c \leq 41$  MPa, the following simple criterion for sufficient reinforcement can be used:

$$\sum \frac{A_{s_i}}{b s_i} \sin \alpha_i \geq 0.003, \quad (2.13)$$

where  $A_{s_i}$  is the total area of surface reinforcement at spacing  $s_i$  in the  $i$ -th layer of reinforcement crossing the strut at an angle  $\alpha_i$  to the axis of the strut. It should be noted that rigorous derivation of this condition requires  $\sin \alpha_i$  to be replaced by  $\sin^2 \alpha_i$ . The code also specifies that deep beams should contain vertical and horizontal web reinforcement with ratios not smaller than 0.25% and 0.15%, respectively. The larger amount of vertical reinforcement is justified with experimental studies showing its higher efficiency. The relatively low  $v_s$ -factor of 0.34 for struts in tension members reflects the fact that these struts need to transfer compression across cracks. An interesting experimental verification of the ACI efficiency factors can be found in a paper by Brown et al., 2006.

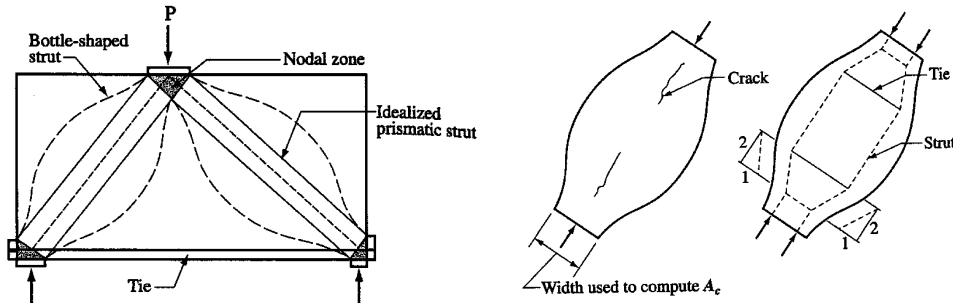


Figure 2.17 Splitting of bottle-shaped struts acc. to ACI 318-08

The expression for the  $v_s$ -factor in EC2 originates from extensive experimental program carried out at the Technical University of Denmark in the late 1970s (Nielsen, 1999). The specimens were T-beams with ordinary or prestressed reinforcement and vertical stirrups. Plasticity approach based on web crushing was used to fit the test results. In terms of minimum web reinforcement for deep beams, EC2 requires 0.20% in each orthogonal direction but not less than 300 mm<sup>2</sup>/m.

EC2 provides an alternative to the strut-and-tie model for beams subjected to concentrated load applied on the top face and located close to the support ( $a_d \leq 2d$ ). The contribution of this load to the design shear force is reduced by a factor of  $a_d/2d \geq 0.25$ . For elements without web reinforcement, the shear so obtained must be smaller than the shear capacity of a slender member with the same cross section. For elements with web

reinforcement, the stirrups located within the central 75% of the clear shear span should be designed to resist the whole reduced shear. In any case, the shear force calculated without reduction should be smaller than  $0.5b_wd\phi v_{fc}'$ .

As evident from Table 2.1, both the ACI and EC2 codes rely on  $v_s$ -factors which do not depend on the strain in the ties and on the angle between the strut and the tie. The ACI code recognizes that flat struts are weaker than steep struts by limiting the applicability of the strut-and-tie model to cases with  $\theta_s \geq 25^\circ$ .



### 3.EXPERIMENTAL PROGRAM

#### 3.1 INTRODUCTION

An experimental program involving ten tests of deep beams was conducted in the Mark Huggins Structural Laboratory in the Department of Civil Engineering at the University of Toronto. The main goal of the program was to provide insight into the effect of the following parameters on the behaviour of deep beams: 1) slenderness ( $a/d$  ratio); 2) transverse reinforcement ( $\rho_v$  ratio); 3) loading history (monotonic vs. reversed cyclic); 4) longitudinal reinforcement distribution (single bar vs. multiple bars); and 5) longitudinal reinforcement anchorage (hooks vs. anchor heads).

Eight of the specimens were designed to systematically study the effect of the first three parameters while the other two specimens were made to study the influence of the last two variables. Table 3.1 summarizes the tests.

Table 3.1 Tests summary

Test	a/d	$\rho_v$	Loading History	Longitudinal Reinforcement Distribution	Longitudinal Reinforcement Anchorage
S0M	1.55	0	Monotonic	Multiple bars	Anchor Heads
S0C			Cyclic		
S1M		0.1%	Monotonic		
S1C			Cyclic		
L0M	2.29	0	Monotonic		
L0C			Cyclic		
L1M		0.1%	Monotonic		
L1C			Cyclic		
SB	1.59	0	Monotonic	Single bar	Hooks
MB				Multiple bars	

Note: All the specimens had depth  $h=1200$  mm

In the notation used for the first 8 specimen names S/L stands for short/long, 0/1 for  $\rho_v=0\%/0.1\%$ , and M/C for monotonic/cyclic. For the last 2 tests SB is an abbreviation for “single bar” and MB stands for “multiple bars”.

The specimens were intended to represent heavily loaded members from engineering practice or, in other words, members working with high diagonal compression stresses in the concrete. They were also designed to have close flexural and shear failure loads assuming that the longitudinal bars were made of mild steel. Flexural yielding was then suppressed by using high-strength steel.

The values of  $a/d$  ratio were chosen such that specimens S0M/C, S1M/C, SB, and MB could be easily classified as deep beams while L0M/C and L1M/C are in the zone of transition from deep to slender beams, i.e. in the zone of moderately-deep beams (see 1.2 and 1.3). It was believed that tests within the transition zone could provide valuable insight into the two mechanisms of shear transfer (beam action controlling the behaviour of slender beams and strut-and-tie action controlling deep beams) and how they interact.

The low ratio of transverse reinforcement is aimed to be representative of traditional construction practices. The values 0% and 0.1% were chosen to examine if small amount of stirrups would lead to a significant improvement of the behaviour of deep beams especially under reversed cyclic loading.

The boundary conditions of the test specimens are shown in Figure 3.1 Both the loading and the supports are direct. This simple scheme was chosen to make the diagonal strut action clearly defined between the loading and support points and to study how effective that action is under reversed cyclic loading.

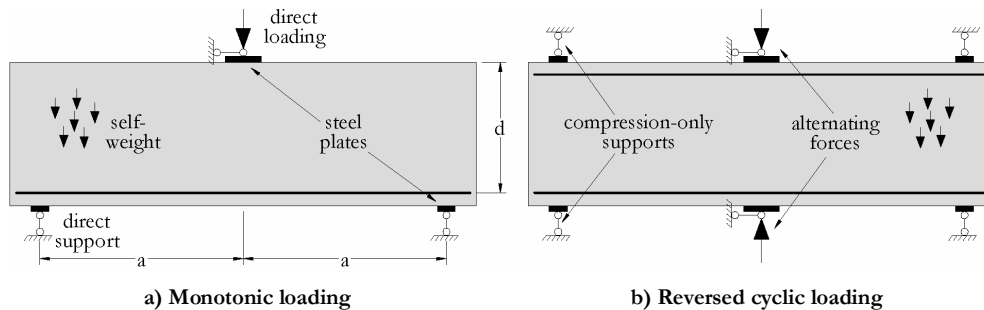


Figure 3.1 Loading and support conditions

Specimens SB and MB have the same amount of longitudinal reinforcement but different number of bars - one and four, respectively. The single bar is anchored with anchor heads while the four bars are anchored with lap-spliced hooks. The solution with the single bar and anchor heads represents an extreme case of reinforcement detailing of large members. The SB and MB tests were expected to provide information on the effects of bond conditions, concrete crushing/splitting around large anchor heads, and



effectiveness of lap-splices in deep beams. Generally, multiple bars with small diameters are more effective in engaging the surrounding concrete than fewer bars with large diameters. Splitting of the concrete cover along large bars leads to further bond deterioration.

### 3.2 SPECIMENS

#### 3.2.1 Dimensions and Reinforcement

All the specimens have the same cross section- 1200 mm deep and 400 mm wide (see Figure 3.2 and Figure 3.3). This solution allowed construction of simple formwork which could be used multiple times for elements with different lengths. Specimens S0M/C, S1M/C, SB, and MB have overall lengths of 3900 mm and spans of 3400 mm while specimens L0M/C and L1M/C- overall lengths of 5500 mm and spans of 5000 mm.

The longitudinal reinforcement of specimens S0M/C, S1M/C, L0M/C, and L1M/C is symmetric (top and bottom) and consists of six US #8 deformed bars ( $A_s=3060 \text{ mm}^2$ ,  $\rho=0.70 \%$ ) distributed in two layers of three bars with 50 mm concrete cover. Specimen SB has just one #18 deformed bar ( $A_s=2580 \text{ mm}^2$ ,  $\rho=0.60 \%$ ) which is the largest reinforcing bar according to the ASTM standard (see Figure 3.4). Specimen MB has four bars - 1x25M and 3x30M ( $A_s=2600 \text{ mm}^2$ ,  $\rho=0.61 \%$ ) arranged in one layer. The anchorage of the #8 and #18 bars is provided by circular anchor heads which were fabricated and friction-welded to the ends of the bars by the Headed Reinforcement Corp., California, US. The 25M and 30M bars are anchored by lap-spliced hooks made of 25M bars. The length of the lap splice is insufficient according to the CSA code. This solution was inspired by similar detailing in the 35 year old slab bridge in Laval, Quebec, which failed in shear in September 2006. The distance from the axis of the longitudinal reinforcement to the bottom face of beams SB and MB is 130 mm. It was determined by the large heads of the #18 bar and was intentionally kept equal for the two specimens to allow for direct comparisons.

The desired low ratio of transverse reinforcement ( $\rho_v=0.10 \%$ ,  $\rho_{vf}=0.49 \text{ MPa}$ ) for specimens S1M/C and L1M/C was achieved with #3 stirrups at 350 mm.

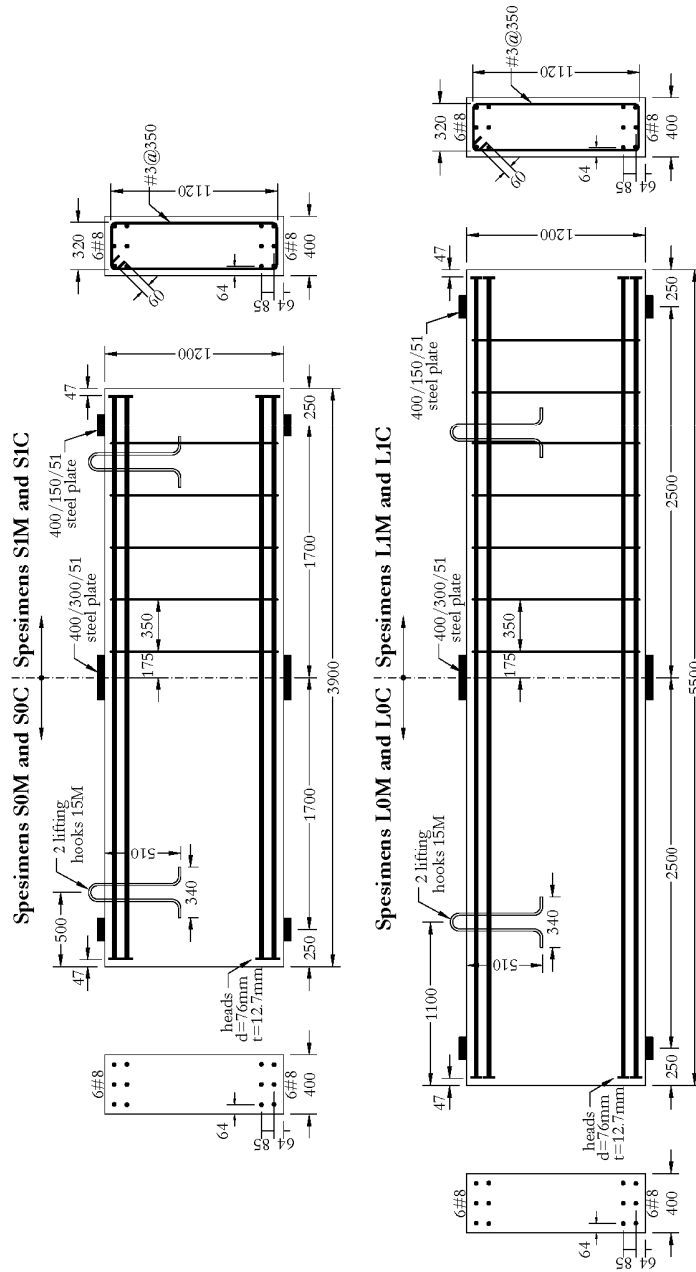


Figure 3.2 Specimens S0M/C, S1M/C, L0M/C, and L1M/C- dimensions and reinforcement

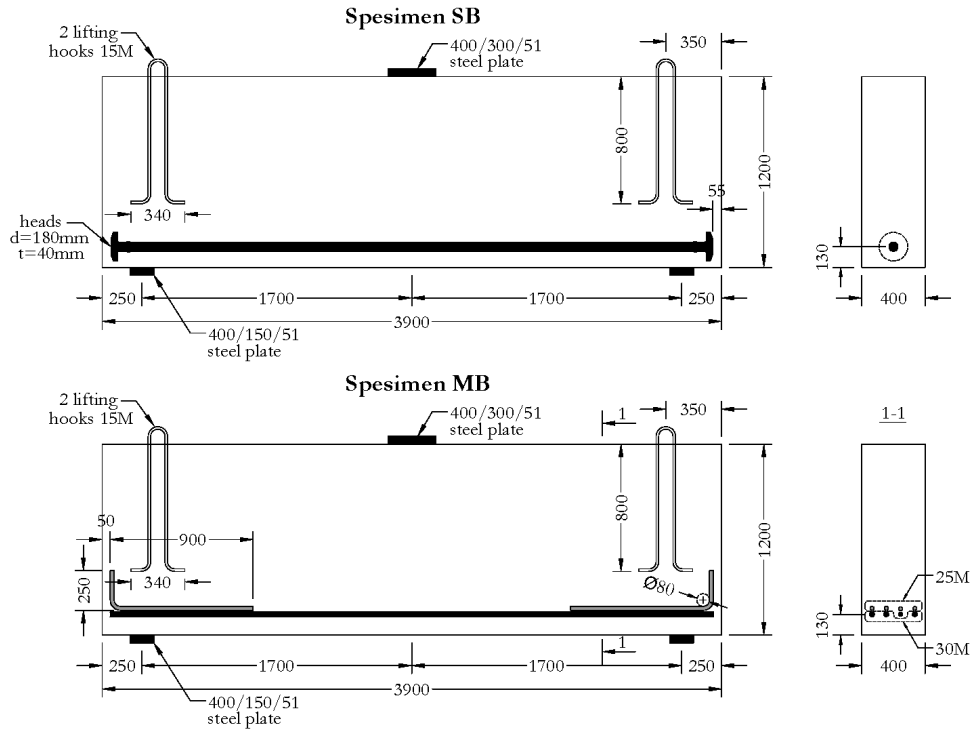


Figure 3.3 Specimens SB and MB- dimensions and reinforcement

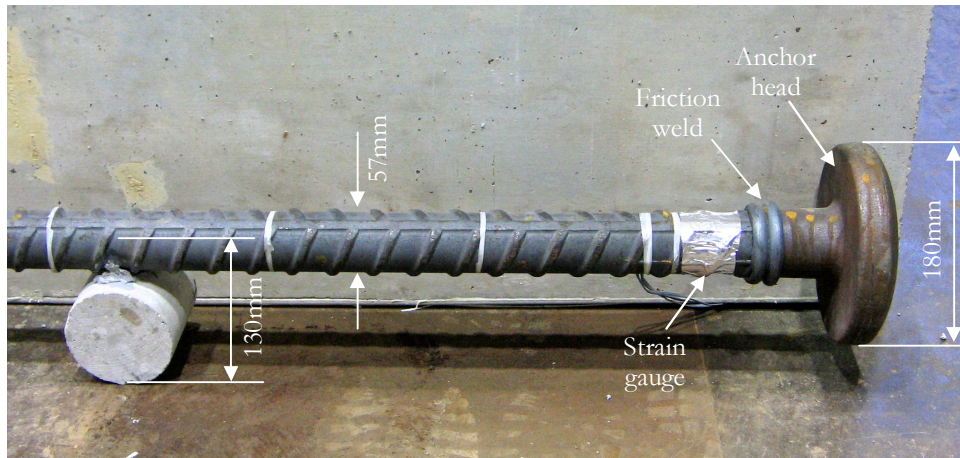


Figure 3.4 #18 bar with anchor heads

### 3.2.2 Construction

The specimens were cast two at a time in wooden forms in the Mark Huggins Structural Laboratory. The concrete was supplied by a local-ready-mix supplier in a single truck and consequently beams from the same cast had practically identical concrete properties. The cast pairs S0M/C, S1M/C, L1M/C, L0M/C, and SB/MB were chosen to allow for clear assessment of the effect of the loading history (the first four pairs) and the effect of the distribution of the longitudinal reinforcement (the last pair). The specimens were kept covered with wet burlap and polyethylene in the form for seven days after casting. Figure 3.5 shows pictures from different stages of the construction process.



Figure 3.5 Construction process

### 3.2.3 Materials

#### 3.2.3.1 Concrete

All ten specimens had the following target concrete properties: compressive strength of 30 MPa, maximum aggregate size 20 mm, and slump 75 mm. From past experience it was known that the local supplier provides concrete with strength of about 10 MPa higher than the specified strength. For this reason it was decided to order concrete with a specified 28 day compressive strength of 20 MPa.

Cylinder compressive tests were performed to obtain the development of compressive strength with time and its value at the time of the beam tests (see Figure 3.6). Fifteen cylinders with dimensions 152/305 mm (6"/12") were prepared from each batch of concrete. Three of them were used to find the standard concrete strength. They were tested after twenty-eight days of curing under standard temperature and humidity. The other twelve cylinders were cured similarly to the beams: in a curing room for seven days and in the laboratory for the rest of the time. They were tested in sets of three at 7<sup>th</sup>, 14<sup>th</sup>, and 28<sup>th</sup> days after casting, and at the time of the beam test. The full stress-strain response was obtained only for the three cylinders tested simultaneously with the beams (see Figure 3.6). A typical stress-strain curve is shown in Figure 3.7.

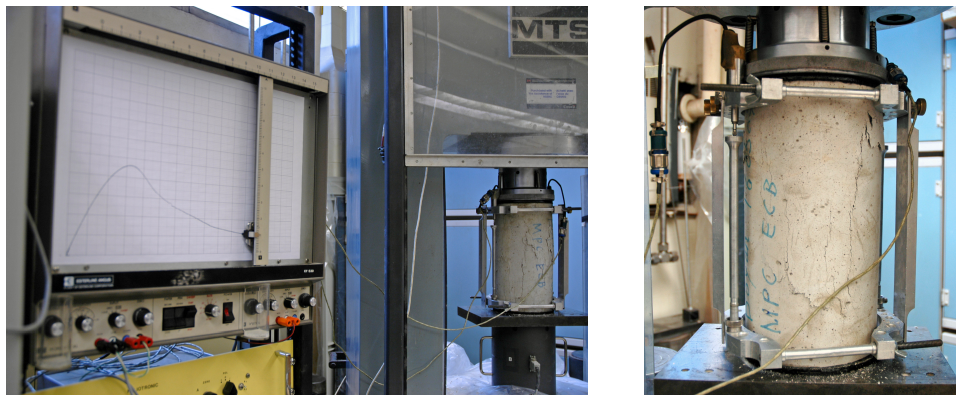


Figure 3.6 Cylinder compressive test – specimens SB and MB



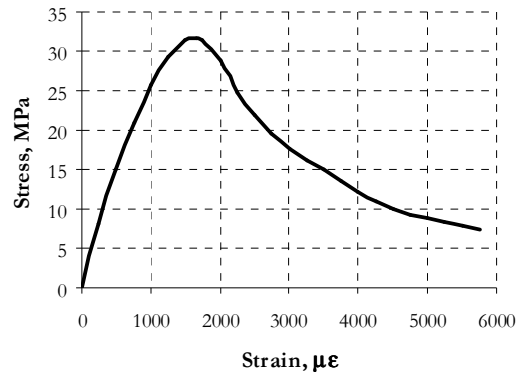


Figure 3.7 Concrete in compression – specimens SB and MB

The modulus of rupture was also obtained experimentally by testing 152/152/533 mm (6"/6"/21") prisms under four-point bending (see Figure 3.8). Three prisms were prepared from each concrete batch and cured entirely in standard conditions. The tests for all the batches were performed within a day after all the beam tests had been completed.



Figure 3.8 Modulus of rupture test – specimens SB and MB

The values of the cylinder compressive strength at testing days as well as the values of the modulus of rupture are presented in Table 3.2. The full set of concrete test data can be found in Appendix A.

Table 3.2 Concrete tests results

Property	S0M/C	S1M/C	SB/MB	L0M/C	L1M/C
Standard cylinder strength (28 days) (MPa)	31.4	28.6	20.2	26.1	32.5
Cylinder strength at day of test (MPa)	34.2	33.0	30.5	29.1	37.8
Strain at maximum stress at day of test ( $\mu\epsilon$ )	1630	1630	1460	1470	1770
Concrete age at day of test (days)	144	119	204	151	171
Modulus of rupture (MPa)	4.3	3.9	3.6	3.7	3.7

Note: Each value in the table is obtained as an average of the results from three tests

### 3.2.3.2 Steel

The headed longitudinal reinforcement was provided by the Headed Reinforcement Corp. together with mill certificate indicating yield stress 652 MPa and tensile strength 862 MPa. The yield stress was used for design of the specimens. No additional tests were performed since no yielding of the bars was expected.

The 30M, 25M, and #3 bars were available in stock in the Mark Huggins Structural Laboratory. No tests on the 25M and 30M bars were performed. Two samples of #3 bars were tested in tension. They had practically identical stress-strain responses characterized by a yield strain of 0.24%, a yield stress of 490 MPa, a yield plateau up to strain of about 2.5 %, a tensile strength of 600 MPa, a strain at maximum stress  $\sim 15$  %, and a ultimate strain  $\sim 22$  %. One of the stress-strain curves is shown in Figure 3.9. This behaviour can be described as quite ductile (ratio ultimate strain to yield strain of about 92) with relatively small strain hardening (ratio tensile strength to yield stress of 1.22).

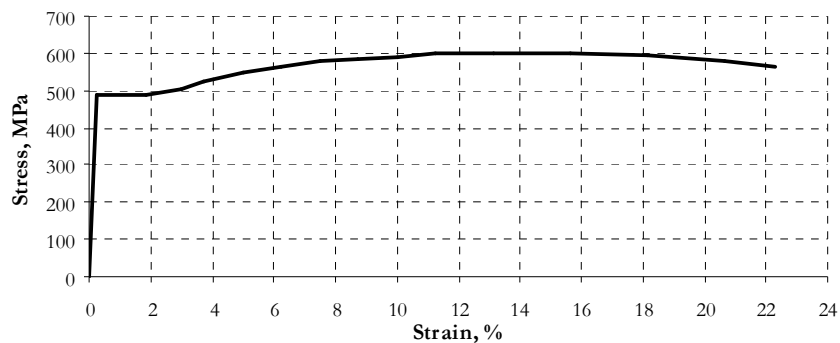


Figure 3.9 Tensile coupon test - #3 bars

### 3.3 TEST SETUP

The test setup for the cyclic tests (S0C, S1C, L0C, and L1C) is shown in Figure 3.10 and Figure 3.11. The top load was applied by a Baldwin hydraulic machine controlled by oil pressure. The load path is schematically shown in Figure 3.10 with grey arrows. The head of the machine has a large spherical hinge allowing for free rotation of the top loading plate and restraining its translation in the horizontal plane. The bottom support plates were seated on rollers to guarantee free elongation of the specimen. Plaster with thickness of about 10 mm was cast between the steel plates and the beam to provide a uniform distribution of the applied stresses. The rollers were installed on stiff steel supports which in turn were bolted to a steel box girder consisting of two standard I-sections welded together. The closed steel section was formed to resist torsion caused by eccentricities in the system and to avoid differential displacements between the two I-sections. Local buckling under the concentrated loads was prevented by a series of stiffeners. The girder was simply supported on two steel pedestals sitting on the strong floor.

The bottom load was applied by four hydraulic jacks installed between the specimen and the steel box girder. The load path is schematically shown in Figure 3.10 with black arrows. The jacks restrained the translation of the bottom loading plate in the horizontal plane and its rotation around the vertical axis. The concrete and the steel beams were connected by “yokes” at the location of the specimen supports. The horizontal parts of the yokes were made of standard steel box sections while their vertical parts were of high-strength steel rods. The steel boxes and the rods were connected through spherical hinges to allow for free elongation of the specimen. The four jacks, the concrete beam, the box girder, and the yokes, form a self equilibrated system. Gaps form between the rollers and the bottom support plates caused mainly by elongation of the rods, bending of the box beams, and straining of the plaster.

An additional lateral support of the system was provided by two thin steel rods ( $d_r=16$  mm) connected to the concrete beam and to “hoops” installed around the columns of the Baldwin machine. The connection between the rods and the “hoop” was made to be effective when the rods elongate and ineffective when the rods tend to shorten. In other words, the rods were capable of transmitting tension only. A concern was the fact that deflection of the specimen causes inclination of the rods and a vertical component of the tension force in them. This component adds to the resistance of the concrete beam and could lead to an overestimation of the strength of the specimens. Calculations showed that the additional resistance is less than 1 % of the load-bearing capacity of the beams and can be neglected. No significant tendency for out-of-plane movement of the specimens was observed during the tests.



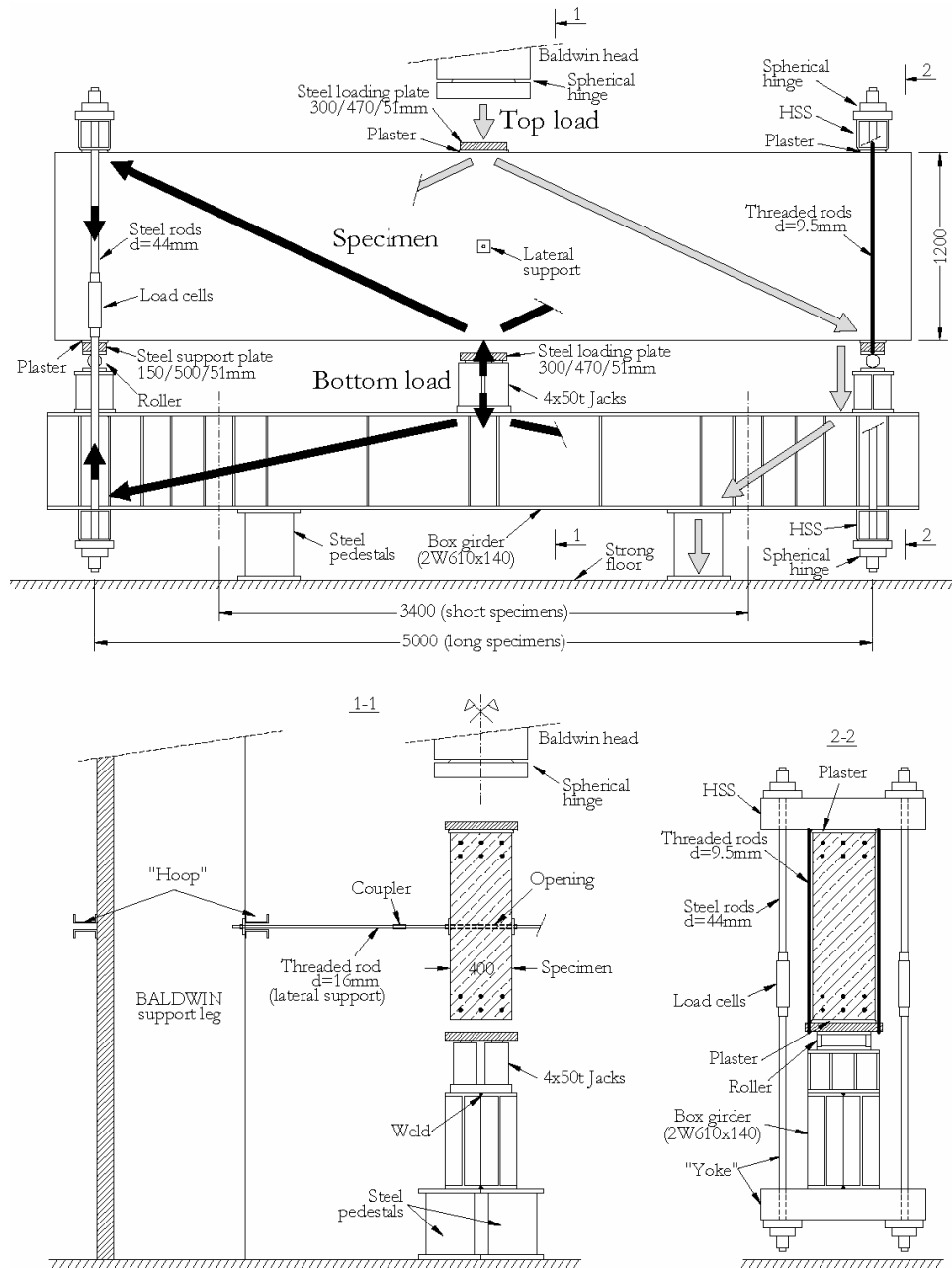


Figure 3.10 Test setup for cyclic tests – scale drawing

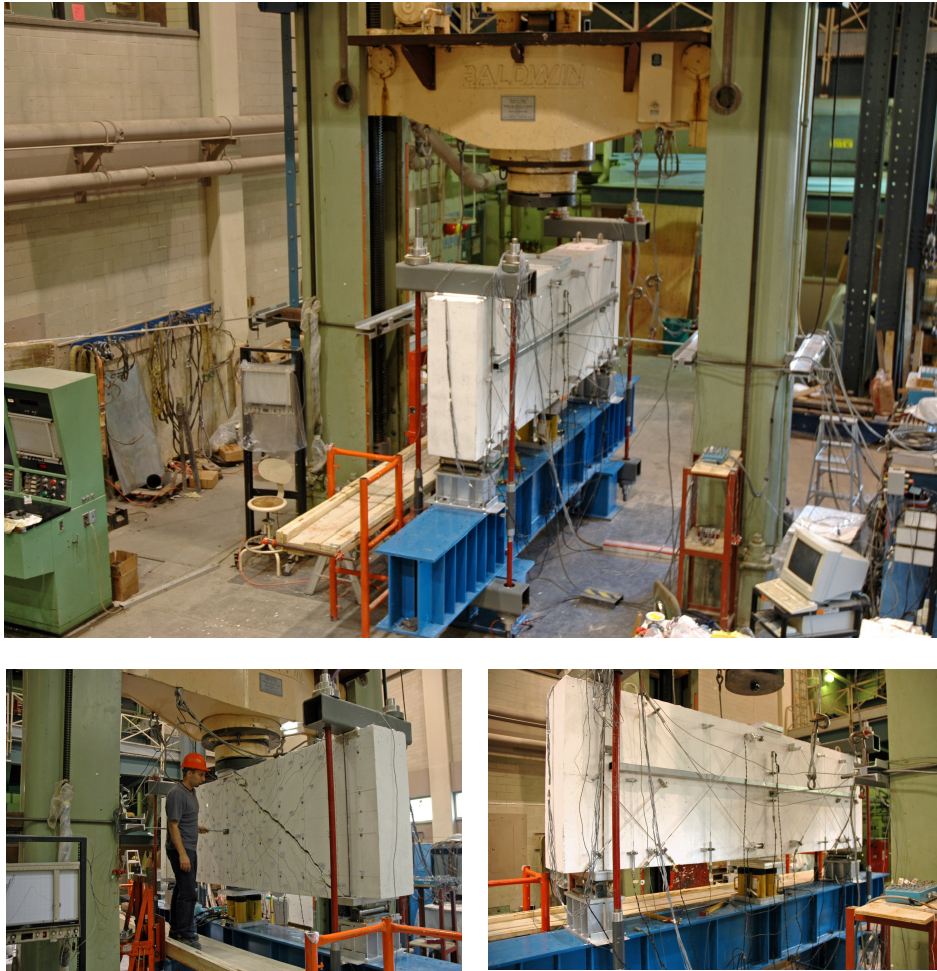


Figure 3.11 Test setup for cyclic tests – general view

The test setup for monotonic tests S0M, S1M, L0M, and L1M was very similar to the one shown in Figure 3.10 and Figure 3.11. The only difference was that the four jacks and the vertical “hoops” were not installed because the bottom load was not needed.

Tests SB and MB were performed with a quite different setup. Since they did not have companion cyclic tests, there was no need to be tested on the steel box girder. Therefore, a simpler setup was used (see Figure 3.12). The beams were loaded with the Baldwin machine and were supported on two rollers. The rollers were installed on stiff box

sections which helped to distribute the forces more uniformly to the strong floor. No additional lateral support was used because the out-of-plane movement of the specimen was restrained by the loading head and by the rollers through friction at the interfaces. Concrete splitting and lateral spalling was expected around the anchor heads of specimen SB (Thompson et al., 2005 and 2006). In order to prevent falling of large concrete pieces, the two ends of the beam were equipped with lateral steel pipes connected to vertical I-sections which were in turn bolted to the supporting box sections (see Figure 3.12). A gap of about 5 mm was left between the pipes and the sides of the specimen.

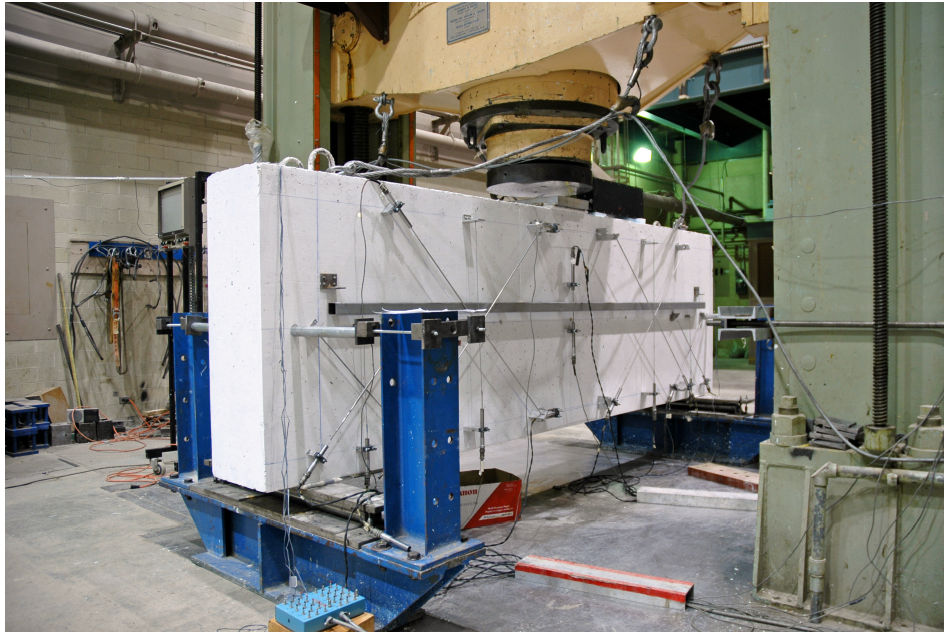


Figure 3.12 Test setup for specimen SB and MB

### 3.4 INSTRUMENTATION

Various quantities describing the local and global response of the test beams were measured by means of different types of instrumentation. These quantities can be arranged in four main groups: applied forces and support reactions, relative displacements between points on the concrete surface, strains on the surface of the reinforcing bars, and crack widths.

The top applied force was measured by the embedded load cell in the head of the Baldwin machine (see Figure 3.10). Load cells were also used to measure the reactions on

the top supports under the action of the bottom load. They were installed on the four rods connecting the concrete beam to the steel box girder (see Figure 3.10). The lengths of the rods were adjusted before each test such that they all received approximately equal tension. In this way the torsional effects on the specimen were minimized. As an additional check a pressure gauge was installed on the bottom jacks to measure the oil pressure in them.

Relative displacements between points on the concrete surface were measured on both sides of the specimens. The longitudinal axis of the specimens was aligned east-west and the south side was covered with a 300 mm by 300 mm grid of “Zürich” targets (see Figure 3.13). Zürich gauges were used to measure the length of the four sides and the two diagonals of each square of the grid at each stage of loading (see Section 3.5). The geometric compatibility between the six readings in a square (note that any of the readings can be derived from the other five) was checked through a routine embedded in the data acquisition software and in case of error the readings were repeated. The length of the sides of the squares was chosen to be roughly equal to the expected distance between the major cracks. In this way the strains calculated over a square of the grid could be approximately interpreted as average concrete strains. The “Zürich” data was also intended to provide information about the deformed shape of the specimens at different load levels.

The north sides of the beams were instrumented with sixteen linear variable differential transformer transducers (LVDT transducers or LVDTs) shown schematically in Figure 3.14 together with their gauge lengths and notation. The LVDTs provide continuous readings of the change of distance between their ends. LVDTs BH and TH were used to measure the average strains along the top and bottom reinforcement at the zone of maximum bending moment. Their gauge length was selected to accommodate several cracks. BV and TV were installed to measure the beam mid-span deflection as a vertical distance between point C and a straight line connecting points A and B. The line AB was defined by a steel box section hanging on thin steel wires connected in turn to L-shaped steel mounts at A and B. BV and TV were connected to the box section and to the face of the beam at point C. They were shifted 30 mm east to not interfere with the lateral support (see Figure 3.10 and Figure 3.11). Two sets of three LVDTs (ES-TW-BE, ES-TE-BW, ES-V and WS-TW-BE, WS-TE-BW, WS-V) were used to measure deformations in the vicinity of the bottom supports where significant “activity” was expected. And finally, two sets of three LVDTs (EL-TW-BE, EL-TE-BW, EL-V and WL-TW-BE, WL-TE-BW, WL-V) were installed to measure deformations at the middle of the shear spans over the effective depth of the section. Each set of three LVDTs represents a strain rosette and provides sufficient data to calculate the average principal strains and principal directions over the covered zone.

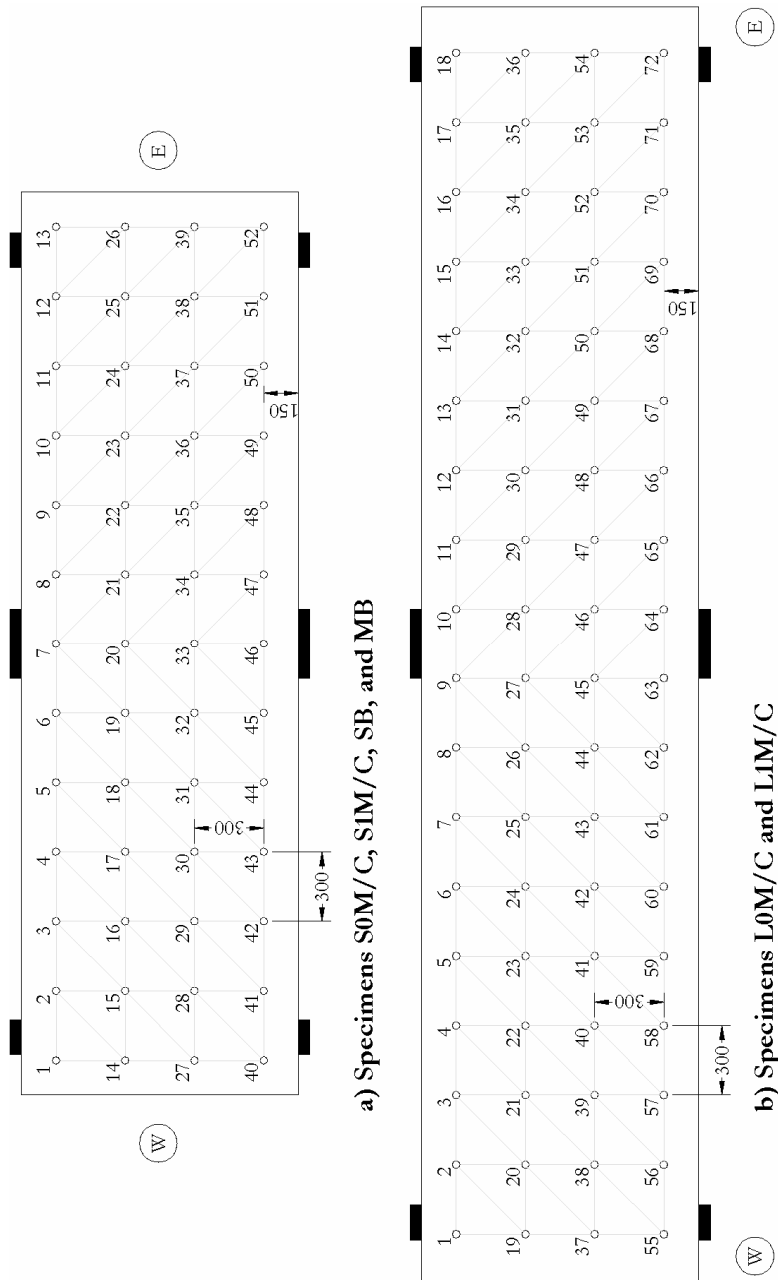


Figure 3.13 Zürich targets on the south face

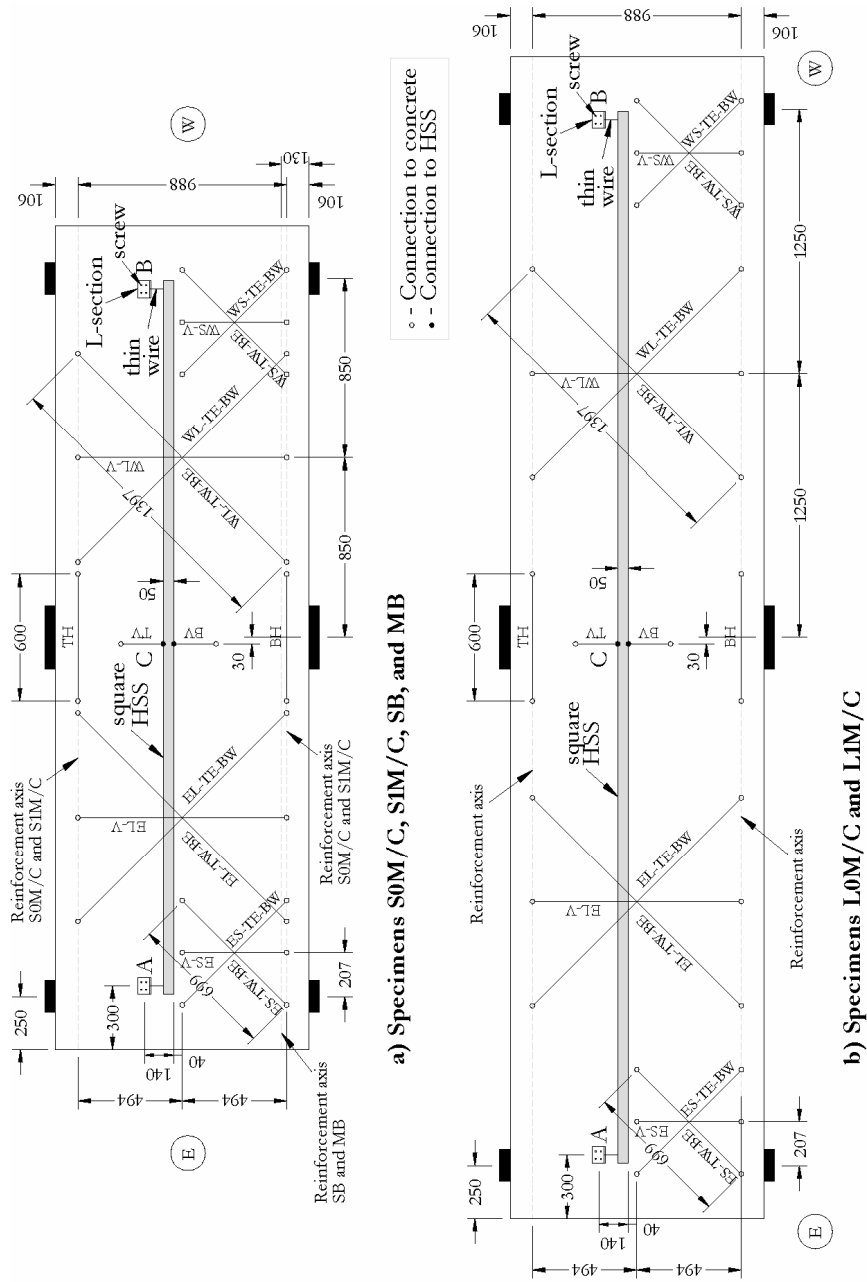


Figure 3.14 LVDTs on the north face

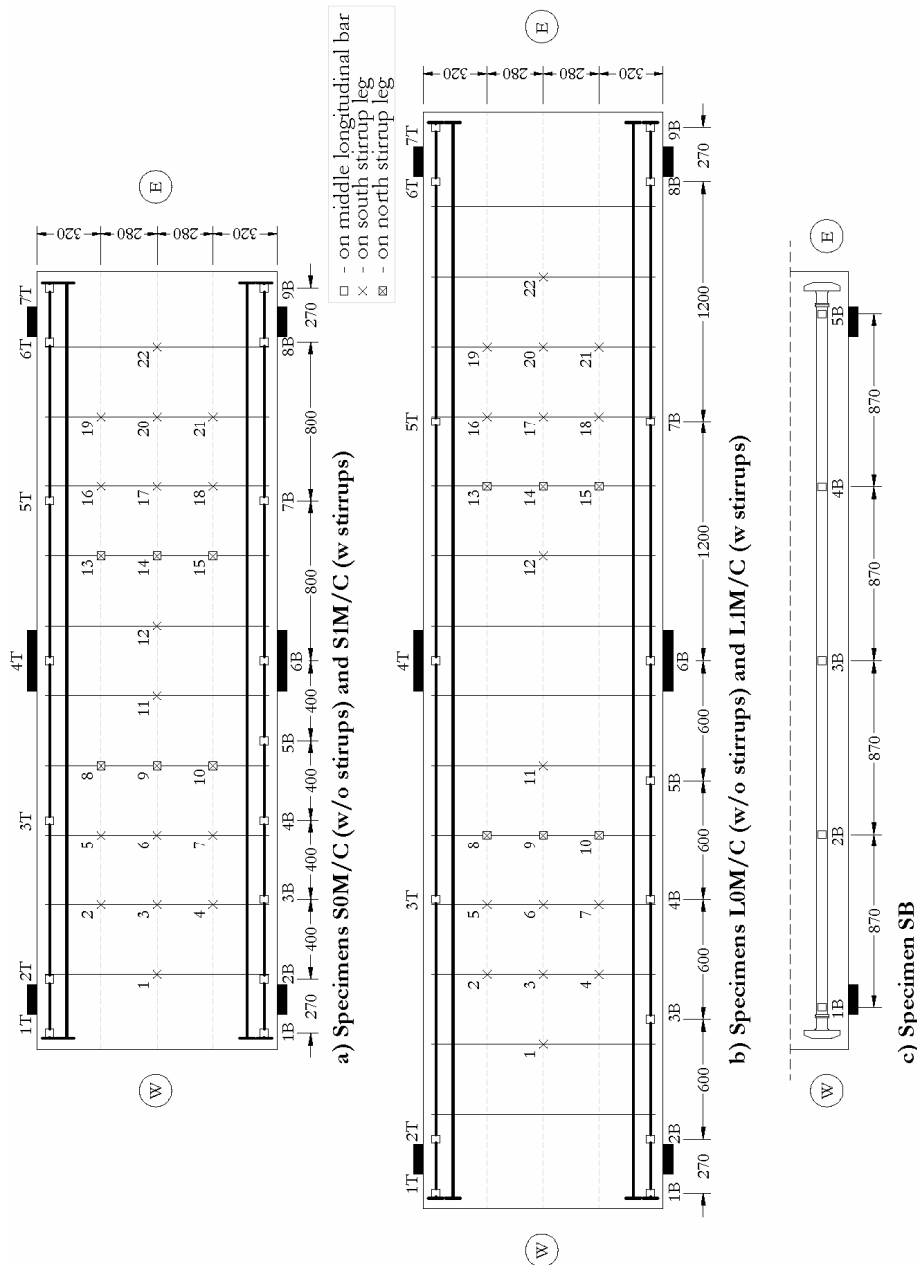


Figure 3.15 Strain gauges

The steel strains were measured by strain gauges with a length of 5 mm glued on the surface of the bars (see Figure 3.15). The gauges on the longitudinal reinforcement were expected to provide information on how the tension varies along the span. They were installed on the sides of the bars to avoid deformations from bending due to dowel action. The gauges on the transverse reinforcement were arranged to cover a large part of the shear span where significant concrete cracking and steel yielding was expected. Most were glued on the south legs of the stirrups and a few on the north legs to check if there was significant difference between the deformations on both sides of the beams. Specimen MB had no strain gauges due to time constraints involving closing the laboratory for major renovations.

The cracks were marked and measured with a comparator gauge at each load stage (see 3.5). Finally, a series of high-resolution high-speed pictures were taken and the tests were recorded on standard definition video.

### 3.5 LOADING HISTORY

A typical monotonic loading history (tests S0M, S1M, L0M, L1M, SB, and MB) is shown in Figure 3.16a). The top load was applied in steps with the load being reduced by about 10% during a “load stage” to allow for safe Zürich readings, crack marking, crack measurement, and taking pictures. The first load stage took place when significant flexural cracking was observed. The loading then proceeded with about constant load increments. The load increment size was chosen such that the total number of load stages per test was of the order of six. In many occasions, however, extra load stages were performed right after a fast increase in deformations caused by cracking or crushing. Each monotonic test was completed within a day.

A typical cyclic loading history (tests S0C, S1C, L0C, and L1C) is shown in Figure 3.16b). The planning of the cyclic tests was facilitated by the fact that each of them was performed right after its companion monotonic test. The reversal of the load including the self-weight of the beam was assumed to take place under a bottom load of  $G/2$  ( $G$  is the weight of the beam) corresponding to zero mid-span moment and zero shear at the middle of the shear spans. In order to induce symmetric damage in the specimens, the loading history was kept symmetric with respect to that load level. The first full unloading was done when the cracking along the bottom reinforcement approached the support zones and major shear cracks reached the top loading plate. The loading proceeded with groups of three cycles with constant amplitudes. If there was a large increase in deformations between the second and the third cycle in a group compared to the increase between the first and the second cycle, a fourth cycle was performed. The amplitude increment between the groups of cycles was kept approximately constant. The third group had maximum load amplitude close to the monotonic capacity and was followed



by monotonic loading up to failure. Unlike the other cyclic specimens, S1C was subjected to four groups of cycles before being loaded to failure. The load stages at which readings were taken differed from test to test to reflect the specifics of each specimen and to comply with time constraints. The duration of the cyclic tests varied between three and six days.

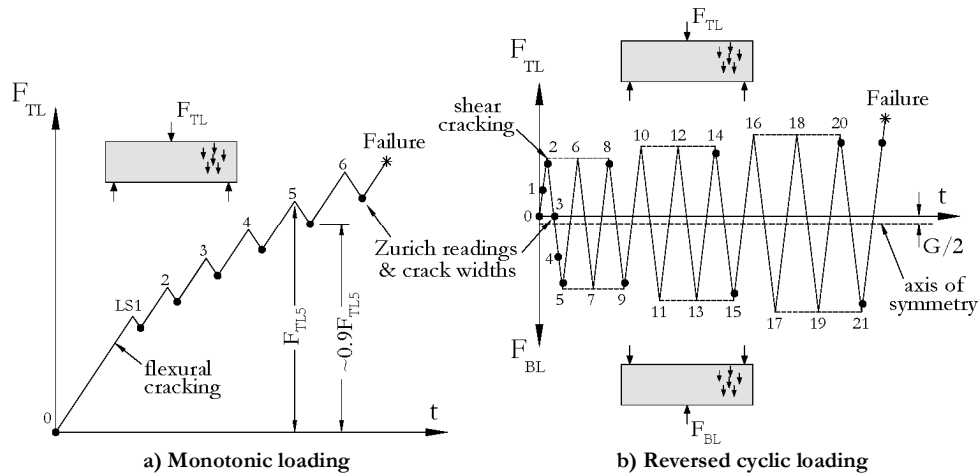


Figure 3.16 Loading histories

The described loading history was not meant to represent a particular type of real excitation. The goal was rather to examine the behaviour of the specimens under quite severe short-term fully reversed cyclic loading. A typical earthquake excitation differs from the chosen loading history in three main respects. First, an earthquake action is better represented in displacements. The displacement histories imposed on different members, in different structures, under different earthquake excitations have much more in common than the respective force histories. In this particular case the longitudinal reinforcement was expected to remain elastic and so the proportionality between forces and displacements was valid to a large extent. Besides, the post peak behaviour was not of primary interest because of the expected brittle shear failures. Second, a typical earthquake record consists of dozens of cycles with increasing amplitude. The low amplitude cycles have some contribution to the degradation of the load-bearing mechanisms. They were omitted in the chosen loading history to allow for undisturbed propagation of shear cracks before the first load reversal. These cracks were expected to have less global roughness and therefore less capacity to transfer shear. The number of cycles was kept small to avoid fatigue-type action. Third, the duration of strong earthquake does not exceed several minutes. The tests duration was much longer in order

to collect valuable information about the deformed shape of the elements, the propagation of cracks and their widths.

The exact loading histories for tests S0C, S1C, L0C, and L1C are given in Appendix B.

## 4. TEST RESULTS AND DISCUSSION

### 4.1 DATA PROCESSING

#### 4.1.1 General

The data acquisition system was launched shortly before the beginning of each test when the element experiences selfweight only and continued until a significant drop of resistance was observed. The readings from the load cells, from LVDTs, and strain gauges were set to close to zero just prior to the test. These small initial values were later subtracted from the rest of the readings. In this way the results have meaning of increment of forces, displacements, and strains with respect to their values prior to loading. Therefore, deformations caused by self-weight and shrinkage were not captured.

#### 4.1.2 Data from load cells and pressure gauges

The readings from the load cell of the Baldwin machine (see Figure 3.10) were directly used to quantify the top load applied on the specimens. As one estimate of the magnitude of the bottom load the measured oil pressure was multiplied by the total area of the bottom jacks. This approach neglects the friction in the hydraulic jacks and therefore overestimates the load when loading and underestimates it when unloading. The result appears as unrealistically large hysteretic loops on a force-displacement plot. A more accurate estimate of the bottom load ( $F_{BL}$ ) was obtained by using the load cells installed on the vertical rods (see Figure 3.10). The following formulas were derived by considering vertical equilibrium of the specimens:

$$F_{BL} \approx G - 2R_{roller} \quad \text{when } F_{BL} < G \quad \text{and} \quad (4.1)$$

$$F_{BL} \approx G + F_{LC} \quad \text{when } F_{BL} \geq G \quad (4.2)$$

Where  $G$  is the weight of the specimen assuming a concrete weight of  $24 \text{ kN/m}^3$ ,  $R_{roller}$  is the reaction force per roller, and  $F_{LC}$  is the total force in the four load cells. The weight of specimens S0M/C, S1M/C, SB, and MB equals  $(3.9 \times 1.2 \times 0.4) \times 24 = 44.9 \text{ kN}$  while that of specimens L0M/C and L1M/C equals  $(5.5 \times 1.2 \times 0.4) \times 24 = 63.4 \text{ kN}$ . Expressions (4.1) and (4.2) would be exact if the yokes had no weight.  $R_{roller}$  was not measured and therefore  $F_{BL}$  was unknown when less than  $G$ .

The shear at the middle of the shear span (see Figure 3.16) can be expressed as:

$$V_{TL} \approx \frac{F_{TL}}{2} + \frac{G}{4}, \quad (4.3)$$

$$V_{BL} \approx \frac{F_{LC}}{2} + \frac{G}{4}. \quad (4.4)$$

These equations show that to keep symmetry in terms of shear force, symmetry must be kept between the top load  $F_{TL}$  and the total force  $F_{LC}$  in the rods connecting the concrete beam to the steel girder. This conclusion facilitated the testing because forces  $F_{TL}$  and  $F_{LC}$  were measured directly. Equations (4.3) and (4.4) would be exact if the yokes and the concrete beyond the supports had no weight. Equation (4.4) can be used only if the contact between the specimen and the rollers has been overcome.

#### 4.1.3 Zürich data

The Zürich targets can be connected to form a “truss” consisting of horizontal, vertical, and diagonal members (see Figure 3.13). The elongation/shortening of the “truss” members is obtained by subtracting their measured initial lengths from the measured lengths at the load stage of interest. The principle of virtual work was used to obtain the displacements of each target in the horizontal and vertical directions and to draw the deformed shape of the grid. Note that the “truss” shown in Figure 3.13 includes only one diagonal in each square of the grid. Calculations with the other set of diagonals showed that the choice of diagonal readings has little effect on the final results. Having the displacements of the targets, the average linear strain between any two of them can be calculated from simple geometrical relations.

In order to calculate the strain distribution over the grid, each of its triangles was treated as a three-node finite element with two degrees of freedom at each node and linearly varying displacements over the element’s area. The strains within each element are constant and their values were obtained by imposing the displacements from the “truss” analysis to the vertices of the finite elements. Compatibility equations were used to calculate the principal strains and their directions.

The above procedure was developed by the author for the purpose of this investigation and has been found to be a valuable tool for studying the deformations of the tested beams.

#### 4.1.4 LVDT data

LVDTs TV and BV had very close readings which were averaged to obtain the vertical mid-span displacement of the beams. The rest of the LVDTs were used to calculate average linear strains over their gauge lengths (see Figure 3.14). The average strains are equal to the displacement readings from the LVDTs divided by the gauge lengths. The strains from the four sets of three LVDTs were further processed to obtain the average principal strains and their directions by using compatibility equations.

#### 4.1.5 Strain gauges

The readings from the strain gauges had units of  $\mu\epsilon=(Strain\times 10^{-6})$  and no further processing was needed.

#### 4.1.6 Sign convention for loads and displacements

The top load and the downwards mid-span displacement are considered positive throughout this thesis. Inversely, the bottom load and the upwards mid-span displacement are considered negative.

## 4.2 TEST L0M

### 4.2.1 Global behaviour

The global behaviour of specimen L0M is demonstrated in Figure 4.1 and Figure 4.2. Figure 4.1 contains the “top load vs. mid-span displacement” plot with indicated load stages and important events. The four pages of Figure 4.2 show the crack patterns and the crack widths at each load stage as well as the change of deformed shape between each two consecutive load stages. The calculation of “incremental” deformed shapes is suggested by the author as an appropriate approach for illustrating the progress of deformations with increasing load. The last two plots in Figure 4.2 show the deformed shape of the specimen at the last load stage and a photograph of the beam taken after the test. The cracks depicted with thick lines are the cracks which formed during the load increment in question. All the deformed shapes are magnified to a mid-span displacement equivalent to 200 mm while the displacement measured by the vertical LVDT's is indicated at the bottom right corner of the plots as a fraction of the displacement at peak load  $\Delta_w$ . Thus only 6% of the total displacement was caused by the 350 kN applied between Load Stages 0 and 1, while 16% was caused by the 40 kN applied between Load Stages 6 and 7.

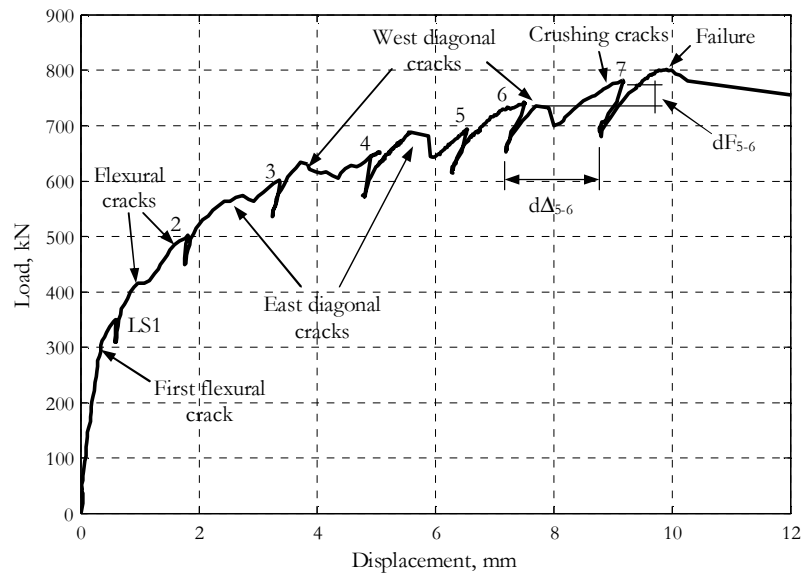


Figure 4.1 Load – displacement response - specimen L0M

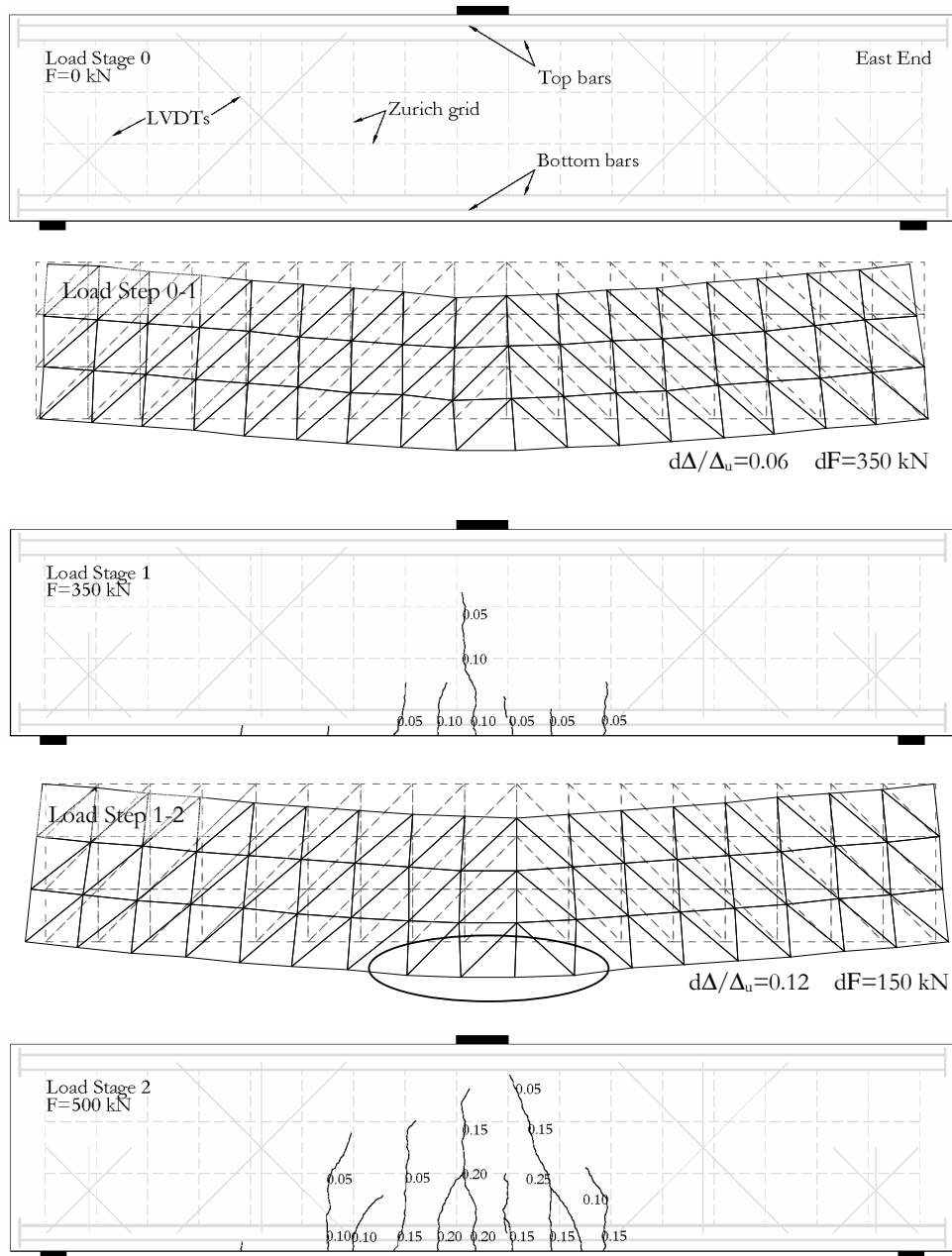


Figure 4.2 Cracks and deformed shapes - specimen L0M

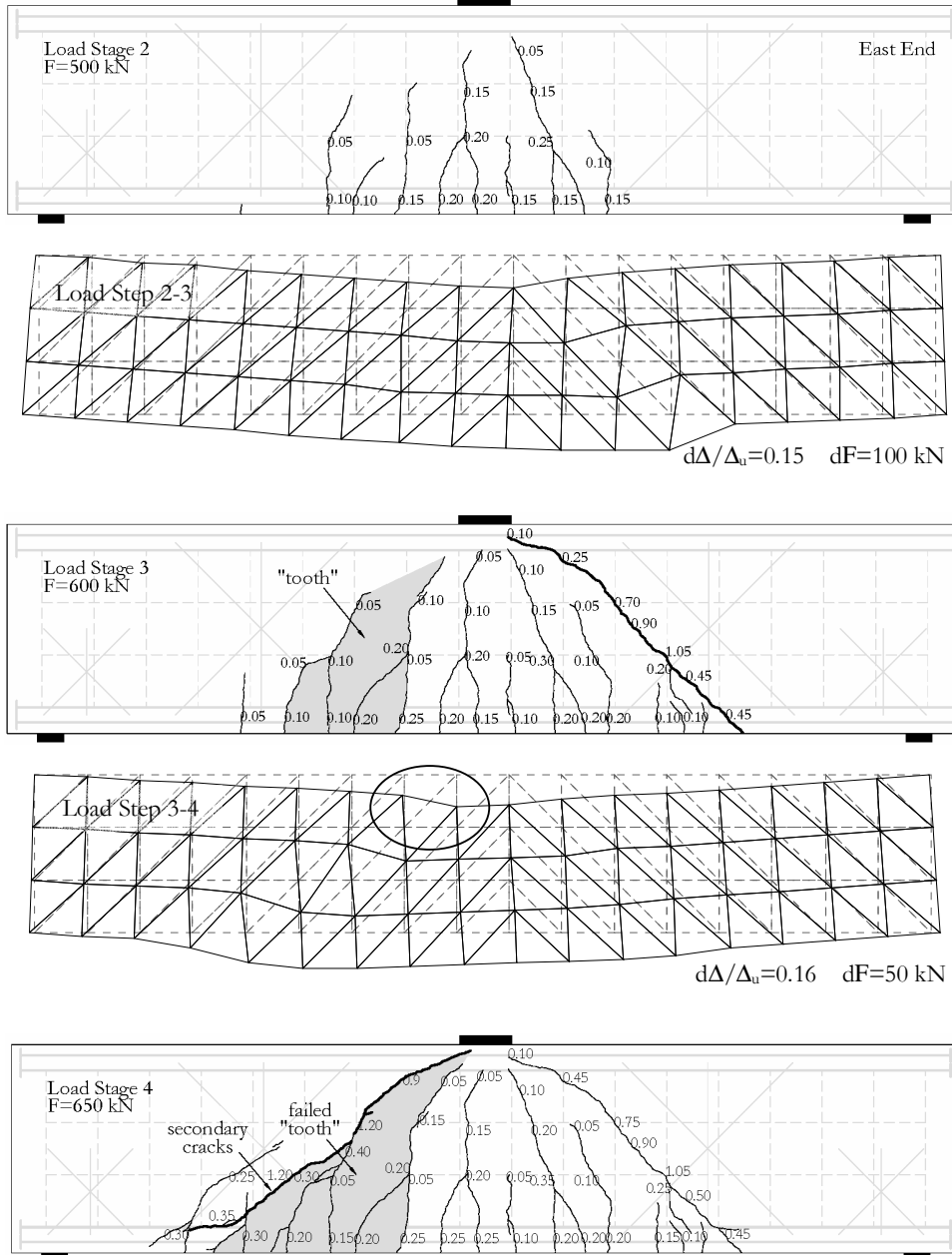


Figure 4.2 – cont



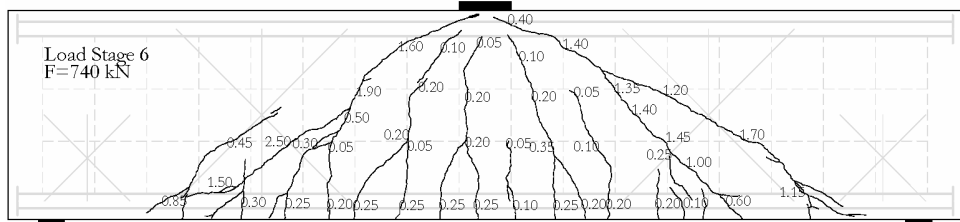
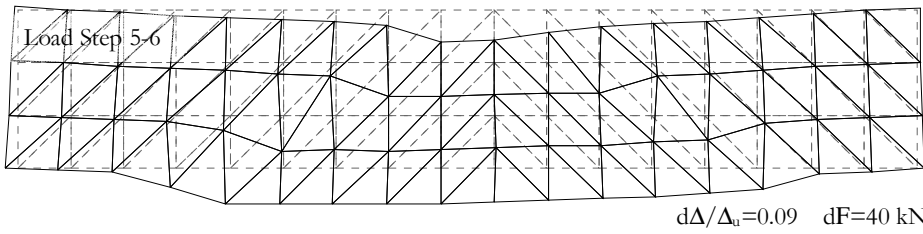
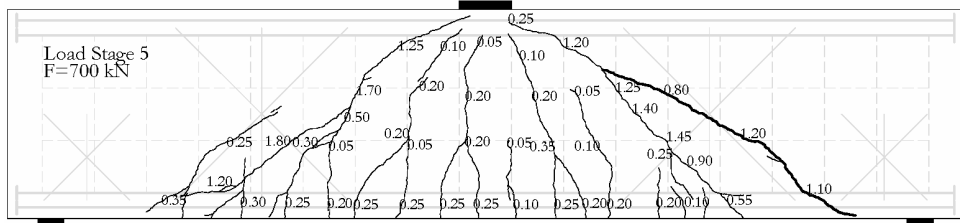
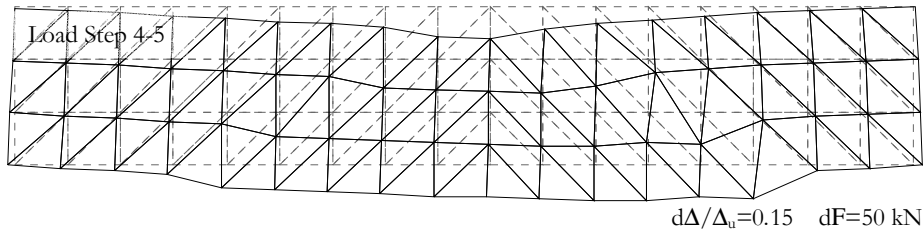
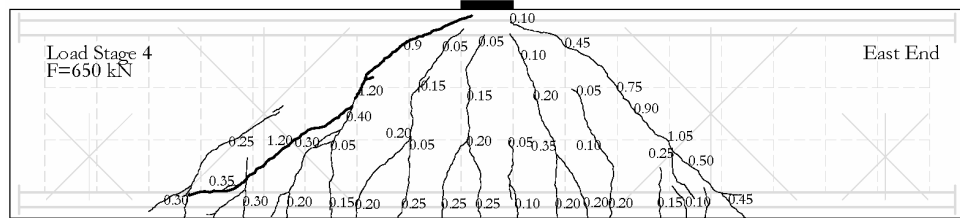


Figure 4.2 – cont

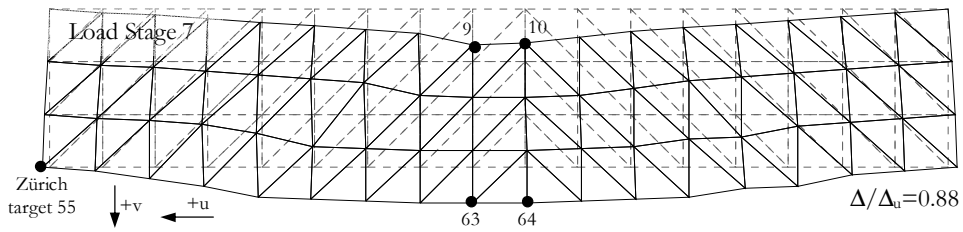
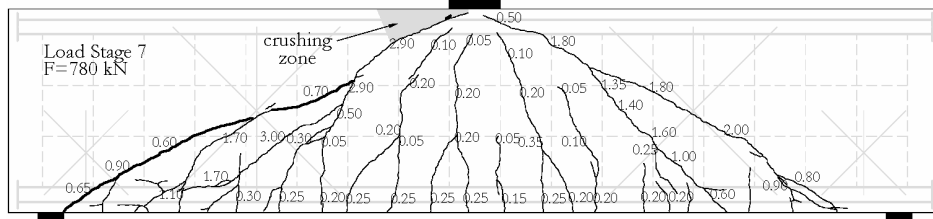
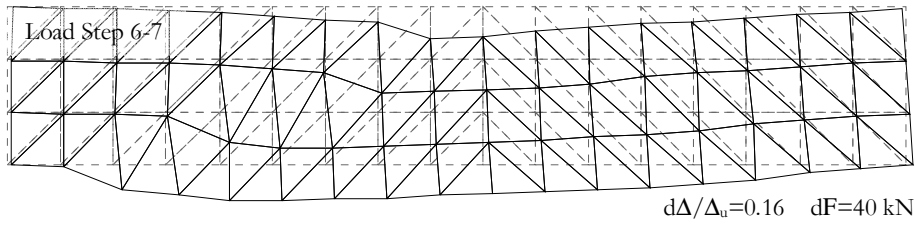
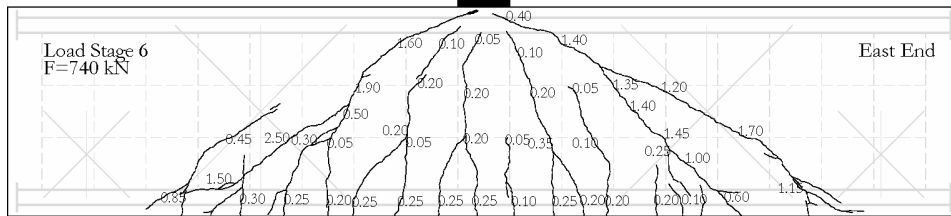


Figure 4.2 – cont

The force-displacement plot remained almost linear up to load of about 300 kN when the first flexural crack appeared at mid-span (see Figure 4.1 and Figure 4.2). The formation and propagation of flexural cracks continued with increasing load over the first two to three load steps. The deformed shape at this stage is characterized by a concentration of curvature in the cracked zone of the beam.

The first flexure-shear crack developed with a significant displacement increase at a load of about 575 kN on the east side of the specimen. It propagated from the flexural-tension side of the section at distance of about  $d$  from mid-span and penetrated the compression zone under the loading plate. Flatter secondary cracks were observed near the bottom reinforcement. A very similar crack occurred on the west side at a load of about 630 kN. The incremental deformed shape at this stage is characterized by a concentration of shear deformations along the diagonal cracks. Another pair of symmetrical cracks developed at 690 kN /720 kN on the east/west side, respectively. They run from near the inner edges of the supports plates and joined the previous inclined cracks near the top of the section. Secondary cracks were observed again with some of them were aligned with the longitudinal bars. Short cracks indicating concrete crushing were noticed at Load Stage 7 near the loading plate. They developed just under its west edge and were approximately parallel to the line connecting the west support and the loading point (see Figure 4.3a). The specimen failed at a load of 801.1 kN and a displacement of 10.0 mm along the most west diagonal crack with crushing at the compression zone near the loading plate (see Figure 4.3b) followed by a fast drop of resistance. A wide splitting crack propagated from the edge of the loading plate towards the west support above the critical shear crack.

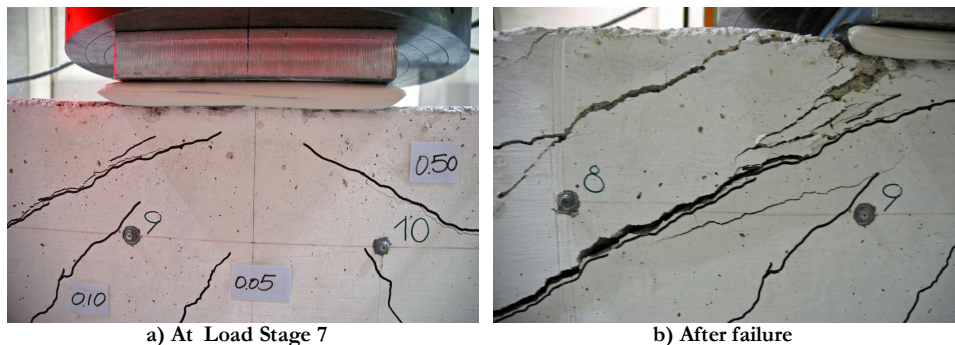


Figure 4.3 Crushing of concrete near loading plate – specimen L0M

The flexure-shear cracks were wider than the flexural cracks throughout the test. They were widest near the mid-depth of the section and reached 2-3 mm at Load Stage 7. No longitudinal splitting cracks were observed on the bottom face of the beam. The concrete

around the anchor heads and above the outer diagonal cracks remained uncracked as well.

The observed behaviour of specimen L0M can be explained in the following way. Initially the specimen behaves as a linear elastic body (see Figure 4.1). The maximum tensile stresses develop at the bottom side of the mid-span section associated with the maximum bending moment. The element cracks when the stresses exceed the tensile strength of the concrete. Vertical cracks propagate towards the loading plate (see Load Stage 1 in Figure 4.2). A free-body diagram of the reinforcement over the shear span shows that it is subjected to pulling force at mid-span and is free of force at the end. Consequently, its equilibrium in the horizontal direction is provided by the forces of interaction with the surrounding concrete (bond forces along the bar and/or direct compression upon the anchor heads) oriented predominantly towards the supports. The increasing bond forces cause formation of other vertical cracks at some distance from mid-span (see Load Stages 1 and 2 in Figure 4.2). The vertical displacement at this stage is caused mainly by elongation of the bottom reinforcement in the cracked middle zone of the beam (see Load Stages 0-1 and 1-2 in Figure 4.2).

The piece of concrete between any two major neighbouring cracks can be viewed as a cantilever or “tooth” fixed at the top part of the section (see Load Stage 3 in Figure 4.2). The bond force from the bottom reinforcement tends to bend the cantilever towards the mid-span section. The bending is restrained by the roughness of the cracks on both sides of the “tooth” (aggregate interlock) and by the shear resistance of the bottom reinforcement (dowel action). The stiffness of the aggregate interlock decreases with increasing width of the cracks because the slip needed to activate contact between the rough crack surfaces increases. The resistance of both actions decreases significantly when flat secondary cracks develop at the bottom part of the beam (see Load Stage 4 in Figure 4.2). This results in increased bending of the tooth and the crack on its tension side propagates towards the loading point. When the tip of this crack reaches the vicinity of the loading plate, the cantilever can be considered failed (see Load Stage 4 in Figure 4.2) and its resistance in terms of force acting on the bottom reinforcement drops drastically. At this moment the beam could be visualized without the failed “tooth” since it is almost free of stresses other than those associated with stabilization of the flexural-compression zone. The observed sudden displacement increase can be now explained by elongation of the “freed” longitudinal reinforcement and deformations of the concrete near the loading point under the action of diagonal compression (see Load Stage 3-4 in Figure 4.2).

Further load increase leads to failure of more cantilevers until the cracking reaches the support plates (see Load Stages 5 and 7 in Figure 4.2). The cracks are flatter near the ends of the beam partly because of the fanning compression from the support reactions (see

4.3.2 for further discussion on this issue). The loss of cantilevering action results in almost constant tension in the reinforcement along the shear span and therefore is equivalent to loss of beam action. The member can be again visualized without its cracked part. The load is now carried predominantly by arch action involving direct diagonal compression between the loading and support points as well as tension in the bottom reinforcement. The interaction between the reinforcement and the surrounding concrete is concentrated at the support zones. The zone above the diagonal cracks at the vicinity of the loading plate has become more slender and deformable and its crushing causes the failure of the beam (see Figure 4.3 and Load Stage 7 in Figure 4.2). Other potential failure mode involves concrete crushing above the diagonal cracks at the vicinity of the support plates (see Figure 2.4).

For the sake of convenience, the zone above the diagonal cracks at the vicinity of the loading plate will be called the critical loading zone.

#### 4.2.2 Kinematic model

A simple kinematic model for non-slender beams without transverse reinforcement similar to specimen L0M is proposed (see Figure 4.4). The model attempts to describe the deformed shape of the element prior to failure using just two input parameters (degrees of freedom): 1) the average strain in the bottom longitudinal reinforcement over the shear span,  $\epsilon$ , and 2) the shear deformation at the critical loading zone,  $\Delta$ .

The bottom reinforcement is represented by a horizontal deformable tie. The strains along the tie are assumed constant and equal to the first input parameter (degree of freedom). The concrete “teeth” are modeled by diagonal struts connected to the tie and joining together at the loading point. The hinges between the struts and the tie represent the bond between the concrete and the longitudinal reinforcement. The struts are assumed rigid in order to reflect the fact that the failed concrete cantilevers are almost free of stresses/strains. The hinge between the struts at the loading point symbolizes the flexible base of the “teeth”. The concrete above the diagonal cracks is represented by a body which has rigid and deformable parts. The rigid part models the intact concrete subjected to low stresses/strains while the deformable part accounts for the crushing of concrete at the critical loading zone and consists of a vertical sliding mechanism. The slip along the mechanism is equal to the second input parameter (degree of freedom) of the model. The sliding mechanism is oriented vertically because concrete crushing is characterized by sliding along planes at angle of approximately  $45^\circ$  to the direction of principal compression. Additionally, the top reinforcement is very stiff in the horizontal direction and much softer as a dowel in the vertical direction.

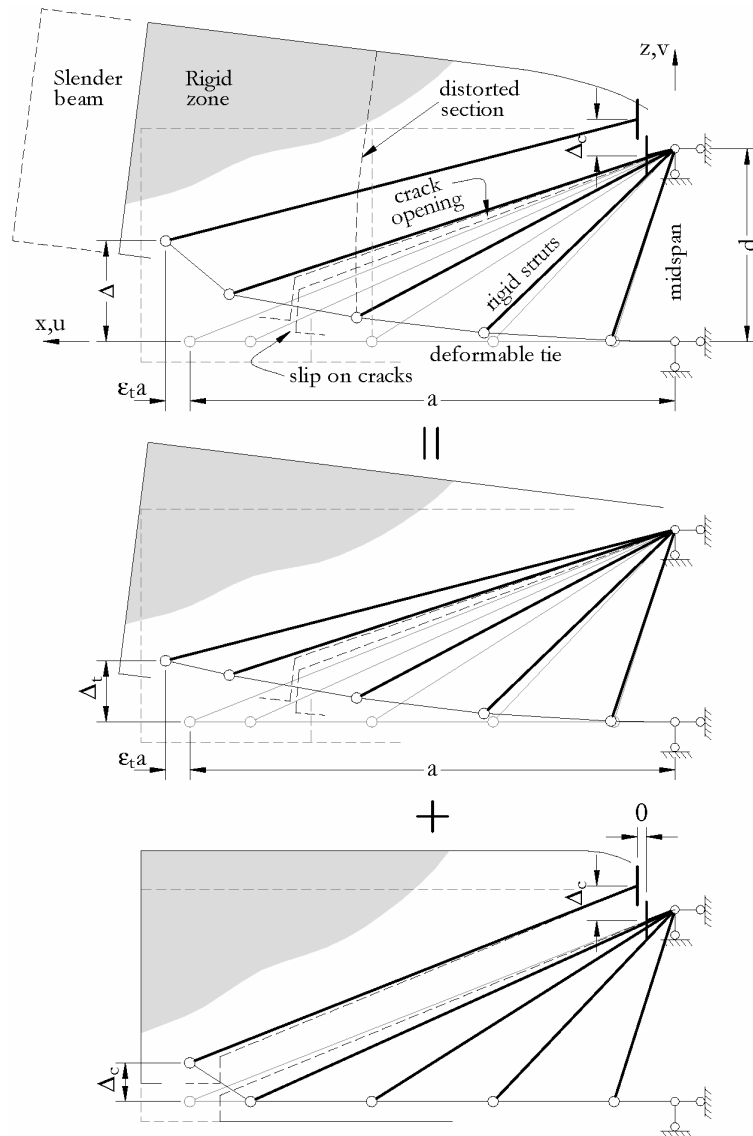


Figure 4.4 Kinematic model

The behaviour of the kinematic model can be more easily understood if the final deformation is reached in two steps (see the last two drawings in Figure 4.4). First, the tie lengthens while the sliding mechanism remains locked. At this stage the struts and the

rigid body rotate around the loading point. The relative rotation between neighbouring struts is associated with opening of the flat parts of the cracks near the mid-depth of the section and slip along the steep parts of the cracks near the bottom of the beam. It can be easily shown that both the opening and the slip increase when moving away from the mid-span section. Second, the sliding mechanism slips and the rigid body translates vertically causing additional opening and/or slip along the outer flexure-shear cracks. It should be noted that the cracks shown in Figure 4.4 are based on the assumption of rigid concrete “teeth”. In reality, the longitudinal reinforcement strains the surrounding concrete and causes closely-spaced narrow cracks at the bottom part of the element.

Based on the above assumptions, the following expressions for horizontal ( $u$ ) and vertical ( $v$ ) displacements can be derived:

- Bottom chord

$$u_{bot} = \varepsilon_t x \quad (4.5)$$

$$v_{bot} = \varepsilon_t \frac{x^2}{d_v} = \Delta_t \left( \frac{x}{a} \right)^2 \quad 0 \leq x < a \quad (4.6)$$

$$v_{bot} = v_{top} \quad x = a \quad (4.7)$$

- Top chord

$$u_{top} \equiv 0 \quad (4.8)$$

$$v_{top} = 0 \quad x = 0 \quad (4.9)$$

$$v_{top} = \frac{\varepsilon_t a}{d_v} x + \Delta_t = \Delta_t \frac{x}{a} + \Delta_t \quad 0 < x \leq a \quad (4.10)$$

where  $\Delta_t$  is the vertical mid-span displacement associated with elongation of the bottom chord.

The above equations show that the deformed shape of the bottom chord is parabolic while the top chord remains straight. If the mid-span displacement of the beam is known, the slip in the sliding mechanism can be obtained from equation (4.10) by setting  $x=a$  and  $v_{top}=\Delta$ :

$$\Delta_t = \Delta - \frac{\varepsilon_t a^2}{d_r} = \Delta - \Delta_t. \quad (4.11)$$

The kinematic model is now applied to the west shear span of specimen L0M at the last stage of loading. Input parameters  $\varepsilon$  and  $\Delta$  can be calculated from the experimentally-obtained deformed shape of the beam (see Load Stage 7 in Figure 4.2) by using the following simple geometrical relations and equation (4.11):

$$\begin{aligned} \varepsilon_t &= \frac{u_{55} - 0.5(u_{63} + u_{64})}{8.5 \times 300} = \frac{2.44 - 0.5(-0.269 - 0.607)}{2550} = 1130 \mu\varepsilon \\ \Delta &= \frac{v_{63} + v_{64}}{2} + \frac{0.5(u_9 + u_{10}) - 0.5(u_{63} + u_{64})}{3 \times 300} 8.5 \times 300 = \\ &= \frac{9.71 + 9.61}{2} + \frac{0.5(0.010 + 0) - 0.5(-0.269 - 0.607)}{900} 2550 = \\ &= 9.66 + 1.25 = 10.9 \text{ mm} \\ \Delta_t &= \frac{0.00113 \times 2550^2}{990} = 7.42 \text{ mm} \\ \Delta_t &= 10.9 - 7.42 = 3.48 \text{ mm} \end{aligned}$$

where  $u_i$  and  $v_i$  are the horizontal and vertical displacements of Zürich target  $i$  with positive directions denoted in Figure 4.2. Note that  $\Delta$  consists of two parts. The first part is equivalent to the mid-span displacement measured by the vertical LVDTs, while the second part comes from rotation of the middle section of the beam caused by unsymmetrical deformations in the two shear spans. According to Figure 4.1, the mid-span displacement at Load Stage 7 was about 9 mm which is slightly smaller than the 9.66 mm calculated above. This difference can be attributed to the fact that the displacement obtained from the deformed shape of the specimen is affected by errors in as many as 156 Zürich readings.

Figure 4.5 shows comparison between the displacements calculated from equations (4.5) to (4.10) and the corresponding experimental values. The horizontal displacements of the kinematic model agree very well with the test data. The negligibly small values along the top edge confirm that the sliding deformations near the loading point are oriented in a vertical direction. The match in terms of vertical displacements along the top chord of the beam seems reasonable as the theoretical and experimental results differ more significantly near the loading point. The kinematic model assumes that the whole deformation of the uncracked top part of the beam is concentrated between two Zürich targets while in reality it is spread over a longer area (see Load Stage 7 in Figure 4.2). The



match in terms of vertical displacements along the bottom chord is almost perfect over the inner half of the shear span but is unsatisfactory near the supports. This shows that the outer diagonal struts shorten significantly, engaged by the top part of the beam in its vertical translation. The shortening is related to diagonal compression forces in the cracked concrete and indicates the existence of a load-bearing mechanism supplementing the discussed arch action.

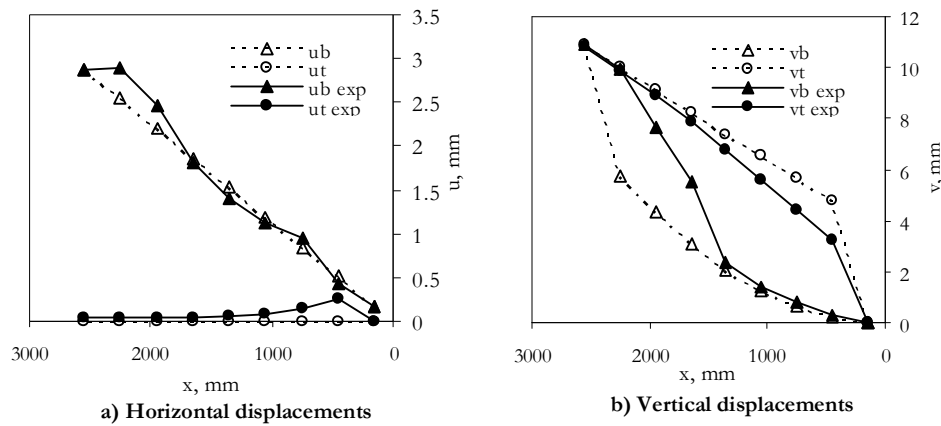


Figure 4.5 Displacements – west side of specimen L0M, Load Stage 7

It is worthwhile to note that the kinematic model reflects the fact that plane sections in deep beams do not remain plane. Figure 4.4 shows a distorted cross section with shape very similar to the experimentally-obtained shapes (see Load Stage 7 in Figure 4.2).

Figure 4.4 also indicates that the model could be extended for application to longer beams, or to non-slender beams at early stages of loading when the flexure-shear cracks have not reached the support plates. This could be done by introducing the cracked length along the bottom chord as a third input parameter.

#### 4.2.3 Chord strains

Figure 4.6 shows the flexural strains obtained from LVDTs BH and TH (see Figure 3.14). The plot of load vs. average bottom strain resembles very much a plot of axial force vs. average strain of a reinforced concrete element subjected to pure tension. It can be seen that the first cracking took place at load of about 300 kN. Assuming that plane sections remained plane and that the concrete and the steel behaved linearly, the cracking flexural stress at the bottom face of the beam equals 3.3 MPa which agrees well with the experimentally-obtained modulus of rupture of 3.7 MPa (see 3.2.3.1). The straight line

under the experimental curve is obtained by neglecting the tension stiffening effect and assuming that the lever arm of the internal forces at the mid-span section is approximately  $0.95d=998$  mm. The plot of load vs. average top strain has the expected shape up to a load of about 575 kN when the strain starts switching from compressive to tensile. The negative strains are not surprising since LVDT TH is located at the flexural compression side of the section. The tensile strains, on the other hand, are caused by diagonal cracks penetrating the compression zone under the loading plate (see Figure 4.2).

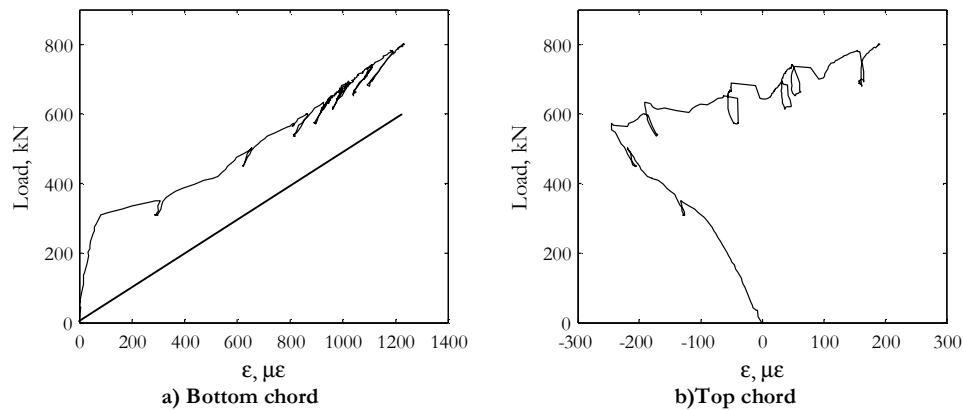


Figure 4.6 Flexural strains – specimen L0M

Figure 4.7 shows the variation of the bottom-chord strains along the span of the specimen. Plot a) shows the results from the strain gauges (see Figure 3.15). The gauges measure local steel strains and their values depend to a large extent on the position of the gauge with respect to cracks. The closer the gauge is to a crack, the higher the steel strain. The variation of the strain profile with increasing load shows clearly how the load-bearing mechanism transforms from beam action (triangular profile) towards arch action (constant profile). The readings from the two most western gauges indicate that the anchor heads were not activated and that the anchorage of the reinforcement was provided almost entirely by bond over a length of just 270 mm. The high effectiveness of the bond could have partly resulted from the clamping stresses from the support reaction which reached a magnitude of 6.7 MPa at failure. Plot b) shows the results from the Zürich readings (see Figure 3.13) at the last load stage. These readings measure average concrete strains over lengths of 300 mm and their values depend to a large extent on the number of cracks located within the gauge length. The larger the number of cracks, the higher the average strain. The horizontal line on the plot represents the average strain over the west shear span. Its value was used earlier as an input for the kinematic model. Both plots in Figure 4.7 indicate that the maximum strains occurred at some distance

from the inner edges of the support plates. An attempt to explain this observation is made in Chapter 5.

The values of the bottom-chord strains in Figure 4.6a) and Figure 4.7 show that the reinforcement was far from yielding. The maximum steel strain is close to  $1800 \mu\epsilon$  which is significantly less than the  $3260 \mu\epsilon$  yield strain.

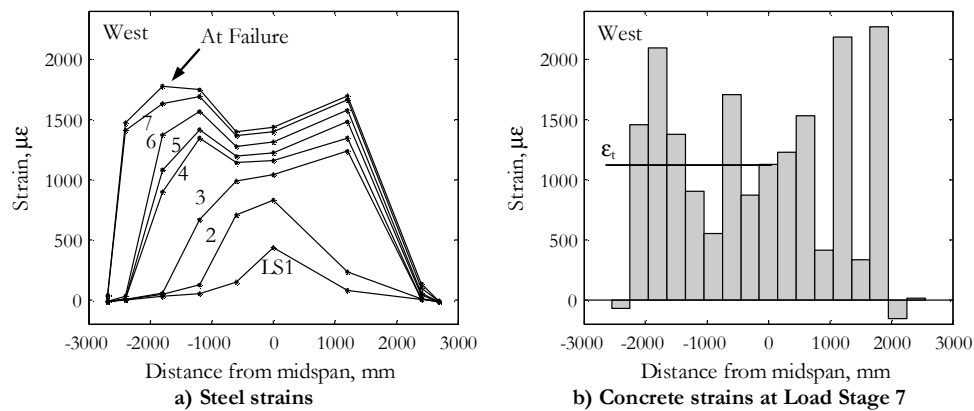


Figure 4.7 Bottom-chord strains – specimen L0M

Figure 4.8 has the same format as Figure 4.7 but shows the variation of the top-chord strains. The readings from the strain gauges show that up to the third load stage the steel strains were increasingly compressive with approximately a triangular profile over the span. Gauge 5T seemed damaged since it measured very high strain at a load of 50 kN compared to the strain increments corresponding to the following load steps of 50 kN. After Load Stage 3 the gauges located away from the mid-span section measured decreasing compression and even tension in the top reinforcement. This behaviour is consistent with transition from beam action to arch action. The beam mechanism is associated with bending and the top strains follow the shape of the moment diagram. The arch mechanism, on the other hand, is characterized by direct diagonal compression which is accompanied by tension along the vertical and horizontal sides of the uncracked “triangular” blocks of the beam. The Zürich readings agree relatively well with the strain-gauge readings since the compatibility between concrete and steel strains is valid in the absence of cracks. An exception is the mid-span location where the Zürich gauges detected diagonal cracks penetrating in the compression zone. The compressive strains were relatively small ( $<400 \mu\epsilon$ ) since the axis of the top chord is located at 150 mm below the top edge of the specimen where crushing took place (see Figure 4.3).

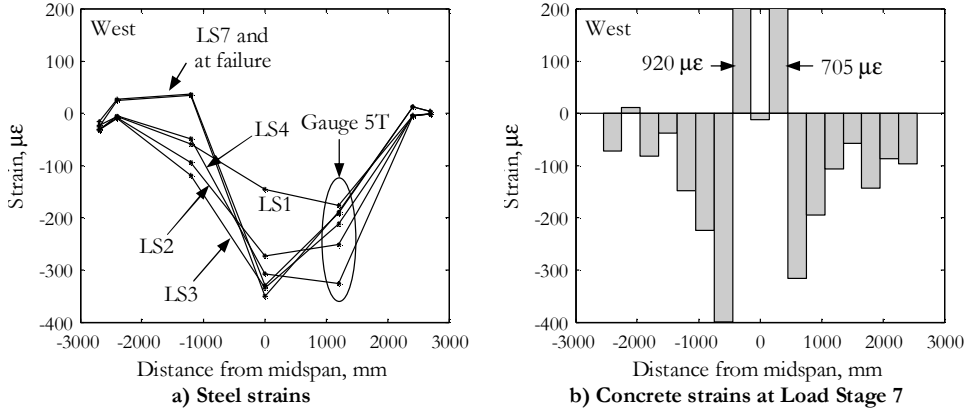


Figure 4.8 Top-chord strains – specimen L0M

#### 4.2.4 Web strains

Figure 4.9 shows the results from the two sets of three LVDTs located at the middle of the shear spans and covering the chord-to-chord depth (effective shear depth) of the beam (see Figure 3.14). The top two plots illustrate the relation between the top load and the strains along the measuring devices. The strains measured prior to diagonal cracking are consistent with linear elastic behaviour: the  $135^\circ$  diagonals lengthen, the  $45^\circ$  diagonals shorten, and the verticals remain almost undeformed. On the other hand, the strains measured after the development of cracks along the entire bottom chord of the beam can be explained by the kinematic model (see 4.2.2). The top ends of the LVDTs are located on the rigid part of the model while the bottom ends - on the tie. The following expressions can be then derived:

$$\epsilon_{45} = \frac{v_{top}(a/2 - d_v/2) - v_{bot}(a/2 + d_v/2) + u_{bot}(a/2 + d_v/2)}{2d_v}, \quad (4.12)$$

$$\epsilon_{90} = \frac{v_{top}(a/2) - v_{bot}(a/2)}{d_v}, \quad (4.13)$$

$$\epsilon_{135} = \frac{v_{top}(a/2 + d_v/2) - v_{bot}(a/2 - d_v/2) - u_{bot}(a/2 - d_v/2)}{2d_v}, \quad (4.14)$$

where  $u_{bot}$ ,  $v_{bot}$ , and  $v_{top}$  are given by (4.5) - (4.10). The above equations will be now applied to the west shear span of specimen L0M at the last stage of loading. As shown in subsection 4.2.2, the input parameters  $\epsilon_i$  (average strain in the bottom longitudinal

reinforcement over the shear span) and  $\Delta_c$  (shear deformation at the critical loading zone) have values of 1130  $\mu\epsilon$  and 10.9 mm, respectively, while  $\Delta_b$  (mid-span displacement coming from elongation of the bottom chord) equals 7.42 mm.

Considering equations (4.1), (4.2), and (4.6):

$$u_{bot} = 0.00113x, \text{ mm}$$

$$v_{bot} = 7.42 \times \left( \frac{x}{2550} \right)^2 = 1.141 \times 10^{-6} x^2, \text{ mm}$$

$$v_{top} = \frac{7.42x}{990} + 3.48 = 0.00291x + 3.48, \text{ mm}$$

By substituting the above expressions into equations (4.12), (4.13), and (4.14):

$$\epsilon_{45} = \frac{0.00291 \times 780 + 3.48 - 1.141 \times 10^{-6} \times 1770^2 + 0.00113 \times 1770}{2 \times 990} = 0.0021 = 2100 \mu\epsilon$$

$$\epsilon_{90} = \frac{0.00291 \times 1275 + 3.48 - 1.141 \times 10^{-6} \times 1275^2}{990} = 0.00538 = 5380 \mu\epsilon$$

$$\epsilon_{135} = \frac{0.00291 \times 1770 + 3.48 - 1.141 \times 10^{-6} \times 780^2 - 0.00113 \times 780}{2 \times 990} =$$

$$= 0.00356 = 3560 \mu\epsilon$$

The results from the above calculations are shown in the last column of Table 4.1 together with the corresponding strains measured by the LVDTs. The table contains also results for the east shear span of specimen L0M at load stages 5, 6, and 7. The last three rows show the experiment-to-prediction ratios for the four considered cases. It can be seen that the agreement along the verticals and along the 135° diagonals is reasonably good. The kinematic model overestimates the tensile strain along the 45° diagonal because, as discussed in 4.2.2, it neglects the compressive strains along the flat diagonal struts.

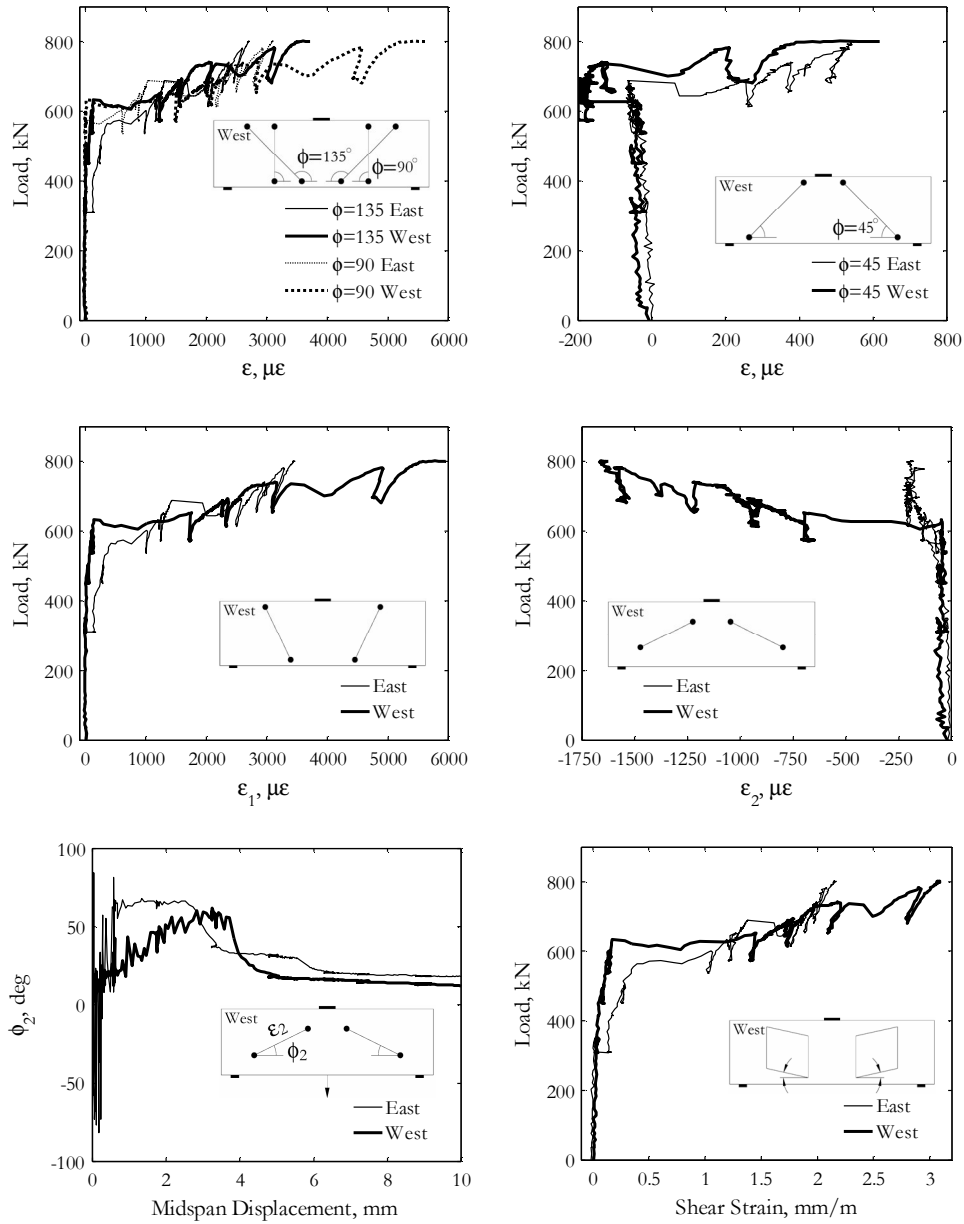


Figure 4.9 Strains in the web at mid shear span – specimen L0M

Table 4.1 Web strains and kinematic model – specimen L0M

	Quantity	LS 5 East side	LS 6 East side	LS 7 East side	LS 7 West side
Input from Zürich readings	$\epsilon_s$ ( $\mu\epsilon$ )	904	1004	992	1130
	$\Delta$ , (mm)	7.14	8.16	8.43	10.9
Kinematic Model	$\Delta_t$ , (mm)	5.94	6.59	6.51	7.42
	$\Delta_c$ , (mm)	1.20	1.57	1.92	3.48
	$\epsilon_{45}$ , ( $\mu\epsilon$ )	887	1106	1276	2100
	$\epsilon_{90}$ , ( $\mu\epsilon$ )	2712	3253	3582	5380
	$\epsilon_{135}$ , ( $\mu\epsilon$ )	2051	2398	2553	3560
LVDT readings	$\epsilon_{45}$ , ( $\mu\epsilon$ )	260	370	480	280
	$\epsilon_{90}$ , ( $\mu\epsilon$ )	2190	2500	2800	4520
	$\epsilon_{135}$ , ( $\mu\epsilon$ )	2050	2270	2460	3070
Ratio of LVDT values to model values	$\epsilon_{45}$ ratios	0.29	0.33	0.38	0.13
	$\epsilon_{90}$ ratios	0.81	0.77	0.78	0.84
	$\epsilon_{135}$ ratios	1.00	0.95	0.96	0.86

The principal strains, the direction of principal compression, and the shear strains were used to generate the bottom four plots in Figure 4.9. It can be immediately noticed that the principal compressive strain on the west side of the beam reaches values as high as -1600  $\mu\epsilon$  indicating concrete crushing over the web at the middle of the shear span. This result seems unrealistic considering the observed behaviour and failure mode (see 4.2.1). The reason for the inconsistency is that the principal strains were obtained from the measured diagonal and vertical strains through compatibility equations. The conditions for strain compatibility are based on the assumption that the horizontal and the vertical displacements of the points from a deforming body vary linearly in the two orthogonal directions. In other words, a square from an undeformed body transforms into parallelogram when deformations take place. This is graphically demonstrated in the middle drawing of Figure 4.10 by using the measured strains at the last load stage multiplied by a factor of 100. The strain along the 45° diagonal is relatively small and was neglected for convenience. The transformation from square to parallelogram can be subdivided into two stages. First, the two diagonals and the vertical are scaled to their deformed lengths and “pinned” together at their midpoints. Second, the diagonals are rotated around the “pin” such that their ends and the end points of the vertical form a parallelogram. The resulting shape shows that the vertical extension to  $\epsilon_{90}=0.45$  was obtained at the expense of significant shortening in the horizontal direction and therefore significant principal compressive strain. The last drawing in Figure 4.10 is aimed to represent what really happened in the web of specimen L0M. The deformed diagonals

and the vertical are arranged such that the top and bottom horizontal strains correspond approximately to the values obtained from the Zürich readings at the last load stage. The resulting shape resembles the experimentally-obtained deformed shape of the beam (see Load Stage 7 in Figure 4.2) and shows that the strains in all directions are mostly tensile. A comparison between the second and the third drawing in Figure 4.10 clearly shows that the application of compatibility equations over the entire depth of a beam can lead to misleading results.

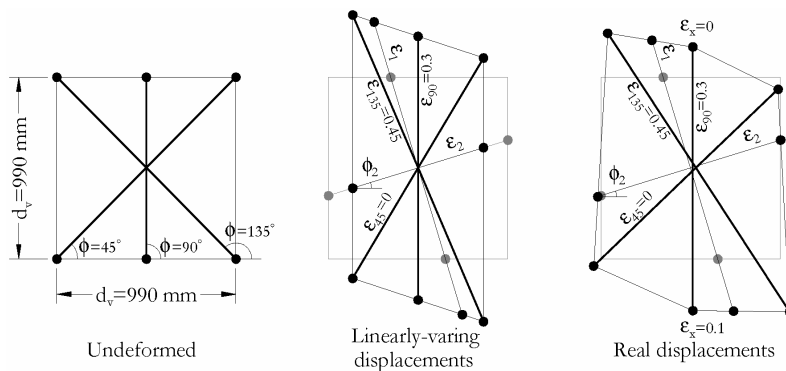


Figure 4.10 Linearly-varying versus real web displacements – west side of specimen L0M at Load Stage 7

Figure 4.11 shows web strains between targets from the Zürich grid. The top left drawing confirms the conclusion that the diagonal compressive strains at the middle of the shear span were relatively low. The bottom left drawing shows the strains along lines fanning from the loading point. They are compressive and almost monotonically increasing from zero at mid-span to about  $-600 \mu\epsilon$  along the flattest diagonals. These values could be considered as consisting of three components: a strain associated with opening of cracks, a strain associated with slip on cracks, and a strain coming from deformations of the concrete between the cracks. The strains along lines 41-58 and 42-59 indicate that the last component contributed with compressive strain of the order of  $-200 \mu\epsilon$ . These results demonstrate once again that the arch action is accompanied by a load-bearing mechanism which relies on diagonal compression through the cracked part of the beam. The plot on the right side of Figure 4.11 shows the variation of the average strain along line 9-56 with increasing load. It can be seen that the strain switches from slightly tensile to compressive at a load of about 600 kN. This is another way of spotting the transition from beam action characterized by bending to arch action characterized by direct diagonal compression.



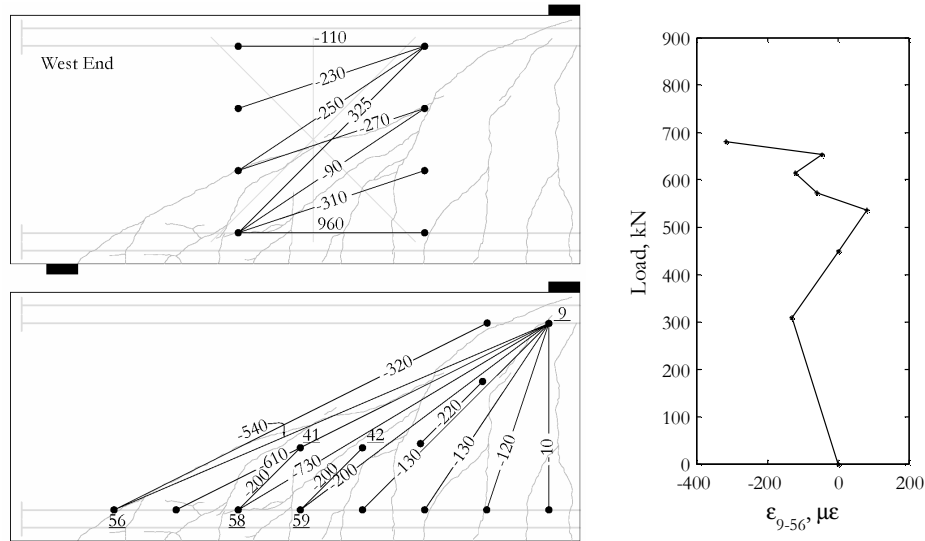


Figure 4.11 Diagonal web strains – specimen L0M at Load Stage 7

Figure 4.12a) shows the orientation of the principal compressive strains over the Zürich grid at the last load stage. The compression “flows” from the loading point towards the supports in accordance with the arch action. Plots b), c), and d) in the same figure show the distribution of the principal tensile strains, principal compressive strains, and shear strains, respectively. The strain values over the cracked part of the beam should be looked at with caution since they depend to a large extent on the cracks running through the triangle in question. For example, the tensile strain within the top triangle on row 2 column 7 is  $16913 \mu\epsilon$ . This value is extremely large if interpreted as an average strain of cracked concrete and is caused by two wide cracks crossing the triangle. Another example is the compressive strain within the bottom triangle on row 3 column 4. Its value is  $-1354 \mu\epsilon$  which is slightly less than the strain at peak concrete stress. At the same time, as shown earlier, the strain in the concrete between the cracks in this zone is  $-200 \mu\epsilon$ . This discrepancy can be explained by slip on the cracks which appears as principal compression in terms of average strains. The strain values over the intact part of the beam are more meaningful. For example, the compressive strain within the top triangle on row 1 column 7 is  $-532 \mu\epsilon$ . This value is relatively high and consistent with the observed crushing at the west edge of the loading plate.

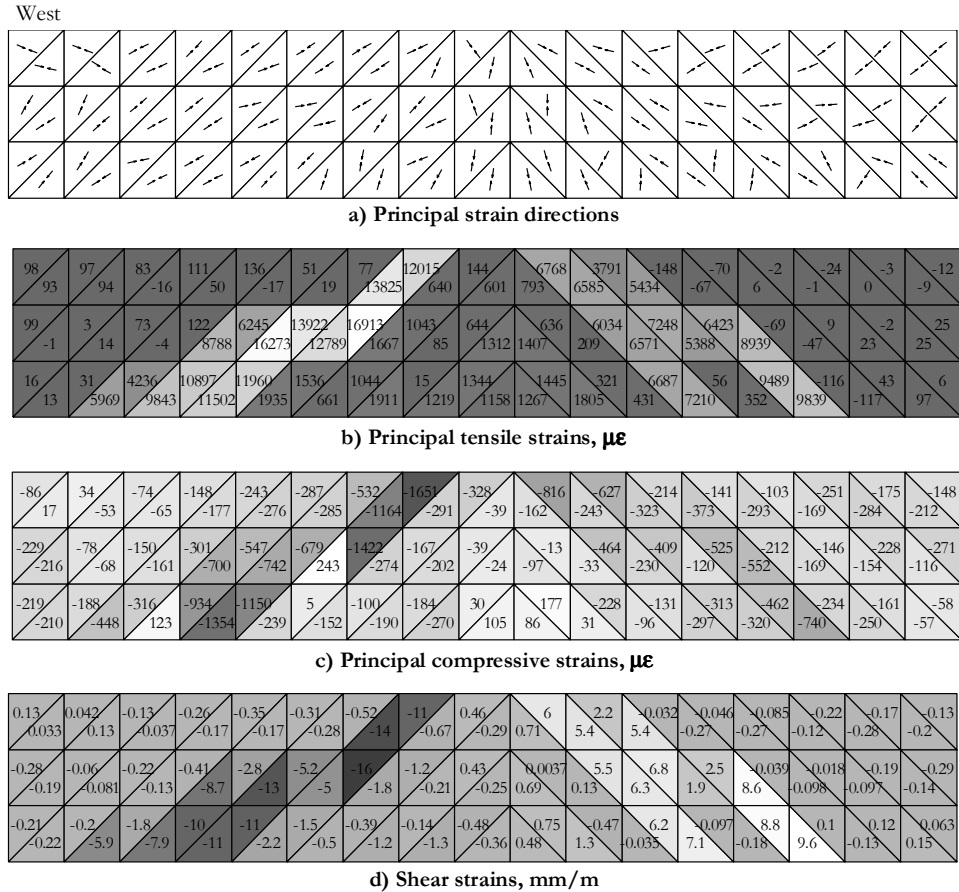


Figure 4.12 Local web strains – specimen L0M at Load Stage 7

Figure 4.13 shows the average strains measured over the verticals of the Zürich grid. As would be expected, the strains prior to diagonal cracking of the web were negligible. The beam started expanding transversally between Load Stages 2 and 3 when the first “tooth” failed on the east side of the loading point. The expansion continued with increasing load and approached the inner edge of the west support plate between Load Stages 6 and 7. The vertical strains under the loading plate and above the support plates remained practically zero. The kinematic model (see 4.2.2 and Figure 4.4) can be used once again for interpretation of the experimental results. The vertical  $\mu\epsilon$  strains can be expressed as:

$$\varepsilon_v = \frac{v_{top}(x) - v_{bot}(x)}{d_v} = \frac{\Delta_t}{d_v} \left[ \frac{\Delta_c}{\Delta_t} + \frac{x}{a} - \left( \frac{x}{a} \right)^2 \right], \quad (4.15)$$

where  $v_{top}$ ,  $v_{bot}$ , and  $\Delta_t$  are given by (4.5) - (4.10). The denominator of (4.15) is equal to the vertical dimension of the “loop” plotted in Figure 4.5b). The above equation was used to calculate the transverse strains in both shear spans of specimen LOM at the last stage of loading. The result is shown in Figure 4.13 with a broken line.

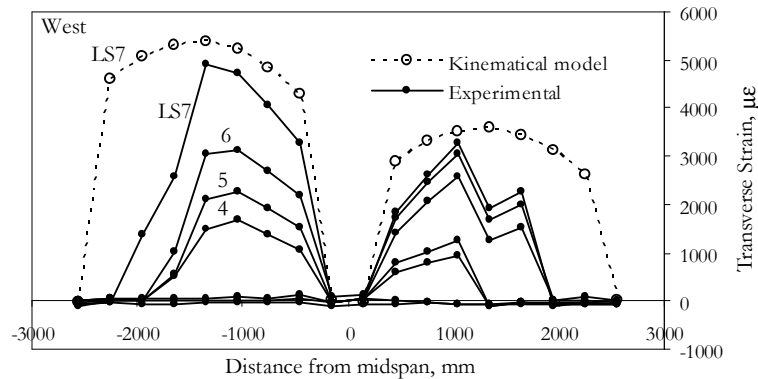


Figure 4.13 Transverse web strains – specimen LOM

#### 4.2.5 Support zone strains

Figure 4.14 shows the results from the two sets of three LVDTs located above the supports and spanning from the bottom chord to the centroidal axis of the beam (see Figure 3.14). The readings along the west 135° diagonal are practically zero up to load of about 720 kN when sudden extension is detected. This strain “jump” is caused by a diagonal crack which propagated from the inner edge of the support plate and crossed the gauge length of the measuring device (see Load Stage 7 in Figure 4.2). The readings along the east 135° diagonal remained negligible throughout the test because the cracking did not reach the east support plate. The 45° LVDTs are approximately aligned with the compression flow above the supports and measured very small negative strains at both ends of the specimen. This result however can not be used to draw firm conclusion about the compression demands on the concrete at those zones. The reason is that the compression stresses decrease very quickly when moving away from the support plates while the LVDTs measure average strain over relatively long gauge lengths. A similar comment could be made about the results from the Zürich readings at the same zones

(see Figure 4.12c). The strain history along the verticals is very similar to that along the  $135^\circ$  diagonals.

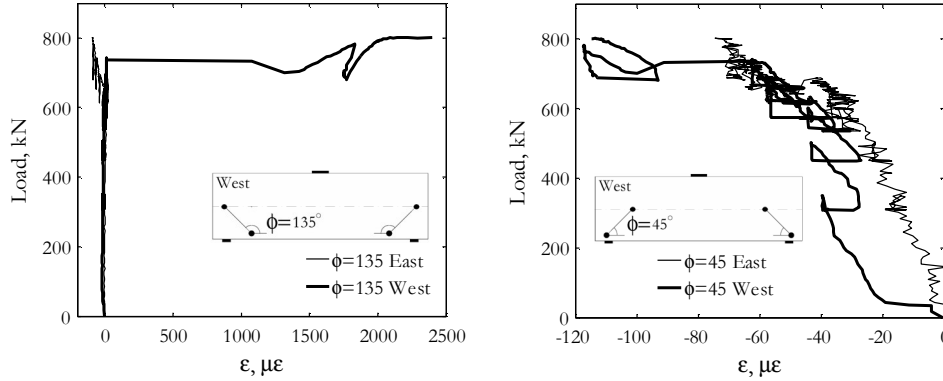


Figure 4.14 Support zone strains – specimen L0M

#### 4.2.6 Shear strength

As mentioned earlier, specimen L0M failed under a top load of 801.1 kN. Hence, from equation (4.3):

$$V_{u,exp} = \frac{801.1}{2} + \frac{63.4}{4} = 416.4 \text{ kN}$$

This result will be compared with the prediction of the CSA shear provisions. According to the procedure presented in 2.2.2.2, the strength prediction of the strut-and-tie model is calculated from:

$$\begin{aligned} V_{u,STM} &= 0.85 \times 29.1 \times 2x_u \times 400 / 1000 = 19.79x_u \text{ kN, mm} \\ &\leq 0.85 \times 29.1 \times 150 \times 400 / 1000 = 1484 \text{ kN} \end{aligned}$$

where  $2x_u = 2 \times \min(x_b, x_s, x_d, x_y)$  is the critical width of the top node regions (see Figure 2.13) with  $x_b$ ,  $x_s$ ,  $x_d$ , and  $x_y$  corresponding to limit on the horizontal stress in the bottom node regions, limit on the vertical stress in the bottom node regions, on the stress in the strut near the supports, and on the stress in the tie, respectively. The values of  $x_b$ ,  $x_s$ , and  $x_y$  are obtained from equations (2.3), (2.6), (2.7), and (2.11) as follows:

$$y_b = 0.441 \times 210 = 92.6 \text{ mm}$$

$$x_b = \frac{-(2275 + 150/2) + \sqrt{(2275 + 150/2)^2 + 4 \times 92.6 \times (1095 - 92.6)}}{2} = 38.9 \text{ mm}$$

$$x_p = 0.441 \times 150 = 66.2 \text{ mm}$$

$$y_y = \frac{3060 \times 652}{2 \times 0.85 \times 29.1 \times 400} = 100.8 \text{ mm}$$

$$x_y = \frac{-(2275 + 150/2) + \sqrt{(2275 + 150/2)^2 + 4 \times 100.8 \times (1095 - 100.8)}}{2} = 41.9 \text{ mm}$$

The value of  $x_d$  is calculated from equation (2.10) by using the following iterative procedure:

- 1) Assume value of  $x_d$ , say 30 mm.
- 2) Calculate  $V$ :

$$V = 19.79 \times 30 = 593.7 \text{ kN}$$

- 2) Calculate  $y_d$  from (2.4):

$$y_d = \frac{1095 - \sqrt{1095^2 - 4 \times 30 \times (2275 + 150/2 + 30)}}{2} = 69.6 \text{ mm}$$

- 3) Calculate  $T$  and  $\varepsilon_s$ :

$$T = 0.85 f_c' \times 2 y_d b = 0.85 \times 29.1 \times 2 \times 69.6 \times 400 / 1000 = 1377.2 \text{ kN}$$

$$\varepsilon_s = \frac{T}{E_s A_s} = \frac{1377200}{200000 \times 3060} = 2.25 \times 10^{-3}$$

- 4) Calculate  $\theta_s$ :

$$\cot \theta_s = T / V = 1377.2 / 593.7 = 2.32 \rightarrow \theta_s = 23.3^\circ$$

- 5) Calculate  $\varepsilon_1$  from (2.9):

$$\varepsilon_1 = \varepsilon_s + (\varepsilon_s + 0.002) \cot^2 \theta_s = 0.00225 + (0.00225 + 0.002) \times 2.32^2 = 0.0251$$

- 6) Calculate  $f_{cu}$  from (2.8):

$$f_{cu} = \frac{29.1}{0.8 + 170 \times 0.0251} = 5.74 < 0.85 \times 29.1 = 24.7 \text{ MPa}$$

- 7) Calculate  $m_f$ :

$$w_b = l_{b2} \sin \theta_s + b_a \cos \theta_s = 150 \times \sin 23.3^\circ + 210 \times \cos 23.3^\circ = 252 \text{ mm}$$

8) Calculate new value of  $x_d$  using the right hand side of (2.10):

$$x_d' = \frac{5.74 \times 252 \times \sin 23.3^\circ}{2 \times 0.85 \times 29.1} = 11.6 \text{ mm}$$

and return to step 2 with revised value of  $x_d = (30 + 11.6) / 2 = 20.8$  mm. The iteration process continues until  $x_d$  and  $x_d'$  converge to a single value. Summary of the iterations is presented in the table below.

$x_d$ (mm)	$y_d$ (mm)	V (kN)	T (kN)	$\epsilon_s$ ( $\mu\epsilon$ )	$\theta_s$ (deg)	$\epsilon_1$ ( $\mu\epsilon$ )	$f_{cu}$ (MPa)	$w_b$ (mm)	$x_d'$ (mm)
30	69.6	593.6	1377.9	2251	23.3	25157	5.73	252	11.6
20.8	47.0	411.2	930.3	1520	23.8	19535	7.06	253	14.6
17.7	39.7	349.9	785.1	1283	24.0	17807	7.60	253	15.8
16.8	37.5	331.5	741.9	1212	24.1	17303	7.78	253	16.2
16.5	36.9	326.3	729.7	1192	24.1	17160	7.83	253	16.3

As a result:

$$x_d = \min(38.9, 66.2, 41.9, 16.4) = 16.4 \text{ mm}$$

and

$$V_{u,STM} = 19.79 \times 16.4 = 324.6 \text{ kN} < 1484 \text{ kN}$$

Calculations analogous to those above and calculations based on the sectional model of the CSA code were performed for a series of cases obtained by varying the length of the shear span of specimen L0M. The results are shown in Figure 4.15. The node-crushing curve on the plot consists of constant and hyperbolic parts coming from the limits on the vertical and horizontal stresses in the support node region, respectively. The hyperbolic part of the curve is proportional to the yielding curve because the limit on the horizontal nodal stress does not depend on the  $a/d$  ratio. It can be seen that the controlling failure mode within the strut-and-tie model is strut crushing. The shear-strength curve is represented by the maximum among the strut-crushing curve and the sectional-model curve. Members within the covered range of  $a/d$  ratios are predicted to fail in shear, because the shear-strength curve has smaller ordinates than the flexural-yielding curve.

Finally, since specimen L0M is located on the left hand side of the intersection of the bottom curves in Figure 4.15:

$$V_{u,pred} = V_{u,STM} = 324.6 \text{ kN}$$

and

$$V_{u,exp} / V_{u,pred} = 416.4 / 324.6 = 1.28$$

The prediction of the CSA code implies that arch action would be activated prior to failure of specimen L0M. This conclusion agrees with the observed behaviour.

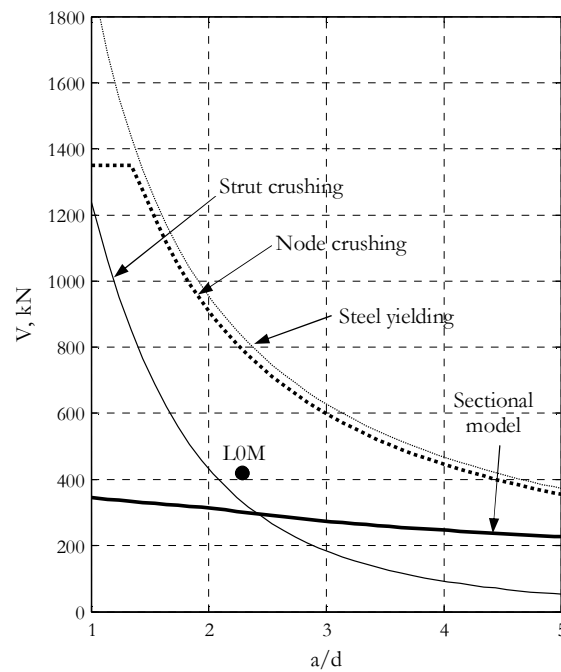


Figure 4.15 Experimental Strength vs. CSA code prediction— specimen L0M

### 4.3 SPECIMENS S0M/C, S1M/C, L0M/C, AND L1M/C

#### 4.3.1 Effect of transverse reinforcement – specimens L1M and L0M

Figure 4.16 shows the “top load vs. mid-span displacement” curves of specimens L1M and L0M while Figure 4.17 compares the crack patterns and crack widths of the two beams. The first and the last diagrams in Figure 4.17 show respectively specimens L0M and L1M just prior to failure. The middle diagram illustrates the cracked state of beam L1M under the failure load of beam L0M.

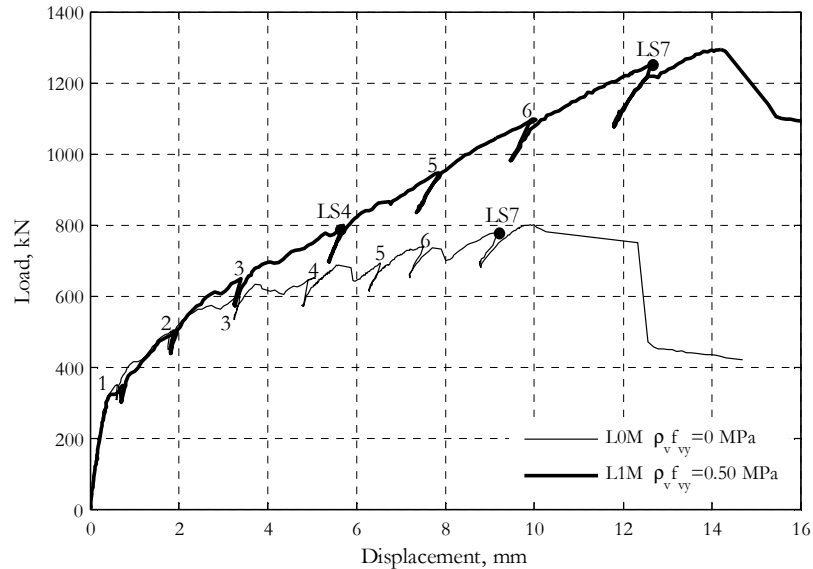


Figure 4.16 Load – displacement response - specimens L1M and L0M

Specimens L1M and L0M behaved almost identically up to first diagonal cracking (see Figure 4.16) after which L1M was noticeably stiffer. The flexure-shear cracks in specimen L1M appeared in a very similar order and with very similar shapes to those in L0M but propagated more gradually towards the loading point (see Figure 4.17). Specimen L1M developed its full crack pattern at a load of about 860 kN when a flat diagonal crack propagated from near the west support plate. The following load increase resulted in a gradual widening of the existing cracks until the beam failed at load of 1295.1 kN and a displacement of 14.2 mm. The failure mode involved crushing at the compression zone near the loading plate and was very similar to that of specimen L0M.



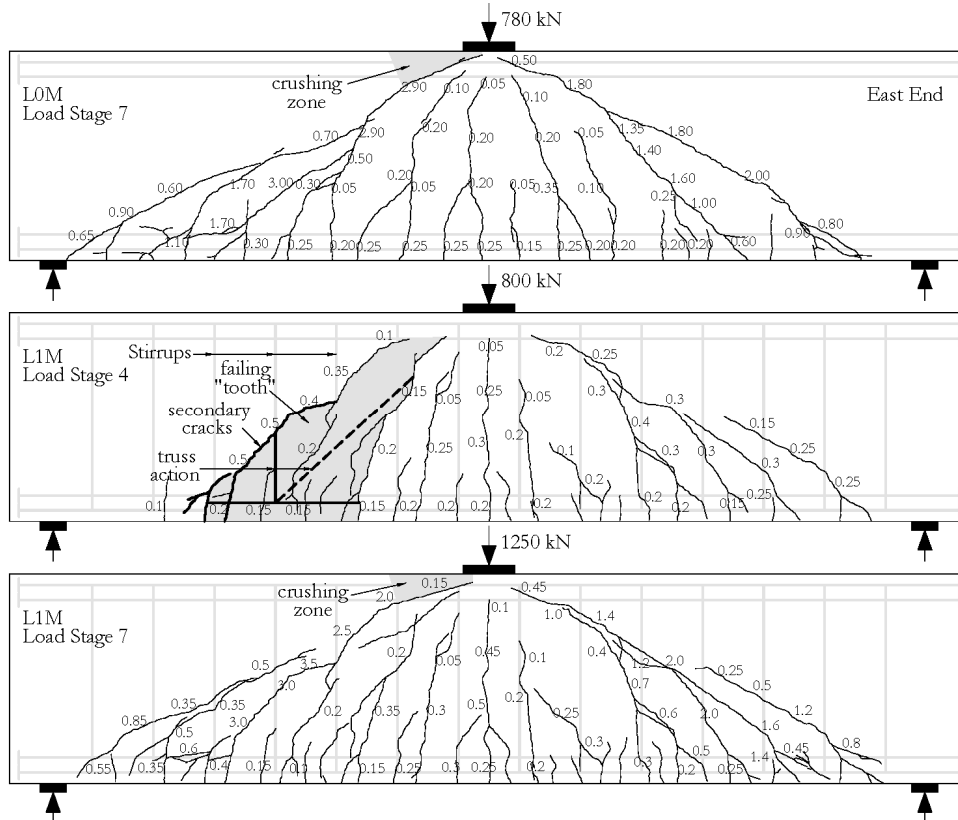


Figure 4.17 Cracks – specimens L1M and L0M

The observed behaviour of specimen L1M and its differences from that of specimen L0M can be explained as follows. In the uncracked stage and in the phase of flexural cracking the transverse reinforcement has no influence on the element behaviour because it does not cross cracks and because its stiffness is significantly smaller than the stiffness of the surrounding concrete. The stirrups become effective when a concrete cantilever (or “tooth”) starts to fail (see Figure 4.17). The vertical cracks turn towards the loading plate and flat secondary cracks develop in the bottom part of the beam. Their propagation is restrained by the stirrups and the “tooth” fails more gradually as compared to the “teeth” of specimen L0M. The loss of cantilevering action is followed by the formation of a truss-type load-bearing mechanism which involves diagonal compression in the cracked concrete and tension in the transverse reinforcement. Its capacity is dictated by the yield capacity of the stirrups. The truss action results in reduced tension in the longitudinal reinforcement beyond the failed concrete cantilever and delays the following “teeth”

failures (compare Load Stage 4 of specimen L1M and Load Stage 7 of L0M in Figure 4.17).

Further load increase leads to failure of more cantilevers until the cracking reaches the support plates (see Load Stage 7 of specimen L1M in Figure 4.17) and the truss action gets fully activated. Figure 4.18 shows the arch action in specimen L0M and the truss action in specimen L1M under the maximum measured top loads. The self weight of the beams is neglected. The complete truss action consists of diagonal compression through the cracked concrete, yield tension forces in the stirrups ( $2A_s f_{ty} = 2 \times 70 \times 490 = 68.6$  kN), arching compression in the uncracked top part of the beam, and varying tension along the bottom reinforcement. The fanning compression crosses steep cracks and therefore relies on aggregate interlock at the crack faces. The deformability of the truss mechanism is less than that of the arch mechanism for three reasons. First, the tensile deformations along the bottom chord are not constant along the shear span but decrease away from the mid-span section. Second, the critical loading zone is subjected to smaller compression and deforms less for a given applied load. And third, the line of thrust in the uncracked part of the beam is shifted upwards resulting in reduced tensile deformations along the top edge. There are also three reasons for why the load-bearing capacity of the truss mechanism is larger than that of the arch mechanism. First, the compression demands on the support zones and on the critical loading zone are reduced. Figure 4.18 demonstrates that the crushing of the critical loading zones of specimens L1M and L0M took place under similar forces (1135.8 kN for L1M vs. 987.4 kN for L0M) but the applied load on specimen L1M was significantly higher (1295.1 kN vs. 801.1 kN). The small difference between the strut crushing forces could be associated with geometrical differences between the two crushing zones and difference in the concrete strengths of the beams (37.8 MPa for specimen L1M vs. 29.1 MPa for L0M). Second, the compression softening effect at the support zones is also reduced as a result of less tension in the longitudinal reinforcement and a steeper slope of the compression flow (see 2.2.2.2). And third, the stability of the uncracked top part of the beam is improved due to the shifted line of thrust.

Specimen L1M has a low percentage of transverse reinforcement ( $\rho_t = 0.001 < f_{ti}/f_{ty} = 0.004$ ) and the stirrups yielded almost simultaneously with the development of diagonal cracks. This is one reason they were not able to alter significantly the crack pattern observed in specimen L0M. The above analysis would be different if specimen L1M was heavily reinforced in transverse direction. The specimens of Alcocer and Uribe (see 2.1.2), for example, had stirrups with ratio of 0.53% which resulted in closely-spaced diagonal cracks and relatively uniform distribution of damage over the shear span (see Figure 2.11).

It is important to note that the load-bearing capacity of specimens with transverse reinforcement is less sensitive to the depth and the shape of the critical loading zone

because its shear capacity constitutes just part of the shear capacity of the beam. The balance of vertical forces at a section close to the loading plate of specimen L1M shows that only 46.8% of the ultimate shear force was carried above the critical diagonal crack. In the case of members with large amounts of stirrups the failure of the beam can be triggered by crushing of the concrete under the critical crack (see Figure 2.4b).

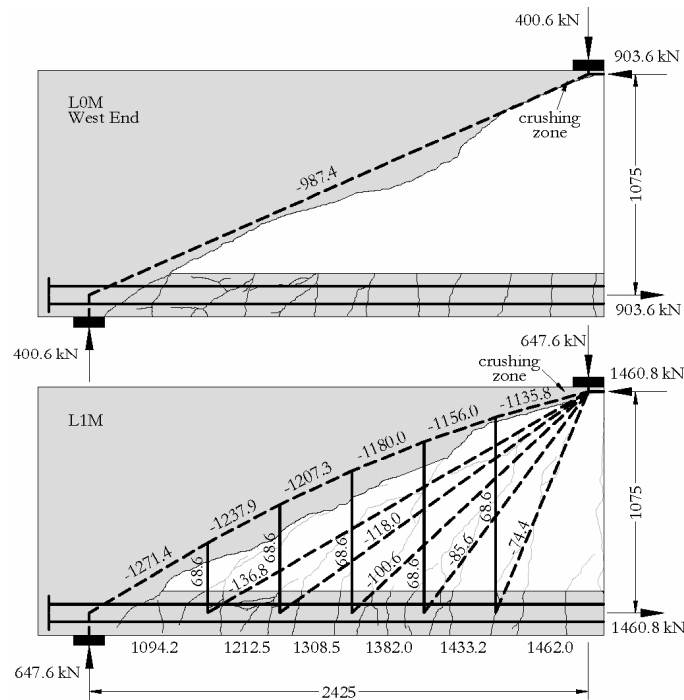


Figure 4.18 Distribution of internal forces – specimens L1M and L0M at failure

Figure 4.19 compares the flexural strains (BH and TH in Figure 3.14) of specimens L1M and L0M. The match at the bottom of the section is almost perfect. As expected, the transverse reinforcement had no effect on the flexural response. The difference between the strains along the top chord is a consequence of the shape of the diagonal cracks penetrating into the compression zone (see Figure 4.17). The cracks of specimen L1M were flatter and penetrated less than those of specimen L0M.

Figure 4.20a) compares the strain distributions along the bottom reinforcement (gauges 1B to 9B in Figure 3.15) of specimens L1M and L0M. The two bottom curves correspond to applied load of approximately 800 kN. Their mid-span values are very similar but the shapes differ significantly. The “parabolic” shape corresponding to

specimen L1M is in good agreement with the truss action discussed above while the almost constant profile of specimen L0M confirms the development of arch action. The top curve represents the strain variation at the last load stage of specimen L1M. Its maximum value is about  $2550 \mu\epsilon$  which is significantly less than the  $3260 \mu\epsilon$  yield strain of the steel. Figure 4.20b) compares the strain distributions along the top reinforcement (gauges 1T to 7T in Figure 3.15). The top edge of specimen L1M did not experience tensile strains because of the beneficial effect of the shifted line of thrust.

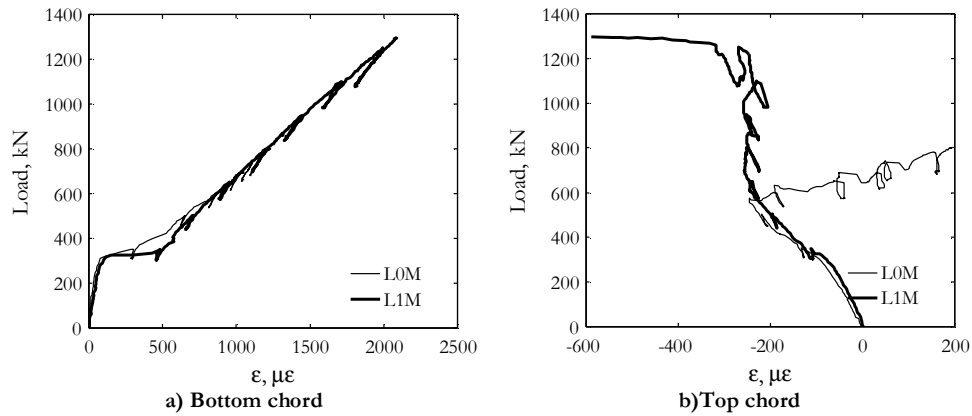


Figure 4.19 Flexural strains – specimens L1M and L0M

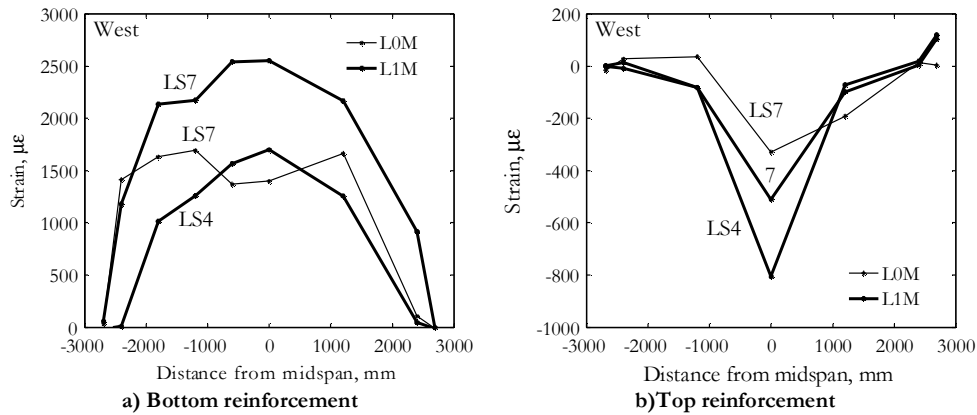


Figure 4.20 Longitudinal reinforcement strains – specimens L1M and L0M

Figure 4.21a) shows the results from the strain gauges attached to the surface of the stirrups (see Figure 3.15). Considering that the gauges were located at some distance from

the cracks, it can be stated that the steel strains at the cracks reached the yield limit right after cracking. Figure 4.21b) shows the average transverse strains of the west webs of specimens L1M and L0M as measured by Zürich gauges. The strains at Load Stage 4 of specimen L1M are significantly smaller than those at Load Stage 7 of L0M even though at these load stages the two beams were subjected to approximately equal loads. The reason for this difference is that the transverse reinforcement delays the development of the full crack pattern. The great similarity between the strain profiles at failure can be explained through the kinematic model (see 4.2.2). It was developed for elements without transverse reinforcement and its application to beams with stirrups could be questioned mainly because of two reasons. First, the assumption for constant strain along the longitudinal reinforcement is not valid (see Figure 4.20a), and second, the assumption for rigid diagonals is in contradiction with the compression in the cracked concrete (see Figure 4.18). Specimen L1M is however very lightly reinforced in the transverse direction and the violation of the two assumptions is considered small. Analysis of equation (4.15) shows that the transverse strain is directly proportional to the mid-span displacement  $\Delta_c$  associated with elongation of the bottom chord and increases with the ratio  $\Delta_c/\Delta_f$ . The strains along the longitudinal reinforcement of specimen L1M are larger than those of L0M and therefore the same applies to the values of  $\Delta_c$ . The displacement  $\Delta_c$  associated with deformations in the critical loading zone is expected to have a similar magnitude for the two specimens since in both cases the concrete was on the verge of crushing there. In conclusion, the transverse strains at failure of specimen L1M are almost equal to those of L0M as a consequence of a larger displacement  $\Delta_c$  and a smaller  $\Delta_c/\Delta_f$  ratio. Calculations for L1M were performed with  $\epsilon_f=1830 \mu\epsilon$  and  $\Delta_c=13.6$  mm resulting in  $\Delta_c/\Delta_f=12.0$  mm and  $\Delta_c/\Delta_f=0.13$  vs.  $\Delta_c=7.4$  mm and  $\Delta_c/\Delta_f=0.47$  for specimen L0M.

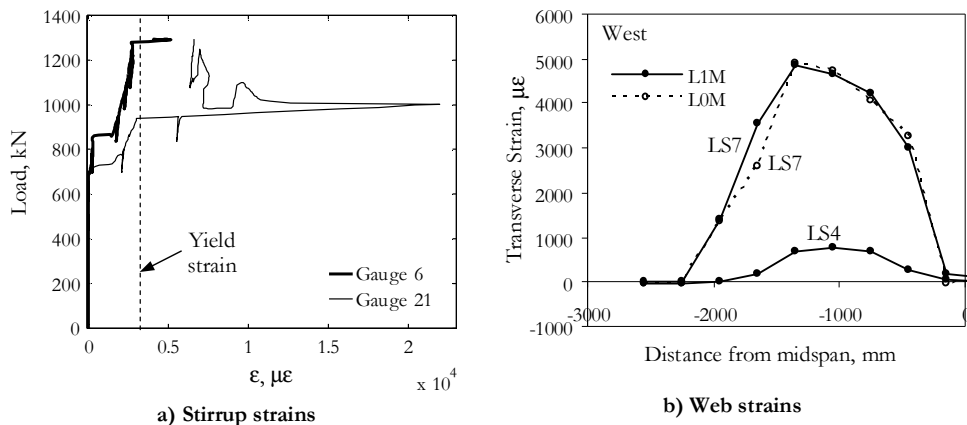


Figure 4.21 Transverse strains – specimens L1M and L0M

Similarly to specimen L0M (see 4.2.6), specimen L1M is used for comparison with the predictions of the CSA shear provisions. The experimental value of the shear strength of the beam is:

$$V_{u,\text{exp}} = \frac{1295.1}{2} + \frac{63.4}{4} = 663.4 \text{ kN}$$

The prediction based on strut crushing (see 2.2.2.2) is obtained as follows:

1) Calculate  $F_v$  and  $\theta_{s1}$ :

$$F_v = \frac{0.001 \times 2275 \times 400 \times 490}{2 \times 1000} = 223.0 \text{ kN}$$

$$\theta_{s1} \approx \tan^{-1} \frac{d}{a_d/2 + l_{b1}/2} = \tan^{-1} \frac{1095}{2275/2 + 150/2} = 42.1^\circ$$

2) Calculate the difference between  $T_f$  and  $T$ :

$$\Delta T = T_f - T = F_v \cot \theta_{s1} = 223.0 \times \cot 42.1^\circ = 247.0 \text{ kN}$$

3) Assume value of  $x_d$ , say 30 mm.

4) Calculate  $V$  from (2.5):

$$V = 0.85 \times 37.8 \times 2 \times 30 \times 400 / 1000 = 771.1 \text{ kN}$$

5) Calculate  $y_d$  from (2.4):

$$y_d = \frac{1095 - \sqrt{1095^2 - 4 \times 30 \times (2275 + 150/2 + 30)}}{2} = 69.6 \text{ mm}$$

6) Calculate  $T$  and  $\varepsilon_s$ :

$$T = 0.85 f_c' \times 2 y_d b - \Delta T = 0.85 \times 37.8 \times 2 \times 69.6 \times 400 / 1000 - 247.0 = 1542 \text{ kN}$$

$$\varepsilon_s = \frac{T}{E_s A_s} = \frac{1542000}{200000 \times 3060} = 2.52 \times 10^{-3}$$

7) Calculate  $\theta_s$ :

$$\cot \theta_s = T / V = 1542 / 771.1 = 2.00 \rightarrow \theta_s = 26.6^\circ$$

8) Calculate  $\varepsilon_1$  from (2.9):

$$\varepsilon_1 = \varepsilon_s + (\varepsilon_s + 0.002) \cot^2 \theta_s = 0.00252 + (0.00252 + 0.002) \times 2.00^2 = 0.0206$$

9) Calculate  $f_{ct}$  from (2.8):

$$f_{ct} = \frac{37.8}{0.8 + 170 \times 0.0206} = 8.78 < 0.85 \times 37.8 = 32.1 \text{ MPa}$$

10) Calculate  $w_b$ :

$$w_b = l_{b2} \sin \theta_s + h_a \cos \theta_s = 150 \times \sin 26.6^\circ + 210 \times \cos 26.6^\circ = 255 \text{ mm}$$

11) Calculate  $x_d$  using the right hand side of (2.10):

$$x_d' = \frac{8.78 \times 255 \times \sin 26.6^\circ}{2 \times 0.85 \times 37.8} = 15.6 \text{ mm}$$

and return to step 4 with revised value of  $x_d = (30 + 15.6) / 2 = 22.8$  mm. The iteration process continues until  $x_d$  and  $x_d'$  converge to a single value. Summary of the iterations is presented in the table below.

$x_d$ (mm)	$y_d$ (mm)	V (kN)	T (kN)	$\epsilon_s$ ( $\mu\epsilon$ )	$\theta_s$ (deg)	$\epsilon_1$ ( $\mu\epsilon$ )	$f_{cu}$ (MPa)	$w_b$ (mm)	$x_d'$ (mm)
30	69.6	593.6	1131.0	1848	27.7	15817	8.34	256	20.0
25.0	57.3	495.0	886.0	1448	29.2	12494	9.95	256	25.2
25.1	57.4	496.5	889.7	1454	29.2	12543	9.92	256	25.1

Additional calculations showed that strut crushing is the controlling failure mode within the strut-and-tie model and that the sectional model of the CSA code predicts ultimate shear of 606.9 kN. Finally:

$$V_{u,pred} = \max(571.1, 606.9) = 606.9 \text{ kN}$$

and

$$V_{u,exp} / V_{u,pred} = 663.4 / 606.9 = 1.09$$

### 4.3.2 Effect of beam slenderness - specimens S0M and L0M

Figure 4.22 shows the “top load vs. mid-span displacement” curves of specimens S0M and L0M while Figure 4.23 compares the crack patterns and the crack widths of the two beams. The first and the third drawings in Figure 4.23 show specimens L0M and S0M under approximately equal mid-span bending moments (752.3 kN.m and 766.2 kN.m, respectively). The second and the fourth drawings illustrate the cracked state of the two beams prior to failure.

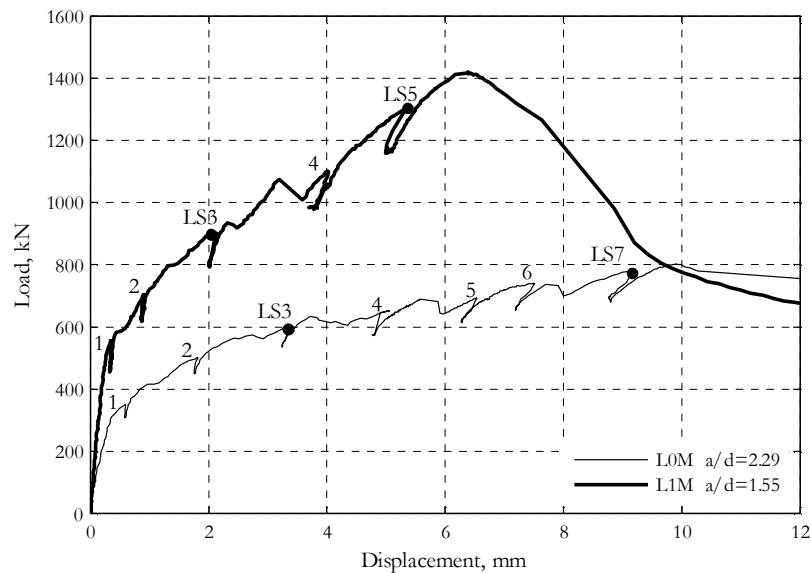


Figure 4.22 Load – displacement response - specimens S0M and L0M

Specimen S0M behaved linearly up to load of about 500 kN when the first flexural crack occurred near the mid-span section (see Figure 4.22 and Figure 4.23). The subsequent load increase caused the gradual formation of very flat cracks running from the bottom of the beam towards the mid-span mid-depth zone. The cracked area reached the support plates at a load of about 1100 kN when a wide diagonal crack developed on the east side of the beam. It propagated almost instantaneously from the support zone towards the loading point and resulted in a significant reduction in stiffness. The following load stages were characterized by minor extension of the existing cracks. Significant creep deformations were noticed while taking Zürich readings at Load Stage 5. The element failed along the wide diagonal crack with crushing near the loading plate under a load of 1419.5 kN and a mid-span displacement of 6.4 mm.



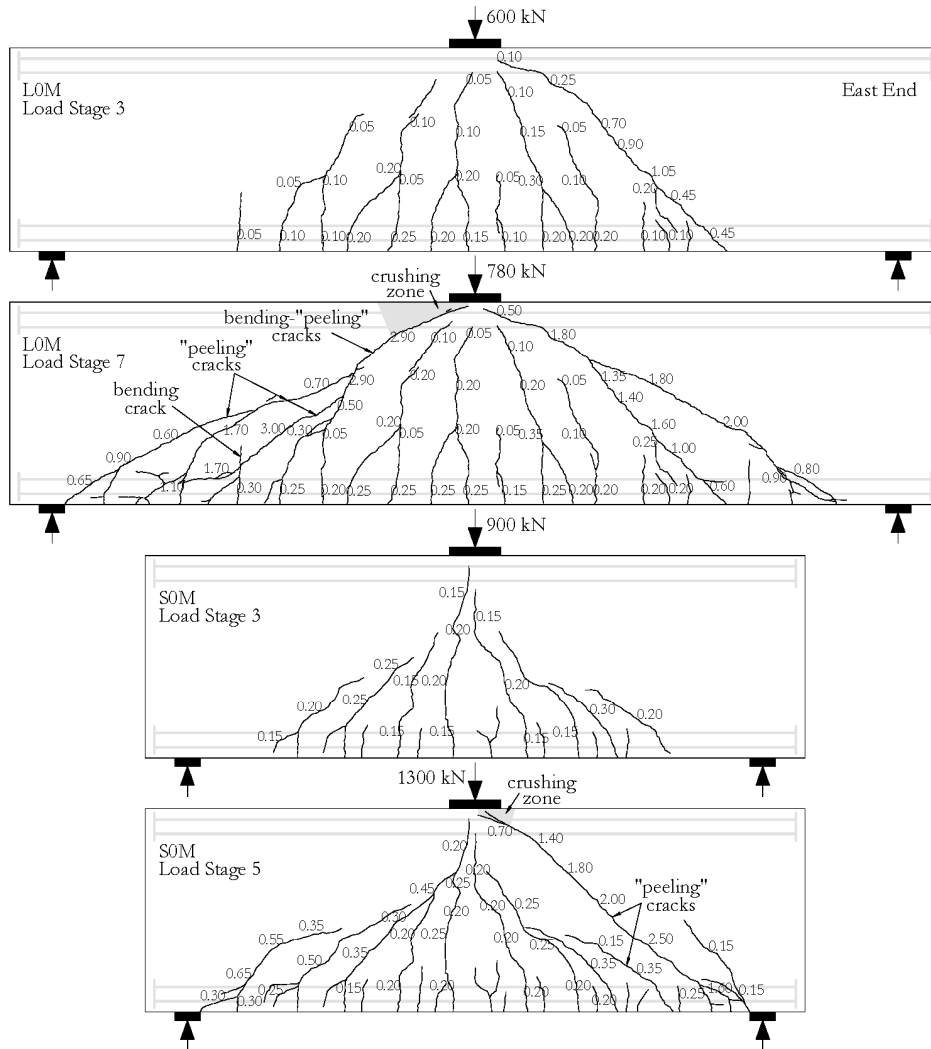


Figure 4.23 Cracks – specimens S0M and L0M

Figure 4.24 compares the balance of forces at the crushing zones of specimens L0M and S0M at failure. The calculations are based on the simple model shown in the first drawing of Figure 4.18. It can be seen that the larger strength of specimen S0M ( $709.8 \text{ kN} / 400.6 \text{ kN} = 1.77$ ) is a result of steeper and larger diagonal compression force. The steeper slope of the compression flow is simply a consequence of the shorter span of S0M. The larger diagonal compression capacity can not be attributed to difference in the concrete

strengths of the beams because specimen SOM had slightly weaker concrete than LOM (34.2 MPa vs. 37.8 MPa). The real reason for this effect is that the critical loading zone of SOM is deeper, less slender, and more tapered as evident from Figure 4.24.

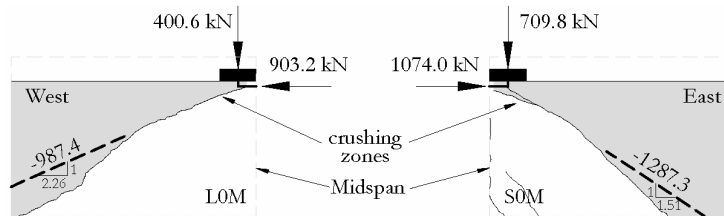


Figure 4.24 Critical loading zones at failure—specimens SOM and LOM

Figure 4.25 is intended to demonstrate why and how the beam slenderness ratio changes the crack pattern and affects the geometry of the critical loading zone. It shows two extreme cases: a) a beam experiencing mostly bending deformations; and b) a beam experiencing no bending deformations. The pure bending case is achieved by very large slenderness ratio, say  $a/d=10$ . The cracks are almost vertical and propagate simultaneously above the mid-depth of the beam. The length of the cracked part of the shear span is not affected by the presence of transverse reinforcement for a given mid-span moment. The tension in the bottom reinforcement reduces linearly from its maximum value at the mid-span section to zero at the support sections. The “no bending” case is achieved by a very large depth of the section, say  $H=a=10d$ , over the shear span. The cracks are flat and form one after another resembling “peeling” of concrete pieces. The presence of transverse reinforcement delays the “peeling” and reduces the length of the cracked part of the shear span for a given mid-span moment. The tension in the reinforcement is almost constant over the cracked zone and quickly decreases to zero within the intact concrete.

Usually, beams have slenderness ratios between 0.5 and 6 and a constant depth along the span. The two effects demonstrated in Figure 4.25 interact and produce complex crack patterns. The smaller the slenderness ratio is, the smaller the bending deformations, the more dominant the “peeling” effect, the deeper the critical loading zone, the higher the diagonal compression capacity. This conclusion is confirmed by the crack patterns of specimens LOM and SOM shown in Figure 4.23. At Load Stage 3 both elements experience equal bending moments at their mid-span sections but specimen LOM is longer and bends more. As a result, its cracked zone is wider and the cracks deviate “later” towards the loading point causing a more slender critical loading zone prior to failure (see Load Stage 5 of specimen SOM and Load Stage 7 of LOM in Figure 4.23). An additional reason for the rather flat cracks of beam SOM is that it appeared to have

weaker aggregate. Figure 4.26 shows the broken prisms from the modulus of rupture tests performed for specimens S0M and L0M (see Figure 3.8). The crack surface in the left picture seems to be smoother since most of the aggregates were cleaved. Smoother cracks mean weaker aggregate interlock and early failure of the concrete “teeth”.

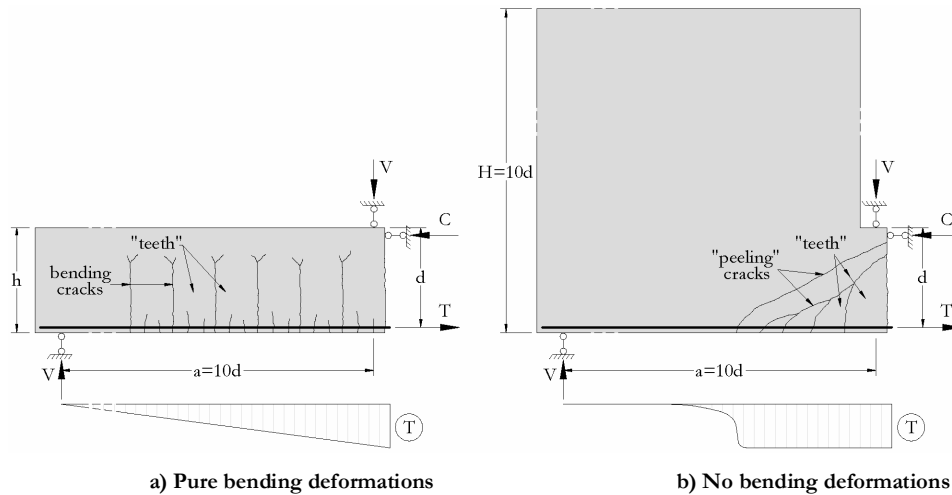


Figure 4.25 Effect of beam slenderness on the crack pattern



a) Prism from specimen S0M



b) Prism from specimen L0M

Figure 4.26 Crack roughness– specimens S0M and L0M

The smaller vulnerability of the critical loading zone of specimen S0M in comparison to that of L0M can be also demonstrated through the kinematic model presented in 4.2.2. It is applied to the failed east side of beam S0M at the last stage of loading. Calculations were performed with  $\epsilon_r=1400 \mu\epsilon$  and  $\Delta=6.2$  mm resulting in  $\Delta_r=4.6$  mm and  $\Delta_c=1.6$  mm vs.  $\Delta_r=7.4$  mm and  $\Delta_c=3.5$  mm for specimen L0M (see 4.2.2). As discussed earlier, the

displacement  $\Delta_c$  is a measure of the deformations in the critical loading zone of the beams. As expected, specimen S0M had a less deformable critical zone in comparison to that of L0M ( $1.6 \text{ mm} / 3.5 \text{ mm} = 0.43$ ). This is also evident from Figure 4.27 which shows the amplified ( $\times 30$ ) deformed shapes of the two specimens at their last load stages. The deformations of the crushing zone of specimen S0M are clearly smaller than those of L0M. The figure also demonstrates that the displacement  $\Delta_c$  “engages” a shorter zone of the bottom part of specimen S0M than it does in the case of L0M. This observation is consistent with the crack patterns of the two beams (see Figure 4.23). The engaged bottom zones are in reality the deformable zones with flat secondary cracks.

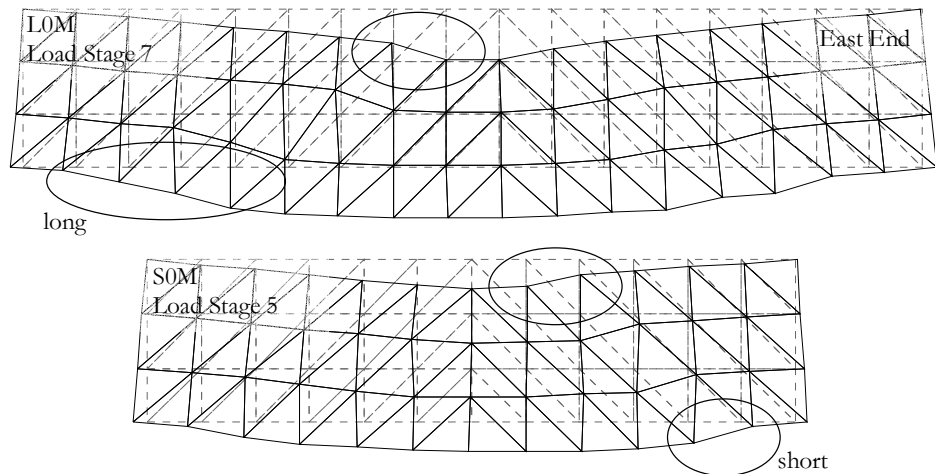


Figure 4.27 Deformed shapes – specimens S0M and L0M

Figure 4.28 compares the flexural response (BH and TH in Figure 3.14) of specimens S0M and L0M in terms of mid-span bending moment vs. flexural strain. Since the two beams have identical cross sections and very similar material properties, comparable flexural responses can be expected. Figure 4.28a) shows the flexural strains along the bottom chords of the beams. The two curves agree very well in terms of initial uncracked response and bending moment at flexural cracking. The larger post-cracking strains of specimen S0M indicate weaker tension stiffening effect in comparison to that of L0M. The reason for this effect could be a difference in the number and in the width of the cracks located within the gauge length of LVDT BH. Figure 4.28b) shows the flexural strains along the top chords of the beams. The two curves have a very similar overall shape and agree almost perfectly prior to the first major diagonal cracking. It is interesting to note that the curvature of the lines changes its sign even without the presence of flexure-shear cracks penetrating into the compression zone. This effect can be attributed

to the deep flexural cracks which propagated above the center line of the top chords (see Figure 4.23).

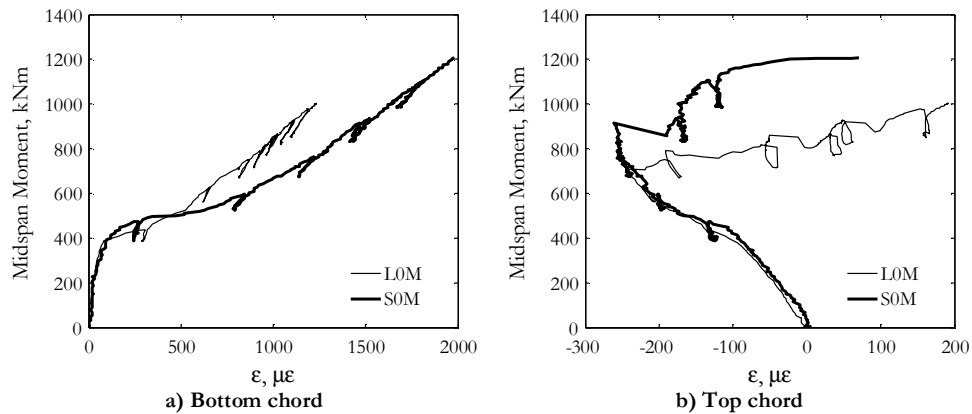


Figure 4.28 Flexural strains—specimens S0M and L0M

Figure 4.29a) shows the variation of the strains along the bottom reinforcement (gauges 1B to 9B in Figure 3.15) of specimens S0M and L0M. At Load Stage 3 both beams experienced similar mid-span bending moments and expectedly the strain readings at the middle section were almost identical. The strain curves confirm the conclusion that the cracked zone of the short beam is slightly shorter than that of the long one. At the last load stages the strain profiles became flat which indicates that in both specimens arch action was almost fully activated. The readings from S0M are higher than those from L0M because the short beam sustained higher bending moments. Strain gauge B8 of S0M was located very close to the critical shear crack (see Figure 3.15 and Figure 4.23) and read a maximum strain of 2500  $\mu\epsilon$  which is less than the yield strain of 3750  $\mu\epsilon$ . Strain gauge B9 of the same beam was attached to the bar just next to the anchor head and read strain of only 250  $\mu\epsilon$  corresponding to stress of 50 MPa. Knowing that the head area is ten times larger than the cross-sectional area of the bar, it can be concluded that the contact compression stress acting on the face of the anchor head reached 5.6 MPa which is significantly less than the concrete compression strength of 34.2 MPa.

Figure 4.29b) shows the variation of the strains along the top reinforcement (gauges 1T to 7T in Figure 3.15) of specimens S0M and L0M. The difference between the readings at the mid-span section can be attributed to difference in the relative location of the gauges with respect to the deep flexural cracks. Strain gauge T6 of S0M read quite high strains throughout the test which indicated that it had been damaged.

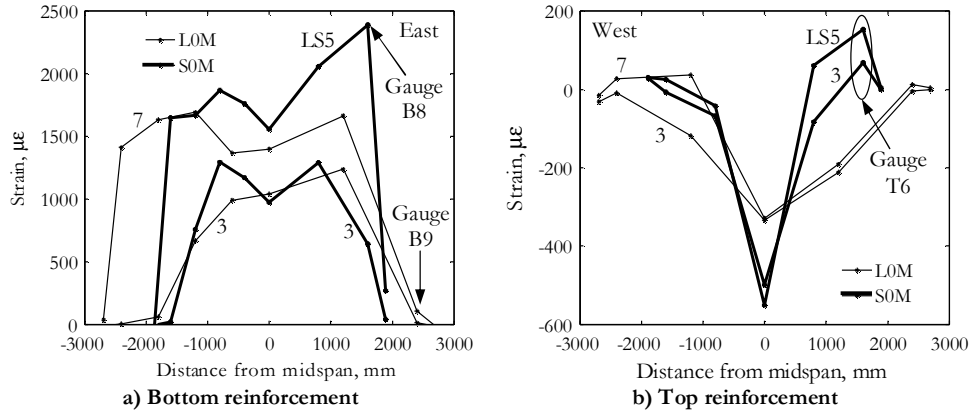


Figure 4.29 Longitudinal reinforcement strains – specimens S0M and L0M

Figure 4.30a) shows the variation of the transverse web strains along the failed shear spans of specimens S0M and L0M prior to failure. Also shown are the predictions of the kinematic model (see 4.2.2). The strains of the long beam are significantly larger than those of the short one even though L0M resisted a smaller load and had a smaller mid-span bending moment than S0M did. This observation can be explained through the kinematic model if (4.15) is written for the middle of the shear span ( $x/a=0.5$ ):

$$\varepsilon_v = \frac{1}{d_v} (\Delta_c + 0.25\Delta_v) \quad (4.16)$$

The deformation  $\Delta_c$  of the critical loading zone of specimen S0M is smaller than that of L0M as shown and justified earlier. The displacement  $\Delta_v$  of the short beam was shown to be smaller as well. This can be justified by recalling that  $\Delta_v$  is a result of the elongation of the bottom chord of the beams and equals  $\varepsilon_c a^2 / d_v$ . Specimen S0M sustains higher mid-span bending and therefore has a larger average chord strain  $\varepsilon_c$  but its shear span  $a$  is smaller than that of L0M.

Figure 4.30b) shows the top load plotted as a function of the transverse web strain at the middle of the failed shear spans (WL-V and EL-V in Figure 3.14) of specimens S0M and L0M. Also indicated are the strain predictions of the kinematic model for the last load stages of the tests. The plot demonstrates clearly the significant creep deformations that took place while the beams were last unloaded for Zürich readings. The creep is a result of the high compression stresses on both sides of the loading plates and affects the  $\Delta_c$  term of the kinematic model.

Figure 4.30 can be used to analyze how the effect of transverse reinforcement changes with decreasing shear-span-to-effective-depth ratio. The smaller the  $a/d$  ratio is, the smaller the transverse strains, the smaller the stresses in the stirrups, and therefore the smaller their effect on the load-bearing capacity of the beam.

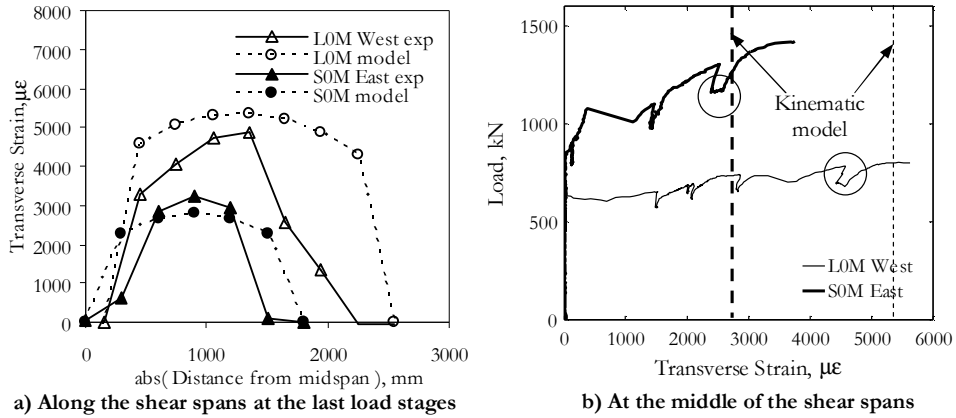


Figure 4.30 Transverse web strains– specimens S0M and L0M

Figure 4.31 shows the support zone strains measured in a direction close to that of the compression flow above the supports plates. Specimen S0M carried a larger load and experienced higher negative strains. Their values however remained significantly smaller than the concrete strain at peak stress.

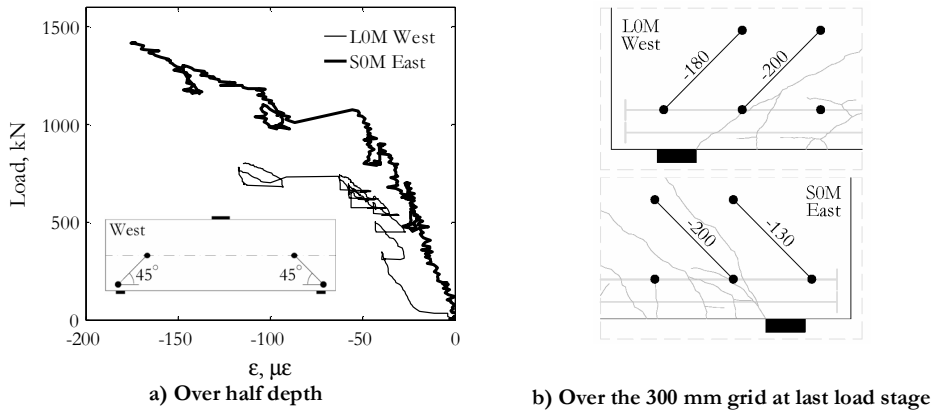


Figure 4.31 Support zone strains– specimens S0M and L0M

### 4.3.3 Effect of loading history – specimens L0C and L0M

Figure 4.32 shows the full hysteretic response of specimen L0C in terms of top/bottom load vs. mid-span displacement together with the load – displacement curve of the companion monotonic test L0M. Figure 4.33 compares the crack patterns and crack widths of the two beams at various load stages.

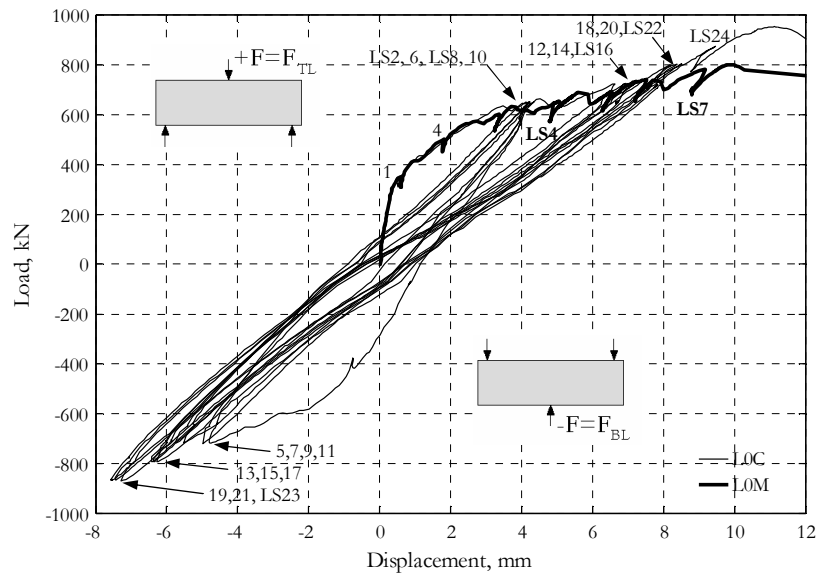


Figure 4.32 Load – displacement response- specimens L0C and L0M

Specimen L0C was first monotonically loaded to a top load of 650 kN to allow for major shear cracks to develop and extend towards the loading point (see Figure 4.32 and Figure 4.33). The load was then reversed to -715 kN and again brought to +650 kN in which way a full load cycle was performed. The different magnitude of top and bottom loads provided the same magnitude of shear at the middle of the shear spans. The zone of cracked concrete was relatively symmetric with respect to the longitudinal axis of the beam. The propagation of the top flexural cracks was stopped by the bottom diagonal cracks developed during the initial monotonic loading. The top flexure-shear cracks crossed the bottom diagonal cracks with a slight shift at the points of intersection. The third push to -715 kN caused the development of a major diagonal crack on the east side of the specimen. That was the reason an extra (fourth) cycle with an amplitude +650 kN/-750 kN was performed. No additional damage was however observed and the loading proceeded with a group of three cycles with amplitudes of +725 kN/-790 kN. The cracks caused by positive load were now on average wider and covered almost the



entire bottom chord of the beam while those caused by negative load did not reach the top support plates. The last group of three cycles had positive amplitude of 800 kN which equaled the load-bearing capacity of the monotonically-tested specimen L0M. Irrespective of the high load, the concrete around the loading and support plates seemed intact and a progressive shift of hysteresis loops was not observed. The element was then pushed monotonically to failure with one intermediate load stage at +870 kN. The width of the major diagonal crack on the west side of the loading point reached 4 mm. Specimen L0C failed under a top load of +953.0 kN and displacement of 11.1 mm with widening of the most west diagonal crack and crushing of the concrete near the top loading plate. This failure mode resembles very much that of specimen L0M as demonstrated by the photographs in Figure 4.34.

Generally, specimen L0C showed an insignificant increase of displacements under consecutive cycles with a constant load amplitude. It was observed that the increase was usually accompanied by a minor extension of existing cracks. The hysteresis loops were narrow and the displacement under zero applied load remained relatively small throughout the test. Residual deformations were observed mainly along the major diagonal cracks.

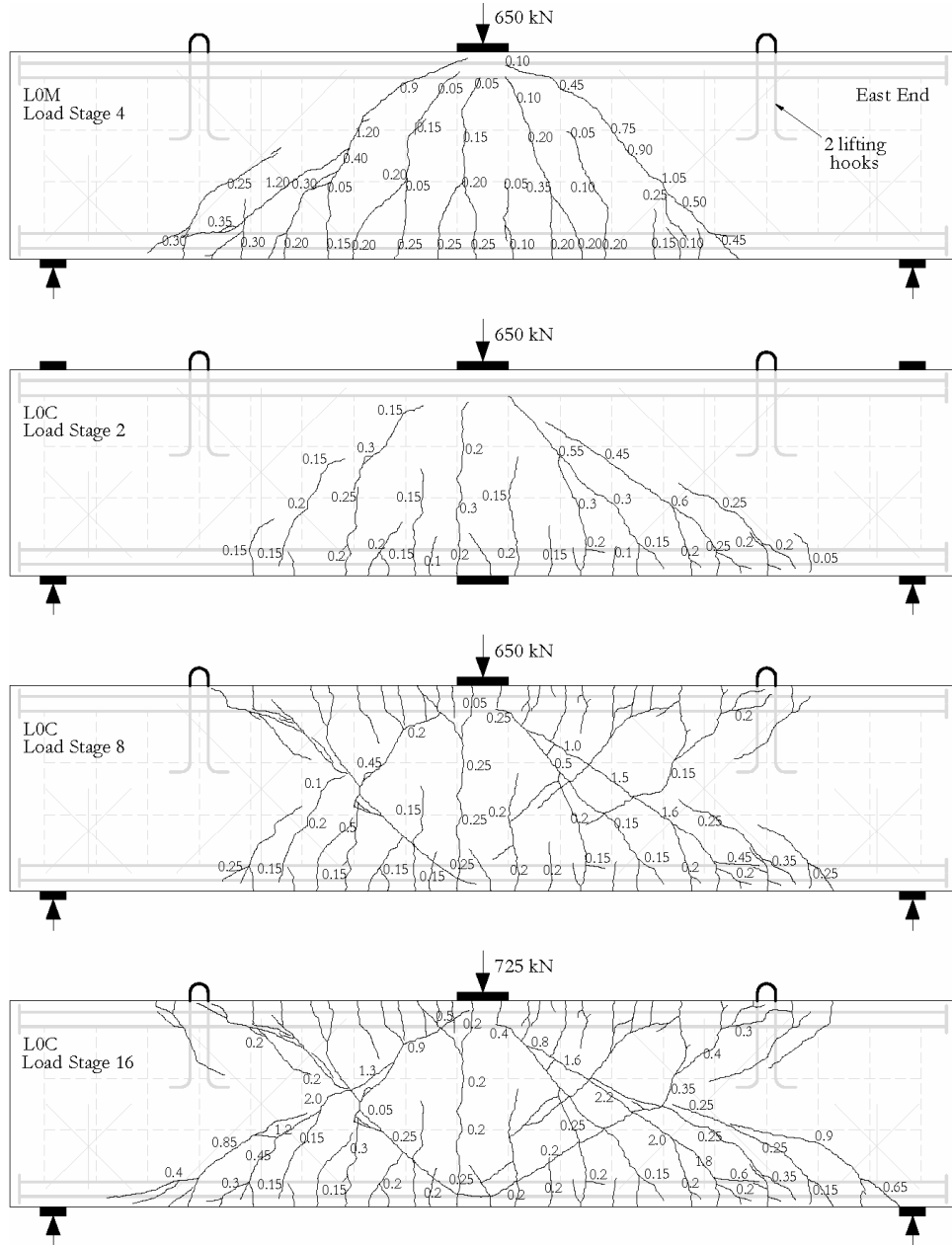


Figure 4.33 Cracks – specimens L0C and L0M

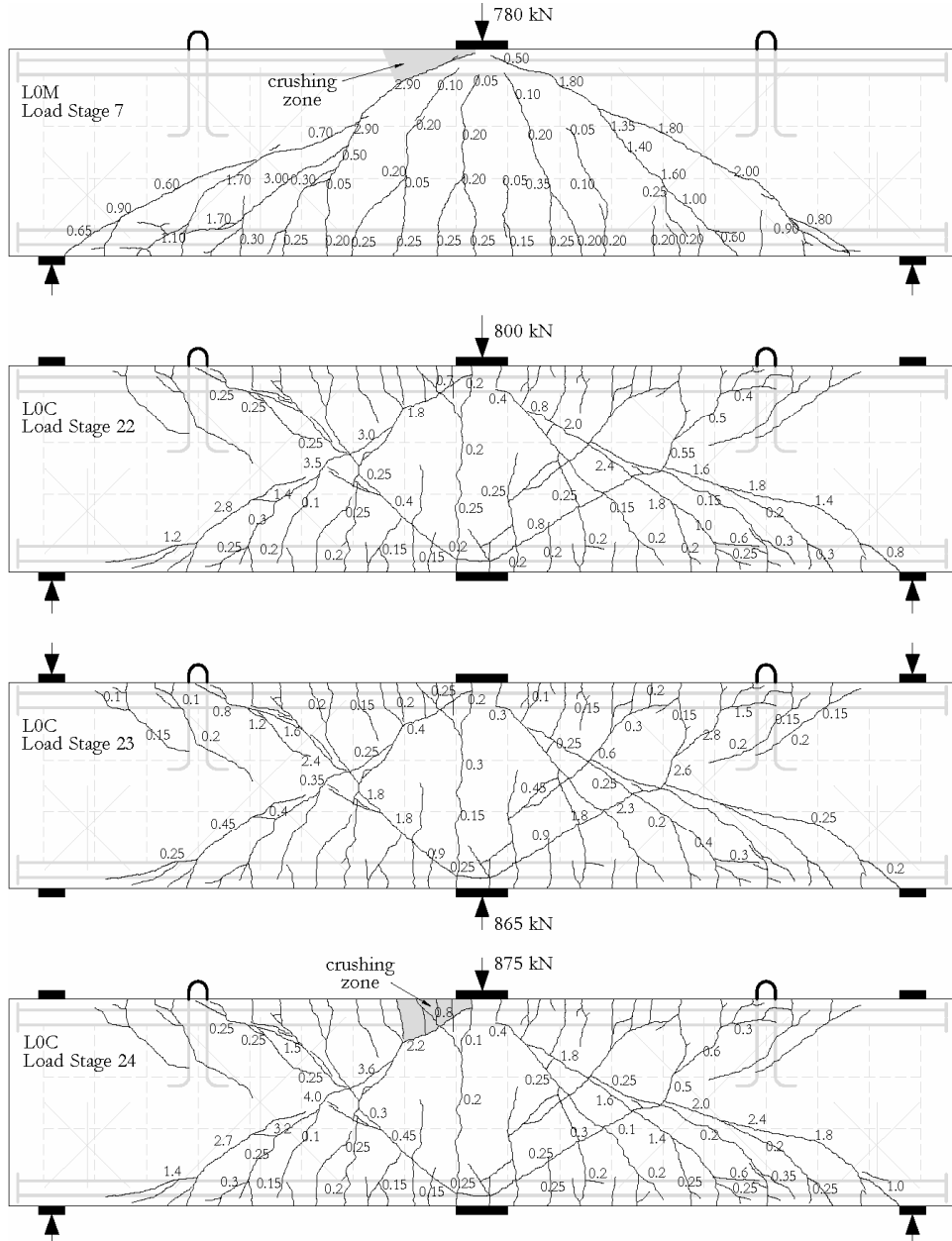


Figure 4.33 - cont



Figure 4.34 Specimens L0M and L0C after failure

Figure 4.35 shows a bilinear representation of the load-displacement response of specimen L0C under cycles with constant load amplitude. The straight lines connect the vertices of the hysteresis loops to the point of zero mid-span shear and zero total displacement. The total displacement equals the displacement  $\delta_c$  under the self-weight of the beam before the application of the concentrated load plus the measured displacement  $\Delta$  after the beginning of the test. The bilinear idealization does not account for residual deformations and is characterized by slopes  $k_p$  and  $k_n$  under positive and negative load, respectively. As would be expected, the secant stiffness decreases with increasing amplitude of the load cycles. It is interesting to note however that  $k_p$  decreases faster than  $k_n$  resulting in a kink at the point of load reversal. The kink seems negligible during the first group of cycles but becomes significant for the later groups. Ideally, if the beam was perfectly symmetrical, the slopes  $k_p$  and  $k_n$  would have been equal. The symmetry of specimen L0C is violated by the two pairs of 15M lifting hooks installed near its top ends (see Figure 3.2 and Figure 4.33). They did not have a significant effect on the behavior of the beam prior to the second group of cycles because the concrete around them was still largely uncracked (see Load Stage 8 in Figure 4.33). The hooks got activated when diagonal cracks crossed their legs (see Load Stages 16 and 22 in Figure 4.33). The negative load was then resisted by a relatively stiff truss action similar to that in specimen L1M while the positive load was carried by a relatively soft arch action as that in L0M (see Figure 4.18). As discussed in 2.2.2.2, the transverse reinforcement (or in this case the hooks), can be effective even if they do not extend to the flexural compression chord of the member. The hooks are also the reason for the observed delayed “peeling” cracks between them and the top support plates.

The bilinear idealization allows for another interesting comment to be made. The displacement under gravity load increased from cycle to cycle because the beam was getting progressively softer. The same is valid at load  $-G$  where the whole weight of the beam is balanced at the middle of the span.

Figure 4.35 contains also an idealization of a typical hysteresis loop. At point  $a$  the beam is subjected to peak top load. The cracks caused by positive load are widely open while those caused by negative load are relatively well closed under the action of clamping stresses. During the unloading from point  $a$  to point  $b$  the status of the closed cracks remains essentially unchanged. The elasticity of the reinforcing bars and that of the concrete narrows the opened cracks but does not close them completely. The residual deformation at point  $b$  can be attributed to plastic deformations in the concrete at the zones of high compression, permanent damage at the cracks, and irreversible slip between the bars and the surrounding concrete. When the load reverses, the closed cracks open quickly while the previously open cracks close gradually. The result of that is a visible kink at point  $b$  and increasing tangent stiffness between points  $b$  and  $c$ . Section  $c-d$  is governed mainly by elongation of the top reinforcement and has an almost constant slope. The increasing negative load leads to increasing compressive stresses and development of plastic deformations in the concrete around the loading and support plates. The softening of the concrete at those zones together with minor extension of cracks results in a slight softening in the global load-displacement response between points  $d$  and  $e$ . The following unloading branch is initially steep and its slope decreases gradually between points  $e$  and  $f$ . This shape resembles the shape of the unloading curves observed in tests of concrete cylinders subjected to cyclic compression. It is also indicative of the presence of friction-type mechanisms such as aggregate interlock along the flexure-shear cracks as well as bond between the steel and the concrete. At point  $f$  the rough faces of the closing cracks start getting in firm contact and the slope of the unloading branch increases until the load reverses again at point  $g$ . The load cycle is completed by loading back to peak top load. The displacement shift between points  $a$  and  $i$  is a result of extension of cracks, cyclic degradation of the concrete in the zones with high compression, smoothening of the crack faces, and deterioration of the bond between the reinforcement and the concrete.

It is interesting to note that the negative residual displacements are on average slightly larger than the positive ones. It is also evident from Figure 4.35 that the bottom half of a typical hysteresis loop is a little wider than the top half. An explanation for this can be found by examining the crack pattern of specimen L0C (see Load Stages 22 and 23 in Figure 4.33). The lifting hooks restrained the flat secondary cracks which resulted in more effective aggregate interlock along the steep parts of the primary flexure-shear cracks and more pronounced friction-type behaviour under negative load.

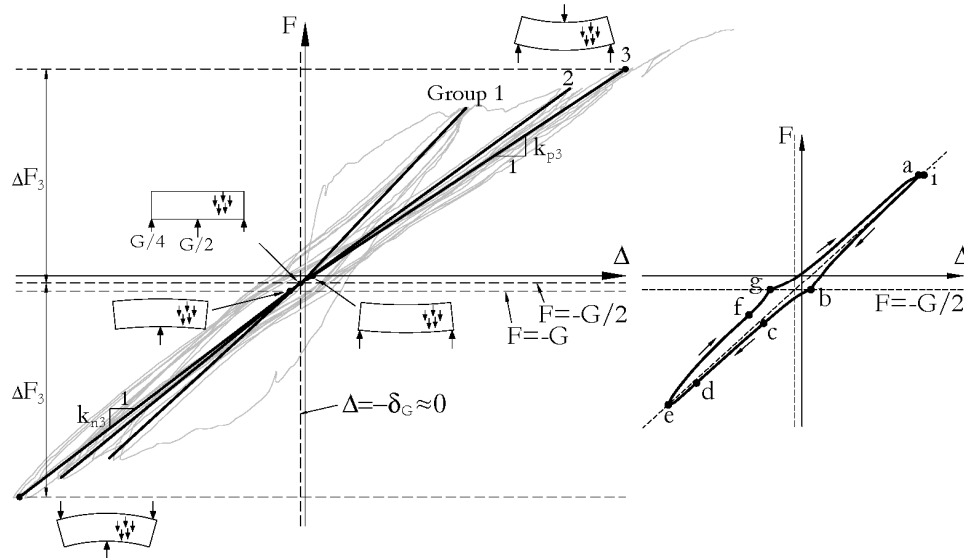


Figure 4.35 Idealized hysteretic behaviour – specimen L0C

Figure 4.36 shows the positive and negative envelopes of the load-displacement response of specimen L0C together with the envelope curve of specimen L0M. As expected, the three curves are initially almost coincident. The negative envelope deviates from the other two curves in agreement with the discussed role of the lifting hooks. It is surprising however that the cyclically-loaded beam was so much stronger than the monotonically-tested specimen (801.1 kN for L0M vs. 953.0 kN for L0C). An explanation for this result can be found by looking at the potential crushing zones of the two specimens. The concrete around the support plates of specimens L0C was not significantly affected by the cyclic load because it was not subjected to reversed forces. For example, the bottom support zones experienced high diagonal compression under positive load but remained almost free of stresses under negative load. The concrete around the loading plates of specimen L0C was expected to be weaker than that of specimen L0M because it was subjected to alternating horizontal tension and diagonal compression. However, the small displacement shifts between hysteresis loops with the same load amplitude show that this effect was negligible. The strength of the concrete is not the only parameter which controls the failure of the critical loading zone. Other important factors are the depth and the shape of the zone as well as the global roughness of the critical diagonal crack. The deeper the critical loading zone is, the larger its compression capacity. The rougher the critical diagonal crack is, the larger the shear transferred through it and the smaller the compression demand on the critical loading zone. Figure 4.37 demonstrates clearly that the crushing zone of specimen L0C was deeper, less slender, and more tapered than that

of specimen L0M. The photographs in Figure 4.34 show that the critical diagonal crack of specimen L0C was rougher than that of L0M. It can be therefore concluded that the higher capacity of specimen L0C in comparison to that of L0M is a result of deeper critical loading zone and rougher critical crack. It is important to note that neither the depth of the critical loading zone nor the roughness of the critical crack was influenced by the load reversals because the “positive” crack pattern of specimen L0C was determined by the initial monotonic loading (see Load Stage 2 in Figure 4.33). The exact path of the critical diagonal crack is rather a function of random factors such as local variations of material properties and aggregate placement over the shear span.

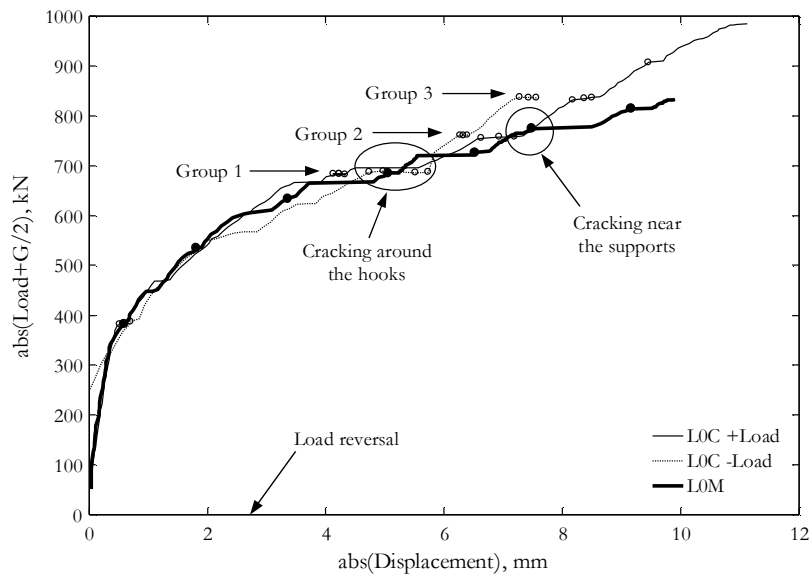


Figure 4.36 Envelope curves - specimens L0C and L0M

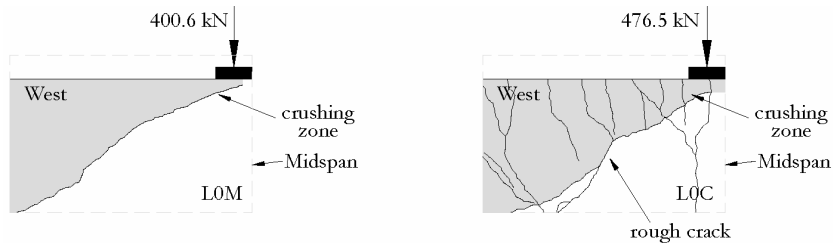


Figure 4.37 Critical loading zones at failure— specimens L0C and L0M

Figure 4.36 and Figure 4.33 show also that the geometry of the critical loading zone affected the behaviour of the beams only after the cracking had reached the bottom support plates or, in other words, only after the arch action had been almost fully activated. The arch action relies very much on the concrete above the diagonal cracks and, therefore, the deformations of the critical loading zones contribute significantly to the mid-span displacement of the beam.

Figure 4.38 compares the deformed shape of specimens L0M at the last load stage to those of L0C at the end of the last group of load cycles. The three diagrams allow for direct comparisons because they correspond to similar load levels and have been equally amplified. The deformations of the crushing zone of specimen L0C seem to be smaller than those of L0M in agreement with the conclusions made in the previous paragraph. A close examination of the second plot reveals slight kinks along the top and bottom chords of the beam which are result of the imperfect contact along the “negative” diagonal cracks (see also Load Stage 22 in Figure 4.32). These cracks could be a reason for small reduction of the mid-span displacement. The magnitude of this reduction can be estimated by subtracting the mid-span displacement from the maximum vertical displacement measured along the tension chord of the beam. The result for Load Stage 22 is 0.5 mm which represents only 6% of the mid-span displacement. The last diagram in Figure 4.38 demonstrates clearly that the lifting hooks played an important role in the load-bearing mechanisms resisting negative loads. The sharp kinks near the hooks together with the relatively narrow cracks at those zones (see Load Stage 23 in Figure 4.33) show that the two sets of four 15M bars did not yield.

Figure 4.39 shows the flexural response (BH and TH in Figure 3.14) of specimens L0C and L0M together with an idealization of the first hysteresis loop from the cyclic test. The bottom flexural strain is resolved into two components: 1) strain coming from vertical cracks and deformations in the concrete between them, and 2) strain coming from diagonal cracks. The behaviour associated with the first strain component can be explained in the following way. The monotonic part  $0-a-b$  has the well-know shape determined by linear material behaviour prior to cracking and gradual loss of tension in the concrete afterwards. The unloading branch  $b-c$  is governed by shortening of the elastic reinforcement. The residual deformation at point  $c$  comes mainly from irreversible slip between the reinforcing bars and the surrounding concrete. The loading in the opposite direction causes clamping of the cracks and compressive strains in the concrete between them. The unloading to point  $e$  is characterized by closed cracks and partial recovery of the concrete strains. The reloading  $e-f$  finishes with a larger strain than that at point  $b$  as a consequence of a minor extension of the flexural cracks and cyclic bond degradation. The second strain component remains zero up to point  $b$  when diagonal cracks caused by negative load propagate into the bottom chord. Their widening results in increasing



tensile strain between points *b* and *i*. The diagonal cracks do not close well and the strain after reloading remains larger than zero.

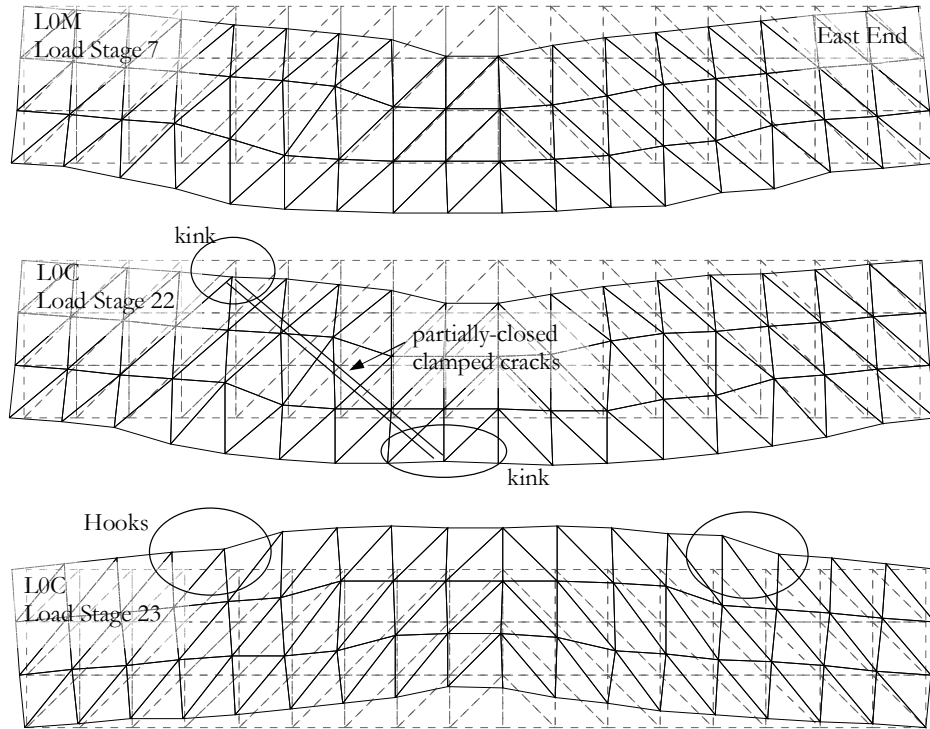


Figure 4.38 Deformed shapes – specimens L0C and L0M

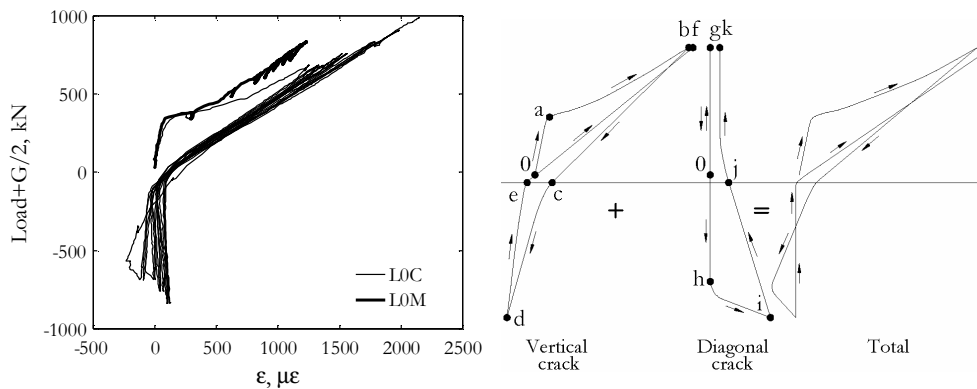


Figure 4.39 Bottom flexural strains – specimens L0C and L0M

Figure 4.40a) shows the variation of the strains along the bottom reinforcement (gauges 1B to 9B in Figure 3.15) of specimen L0C at load reversal. They were obtained as an average of the strains at load  $-G$  and load 0 because, as discussed in 4.1.2, values of the bottom load smaller than  $G$  were not measured. The shape of the curves resembles the shape of the bending-moment diagram under a load of  $-G/2$ , i.e. zero at mid-span and parabolic in each of the shear spans. Figure 4.40b) shows the bottom-reinforcement strains of specimens L0C and L0M at various load stages of positive load. The three sets of curves corresponding to the three groups of load cycles show that the strain increase caused by load repetitions becomes smaller with increasing load amplitude. In fact, the set of curves corresponding to the third group of cycles appears almost as a single line. This trend can be explained by the state of cracking (see Figure 4.33). The higher is the load amplitude, the more developed the crack pattern, the smaller the crack extensions under load repetitions.

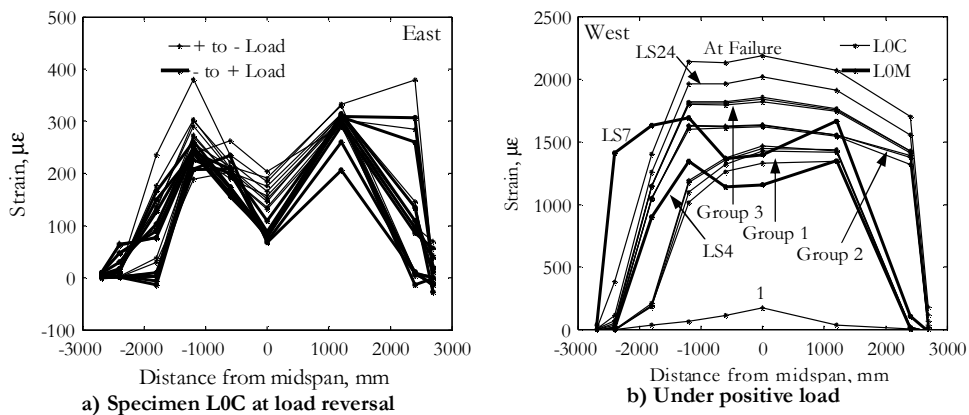


Figure 4.40 Bottom reinforcement strains – specimens L0C and L0M

The top two plots in Figure 4.41 show the web behaviour along the  $135^\circ$  diagonals located at the middle of the failed shear spans of specimens L0C and L0M. The strain along the diagonals is controlled by the relative diagonal displacements at the flexure-shear cracks caused by positive load (see Figure 4.33). The major contribution is the width of the cracks since the  $135^\circ$  diagonals are almost perpendicular to them. At point *a* the cracks are widely open under the action of peak positive load. The unloading branch *a-b* is governed by shortening of the elastic reinforcement and recovery of deformations in the inelastic concrete on both sides of the top loading plate. The residual deformation at point *b* comes mainly from plastic deformations at the loading zone and permanent damage at the cracks. The loading in the opposite direction causes clamping of the cracks but their misaligned and damaged faces do not allow for full contact to be reached. The unloading to point *d* is characterized by decreasing clamping stresses and no change in

the width of the cracks. The reloading  $d-e$  finishes with a larger strain than that at point  $b$  as a consequence of cyclic degradation of the concrete on both sides of the top loading plate and smoothening of the faces of the diagonal cracks.

The bottom two plots in Figure 4.41 show the web behaviour along the verticals located at the middle of the failed shear spans of specimens L0C and L0M. The strain along the verticals is controlled by the relative vertical displacements at the two intersecting systems of flexure-shear cracks (see Figure 4.33). If we assume that these displacements are proportional to the width of the cracks, the transverse strain can be obtained as a linear combination of the strains measured along the  $45^\circ$  and  $135^\circ$  diagonals.

Comparison between the plots in Figure 4.39, Figure 4.40, and Figure 4.41 reveals that, in relative terms, the web of specimen L0C was more prone to residual deformations and cyclic degradation than its chords were.

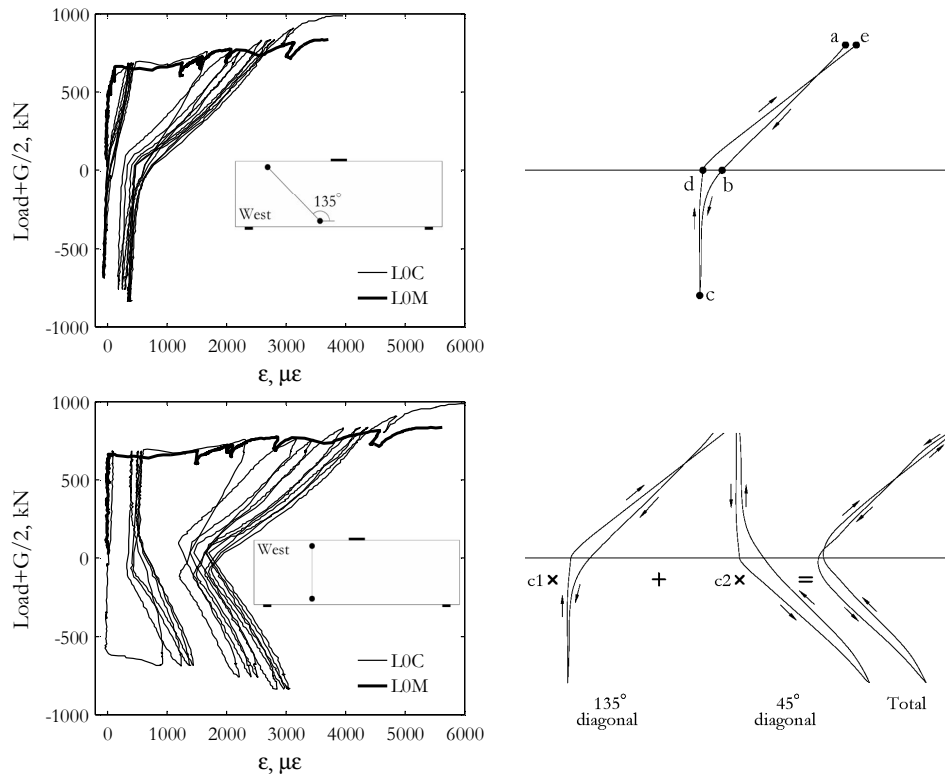


Figure 4.41 Strains in the web at mid shear span – specimens L0C and L0M

Figure 4.42 shows the support-zone behaviour along the verticals located at the bottom half of specimens L0C and L0M. The strain along the verticals is controlled by the relative vertical displacements at the flat “peeling” cracks which are in turn related to the relative displacements at the middle of the major diagonal cracks (see Figure 4.33). If the two displacements were proportional to each other, the actual hysteresis loops would be well represented by the idealized loop drawn with a dashed line. In reality, the negative load has almost no influence on the cracks near the bottom supports because it causes direct diagonal compression between the bottom loading plate and the top supports. This is reflected in the correct idealized loop drawn with a solid line.

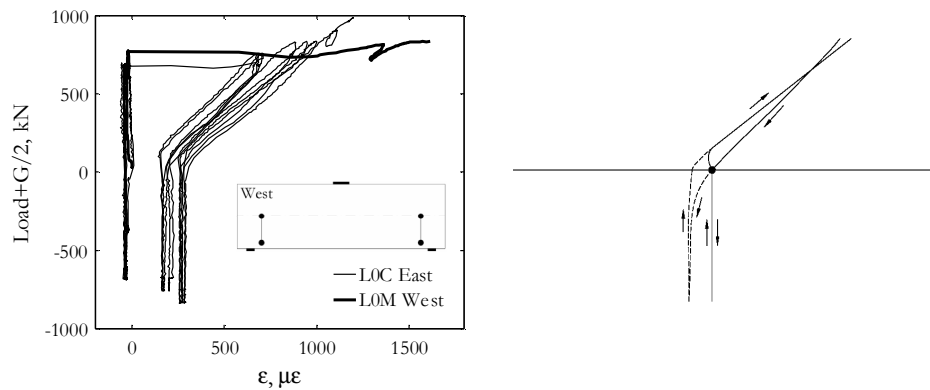


Figure 4.42 Support zone strains – specimens L0C and L0M

#### 4.3.4 Load-displacement response and failure

Figure 4.43, Figure 4.44, Figure 4.45, and Figure 4.46 show the full load-displacement response of specimens S0M/C, S1M/C, L0M/C, and L1M/C. The first two figures are for the short specimens while the second two are for the long ones. Each plot compares the monotonic and cyclic responses of beams with otherwise identical properties.

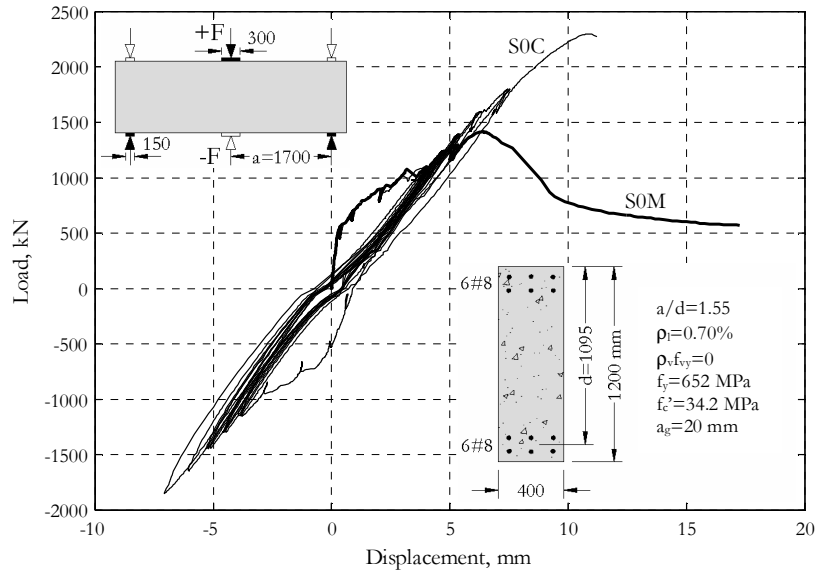


Figure 4.43 Full load-displacement response – specimens S0M and S0C

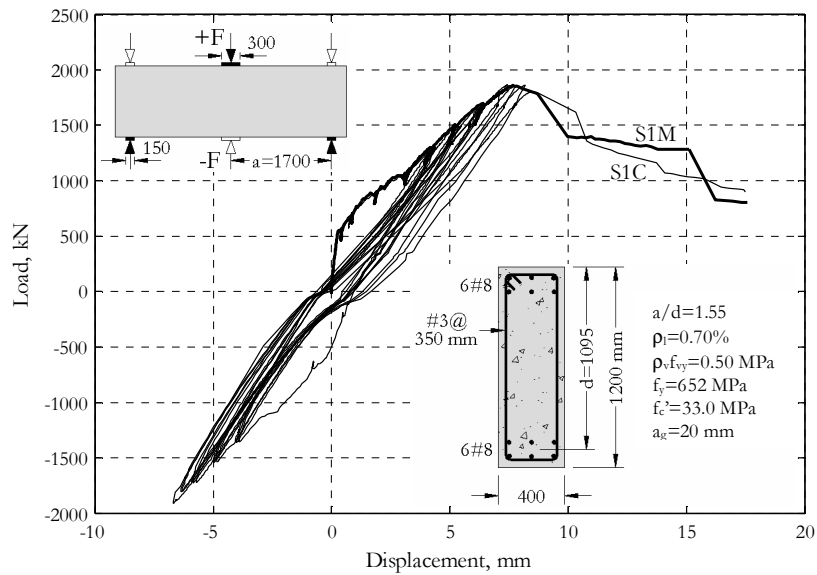


Figure 4.44 Full load-displacement response – specimens S1M and S1C

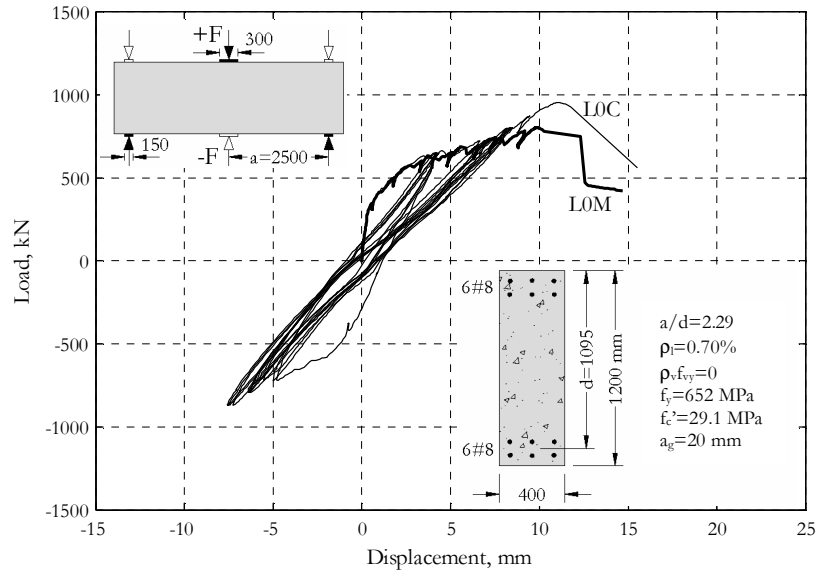


Figure 4.45 Full load-displacement response – specimens L0M and L0C

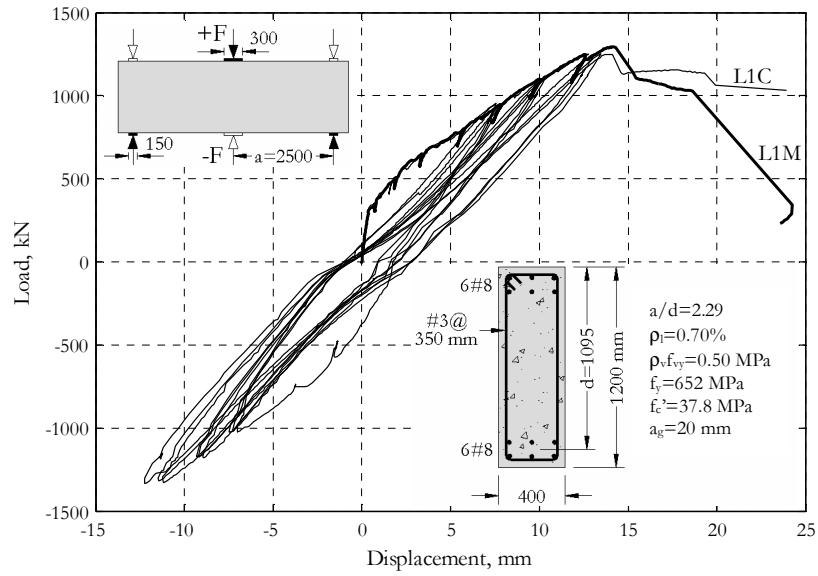


Figure 4.46 Full load-displacement response – specimens L1M and L1C

The four cyclically-tested specimens have very similar hysteretic behaviour characterized by small energy dissipation (narrow hysteretic loops), small cyclic degradation (small increase in displacements under consecutive cycles with constant load amplitude), small residual displacements, and low ductility (fast drop of resistance after peak load). A closer look at the plots shows that the beams with stirrups have slightly wider loops and slightly larger residual displacements than the beams without stirrups. The reason for this is the yielding of the transverse reinforcement at the flexure-shear cracks. The plastic elongation of the stirrups under peak load prevented effective clamping of the cracks upon unloading. The plots also show that specimens S1C and L1C failed during the last group of load cycles which is consistent with the relatively high displacement shift between the first and the third cycles with maximum load amplitude.

More test data for specimens S0M/C, S1M/C, L0M/C, and L1M/C is presented in Appendix B.

Figure 4.47 shows the positive envelopes of the load-displacement response of specimens S0M/C, S1M/C, L0M/C, and L1M/C. In the linear elastic range the curves are clearly grouped according to the beam slenderness and, expectedly, the short elements were stiffer than the long ones. The agreement between the curves in each group continues in the range of flexural cracking, because during this phase the stirrups were not crossed by cracks and experienced very small strains. The divergence between the envelopes of specimens with and without transverse reinforcement corresponds to first flexure-shear cracking. Beams with stirrups started the transition to a relatively stiff truss-type load-bearing mechanism while those without stirrups – to a relatively soft arch action (see 4.3.1). The other visible branching corresponds to cracking near the support plates of the specimens without transverse reinforcement. This is the stage at which the arch action was almost fully activated and the response of the elements became very much dependent on the properties of the zones subjected to high compression, namely the loading and support zones (see 4.3.3). Particularly important were the critical loading zones because, as evident from Figure 4.48, their crushing caused the failure of all the specimens. Figure 4.49 shows close-up photographs of the crushed zones of specimens S0M and S0C after failure. It can be seen that the critical loading zone of the beam subjected to cyclic loading was significantly deeper than that of the beam tested monotonically. As a consequence, the load-bearing capacity of specimen S0C was 1.62 times larger than that of S0M. It is important to note that this difference can not be related to the load reversals because the “positive” crack pattern of specimen S0C was almost fully developed during the initial monotonic part of the loading history. In contrast to the envelope curves of beams without stirrups, the two pairs of curves corresponding to specimens with transverse reinforcement show an almost perfect match up to failure.

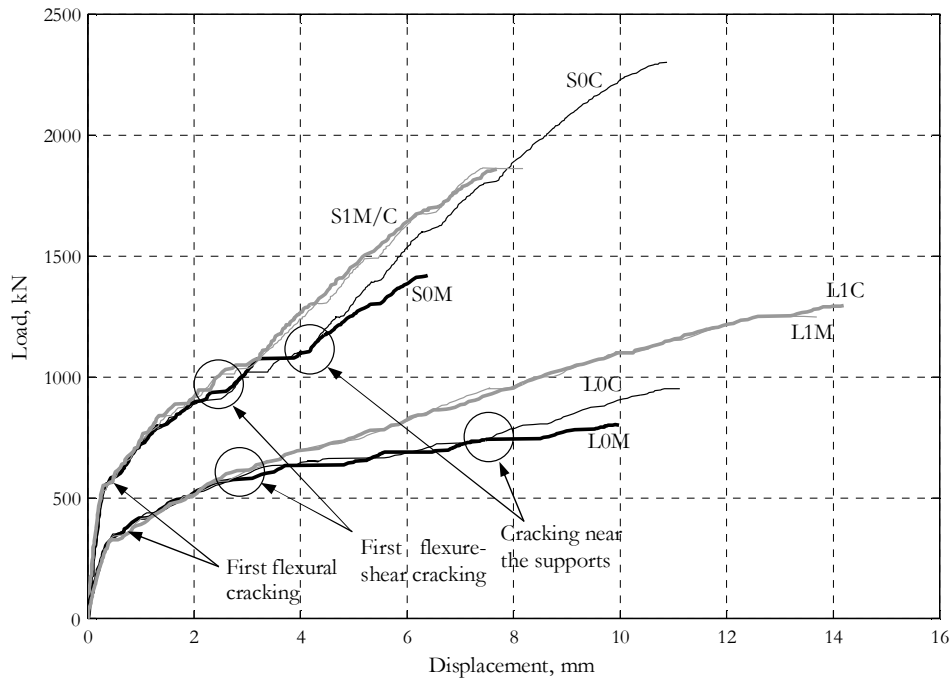


Figure 4.47 Envelope curves – specimens S0M/C, S1M/C, L0M/C, L1M/C

In conclusion, load reversals had a negligible effect on the response of the tested beams since they did not cause significant cyclic degradation and did not alter the crack pattern which would have developed under positive monotonic load. The former is evident from the full load-displacement curves (see Figure 4.43 - Figure 4.47) while the later is a direct consequence of the choice of loading history (see 3.5).

The scatter in terms of the ultimate response of identical beams without stirrups (compare curve S0M to S0C and curve L0M to L0C in Figure 4.47) was mainly a result of scatter in the depth of the critical loading zones. These zones are bound by the critical diagonal cracks whose exact path is a function of random factors such as variations of material properties over the shear span. As evident from Figure 4.47, the scatter decreased with increasing  $a/d$  ratio. This trend can be explained through the fact that the importance of the arch mechanism, and therefore the importance of the depth of the critical loading zone, decreases with increasing beam slenderness.



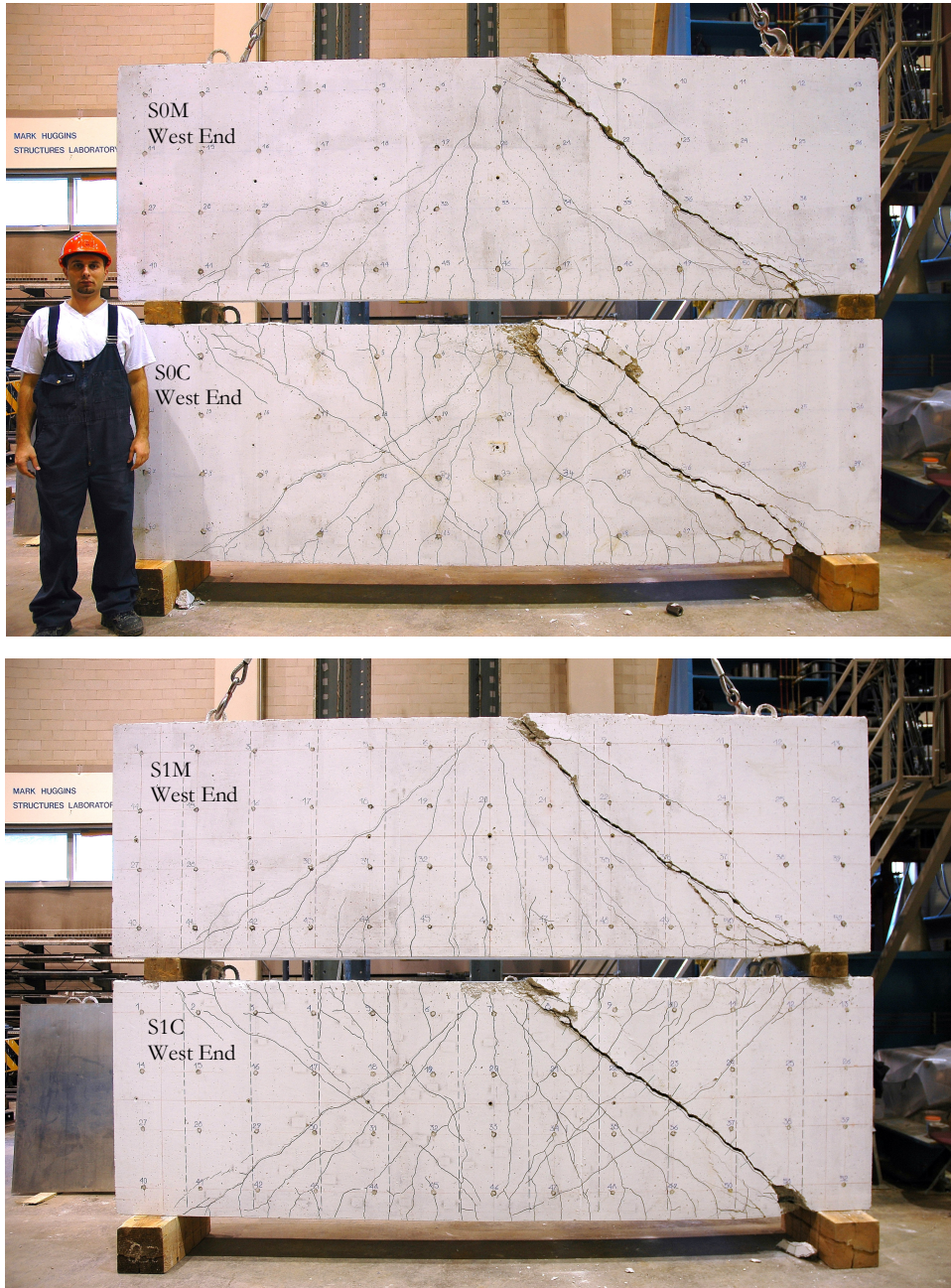


Figure 4.48 Specimens S0M/C, S1M/C, L0M/C, and L1M/C after failure

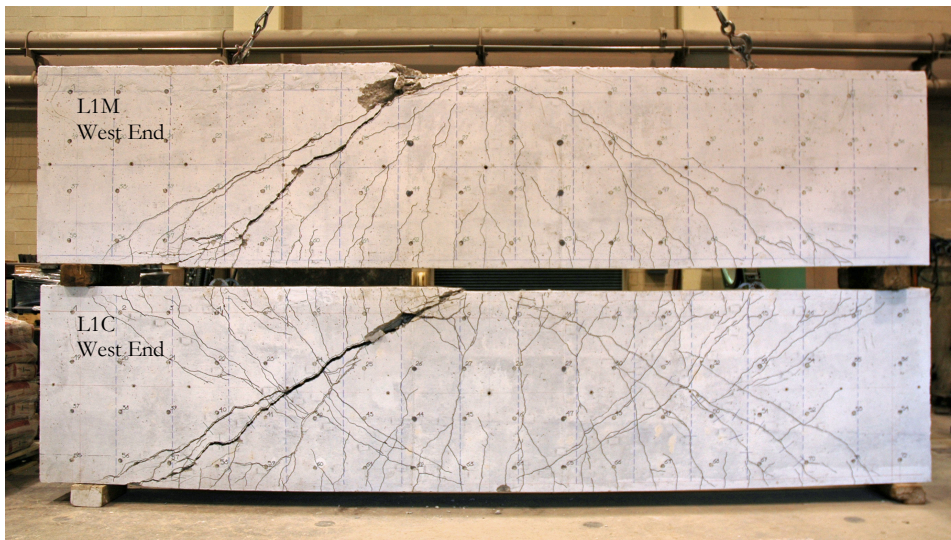


Figure 4.48 – cont





Figure 4.49 Critical loading zones after failure – specimens S0M (on the left) and S0C (on the right)

Identical beams with transverse reinforcement exhibited negligible scatter (compare curve S1M to S1C and curve L1M to L1C in Figure 4.47) mainly because of two reasons. First, the stirrups had some influence on the propagation of diagonal cracks and reduced the scatter in terms of depth of the critical loading zones. And second, specimens S1M/C and L1M/C developed truss-type load-bearing mechanism in which a significant part of the shear was carried below the critical cracks. As a consequence, the global response of the beams was less sensitive to variations in the depth of the crushing zones.

Very similar trends and magnitude of scatter were observed in the test results of Leonhardt and Walther (1961), as well as in the results of Rogowsky, MacGregor, and Ong (1986) (see Figure 2.2 and Figure 2.5).

#### 4.3.5 Shear Strengths

Table 4.2 contains the experimentally-obtained shear strengths of specimens S0M/C, S1M/C, L0M/C, and L1M/C together with the corresponding CSA code predictions (see 2.2.2.2). The ultimate shear force  $V_{u,exp}$  is calculated at the middle of the shear spans using (4.3) while  $V_{u,pred}$  is obtained by neglecting the effect of the distributed load from self weight. The last column of Table 4.2 shows that the CSA code renders conservative predictions for all the specimens but S0M which has an experiment-to-prediction ratio slightly smaller than 1.

Table 4.2 Experimental shear strength vs. CSA code prediction – specimens S0M/C, S1M/C, L0M/C, and L1M/C

Specimen	a/d	$f_c'$ (MPa)	$F_{TL,u,exp}$ (kN)	$V_{u,exp}$ (kN)	$V_{u,pred}$ (kN)	$\frac{V_{u,exp}}{f_c'bd}$	$\frac{V_{u,pred}}{f_c'bd}$	$\frac{V_{u,exp}}{V_{u,pred}}$
S0M	1.55	34.2	1420	721	747	0.0481	0.0498	0.97
S0C	1.55	34.2	2301	1162	747	0.0776	0.0498	1.56
S1M	1.55	33.0	1860	941	828	0.0651	0.0573	1.14
S1C	1.55	33.0	1864	943	828	0.0653	0.0573	1.14
L0M	2.29	29.1	801	416	324	0.0327	0.0254	1.28
L0C	2.29	29.1	953	492	324	0.0386	0.0254	1.52
L1M	2.29	37.8	1295	663	607	0.0401	0.0367	1.09
L1C	2.29	37.8	1253	642	607	0.0388	0.0367	1.06
Average								1.219
COV								0.177

Figure 4.50 shows the variation of the normalized shear strength as a function of the shear-span-to-effective-depth ratio. The CSA curves are generated for a concrete strength of 30 MPa by varying the length of the shear span and setting the rest of the parameters equal to those of the tested beams. The ordinates of the eight experimental points were slightly adjusted in order to comply with the experiment-to-prediction ratios in Table 4.2. If we assume that specimens S0M and S0C are well represented by an average strength value (see the gray point in the plot), two distinct trends in the experimental data can be pointed out. First, the shear strength decreases significantly with increasing shear-span-to-effective-depth ratio, and second, the strength improvement caused by the transverse reinforcement increases with increasing  $a/d$  ratio. As evident from the plot, the CSA code captures well both these trends. It can also be seen that the code curves represent a lower bound of the scattered experimental points of the specimens without stirrups. This is a favorable result because, as discussed in 4.3.4, the shear strength of non-slender beams with no web reinforcement is sensitive to random factors.

Table 4.3 compares experiment-to-prediction ratios for the eight specimens given by the CSA, ACI, and EC2 codes (see 2.2.2.3). It can be seen that ACI and EC2 produce rather unconservative predictions for most of the tested beams with the lowest experiment-to-prediction ratio being equal to 0.68.

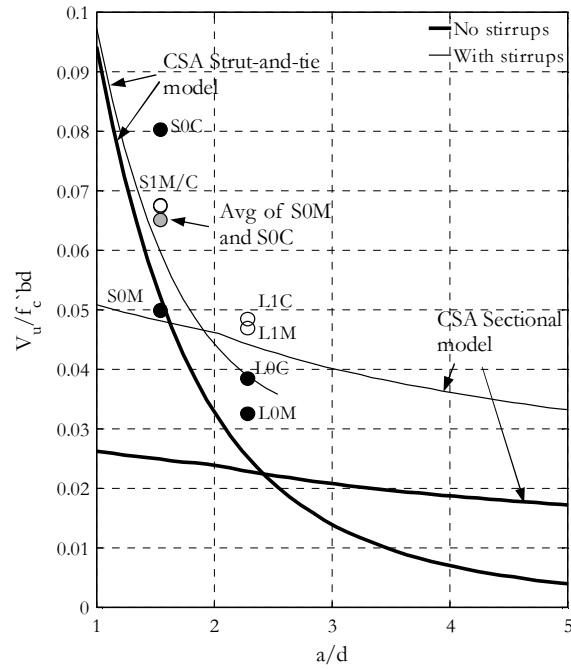


Figure 4.50 Experimental shear strength vs. CSA code prediction – specimens S0M/C, S1M/C, L0M/C, and L1M/C

Table 4.3 Experimental shear strength vs. CSA, ACI and EC2 code predictions – specimens S0M/C, S1M/C, L0M/C, and L1M/C

Specimen	a/d	$V_{u,exp}$ (kN)	$V_{u,exp}/V_{u,pred}$		
			CSA	ACI	EC2
S0M	1.55	721	0.97	0.74	0.73
S0C	1.55	1162	1.56	1.19	1.17
S1M	1.55	941	1.14	0.95	0.93
S1C	1.55	943	1.14	0.95	0.93
L0M	2.29	416	1.28	1.01	0.68
L0C	2.29	492	1.52	1.20	0.80
L1M	2.29	663	1.09	0.78	0.78
L1C	2.29	642	1.06	0.75	0.75
Average			1.22	0.95	0.85
COV			0.177	0.194	0.189

Figure 4.51 is analogous to Figure 4.50, but includes ACI and EC2 prediction curves (see 2.2.2.3). Plot b) shows that EC2 underestimates the rate at which the shear strength decreases with increasing  $a/d$  ratio. This is an indication that the assumption for almost constant strut efficiency factor  $v_s$  does not reflect the true behaviour. The lower limit on the angle  $\theta_s$  between struts and ties, imposed in the ACI code, compensates for this deficiency only to a certain extent (see plot a). It is also interesting to note that, according to EC2, transverse reinforcement of 0.1% has no effect on the shear strength of long beams with sectional and material properties identical to those of the tested specimens. In fact, the EC2 empirical expression for members without web reinforcement gives larger shear-strength prediction than the variable-angle truss model with cracks at  $45^\circ$  (see 2.2.2.1).

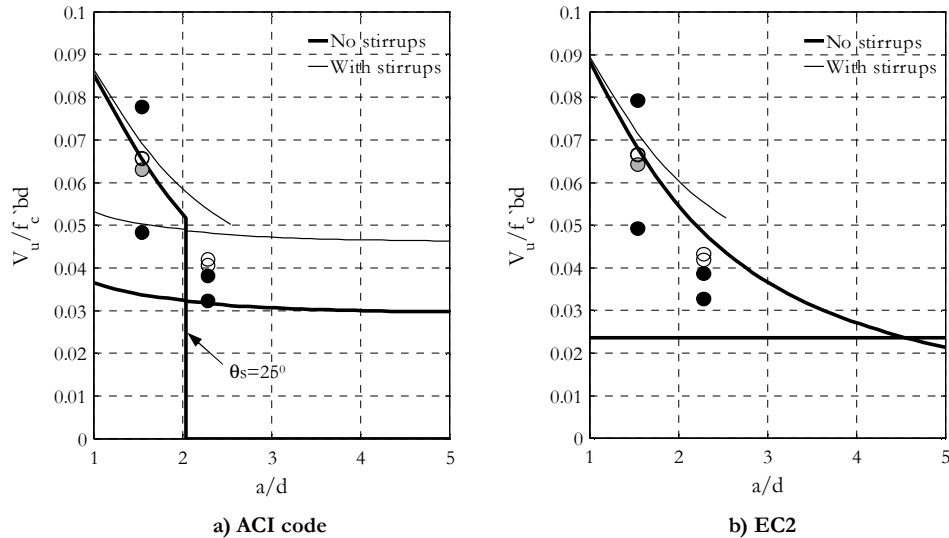


Figure 4.51 Experimental shear strength vs. ACI and EC2 code predictions – specimens S0M/C, S1M/C, L0M/C, and L1M/C

#### 4.4 SPECIMENS MB AND SB

Figure 4.52 shows the “top load vs. mid-span displacement” curves of specimens MB and SB. Figure 4.53 compares the crack patterns and crack widths of the two beams. The first six crack diagrams correspond to three load levels while the last two plots show the crack state of the specimens at the last load stage prior to failure. Figure 4.54 contains photographs of the beams taken soon after failure. The display on top of the specimens shows the magnitude of the top load at that instant of time.

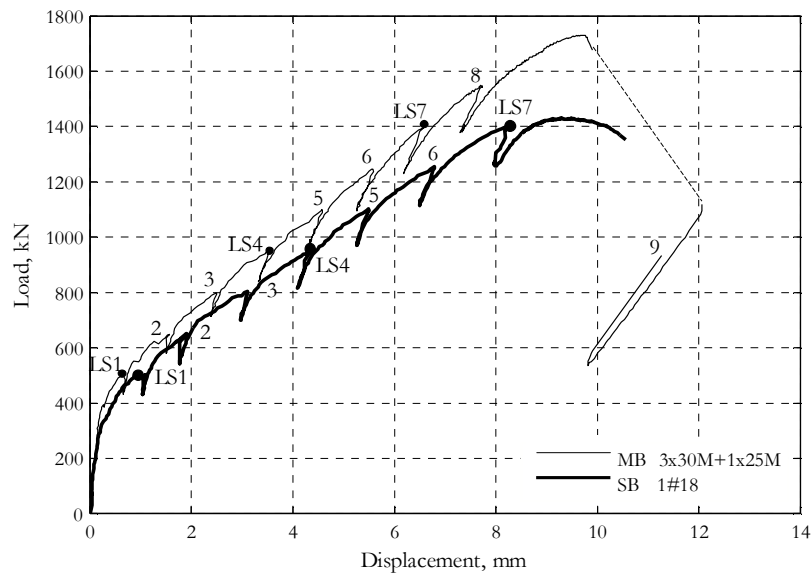


Figure 4.52 Load – displacement response- specimens MB and SB

Specimen MB behaved linearly up to load of about 400 kN when flexural cracking took place at the bottom of the mid-span section (see Figure 4.52 and Figure 4.53). The following loading to 800 kN resulted in propagation of two flexural and two steep flexure-shear cracks together with several short vertical cracks in-between. Short flat cracks were observed at the inner ends of the lap splices between the straight bottom bars and the anchor hooks. Further loading caused formation of more flat cracks along the splices and at load of 1100 kN the cracking had already “arrived” at the inner edges of the support plates. At the last load stage the maximum width of the flexure-shear cracks and that of the splice cracks reached 3.5 mm and 1.6 mm, respectively. Specimen MB failed at a load of 1731.2 kN and a displacement of 9.6 mm with widening of the east flexure-shear crack and splitting along the lap splice (see Figure 4.54). The post-peak resistance decreased quickly to about 1100 kN when it was decided that additional set of Zürich

readings would provide valuable information about the mechanism of failure. In order to stop the growth of deformations, the beam was unloaded to about 530 kN and the load was again increased to 930 kN where the ninth load stage was performed.

Specimen SB developed just three primary cracks – one flexural at the middle and two steep flexure-shear cracks on both sides of the mid-span section (see Figure 4.52 and Figure 4.53). The first cracking took place under a load of about 320 kN while the flexure-shear cracks reached the vicinity of the loading plate at a load of about 600 kN. Inspection of the bottom face of the beam at Load Stage 1 (500 kN) revealed the initiation of splitting cracks along the reinforcing bar at the vicinity of the three primary cracks (see Figure 4.53). Loading to 800 kN caused the formation of flat secondary cracks at the bottom of the two flexure-shear cracks and propagation of the splitting cracks all the way to the inner edges of the support plates. Several short cracks, oriented perpendicularly to the reinforcing bar, had also appeared on the bottom face of the specimen. Further loading did not lead to formation of new cracks but to extension of the splitting cracks above the supports towards the anchor heads. At the last stage of loading the maximum width of the flexure-shear cracks and that of the splitting cracks reached 3.5 mm and 2 mm, respectively. Specimen SB failed in a very brittle manner at load of 1431.3 kN and displacement 9.5 mm with crushing at the compression zone on the east side of the loading plate (see Figure 4.54).



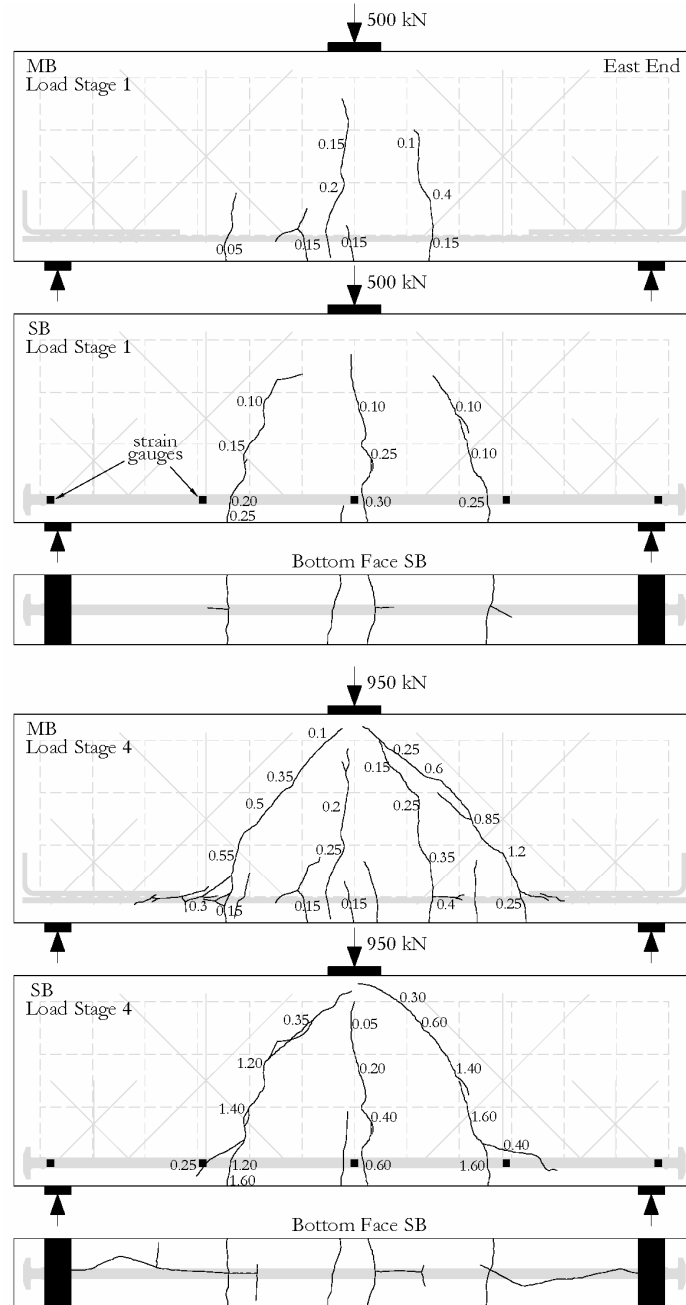


Figure 4.53 Cracks – specimens MB and SB

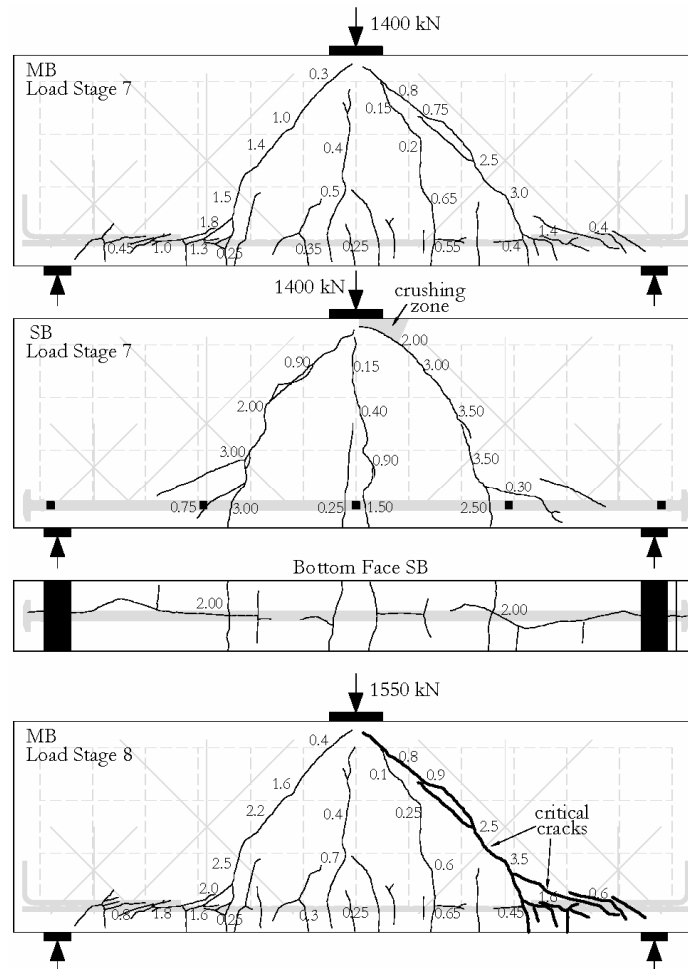


Figure 4.53 - cont

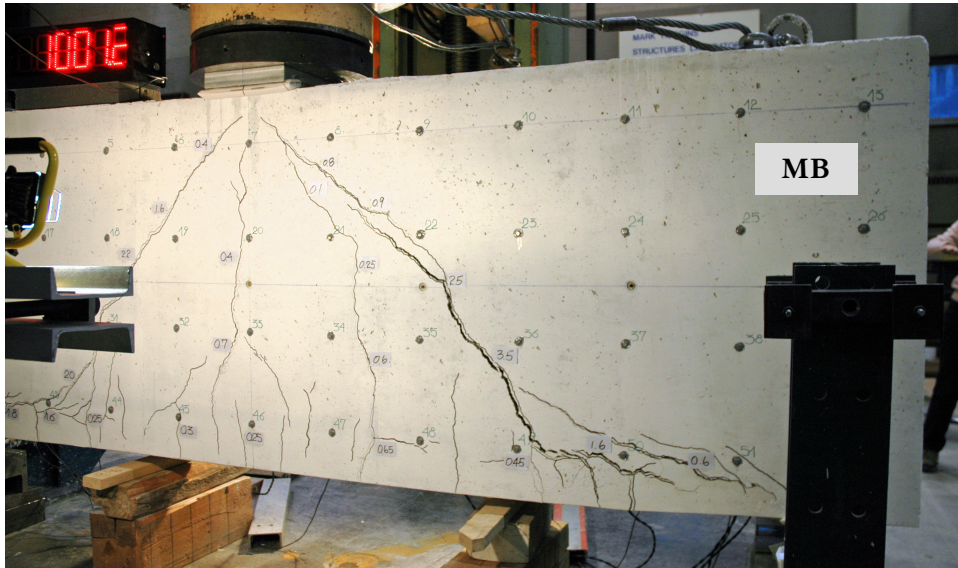


Figure 4.54 Failure – specimens MB and SB

The described behaviour of specimen MB can be explained in the following way. The initial flexural and flexure-shear cracking were not affected by the presence of the lap-spliced hooks and developed in the usual manner for deep beams. The cracking along the lap splices, on the other hand, can be attributed to the combined action of two mechanisms. First, the concrete between the spliced bars transmits high shear which causes a series of short inclined cracks, and second, the dowel action of the bottom layer of reinforcing bars tends to separate them from the above overlapping bars. Both effects would have been significantly reduced if specimen MB was provided with transverse reinforcement. The stirrups participate in a truss mechanism against the shear and restrain the splitting caused by dowel action. In the absence of such transverse reinforcement, however, the cracking between the two layers of bars was almost equivalent to failure of the lap splice. This resulted in full development of arch action consisting of constant tension in the bottom reinforcement and diagonal compression between the loading and support points. Furthermore, the anchor hooks became ineffective and the tension in the chord of the arch was resisted only by bond above the support plates. The failure of specimen SB was caused by a pullout failure at the zone of the east support. It is important to note that the breakdown of the lap splices did not allow formation of “peeling” cracks near the supports. In this way the critical flexure-shear crack was quite steep and the aggregate interlocking of its faces may have contributed to the high load-bearing capacity of the beam.

The behaviour of specimen SB can be interpreted as follows. Similarly to specimen MB, the initial flexural and flexure-shear cracking had the expected pattern. The splitting cracks on the bottom face of the beam were caused by circumferential tensile stresses around the very large #18 bar associated with bond between the deformed surface of the steel and the surrounding concrete. The splitting took place under the bar because the concrete cover there was smaller than the side cover (see Figure 3.3). If specimen SB had stirrups, they would have restrained the opening of the splitting cracks. In the absence of stirrups, however, the splitting was almost equivalent to complete loss of bond. As a result, arch action was fully activated without development of “peeling” cracks near the supports. The flat secondary cracks on the sides of the beam are attributed primarily to dowel action of the reinforcing bar. The concrete in front of the anchor heads was able to resist the diagonal compression associated with the arch action and specimen SB failed due to crushing of the critical loading zone on the east side of the loading plate (see Load Stage 7 in Figure 4.53). The failure was very brittle in agreement with the inherent brittleness of the concrete. The sudden release and shortening of the bottom bar caused impact and crushing at the bottom half of the critical crack (see Figure 4.54). Other possible explanation for the explosive damage at that location is a sudden failure of a shear key formed by the rough faces of the wide flexure-shear crack. If specimen SB had contained top bars, they would have acted as dowels and would have made the failure less

brittle. Similarly to specimen MB, part of the load-bearing capacity can be attributed to interlocking at the steep critical crack.

One of the clear differences between specimens SB and MB is that the former developed splitting cracks while the later did not. This outcome is not surprising since it is well-known that bars with larger diameters create greater circumferential tensile stresses for a given magnitude of bond stresses.

According to Figure 4.52, specimen MB was stiffer and stronger than specimen SB. The difference in terms of stiffness can be attributed to two reasons. First, the tension stiffening of the four small bars was larger than that of the single large bar. Generally, multiple bars with small diameters are more effective in engaging the surrounding concrete than a single large bar. More importantly, as mentioned above, the splitting cracks in specimen SB resulted in almost complete loss of interaction between reinforcement and concrete. Second, as evident from Figure 4.53, the critical loading zones of specimen MB were on average deeper and, therefore, less deformable than those of SB. The difference in the geometry of the critical loading zones explains also the difference in strength between the two beams. In fact, the critical loading zones of specimen MB were deep enough to resist a diagonal compression corresponding to pullout of the reinforcing bars.

Figure 4.55 compares the deformed shape of specimen MB after failure to that of specimen SB just prior to failure. Both shapes are amplified by a factor of 20. In order to make the interpretation of the kinematics of the beams easier, the three displacement restraints were chosen such that the mid-span section remains in its original position. It is evident that the elongation of the bottom chord within the east shear span of specimen MB is much larger than that of SB (9.0 mm or 5000  $\mu\epsilon$  vs. 4.4 mm or 2400  $\mu\epsilon$ ) even though the load on the former beam was smaller than that on the later one (930 kN vs. 1400 kN). This is a proof that the failure of specimen MB was caused by pullout of the reinforcing bars at the vicinity of the east support. The large elongation can not be devoted to yielding of the reinforcement because the beam with four bars did not maintain high post-peak resistance (see Figure 4.52). Another interesting observation is that the deformations in the critical loading zone of specimen MB are much smaller than those of SB. This is consistent with the fact that the beam with the single bar failed due to concrete crushing in that zone.

Figure 4.56a) compares the flexural response along the bottom chords (BH in Figure 3.14) of specimens MB and SB. The plot shows that the beam with a single bar cracked earlier than the beam with four bars even though the two cases are identical from the point of view of sectional analysis. The reason for this difference could be concentration of shrinkage stresses and/or load related stresses around the stiff #18 bar. The post-

cracking response demonstrates again that the strain stiffening effect was smaller in the case of specimen SB. Neither of the curves has a flat top and therefore flexural yielding did not occur.

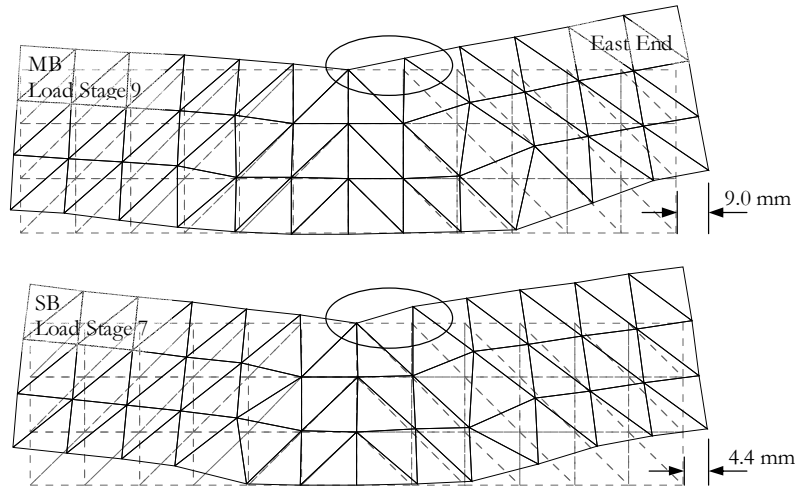


Figure 4.55 Deformed shapes – specimens MB and SB

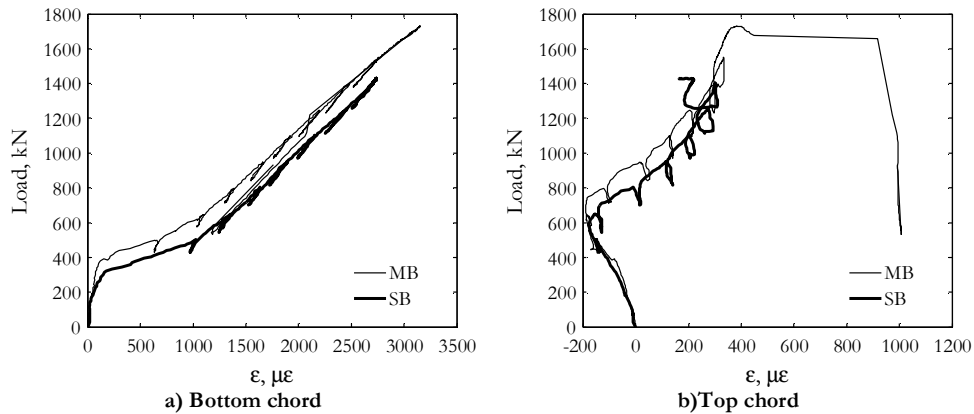


Figure 4.56 Flexural strains – specimens MB and SB

Figure 4.56b) compares the flexural response along the top chords (TH in Figure 3.14) of the beams. The two curves agree well up to the final load stages where a clear divergence takes place. The ultimate response of specimen SB is characterized by a negative strain increment while that of MB – by increasing tensile strain. This difference can be

explained if we recall that the top flexural strain consists of two components: 1) compressive strain in the concrete; and 2) apparent tensile strain coming from cracks in the loading zone. Specimen SB failed with crushing on the east side of the loading plate and its ultimate response was governed by the first strain component. In contrast, specimen MB failed with widening of the east diagonal crack and the second strain component therefore had a dominant role.

Plot a) in Figure 4.57 shows the strains measured on the surface of the #18 bar at various load stages, while plot b) illustrates the chord strains measured on the south face of specimen SB at the last stage of loading. Comparison between the two plots demonstrates that there was almost no compatibility between steel and concrete strains. The flat curves in plot a) represent clear evidence that arch action was fully activated. The strain just next to the west anchor head reached  $2100 \mu\epsilon$  which corresponds to a stress of 420 MPa. This stress can be used to calculate the maximum compressive stress which developed in the concrete in front of the anchor heads. Considering that the area of the head is about 10 times larger than the cross-sectional area of the bar, the concrete stress equals  $420/9=46.7$  MPa. This value is 1.53 times the cylinder strength of the concrete on the day of the test.

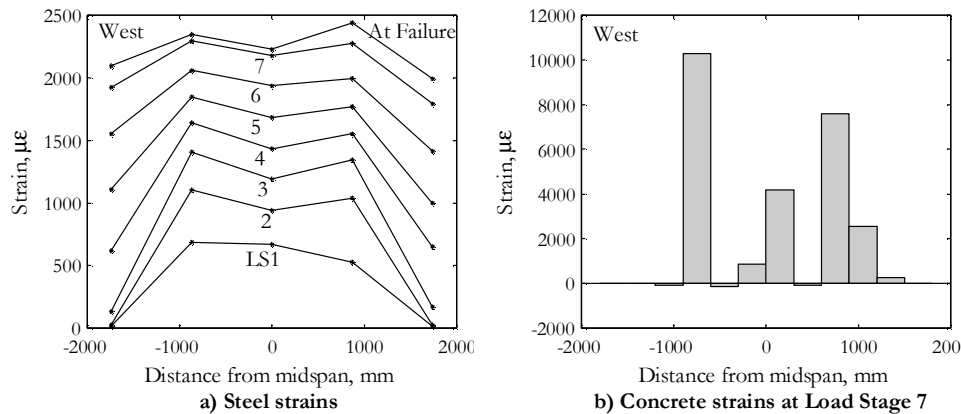


Figure 4.57 Bottom-chord strains – specimen SB

In order to study the damage around the anchor heads, the bottom-east corner of specimen SB was cut into four prisms according to the scheme in Figure 4.58a). The cutting was done by diamond saw as shown in the photograph in Figure 4.58b). After the cutting, the prisms and the cut face of the beam were watered and allowed to partially dry so that the moisture in the cracks made the cracks more visible. The photograph in Figure 4.58c) shows that there was a large vertical crack in front of the anchor head.

Examination of the concrete in the prisms containing the anchor head revealed no signs of crushing of the concrete (see Figure 4.58d).

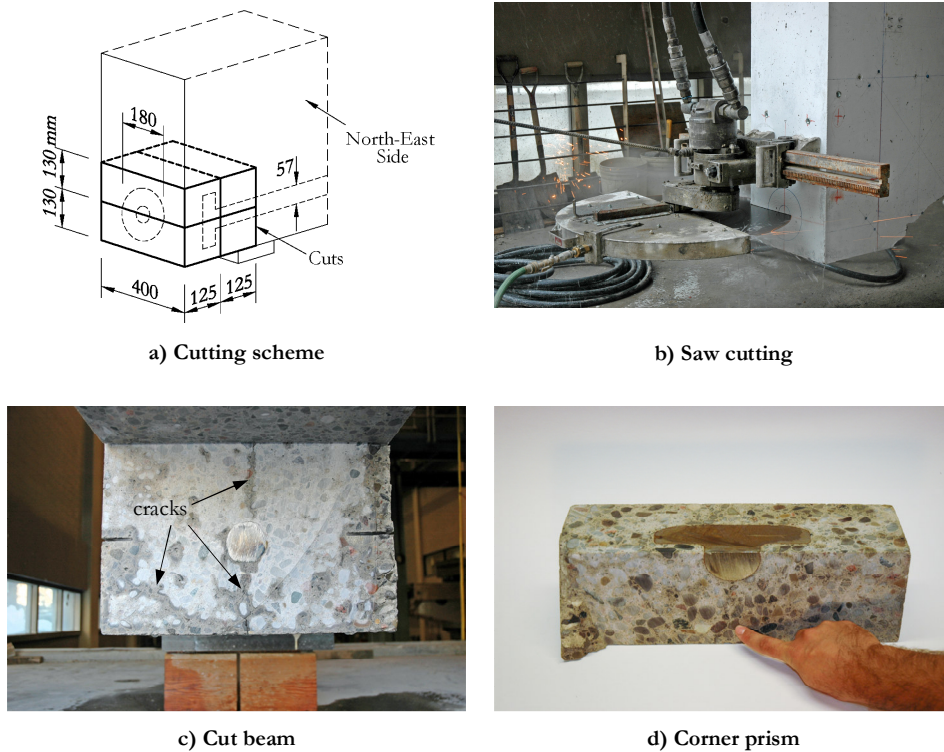


Figure 4.58 Damage around anchor heads – specimen SB

The strut-and-tie model in Figure 4.59a) is intended to demonstrate how highly-disturbed and complex is the stress field around the anchor heads. The tension force in the reinforcing bar is balanced by bond forces along the bar and by direct compression upon the anchor head (head bearing). The principal compression trajectories spread when moving away from the reinforcement because the diameter of the bar and that of the anchor head are much smaller than the dimensions of the cross section of the beam. The widening of the compression flow is possible by virtue of co-existing tensile and compressive circumferential stresses. The tensile stresses cause splitting cracks which in turn result in redistribution of internal stresses. For the sake of simplicity, the strut-and-tie model does not reflect the tensile stresses which occur in planes parallel to the plane of the beam. The compressive circumferential stresses, on the other hand, provide lateral



confinement of the concrete in front of the anchor head, which is probably the main reason for the high values of the head bearing stresses calculated above.

Figure 4.59b) shows how the bond and the head bearing contributions varied with increasing tension in the reinforcing bar of specimen SB. The tension in the bar  $T$  is obtained from the strain gauge located above the inner edge of the east support (see Figure 3.15), the head bearing component  $T_{hb}$  comes from the gauge installed just in front of the east anchor head, and the bond component  $T_b$  equals the difference between  $T$  and  $T_{hb}$ . The plot shows that before Load Stage 3 the tensile force was balanced entirely by bond. After Load Stage 3 the bond resistance decreased quickly and at failure it was equilibrating just 18.4% of  $T$ . The reason for the sudden change at a load of about 800 kN is the propagation of a splitting crack between the east flexure-shear crack and the east support plate. It should be noted that the splitting at the ends of specimen SB may have been partially restrained by the steel support plates. Another interesting outcome from Figure 4.59b) is that the 10%-unloading of the beam, performed at each load stage, did not lead to reduction of the head bearing. This observation can be explained by taking into account that the slip deformations between bar and concrete are compatible with the deformations in the concrete in front of the anchor head. If the slip deformations are decreasing, so are the deformations in front of the head, and so are the bearing stresses in front of the head. However, the slip deformations do not decrease much upon unloading because the bond mechanism is of frictional type. As a result, the strain and stress state in front of the anchor head remains unchanged while the load on the beam is being reduced.

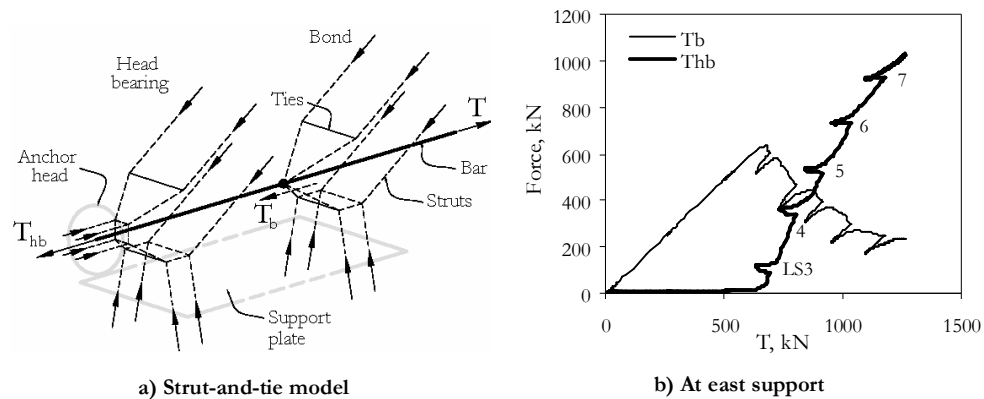


Figure 4.59 Head bearing and bond – specimen SB

The mid-span shear at failure  $V_{u,exp}$  of specimens MB and SB was calculated from (4.3) and equals 876.7 kN and 726.7 kN, respectively. The CSA code (see 2.2.2.2) predicts

ultimate shear force  $V_{u,pred}=719.7$  kN ( $V_{u,exp}/V_{u,pred}=1.22$  for MB and 1.01 for SB) corresponding to strut crushing. The calculations were performed considering  $a=1700$  mm,  $d=1070$  mm,  $b=400$  mm,  $l_{b1}=l_{b2}=150$  mm,  $A_s=2580$  mm<sup>2</sup>,  $\rho_b=0\%$ ,  $f'_c=30.5$  MPa,  $a_g=20$  mm, and  $f_y=652$  MPa. Failure modes involving lap splice failure and pullout of the bars of specimen MB were not considered. The complex support zone of specimen SB was treated as a standard two-dimensional compression-compression-tension (CCT) node region.

#### 4.5 SUMMARY OF EXPERIMENTAL RESULTS

Table 4.4 provides a summary of the experimental results of the 10 large beams tested in this study. It is interesting to compare specimens SB and S0M. The beam with a single #18 bar had slightly larger  $a/d$  ratio ( $1.59/1.55=1.03$ ), smaller reinforcement ratio ( $0.60/0.70=0.86$ ), and slightly weaker concrete ( $30.5 \text{ MPa}/34.2 \text{ MPa}=0.89$ ), but yet it resisted slightly larger shear than the beam with 6 bars #8 ( $727 \text{ kN}/721 \text{ kN}=1.01$ ). This result could be explained by the patterns of cracks which developed in the two beams (see Figure 4.23 and Figure 4.53). Specimen S0M had a flat critical diagonal crack which resulted in a relatively slender and, therefore, relatively weak critical loading zone. In contrast, the critical loading zone of SB was relatively strong because the poor bond between the concrete and the single reinforcing bar prevented propagation of flat flexure-shear cracks.

The maximum crack widths  $w_{max}$  and the ratio  $\Delta_u/a$  shown in the table are indicators of how much warning the deep beams gave prior to failure. It is interesting to compare these numbers with experimental results from large but slender beams without web reinforcement. A good example for such tests are those of beams with  $d=1400 \text{ mm}$  and  $a/d=2.89$  reported by Sherwood, Bentz, and Collins (2007). These specimens had a reinforcement ratio of either 0.83 or 1.33 and an average concrete strength of 42.4 MPa. The average  $w_{max}$  and  $\Delta_u/a$  from these experiments equal 0.85 mm and  $2.56 \times 10^{-3}$ , respectively, compared to the 3.27 mm and  $5.05 \times 10^{-3}$  for the beams in the current study (see Table 4.4). This comparison demonstrates that slender beams fail in a much more sudden manner than deep beams.

The last column in Table 4.4 shows the experiment-to-prediction ratios based on the current CSA code. It can be seen that 7 of the 10 values lie between 0.97 and 1.22 which for shear critical deep beams are excellent results. The most conservative of the CSA predictions is that for SOC which, as discussed in 4.3.4, had very deep critical loading zone. The other two rather conservative predictions correspond to beams L0M and L0C. These specimens are in the transition zone between deep and slender members where current design code predictions have been shown to be very scattered (see Subsection 1.4). The following chapter presents a modified strut-and-tie model which is aimed at improving the CSA model for this transition zone.

Table 4.4 Summary of experimental results and CSA code predictions

Specimen	a/d	$\rho_l$ (%)	$\rho_v f_y$ (MPa)	$f'_c$ (MPa)	d (mm)	$w_{max}^{**}$ (mm)	$\Delta_u$ (mm)	$\Delta_u/a$ $\times 10^{-3}$	$V_{u,exp}$ (kN)	$V_{u,CSA}$ (kN)	$\frac{V_{u,exp}}{V_{u,CSA}}$	
S0M	1.55	0.70	0	34.2	1094	2.50	6.4	3.8	721	747 <sup>*</sup>	0.97	
S0C	1.55	0.70	0	34.2	1094	3.70	10.9	6.4	1162	747 <sup>*</sup>	1.56	
S1M	1.55	0.70	0.497	33.0	1094	2.30	7.7	4.5	941	828 <sup>*</sup>	1.14	
S1C	1.55	0.70	0.497	33.0	1094	4.20	8.4	4.9	943	828 <sup>*</sup>	1.14	
L0M	2.29	0.70	0	29.1	1094	2.00	10.0	4.0	416	324 <sup>*</sup>	1.28	
L0C	2.29	0.70	0	29.1	1094	4.00	11.1	4.4	492	324 <sup>*</sup>	1.52	
L1M	2.29	0.70	0.497	37.8	1094	3.50	14.2	5.7	663	607 <sup>***</sup>	1.09	
L1C	2.29	0.70	0.497	37.8	1094	3.50	13.7	5.5	642	607 <sup>***</sup>	1.06	
SB	1.59	0.60	0	30.5	1070	3.50	9.5	5.6	727	720 <sup>*</sup>	1.01	
MB	1.59	0.61	0	30.5	1070	3.50	9.6	5.6	877	720 <sup>*</sup>	1.22	
Average						3.27	Average		5.05	Average		1.198
											COV	0.168

Note: b=400 mm

\*\* From the last load stage

\* governed by strut-and-tie model, strut crushing

\*\*\* governed by sectional model

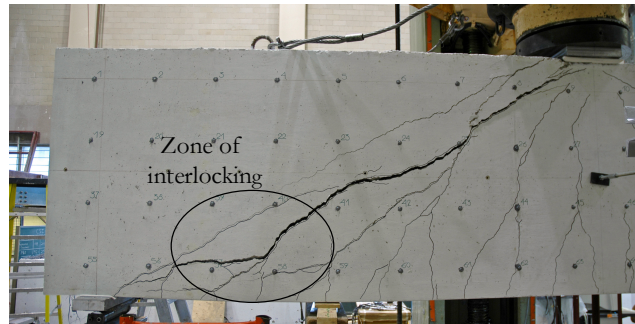
## **5.IMPROVED STRUT-AND-TIE MODEL FOR DEEP BEAMS WITHOUT WEB REINFORCEMENT**

### **5.1 FORMULATION AND SOLUTION PROCEDURE**

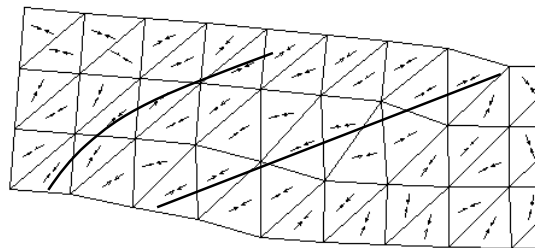
As suggested in Section 1.4, moderately-deep beams without web reinforcement may fail after the beam action has broken down, but before the arch action has fully developed. The detailed experimental program performed (see Chapters 3 and 4) confirmed this assumption and provided valuable information to help develop an improved strut-and-tie model for this situation.

Figure 5.1a) shows a photograph of specimen LOM taken after failure. Below the photograph is the experimentally-obtained deformed shape at 98% of the failure load with indicated directions of the principal compressive strains. The last plot in the figure shows the proposed improved strut-and-tie model (ISTM) for non-slender beams. The model is based on the assumption that the beam fails by diagonal crushing at the support zones after the cracks have spread over the entire bottom chord. Part of the shear force is carried under the critical flexure-shear crack (residual beam action) and the rest of it above the crack (arch action).

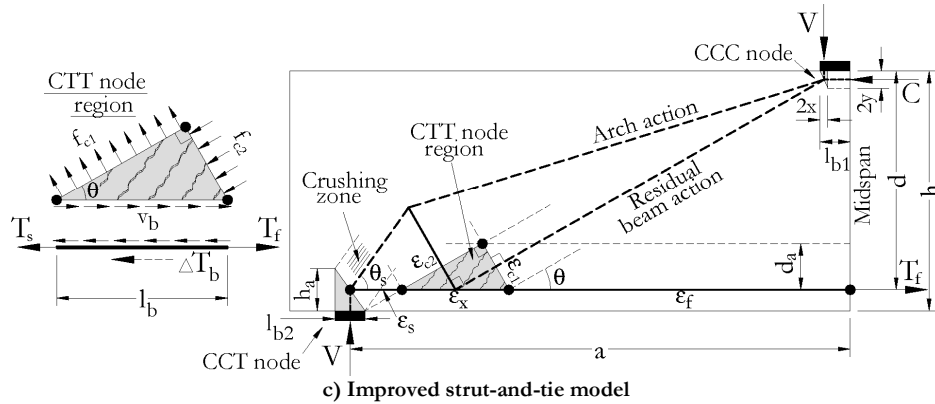
The residual beam action consists of a diagonal compression – diagonal tension mechanism through cracked concrete and is associated with reduced tension in the bottom chord near the supports. The existence of diagonal compression was indicated by the kinematics of the tested beams (see 4.2.2) and confirmed by the measured negative strains in the cracked webs (see 4.2.4). The residual resistance of the beam action depends on the ability of the cracked concrete to transfer diagonal tension, which in turn depends on the ability of the cracks to transfer shear. The interlocking of the cracks diminishes with increasing crack widths associated with increasing strain in the longitudinal reinforcement. The zone of interlocking is located near the supports where the cracks are well controlled by the reinforcing bars and where the tendency for slip on the cracks is highest (see 4.2.2). This is also a zone of potential dowel action of the bottom reinforcement.



a) Specimen L0M after failure



b) Specimen L0M – deformed shape and principal compressive strain trajectories



c) Improved strut-and-tie model

Figure 5.1 Specimen L0M and improved strut-and-tie model

As shown in Figure 5.1c), the residual beam action is modelled by a strut and a tie connected to the bottom chord at a compression-tension-tension (CTT) node representing the zone of aggregate interlocking. According to EC2, the depth with effectively controlled cracks can be calculated as:

$$d_a = \min \left[ 2.5 \frac{b_a}{2}, \frac{b-2y}{3} \right] \approx \min \left[ 2.5 \frac{b_a}{2}, 0.3b \right]. \quad (5.1)$$

This expression is preferred because of its simplicity. In reality,  $d_a$  depends on many other factors such as bar diameters and distribution of the reinforcement over the bottom part of the section.

The behaviour of the CTT node region is modeled by the Modified Compression Field Theory (MCFT) which includes equilibrium, compatibility, and material stress-strain relations for cracked reinforced concrete subjected to in-plane stresses (Vecchio and Collins, 1986). This solution is motivated by the observed behaviour of the zones of aggregate interlocking. Their relatively regular crack pattern (see Figure 5.1a) and approximately straight bottom contour (see Figure 5.1b) resemble the deformations of the panel elements used for development of the MCFT (see Figure 5.2). The basic assumption of the MCFT is that the average direction of the principal compressive stresses coincides with the average direction of the principal compressive strains and that the critical cracks are parallel to this direction. The inclined cracks depicted in Figure 5.1c) are not aligned with the principal stress/strain direction in order to reflect the rotation of cracks observed in the zones of interlocking (see Figure 5.1a). The stress and strain state of the CTT node can be fully determined for given vertical stress  $f_v$ , angle  $\theta$  between the longitudinal reinforcement and the principal compression direction, and average horizontal strain  $\epsilon_x$ . In addition, an estimate of the average distance between the cracks is required.

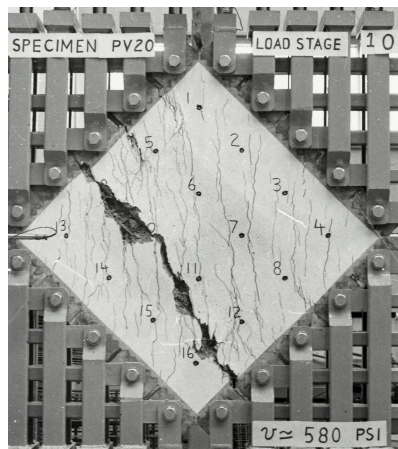


Figure 5.2 Panel tests (Vecchio and Collins, 1986)

The stress  $f_x$  is assumed zero which is equivalent to neglecting the effect of the dowel action on the node. The angle  $\theta$  is determined for given  $a$ ,  $d$ ,  $b$ ,  $l_{b1}$ ,  $l_{b2}$ ,  $x$ , and  $y$  by considering the geometrical conditions indicated in Figure 5.1c). The physical meaning of these conditions can be understood if the tension side of the node region is viewed as almost coincident with the flattest crack in the support zone (see also Figure 5.1a). An algebraic expression for  $\theta$  is derived in Appendix C. The strain  $\epsilon_x$  can be generally calculated as average of the strains in the longitudinal reinforcement on both sides of the node. For the sake of simplicity, however,  $\epsilon_x$  is taken equal to the average flexural strain  $\epsilon_f$ . The average distance between vertical cracks in the CIT node region is calculated from:

$$s_{mc} = 0.1 \frac{d_b}{\rho_{eff}} + \frac{d_a}{2}, \quad (5.2)$$

where  $d_b$  is the diameter of the longitudinal bars and  $\rho_{eff}$  equals  $A_s/(b_a/2+d_a)b$ . The average spacing  $s_{mc}$  of horizontal cracks is assumed infinitely large because of the absence of transverse reinforcement.

Considering horizontal equilibrium of the reinforcement within the node (see the left hand side of Figure 5.1c) and neglecting the tension stiffening effect of the concrete around the longitudinal reinforcement:

$$\epsilon_s = \epsilon_f - \frac{bl_b \cdot v_b (f_x = 0, \theta, \epsilon_x = \epsilon_f)}{E_s A_s}, \quad (5.3)$$

where  $l_b = d_a(\tan\theta + \cot\theta)$  and  $v_b$  is the average shear stress acting in the node region. Considering equilibrium of the concrete within the node (Mohr's circle):

$$v_b = f_{c1} \cot\theta. \quad (5.4)$$

According to the constitutive relations of the MCFT:

$$f_{c1} = \frac{0.33\sqrt{f_c'}}{1 + \sqrt{500\epsilon_{c1}}} \leq \frac{0.18\sqrt{f_c'}}{0.31 + \underbrace{\frac{24w}{a_g + 16}}_{v_{i,u}}} \tan\theta \quad \text{MPa, mm} \quad (5.5)$$

where  $\epsilon_{c1}$  is the average principal tensile strain within the node region,  $w = \epsilon_{c1}s_{mc}/\sin\theta$  is the width of the critical cracks, and  $a_g$  is the maximum aggregate size. The left part of this expression models the tension stiffening effect which is limited by the capacity of the



critical inclined cracks  $v_{i,u}$  to transfer shear through aggregate interlock. The actual shear stress  $v_{i,c}$  acting on the crack faces equals  $v_b$ .

Using conditions for strain compatibility:

$$\varepsilon_{c1} = \varepsilon_x + (\varepsilon_x - \varepsilon_{c2}) \cot^2 \theta \approx \varepsilon_f (1 + \cot^2 \theta) \quad (5.6)$$

and

$$\gamma_{xy} = (\varepsilon_{c1} - \varepsilon_{c2}) \sin 2\theta \approx \varepsilon_f (1 + \cot^2 \theta) \sin 2\theta = 2\varepsilon_f \cot \theta, \quad (5.7)$$

where  $\gamma_{xy}$  is the average shear deformation in the node region. The average principal compressive strain  $\varepsilon_2$  is neglected since its absolute value is expected to be much smaller than  $\varepsilon_f$ . As evident from Figure 5.1c), the node region can not develop high compressive stresses because the vertical component of their resultant force must equilibrate the relatively small vertical component of the resultant of the principal tensile stresses.

Finally, the local strain in the longitudinal reinforcement, occurring at the critical cracks, is calculated from:

$$\varepsilon_{ser} = \varepsilon_f + \frac{f_{c1} + v_{i,c} \cot \theta}{E_s \rho_{eff}} = \varepsilon_f + \frac{f_{c1} (1 + \cot^2 \theta)}{E_s \rho_{eff}}. \quad (5.8)$$

Figure 5.3 shows the behaviour of the above-formulated CTT node region. The plots are generated for the cross-sectional properties of specimen LOM. The angle  $\theta$  is related to the slenderness of the beam while the strain  $\varepsilon_f$  is a measure of the magnitude of the applied load. The more slender is the beam, the smaller the angle  $\theta$ . The larger the load on the beam, the larger the strain  $\varepsilon_f$ . As evident from the figure, both surfaces have distinct kink at  $\theta = \theta_k \approx (40^\circ - 50^\circ)$  which corresponds to  $a/d$  ratio between 1.25 and 1.65. Node regions with  $\theta < \theta_k$  are controlled by tension stiffening while those with  $\theta > \theta_k$  - by slip on the critical cracks (see (5.5)). Plot b) shows that the residual beam action has a peak at  $a/d \approx (1.25 - 1.65)$  and weakens with increasing load.

The arch action shown in Figure 5.1c) consists of a compression mechanism through uncracked concrete and is associated with constant tension along the bottom chord. Its strength depends on the ability of the loading and support zones to resist diagonal compression. The arch action is modeled by two struts and a bottom CCT node region. The crushing strength of the support strut is calculated in accordance with the CSA code procedure which accounts for compression softening effect (see 2.2.2.2).

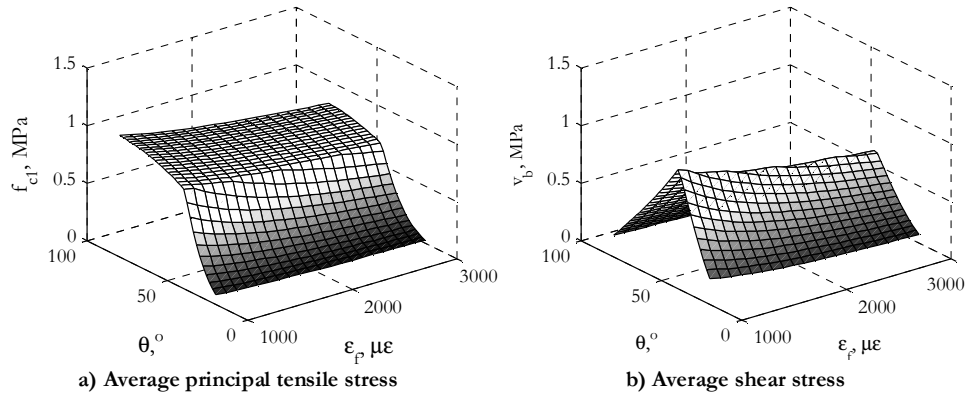


Figure 5.3 Behaviour of CTT node region—specimen L0M

Table 5.1 summarizes the stress and strain conditions of the CTT and CCT node regions. Both zones are modeled by the MCFT. The CTT node is associated mainly with aggregate interlock while the CCT node with diagonal crushing. It should be noted that the principal tensile stresses in the CCT region are neglected because they are not needed for the equilibrium of the support node.

Table 5.1 Comparison between the CTT and CCT node regions

Quantity	CTT node (residual beam action)	CCT node (arch action)
$\epsilon_2$	0	Crushing strain
$f_{c2}$	In vertical equilibrium with the principal tensile stresses	Crushing stress accounting for compression softening
$\epsilon_{c1}$	Compatible with the horizontal tensile strains and the diagonal compressive strains	
$f_{c1}$	Stress associated with tension stiffening limited by aggregate interlock	0

The top CCC node region of the improved strut-and-tie model is shared by both load-bearing mechanisms. Its dimensions can be determined such that it is under “hydrostatic” pressure with intensity  $0.85f'_c$  (see 2.2.2.2 and Figure 5.1c). In order to simplify the procedure, a solution with a horizontal nodal stress of  $0.85f'_c$  and  $x = l_{bt}$  is adopted.

The residual beam action and the arch action interact where the diagonal tension from the beam action diverts the compression flow of the arch action. This is confirmed by the

shape of the compression trajectories shown in Figure 5.1b). The weaker the residual beam action is, the smaller the kink between the two struts of the “arch”. In the limit case of zero beam action, the compression in the web “flows” directly from the loading point to the supports and the proposed ISTM “converges” to the CSA STM discussed in 2.2.2.2.

The improved strut-and-tie model is expected to result in higher strength predictions than the current CSA model for moderately-deep beams without web reinforcement. For a given applied load, the allowance for residual beam action leads to a steeper support strut and a smaller strain in the bottom chord near the support. The larger the angle  $\theta_s$ , the smaller the compression demand on the strut. The larger the angle  $\theta_s$  and the smaller the strain  $\epsilon_s$ , the smaller the compression softening effect.

A suitable procedure for performing calculations with the above equations is as follows:

- 1) Calculate  $d_a$  and  $\theta$  from (5.1) and Appendix C, respectively. In order to simplify the calculations, use  $x=l_{b1}$  and  $y=0$ .
- 2) Calculate  $s_{mc}$  from (5.2).
- 3) Assume an initial value of  $y$  (say  $y=0.05d$ ) and calculate  $x$  from (2.3). In this way the top node region will be subjected to hydrostatic stress state. The calculations can be simplified by considering  $x=l_{b1}$ . Note that with  $x=l_{b1}$ , where  $l_{b1}$  represents one-half of the width of the loading element, the procedure can be also applied to the end shear spans of beams subjected to symmetric four-point bending.
- 4) Calculate  $C=T_f=2yb \cdot 0.85f'_c$ .
- 5) Calculate  $V$  considering equilibrium of the shear span:

$$V = T_f \frac{d - y}{a - l_{b1} + x}. \quad (5.9)$$

- 6) Calculate  $\epsilon_f$  as equal to  $T_f/E_s A_s$ .
- 7) Calculate  $\epsilon_s$  using (5.3), (5.4), (5.5), and (5.6).
- 8) Calculate  $\theta_s$  and the compression force  $D$  in the support strut:

$$\theta_s = \tan^{-1} \frac{V}{E_s A_s \epsilon_s}, \quad (5.10)$$

$$D = V / \sin \theta_s. \quad (5.11)$$

- 9) Calculate the compression capacity of the support strut:

$$D_u = b \cdot (l_{b2} \sin \theta_s + b_a \cos \theta_s) f_{cu}, \quad (5.12)$$

where  $f_{cu}$  is calculated from (2.8) and (2.9).

10) Calculate new values for  $T_f$  and  $y$ :

$$T_f' = E_s A_s \varepsilon_s \frac{D_u}{D} + b d_a (\tan \theta + \cot \theta) v_b, \quad (5.13)$$

$$y' = T_f' / 2b \cdot 0.85 f_c' \quad (5.14)$$

and return to step 4 with the average of  $y$  and  $y'$ .

The calculations continue until  $D_u/D \approx 1$ . The final value of  $V$  represents the shear-strength prediction  $V_u$ .

Another way of expressing the shear strength is:

$$V_u = D_u \sin \theta = V_a + V_b = V_a + b d_a v_b, \quad (5.15)$$

where  $V_a$  and  $V_b$  are the vertical components of the forces acting in the top strut of the arch mechanism and in the strut of the beam mechanism, respectively.

## 5.2 COMPARISON WITH EXPERIMENTS

### 5.2.1 Specimens S0M/C and L0M/C

The solution procedure described above is applied first to specimen L0M:

$$1) \quad d_a = \min \left[ 2.5 \frac{210}{2}, 0.3 \times 1200 \right] = \min[263, 360] = 263 \text{ mm}$$

$$A = 263 / 2 = 131$$

$$B = -2500 + 150 / 2 = -2425$$

$$C = 263 / 2 + 105 + 1095 = 1331$$

$$\theta = \tan^{-1} \left[ \frac{2425 - \sqrt{2425^2 - 4 \times 131 \times 1331}}{2 \times 131} \right] = 29.52^\circ$$

$$2) \quad \rho_{eff} = \frac{3060}{(210/2 + 263) \times 400} = 0.0208$$

$$s_{max} = 0.1 \frac{25.4}{0.0208} + \frac{263}{2} = 122 + 131 = 253 \text{ mm}$$

$$\text{Assume } y = 0.05d = 0.05 \times 1095 = 55 \text{ mm}$$

$$3) \quad x = \frac{-(2275 + 150/2) + \sqrt{(2275 + 150/2)^2 + 4 \times 55 \times (1095 - 55)}}{2} = 24.1 \text{ mm}$$

$$4) \quad C = T_f = 2 \times 55 \times 400 \times 0.85 \times 29.1 / 1000 = 1088 \text{ kN}$$

$$5) \quad V = 1088 \frac{1095 - 55}{2500 - 150 + 24.1} = 476.8 \text{ kN}$$

$$6) \quad \epsilon_f = \frac{1088000}{200000 \times 3060} = 1.778 \times 10^{-3}$$

$$7) \quad \epsilon_{c1} = 1.778 \times 10^{-3} \times (1 + \cot^2 29.52^\circ) = 7.32 \times 10^{-3}$$

$$w = 7.32 \times 10^{-3} \times 253 / \sin 29.52^\circ = 7.32 \times 10^{-3} \times 513 = 3.76 \text{ mm}$$

$$v_{c1,w} = \frac{0.18 \sqrt{29.1}}{0.31 + \frac{24 \times 3.76}{20 + 16}} = 0.344 \text{ MPa}$$

$$f_{c1} = \frac{0.33 \sqrt{29.1}}{1 + \sqrt{500 \times 7.32 \times 10^{-3}}} = 0.611 \leq 0.344 \tan 29.52^\circ = 0.195 \text{ MPa} \rightarrow$$

$$\rightarrow f_{c1} = 0.195 \text{ MPa}$$

$$v_b = 0.195 \times \cot 29.52^\circ = 0.344 \text{ MPa}$$

$$l_b = 263 \times (\tan 29.52^\circ + \cot 29.52^\circ) = 613 \text{ mm}$$

$$\epsilon_s = 1.778 \times 10^{-3} - \frac{400 \times 613 \times 0.344}{200000 \times 3060} = 1.640 \times 10^{-3}$$

$$8) \quad \theta_s = \tan^{-1} \frac{476800}{200000 \times 3060 \times 1.640 \times 10^{-3}} = 25.40^\circ$$

$$D = 476.8 / \sin 25.40^\circ = 1111 \text{ kN}$$

$$9) \quad \varepsilon_1 = 1.640 \times 10^{-3} + (1.640 \times 10^{-3} + 0.002) \cot^2 25.40^\circ = 0.01779$$

$$f_{cu} = \frac{29.1}{0.8 + 170 \times 0.01779} = 7.61 < 0.85 \times 29.1 = 24.7 \text{ MPa}$$

$$D_u = 400 \times (150 \times \sin 25.40^\circ + 210 \times \cos 25.40^\circ) \times 7.61 / 1000 = 773.4 \text{ kN}$$

$$D_u / D = 773.4 / 1111 = 0.696 \neq 1 \rightarrow \text{Second iteration is needed.}$$

$$10) \quad T_j' = 200000 \times 3060 \times 1.640 \times 10^{-3} \times 0.696 / 1000 +$$

$$+ 400 \times 263 \times (\tan 29.52^\circ + \cot 29.52^\circ) \times 0.344 / 1000 =$$

$$= 698.6 + 84.4 = 783.0 \text{ kN}$$

$$y' = 783000 / (2 \times 400 \times 0.85 \times 29.1) = 39.6 \text{ mm}$$

The second iteration is performed with  $y = (55 + 39.6) / 2 = 47.3 \text{ mm}$ . Summary of all the iterations is presented in the table below.

Quantity	Iteration #			
	1	2	3	4
y (mm)	55.0	47.3	45.9	45.7
x (mm)	24.1	20.9	20.3	20.2
C=T <sub>f</sub> (kN)	1088.3	935.7	907.7	903.8
V (kN)	476.8	413.5	401.8	400.1
ε <sub>f</sub> (με)	1778	1529	1483	1477
ε <sub>cl</sub> (με)	7323	6296	6108	6081
w (mm)	3.8	3.2	3.1	3.1
v <sub>ci,u</sub> (MPa)	0.344	0.394	0.404	0.406
f <sub>cl</sub> (MPa)	0.195	0.223	0.229	0.230
v <sub>b</sub> (MPa)	0.344	0.394	0.404	0.406
ε <sub>s</sub> (με)	1641	1371	1321	1315
θ <sub>s</sub> (deg)	25.40	26.23	26.42	26.44
D (kN)	1111	935.6	903.0	898.5
ε <sub>1</sub> (με)	17785	15262	14780	14713
f <sub>cu</sub> (MPa)	7.61	8.57	8.78	8.81
D <sub>u</sub> (kN)	773.4	873.3	895.3	898.5
D <sub>u</sub> /D	0.696	0.933	0.991	1.000
T <sub>f</sub> ' (kN)	783.0	879.7	900.8	903.8
y' (mm)	39.6	44.5	45.5	45.7

As evident from the last column of the table, the ISTM predicts that specimen L0M would fail under a shear force of 400.1 kN. Note that the predicted failure shear for this specimen using the current CSA strut-and-tie model was 324.2 kN. In addition, considering equation (5.15):

$$V_b = 400 \times 263 \times 0.406 / 1000 = 42.7 \text{ kN}$$

Analogous calculations were performed for a series of beams with varying lengths of shear span and cross-sectional properties identical to those of specimens S0M/C and L0M/C. Since the two pairs of beams had different concrete strengths, an average value of 30 MPa was used. The results of the calculations, including a curve giving the “residual beam action” corresponding to  $V_b$ , are shown in Figure 5.4. Shown also are the experimentally-obtained shear strengths of specimens S0M/C and L0M/C, the prediction of the CSA strut-and-tie model, and the prediction of the CSA sectional model. As evident from the plot, the ISTM produced better predictions than the strut-and-tie model of the CSA code. This is particularly true if beams S0M and S0C are represented by their average shear strength. Note also that the transition from “sudden shear tension failures” to “gradual shear compression failures” is now predicted at  $a/d=2.8$  rather than  $a/d=2.4$ . The bottom curve in the figure shows that the residual beam action has a peak at  $a/d$  of about 1.4 and diminishes with increasing shear-span-to-effective-depth ratio. It should be noted that the “residual beam action” curve can not be obtained by simply subtracting the ordinates of the CSA STM curve from those of the ISTM curve.

Figure 5.4 also contains data point “10T0” at  $a/d=2.91$  which corresponds to a four-point bending test performed at Oregon State University (Higgins et al., 2004). Specimen 10T0 was considered particularly relevant to this discussion because it had sectional and material properties very similar to those of specimens S0M/C and L0M/C. Among the properties of the “Oregon” beam are  $d=1151$  mm,  $\rho=0.74$  %,  $f_c'=31.8$  MPa,  $a_g=20$  mm,  $b_{b1}=b_{b2}=102$  mm,  $b_a=137$  mm. It can be seen that the CSA code gives an excellent estimate of the failure load of 01T0. In addition, it is predicted that the beam would fail upon breakdown of beam action. Figure 5.5 shows a photograph of specimen 10T0 after failure. The fact that there is no visible evidence for concrete crushing at the loading and support zones indicates that the failure was indeed of shear tension type.

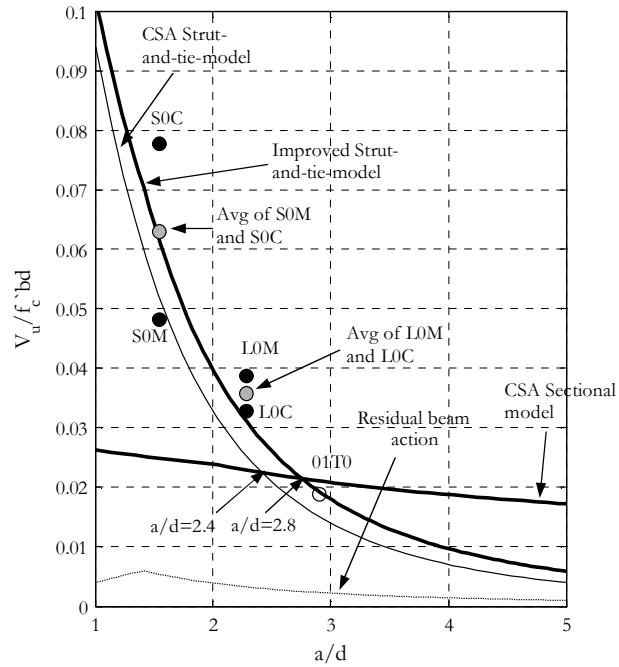


Figure 5.4 Experimental shear strength, CSA model, and Improved strut-and-tie model – specimens S0M/C and L0M/C



Figure 5.5 Failure of specimen 01T0 tested by Higgins et al. (2004)



Table 5.2 compares the predictions of the CSA code supplemented by the improved strut-and-tie model to the predictions of the CSA code alone. It can be seen that column “ $V_{u,CSA}$  or  $V_{u,ISTM}$ ” differs from column “ $V_{u,CSA}$ ” in the case of specimens S0M/C and L0M/C only. By definition, the ISTM is not applicable to beams S1M/C and L1M/C which contain stirrups. Specimens SB and MB did not have significant residual beam action because their reinforcement lost interaction with the surrounding concrete as a result of splitting of the concrete cover and lap-splice failure, respectively. As shown at the bottom of the table, the ISTM improved the average experiment-to-prediction ratio from 1.198 to 1.108 and reduced the coefficient of variation from 0.168 to 0.126. The data in the last three columns of Table 5.2 will be discussed in Section 5.3.

**Table 5.2 Predictions of the CSA code supplemented by the ISTM vs. predictions of the CSA code alone – specimens S0M/C, S1M/C, L0M/C, L1M/C, SB, and MB**

Specimen	a/d	$V_{u,exp}$ (kN)	$V_{u,CSA}$ (kN)	$V_{u,CSA}$ or $V_{u,ISTM}$ (kN)	$\frac{V_{u,exp}}{V_{u,CSA}}$	$\frac{V_{u,exp}}{\left(\frac{V_{u,exp}}{V_{u,CSA}}\right)}$ or $\frac{V_{u,exp}}{V_{u,ISTM}}$	$\Delta_{u,exp}$ (mm)	$\Delta_{u,pred}$ (mm)	$\frac{\Delta_{u,exp}}{\Delta_{u,pred}}$
S0M	1.55	721	747	873	0.97	0.83	6.4	9.0	0.71
S0C	1.55	1162	747	873	1.56	1.33	10.9	9.0	1.21
S1M	1.55	941	828	828	1.14	1.14	7.7	-	-
S1C	1.55	943	828	828	1.14	1.14	8.4	-	-
L0M	2.29	416	324	400	1.28	1.04	10.0	12.6	0.79
L0C	2.29	492	324	400	1.52	1.23	11.1	12.6	0.88
L1M	2.29	663	607	607	1.09	1.09	14.2	-	-
L1C	2.29	642	607	607	1.06	1.06	13.7	-	-
SB	1.59	727	720	720	1.01	1.01	9.5	-	-
MB	1.59	877	720	720	1.22	1.22	9.6	-	-
Average					1.198	1.108	Average		0.900
COV					0.168	0.126	COV		0.244

Figure 5.6 shows the ratio between the shear-strength prediction of the ISTM used in combination with the CSA sectional model and the prediction of the CSA code. The larger this ratio is, the larger the predicted effect of the residual beam action on the shear strength. As it would be intuitively expected, the curve has maximum ordinates in the range of transition from deep to slender beams. Deep members have very steep diagonals and naturally develop almost pure arch action while slender members fail immediately after the beam action breaks down. In the later case the residual beam action has significance for the post-peak response only. The experimental points, shown in the same plot, are on average closer to the  $V_{u,ISTM}/V_{u,CSA}$  curve than to the line  $V_u/V_{u,CSA}=1$ .

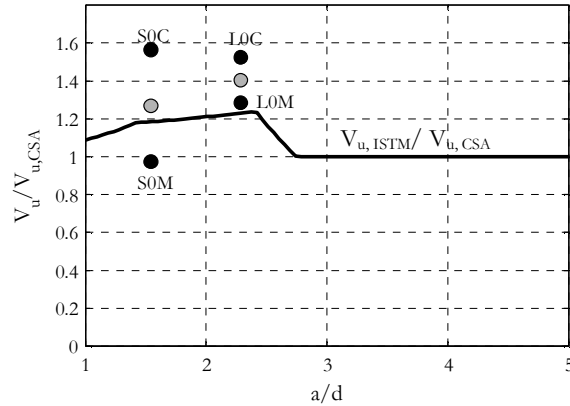


Figure 5.6 Effect of residual beam action on the shear strength – specimens S0M/C and L0M/C

The experimental data from tests S0M/C and L0M/C allows for more detailed verification of the proposed improved model to be performed. Figure 5.7 compares the predicted strains in the bottom chord of the beams (see plot a) to the strains in the reinforcement measured at ultimate load (see plot b). For the sake of simplicity, plot b) includes curves from the two monotonic tests only. The data from tests S0C and L0C can be found in Appendix B. The theoretical curves in plot a) can be assumed meaningful up to an  $a/d$  ratio of about 2.8 because more slender beams are expected to fail before the cracking has reached the supports. It can be seen that the ISTM captures the shape of the strain profiles and predicts the magnitude of the strains with reasonable accuracy. This conclusion is reinforced by the fact that the experimental values vary depending on the exact position of the strain gauges with respect to cracks. The location of the measured maximum strains coincides approximately with the location of the TTC node region of the improved strut-and-tie model (see Figure 5.1). The slip on the cracks at these zones is accompanied by an additional separation of their rough faces which results in increased strains in the bottom bars. The magnitude of this effect seems to be well predicted by equation (5.8) of the MCFT.

Figure 5.8 compares the predicted and measured widths of the cracks near the supports of the failed shear spans of specimens S0M and L0M. The estimated maximum widths of 1.7 mm (short beam) and 3.2 mm (long beam) agree relatively well with the measured values of 1.6 mm and 1.7 mm, respectively. It should be noted, however, that the widest crack in L0M occurred at some distance from the theoretical node region depicted with a gray triangle.

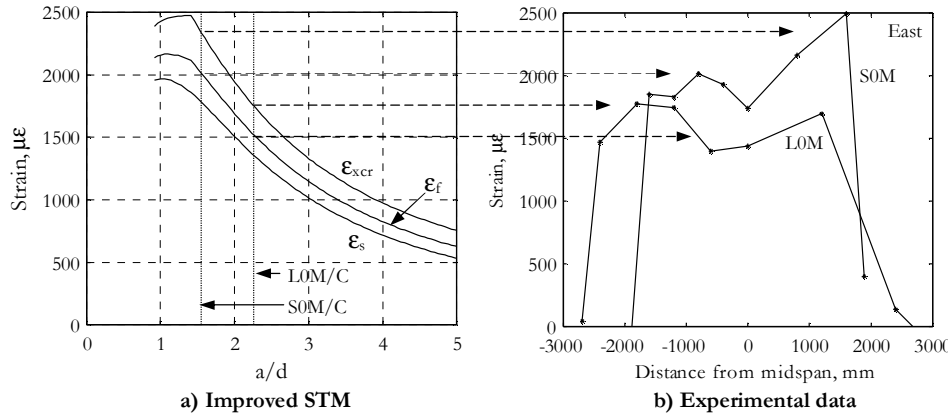


Figure 5.7 Chord strains acc. to the ISTM – comparison with specimens S0M and L0M

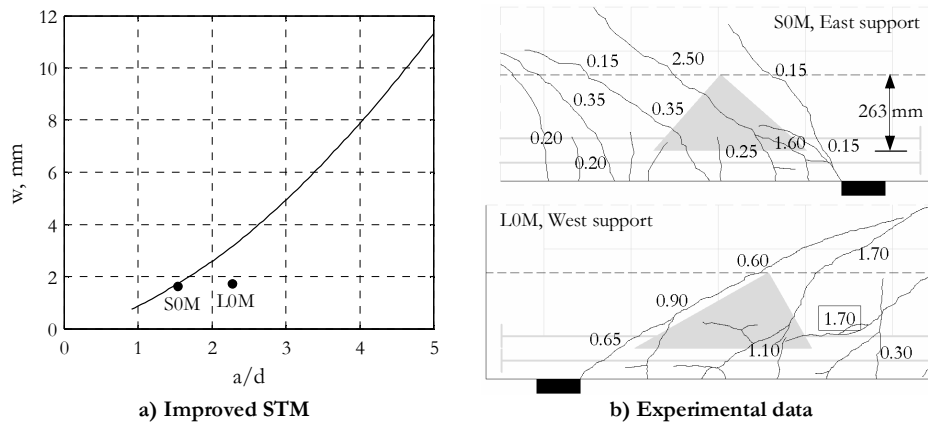


Figure 5.8 Crack widths acc. to the ISTM – comparison with specimens S0M and L0M

The last comparison with the data from specimens S0M and L0M is shown in Figure 5.9 and has to do with the average shear strains near the supports. The improved strut-and-tie model seems to capture the trend indicated by the experimental values. According to the model, the more slender the beam is, the smaller the angle  $\theta$ , and the larger the shear strain  $\gamma_{xy}$  for a given flexural strain  $\epsilon_f$  (see equation (5.7)). This trend is less pronounced in the actual calculations because, as evident from Figure 5.7,  $\epsilon_f$  decreases with increasing  $a/d$  ratio. In terms of magnitude, the predicted shear strains are about two-thirds of the corresponding test values.

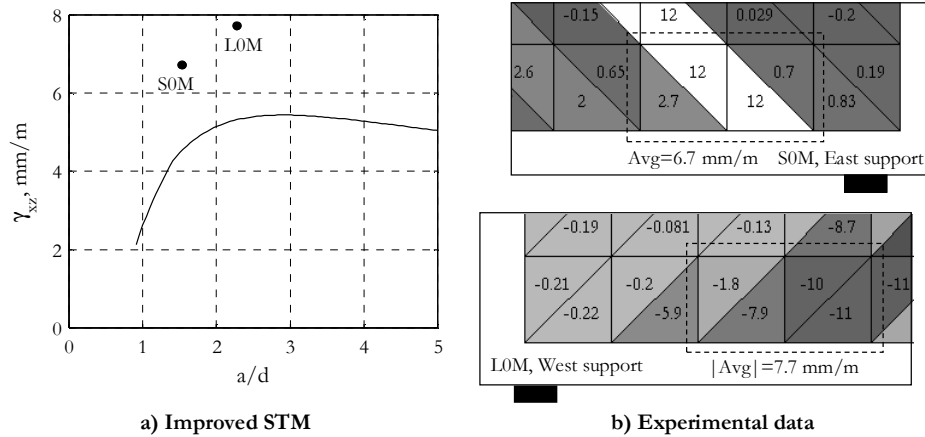


Figure 5.9 Shear strains acc. to the ISTM – comparison with specimens SOM and LOM

### 5.2.2 Shear database

The suggested improved strut-and-tie model was applied to the database of 1849 shear tests described briefly in 2.1.1 (Collins, Bentz, and Sherwood, 2008). The number of tests was reduced by excluding the cases to which the ISTM is not applicable, namely: simply supported beams with cantilevers, flexural failures (as defined by the authors of the database), specimens with FRP, specimens with bar cutoffs, Tee sections, specimens made of lightweight concrete (density smaller than  $2.3 \text{ t/m}^3$ ), distributed loads. In addition, the rather impractical cases of  $(b_u/2)/d > 0.25$  and  $l_{b2}/d > 0.5$  were removed as well. As a result, the following verification is performed with 848 data records. Since the database does not contain bar diameters, the horizontal distance between the cracks is calculated with  $d_b = 12 \text{ mm}$ . Trial calculations with different values showed that the size of the bars has little effect on the shear-strength predictions. Also, the calculations were performed using  $x = l_{b1}$  in Step 3) of the solution procedure described in Section 5.1.

Figure 5.10 compares the results from the CSA code to those from the improved strut-and-tie model used in combination with the CSA sectional model for slender members. The plots demonstrate that the proposed model gives less conservative average experiment-to-prediction ratio (1.115 for the ISTM vs. 1.264 for the CSA model), smaller coefficient of variation (0.222 for the ISTM vs. 0.250 for the CSA model), more uniform safety (less variation of the average experiment-to-prediction ratio and the  $COV$  with varying slenderness of the member), but a large percentage of unconservative predictions (33.1% for the ISTM vs. 19.7% for the CSA model). This comparison is performed only for specimens with  $a/d$  ratio between 0.5 and 3, 534 in number, because this is the approximate range in which the calculations are governed by the strut-and-tie models

over the sectional model. A summary of the properties of the members and results from the calculations is presented in Appendix D.

The positive outcome from the detailed verification with tests S0M/C and L0M/C (see 5.2.1) and the obtained uniform safety for a large number of experiments (see Figure 5.10b) demonstrate that the proposed improved strut-and-tie model is consistent with physical observations and explains reasonably well the transition from deep to slender beams. As evident from Figure 5.10a), the CSA model is most conservative and gives the largest scatter in the range of  $a/d$  between 1.5 and 2.5. The ISTM damps down this effect by predicting that the residual beam action has a maximum magnitude for approximately the same range of  $a/d$  values (see Figure 5.11).

The reduction in terms of scatter of the experiment-to-prediction ratios, provided by the improved strut-and-tie model, can be considered reasonably good if we recall that the shear-strength of non-slender members without web reinforcement is naturally scattered. As shown in 2.1 and 4.3.4, the difference in strength between seemingly identical beams can be as large as 60-70%. In addition, the load-bearing capacity is strongly influenced by the detailing of the loading and support zones (Collins and Mitchell, 1991). It should be also noted, that neither the CSA STM nor the ISTM accounts explicitly for failure caused by crushing at the critical loading zone. This failure mode has been reported by many researchers (see 2.1) and was observed in the tests performed as part of this study (Chapters 3 and 4). Is it possible, however, that top crushing is indirectly accounted for? If, for example, beams with increasing length and fixed other properties are considered, the diagonal struts are becoming weaker and weaker because of increasing compression softening at the support zones. On the other hand, as discussed in 4.3.2, the struts are becoming weaker also because the critical loading zone is becoming shallower and more slender. Identical reasoning can be applied in the case of decreasing amounts of bottom reinforcement: less reinforcement results in larger softening and shallower compression zone. It can be therefore concluded, that the load-bearing capacity of the loading and support zones follow similar trends and a good model for one of them may approximately represent the other.

The only feature of the improved strut-and-tie model that is a cause for some concern is the relatively large number of unconservative predictions. However, since the ISTM is too complicated for design purposes, it should be viewed as a model capable of predicting the average ultimate response of non-slender beams.

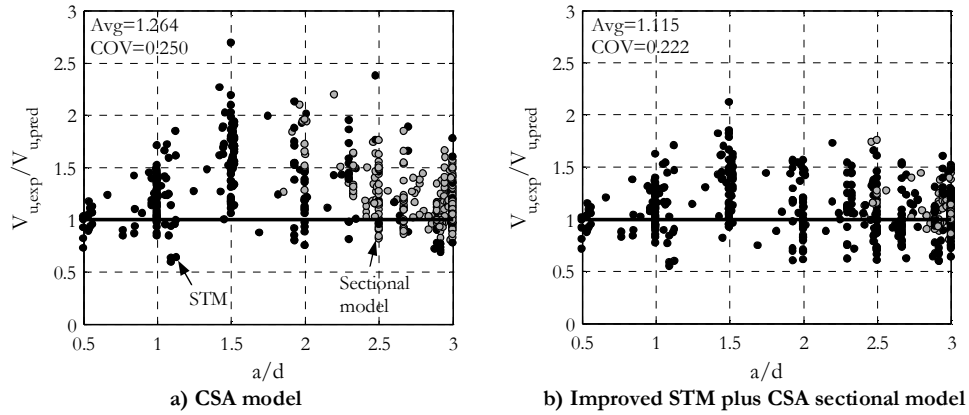


Figure 5.10 Experiment-to-prediction ratios – shear database - 534 test results

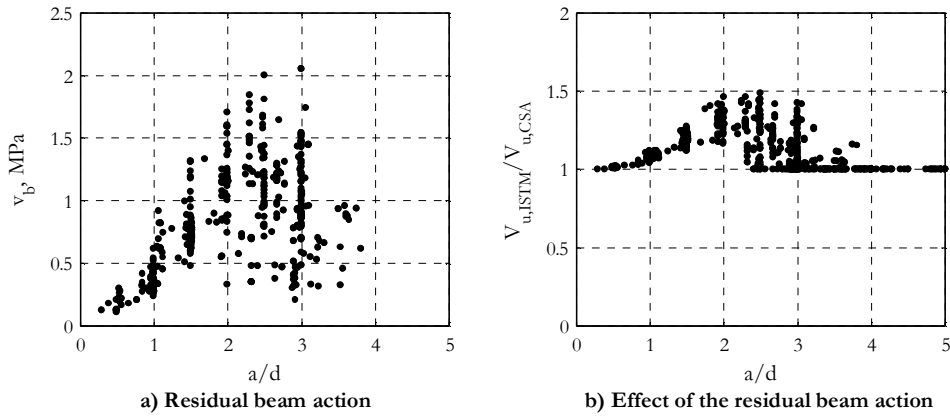


Figure 5.11 Predicted residual beam action and its effect on the shear strength – shear database

### 5.3 DEFORMATIONS

Figure 5.12 shows the proposed improved strut-and-tie model together with the kinematic model presented in 4.2.2. The correspondence between the two is evident. The ISTM is aimed at predicting the load-bearing capacity of non-slender beams. Its struts and ties should not be seen as real truss elements which shorten/lengthen and remain straight. Their function is rather to represent the flow of internal forces and to provide an estimate of important local deformations such as  $\epsilon_s$ ,  $\epsilon_t$ , and  $\gamma_{xy}$ . The kinematic model, on the other hand, provides relationships between the local and global deformations and can

be viewed as a set of compatibility conditions on the scale of the whole beam. Considering Figure 5.12 and taking into account (5.7):

$$\varepsilon_{t,u} \approx \varepsilon_f, \quad (5.16)$$

$$\Delta_{v,u} = \gamma_{xy} l_b = 2\varepsilon_f l_b \cot \theta = 2\varepsilon_f d_a (1 + \cot^2 \theta). \quad (5.17)$$

These relations show that the local compatibility condition (5.7) of the ISTM “couples” the two degrees of freedom of the kinematic model  $\varepsilon_t$  and  $\Delta_v$  by means of the strain  $\varepsilon_f$ .

The mid-span displacement at ultimate load can be now expressed by substituting equations (5.16) and (5.17) into the basic equation (4.10) of the kinematic model:

$$\Delta_u = \frac{\varepsilon_{t,u} a^2}{d_v} + \Delta_{v,u} = \varepsilon_f \left[ \frac{a^2}{d_v} + 2d_a (1 + \cot^2 \theta) \right]. \quad (5.18)$$

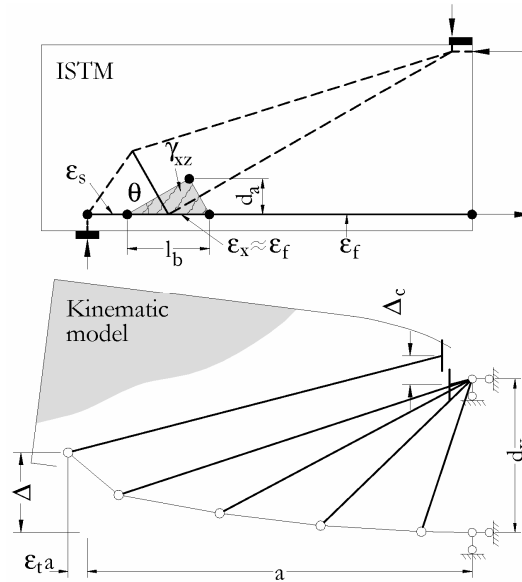


Figure 5.12 Improved strut-and-tie model and kinematic model

Figure 5.13 compares the displacement prediction based on equation (5.18) with the results from tests S0M/C and L0M/C. The ultimate displacements of the specimens are obtained from the readings of the vertical LVDTs installed in the middle of the span (see Figure 3.14), while the experimental values of  $\Delta_{v,u}$  are derived from the Zürich readings

taken at the last load stage (see 4.2.2). Since the last load stage was performed before failure, the true values of  $\Delta_{c,u}$  are probably slightly larger than those shown in the plot. It is also important to note that  $\Delta_{c,u}$  is taken as average of the deformations of the critical loading zones on both sides of the top loading plate. The figure demonstrates that the improved strut-and-tie model, used in combination with the kinematic model, captures well the trend indicated by the experimental points. It can be seen that the shear deformations along the critical diagonal crack contribute significantly to the mid-span displacement at the maximum load.

The actual numbers from this comparison are shown in the last three columns of Table 5.2. It can be seen that, on average, the suggested model gives a slightly high estimate of the measured ultimate mid-span displacement of specimens S0M/C and L0M/C (average experiment-to-prediction ratio of 0.90). This result can be attributed to the fact that the model neglects the tension stiffening effect of the concrete surrounding the bottom longitudinal reinforcement. The table also shows that the ultimate displacement of specimens SB and MB are significantly larger than that of S0M (9.5 mm and 9.6 mm vs. 6.4 mm). Among the reasons for this difference is probably the absence of residual beam action in the case of a beam with poor bond and in the case of a beam with inadequate lap-splice.

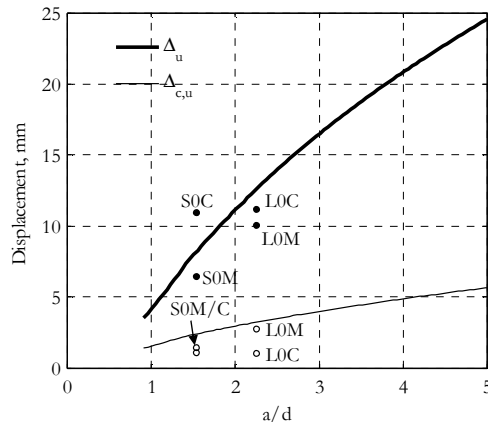


Figure 5.13 Ultimate displacement according to the improved STM used together with the kinematic model – comparison with specimens S0M/C and L0M/C

In conclusion, the proposed improved strut-and-tie model and the kinematic model can be used to obtain the shear strength and the ultimate deformed shape of non-slender beams without web reinforcement.



## 6. COMPARISON BETWEEN EXPERIMENTAL RESULTS AND VecTor2 ANALYSES

### 6.1 INTRODUCTION

Non-linear finite element procedures currently represent the most complex and advanced tools for predicting the response of reinforced concrete structures. They incorporate models from various constitutive frameworks such as non-linear elasticity, plasticity, continuum damage mechanics, smeared fixed/rotating crack models, microplane models (CEB-FIP, 2008). Each of these approaches has proven effective in some applications and less effective in others.

VecTor2 is a finite element program for 2D static and dynamic analysis of reinforced concrete structures. It has been developed over the last 18 years by Prof. Vecchio and his research group at the University of Toronto. Used in this study is VecTor2, Revision 6.0 from the 8<sup>th</sup> of February, 2008. The basic models implemented into the program include the Modified Compression Field Theory (MCFT – Vecchio and Collins, 1986) and the Disturbed Stress Field Model (DSFM – Vecchio, 2000). Both the MCFT and the DSFM fall into the category of smeared rotating crack models, as the later is built on the concepts of the former. The main difference between the DSFM and the MCFT lies in the reorientation of the stress and strain fields. As discussed in subsection 5.1, the basic assumption of the MCFT is that the average direction of the principal compressive stresses coincides with the average direction of the principal compressive strains and that the critical cracks are parallel to this direction. In contrast, the DSFM explicitly accounts for slip deformations at the critical cracks which results in delayed rotation of the stress field with respect to the strain field. The critical cracks in the DSFM are kept perpendicular to the direction of the principal tensile stresses.

The goal of this chapter is to compare the predictions of VecTor2 to the data from the tests performed as part of this study (see Chapter 3 and Chapter 4). The comparisons are done in global terms: load-displacement response, deformed shapes, crack patterns, and failure modes. In order to simulate the usual situation for engineering practice, it is assumed that the only information available prior to the analysis being performed is the geometry, boundary conditions, and basic material properties. With a few exceptions which are discussed later, the default options available in VecTor2 are chosen.

## 6.2 MODELING

Figure 6.1 shows the finite element models of specimens S0M/C, S1M/C, L0M/C, and L1M/C. As is evident from the plot, advantage is taken of the presence of the plane of symmetry passing through the mid-span section of the beams. The models are built with four-node rectangular elements with two translational degrees of freedom at each node. The loading and support plates are not explicitly modeled. The longitudinal reinforcement and the bars of the lifting hooks are represented by truss elements (Reinf. 1 and 3), while the stirrups are modeled as smeared reinforcement in the elements of the web (see the elements shaded gray). One of the nodes located within the width of the bottom support plate is restrained against vertical movement. The small eccentricity between the vertical restraint and the axis of the support does not affect the length of the shear span because, as it will become clear later, the resultant of the applied reaction forces acts at the center of the support plate. Connected to the restrained node is a short vertical truss element (Reinf. 2) whose other end is restrained against horizontal movement. The function of the short element will be discussed later in relation to the use of post processor Augustus developed by Prof. Bentz at the University of Toronto. It can be seen, however, that the truss bar does not affect the stiffness characteristics of the model.

In terms of constitutive modeling, the Disturbed Stress Field Model (DSFM) is used with default models for compression post-peak response of the concrete, compression softening, tension stiffening, tension softening, confinement, concrete dilation, cracking, crack width check, hysteretic response of the steel, dowel action, and buckling of the rebars. Non-default models were used only for the pre-peak compression response of the concrete (Popovic NSC model instead of Hognestad parabola) and for the hysteretic response of the concrete (Palermo 2002 with decay instead of non-linear with plastic offsets). It is well known that the parabola of Hognestad is a rather approximate representation of the true stress-strain response of concrete. Palermo 2002 hysteretic model (Palermo and Vecchio, 2004) is preferred because it includes improved non-linear unloading and stiffness degradation upon reloading. The properties of the concrete, supplied as an input to VecTor2, include the experimentally-obtained cylinder strength, strain at peak stress, and maximum aggregate size. The steel was defined by yield strength, ultimate strength, elastic modulus, strain hardening modulus, and strain hardening strain.

The basic modeling assumption regarding the loading conditions is that the loading and support plates apply uniform stresses perpendicular to the face of the beams. This simplification is motivated by the presence of a relatively soft and weak material (plaster) between the steel plates and the concrete surface. The total loading on the beams is resolved into the load cases depicted in Figure 6.2. Load case 1 represents the uniformly-distributed weight of the specimens. Load cases 2 and 4 contain forces which balance the

self weight of the beams at the bottom supports and at the bottom loading plate, respectively. Finally, Load cases 3 and 5 model the top/bottom mid-span loads and the corresponding bottom/top support reactions. Shown in Figure 6.2 is also the variation of the loads from the different load cases. Since VecTor2 does not allow for arbitrary variation to be defined, a load cycle from tests S0C, S1C, L0C, and L1C is resolved into four steps. Each step is run as a separate analysis with initial stiffness matrix taken from the last stage of the previous step. In VecTor2 this is done with the help of so-called seed files.

Physically, Step 1 corresponds to a cycle of loading and unloading performed by the Baldwin machine while the beam is seated on the bottom rollers. Step 2, on the other hand, models the loading range over which the bottom jacks overcome the weight of the beam. Steps 2, 3 and 4 all together represent a cycle of loading and unloading performed by the bottom jacks. Finally, Step 4 alone is a reverse to Step 2: the weight of the beam is gradually transferred from the bottom jacks to the bottom supports. Note that in Step 3 the applied forces are in equilibrium in the vertical direction and, therefore, the vertical restraint force is zero. This complicates the reading of the loads in post processor Augustus. In order to overcome this problem, a vertical force of  $(F_{BL}-G)/6$  is applied upon the aforementioned short truss element (see zone A in Figure 6.1 and Load case 5 in Figure 6.2). This force does not affect the behaviour of the model but causes a vertical restraint force whose magnitude can be easily related to the magnitude of the bottom applied load.

It is important to note that the assumed uniform distribution of the stresses applied by the loading and support plates requires the use of a force-controlled analysis. This approach does not allow for prediction of the post peak response but suits the way the loading histories for tests S0C, S1C, L0C, and L1C were defined.

The input files for specimens S1C and L0M are shown in Appendix E. The input for the rest of the beams is not presented for the sake of brevity.

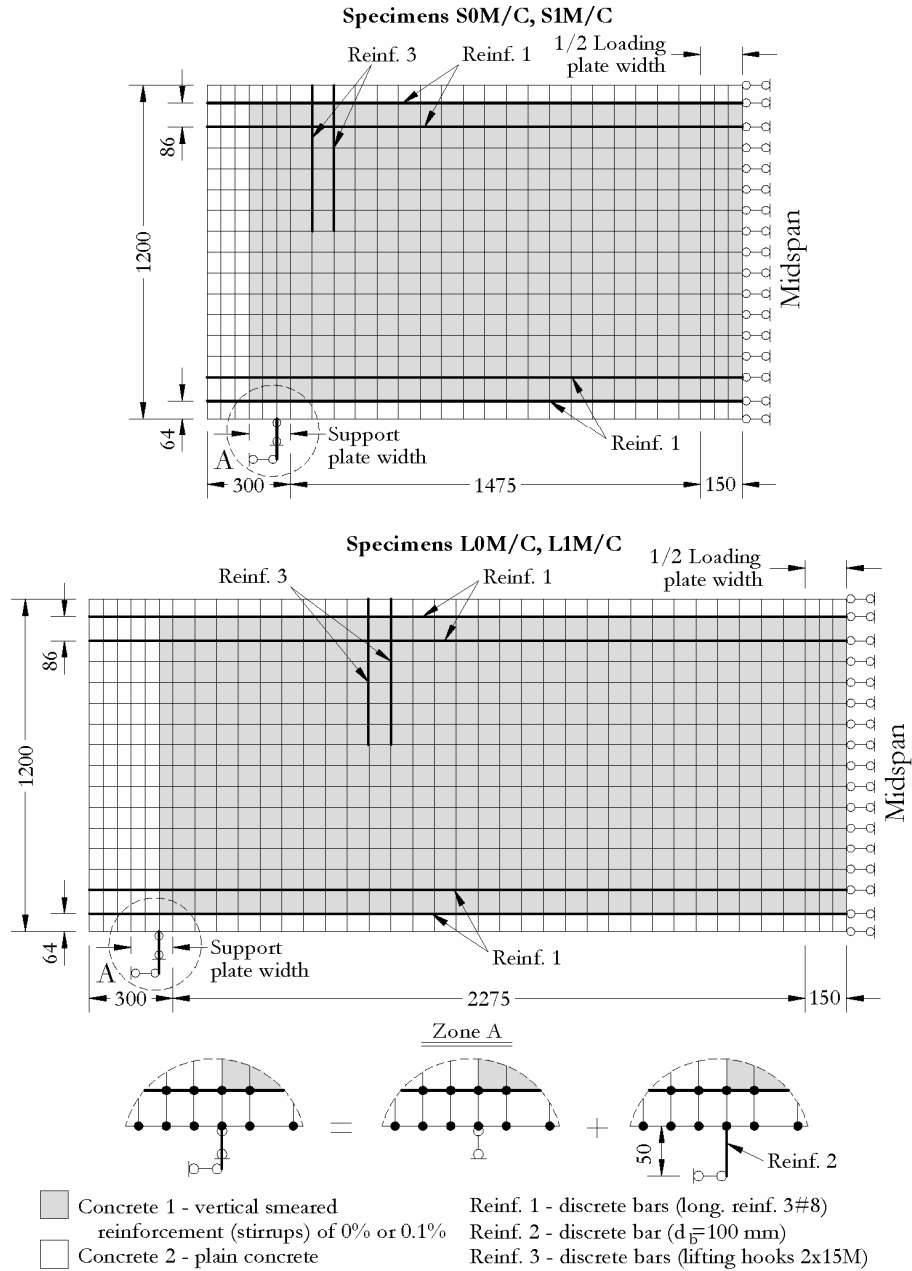


Figure 6.1 Finite element models - mesh and support conditions

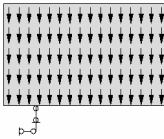

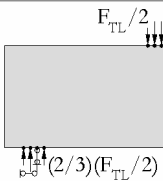
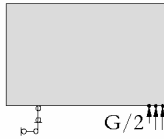
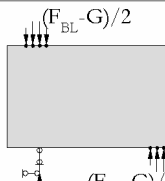
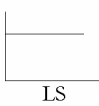
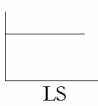
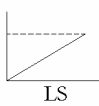
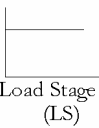
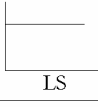
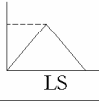
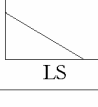
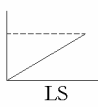
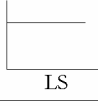
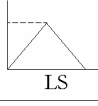
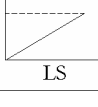
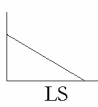
		Load case 1	Load case 2	Load case 3	Load case 4	Load case 5
						
Monotonic load					—	—
Reversed cyclic load - 1 cycle	Step 1				—	—
	Step 2			—		—
	Step 3		—	—		
	Step 4			—		—

Figure 6.2 Finite element models – loading conditions

### 6.3 RESULTS

Figure 6.3 compares the predicted load-displacement response of the monotonically-loaded specimens S0M, S1M, L0M, L1M to their measured response (left hand side plots) and to the measured response of specimens S0C, S1C, L0C, and L1C (right hand side plots). It can be seen that VecTor2 captured well the uncracked behaviour of the beams with the exception of specimens L0M and L0C whose initial stiffness is slightly underestimated. Similarly good are the results in the zone of transition from beam action to arch action for beams without stirrups, and from beam action to truss action for beams with transverse reinforcement. However, VecTor2 seems to overestimate the load-bearing capacity of the arch and truss mechanisms (see the experiment-to-prediction ratios at the top left corner of the plots). Most unconservative is the prediction for specimen S0M with an experiment-to-prediction ratio of 0.64 (see the top plot on the

left). This result appears less worrisome if the significant scatter between tests S0M and S0C is taken under consideration. In fact, the predicted monotonic response represents an almost perfect envelope to the response of specimen S0C (see the top plot on the right). However the strength prediction for beam L1M is a cause for real concern since it results in an experiment-to-prediction ratio of 0.73 for both L1M and L1C (see the bottom two plots in the figure). The most accurate prediction is for specimen S1M with an experiment-to-prediction ratio of 0.92 (see the left plot on the second row). These unconservative results are consistent with findings for deep beams containing little or no web reinforcement reported by Vecchio (2000). In the same publication he shows that rotating crack models such as the MCFT can provide a viable and accurate method for the analysis of slender lightly-reinforced beams which fail in shear.

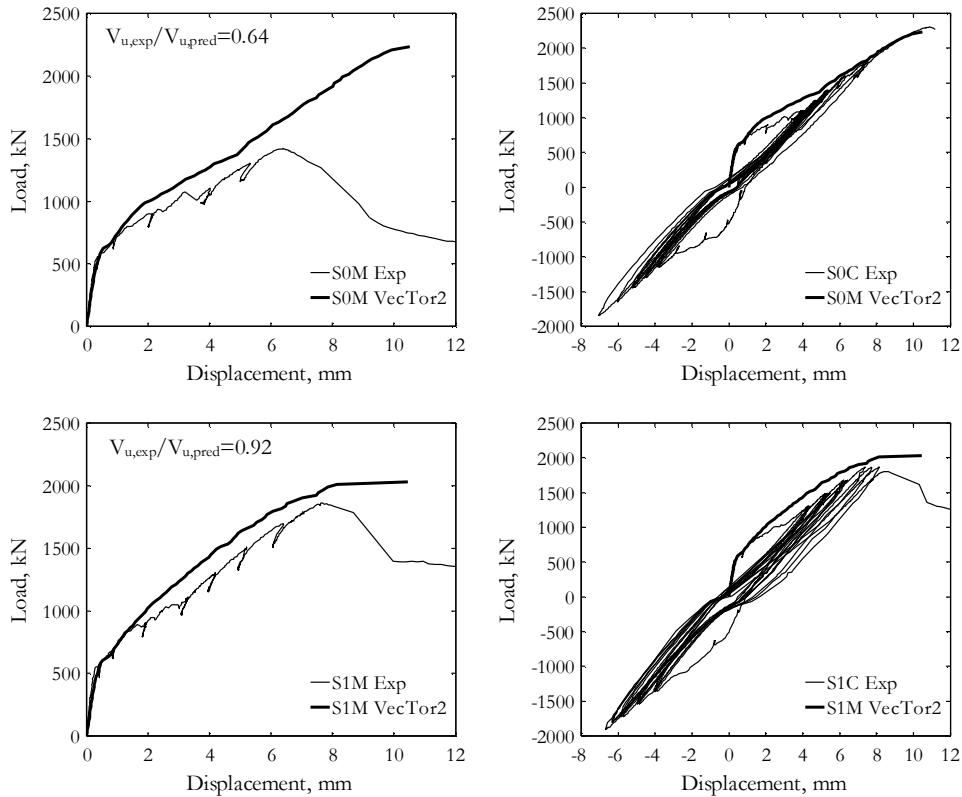


Figure 6.3 Experimentally-obtained load-displacement response vs. predictions from monotonic VecTor2 analysis—specimens S0M/C, S1M/C, L0M/C, and L1M/C

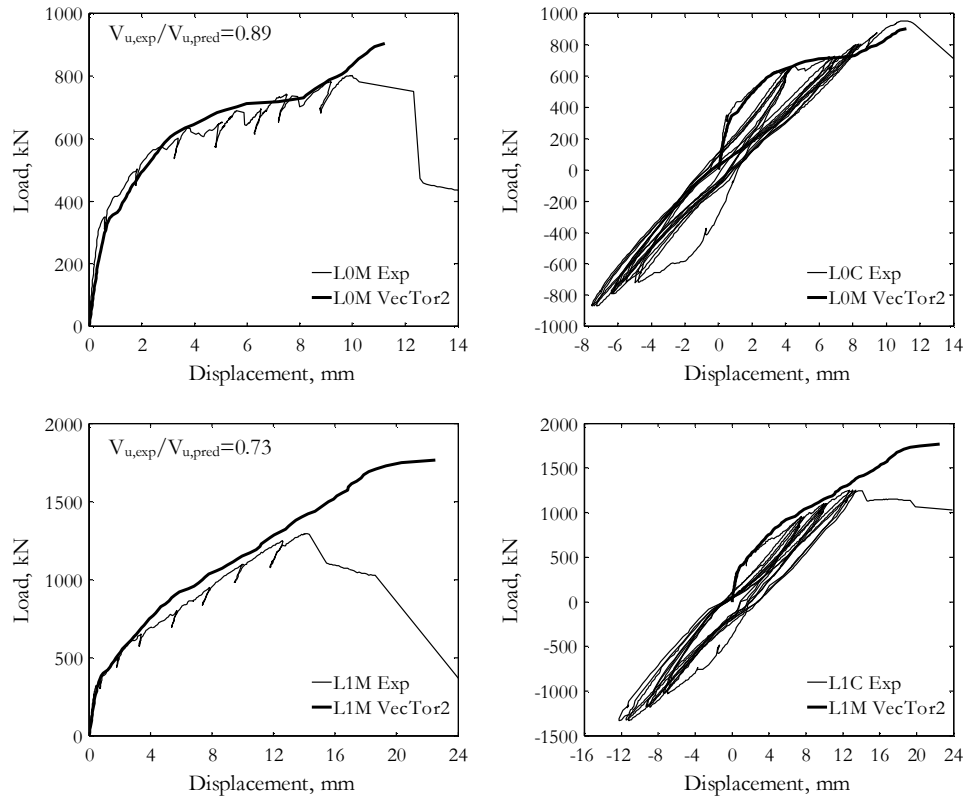


Figure 6.3 cont

Figure 6.4 and Figure 6.5 show respectively the crack patterns and the deformed shapes of the beams just prior to failure as predicted by VecTor2 for both monotonically and cyclically loaded specimens. Shown for comparison are also the experimentally-obtained crack diagrams and the deformed shapes of the grid of Zürich targets in the failed shear spans. The Zürich grid seems more “slender” than the specimens because it occupies only the middle 75% of their depth. It can be seen that in the case of beams S0M, L0M/C, and L1M/C a “band” of flexure-shear cracks covers the zone just above the bottom longitudinal reinforcement and “deviates” towards the top loading point at distance of about  $0.5d$  (short beams) to  $1d$  (long beams) from the mid-span section. In contrast, the experimentally-observed critical diagonal cracks run almost straight between the inner edges of the supports and the top loading zone. The significance of this difference is related to the geometry of the critical loading zones: the shallower the band of cracks, the deeper and more tapered the critical loading zone. As a result, VecTor2 underestimates the transverse deformations which take place near the edges of the

loading plates. As evident from the plots in Figure 6.5, the top contour of the finite element mesh of specimens S0M, L0M/C, and L1M/C remained almost straight, while in reality the top edge of the beams deformed significantly. According to the terminology of the kinematic model developed in 4.2.2, the results from VecTor2 imply that the mid-span vertical displacement of the beam comes almost entirely from elongation of the bottom reinforcement, i.e.  $\Delta = \Delta_t + \Delta_c \approx \Delta_c$ .

In the case of specimens S1M/C, VecTor2 predicted a deep band of diagonal cracks which resemble the crack pattern observed in the tests. Consistent with this result are the visible shear distortions at the critical loading zones of the model. As far as specimen S0C is concerned, the predicted cracking has an unusual pattern which is probably a result of the cyclic constitutive models used in the analysis.

It is interesting to note that in all eight cases VecTor2 predicts late occurrence of horizontal cracks at mid-height at face end of beam beyond the support. It is believed that these cracks do not influence the ultimate behaviour of the model because they do not affect the diagonal strut which forms in the web. Cracking of this type was not noticed during the tests, even though it seems consistent with the flow of stresses in the concrete above the critical diagonal cracks. An example of experimentally-observed end cracks are the tests of Alcocer and Uribe, 2008 (see Figure 2.11).

The two different crack patterns predicted by VecTor2 resulted in two different failure modes: beams with a shallow band of flexure-shear cracks (S0M, L0M/C, and L1M/C), including beam S0C, failed due to crushing at the support zone, while those with deep band of cracks (S1M/C) failed due to crushing at the critical loading zone. The first type of failure is demonstrated in Figure 6.6a). The top plot on the left shows the distribution of the principal compressive stresses in the web of beam L0M under maximum load. The short white lines indicate the direction and the relative magnitude of the stress. Elements with compressive stress less than 2 MPa and those with tensile principal stresses are shown in white. It can be seen that the zone of diagonal compression forms an almost ideal bottle-shaped strut as defined, for example, by the ACI code (see Figure 2.17). It should be noted, however, that this shape is possible only because VecTor2 predicts an unrealistically shallow band of flexure-shear cracks which determines the bottom contour of the strut. The failure of the bottle-shaped strut could take place at either of its ends where the compressive stresses are relatively high. The top plot on the right demonstrates that specimen L0M failed with crushing at the support zone. It can be seen that some of the finite elements at the bottom end of the strut start undergoing distress while the elements near the loading plate are still within the ascending branch of the compressive stress-strain curve. It is interesting to notice that the peak compressive stresses at these two zones differ significantly. The elements near the support experience compression softening due to the high principal tensile strains coming from compatibility with the



tensile strains in the bottom reinforcement. In addition, VecTor2 includes a routine called “crack width check” which additionally reduces the compression capacity once a given crack width limit ( $w=a_g/5$  by default) is exceeded. On the other hand, the elements at the top end of the strut are under biaxial compression which, according to the default constitutive models in VecTor2, leads to a slightly enhanced compressive strength. Finally, the bottom plot in Figure 6.6a) shows the deformed shape of specimen L0M corresponding to the first unconverged load stage.

A similar analysis of the causes of failure can also be performed for specimens S1M/C. For the sake of brevity, however, Figure 6.6b) contains only the post-failure deformed shape of beam S1M. It can be seen that VecTor2 predicted excessive shear deformations in the critical loading zone. This failure mode seems very similar to the experimentally-observed failures of all eight specimens.

Figure 6.7, Figure 6.8, Figure 6.9, and Figure 6.10 show the load-displacement response of all eight specimens as obtained from the tests and as predicted by VecTor2. Each plot contains monotonic and cyclic response of beams with the same length and the same amount of transverse reinforcement. The predictions are shifted to the right of the origin of the plots in order to avoid overlapping with the experimental hysteresis loops. The left pairs of curves display once again the significant scatter in the ultimate behaviour of the seemingly identical pairs of beams S0M/C and L0M/C. The right pairs of curves, on the other hand, show that VecTor2 predicts a relatively small effect of load reversals with strength reductions varying between 1.1% (beams L1M/C) and 15.0% (beams S0M/C). A comparison between experiment and analysis shows good agreement in terms of overall hysteretic response. As evident from Figure 6.9, VecTor2 captured the effect of the lifting hooks consisting of relatively high unloading/reloading stiffness under negative load. The same plot shows also that the finite element analysis predicts correctly the significant decrease in the “positive” unloading/reloading stiffness between the first and the second groups of load cycles. In fact, this is the load range over which specimen L0C developed flat diagonal cracks causing a significant loss of beam action. It should be noted, however, that VecTor2 underestimates the residual displacements and overestimates the stiffness degradation under consecutive cycles with constant load amplitude. A possible reason for the former discrepancy is that the finite element analysis does not account for residual slip deformations at the cracks, while the experimental observations showed the presence of permanent damage along the main diagonal discontinuities. The later discrepancy, on the other hand, is related mainly to the hysteretic model for concrete subjected to compression.

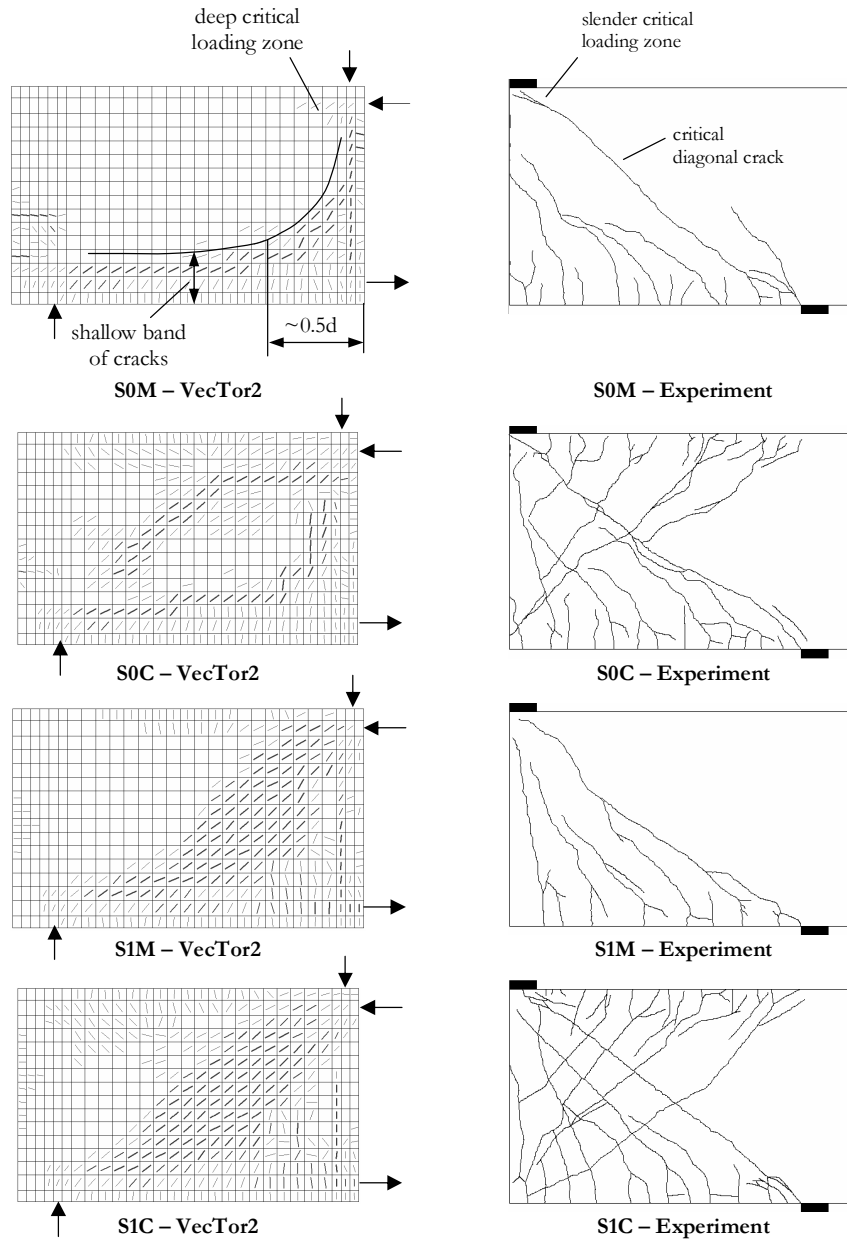


Figure 6.4 Crack patterns from VecTor2 analysis – specimens S0M/C, S1M/C, L0M/C, and L1M/C

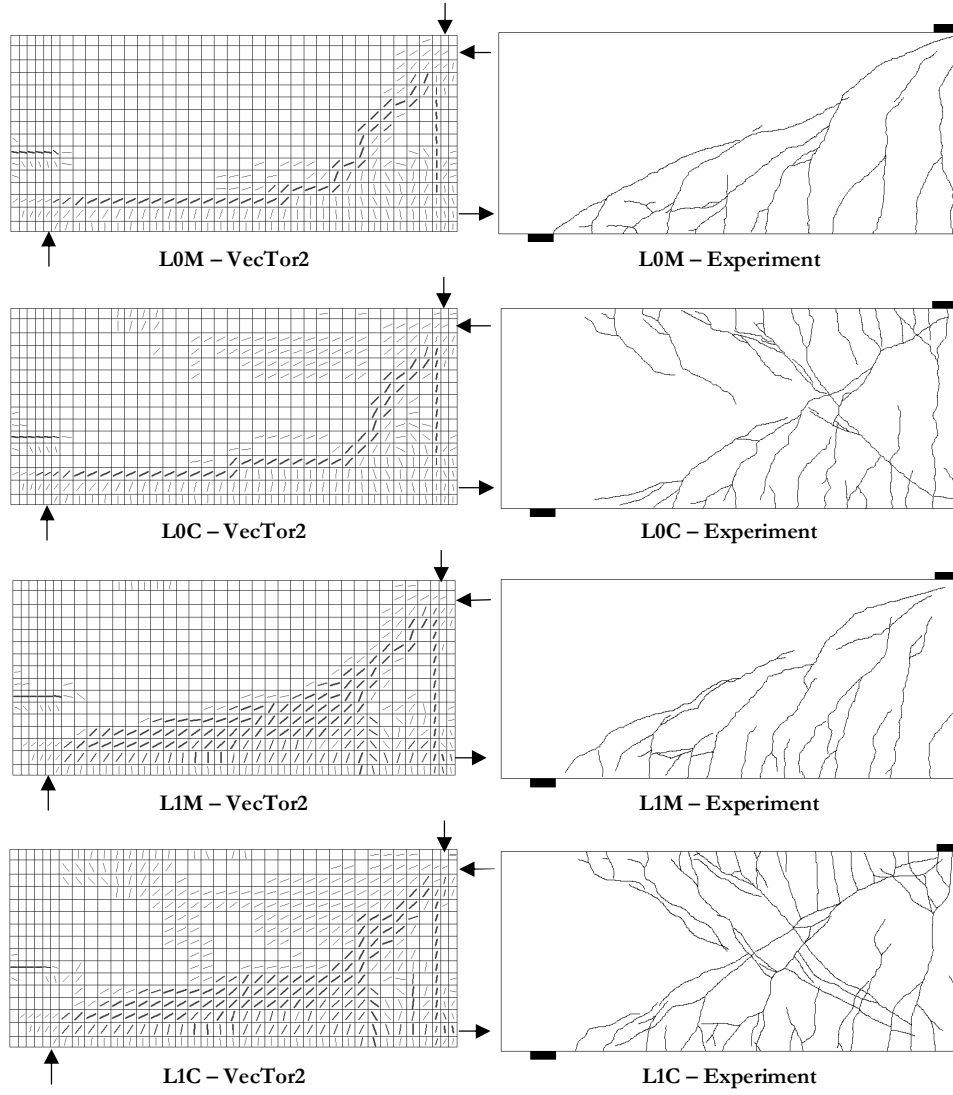


Figure 6.4 cont

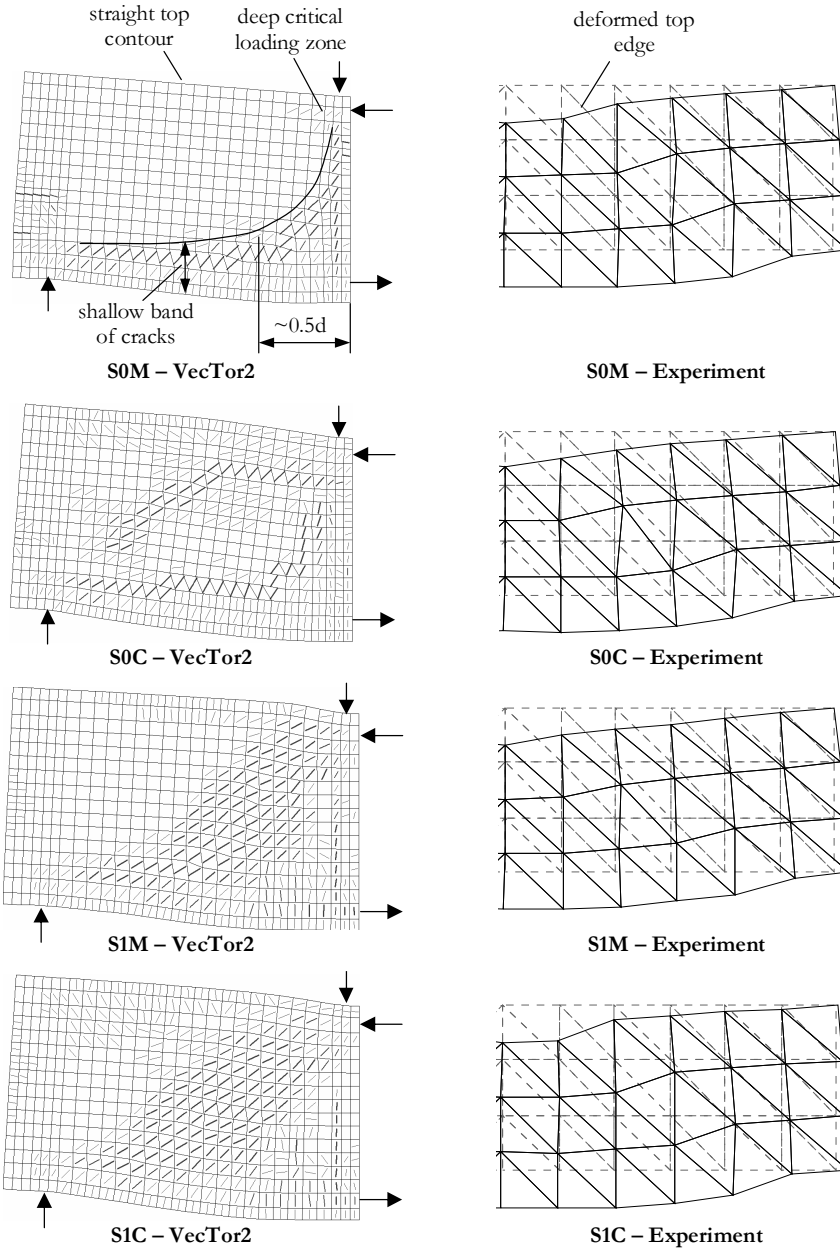


Figure 6.5 Deformed shapes from VecTor2 analysis – specimens S0M/C, S1M/C, L0M/C, and L1M/C

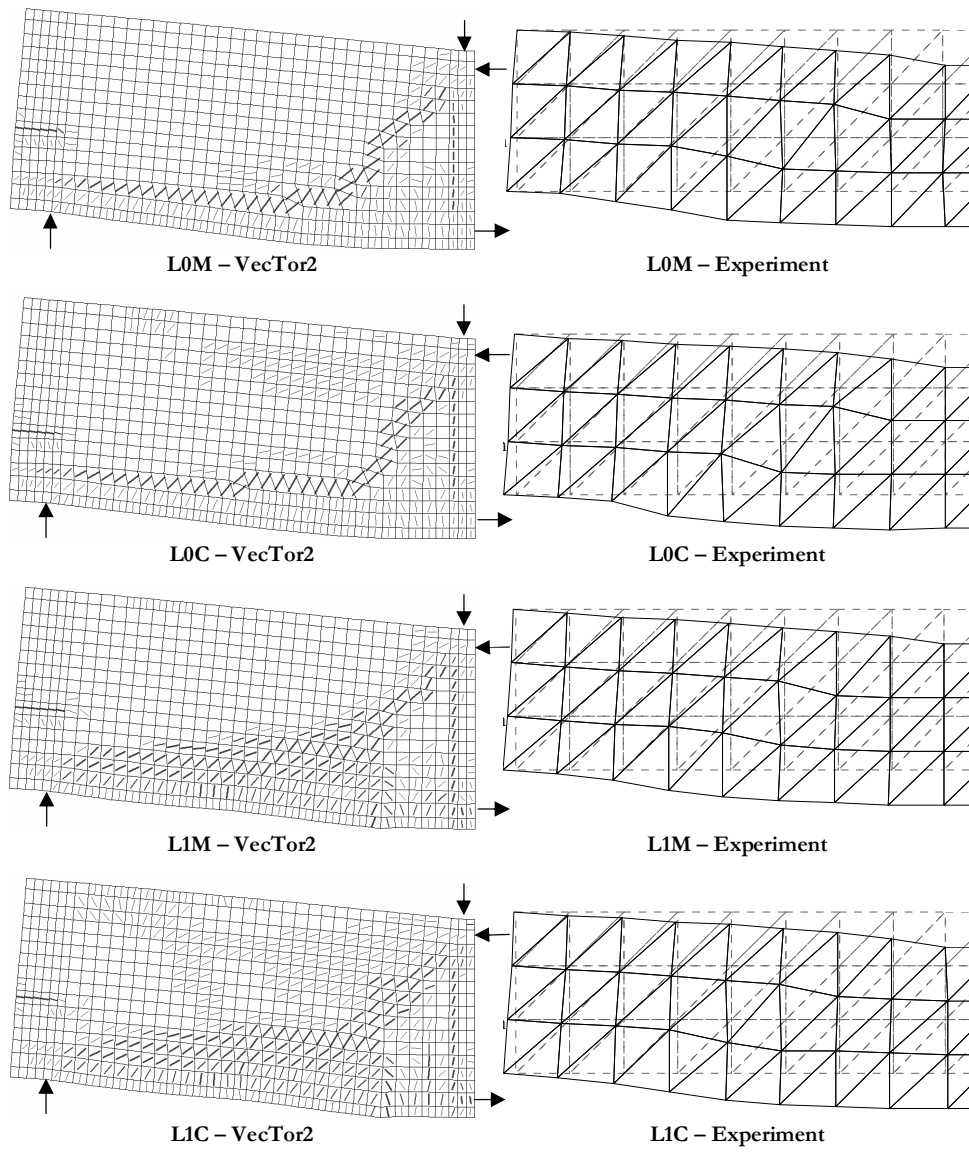
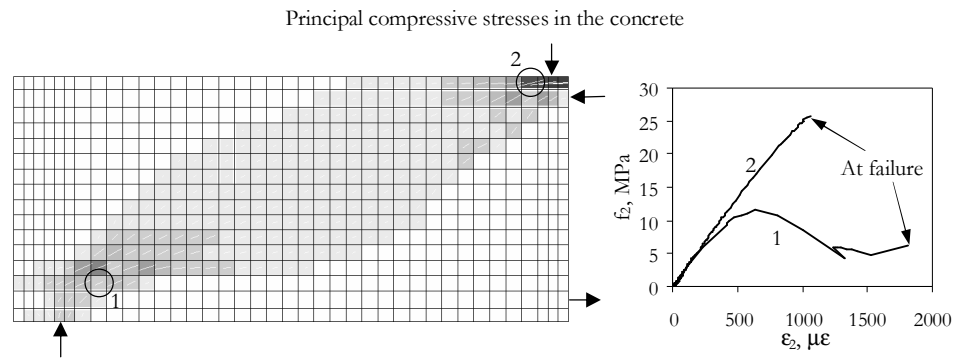
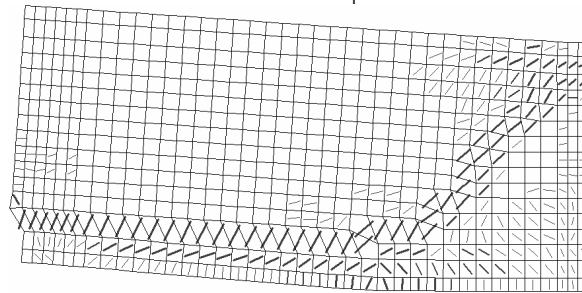


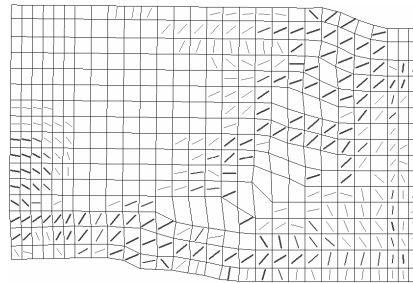
Figure 6.5 cont



Deformed shape



a) Crushing at the support zone – specimen L0M



b) Crushing at the critical loading zone – specimen S1M

Figure 6.6 Failure modes predicted by VecTor2

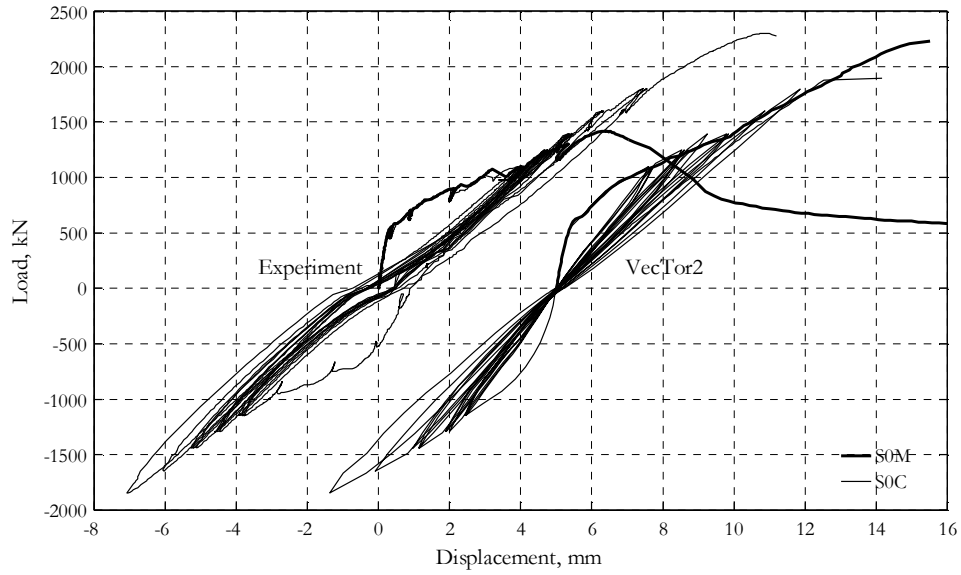


Figure 6.7 Experimentally-obtained load-displacement response vs. VecTor2 predictions – specimens S0M and S0C

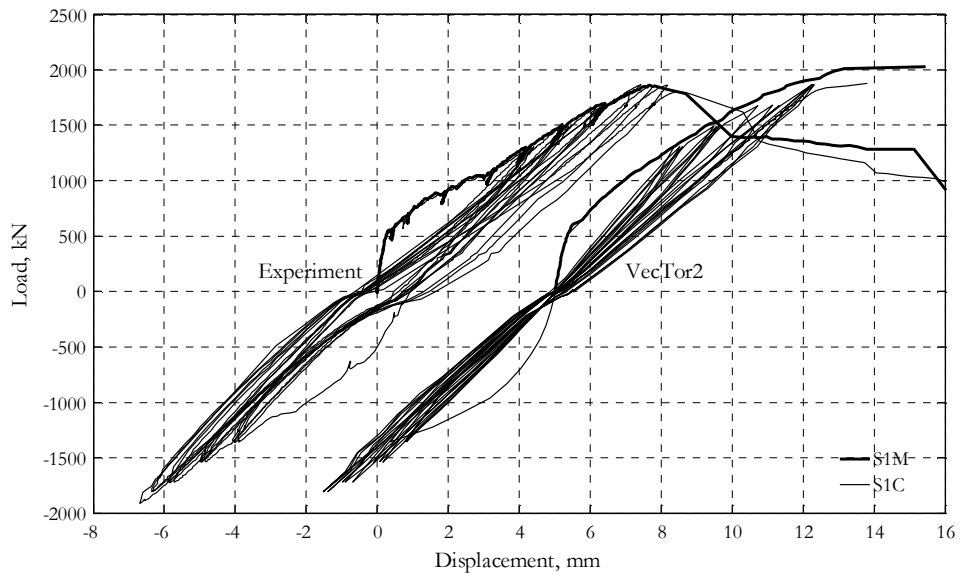


Figure 6.8 Experimentally-obtained load-displacement response vs. VecTor2 predictions – specimens S1M and S1C

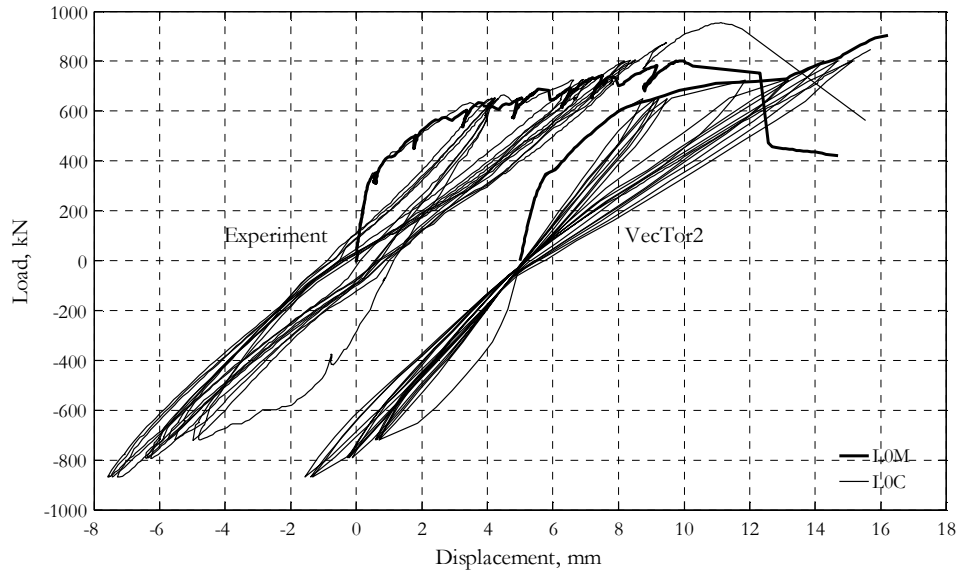


Figure 6.9 Experimentally-obtained load-displacement response vs. VecTor2 predictions – specimens L0M and L0C

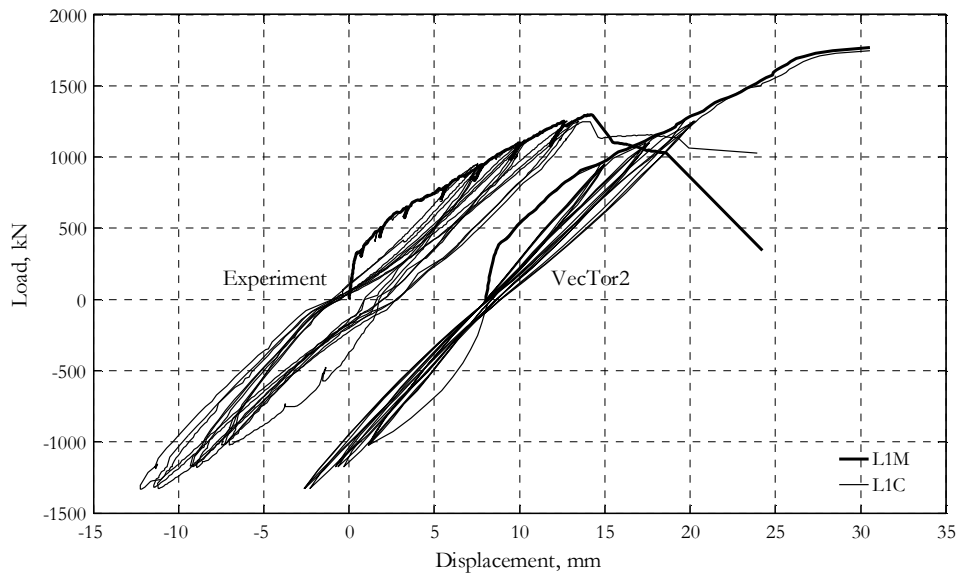


Figure 6.10 Experimentally-obtained load-displacement response vs. VecTor2 predictions – specimens L1M and L1C



In addition to the force-controlled analyses presented above, specimen L0M was also analyzed under controlled displacements. The steel support plate was modeled and its bottom middle node was restrained against vertical movement. The loading plate was assumed rigid and, therefore, the top nodes located within the width of the plate were prescribed equal downward displacement. The results showed almost no difference in terms of pre-peak response obtained from force- and displacement- controlled analyses. The post-peak response captured under controlled displacements was characterized by a sudden drop of resistance to about 12% of the maximum load. As evident from Figure 6.3, specimen L0M failed in a less brittle manner.



## 7. SUMMARY AND CONCLUSIONS

A review of a large number of tests of deep beams, coupling beams, and shear walls (Section 2.1) revealed the following general trends in the ultimate response of this type of structural elements. The shear strength of members without web reinforcement is very sensitive to the shear-span-to-effective-depth ratio ( $a/d$  ratio). For example, a beam without stirrups ( $\rho_v=0\%$ ) and  $a/d=1$  can be up to 6 times stronger than a similar beam with  $a/d=3$ . Transverse reinforcement enhances the shear strength, and this enhancement increases with increasing  $a/d$  ratios. However, heavily reinforced members, whose stirrups remain elastic up to failure, seem to be almost insensitive to variations of  $\rho_v$ . Even though shear failures are inherently brittle, members with transverse reinforcement fail in a more gradual manner with opening of wide diagonal cracks and spalling of concrete in the zones adjacent to supports and applied loads. Another favorable characteristic of members containing web reinforcement is that they exhibit relatively little scatter in terms of ultimate response. On the contrary, some studies show that the scatter in shear strength of seemingly identical deep beams without stirrups can be as large as 60-70%. The data also indicate that this scatter decreases with increasing  $a/d$  ratio.

Experimental studies devoted to the effects of earthquake-like cyclic loads have been focused predominantly on failure modes which involve yielding of the flexural reinforcement. Furthermore, the specimens are typically reinforced in two orthogonal directions. Test results show that the interaction between flexure and shear in non-slender members results in reduced flexural capacity. More importantly, however, the displacement ductility capacity of this type of elements is rather low as it rarely exceeds 3. Comparisons between identical specimens subjected to monotonic and cyclic load show that the type of loading history has little effect on the overall response.

The experimental program described in Chapter 3 included 10 tests of non-slender simply-supported beams with no or small amounts of transverse reinforcement subjected to monotonic and reversed cyclic load. The beams were designed to fail shortly before yielding of the flexural reinforcement. The longitudinal bars were anchored by anchor heads with the exception of the bars of specimen MB which were developed by lap-spliced hooks. The emphasis was on studying the load-bearing mechanisms which develop in this type of elements and how they change over the course of different loading histories.

Specimen L0M is a typical example of moderately-deep beam without web reinforcement. It was decided that a detailed analysis of all aspects of its behaviour (Section 4.2) would provide a solid basis for understanding the behaviour of the rest of the specimens and would allow for comprehensive comparisons. The crack diagrams at each load stage, shown together with the change of deformed shape over each load step, provided a complete picture of the progress of deformations with increasing applied load. Based on these and other results, a kinematic model capable of describing the ultimate deformed shape of non-slender beams without web reinforcement was developed. The model has only two degrees of freedom (average strain in the bottom chord and shear deformation in the critical loading zone) and its equations can be viewed as global conditions for compatibility of deformations. These conditions were successfully used for interpretation of various test measurements. It was demonstrated that standard strain compatibility conditions (Mohr's circle) do not apply over the entire depth of a beam and their application can lead to misleading results.

The strains measured along the bottom chord of specimen L0M showed a transition from beam action (triangular strain profile) at low load levels towards arch action (constant profile) prior to failure. Signs of this transition were evident also in the variation of the strain profile along the top chord, in the strains between the loading and support points, and in the orientation of the principal strains on the side face of the beam. Compressive strains in the cracked part of the web indicated that part of the ultimate shear was carried under the critical diagonal crack. The failure of specimen L0M was attributed to crushing at the zone located above the critical crack and near the edge of the loading plate. For the sake of convenience, this zone was defined as the critical loading zone.

Comparison between tests L0M and L1M (Subsection 4.3.1) was used for studying the effect of small amount of transverse reinforcement ( $\rho_r=0\%$  for L0M vs.  $\rho_r=0.1\%$  for L1M). The stirrups caused a more gradual propagation of diagonal cracks but were not able to alter the final crack pattern observed in specimen L0M. The strains along the bottom chord of beam L1M showed a transition from beam action (triangular type profile) to truss action (parabolic type profile). A simple strut-and-tie model revealed that the truss action reduced significantly the compression demand on the critical loading zones. This effect and the difference in the concrete strength of the specimens could explain the fact that beam L1M was almost 63% stronger than L0M.

The results from tests L0M and S0M (Subsection 4.3.2) were used to investigate the effect of decreasing  $a/d$  ratio ( $a/d=2.28$  for L0M vs.  $a/d=1.55$  for S0M). The balance of forces at the loading zones of the beams showed that specimen S0M was about 77% stronger than L0M because of steeper and larger diagonal compression forces. While the steeper slope of the compression flow is a direct consequence of the smaller  $a/d$  ratio, the

larger diagonal compression capacity was attributed to a deeper and less slender critical loading zone. The geometrical difference between the critical loading zones of the two beams was explained through the crack patterns in two ideal cases: a beam with mostly bending deformations (bending cracks) and a beam with no bending deformations (“peeling” cracks). Strain measurements over the depth of the sections showed that specimen L0M exhibited a larger transverse dilation than S0M. This result was found consistent with the increasing effectiveness of stirrups in members with increasing  $a/d$  ratios.

The data from tests L0M and L0C (Subsection 4.3.3) were used to analyze the effect of load reversals (L0M under monotonic load vs. L0C under reversed cyclic load). The various stages of global response, flexural response, response of the web, and response of the support zones of specimen L0C were interpreted with the help of idealized hysteresis loops. Comparison between the load-displacement response of specimen L0M and the positive envelope of the hysteretic response of L0C showed that the two curves diverged at a load corresponding to the breakdown of beam action. Surprisingly, the ultimate response of the cyclically-loaded beam was stiffer than that of the monotonically-tested one. Furthermore, specimen L0C was 19% stronger than L0M. This difference was attributed primarily to the random differences in the geometry of the critical loading zones. It was shown that load reversals had a negligible effect on the response of specimen L0C since they did not cause significant material degradation and did not alter the crack pattern which would have developed under monotonic load.

All of the 8 specimens devoted to a systematic investigation of the effects of transverse reinforcement ( $\rho_v$  ratio), beam slenderness ( $a/d$  ratio), and loading history (monotonic vs. reversed cyclic) failed in a brittle manner due to crushing at the critical loading zones (Subsection 4.3.4). No damage related to the anchorage by anchor heads was observed. All cyclically-tested beams (S0C, S1C, L0C, and L1C) had force-displacement response characterized by small energy dissipation (narrow hysteretic loops), small cyclic degradation (small increase in displacements under consecutive cycles with constant load amplitude), and small residual displacements. The pair of short beams without web reinforcement (specimens S0M/C) followed the pattern observed in pair L0M/C but in this case the cyclically-loaded specimen was as much as 62% stronger than the monotonically-tested one. The pairs of identical specimens with stirrups (S1M/C and L1M/C) subjected to monotonic and reversed cyclic load had practically overlapping load-displacement envelopes.

The scatter in terms of ultimate response of identical beams without stirrups decreased with increasing  $a/d$  ratio (62% for S0M/C vs. 19% for L0M/C) because the importance of the arch mechanism, and therefore the importance of the geometry of the critical loading zone, decreases with increasing beam slenderness. The lack of scatter in identical

beams with stirrups was attributed to two main reasons. First, the stirrups had some influence on the propagation of diagonal cracks and reduced the scatter in terms of depth of the critical loading zones, and second, specimens S1M/C and L1M/C developed a truss-type load-bearing mechanism in which a significant part of the shear was carried below the critical loading zones.

Comparison of the experimentally-obtained shear strengths of specimens S0M/C, S1M/C, L0M/C, and L1M/C to code predictions (Subsection 4.3.4) showed that the current Canadian (CSA) code captured well the trends indicated by the data points. Furthermore, the CSA predictions were reasonably conservative (average experiment-to-prediction ratio of 1.22 and coefficient of variation  $COV=0.177$ ) which is a favourable result considering the scatter in the test data. In contrast, the American (ACI) and European (EC2) codes rendered rather unconservative predictions with average experiment-to-prediction ratios of 0.95 and 0.85, and  $COV$  of 0.194 and 0.188, respectively. It was shown that the constant efficiency factors in the strut-and-tie provisions of EC2 lead to an underestimation of the rate at which the shear strength decreases with increasing  $a/d$  ratios. The limit on the applicability of the strut-and-tie models, imposed in the ACI code, compensates for this deficiency only to a certain extent.

Specimens MB and SB (Section 4.4) developed arch action as a result of two different phenomena. The four bars of the former beam separated from the web because of a lap-splice failure while the single bar of the later beam lost interaction with the surrounding concrete due to splitting of the bottom concrete cover. Lap-spliced anchor hooks proved to be an unreliable solution in cases of deep members without stirrups where the flexural reinforcement is subjected to high tension over the entire shear span. On the other hand, the anchor heads of the #18 ( $\phi=57$  mm) bar of specimen SB were very effective and the beam failed due to crushing at the critical loading zone. It was shown that the stresses in the concrete in front of the anchor heads reached values as high as  $1.53f_c'$ . Close examination of concrete prisms cut from the support zones revealed splitting cracks but no signs of concrete crushing.

The improved strut-and-tie model (ISTM) presented in Chapter 5 is based on the CSA strut-and-tie provisions, but accounts for shear carried under the critical diagonal cracks of non-slender beams without web reinforcement (see the top sketch in Figure 7.1). This supplementary load-bearing mechanism was named “residual beam action” and was modeled by a strut and a tie connected to the bottom chord at a compression-tension-tension (CTT) node. The CTT node represents the diagonally-cracked concrete at the bottom end of the critical flexure-shear cracks where aggregate interlock occurs. The behaviour of this zone was modeled through the Modified Compression Field Theory (MCFT - Vecchio and Collins, 1986). The ISTM produced excellent shear-strength

predictions for specimens S0M/C and L0M/C with an average experiment-to-prediction ratio of 1.107. These predictions, together with the predictions of the CSA code for specimens S1M/C, L1M/C, SB, and MB, resulted in  $V_{u,exp}/V_{u,pred}$  ratios with an average value of 1.108 and coefficient of variation of 0.126 compared to the 1.198 and 0.168 from the CSA code applied to all the specimens. Furthermore, the improved strut-and-tie model was able to capture local effects such as strains along the bottom chord, width of the “peeling” cracks near the supports, and shear strains near the supports of specimens S0M and L0M. Verifications of the proposed model and comparisons with the CSA code were also performed through a large database of shear tests of members without stirrups (Collins, Bentz, and Sherwood, 2008). The results showed that the ISTM, used in combination with the CSA sectional model for slender members, gave a less conservative average experiment-to-prediction ratio than the CSA code (1.115 vs. 1.264), a smaller coefficient of variation (0.222 vs. 0.250), and more uniform safety. Based on all the verifications, it was concluded that the proposed improved strut-and-tie-model is consistent with physical observations and explains well the transition from deep to slender beams.

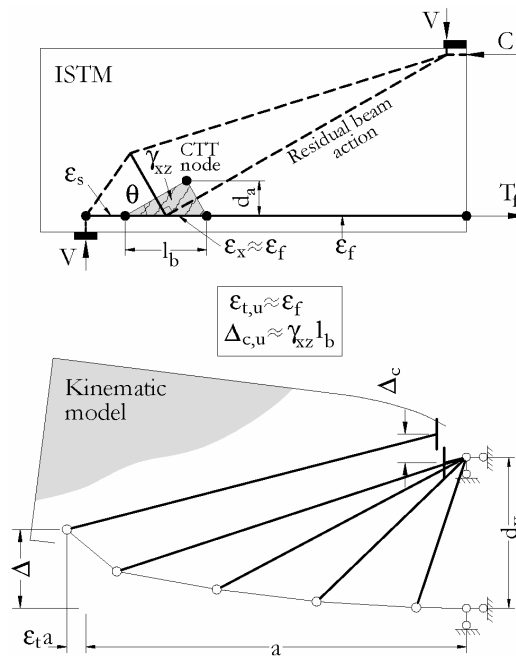


Figure 7.1 Improved strut-and-tie model and kinematic model

It was also shown that the improved strut-and-tie model can be used together with the kinematic model from Chapter 4 for predicting the ultimate mid-span displacement and the deformed shape of non-slender beams without web reinforcement (see Figure 7.1). The ISTM provides an estimate of the shear strength of the member as well as estimates of local deformations such as  $\epsilon_s$ ,  $\epsilon'_s$  and  $\gamma_{xy}$ . The kinematic model, on the other hand, gives relationships between the local and global deformations. The combination of the two models was applied to specimens S0M/C and L0M/C resulting in  $\Delta_{u,exp}/\Delta_{u,pred}$  ratios with an average value of 0.90 and a coefficient of variation of 0.244.

VecTor2 analyses of specimens S0M, S1M, L0M, and L1M (Chapter 6) showed that the finite element program based on the MCFE and on the Disturbed Stress Field Model (DSFM - Vecchio, 2000) was able to capture the load-displacement response of the beams in the linear range and in the range of transition from beam action to arch/truss action. The same was valid for the envelopes of the hysteretic response of specimens S0C, S1C, L0C, and L1C. At the same time, in most of the cases, the predicted zones of cracked concrete did not extend as far above the bottom longitudinal reinforcement as was observed in the tests. It was shown that this resulted in failures caused by crushing of the concrete in the support zones and not in the loading zone as in the tested beams. This could be a reason for the overestimated shear strengths with experiment-to-prediction ratios for the monotonically-tested specimens varying between 0.64 and 0.92. In terms of hysteretic response, the analyses captured the overall shape of the load-displacement loops, but underestimated the residual displacements and overestimated the stiffness degradation under consecutive cycles with constant load amplitude.

Finally, the work on this thesis gave rise to ideas for future research topics. An immediate possibility is to improve and extend the proposed improved strut-and-tie model to beams with small amounts of stirrups such as specimens S1M/C and L1M/C. Further, it is of great interest to examine the kinematics of slender beams and that of beams which contain large amounts of web reinforcement. More generally, the kinematics-based approaches used in this work could be used to study the behaviour of other important non-slender members such as coupling beams, shear walls, and short columns.



## REFERENCES

- ACI-ASCE Committee 326 "Shear and Diagonal Tension," *ACI Structural Journal*, Vol. 59, No. 1, 2, and 3, Jan., Feb., and Mar. 1962, pp. 1-30, 277-334, and 352-1349; also discussion and closure, Vol. 59, No. 10, Oct. 1962, pp. 1323-1349.
- ACI Committee 318 [2008] *Building Code Requirements for Reinforced Concrete (ACI 318-08) and Commentary (318R-08)*, American Concrete Institute, Farmington Hills, 465 pp.
- Alcocer, S.M., Uribe, C.M. [2008] "Monotonic and cyclic behaviour of deep beams designed using strut-and-tie models," *ACI Structural Journal*, Vol. 105, No. 3, pp. 327-337.
- Asin, M. [1999] "The Behaviour of Reinforced Concrete Continuous Deep Beams," *Doctoral Thesis*, Delft University Press, The Netherlands.
- ATC-40 [1996] *Seismic Evaluation and Retrofit of Concrete Buildings- Volume 1*, Applied Technology Council, Redwood City, California, 260 pp.
- Bentz, E.C., Vecchio, F.J., Collins, M.P., [2006] "Simplified Modified Compression Field Theory for Calculating Shear Strength of Reinforced Concrete Elements," *ACI Structural Journal*, Vol. 103, No. 4, pp. 614-624.
- Brown, M.D., Sankovich, C.L., Bayrak O., Jirsa, J.O. [2006] "Behavior and Efficiency of Bottle-Shaped Struts," *ACI Structural Journal*, Vol. 103, No. 3, pp. 348-355.
- CEB-FIP [2008] "Practitioners' Guide to Finite Element Modeling of Reinforced Concrete Structures," *Bulletin 45*. pp. 337.
- Collins, M.P., Mitchell, D. [1986] "A Rational Approach to Shear Design – the 1984 Canadian Code Provisions," *ACI Structural Journal*, Vol. 83, No. 6, pp. 925-933.
- Collins, M.P., Mitchell, [1997] *Prestressed Concrete Structures*, Response Publications
- Collins, M.P., Mitchell, D., Bentz, E.C. [2008] "Shear Design of Concrete Structures," *The Structural Engineer*, Vol. 86, No. 10, pp. 32-39.

- Collins, M.P., Bentz, E.C., Sherwood, E.G. [2008] "Where is Shear Reinforcement Required? Review of Research Results and Design Procedures," *ACI Structural Journal*, Vol. 105, No. 5, pp. 589-599.
- CSA Committee A23.3 [2005] *Design of Concrete Structures*, Canadian Standards Association, Mississauga, Ontario, Canada, 214 pp.
- European Committee for Standardization, CEN, EN 1992-1-1 [2004] *Eurocode 2: Design of Concrete Structures- Part 1-1: General Rules and Rules for Buildings*, Brussels, Belgium, 225 pp.
- European Committee for Standardization, CEN, prEN 1998-3 [2004] *Eurocode 8: Design of Structures for Earthquake Resistance- Part 3: Assessment and Retrofitting of Buildings*, Brussels, Belgium, 89 pp.
- FEMA 356 [2000] *Prestandard and Commentary for Seismic Rehabilitation of Buildings*, Federal Emergency Management Agency, Washington, D.C., 516 pp.
- Fenwick, R.C., Paulay, T. [1968] "Mechanisms of Shear Resistance of Concrete Beams," *Journal of the Structural Division*, ASCE, Vol. 94, No. ST10, pp. 2325-2350.
- Foster, S.J., Malik, A.R. [2002] "Evaluation of Efficiency Factor Models used in Strut-and-Tie Modelling of Nonflexural Members," *Journal of Structural Engineering*, ASCE, Vol. 128, No. 5, pp. 569-577.
- Higgins, C. et al. [2004] "Assessment Methodology for Diagonally Cracked Reinforced Concrete Deck Girders," *Final Report SPR350 SR500-091 for the Oregon Department of Transportation Research Unit*. pp. 328.
- Kani, M., Huggins, M., Wittkopp, R. [1979] *Kani on shear in reinforced concrete*, University of Toronto Press, Toronto, Canada.
- Lee, D. [1982] "An experimental investigation in the effects of detailing on the shear behaviour of deep beams," *Master Thesis*, University of Toronto, Canada.
- Lefas, I.D., Kotsovos, M.D., Ambraseys, N.N [1990] "Behaviour of Reinforced Concrete Structural Walls: Strength, Deformation Characteristics, and Failure Mechanism," *ACI Structural Journal*, Vol. 87, No. 1, pp. 23-31.
- Lefas, I.D., Kotsovos, M.D. [1990] "Strength and Deformation Characteristics of Reinforced Concrete Walls under Load Reversals," *ACI Structural Journal*, Vol. 87, No. 6, pp. 716-726.

- Leonhardt, F., Walther, R. [1961, 1962] "The Stuttgart shear tests, 1961, Contributions to the treatment of the problems of shear in reinforced concrete construction," A translation of articles that appeared in *Beton- und Stahlbetonbau*, Vol. 56, No. 12, and Vol. 57, Nos. 2, 3, 6, 7, and 8.
- Leonhardt, F. [1970] "Shear and Torsion in Prestressed Concrete," *VI. FIP Congress*, Prague.
- Mihaylov, B. [2006] "Analysis of Code Procedures for Seismic Assessment of Existing Buildings: Italian Seismic Code, EC8, ATC-40, FEMA 356, FEMA 440," *Master Thesis*, University of Pavia, ROSE School, Italy.
- Muttoni, A., Schwartz, J., Thürlimann, B., [1996] *Design of Concrete Structures with Stress Fields*, Birkhauser
- Nielsen, M.P. [1999] *Limit Analysis and Concrete Plasticity, Second Edition*, CRC Press
- Palermo, D., Vecchio, F.J. [2004] "Compression Field Modelling of Reinforced Concrete Subjected to Reversed Loading: Formulation," *ACI Structural Journal*, Vol. 100, No. 5, pp. 616-625.
- Paulay, T. [1971a] "Coupling beams of reinforced concrete shear walls," *Journal of the Structural Division*, ASCE, Vol. 97, No. ST3, pp. 843-862.
- Paulay, T. [1971b] "Simulated seismic loading of spandrel beams," *Journal of the Structural Division*, ASCE, Vol. 97, No. ST9, pp. 2407-2419.
- Paulay, T., Priestley, M.J.N. [1992] *Seismic Design of Reinforced Concrete and Masonry Buildings*, John Wiley & Sons
- Reineck, K.H. [2002] "Examples for the Design of Structural Concrete with Strut-and-Tie Models," *ACI SP-208*, pp. 242.
- Rogowsky, D.M., MacGregor, J.G., Ong, S.Y. [1986a] "Tests of reinforced concrete deep beams," *ACI Structural Journal*, Vol. 83, No. 4, pp. 614-623.
- Rogowsky, D.M., MacGregor, J.G. [1986b] "Design of Reinforced Concrete Deep Beams," *Concrete International*, ACI, Vol. 8, No. 8, pp. 49-58.
- Schlaich, J., Schäfer, K., Jennewein, M. [1987] "Toward a Consistent Design of Structural Concrete," *PCI Journal*, Vol. 32, No. 3, pp. 74-150.

- Sherwood, E.G., Bentz, E.C., Collins, M.P. [2007] "Effect of Aggregate Size on Beam-Shear Strength of Thick Slabs," *ACI Structural Journal*, Vol. 104, No. 2, pp. 180-190.
- Thompson, M.K., Ziehl, M.J., Jirsa J.O., Breen, J.E. [2005] "CCT Nodes Anchored by Headed Bars- Part 1: Behavior of Nodes," *ACI Structural Journal*, Vol. 102, No. 6, pp. 808-815.
- Thompson, M.K., Jirsa J.O., Breen, J.E. [2006] "CCT Nodes Anchored by Headed Bars- Part 2: Capacity of Nodes," *ACI Structural Journal*, Vol. 103, No. 1, pp. 65-73.
- Vecchio, F.J., Collins, M.P. [1986] "Modified Compression Field Theory for Reinforced Concrete Elements Subjected to Shear," *ACI Structural Journal*, Vol. 83, No. 2, pp. 219-231.
- Vecchio, F.J. [2000] "Analysis of Shear-Critical Reinforced Concrete Beams," *ACI Structural Journal*, Vol. 97, No. 1, pp. 102-110.
- Vecchio, F.J. [2000] "Disturbed Stress Field Model for Reinforced Concrete: Formulation," *Journal of Structural Engineering*, ASCE, Vol. 126, No. 9, pp. 1070-1077.
- Yang, K.H., Chung, H.S., Lee, E.T., Eun, H.C. [2003] "Shear Characteristics of High-Strength Concrete Deep Beams without Shear Reinforcement," *Engineering Structures*, Vol. 25, No. 10, pp. 1343-1352.
- Zhang, N., Tan, K.H. [2007] "Size Effect in RC Deep Beams: Experimental Investigation and STM Verification," *Engineering Structures*, Vol. 29, No. 12, pp. 3241-3254.

## APPENDIX A. CONCRETE TESTS

### Compressive tests of 152/305 mm (6"/12") cylinders

#### Design properties:

$f_c' = 20$  MPa

$a_g = 20$  mm

Slump = 75 mm

#### Specimens S0M/C

Cast day: 28/03/2007

Slump: 110 mm

Date	Days	$f_c'$ (MPa)			Avg.	
04/04/2007	7	20.14	20.89	22.48	21.2	*
11/04/2007	14	28.24	27.8	26.59	27.5	*
25/04/2007	28	31.8	31.61	31.26	31.6	*
25/04/2007	28	30.26	23.46	32.63	31.4	**
22/08/2007	144	34.61	33.2	34.81	34.2	***

#### Specimens S1M/C

Cast day: 01/05/2007

Slump: 80 mm

Date	Days	$f_c'$ (MPa)			Avg.	
08/05/2007	7	19.41	18.58	18.79	18.9	*
15/05/2007	14	25.77	23.71	24.18	24.6	*
29/05/2007	28	29.22	29.91	29.05	29.4	*
29/05/2007	28	28.86	28.35	20.64	28.6	**
31/08/2007	119	33.3	32.0	33.71	33.0	***

**Specimens SB/MB**

Cast day: 16/05/2007

Slump: 85 mm

Date	Days	$f_c'$ (MPa)			Avg.	
23/05/2007	7	18.26	17.91	17.99	18.1	*
30/05/2007	14	22.42	19.95	20.43	20.9	*
13/06/2007	28	26.14	25.81	22.26	24.7	*
13/06/2007	28	18.84	23.12	18.73	20.2	**
10/12/2007	204	31.66	30.7	29.26	30.5	***

**Specimens L0M/C**

Cast day: 30/05/2007

Slump: 110 mm

Date	Days	$f_c'$ (MPa)			Avg.	
06/06/2007	7	17.33	16.4	17.04	16.9	*
13/06/2007	14	22.32	20.42	19.94	20.9	*
27/06/2007	28	25.09	25.05	25.96	25.4	*
27/06/2007	28	25.37	25.88	26.92	26.1	**
31/10/2007	151	27.22	30.4	29.71	29.1	***

**Specimens L1M/C**

Cast day: 19/06/2007

Slump: 50 mm

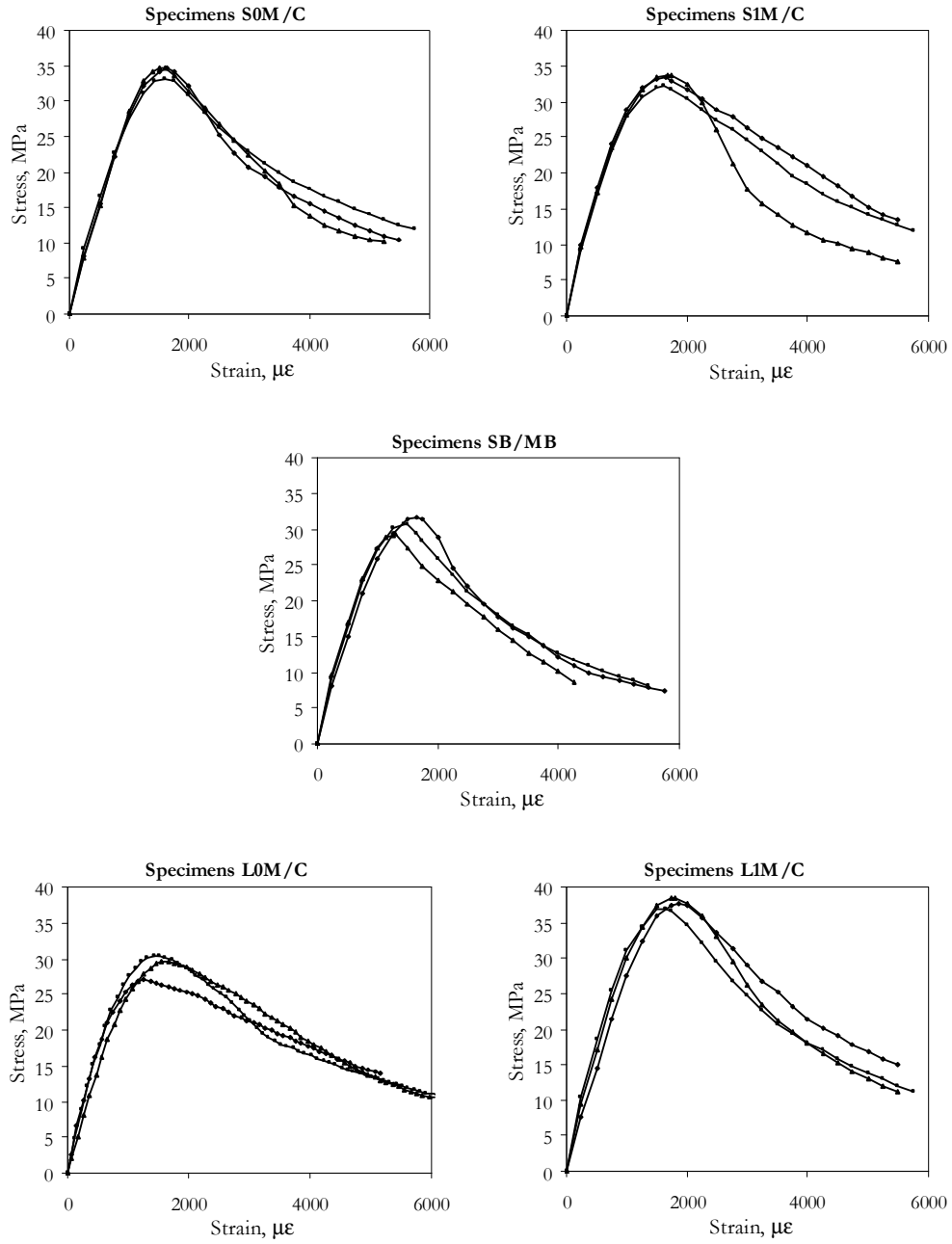
Date	Days	$f_c'$ (MPa)			Avg.	
26/06/2007	7	22.7	22.62	23.64	23.0	*
03/07/2007	14	28.25	29.48	26.47	28.1	*
17/07/2007	28	32.64	32.03	35.87	33.5	*
17/07/2007	28	33.37	34.86	29.26	32.5	**
10/12/2007	171	37.7	37.0	38.58	37.8	***

Note: The values in a grey box were disregarded since they were relatively very low.

\* Cured in standard conditions for the first 7 days.

\*\* Cured in standard conditions (standard cylinder test).

\*\*\* Cured in standard conditions for the first 7 days and tested approximately at the day of the beam test.



**Four-point bending tests of 152/152/533 mm (6"/6"/21") prisms**

Test days: 10 – 11/12/2007

Specimen	Modulus of rupture, (MPa)			Avg.
S0M/C	3.9	4.1	5.0	4.3
S1M/C	3.8	4.0	3.9	3.9
SB/MB	3.2	3.0	4.6	3.6
L0M/C	3.6	3.9	3.8	3.7
L1M/C	3.7	3.7	3.5	3.7

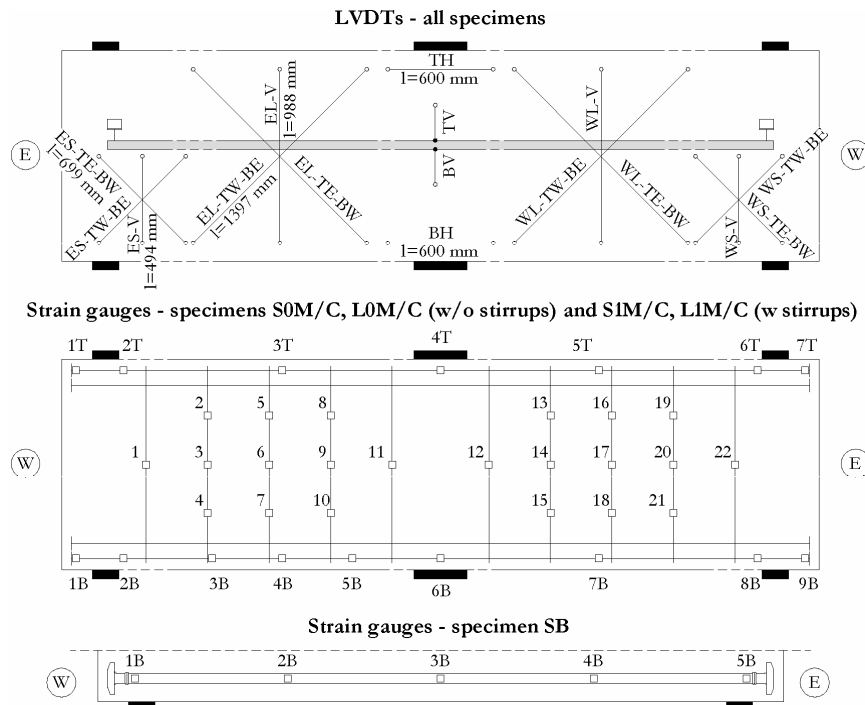


## APPENDIX B. EXPERIMENTAL DATA

### B1. INTRODUCTION

This appendix contains data from tests S0M/C, S1M/C, L0M/C, L1M/C, SB, and MB presented in numerical and graphical form. Detailed description of the experimental program, including geometrical properties of the specimens, results from material tests, test setup, instrumentation, and loading histories, was given in Chapter 3. For the sake of convenience, big part of that information is repeated below and at the beginning of the sections devoted to each individual test.

#### Measuring devices



**Sign convention for loads and displacements**

The downward midspan displacement and the load applied by the Baldwin machine on the top face of the specimens are considered positive. Inversely, the upward midspan displacement and the bottom load applied by the hydraulic jacks are given negative sign.

## B2. SPECIMEN S0M

**Cast day:** March 28<sup>th</sup>, 2007

### Beam properties

Cross section:  $h=1200$  mm,  $b=400$  mm

Effective depth: 1095 mm

Shear span: 1700 mm

Loading plates: 51/300/400 mm

Support plates: 51/150/400 mm

Longitudinal reinforcement:  $\rho_l=0.68\%$ ,  $f_y=650$  MPa

Transverse reinforcement:  $\rho_t=0\%$

Concrete:  $f_c' = 34.2$  MPa,  $\epsilon_c^* = 1630 \mu\epsilon$ ,  $a_g=20$  mm, *Modulus of rupture* = 4.3 MPa

Defects: no significant defects

**Test day:** August 7<sup>th</sup>, 2007

### Test Remarks

Maximum load: 1419.5 kN

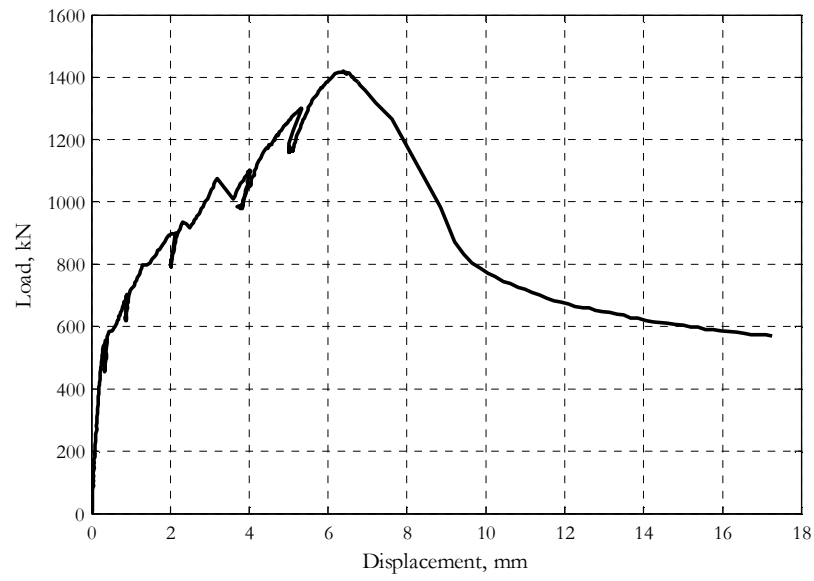
Displacement at maximum load: 6.4 mm

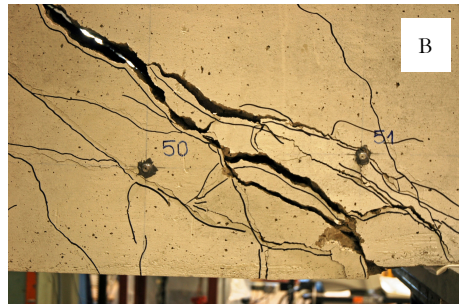
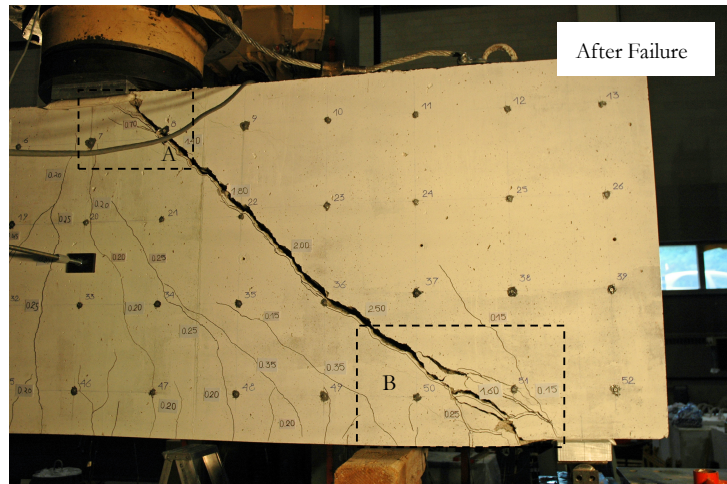
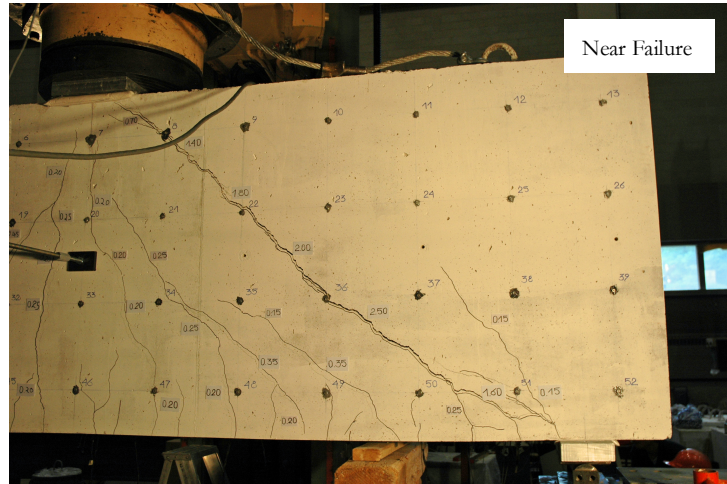
Failure mode: The beam failed suddenly with crushing above the most eastern diagonal crack near the edge of the top loading plate.

Other remarks:

- The formation and propagation of flexure-shear cracks was relatively quick.
- Zürich target 8 fell off at Load Stage 4. It was glued back and the readings over the adjacent squares from the grid were repeated.
- The critical most diagonal crack propagated almost instantaneously during Load Step 4-5.

## Global response



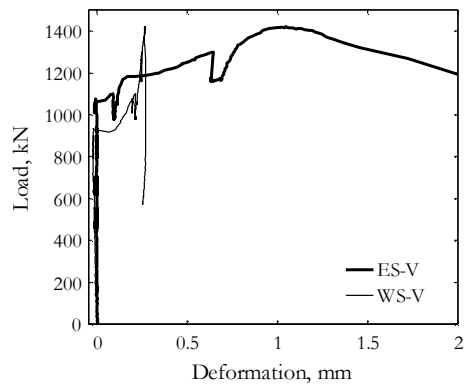
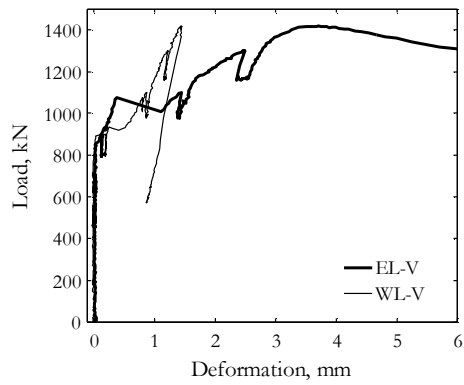
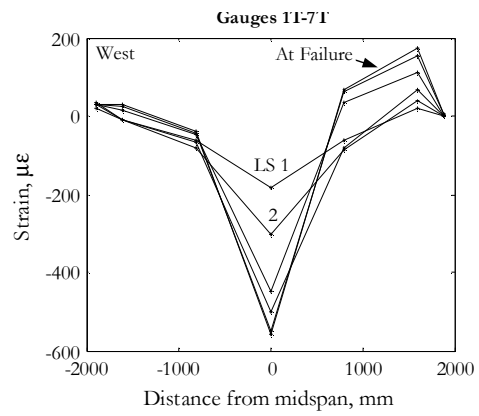
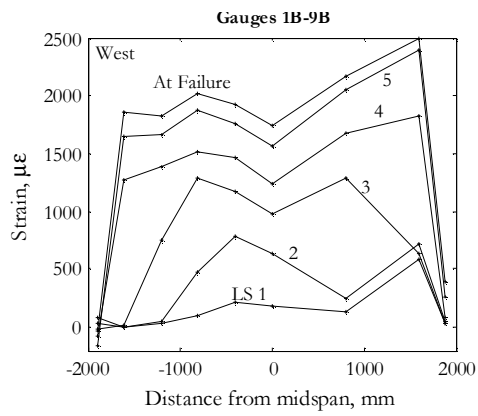
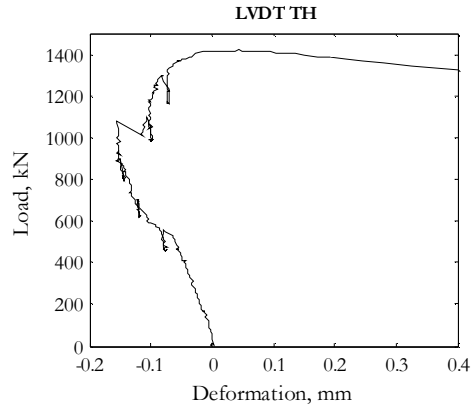
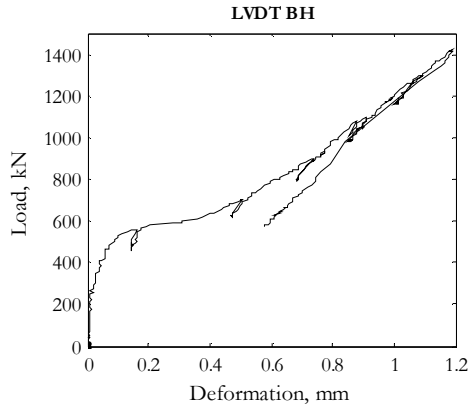


## Data summary

Load Stage	Data Set	Time elapsed	F	$\Delta=(BV+TV)/2$	BH	TH	ES-TE-BW	ES-V	ES-TW-BE	WS-TW-BE	WS-V	WS-TE-BW	EL-TE-BW	EL-V	EL-TW-BE	WL-TW-BE	WL-V	WL-TE-BW	Gauge 7B
(#)	(#)	(min)	(kN)	(mm)	(mm) $\times 10^{-3}$	(mm) $\times 10^{-3}$	(mm) $\times 10^{-3}$	(mm) $\times 10^{-3}$	(mm) $\times 10^{-3}$	(mm) $\times 10^{-3}$	(mm) $\times 10^{-3}$	(mm) $\times 10^{-3}$	(mm)	(mm)	(mm)	(mm)	(mm)	(mm)	( $\mu\epsilon$ )
-	37	56	231.3	0.1	11	-23	0	-2	-6	-4	-14	-20	0.00	0.02	0.02	-0.02	-0.01	-0.02	74
-	60	63	420.1	0.2	56	-48	1	-5	-12	-3	-12	-28	0.01	0.01	0.01	0.00	-0.01	-0.04	104
1	76	67	556.4	0.4	161	-80	2	-4	-17	0	-18	-37	0.00	0.02	0.00	0.00	-0.01	-0.07	127
-	102	116	587.6	0.5	281	-100	4	-3	-16	11	-16	-30	0.02	0.02	0.01	0.05	0.00	-0.07	208
-	105	117	611.4	0.7	360	-104	4	-3	-15	10	-15	-31	0.03	0.02	0.00	0.13	-0.02	-0.06	214
-	111	119	653.3	0.8	439	-116	2	-3	-18	11	-19	-32	0.04	0.02	-0.01	0.15	-0.01	-0.07	228
2	119	121	704.5	0.9	506	-120	5	-3	-18	13	-17	-32	0.07	0.03	-0.01	0.21	-0.01	-0.07	242
-	148	157	730.1	1.1	536	-132	2	-5	-24	5	-23	-47	0.05	0.02	0.00	0.33	-0.02	-0.10	299
-	153	158	768.9	1.2	581	-132	5	-5	-23	6	-23	-49	0.09	0.03	-0.02	0.42	-0.01	-0.11	317
-	157	159	797.6	1.4	626	-138	6	-6	-23	9	-24	-51	0.24	0.03	-0.02	0.48	-0.01	-0.12	702
-	160	160	825.8	1.6	656	-140	7	-7	-24	7	-24	-51	0.41	0.03	-0.01	0.54	0.01	-0.10	1041
-	164	160	847.6	1.7	686	-144	8	-4	-26	6	-24	-50	0.52	0.02	-0.02	0.61	0.01	-0.10	1170
-	167	161	872.0	1.9	697	-149	10	-3	-28	7	-24	-50	0.57	0.10	-0.05	0.65	0.02	-0.10	1275
3	173	163	901.4	2.1	735	-150	11	-3	-29	29	-23	-57	0.66	0.13	-0.05	0.89	0.19	-0.14	1290
-	205	207	926.4	2.3	773	-154	12	-3	-30	73	-21	-57	0.73	0.17	-0.04	1.00	0.24	-0.15	1343
-	212	210	948.3	2.7	776	-153	15	-4	-33	566	117	-79	0.78	0.22	-0.04	1.38	0.56	-0.03	1390
-	216	211	972.6	2.8	791	-155	20	-4	-33	614	130	-82	0.81	0.24	-0.04	1.47	0.61	0.00	1418
-	220	212	1000.1	2.9	818	-154	18	-4	-33	679	150	-87	0.88	0.30	-0.04	1.55	0.67	0.01	1466
-	223	213	1028.9	3.0	836	-154	22	-7	-34	732	169	-91	0.90	0.32	-0.04	1.67	0.72	0.03	1500
-	227	213	1066.4	3.1	866	-156	30	-10	-37	785	191	-98	0.96	0.35	-0.04	1.74	0.78	0.04	1562
4	241	215	1098.9	4.0	911	-107	1260	86	-72	869	212	-97	2.17	1.44	0.06	1.87	0.87	0.06	1672

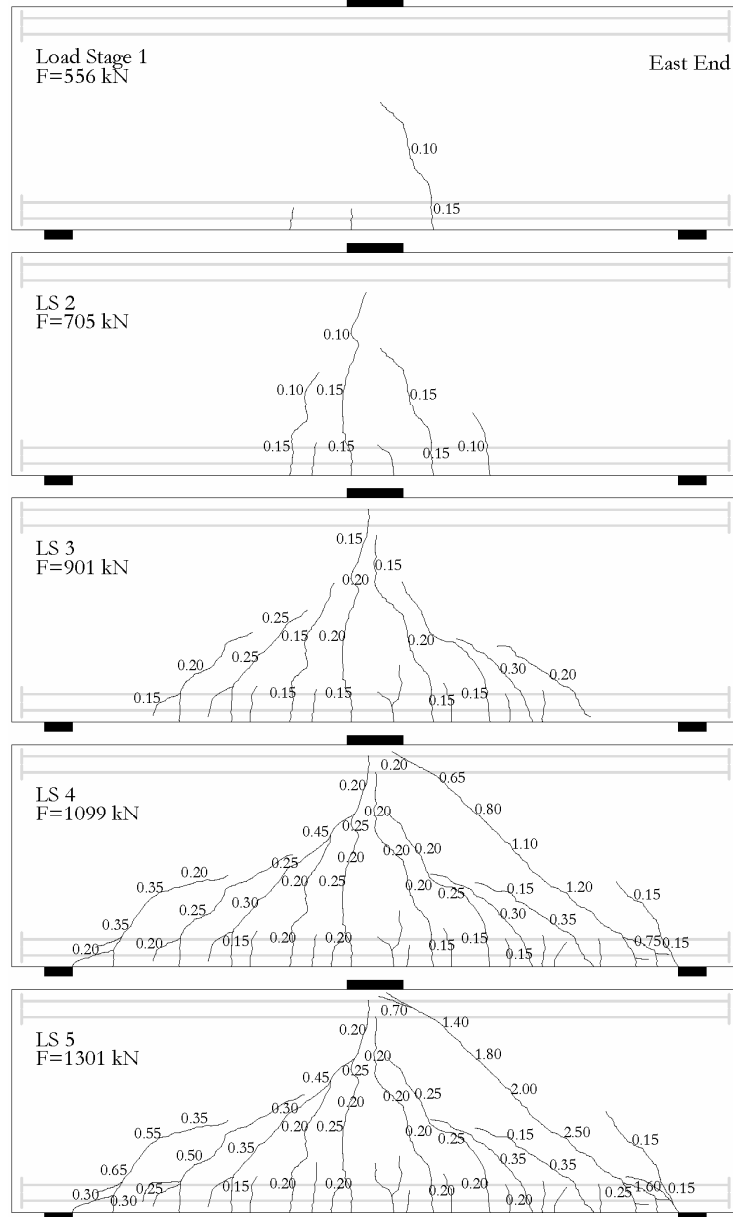
Load Stage	Data Set	Time elapsed	F	$\Delta = (BV + TV)/2$	BH	TH	ES-TE-BW	ES-V	ES-TW-BE	WS-TW-BE	WS-V	WS-TE-BW	EL-TE-BW	EL-V	EL-TW-BE	WL-TW-BE	WL-V	WL-TE-BW	Gauge 7/B
-	282	285	1120.1	4.2	941	-100	1383	119	-69	940	225	-96	2.14	1.59	0.11	1.98	0.97	0.09	1698
-	285	286	1149.5	4.3	956	-102	1435	133	-75	971	230	-102	2.21	1.64	0.12	2.03	0.98	0.09	1733
-	288	288	1173.3	4.4	971	-104	1496	150	-74	1007	235	-101	2.28	1.71	0.13	2.10	1.01	0.10	1763
-	297	291	1198.9	4.6	1001	-98	1676	326	-81	1044	236	-103	2.44	1.89	0.26	2.18	1.05	0.11	1784
-	304	293	1224.5	4.8	1016	-95	1805	423	-89	1075	238	-106	2.56	2.02	0.31	2.22	1.08	0.12	1832
-	308	294	1250.1	4.9	1039	-91	1928	497	-96	1110	244	-110	2.68	2.14	0.39	2.29	1.11	0.12	1859
-	314	295	1271.4	5.1	1061	-89	2019	543	-95	1141	242	-111	2.79	2.27	0.41	2.34	1.15	0.14	1880
5	319	298	1300.8	5.3	1091	-81	2198	640	-103	1200	246	-115	3.00	2.49	0.51	2.43	1.21	0.16	2056
-	361	361	1325.1	5.6	1110	-72	2459	776	-108	1263	250	-119	3.28	2.83	0.65	2.55	1.29	0.16	2013
-	365	362	1348.3	5.7	1133	-63	2544	812	-113	1293	255	-122	3.39	2.91	0.68	2.59	1.32	0.18	2041
-	370	364	1373.3	5.9	1151	-51	2657	859	-115	1330	260	-128	3.53	3.07	0.72	2.65	1.37	0.19	2102
UL	380	366	1419.5	6.4	1189	42	3133	1045	-122	1407	263	-129	4.07	3.71	1.02	2.79	1.44	0.21	2163
-	397	367	1319.5	7.2	1136	402	4453	1458	-123	1377	263	-126	5.52	5.70	1.94	2.66	1.40	0.21	2068
-	399	368	982.0	8.9	844	1533	8019	2782	-80	1131	268	-100	9.11	11.18	4.56	2.07	1.15	0.21	1615
-	401	368	832.0	9.4	761	1804	9249	3179	-68	1057	267	-93	10.20	12.89	5.50	1.92	1.08	0.20	1540
-	406	368	744.5	10.4	701	2116	11004	3749	-56	997	265	-88	11.52	15.33	6.70	1.80	1.02	0.19	1511
-	417	369	660.8	12.5	641	2436	14278	4877	-30	926	260	-81	14.58	19.98	9.40	1.64	0.95	0.19	1590
-	443	371	570.1	17.3	581	2951	18913	7529	3	847	251	-77	21.64	28.08	15.52	1.49	0.87	0.19	1180

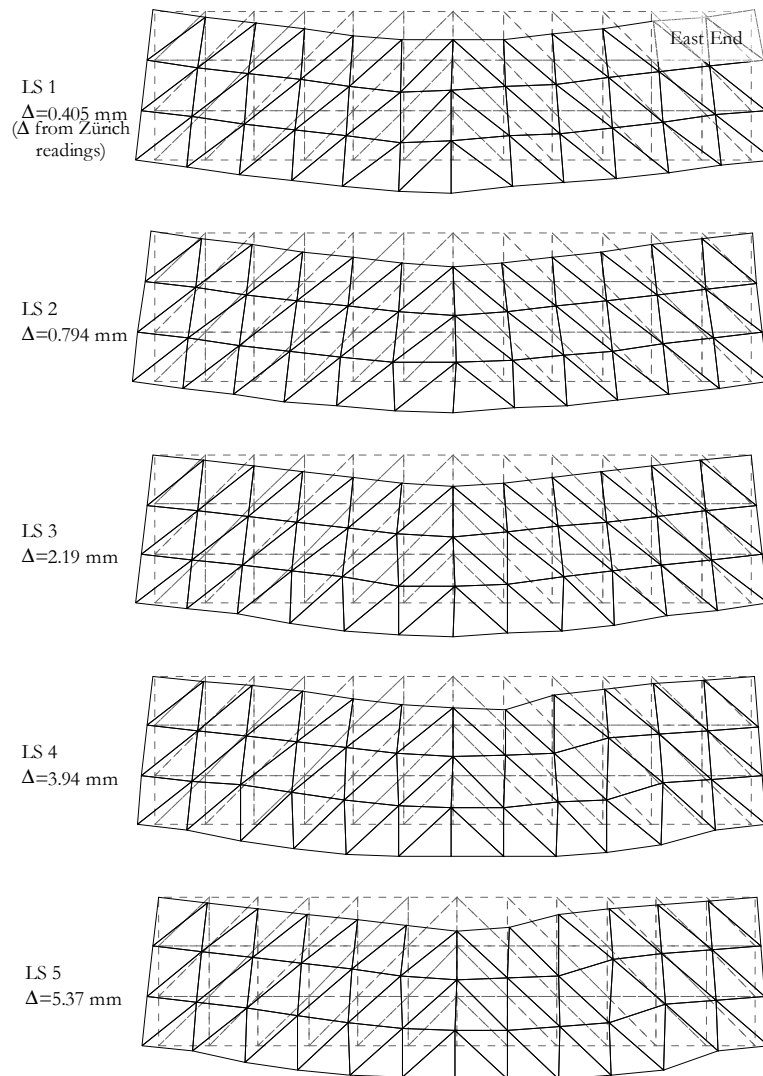
Note: The data from most of the strain gauges is not presented for the sake of brevity.



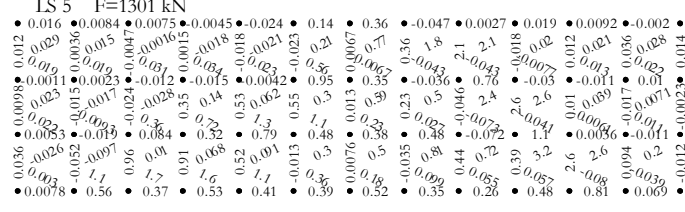
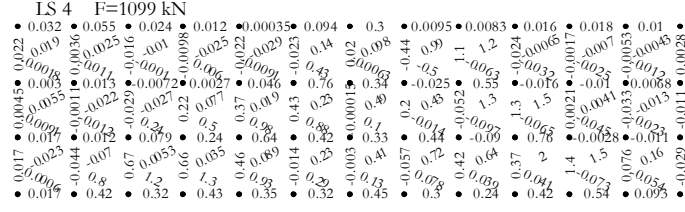
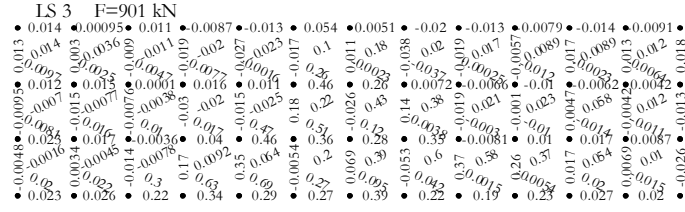
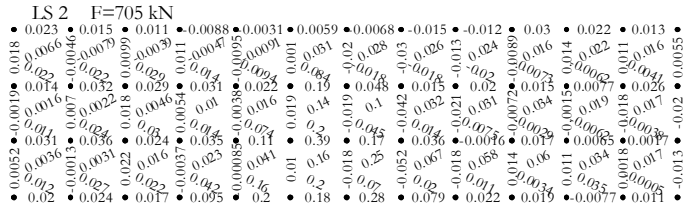
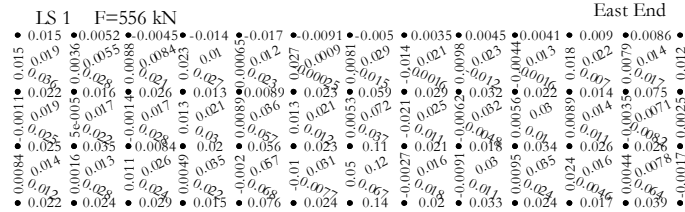


Crack Diagrams, crack widths in (mm)



**Deformed shapes amplified to midspan displacement equivalent to 200 mm**

Zürich readings over 300/300 mm grid, deformations in (mm)



### B3. SPECIMEN S0C

Cast day: March 28<sup>th</sup>, 2007

#### Beam properties

Cross section:  $b=1200$  mm,  $b_f=400$  mm

Effective depth: 1095 mm

Shear span: 1700 mm

Loading plates: 51/300/400 mm

Support plates: 51/150/400 mm

Longitudinal reinforcement:  $\rho_l=0.68\%$ ,  $f_y=650$  MPa

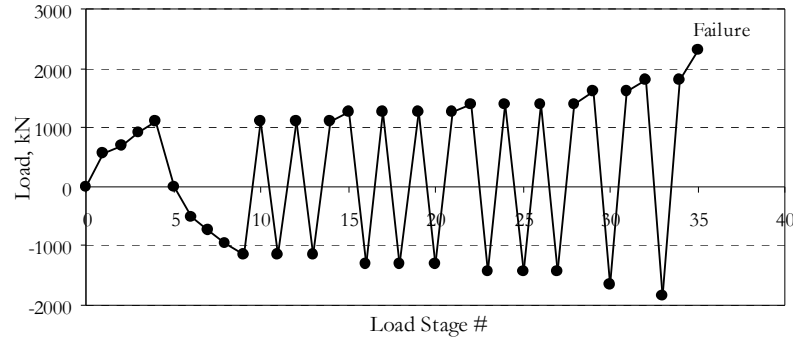
Transverse reinforcement:  $\rho_v=0\%$

Concrete:  $f_c' = 34.2$  MPa,  $\epsilon_c' = 1630 \mu\epsilon$ ,  $a_g = 20$  mm, *Modulus of rupture* = 4.3 MPa

Defects: no significant defects

Test days: August 16<sup>th</sup> – 24<sup>th</sup>, 2007

#### Loading history



#### Test Remarks

Maximum positive load: 2301.0 kN

Maximum negative load: 1848.5 kN

Displacement at failure: +10.9 mm

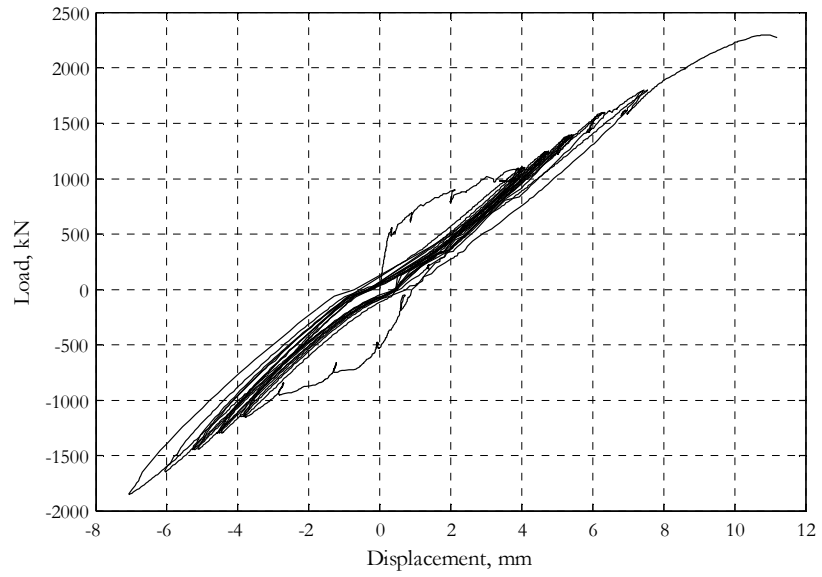
Failure mode: The beam failed in a very brittle manner with load crushing of concrete above the most eastern diagonal crack near the edge of the top loading plate.

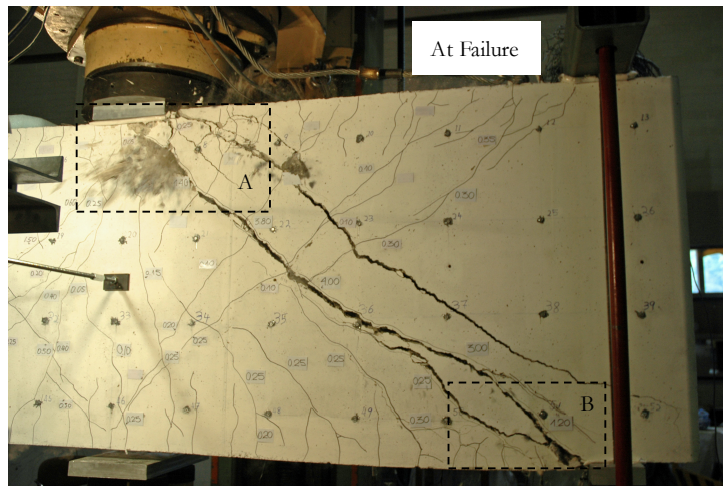
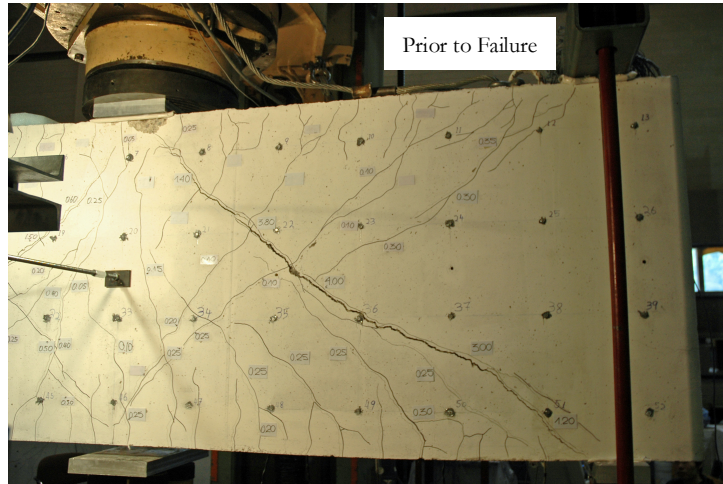
Other remarks:

- The formation and propagation of flexure-shear cracks was relatively quick.
- The north lateral support was loosening under positive load throughout the test.

- The threaded rods which connected the top and bottom support plates were loosened prior to Load Stage 34.

Global response





## Data summary

Load Stage	Data Set	Time elapsed	F	$\Delta=(BV+TV)/2$	BH	TH	ES-TE-BW	ES-V	ES-TW-BE	WS-TW-BE	WS-V	WS-TE-BW	EL-TE-BW	EL-V	EL-TW-BE	WL-TW-BE	WL-V	WL-TE-BW	Gauge 7B
(#)	(#)	(min)	(kN)	(mm)	(mm) $\times 10^{-3}$	(mm) $\times 10^{-3}$	(mm) $\times 10^{-3}$	(mm) $\times 10^{-3}$	(mm) $\times 10^{-3}$	(mm) $\times 10^{-3}$	(mm) $\times 10^{-3}$	(mm) $\times 10^{-3}$	(mm)	(mm)	(mm)	(mm)	(mm)	(mm)	( $\mu\text{E}$ )
-	14	29	9.2	0.0	0	3	0	0	2	0	0	-2	-0.03	-0.03	-0.01	0.00	0.01	0.01	0
1	86	62	558.5	0.3	53	-51	11	-10	-21	7	-12	-30	0.01	-0.01	-0.04	0.01	0.00	-0.02	59
2	126	116	697.3	0.9	282	-65	14	-3	-30	16	-12	-30	0.12	-0.03	-0.04	0.16	0.00	-0.05	81
3	179	157	901.7	2.1	438	-69	23	-2	-50	27	-16	-53	0.85	0.17	-0.10	0.69	0.38	-0.11	1052
4	251	212	1098.5	3.9	617	20	824	592	-109	1253	36	-103	2.05	1.19	-0.04	1.65	1.51	0.23	1355
5	551	1295	-1.8	0.9	83	77	260	200	-35	369	25	-20	0.58	0.37	0.02	0.57	0.55	0.12	276
6	683	1465	-526.5	-0.1	-48	285	137	129	-17	225	18	-1	0.22	0.16	0.11	0.32	0.40	0.17	58
7	766	1553	-748.2	-1.2	-54	463	119	117	-14	194	17	-6	0.16	0.15	0.41	0.21	0.75	0.94	1
8	843	1612	-950.7	-2.8	12	666	123	111	-21	201	16	-17	-0.07	0.78	1.50	0.14	1.37	1.71	62
9	938	1673	-1149.2	-3.8	33	792	123	111	-26	197	13	-17	-0.14	1.17	1.97	0.05	1.79	2.27	62
-	1016	1731	-344.0	-1.8	38	353	146	113	-30	239	13	-20	0.00	0.70	1.05	0.15	1.17	1.23	106
-	1056	1745	192.7	0.4	162	69	307	189	-51	418	17	-35	0.58	0.64	0.32	0.63	0.92	0.43	340
10	1218	1766	1105.4	4.0	694	67	1164	685	-138	1536	158	-109	2.60	1.88	0.08	2.11	1.99	0.46	1463
-	1418	5683	0.7	0.5	97	119	341	236	-26	497	95	-16	0.69	0.71	0.25	0.67	1.00	0.41	231
-	1460	5736	-482.9	-1.6	43	390	237	196	-30	333	82	-25	0.14	0.91	1.08	0.26	1.43	1.30	129
11	1517	5744	-1147.5	-3.8	54	822	210	179	-31	261	82	-25	-0.07	1.48	2.15	0.08	2.12	2.42	98
-	1552	5781	-375.6	-1.8	50	373	206	171	-27	297	89	-14	0.24	0.98	1.16	0.19	1.41	1.37	118
-	1598	5793	326.2	1.2	251	69	581	348	-59	712	89	-44	1.13	1.03	0.25	1.02	1.30	0.42	535
12	1688	5811	1098.5	4.0	710	69	1246	735	-135	1611	211	-113	2.77	1.99	0.15	2.17	2.17	0.53	1468
-	1716	5851	419.2	1.9	324	57	742	462	-82	981	133	-59	1.40	1.21	0.19	1.31	1.46	0.42	663
-	1732	5857	-110.1	-0.1	55	160	290	229	-36	433	120	-26	0.36	0.70	0.46	0.47	1.04	0.60	162

Load Stage	Data Set	Time elapsed	F	$\Delta=(BV+TV)/2$	BH	TH	ES-TE-BW	ES-V	ES-TW-BE	WS-TW-BE	WS-V	WS-TE-BW	EL-TE-BW	EL-V	EL-TW-BE	WL-TW-BE	WL-V	WL-TE-BW	Gauge 7B
13	1806	5865	-1146.2	-3.9	50	830	202	188	-34	262	111	-26	-0.07	1.56	2.17	0.05	2.17	2.47	98
-	1853	5908	-418.0	-1.9	49	398	210	191	-28	293	119	-14	0.07	1.04	1.24	0.18	1.51	1.46	113
-	1887	5934	71.8	0.1	114	96	313	214	-38	425	124	-22	0.47	0.71	0.37	0.53	1.03	0.50	218
14	2000	5950	1104.2	4.1	716	71	1274	754	-139	1650	242	-114	2.66	2.01	0.16	2.22	2.22	0.56	1480
15	2051	5990	1248.5	4.7	816	77	1445	868	-157	1857	281	-124	2.99	2.25	0.15	2.46	2.40	0.61	1677
-	2076	6021	554.2	2.5	414	66	927	588	-99	1267	192	-74	1.78	1.50	0.20	1.57	1.71	0.48	862
-	2089	6022	2.5	0.5	114	104	393	294	-40	613	162	-21	0.63	0.74	0.27	0.71	1.11	0.46	232
-	2117	6030	-402.6	-1.5	44	346	249	234	-36	387	151	-23	0.11	0.96	1.06	0.24	1.44	1.30	130
16	2182	6037	-1295.1	-4.5	55	924	212	205	-35	303	144	-23	-0.11	1.72	2.43	0.05	2.42	2.77	96
-	2209	6068	-469.0	-2.3	49	456	220	206	-34	335	147	-20	0.04	1.15	1.40	0.15	1.67	1.69	116
-	2288	6080	648.5	2.6	462	66	947	567	-100	1232	183	-78	1.87	1.55	0.20	1.64	1.78	0.49	963
17	2354	6092	1247.3	4.7	823	70	1475	880	-159	1915	308	-123	3.02	2.30	0.15	2.49	2.46	0.64	1680
-	2371	6120	601.7	2.5	421	55	953	603	-98	1276	203	-72	1.75	1.49	0.20	1.60	1.74	0.49	810
-	2379	6121	14.7	0.5	111	102	397	296	-41	576	172	-20	0.61	0.74	0.28	0.69	1.13	0.48	222
-	2439	7163	-398.4	-1.6	51	350	256	237	-30	392	161	-18	0.12	1.00	1.12	0.24	1.48	1.34	122
18	2509	7171	-1294.1	-4.5	63	940	223	219	-30	320	152	-18	-0.07	1.75	2.47	0.04	2.46	2.84	91
-	2534	7203	-505.0	-2.4	56	477	229	216	-30	332	153	-15	0.03	1.22	1.45	0.17	1.74	1.75	107
-	2549	7205	0.0	-0.3	88	130	282	229	-30	405	158	-20	0.28	0.73	0.55	0.40	1.09	0.68	146
-	2590	7216	406.7	1.7	318	79	753	464	-75	944	144	-58	1.42	1.26	0.23	1.27	1.53	0.46	648
19	2693	7230	1246.7	4.7	826	68	1492	899	-157	1965	318	-123	3.10	2.30	0.16	2.54	2.52	0.67	1673
-	2718	7273	569.8	2.6	424	48	986	632	-102	1329	214	-74	1.85	1.51	0.21	1.68	1.81	0.52	868
-	2732	7274	14.4	0.5	113	101	439	335	-42	606	182	-20	0.65	0.80	0.30	0.71	1.16	0.48	219
-	2760	7293	-386.8	-1.5	53	341	286	264	-36	421	168	-22	0.13	1.04	1.13	0.24	1.51	1.36	124
20	2827	7302	-1297.1	-4.6	66	948	236	241	-38	324	158	-24	-0.08	1.81	2.52	0.04	2.50	2.89	90
-	2869	7341	-548.0	-2.5	63	501	244	236	-34	348	163	-13	0.04	1.29	1.55	0.16	1.83	1.87	111

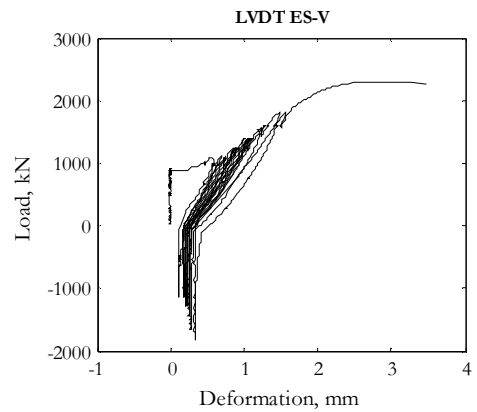
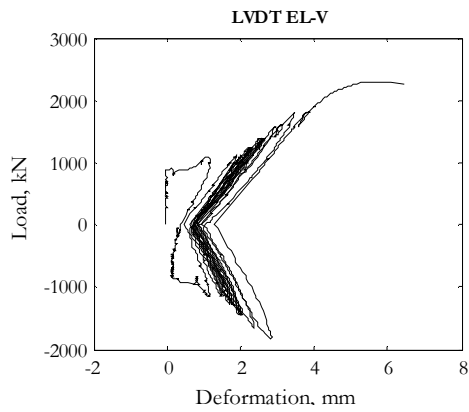
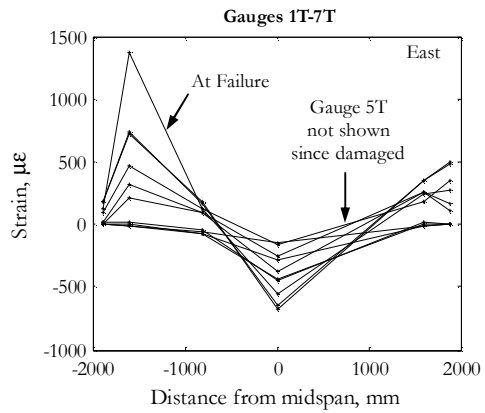
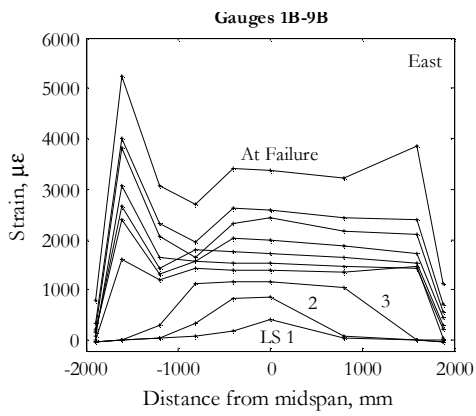
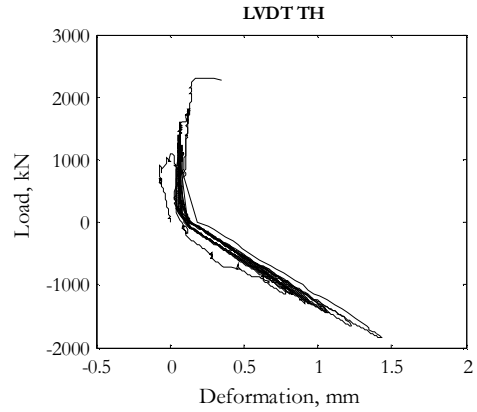
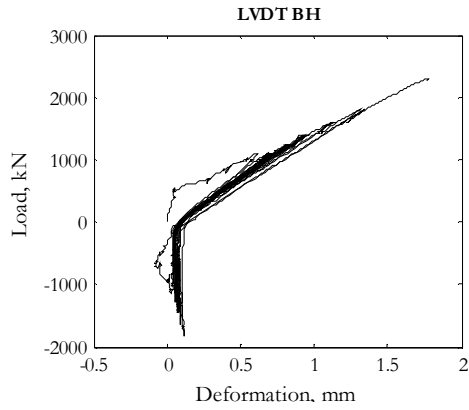


Load Stage	Data Set	Time elapsed	F	$\Delta = (BV+TV)/2$	BH	TH	ES-TE-BW	ES-V	ES-TW-BE	WS-TW-BE	WS-V	WS-TE-BW	EL-TE-BW	EL-V	EL-TW-BE	WL-TW-BE	WL-V	WL-TE-BW	Gauge 7B
-	2904	7399	0.0	-0.2	89	124	306	248	-34	434	173	-12	0.34	0.74	0.53	0.45	1.10	0.67	148
-	2953	7417	412.9	1.8	330	71	781	485	-81	999	153	-56	1.44	1.31	0.24	1.29	1.54	0.48	651
21	3060	7438	1249.8	4.8	833	59	1521	914	-160	2007	332	-123	3.08	2.32	0.16	2.56	2.52	0.67	1666
22	3111	7482	1394.2	5.3	930	59	1692	1021	-179	2209	366	-136	3.42	2.54	0.16	2.79	2.72	0.71	1855
-	3136	7533	676.7	2.9	479	42	1119	721	-111	1502	239	-84	2.00	1.66	0.21	1.81	1.92	0.57	925
-	3147	7534	130.2	0.6	148	77	520	390	-52	728	180	-28	0.68	0.85	0.28	0.80	1.22	0.49	218
-	3375	10043	-346.3	-1.4	57	318	292	277	-38	445	167	-26	0.14	1.01	1.08	0.27	1.50	1.28	124
23	3457	10051	-1439.0	-5.1	73	1059	246	252	-36	337	157	-26	-0.10	1.97	2.78	0.00	2.73	3.17	84
-	3480	10081	-642.5	-2.9	69	565	253	251	-36	353	163	-15	0.03	1.42	1.75	0.14	2.02	2.10	104
-	3491	10082	-2.6	-0.4	98	128	317	266	-36	434	171	-15	0.34	0.81	0.62	0.42	1.20	0.77	144
-	3536	10096	401.0	1.8	324	72	810	507	-85	997	150	-61	1.47	1.34	0.25	1.33	1.60	0.50	637
24	3647	10110	1392.3	5.3	941	66	1724	1052	-178	2209	379	-138	3.44	2.58	0.17	2.84	2.76	0.74	1856
-	3667	10138	687.3	3.1	498	44	1166	757	-117	1517	243	-94	2.08	1.74	0.23	1.90	2.01	0.60	964
-	3678	10139	146.2	0.9	166	54	589	423	-60	770	155	-42	0.86	0.95	0.26	0.90	1.30	0.45	246
-	3699	10146	-260.3	-1.1	56	252	293	276	-42	417	160	-30	0.17	0.92	0.97	0.30	1.41	1.17	124
-	3735	10150	-800.5	-3.1	65	627	255	259	-43	333	158	-28	0.01	1.45	1.83	0.12	2.08	2.20	104
25	3781	10155	-1445.0	-5.2	77	1059	247	254	-41	315	150	-28	-0.09	2.00	2.80	0.00	2.80	3.25	87
-	3817	10194	-688.4	-3.2	74	604	251	254	-39	330	160	-15	0.04	1.50	1.84	0.14	2.13	2.26	105
-	3837	10196	-124.5	-1.1	80	224	277	255	-38	396	165	-14	0.18	1.00	0.94	0.32	1.42	1.14	123
-	3884	10240	279.9	1.3	259	75	690	439	-70	853	152	-51	1.23	1.18	0.29	1.12	1.49	0.50	495
-	3941	10249	797.3	3.3	580	63	1213	755	-125	1571	250	-103	2.37	1.88	0.22	2.03	2.11	0.60	1158
26	4008	10257	1395.4	5.4	950	64	1750	1074	-183	2256	390	-141	3.48	2.62	0.18	2.89	2.79	0.76	1878
-	4032	10286	722.9	3.2	532	54	1219	794	-123	1596	257	-94	2.20	1.83	0.24	1.98	2.06	0.62	1019
-	4044	10287	134.2	0.5	151	81	528	400	-53	696	156	-34	0.68	0.85	0.32	0.75	1.23	0.50	204

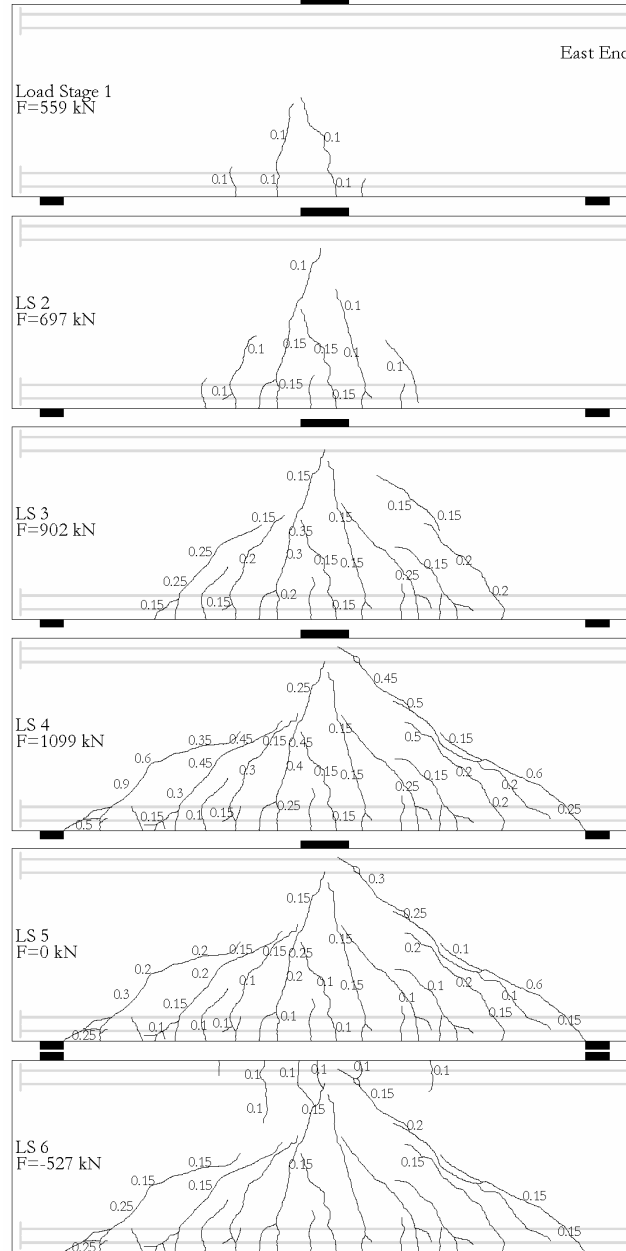
Load Stage	Data Set	Time elapsed	F	$\Delta=(BV+TV)/2$	BH	TH	ES-TE-BW	ES-V	ES-TW-BE	WS-TW-BE	WS-V	WS-TE-BW	EL-TE-BW	EL-V	EL-TW-BE	WL-TW-BE	WL-V	WL-TE-BW	Gauge 7B
-	4068	10293	-358.0	-1.5	59	325	288	279	-40	393	153	-27	0.12	1.07	1.14	0.26	1.58	1.40	124
27	4148	10302	-1444.2	-5.3	79	1070	247	255	-39	322	146	-26	-0.08	2.02	2.86	0.01	2.85	3.29	90
-	4178	10331	-698.2	-3.3	73	607	251	254	-40	328	152	-20	0.04	1.53	1.87	0.12	2.18	2.29	109
-	4198	10333	-145.4	-1.2	81	230	276	256	-42	387	156	-21	0.17	1.01	0.99	0.30	1.47	1.21	125
-	4260	10345	379.4	1.8	318	66	825	529	-87	1009	139	-62	1.48	1.37	0.26	1.39	1.62	0.51	628
28	4379	10360	1396.7	5.4	957	64	1782	1095	-186	2271	399	-141	3.53	2.66	0.17	2.96	2.83	0.77	1883
29	4442	10396	1601.0	6.3	1124	67	2044	1263	-206	2577	455	-158	4.00	2.99	0.17	3.27	3.10	0.85	2143
-	4471	10442	936.7	4.2	711	52	1548	1008	-153	1974	338	-110	2.83	2.27	0.24	2.45	2.44	0.73	1360
-	4480	10443	385.4	2.2	356	35	998	699	-94	1254	176	-62	1.64	1.49	0.28	1.51	1.75	0.56	665
-	4534	11486	-64.7	0.0	102	131	406	349	-50	577	156	-32	0.44	0.82	0.54	0.61	1.21	0.64	160
-	4564	11495	-477.9	-2.0	74	410	297	304	-48	431	152	-33	0.11	1.25	1.42	0.25	1.76	1.64	119
30	4652	11507	-1648.7	-6.0	96	1222	262	276	-51	369	146	-34	-0.04	2.34	3.30	-0.02	3.10	3.66	86
-	4688	11559	-868.6	-4.0	83	740	270	273	-48	374	150	-26	0.09	1.85	2.31	0.09	2.43	2.64	108
-	4710	11561	-297.8	-1.9	90	345	290	277	-48	398	152	-27	0.19	1.27	1.38	0.24	1.75	1.59	120
-	4742	11577	108.5	0.4	180	94	510	362	-59	632	161	-36	0.87	1.10	0.45	0.79	1.39	0.61	263
-	4792	11589	541.7	2.4	443	58	1053	675	-109	1315	192	-86	1.97	1.71	0.27	1.68	1.90	0.60	833
31	4928	11612	1601.0	6.3	1145	65	2109	1287	-208	2658	471	-164	4.15	3.13	0.21	3.30	3.14	0.88	2158
32	5009	11660	1802.9	7.4	1313	117	2442	1497	-233	2944	476	-201	4.68	3.50	0.20	3.99	3.57	0.64	2418
-	5045	11720	1154.8	5.4	905	105	1949	1264	-182	2381	393	-158	3.56	2.81	0.28	3.15	2.97	0.59	1663
-	5066	11721	601.7	3.4	533	84	1400	973	-126	1740	264	-110	2.36	2.05	0.33	2.22	2.30	0.54	953
-	5085	11723	110.8	1.2	219	123	783	621	-68	1005	198	-51	1.18	1.25	0.35	1.22	1.60	0.54	315
-	5117	11750	-292.2	-1.3	90	324	403	401	-53	630	202	-33	0.25	1.24	1.23	0.48	1.85	1.45	132
-	5154	11755	-798.4	-3.3	92	679	344	360	-49	503	198	-33	0.13	1.74	2.11	0.22	2.48	2.46	105
33	5235	11766	-1848.5	-7.1	120	1423	309	330	-51	443	189	-35	0.14	2.88	3.91	-0.01	3.74	4.33	86
-	5256	11803	-1067.9	-5.0	104	937	316	327	-56	449	194	-25	0.25	2.34	2.91	0.12	3.12	3.35	109

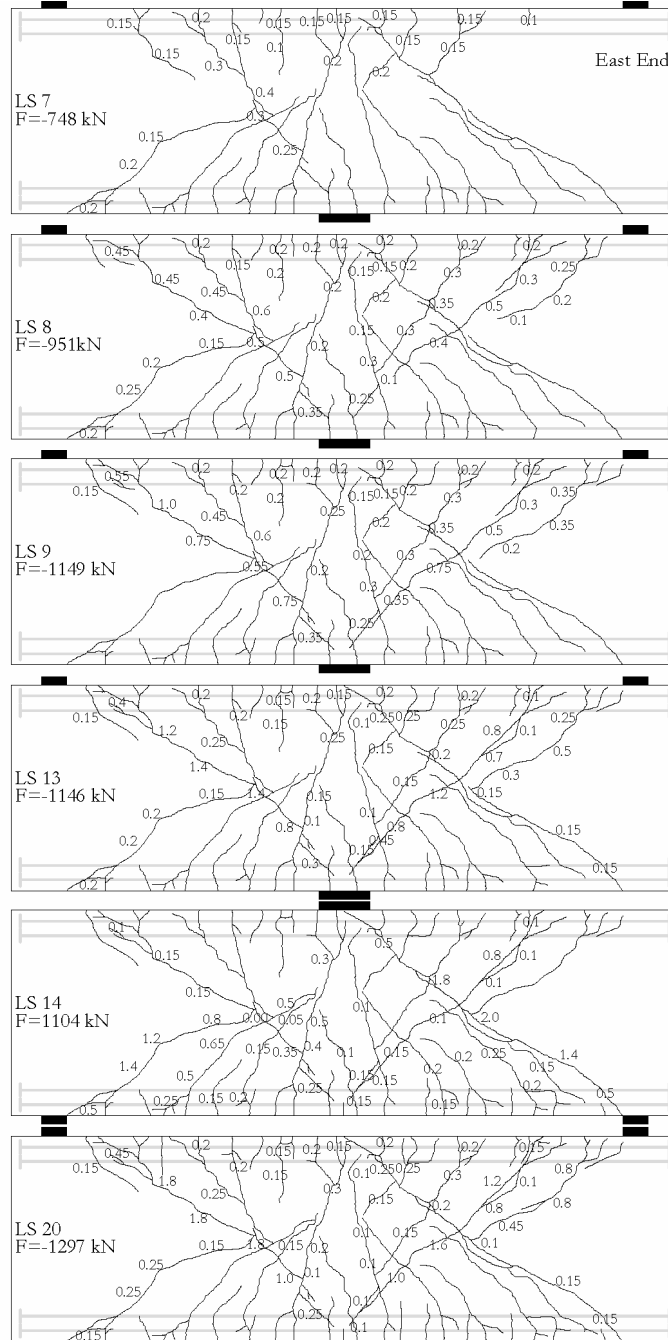
Load Stage	Data Set	Time elapsed	F	$\Delta = (BV+TV)/2$	BH	TH	ES-TE-BW	ES-V	ES-TW-BE	WS-TW-BE	WS-V	WS-TE-BW	EL-TE-BW	EL-V	EL-TW-BE	WL-TW-BE	WL-V	WL-TE-BW	Gauge 7B
-	5266	11804	-477.7	-2.9	111	530	322	330	-56	453	198	-26	0.31	1.78	1.95	0.30	2.43	2.30	119
-	5279	11809	-0.1	-0.7	143	183	372	340	-55	537	203	-34	0.51	1.28	1.03	0.58	1.66	1.07	150
-	5352	11818	719.2	3.3	607	98	1349	874	-130	1524	178	-114	2.71	2.32	0.40	2.30	2.48	0.53	1075
-	5410	11827	1226.0	5.3	947	109	1890	1195	-177	2142	235	-158	3.80	2.99	0.33	3.16	3.09	0.51	1700
34	5476	11834	1803.5	7.5	1341	125	2543	1568	-230	2830	306	-202	5.02	3.80	0.27	4.12	3.79	0.51	2437
UL	5598	11886	2301.0	10.9	1772	241	4216	2903	-298	4018	475	-285	7.18	5.71	0.87	5.55	4.90	0.64	3200
-	5601	11886	2274.8	11.2	1764	342	4662	3477	-299	4018	478	-284	7.73	6.42	1.44	5.50	4.87	0.64	1270

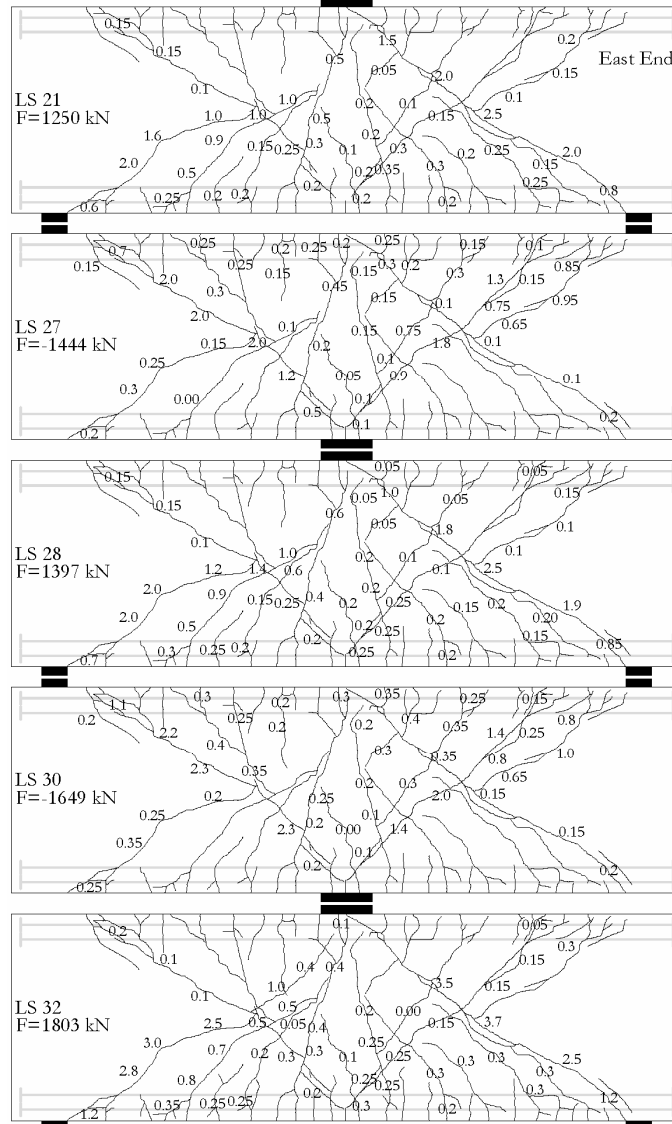
Note: The data from most of the strain gauges is not presented for the sake of brevity.



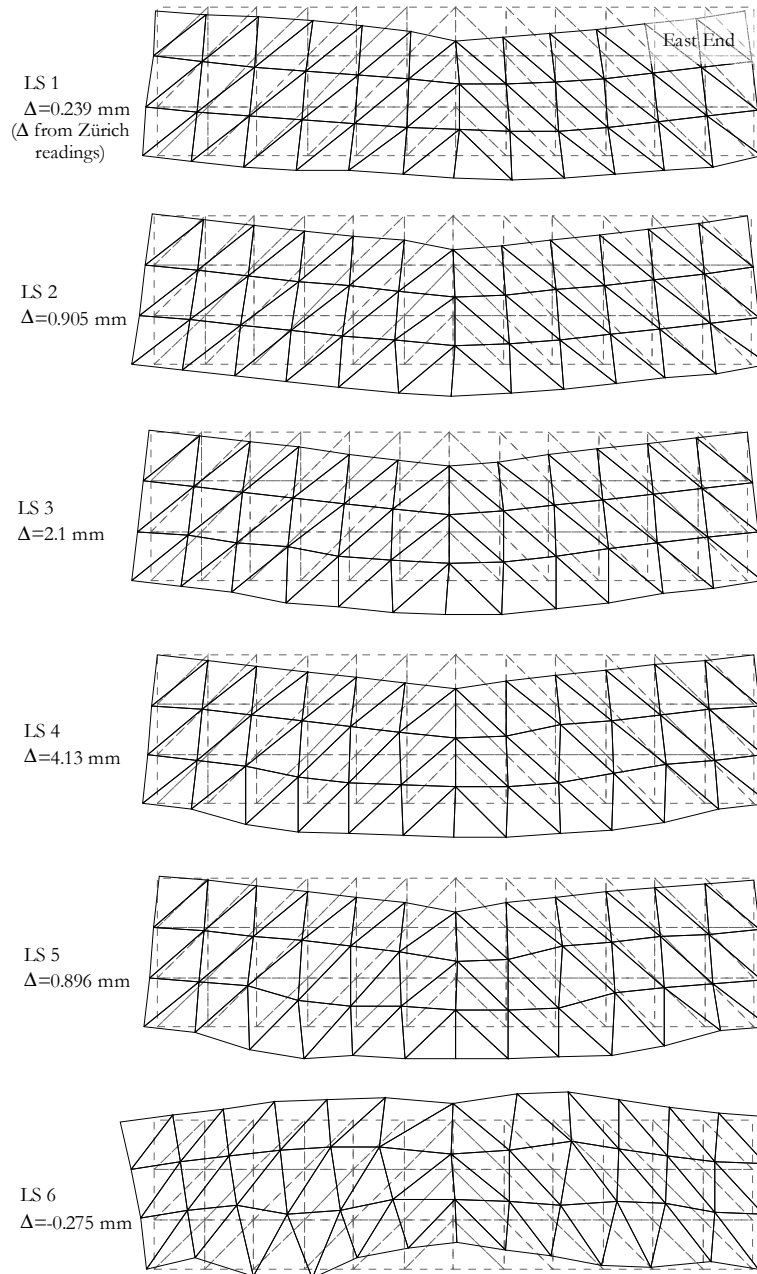
Crack Diagrams, crack widths in (mm)



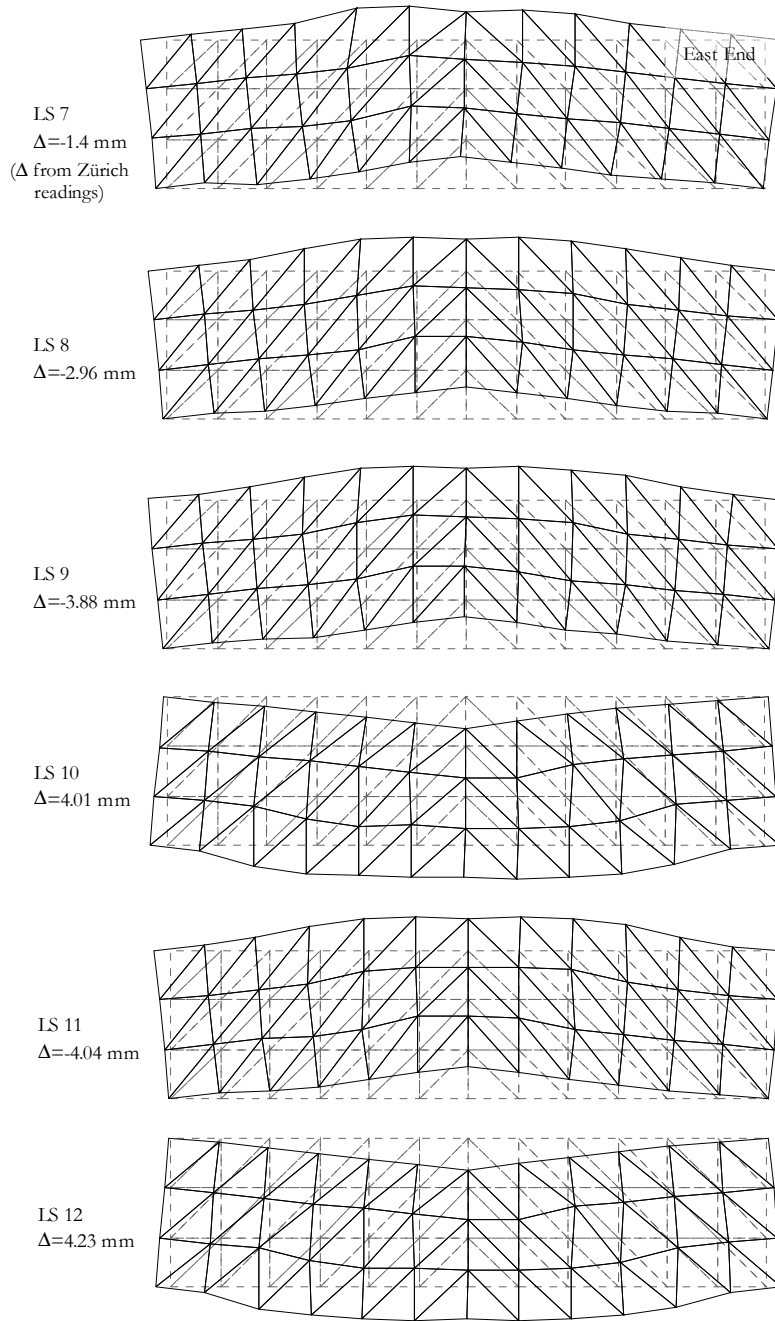


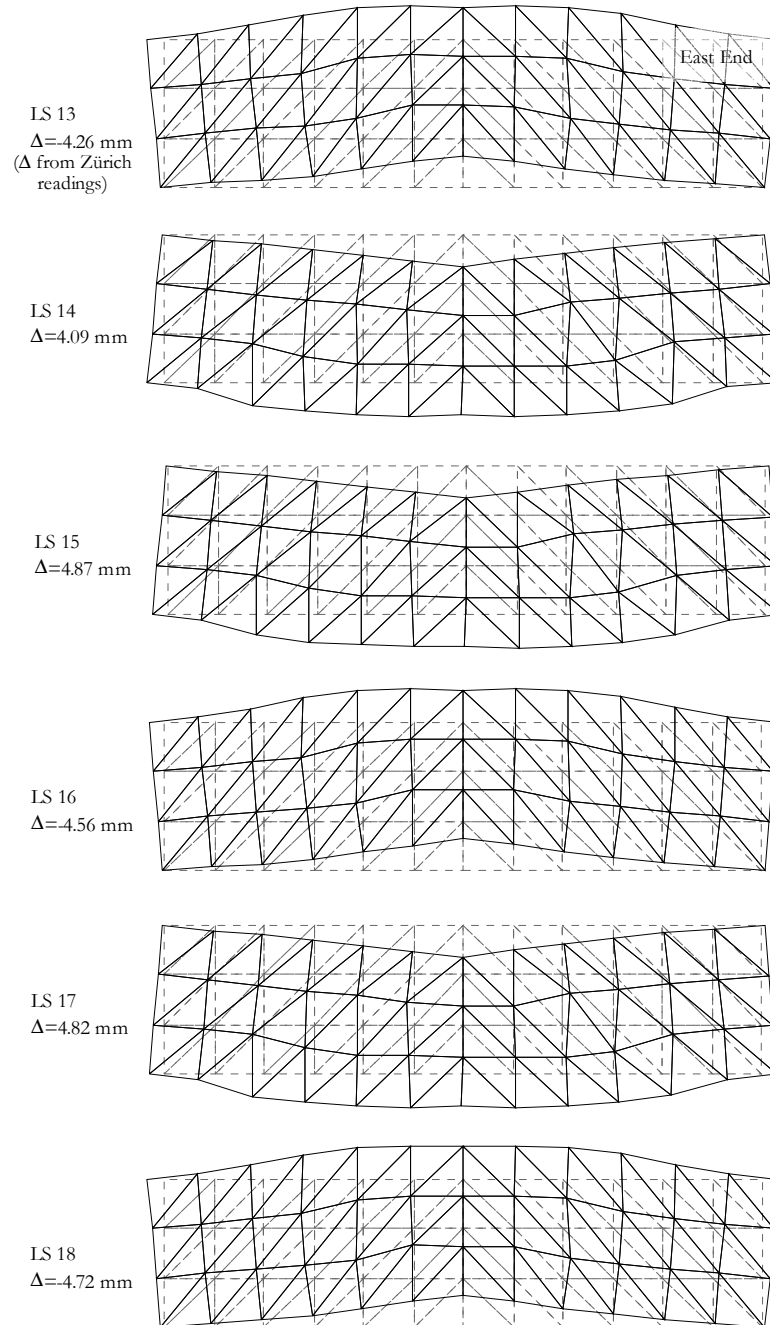


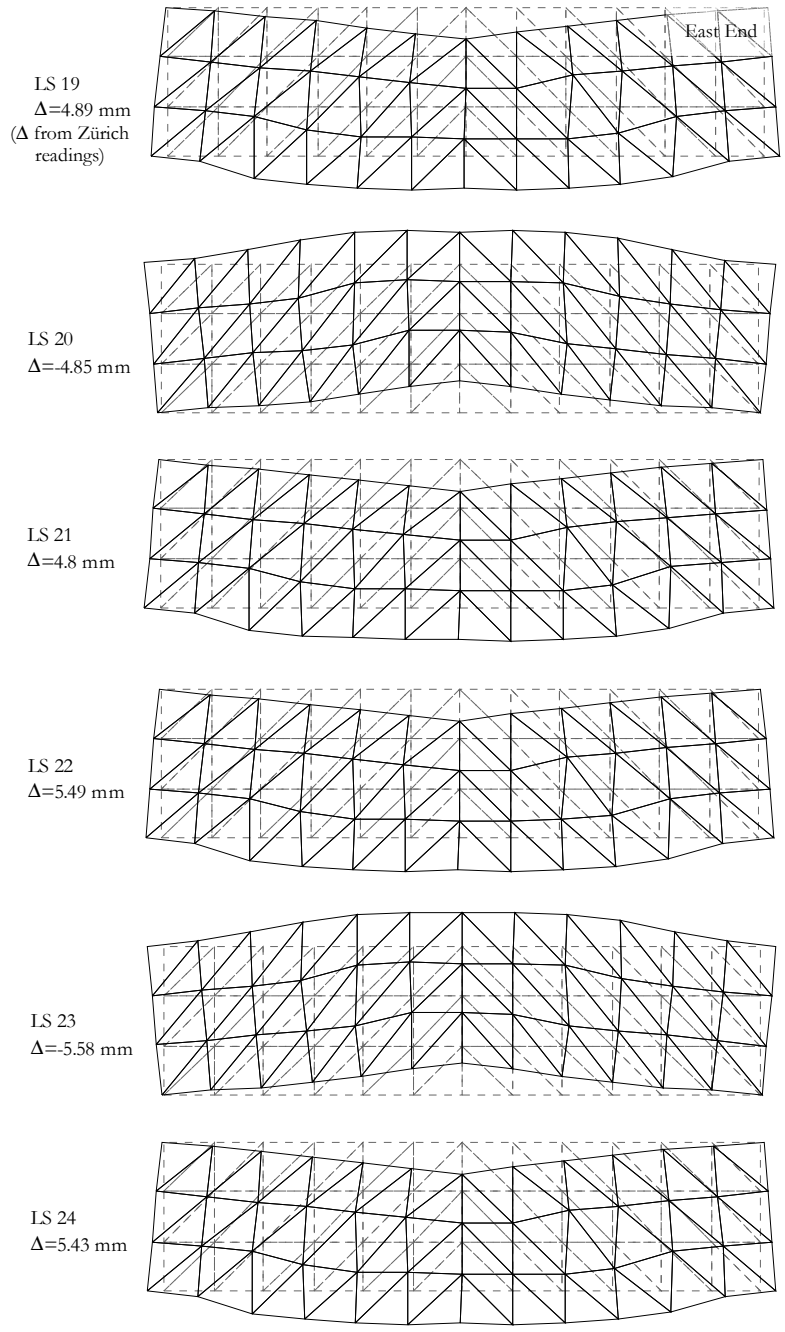
## Deformed shapes amplified to midspan displacement equivalent to 200 mm

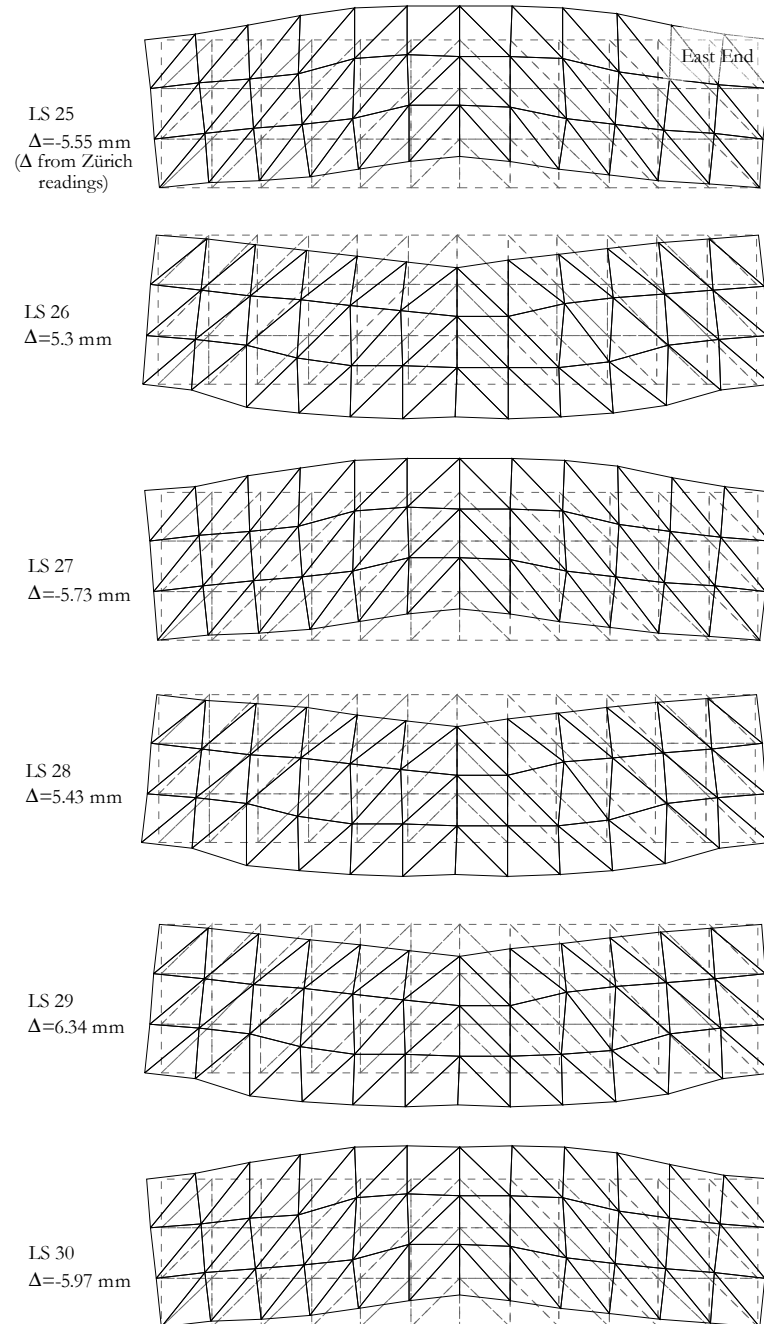


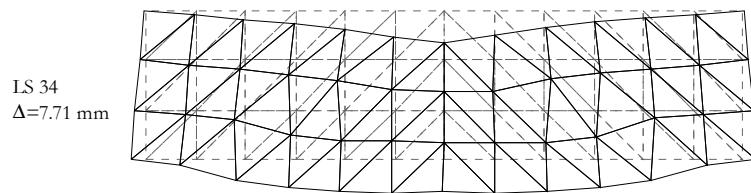
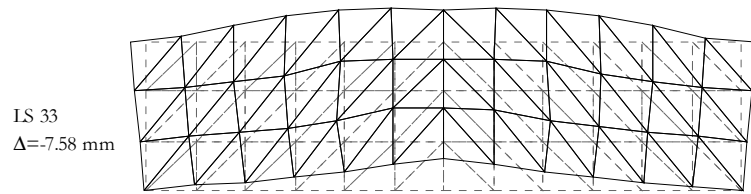
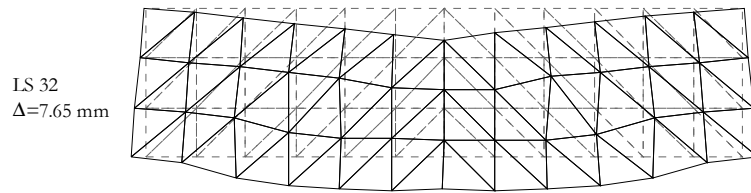
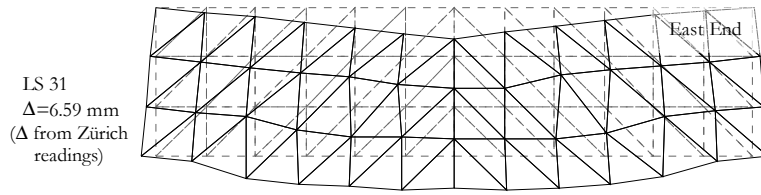




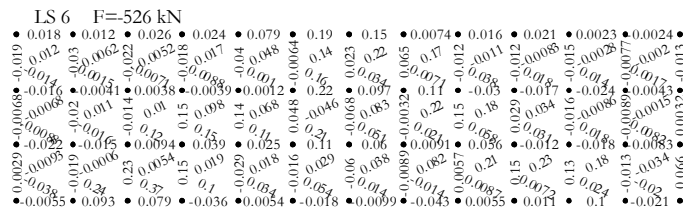
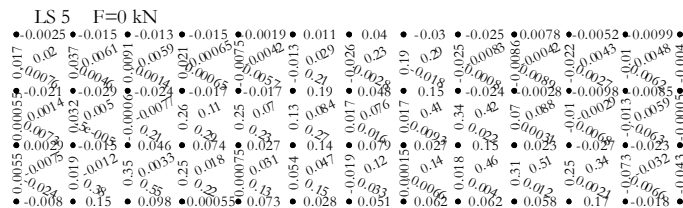
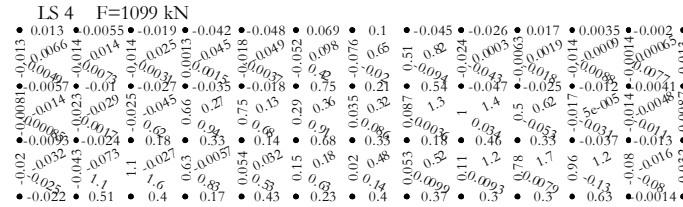
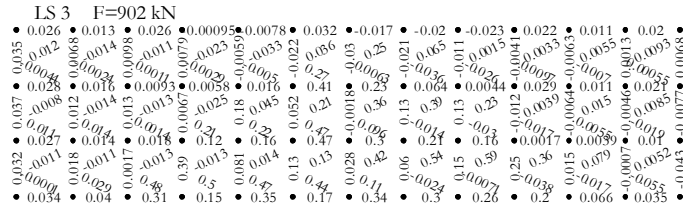
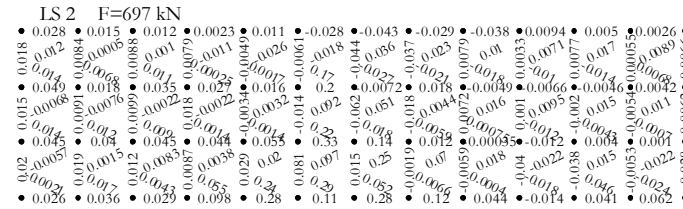
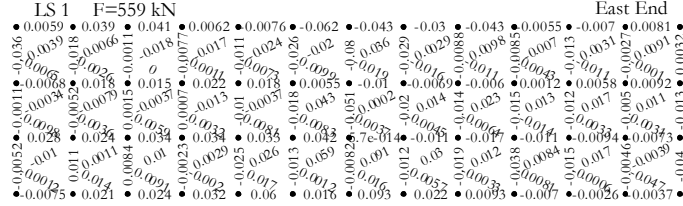


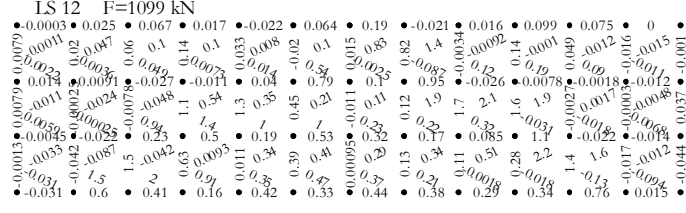
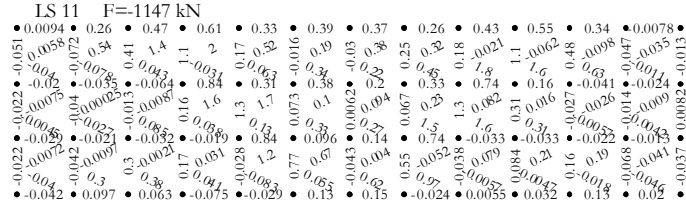
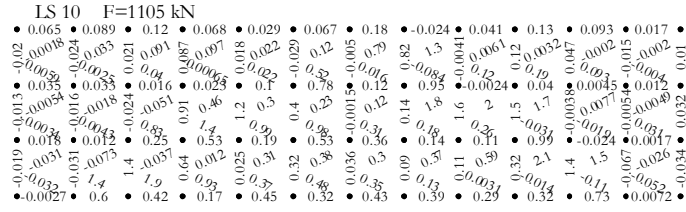
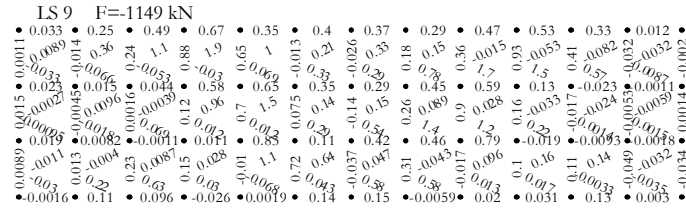
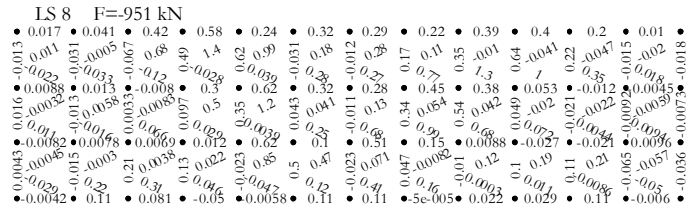
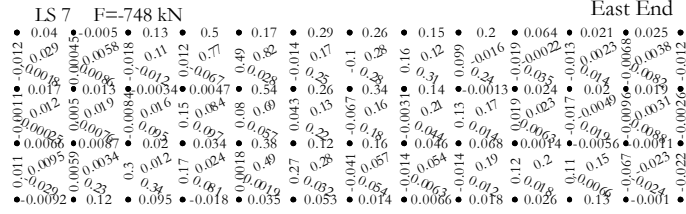


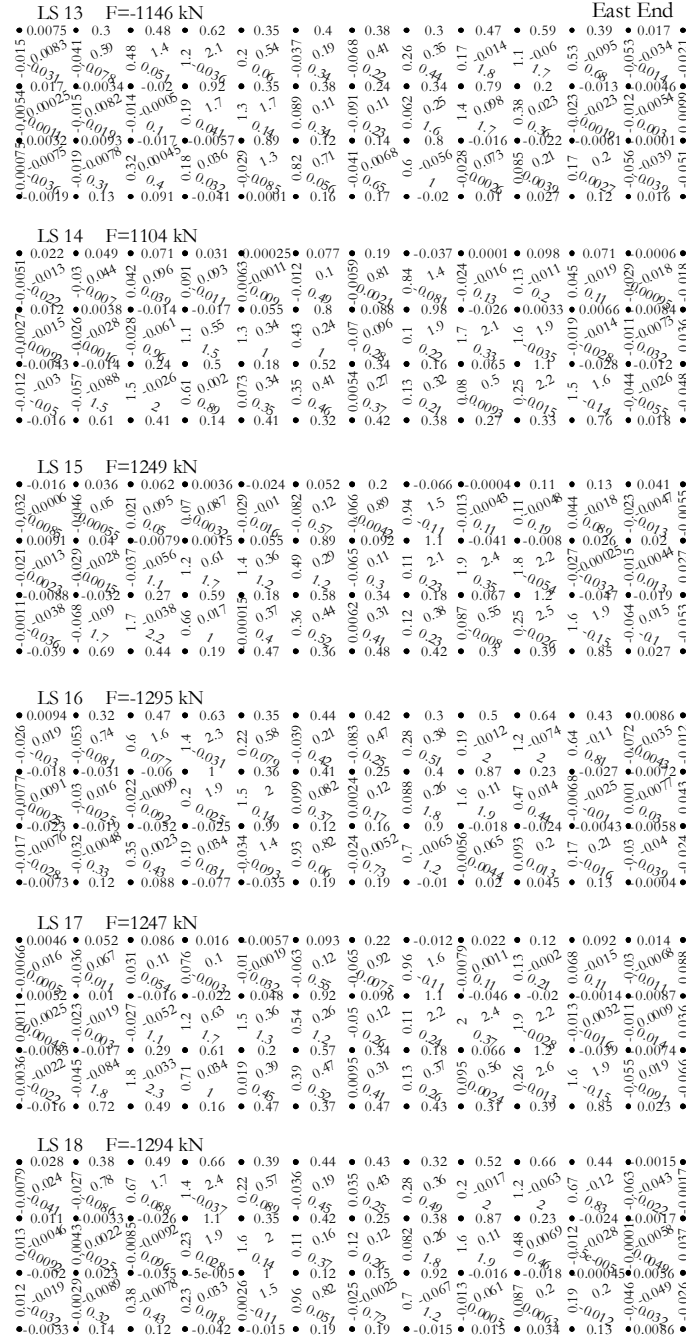




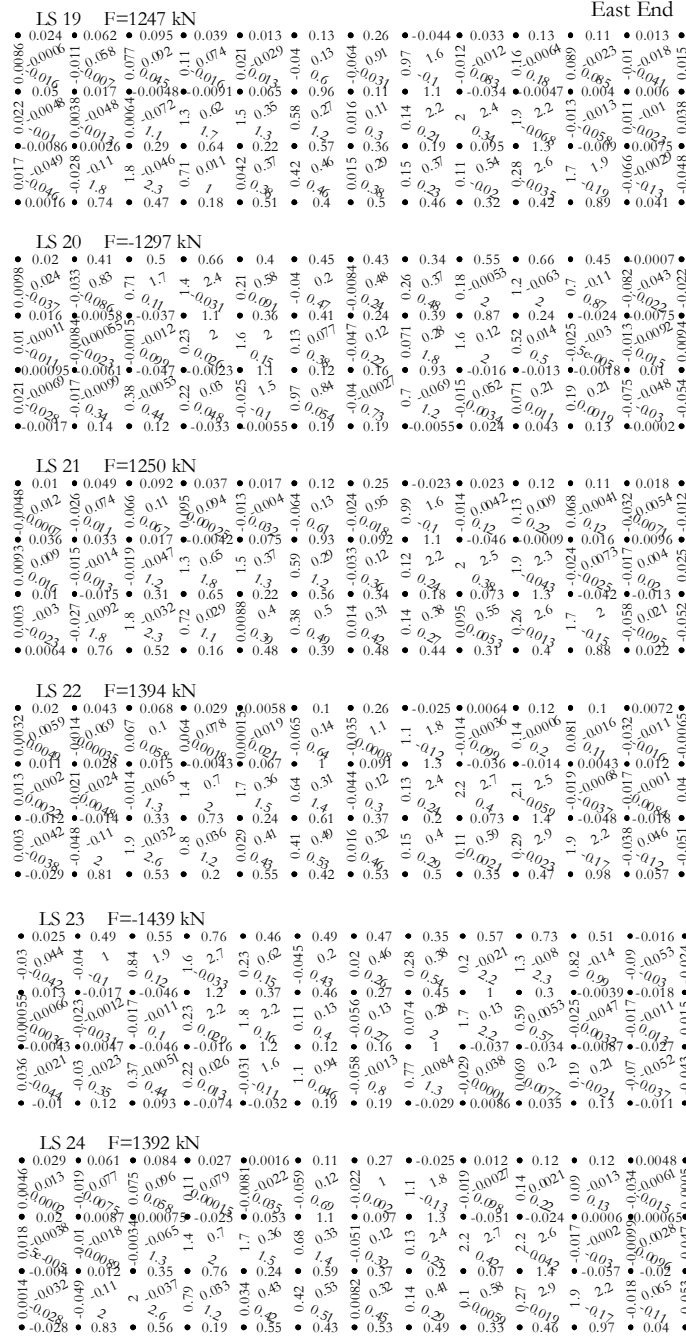
Zürich readings over 300/300 mm grid, deformations in (mm)











LS 25 F=-1445 kN East End

0.06	0.54	0.53	0.73	0.45	0.47	0.35	0.59	0.76	0.54	-0.02
0.01	0.051	1.1	2	1.6	2.7	0.46	0.4	-0.0055	-0.15	-0.044
0.0023	-0.021	-0.038	1.2	0.4	0.095	0.27	0.35	2.3	0.87	-0.037
0.00093	-0.0023	-0.0048	2.2	2.2	0.11	0.12	1.8	0.14	-0.022	-0.012
0.015	0.00088	0.0031	0.1	0.01	0.16	0.33	0.15	0.63	0.00092	0.015
0.00088	-0.00172	-0.0056	-0.061	-0.012	1.2	0.11	0.11	0.033	0.00092	0.0046
0.015	-0.00072	-0.0014	0.4	0.43	0.04	0.016	1.7	0.2	0.011	0.042
0.037	-0.35	0.43	0.22	0.029	-0.11	1.1	0.97	0.0079	0.011	0.036
0.0012	0.14	0.11	-0.062	-0.014	0.21	-0.046	0.81	0.2	-0.015	0.029

LS 26 F=1395 kN

0.06	0.058	0.083	0.046	0.0053	0.13	0.26	-0.038	0.026	0.11	0.1	0.011
0.001	0.012	0.0028	0.069	0.0028	0.004	1	1.8	-0.004	0.005	-0.014	-0.0005
0.0024	0.0079	-0.021	-0.022	0.054	1.1	0.63	0.015	-0.12	0.34	0.16	-0.015
0.007	0.0077	0.021	-0.006	0.71	0.7	0.2	2.5	2.7	2.6	0.0052	0.041
0.007	0.0077	0.021	-0.006	0.71	0.7	0.2	2.5	2.7	2.6	0.0052	0.041
0.014	-0.049	-0.11	2	-0.037	0.84	0.027	1.7	0.021	1.9	-0.024	0.014
0.014	-0.049	-0.11	2	-0.037	0.84	0.027	1.7	0.021	1.9	-0.024	0.014
0.02	-0.776	-0.11	2	-0.037	0.84	0.027	1.7	0.021	1.9	-0.024	0.014
-0.015	0.82	0.53	0.17	0.51	0.41	0.42	0.4	0.34	0.48	0.33	0.97

LS 27 F=-1444 kN

0.033	0.56	0.52	0.75	0.47	0.52	0.51	0.39	0.61	0.76	0.57	0.0003
0.011	0.051	1.1	2	2.8	0.2	0.46	0.38	2.3	1.4	0.075	0.055
0.002	-0.012	-0.035	1.3	0.4	0.091	0.27	0.45	1	0.29	-0.031	0.0051
0.016	0.0023	-0.0048	2.2	2.2	0.11	0.12	1.8	0.14	0.67	0.00094	0.0041
0.016	0.0023	-0.0048	2.2	2.2	0.11	0.12	1.8	0.14	0.67	0.00094	0.0041
0.025	0.0045	0.0023	0.22	0.25	2.3	1.9	0.13	0.63	0.21	-0.012	0.015
0.025	0.0045	0.0023	0.22	0.25	2.3	1.9	0.13	0.63	0.21	-0.012	0.015
0.04	-0.0045	-0.0019	0.41	0.0043	0.012	1.1	0.99	0.017	0.075	0.0055	0.0041
0.0008	0.14	0.11	-0.053	0.0076	0.21	-0.067	0.83	0.2	-0.019	0.012	0.018

LS 28 F=1397 kN

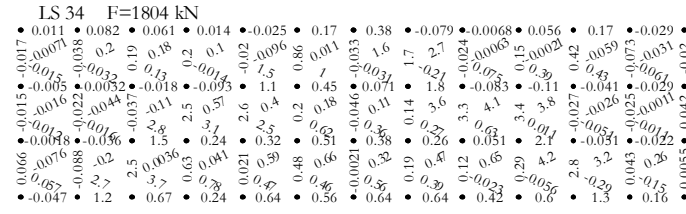
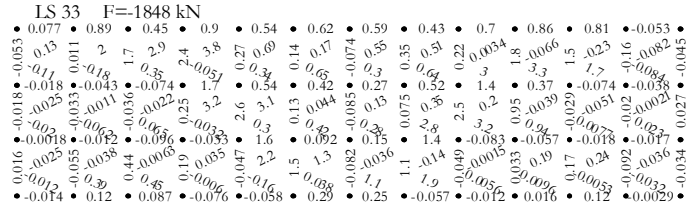
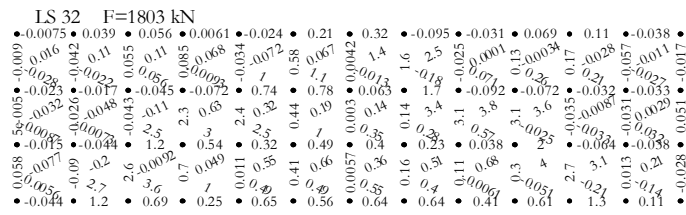
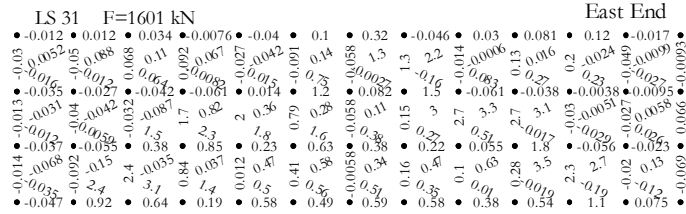
0.031	0.064	0.12	0.06	0.0042	0.11	0.28	-0.037	0.014	0.11	0.12	0.0028
0.0055	0.005	0.088	0.11	0.084	0.12	1.1	1.8	-0.004	0.004	0.013	0.00094
0.019	0.0055	-0.011	-0.024	0.049	1.1	0.097	0.13	-0.052	-0.032	0.0045	0.00015
0.004	0.0004	0.0023	0.025	0.72	0.23	0.12	2.5	2.8	2.2	0.00075	0.0045
0.004	0.0004	0.0023	0.025	0.72	0.23	0.12	2.5	2.8	2.2	0.00075	0.0045
0.0054	0.0032	-0.014	0.065	0.24	0.38	0.36	0.14	0.13	0.27	-0.027	0.017
0.0054	0.0032	-0.014	0.065	0.24	0.38	0.36	0.14	0.13	0.27	-0.027	0.017
0.042	-0.059	-0.11	2	-0.037	0.84	0.027	1.7	0.021	1.9	-0.024	0.014
-0.031	0.84	0.55	0.19	0.5	0.44	0.42	0.4	0.34	0.48	0.33	0.97

LS 29 F=1601 kN

0.032	0.065	0.1	0.039	0.012	0.14	0.31	-0.017	0.051	0.12	0.12	0.0068
0.0096	0.009	0.085	0.12	0.068	0.13	1.2	1.8	-0.0024	0.0045	0.012	0.0037
0.007	0.007	0.017	0.09	0.049	0.12	0.8	0.15	-0.057	-0.027	0.0034	0.00088
0.016	0.012	-0.013	0.027	0.069	0.34	0.15	2.8	3.2	2.5	0.00075	0.001
0.016	0.012	-0.013	0.027	0.069	0.34	0.15	2.8	3.2	2.5	0.00075	0.001
0.0059	0.0045	-0.0061	0.015	0.32	0.32	0.41	0.17	0.24	0.27	-0.038	0.0075
0.0059	0.0045	-0.0061	0.015	0.32	0.32	0.41	0.17	0.24	0.27	-0.038	0.0075
0.006	-0.048	-0.15	2.4	0.022	0.65	0.47	0.17	0.38	0.29	0.0014	0.0075
0.006	-0.048	-0.15	2.4	0.022	0.65	0.47	0.17	0.38	0.29	0.0014	0.0075
0.081	0.59	0.47	0.76	0.45	0.51	0.49	0.35	0.57	0.72	0.61	0.047

LS 30 F=-1649 kN

0.081	0.59	0.47	0.76	0.45	0.51	0.49	0.35	0.57	0.72	0.61	0.047
-0.057	0.089	1.4	2.5	5.1	0.69	0.2	0.4	0.24	1.5	-0.085	-0.18
-0.023	-0.021	-0.073	0.099	1.4	0.38	0.32	0.39	2.5	2.7	0.36	0.0048
-0.008	-0.024	-0.036	-0.019	2.5	2.6	0.12	0.29	0.15	0.06	-0.021	0.0044
-0.008	-0.024	-0.036	-0.019	2.5	2.6	0.12	0.29	0.15	0.06	-0.021	0.0044
-0.024	-0.036	-0.036	-0.12	-0.074	1.3	0.11	1.2	-0.038	0.022	0.0047	0.0058
-0.024	-0.036	-0.036	-0.12	-0.074	1.3	0.11	1.2	-0.038	0.022	0.0047	0.0058
-0.032	0.073	0.047	-0.1	-0.082	0.22	0.24	0.24	-0.02	0.026	0.035	0.16



**B4. SPECIMEN SIM**

**Cast day:** May 1<sup>th</sup>, 2007

**Beam properties**

Cross section:  $b=1200$  mm,  $b=400$  mm

Effective depth: 1095 mm

Shear span: 1700 mm

Loading plates: 51/300/400 mm

Support plates: 51/150/400 mm

Longitudinal reinforcement:  $\rho_l=0.68\%$ ,  $f_y=650$  MPa

Transverse reinforcement:  $\rho_t=0.1\%$ ,  $f_{yt}=490$  MPa

Concrete:  $f'_c = 33.0$  MPa,  $\epsilon'_c=1630 \mu\epsilon$ ,  $a_g=20$  mm, *Modulus of rupture* = 3.9 MPa

Defects: no significant defects

**Test day:** August 30<sup>th</sup>, 2007

**Test Remarks**

Maximum load: 1860.1 kN

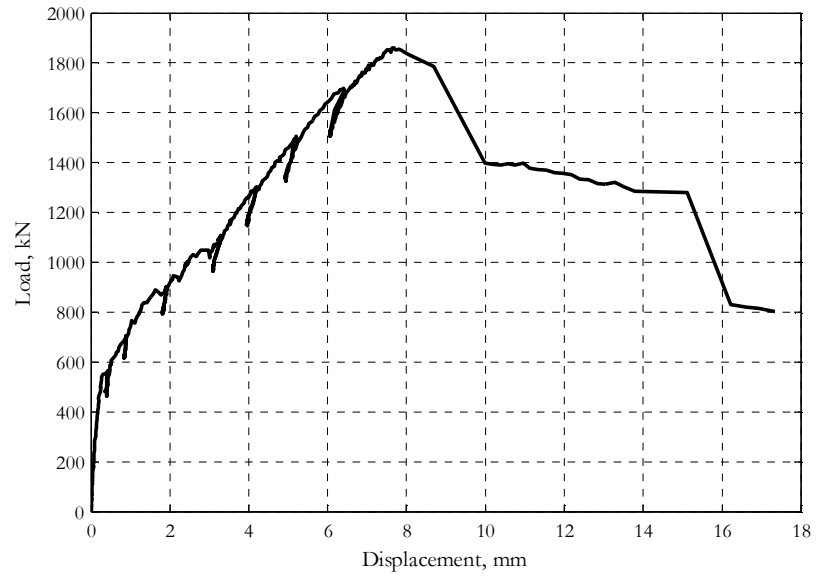
Displacement at maximum load: 7.7 mm

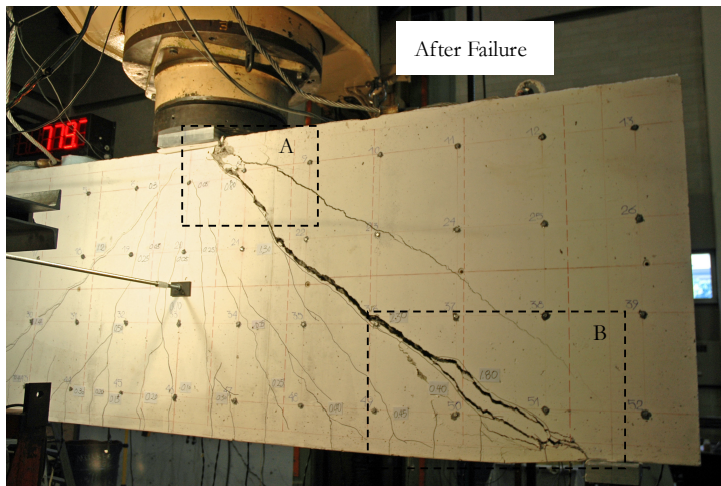
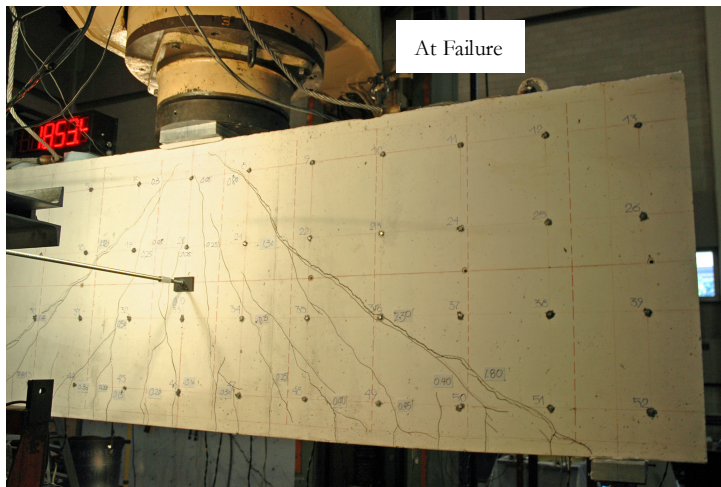
Failure mode: The beam failed in a relatively gradual manner with crushing above the most eastern diagonal crack near the edge of the top loading plate. Sounds indicating rupture of stirrups were heard after the load on the beam has started to decrease.

Other remarks:

- The formation and propagation of flexure-shear cracks was relatively gradual.

Global response





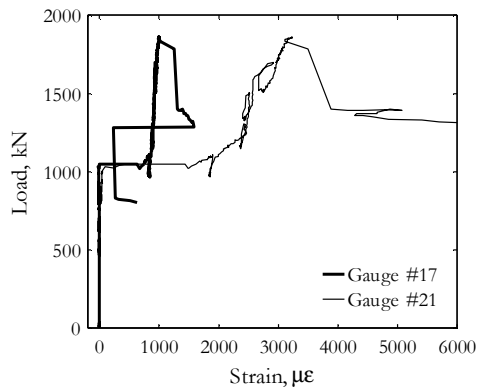
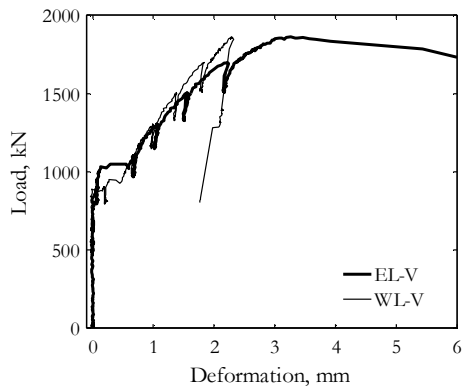
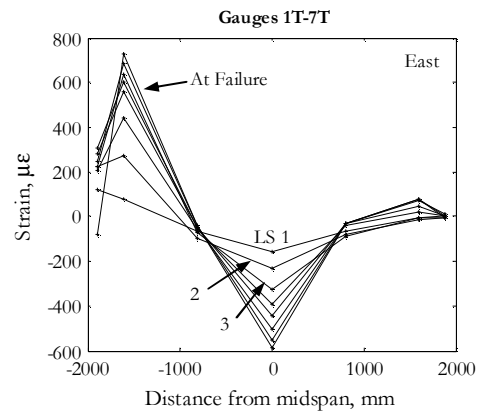
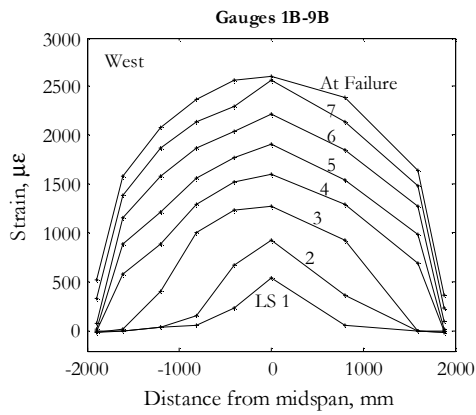
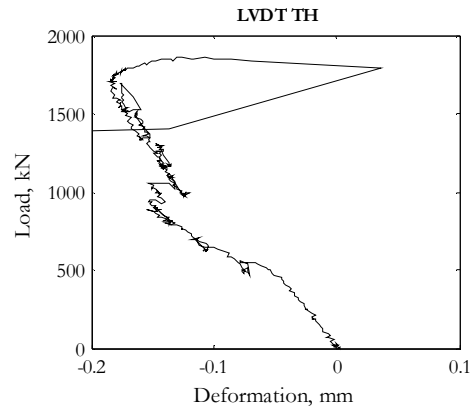
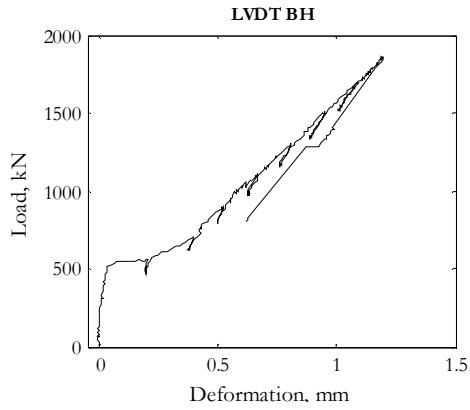
## Data summary

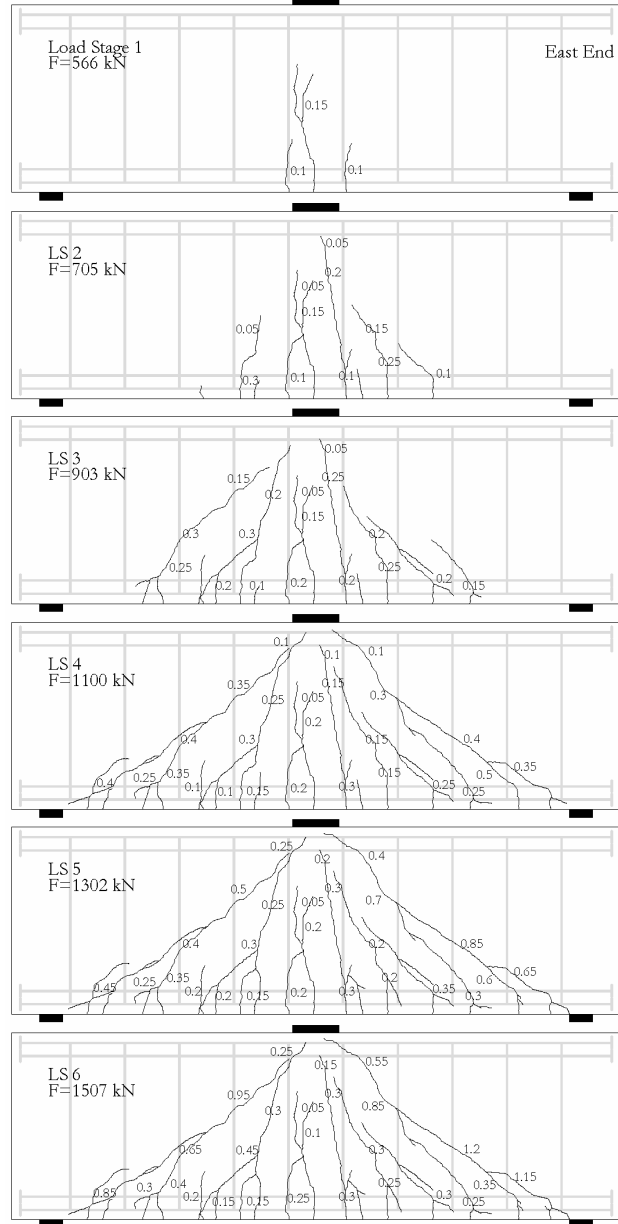
Load Stage	Data Set	Time elapsed	F	$\Delta=(BV+TV)/2$	BH	TH	ES-TE-BW	ES-V	ES-TW-BE	EL-TE-BW	EL-V	EL-TW-BE	WL-TW-BE	WL-V	WL-TE-BW	Gauge 7B	Gauge 17	Gauge 21
(#)	(#)	(min)	(kN)	(mm)	(mm) $\times 10^{-3}$	(mm) $\times 10^{-3}$	(mm) $\times 10^{-3}$	(mm) $\times 10^{-3}$	(mm) $\times 10^{-3}$	(mm)	(mm)	(mm)	(mm)	(mm)	(mm)	( $\mu\epsilon$ )	( $\mu\epsilon$ )	( $\mu\epsilon$ )
-	49	25	370.2	0.2	16	-38	4	-6	-12	0.02	-0.02	-0.02	0.00	-0.02	-0.03	32	-5	-7
1	71	31	565.7	0.4	199	-78	5	-9	-20	0.04	0.00	-0.04	0.03	-0.01	-0.06	58	-2	-3
-	97	63	627.1	0.6	306	-96	5	-10	-19	0.12	0.00	-0.02	0.07	-0.03	-0.07	73	-6	-3
2	105	66	704.7	0.9	397	-112	3	-8	-22	0.27	-0.01	-0.03	0.13	-0.01	-0.08	372	-1	-4
-	132	97	772.5	1.1	431	-125	7	-10	-24	0.33	0.00	-0.04	0.25	-0.02	-0.09	497	-6	1
-	139	99	827.6	1.3	471	-139	5	-8	-26	0.39	-0.01	-0.05	0.30	-0.02	-0.10	619	-10	-4
-	143	101	862.7	1.5	491	-147	6	-11	-29	0.53	0.05	-0.05	0.36	-0.01	-0.08	852	-12	5
3	156	106	902.8	1.9	524	-148	9	-11	-29	0.61	0.08	-0.05	0.78	0.18	-0.12	926	-10	18
-	194	138	931.6	2.1	552	-154	9	-12	-33	0.65	0.08	-0.04	0.88	0.27	-0.16	987	-11	45
-	200	140	960.8	2.3	565	-143	8	-12	-33	0.68	0.09	-0.07	1.18	0.49	-0.19	1005	-12	41
-	208	142	1020.7	2.5	593	-148	11	-11	-34	0.78	0.13	-0.07	1.27	0.56	-0.18	1060	-18	71
-	212	144	1048.8	2.8	618	-153	258	-12	-41	0.97	0.29	-0.07	1.32	0.59	-0.20	1111	-5	443
4	234	150	1099.5	3.3	662	-137	678	-50	-63	1.45	0.70	-0.09	1.44	0.68	-0.21	1292	833	1901
-	269	192	1132.8	3.4	699	-138	729	-48	-69	1.52	0.76	-0.07	1.53	0.72	-0.18	1350	875	2080
-	278	193	1179.5	3.6	727	-143	776	-50	-70	1.61	0.82	-0.08	1.60	0.77	-0.19	1406	873	2238
-	286	195	1218.2	3.8	752	-144	829	-54	-75	1.67	0.90	-0.06	1.69	0.85	-0.17	1452	880	2402
-	293	196	1258.3	4.0	776	-143	894	-60	-78	1.78	0.96	-0.05	1.80	0.91	-0.17	1497	885	2450
5	308	198	1302.3	4.2	811	-147	1003	-72	-84	1.90	1.07	-0.03	1.91	0.99	-0.16	1553	888	2425
-	344	237	1335.7	4.4	844	-153	1097	-76	-91	2.02	1.17	-0.04	2.02	1.09	-0.12	1625	912	2482
-	349	238	1379.7	4.6	867	-155	1156	-80	-93	2.10	1.24	-0.01	2.10	1.14	-0.13	1675	913	2507
-	352	239	1409.1	4.7	887	-156	1218	-85	-98	2.19	1.31	-0.01	2.17	1.20	-0.12	1721	918	2515

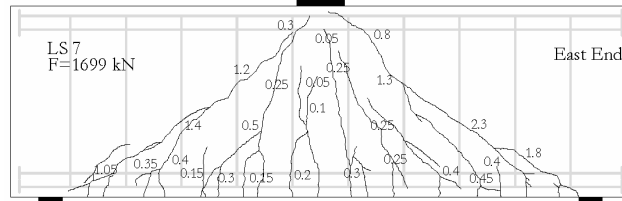
Load Stage	Data Set	Time elapsed	F	$\Delta=(BV+TV)/2$	BH	TH	ES-TE-BW	ES-V	ES-TW-BE	EL-TE-BW	EL-V	EL-TW-BE	WL-TW-BE	WL-V	WL-TE-BW	Gauge 7B	Gauge 17	Gauge 21
-	356	241	1434.4	4.9	906	-158	1282	-90	-100	2.29	1.36	0.01	2.25	1.25	-0.10	1760	917	2515
6	364	243	1506.5	5.2	951	-162	1422	-96	-105	2.45	1.55	0.04	2.41	1.38	-0.09	1845	922	2517
-	396	273	1533.2	5.4	978	-170	1528	-93	-108	2.57	1.66	0.07	2.54	1.48	-0.06	1909	934	2579
-	399	274	1563.9	5.6	998	-173	1600	-94	-112	2.66	1.76	0.10	2.61	1.53	-0.07	1952	933	2574
-	402	275	1591.9	5.8	1016	-174	1673	-94	-114	2.74	1.84	0.12	2.66	1.58	-0.06	1987	928	2589
-	405	276	1633.3	5.9	1043	-175	1753	-92	-119	2.86	1.92	0.13	2.76	1.66	-0.06	2040	938	2704
7	412	279	1698.6	6.4	1091	-174	1980	-70	-123	3.13	2.22	0.24	2.97	1.84	-0.03	2142	939	2913
-	457	308	1725.3	6.7	1110	-183	2140	-28	-125	3.30	2.44	0.33	3.11	1.97	-0.02	2187	973	3004
-	468	309	1752.0	6.8	1128	-178	2207	-16	-127	3.39	2.53	0.36	3.19	2.03	-0.01	2205	968	3030
-	478	311	1777.4	7.0	1142	-173	2282	-2	-129	3.49	2.63	0.40	3.26	2.07	0.01	2250	978	3055
-	490	312	1805.4	7.2	1161	-162	2389	21	-131	3.64	2.77	0.48	3.33	2.14	0.01	2297	985	3105
UL	504	314	1860.1	7.7	1192	-125	2729	51	-131	4.03	3.27	0.72	3.49	2.29	0.06	2390	993	3230
-	512	315	1398.4	10.0	981	-136	6879	578	-97	8.00	9.53	4.36	3.07	2.13	0.10	1972	1305	3886
-	530	317	1285.0	13.8	924	-1796	12455	2857	118	13.35	17.47	8.15	2.94	2.09	0.11	1844	1591	7205
-	535	318	803.6	17.3	617	-1996	18058	3296	196	19.80	27.75	12.71	2.27	1.77	0.18	-35185	631	6305

Notes: The data from LVD's WS-TE-BW, WS-V, and WS-TW-BE as well as the data from most of the strain gauges is not presented for the sake of brevity.

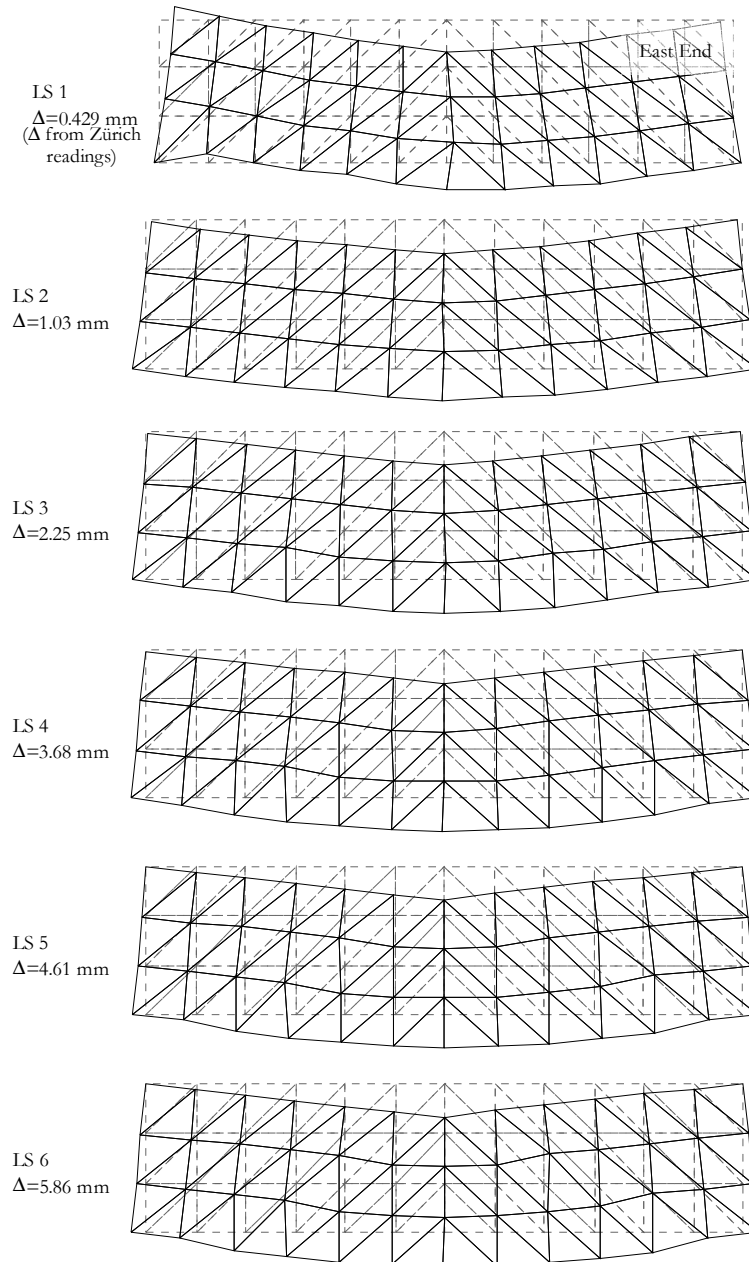


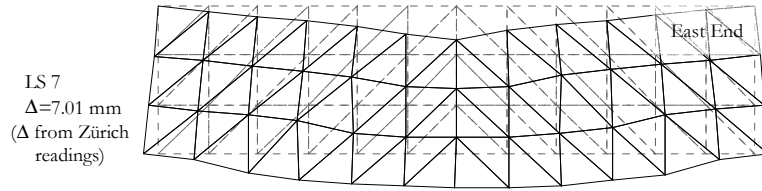


**Crack Diagrams, crack widths in (mm)**



## Deformed shapes amplified to midspan displacement equivalent to 200 mm





Zürich readings over 300/300 mm grid, deformations in (mm)

IS 1 F=566 kN East End  
 • -0.031 • -0.022 • -0.02 • -0.023 • -0.058 • -0.055 • -0.049 • -0.063 • -0.033 • 0.032 • -0.0098 • -0.017 •  
 • -0.037 • -0.0015 • -0.026 • 0.0021 • -0.042 • -0.0058 • -0.0011 • -0.052 • -0.0095 • -0.034 • -0.0096 • -0.0075 • -0.017 •  
 • -0.028 • -0.031 • -0.0099 • -0.022 • -0.05 • 0.01 • -0.0066 • -0.047 • -0.052 • -0.015 • -0.018 • -0.016 • -0.0075 •  
 • -0.046 • -0.05 • 0.014 • -0.0039 • -0.01 • -0.0059 • -0.0036 • -0.052 • -0.0088 • 0.054 • -0.0075 • -0.019 • -0.016 • -0.0075 •  
 • -0.024 • -0.041 • -0.028 • -0.011 • -0.017 • 0.12 • -0.028 • -0.012 • -0.01 • -0.0044 • -0.019 • -0.019 • -0.016 • -0.0075 •  
 • 0.28 • 0.17 • -0.038 • -0.0046 • -0.0027 • -0.052 • 0.0028 • -0.07 • 0.12 • 0.11 • -0.031 • -0.019 • -0.039 • -0.0068 • -0.012 • -0.022 • -0.015 •  
 • -0.051 • -0.023 • -0.01 • -0.015 • 0.036 • 0.046 • 0.17 • -0.032 • -0.032 • -0.01 • -0.013 • -0.011 • -0.0027 • -0.01 • -0.014 • -0.023 •  
 • 0.086 • -0.027 • 0 • -0.015 • 0.036 • 0.046 • 0.17 • -0.032 • -0.032 • -0.01 • -0.013 • -0.011 • -0.0027 • -0.01 • -0.014 • -0.023 •

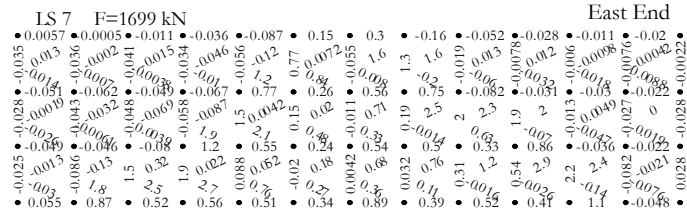
IS 2 F=705 kN  
 • -0.041 • -0.024 • -0.033 • -0.032 • -0.033 • -0.02 • -0.034 • -0.05 • -0.04 • -0.025 • -0.0093 • -0.016 •  
 • -0.025 • -0.0022 • -0.0031 • -0.0015 • -0.0055 • -0.014 • -0.032 • -0.019 • -0.025 • -0.0071 • -0.005 • 0.008 • -0.012 • -0.015 •  
 • -0.018 • -0.025 • -0.0082 • -0.009 • -0.016 • 0.14 • -0.026 • -0.026 • 0.0247 • 0.14 • -0.031 • -0.043 • -0.043 • -0.011 • -0.014 • -0.018 •  
 • -0.036 • -0.032 • -0.012 • -0.003 • -0.033 • -0.009 • 0.15 • -0.087 • -0.027 • -0.026 • -0.0088 • -0.011 • -0.011 • -0.015 • -0.015 •  
 • -0.017 • -0.002 • -0.009 • -0.005 • 0.28 • 0.13 • 0.13 • 0.2 • 0.1 • -0.095 • -0.008 • -0.02 • -0.026 • -0.039 • -0.006 • 0.006 •  
 • -0.028 • -0.017 • -0.008 • -0.0015 • -0.0088 • -0.0065 • -0.026 • 0.08 • 0.25 • -0.12 • 0.14 • 0.098 • -0.024 • -0.028 • -0.012 • -0.0085 •  
 • -0.041 • -0.0015 • -0.022 • 0.0092 • -0.12 • 0.12 • 0.12 • 0.35 • 0.13 • 0.13 • 0.068 • -0.031 • -0.016 • -0.037 • -0.014 •  
 • 0.089 • 0.0015 • -0.022 • 0.0092 • -0.12 • 0.12 • 0.12 • 0.35 • 0.13 • 0.13 • 0.068 • -0.031 • -0.016 • -0.037 • -0.014 •

IS 3 F=903 kN  
 • 0.023 • -0.018 • -0.02 • -0.024 • -0.043 • 0.007 • -0.025 • -0.06 • -0.048 • -0.036 • -0.01 • 0.0024 •  
 • -0.025 • 0.018 • -0.03 • 0.015 • -0.024 • -0.0088 • -0.0099 • -0.0022 • 0.22 • 0.22 • -0.02 • -0.0084 • -0.009 • -0.001 • 0.0024 •  
 • -0.003 • -0.005 • -0.0092 • -0.006 • -0.053 • 0.054 • 0.16 • 0.22 • 0.021 • -0.029 • -0.019 • -0.01 • -0.0074 • -0.003 •  
 • -0.044 • -0.0057 • -0.0034 • -0.001 • -0.001 • 0.15 • 0.0055 • -0.037 • 0.4 • 0.4 • 0.4 • 0.4 • 0.4 • 0.4 • 0.4 • 0.4 •  
 • -0.047 • -0.015 • -0.031 • 0.2 • 0.2 • 0.32 • 0.14 • 0.38 • 0.18 • 0.18 • 0.18 • 0.18 • 0.18 • 0.18 • 0.18 •  
 • -0.1 • -0.063 • -0.037 • -0.013 • -0.022 • -0.02 • 0.21 • -0.0005 • 0.03 • 0.48 • 0.48 • 0.48 • 0.48 • 0.48 • 0.48 • 0.48 •  
 • 0.016 • -0.021 • 0.4 • 0.39 • 0.42 • 0.42 • 0.42 • 0.42 • 0.42 • 0.42 • 0.42 • 0.42 • 0.42 • 0.42 • 0.42 •  
 • 0.037 • 0.01 • 0.25 • 0.27 • 0.25 • 0.25 • 0.18 • 0.46 • 0.46 • 0.46 • 0.46 • 0.46 • 0.46 • 0.46 • 0.46 •

IS 4 F=1100 kN  
 • -0.021 • -0.017 • 0.0037 • -0.012 • -0.02 • 0.063 • 0.094 • -0.0099 • 0.0066 • 0.0042 • 0.021 • 0.0072 •  
 • -0.019 • -0.041 • -0.012 • 0.012 • -0.025 • -0.05 • 0.047 • 0.18 • 0.18 • 0.25 • 0.44 • 0.01 • 0.0025 • 0.012 •  
 • -0.009 • -0.0057 • -0.0045 • -0.003 • 0.0033 • 0.01 • -0.39 • 0.33 • 0.39 • 0.39 • 0.39 • 0.39 • 0.39 • 0.39 •  
 • -0.026 • -0.014 • -0.004 • -0.0038 • -0.029 • -0.024 • 0.021 • 0.48 • 0.48 • 0.48 • 0.48 • 0.48 • 0.48 • 0.48 •  
 • -0.015 • -0.0048 • -0.0045 • 0.73 • 0.73 • 0.73 • 0.73 • 0.73 • 0.73 • 0.73 • 0.73 • 0.73 • 0.73 •  
 • -0.17 • -0.057 • -0.044 • -0.054 • 0.6 • 0.6 • 0.6 • 0.6 • 0.6 • 0.6 • 0.6 • 0.6 • 0.6 •  
 • -0.017 • 0.63 • 1 • 1.2 • 1.2 • 1.2 • 1.2 • 1.2 • 1.2 • 1.2 • 1.2 • 1.2 • 1.2 •  
 • 0.012 • 0.36 • 0.32 • 0.34 • 0.31 • 0.31 • 0.21 • 0.56 • 0.56 • 0.56 • 0.56 • 0.56 • 0.56 • 0.56 •

IS 5 F=1302 kN  
 • -0.029 • -0.021 • 0.033 • -0.041 • 0.064 • 0.085 • 0.14 • -0.077 • -0.046 • -0.033 • -0.014 • -0.029 •  
 • -0.041 • 0.02 • -0.047 • -0.014 • -0.053 • -0.0037 • -0.022 • -0.0066 • 0.77 • 0.77 • 0.77 • 0.77 • 0.77 • 0.77 •  
 • -0.044 • -0.041 • -0.031 • -0.043 • 0.47 • 0.19 • 0.47 • 0.47 • 0.44 • -0.086 • -0.039 • -0.035 • -0.029 • -0.029 •  
 • -0.057 • -0.0072 • -0.0072 • -0.037 • -0.042 • 0.76 • 0.76 • 0.76 • 0.76 • 0.76 • 0.76 • 0.76 • 0.76 •  
 • -0.008 • -0.0083 • -0.0083 • 1.1 • 1.1 • 1.1 • 1.1 • 1.1 • 1.1 • 1.1 • 1.1 • 1.1 • 1.1 •  
 • -0.03 • -0.064 • -0.083 • -0.083 • 0.11 • 0.11 • 0.11 • 0.11 • 0.11 • 0.11 • 0.11 • 0.11 • 0.11 •  
 • 0.04 • 0.38 • 0.37 • 0.39 • 0.36 • 0.36 • 0.36 • 0.36 • 0.36 • 0.36 • 0.36 • 0.36 • 0.36 •  
 • 0.061 • 0.3 • 0.37 • 0.39 • 0.34 • 0.25 • 0.25 • 0.65 • 0.65 • 0.65 • 0.65 • 0.65 • 0.65 •

IS 6 F=1507 kN  
 • 0.0092 • -0.0096 • 0.0023 • -0.0087 • -0.047 • 0.12 • 0.22 • -0.097 • -0.029 • -0.015 • -0.0069 • -0.019 •  
 • -0.018 • 0.007 • -0.027 • 0.0024 • -0.033 • -0.015 • -0.023 • -0.057 • -0.1 • -0.1 • -0.1 • -0.1 • -0.1 • -0.1 •  
 • -0.015 • -0.025 • -0.011 • -0.01 • -0.035 • 0.8 • 0.8 • 0.8 • 0.8 • 0.8 • 0.8 • 0.8 • 0.8 •  
 • -0.017 • -0.014 • -0.027 • -0.029 • -0.032 • -0.06 • -0.07 • -0.1 • -0.1 • -0.1 • -0.1 • -0.1 • -0.1 •  
 • -0.021 • -0.012 • -0.032 • -0.011 • 1.5 • 1.5 • 1.5 • 1.5 • 1.5 • 1.5 • 1.5 • 1.5 •  
 • -0.13 • -0.15 • -0.07 • -0.11 • 1.1 • 1.1 • 1.1 • 1.1 • 1.1 • 1.1 • 1.1 • 1.1 •  
 • 0.032 • 0.69 • 0.47 • 0.49 • 0.43 • 0.43 • 0.32 • 0.79 • 0.79 • 0.79 • 0.79 • 0.79 • 0.79 •  
 • 0.0092 • -0.0096 • 0.0023 • -0.0087 • -0.047 • 0.12 • 0.22 • -0.097 • -0.029 • -0.015 • -0.0069 • -0.019 •  
 • -0.018 • 0.007 • -0.027 • 0.0024 • -0.033 • -0.015 • -0.023 • -0.057 • -0.1 • -0.1 • -0.1 • -0.1 •  
 • -0.015 • -0.025 • -0.011 • -0.01 • -0.035 • 0.8 • 0.8 • 0.8 • 0.8 • 0.8 • 0.8 • 0.8 • 0.8 •  
 • -0.017 • -0.014 • -0.027 • -0.029 • -0.032 • -0.06 • -0.07 • -0.1 • -0.1 • -0.1 • -0.1 • -0.1 • -0.1 •  
 • -0.021 • -0.012 • -0.032 • -0.011 • 1.5 • 1.5 • 1.5 • 1.5 • 1.5 • 1.5 • 1.5 • 1.5 •  
 • -0.13 • -0.15 • -0.07 • -0.11 • 1.1 • 1.1 • 1.1 • 1.1 • 1.1 • 1.1 • 1.1 • 1.1 •  
 • 0.032 • 0.69 • 0.47 • 0.49 • 0.43 • 0.43 • 0.32 • 0.79 • 0.79 • 0.79 • 0.79 • 0.79 • 0.79 •



## B5. SPECIMEN S1C

Cast day: May 1<sup>th</sup>, 2007

### Beam properties

Cross section:  $b=1200$  mm,  $b=400$  mm

Effective depth: 1095 mm

Shear span: 1700 mm

Loading plates: 51/300/400 mm

Support plates: 51/150/400 mm

Longitudinal reinforcement:  $\rho=0.68\%$ ,  $f_y=650$  MPa

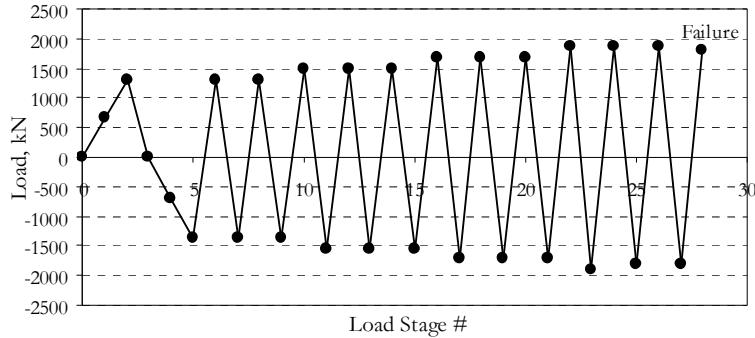
Transverse reinforcement:  $\rho_v=0.1\%$ ,  $f_{yv}=490$  MPa

Concrete:  $f'_c = 33.0$  MPa,  $\epsilon'_c=1630 \mu\epsilon$ ,  $a_g=20$  mm, *Modulus of rupture* = 3.9 MPa

Defects: no significant defects

Test days: September 10<sup>th</sup> – 13<sup>th</sup>, 2007

### Loading history



### Test Remarks

Maximum positive load: 1864.3 kN

Maximum negative load: 1912.5 kN

Displacement at failure: +8.4 mm

Failure mode: The beam failed in a relatively gradual manner with crushing above the most eastern diagonal crack near the edge of the top loading plate after three cycles with constant load amplitude. Sounds indicating rupture of stirrups were heard after the load on the beam has started to decrease.

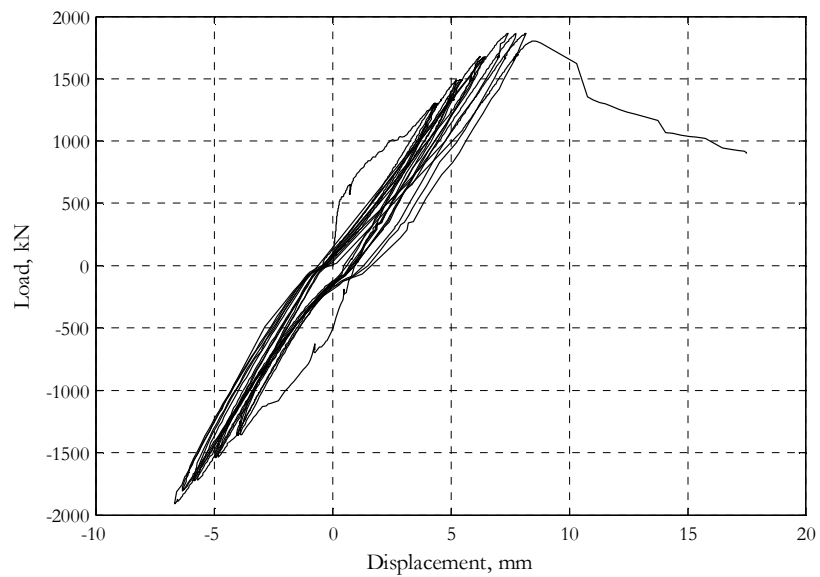
Other remarks:

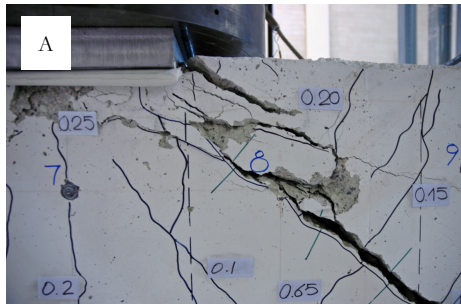
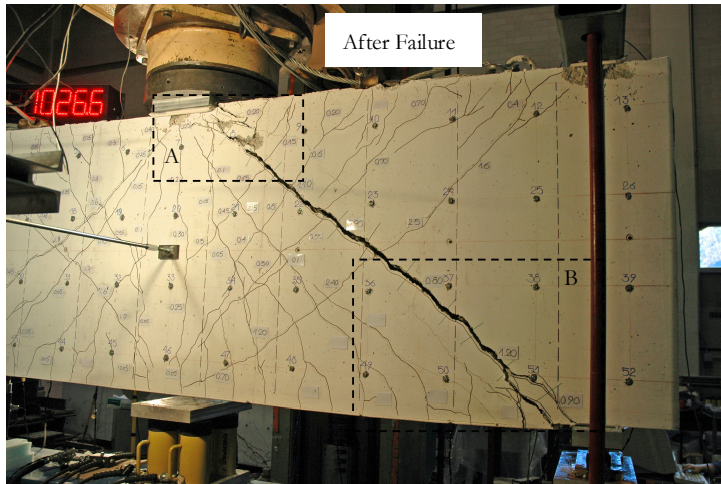
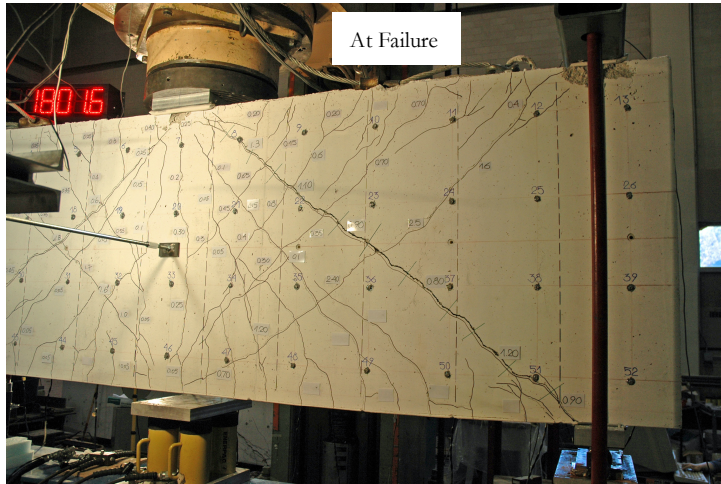
- The formation and propagation of flexure-shear cracks was relatively gradual.



- LVDT BV was moved unintentionally when the beam was unloaded between load stages 14 and 15.
- Noise in the readings from the load cell of the Baldwin machine was noticed just prior to and during Load Stage 15.
- The loading to Load Stage 16 was performed with bolted bottom support rollers.
- A hydraulic valve broke while loading to Load Stage 23 and the beam had to be unloaded very quickly.

Global response





## Data summary

Load Stage	Data Set	Time elapsed	F	$\Delta=(BV+TV)/2$	BH	TH	ES-TE-BW	ES-V	ES-TW-BE	EL-TE-BW	EL-V	EL-TW-BE	WL-TW-BE	WL-V	WL-TE-BW	Gauge 7B	Gauge 12	Gauge 21
(#)	(#)	(min)	(kN)	(mm)	(mm) $\times 10^{-3}$	(mm) $\times 10^{-3}$	(mm) $\times 10^{-3}$	(mm) $\times 10^{-3}$	(mm) $\times 10^{-3}$	(mm)	(mm)	(mm)	(mm)	(mm)	(mm)	( $\mu\epsilon$ )	( $\mu\epsilon$ )	( $\mu\epsilon$ )
-	4	5	16.9	0.0	-2	-2	0	-2	0	0.00	-0.01	0.01	0.00	0.00	0.01	0	-3	-2
1	107	27	651.8	0.7	339	-71	8	-9	-22	0.19	0.00	-0.04	0.12	0.00	-0.05	105	-38	-14
2	221	82	1305.6	4.3	927	11	942	506	-96	2.09	1.29	0.01	2.02	1.09	-0.08	1387	-10	6962
3	268	156	1.7	1.0	139	62	338	181	-17	0.57	0.47	0.09	0.46	0.36	0.06	296	-1	2984
4	313	226	-697.0	-0.7	-61	459	141	103	7	0.16	0.24	0.33	0.12	0.19	0.39	34	419	1561
5	356	272	-1354.4	-3.9	-65	922	111	85	4	-0.09	1.12	1.88	-0.17	1.05	2.09	11	936	1305
-	394	340	-437.7	-1.9	-14	409	120	101	-3	0.01	0.69	1.00	0.01	0.68	1.15	66	325	1656
-	446	1321	161.6	0.2	158	60	250	139	6	0.42	0.59	0.37	0.37	0.53	0.40	246	117	2786
-	486	1327	671.8	2.2	513	41	585	310	-28	1.35	1.08	0.19	1.34	0.93	0.14	789	82	3719
6	554	1338	1303.7	4.3	947	48	1058	577	-73	2.37	1.70	0.15	2.29	1.44	0.03	1419	91	5919
-	575	1340	541.8	2.3	459	62	698	387	-27	1.42	1.18	0.21	1.38	1.01	0.10	752	73	3519
-	593	1350	-85.5	0.3	89	126	336	192	20	0.54	0.67	0.27	0.49	0.56	0.31	178	83	2101
-	615	1357	-602.9	-1.7	-13	461	218	139	20	0.13	0.81	1.03	0.09	0.85	1.22	79	364	894
7	641	1365	-1361.1	-4.0	-59	950	148	107	24	-0.04	1.22	2.00	-0.11	1.21	2.27	12	794	634
-	669	1388	-498.5	-1.9	-20	428	160	107	21	0.07	0.78	1.09	0.04	0.80	1.28	59	269	971
-	692	1399	90.3	0.2	118	68	281	156	10	0.44	0.64	0.35	0.34	0.55	0.43	200	89	2203
-	741	1406	599.3	2.2	474	43	626	336	-21	1.36	1.14	0.21	1.35	1.00	0.15	752	63	3494
8	811	1416	1304.3	4.4	962	42	1089	601	-72	2.40	1.75	0.16	2.36	1.49	0.05	1436	70	5419
-	851	1441	539.3	2.4	459	49	726	402	-26	1.46	1.22	0.21	1.45	1.04	0.13	772	59	2994
-	893	1452	-75.3	0.3	81	115	347	200	15	0.53	0.69	0.29	0.47	0.59	0.33	164	84	1581
-	935	1458	-583.0	-1.8	-10	456	220	144	17	0.13	0.84	1.07	0.06	0.88	1.27	74	319	716

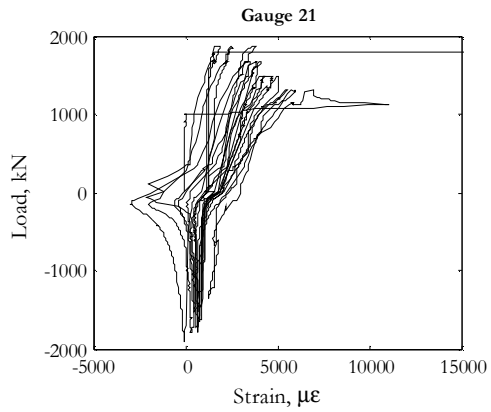
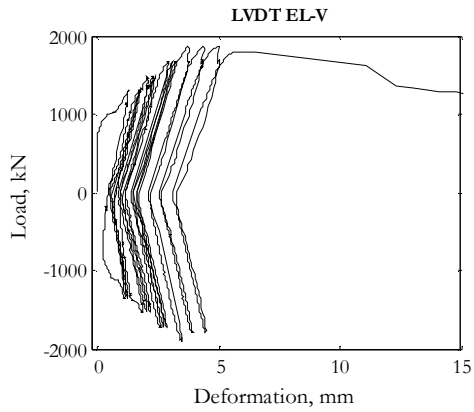
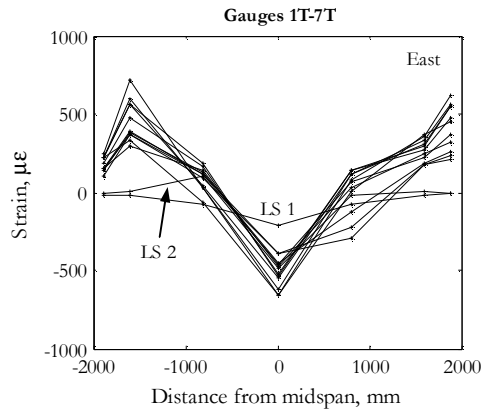
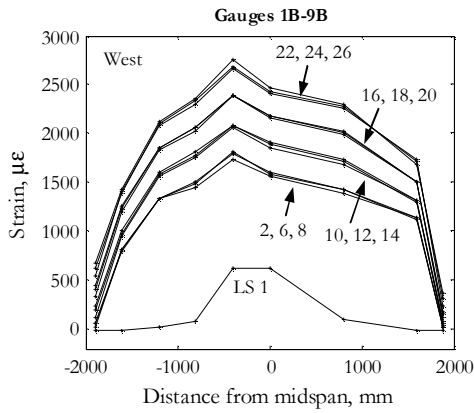
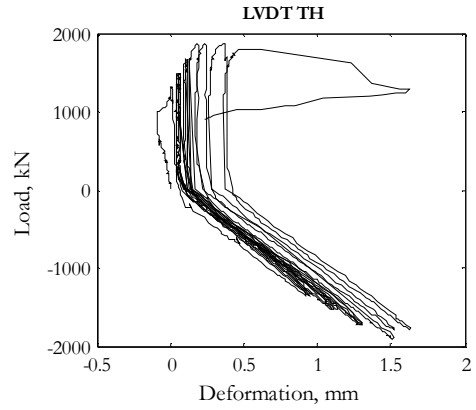
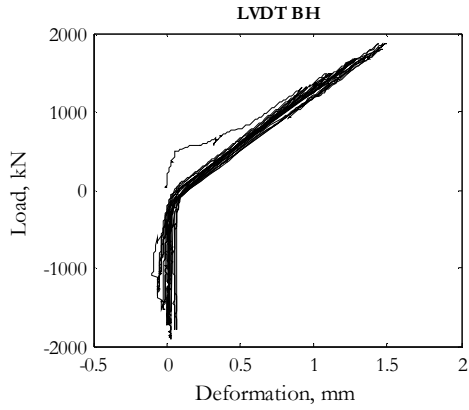
Load Stage	Data Set	Time elapsed	F	$\Delta=(BV+TV)/2$	BH	TH	ES-TE-BW	ES-V	ES-TW-BE	EL-TE-BW	EL-V	EL-TW-BE	WL-TW-BE	WL-V	WL-TE-BW	Gauge 7B	Gauge 12	Gauge 21
9	999	1466	-1349.0	-4.0	-60	954	166	113	20	-0.02	1.25	2.04	-0.09	1.24	2.33	11	761	651
-	1077	1503	-527.6	-2.0	-24	465	172	113	21	0.08	0.82	1.15	0.02	0.82	1.36	55	279	1056
-	1149	1515	241.8	0.9	227	40	422	220	2	0.81	0.84	0.25	0.75	0.70	0.27	369	57	2556
-	1227	1523	811.2	3.0	624	43	791	432	-38	1.72	1.35	0.19	1.69	1.15	0.10	981	60	3487
10	1341	1539	1489.9	5.2	1092	48	1366	786	-88	2.85	2.08	0.21	2.75	1.72	0.05	1674	73	5094
-	1482	1595	713.7	3.2	587	48	1019	600	-34	1.93	1.60	0.30	1.85	1.32	0.19	992	60	2902
-	1501	1596	101.6	1.2	185	79	623	365	6	1.00	1.03	0.31	0.88	0.80	0.27	327	63	1509
-	1549	1606	-403.1	-1.1	-3	343	376	248	20	0.33	0.93	0.94	0.22	0.86	1.06	106	175	366
11	1661	1625	-1537.5	-4.8	-31	1097	256	188	21	0.03	1.82	2.70	-0.08	1.40	2.72	65	823	501
-	1723	1657	-679.7	-2.7	-8	577	263	193	20	0.19	1.36	1.74	0.02	0.99	1.75	89	304	838
-	1748	1664	13.1	-0.4	79	119	323	217	23	0.40	0.85	0.73	0.24	0.56	0.68	144	118	1891
12	1878	1678	1491.8	5.4	1110	57	1485	886	-87	3.12	2.30	0.32	2.87	1.77	0.09	1712	73	4694
-	1900	1686	741.8	3.1	585	62	1082	646	-30	2.04	1.73	0.35	1.88	1.30	0.21	913	56	2531
-	1923	1689	5.1	0.7	138	101	595	369	17	0.97	1.07	0.41	0.73	0.69	0.36	230	84	1039
-	1957	1695	-511.7	-1.7	6	415	406	290	19	0.33	1.27	1.39	0.16	0.90	1.34	123	222	504
13	2023	1702	-1539.9	-4.9	-17	1114	337	257	23	0.14	2.02	2.90	-0.08	1.38	2.80	83	824	654
-	2058	1715	-723.1	-2.9	-4	601	340	256	20	0.25	1.50	1.91	0.05	0.99	1.85	103	334	926
-	2076	1717	-70.3	-0.8	50	174	366	263	21	0.37	1.00	1.00	0.20	0.60	0.87	129	129	1384
-	2171	1736	832.4	3.3	665	63	1029	611	-37	2.16	1.78	0.34	1.98	1.29	0.18	1072	67	3119
14	2263	1748	1492.4	5.5	1125	64	1548	933	-87	3.22	2.40	0.34	2.93	1.79	0.12	1744	84	4294
-	2290	1757	795.6	3.4	639	63	1180	712	-39	2.25	1.88	0.41	2.04	1.36	0.22	1009	65	2476
-	2300	1758	90.5	1.2	190	79	712	430	9	1.22	1.23	0.41	0.94	0.75	0.32	334	69	1316
-	4089	2807	-412.9	-1.3	28	367	478	342	46	0.50	1.35	1.38	0.27	0.84	1.24	147	197	481
15	4161	2816	-1536.9	-5.0	5	1138	405	307	45	0.26	2.16	3.03	0.00	1.35	2.90	105	854	641
-	4204	2871	-707.4	-2.9	20	624	408	306	47	0.39	1.64	2.03	0.13	1.01	1.91	123	354	1041

Load Stage	Data Set	Time elapsed	F	$\Delta=(BV+TV)/2$	BH	TH	ES-TE-BW	ES-V	ES-TW-BE	EL-TE-BW	EL-V	EL-TW-BE	WL-TW-BE	WL-V	WL-TE-BW	Gauge 7B	Gauge 12	Gauge 21
-	4225	2873	-80.0	-0.9	63	203	430	312	45	0.51	1.19	1.14	0.29	0.61	0.95	146	153	1405
-	4291	2883	673.7	2.8	570	93	989	582	-11	2.07	1.85	0.42	1.81	1.20	0.26	919	80	2981
16	4404	2899	1678.1	6.2	1276	110	1859	1145	-87	3.78	2.92	0.47	3.39	2.08	0.19	1979	107	4119
-	4444	2932	921.8	4.0	742	101	1476	915	-34	2.72	2.38	0.56	2.42	1.63	0.31	1198	82	2387
-	4460	2935	1.7	0.9	145	138	817	539	33	1.31	1.50	0.58	0.93	0.84	0.48	266	108	268
-	4484	2940	-503.7	-1.7	20	444	572	434	35	0.55	1.72	1.69	0.30	1.01	1.49	153	228	287
-	4517	2944	-1089.4	-3.7	13	863	514	408	35	0.39	2.06	2.54	0.12	1.24	2.37	127	559	521
17	4564	2951	-1721.4	-5.7	2	1279	482	392	35	0.28	2.59	3.50	-0.01	1.61	3.33	112	939	651
-	4588	2964	-895.7	-3.7	8	760	485	392	34	0.40	2.05	2.51	0.09	1.29	2.37	129	441	864
-	4601	2965	-257.7	-1.6	38	315	498	393	36	0.51	1.53	1.63	0.25	0.93	1.40	146	188	1034
18	4711	3002	1675.6	6.4	1286	117	1979	1253	-89	3.96	3.10	0.54	3.52	2.23	0.26	2007	110	3944
-	4728	3009	921.8	4.2	754	123	1575	1005	-37	2.94	2.55	0.63	2.56	1.77	0.37	1247	84	2334
-	4738	3010	298.9	2.1	325	114	1137	724	7	2.00	1.97	0.61	1.55	1.21	0.45	588	71	1182
-	4755	3016	-205.5	-0.4	44	235	703	527	33	0.86	1.66	1.22	0.56	1.00	1.05	174	148	-275
-	4778	3018	-714.1	-2.6	24	601	598	479	32	0.55	1.99	2.16	0.23	1.26	1.97	141	351	261
19	4833	3025	-1724.0	-5.8	9	1299	537	451	33	0.34	2.72	3.67	0.00	1.75	3.46	113	956	604
-	4846	3034	-845.7	-3.6	12	749	545	450	33	0.48	2.18	2.61	0.12	1.40	2.46	130	429	781
-	4854	3034	-126.9	-1.2	50	254	569	453	34	0.61	1.57	1.60	0.32	0.99	1.37	151	181	1075
20	4965	3051	1678.1	6.4	1290	134	2051	1339	-92	4.08	3.19	0.58	3.59	2.30	0.29	2017	114	3544
-	4979	3059	843.1	3.7	670	131	1563	1018	-28	2.80	2.51	0.67	2.40	1.76	0.42	1019	80	1749
-	5001	3062	-0.6	0.8	135	156	908	628	33	1.46	1.69	0.79	1.02	1.00	0.65	253	144	-142
-	5033	3069	-503.6	-1.8	26	451	661	540	37	0.68	1.94	1.94	0.33	1.24	1.72	149	288	204
-	5065	3072	-1072.1	-3.8	26	867	612	514	35	0.52	2.33	2.78	0.16	1.51	2.62	129	572	522
21	5105	3078	-1722.1	-5.9	8	1308	586	503	37	0.39	2.83	3.76	0.02	1.83	3.52	113	974	699

Load Stage	Data Set	Time elapsed	F	$\Delta=(BV+TV)/2$	BH	TH	ES-TE-BW	ES-V	ES-TW-BE	EL-TE-BW	EL-V	EL-TW-BE	WL-TW-BE	WL-V	WL-TE-BW	Gauge 7B	Gauge 12	Gauge 21
-	5128	3110	-884.4	-3.8	8	765	586	498	36	0.52	2.30	2.74	0.13	1.50	2.53	129	471	909
-	5139	3111	-229.4	-1.6	39	300	600	502	32	0.63	1.73	1.80	0.31	1.10	1.53	145	206	1092
-	5208	3126	1217.4	4.9	972	127	1672	1101	-60	3.40	2.78	0.60	2.96	1.99	0.36	1553	102	2596
22	5287	3136	1864.3	7.4	1442	189	2524	1685	-102	4.73	3.80	0.82	4.05	2.67	0.38	2252	127	3869
-	5310	3171	1171.8	5.3	930	189	2183	1522	-53	3.77	3.34	0.94	3.14	2.26	0.50	1447	93	1868
-	5314	3171	421.2	3.0	419	187	1682	1202	0	2.75	2.66	0.96	2.03	1.63	0.56	732	74	746
-	5338	3175	-81.5	0.8	109	245	1206	927	35	1.66	2.14	1.20	1.12	1.22	0.77	239	151	-2627
-	5366	3178	-596.4	-2.1	34	583	936	824	39	0.85	2.46	2.46	0.38	1.49	2.04	157	339	-1051
-	5396	3181	-1181.4	-4.1	32	1007	866	785	38	0.66	2.87	3.37	0.18	1.75	2.92	133	616	-389
23	5450	3190	-1912.5	-6.7	26	1517	809	756	36	0.51	3.51	4.55	0.03	2.19	4.04	118.69	1079	-34
-	5460	3197	-486.0	-2.9	36	617	830	759	36	0.75	2.54	2.80	0.28	1.59	2.34	146.25	319	203
-	5509	3204	689.9	3.3	620	167	1547	1037	-18	2.97	2.81	0.90	2.33	1.85	0.56	986.88	66	1602
-	5535	3207	1244.9	5.4	1030	174	2021	1387	-58	3.90	3.36	0.89	3.23	2.28	0.48	1616.3	98	1654
24	5593	3213	1863.7	7.7	1471	236	2843	1978	-101	5.17	4.34	1.09	4.23	2.87	0.48	2271.9	121	2542
-	5617	3232	1094.3	5.6	929	243	2499	1819	-46	4.24	3.88	1.25	3.29	2.42	0.61	1504.4	87	1016
-	5623	3232	456.8	3.4	469	242	2030	1520	5	3.24	3.22	1.25	2.22	1.84	0.65	796.88	73	292
-	5665	4208	-84.1	0.9	112	308	1477	1216	52	1.97	2.62	1.62	1.21	1.35	0.91	266.13	220	-1351
-	5692	4211	-591.1	-2.1	58	646	1213	1133	53	1.11	2.99	2.96	0.46	1.68	2.19	174.63	411	-129
-	5716	4214	-1157.7	-4.1	60	1058	1144	1100	51	0.90	3.39	3.84	0.26	1.92	3.06	150.38	666	217
25	5748	4218	-1798.5	-6.3	53	1521	1088	1074	52	0.75	3.89	4.83	0.11	2.25	3.99	133.19	1061	304
-	5776	4238	-975.2	-4.2	48	985	1087	1068	52	0.89	3.38	3.84	0.24	1.95	3.03	146.31	642	489
-	5789	4239	-369.8	-2.2	63	530	1103	1073	52	0.98	2.85	3.01	0.40	1.58	2.08	159.88	366	649
-	5870	4252	1008.7	4.8	865	261	2135	1536	-30	3.88	3.58	1.18	2.99	2.22	0.58	1341.9	82	1308
26	5969	4265	1863.1	8.2	1488	370	3354	2472	-92	5.77	5.06	1.55	4.36	2.98	0.53	2299.4	129	1578
-	5997	4302	1103.7	6.0	945	383	2994	2337	-42	4.82	4.60	1.67	3.37	2.53	0.67	1492.5	86	584

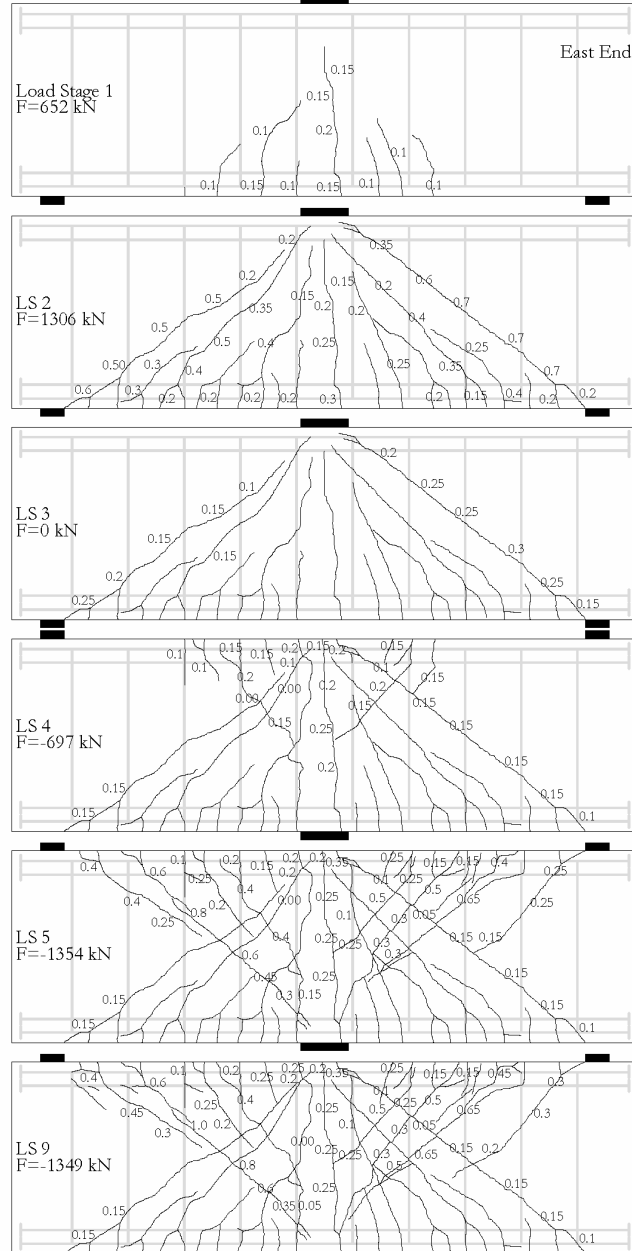
Load Stage	Data Set	Time elapsed	F	$\Delta=(BV+TV)/2$	BH	TH	ES-TE-BW	ES-V	ES-TW-BE	EL-TE-BW	EL-V	EL-TW-BE	WL-TW-BE	WL-V	WL-TE-BW	Gauge 7B	Gauge 12	Gauge 21
-	6003	4303	423.7	3.6	452	381	2486	2000	10	3.74	3.86	1.65	2.25	1.91	0.71	750	64	233
-	6022	4307	-93.7	0.9	108	441	1860	1649	46	2.26	3.26	2.17	1.14	1.45	1.10	241.69	238	-1932
-	6039	4309	-612.6	-2.1	63	761	1532	1521	52	1.30	3.55	3.52	0.45	1.76	2.33	166.63	484	539
-	6057	4310	-1178.5	-4.2	66	1181	1446	1473	52	1.07	3.97	4.39	0.25	2.03	3.18	143.88	755	662
27	6089	4314	-1806.7	-6.4	65	1636	1386	1445	53	0.90	4.46	5.36	0.14	2.33	4.09	130.31	1124	634
-	6113	4346	-998.5	-4.3	57	1100	1379	1430	56	1.01	3.95	4.39	0.27	2.02	3.13	143	761	796
-	6125	4347	-351.5	-2.1	69	626	1401	1437	54	1.15	3.40	3.53	0.43	1.65	2.15	157	455	903
-	6200	4364	1074.3	5.4	928	358	2625	2000	-37	4.49	4.29	1.54	3.18	2.38	0.62	1429.4	83	1192
UL	6290	4378	1803.1	8.4	1463	495	3834	3075	-88	6.27	5.79	1.98	4.33	3.02	0.58	2273.8	147	1649
-	6319	4382	900.6	17.5	815	231	18024	19410	2	20.66	28.33	20.07	3.13	2.42	0.68	1319.4	527	37994

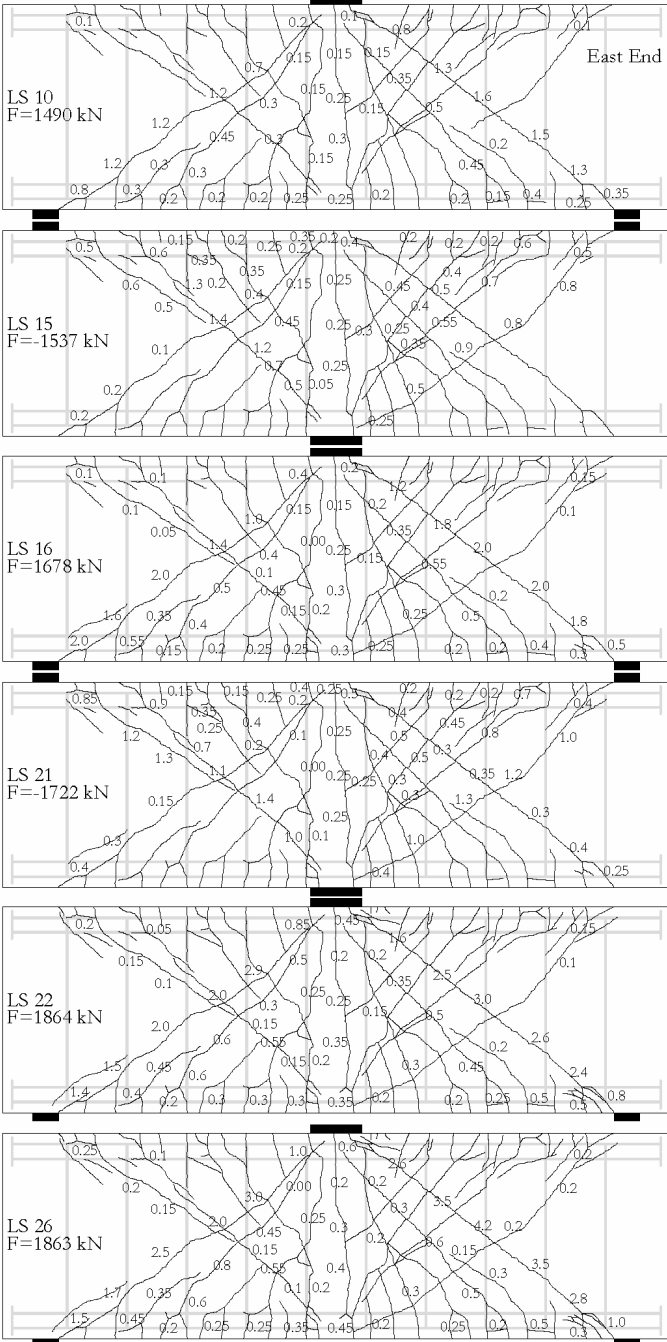
Notes: The data from LVDTs WS-TE-BW, WS-V, and WS-TW-BE as well as the data from most of the strain gauges is not presented for the sake of brevity.

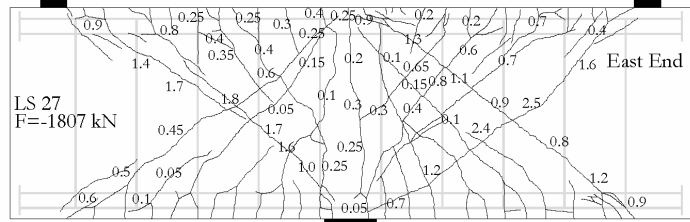




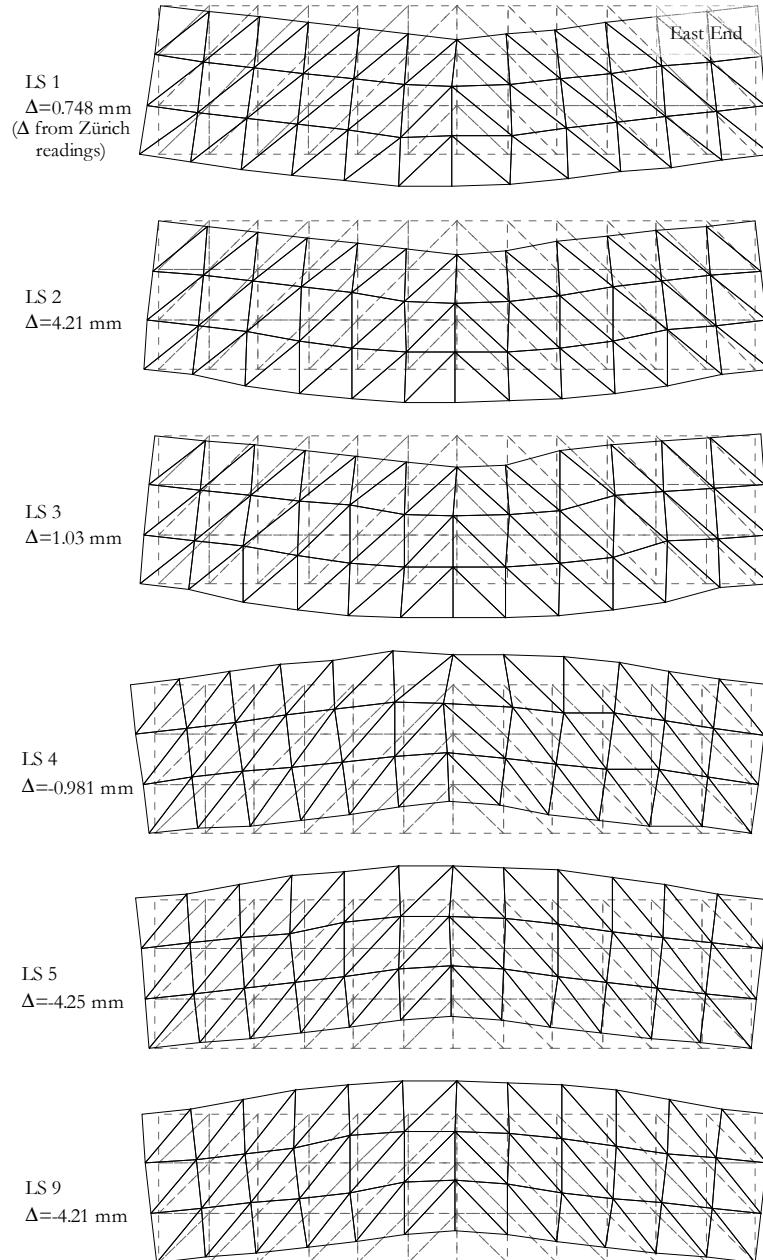
Crack Diagrams, crack widths in (mm)



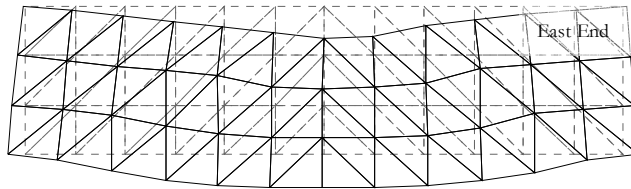




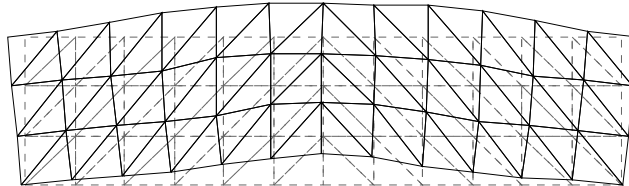
## Deformed shapes amplified to midspan displacement equivalent to 200 mm



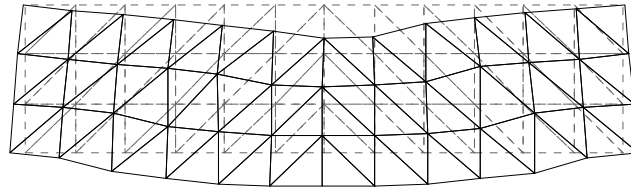
IS 10  
 $\Delta=5.16$  mm  
( $\Delta$  from Zürich  
readings)



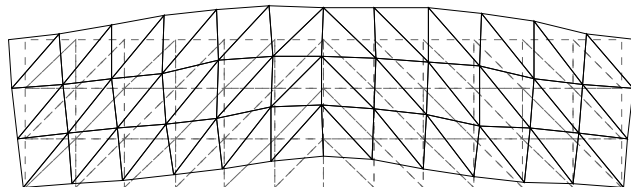
IS 15  
 $\Delta=-5.41$  mm



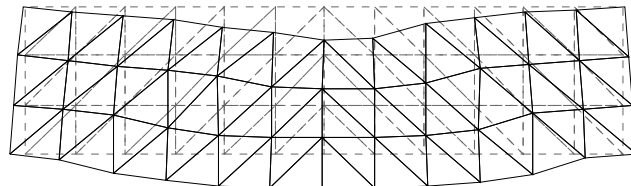
IS 16  
 $\Delta=6.51$  mm



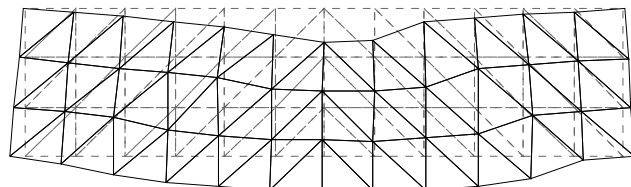
IS 21  
 $\Delta=-6.33$  mm

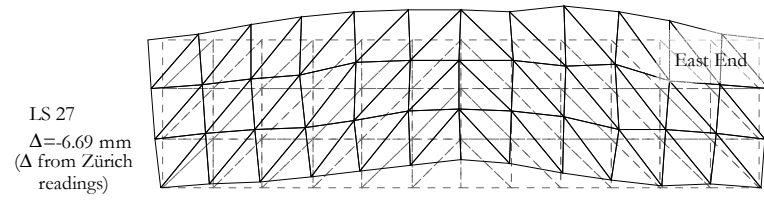


IS 22  
 $\Delta=7.65$  mm



IS 26  
 $\Delta=8.37$  mm





Zürich readings over 300/300 mm grid, deformations in (mm)

LS 1 F=652 kN East End

• -0.006	• 0.0009	• 0.004	• -0.0058	• -0.02	• -0.024	• 0.018	• -0.025	• 0.022	• 0.01	• 0.029	• 0.0073
• 0.013	• 0.0017	• 0.0044	• 0.0095	• 0.016	• 0.0011	• 0.0083	• 0.0094	• 0.13	• 0.014	• 0.003	• 0.0099
• 0.0062	• 0.0097	• 0.0027	• 0.015	• 0.014	• 0.014	• 0.029	• 0.21	• 0.026	• 0.023	• 0.0038	• 0.0075
• 0.0094	• 0.0084	• 0.0064	• 0.0021	• 0.099	• 0.099	• 0.099	• 0.099	• 0.25	• 0.021	• 0.012	• 0.0053
• 0.00074	• 0.0013	• 0.00091	• 0.003	• 0.0079	• 0.0077	• 0.0077	• 0.0077	• 0.12	• 0.017	• 0.015	• 0.019
• 0.02	• 0.014	• 0.0091	• 0.0012	• 0.022	• 0.022	• 0.022	• 0.022	• 0.18	• 0.018	• 0.002	• 0.0088
• 0.014	• 0.014	• 0.0091	• 0.0012	• 0.022	• 0.022	• 0.022	• 0.022	• 0.18	• 0.018	• 0.002	• 0.0088

LS 2 F=1306 kN

• 0.0091	• 0.007	• 0.008	• 0.0093	• -0.0005	• -0.027	• 0.077	• 0.084	• 0.15	• -0.02	• -0.01	• 0.0021
• 0.018	• 0.014	• 0.0086	• 0.016	• -0.0005	• -0.027	• 0.077	• 0.084	• 0.15	• -0.02	• -0.01	• 0.0021
• 0.0038	• 0.0097	• -0.015	• -0.016	• 0.019	• 0.64	• 0.3	• 0.092	• 0.42	• 0.023	• 0.011	• 0.013
• 0.018	• 0.014	• 0.0086	• 0.016	• -0.0005	• -0.027	• 0.077	• 0.084	• 0.15	• -0.02	• -0.01	• 0.0021
• 0.0038	• 0.0097	• -0.015	• -0.016	• 0.019	• 0.64	• 0.3	• 0.092	• 0.42	• 0.023	• 0.011	• 0.013
• 0.018	• 0.014	• 0.0086	• 0.016	• -0.0005	• -0.027	• 0.077	• 0.084	• 0.15	• -0.02	• -0.01	• 0.0021

LS 3 F=0 kN

• 0.0025	• 0.0037	• 0.0099	• 0.015	• 0.0069	• 0.058	• -0.04	• 0.14	• 0.028	• 0.02	• 0.018	• 0.0075
• 0.012	• 0.0008	• 0.0018	• 0.0011	• 0.0086	• 0.0085	• 0.0024	• 0.0025	• 0.0094	• 0.055	• 0.01	• 0.01
• 0.0014	• 0.01	• 0.0033	• -0.0034	• 0.15	• 0.02	• 0.19	• 0.02	• 0.19	• 0.02	• 0.19	• 0.02
• 0.012	• 0.0008	• 0.0018	• 0.0011	• 0.0086	• 0.0085	• 0.0024	• 0.0025	• 0.0094	• 0.055	• 0.01	• 0.01
• 0.0014	• 0.01	• 0.0033	• -0.0034	• 0.15	• 0.02	• 0.19	• 0.02	• 0.19	• 0.02	• 0.19	• 0.02
• 0.012	• 0.0008	• 0.0018	• 0.0011	• 0.0086	• 0.0085	• 0.0024	• 0.0025	• 0.0094	• 0.055	• 0.01	• 0.01

LS 4 F=-697 kN

• 0.0035	• 0.0084	• 0.015	• 0.1	• 0.29	• 0.32	• 0.0076	• 0.34	• 0.16	• 0.017	• 0.0013	• 0.0095
• 0.024	• 0.014	• 0.0055	• 0.023	• 0.003	• 0.018	• 0.064	• 0.21	• 0.18	• 0.00007	• 0.0002	• 0.0055
• 0.0068	• 0.01	• 0.0013	• 0.019	• 0.29	• 0.0012	• 0.56	• 0.026	• 0.062	• 0.0054	• 0.0009	• 0.0021
• 0.0068	• 0.01	• 0.0013	• 0.019	• 0.29	• 0.0012	• 0.56	• 0.026	• 0.062	• 0.0054	• 0.0009	• 0.0021
• 0.0068	• 0.01	• 0.0013	• 0.019	• 0.29	• 0.0012	• 0.56	• 0.026	• 0.062	• 0.0054	• 0.0009	• 0.0021
• 0.0068	• 0.01	• 0.0013	• 0.019	• 0.29	• 0.0012	• 0.56	• 0.026	• 0.062	• 0.0054	• 0.0009	• 0.0021

LS 5 F=-1354 kN

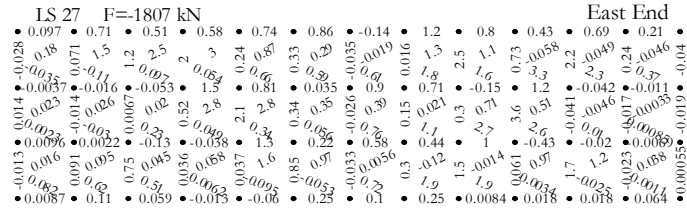
• 0.043	• 0.33	• 0.43	• 0.4	• 0.61	• 0.62	• 0.17	• 0.67	• 0.53	• 0.46	• 0.34	• 0.032
• 0.025	• 0.061	• 0.05	• 0.65	• 0.51	• 1.5	• 1.5	• 0.16	• 0.37	• 0.72	• 0.72	• 0.0082
• 0.0039	• -0.004	• -0.028	• 0.75	• 0.72	• 0.21	• 0.21	• 0.83	• 0.25	• 0.83	• 0.37	• 0.02
• 0.0039	• -0.004	• -0.028	• 0.75	• 0.72	• 0.21	• 0.21	• 0.83	• 0.25	• 0.83	• 0.37	• 0.02
• 0.0039	• -0.004	• -0.028	• 0.75	• 0.72	• 0.21	• 0.21	• 0.83	• 0.25	• 0.83	• 0.37	• 0.02
• 0.0039	• -0.004	• -0.028	• 0.75	• 0.72	• 0.21	• 0.21	• 0.83	• 0.25	• 0.83	• 0.37	• 0.02

LS 9 F=-1349 kN

• 0.026	• 0.32	• 0.4	• 0.37	• 0.56	• 0.59	• 0.075	• 0.68	• 0.54	• 0.42	• 0.34	• -0.025
• -0.056	• 0.83	• 0.0015	• 0.71	• 0.52	• 1.4	• 1.7	• 0.11	• 0.88	• 0.11	• 0.88	• -0.038
• -0.04	• -0.038	• -0.045	• 0.067	• 0.85	• 0.25	• 0.25	• 0.13	• 0.72	• 0.72	• 0.12	• -0.044
• -0.04	• -0.038	• -0.045	• 0.067	• 0.85	• 0.25	• 0.25	• 0.13	• 0.72	• 0.72	• 0.12	• -0.044
• -0.04	• -0.038	• -0.045	• 0.067	• 0.85	• 0.25	• 0.25	• 0.13	• 0.72	• 0.72	• 0.12	• -0.044
• -0.04	• -0.038	• -0.045	• 0.067	• 0.85	• 0.25	• 0.25	• 0.13	• 0.72	• 0.72	• 0.12	• -0.044







**B6. SPECIMEN L0M**

**Cast day:** May 30<sup>th</sup>, 2007

**Beam properties**

Cross section:  $b=1200$  mm,  $b=400$  mm

Effective depth: 1095 mm

Shear span: 2500 mm

Loading plates: 51/300/400 mm

Support plates: 51/150/400 mm

Longitudinal reinforcement:  $\rho_l=0.68\%$ ,  $f_y=650$  MPa

Transverse reinforcement:  $\rho_t=0\%$

Concrete:  $f'_c = 29.1$  MPa,  $\epsilon'_c=1470 \mu\epsilon$ ,  $a_g=20$  mm, *Modulus of rupture* = 3.7 MPa

Defects: no significant defects

**Test day:** October 16<sup>th</sup>, 2007

**Test Remarks**

Maximum load: 801.1 kN

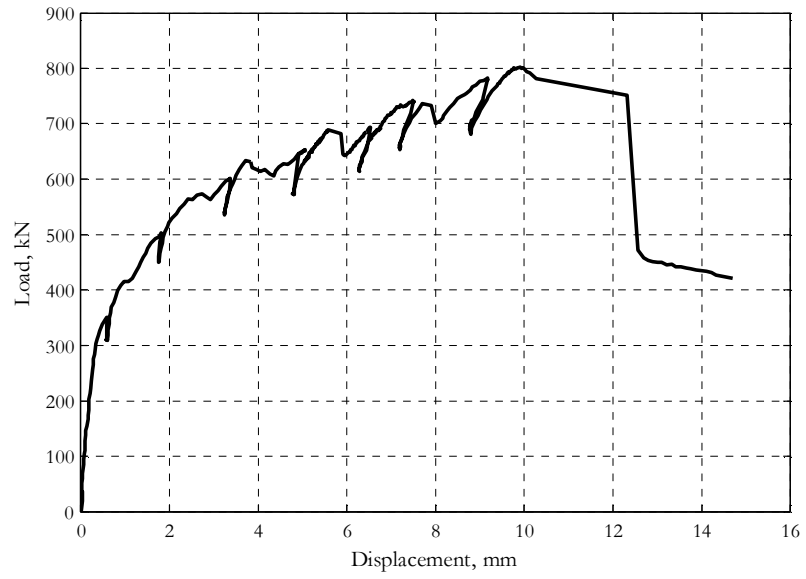
Displacement at maximum load: 10.0 mm

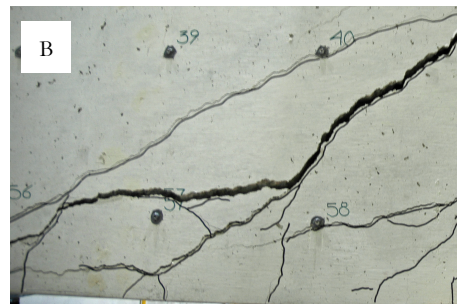
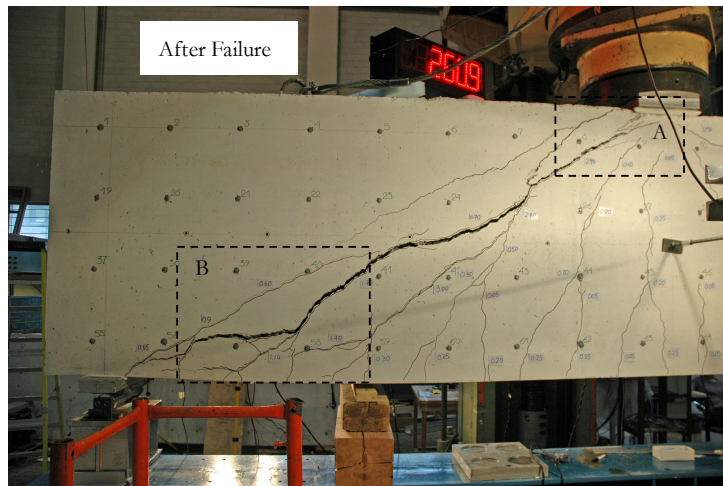
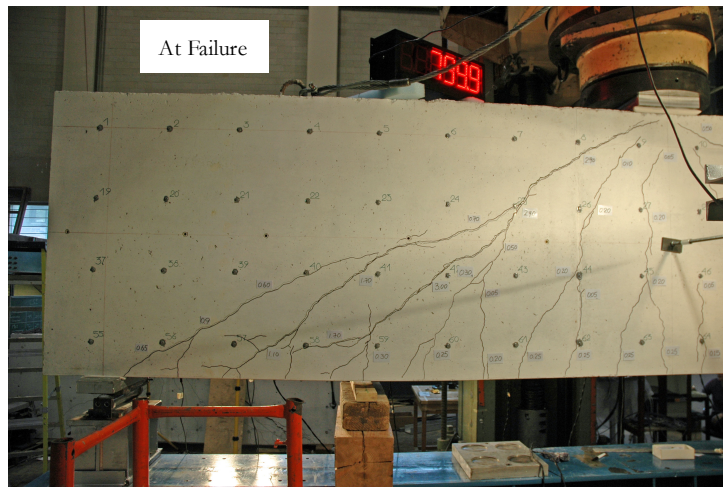
Failure mode: The beam failed with crushing above the most western diagonal crack near the edge of the top loading plate.

Other remarks:

- The formation and propagation of flexure-shear cracks was relatively quick.
- Short diagonal cracks indicating concrete crushing were observed at Load Stage 7 near the west edge of the loading plate.

Global response



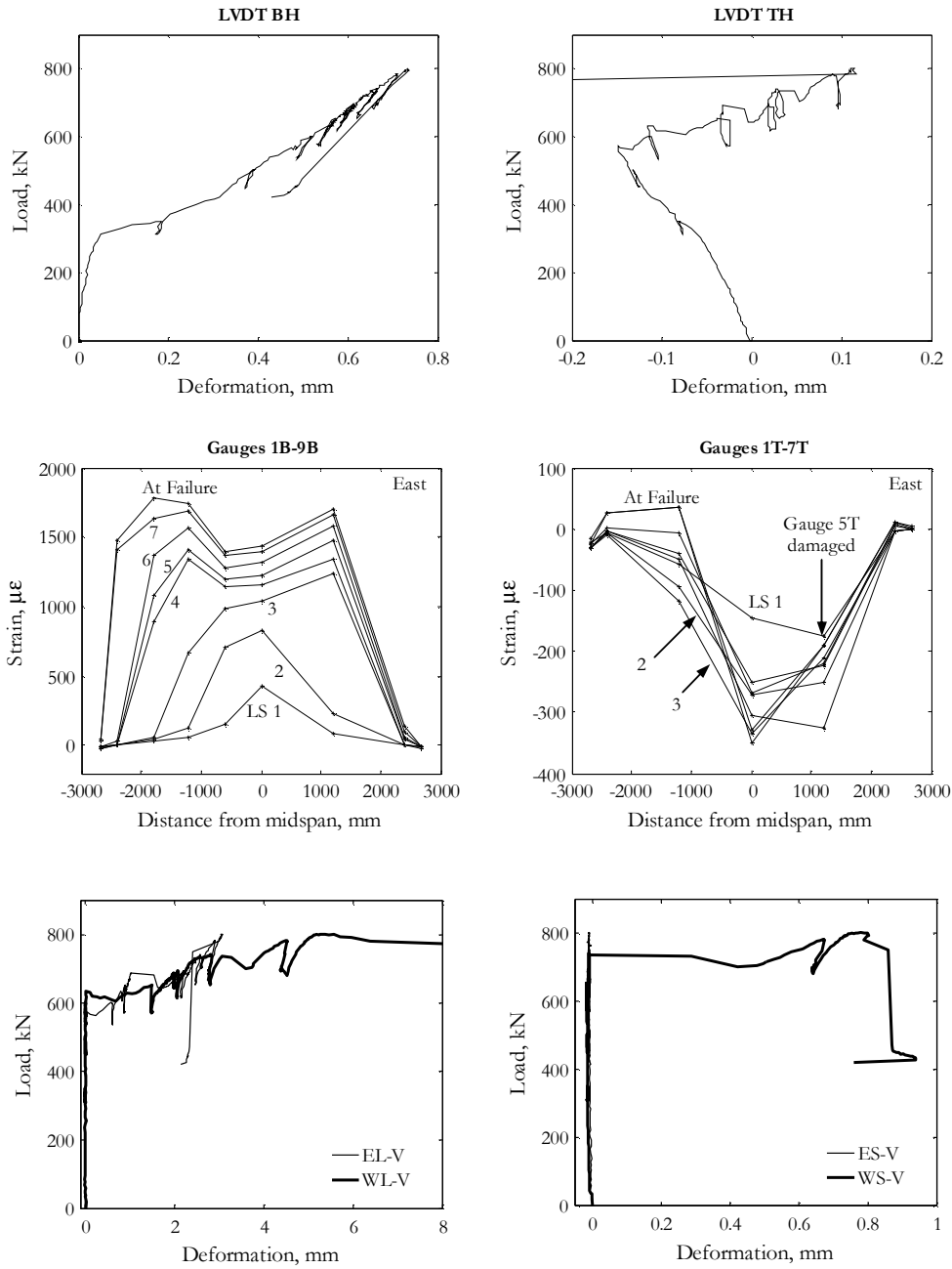


## Data summary

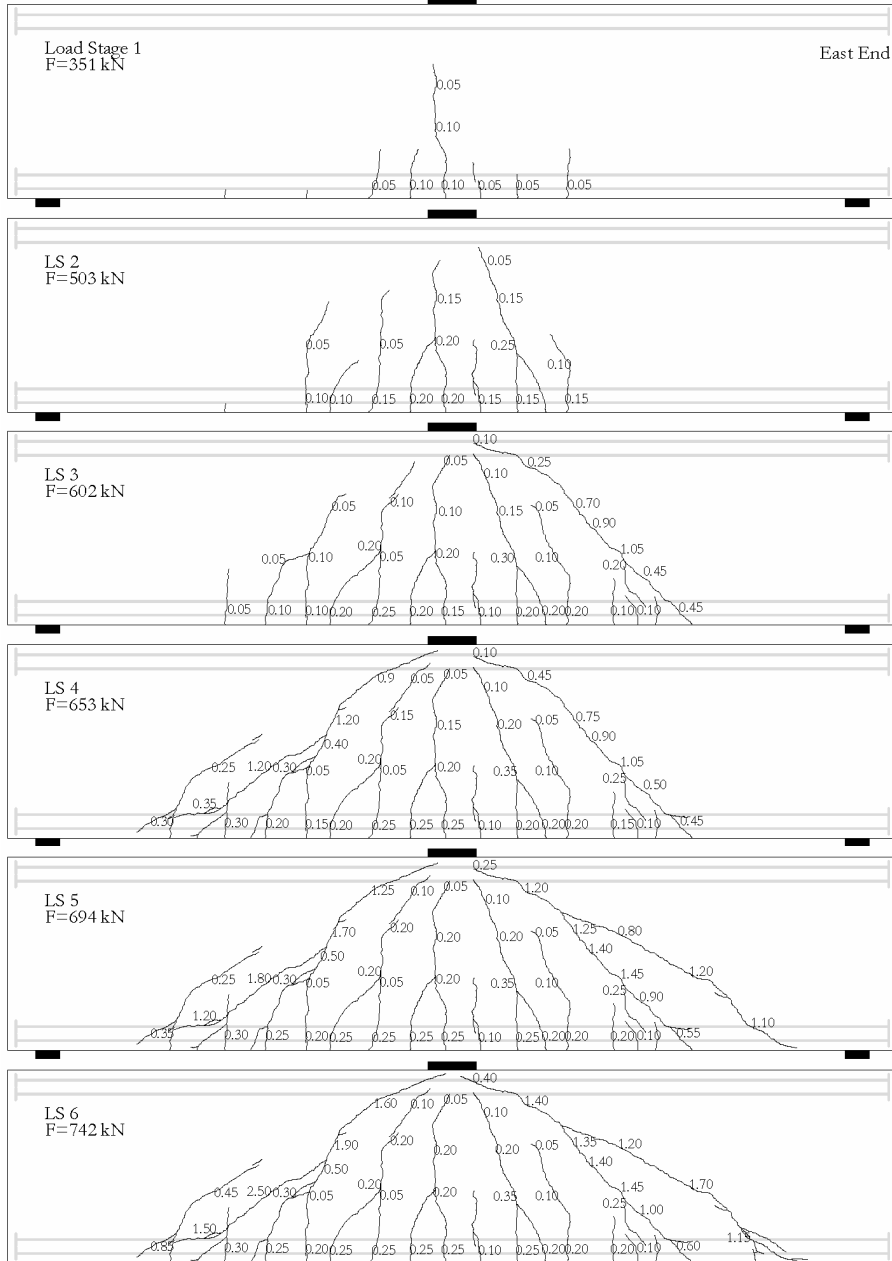
Load Stage	Data Set	Time elapsed	F	$\Delta=(BV+TV)/2$	BH	TH	ES-TE-BW	ES-V	ES-TW-BE	WS-TW-BE	WS-V	WS-TE-BW	EL-TE-BW	EL-V	EL-TW-BE	WL-TW-BE	WL-V	WL-TE-BW	Gauge 4B
(#)	(#)	(min)	(kN)	(mm)	(mm) $\times 10^{-3}$	(mm) $\times 10^{-3}$	(mm) $\times 10^{-3}$	(mm) $\times 10^{-3}$	(mm) $\times 10^{-3}$	(mm) $\times 10^{-3}$	(mm) $\times 10^{-3}$	(mm) $\times 10^{-3}$	(mm)	(mm)	(mm)	(mm)	(mm)	(mm)	( $\mu\text{E}$ )
-	16	19	128.2	0.1	9	-20	-2	-5	-3	-12	-10	-19	-0.01	-0.01	-0.01	-0.01	-0.01	-0.05	16
-	25	23	212.7	0.2	24	-37	-2	-8	-7	-12	-13	-23	-0.01	-0.01	-0.03	-0.03	-0.01	-0.06	30
-	32	24	284.3	0.3	39	-52	3	-5	-10	-12	-14	-26	-0.01	0.01	-0.02	-0.01	0.00	-0.05	41
-	37	24	326.6	0.4	97	-66	2	-7	-12	-12	-14	-27	-0.01	0.00	-0.02	-0.01	-0.01	-0.05	49
1	40	25	350.8	0.6	173	-79	0	-7	-10	-12	-14	-28	0.00	-0.01	-0.02	-0.03	-0.01	-0.08	54
-	58	61	377.8	0.7	219	-90	1	-8	-13	-7	-14	-22	0.18	0.01	-0.03	0.02	0.01	-0.06	59
-	61	62	408.6	0.9	283	-101	3	-8	-15	-7	-14	-23	0.18	-0.01	-0.05	0.01	0.02	-0.06	63
-	64	63	420.5	1.2	316	-112	3	-6	-15	-7	-14	-25	0.20	-0.01	-0.04	0.02	-0.01	-0.06	63
-	66	64	441.1	1.3	333	-118	4	-7	-12	-8	-15	-26	0.27	-0.01	-0.03	0.01	-0.01	-0.06	67
-	68	65	458.6	1.4	345	-122	5	-8	-16	-8	-15	-27	0.29	-0.01	-0.04	0.02	-0.01	-0.07	70
-	71	66	484.9	1.6	372	-128	5	-10	-13	-8	-16	-29	0.33	-0.01	-0.02	0.05	-0.01	-0.06	79
2	74	67	503.0	1.8	393	-132	4	-9	-16	-8	-16	-30	0.35	0.01	-0.04	0.06	-0.01	-0.08	126
-	90	101	514.9	2.0	407	-138	7	-7	-18	-2	-13	-23	0.36	0.00	-0.02	0.08	0.02	-0.06	147
-	92	102	529.9	2.1	421	-140	5	-8	-17	-2	-13	-25	0.39	-0.01	-0.06	0.09	0.00	-0.06	290
-	94	102	547.4	2.2	447	-143	9	-8	-18	-2	-13	-26	0.44	-0.02	-0.04	0.11	0.02	-0.06	458
-	96	103	564.3	2.4	475	-147	7	-12	-21	-3	-14	-28	0.50	-0.02	-0.05	0.13	0.01	-0.04	563
-	103	105	579.3	3.1	495	-125	5	-12	-21	-4	-16	-30	1.20	0.38	-0.07	0.13	-0.01	-0.06	615
3	107	106	601.8	3.4	518	-115	11	-12	-25	-4	-16	-31	1.40	0.59	-0.07	0.14	0.00	-0.06	668
-	127	136	617.4	3.6	536	-114	8	-13	-20	-4	-15	-29	1.53	0.73	-0.07	0.17	0.03	-0.06	725
-	129	136	633.6	3.7	555	-115	9	-11	-25	-4	-15	-30	1.60	0.80	-0.07	0.19	0.01	-0.06	773
4	147	142	653.0	5.1	574	-37	12	-9	-27	-1	-17	-40	1.70	0.89	-0.08	1.76	1.50	-0.28	1345

Load Stage	Data Set	Time elapsed	F	$\Delta=(BV+TV)/2$	BH	TH	ES-TE-BW	ES-V	ES-TW-BE	WS-TW-BE	WS-V	WS-TE-BW	EL-TE-BW	EL-V	EL-TW-BE	WL-TW-BE	WL-V	WL-TE-BW	Gauge 4B
-	202	183	663.6	5.3	586	-33	9	-11	-27	7	-11	-38	1.76	0.96	-0.08	2.00	1.80	-0.27	1355
-	224	184	676.8	5.5	598	-31	6	-14	-27	8	-11	-39	1.81	0.99	-0.09	2.09	1.93	-0.27	1385
5	265	188	694.3	6.5	612	19	-24	-10	-41	7	-12	-40	2.94	2.20	0.37	2.21	2.07	-0.27	1415
-	313	229	704.9	6.8	629	20	-31	-9	-42	10	-11	-40	3.09	2.37	0.45	2.40	2.31	-0.25	1481
-	320	230	718.0	7.0	640	22	-32	-8	-42	10	-11	-40	3.17	2.43	0.47	2.46	2.35	-0.23	1492
-	328	230	729.9	7.1	653	25	-36	-8	-42	10	-11	-41	3.22	2.50	0.49	2.56	2.45	-0.22	1517
6	344	231	742.4	7.5	666	29	-39	-12	-47	9	-11	-44	3.31	2.57	0.53	2.86	2.80	-0.19	1565
-	379	278	753.0	8.7	682	72	-48	-9	-45	1176	606	-80	3.44	2.75	0.61	4.01	4.11	0.20	1598
-	382	280	764.3	8.8	692	78	-51	-4	-47	1211	629	-82	3.51	2.80	0.66	4.13	4.22	0.22	1632
7	389	282	782.4	9.2	708	93	-58	-12	-48	1278	672	-82	3.63	2.90	0.72	4.34	4.52	0.29	1692
UL	442	342	801.1	10.0	738	113	-65	-9	-50	1676	799	-80	3.80	3.07	0.77	5.19	5.56	0.86	1745
-	446	343	751.1	12.3	701	-466	-68	-10	-48	5301	858	-57	2.92	2.40	0.60	10.34	13.16	6.19	1237
-	464	344	420.5	14.7	431	-1727	-68	-10	-37	8297	758	-34	2.58	2.14	0.55	14.49	19.71	11.19	1064

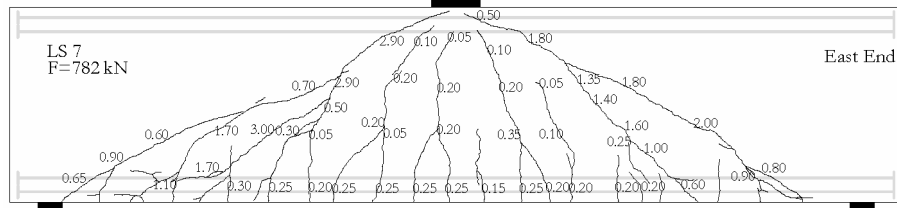
Note: The data from most of the strain gauges is not presented for the sake of brevity.

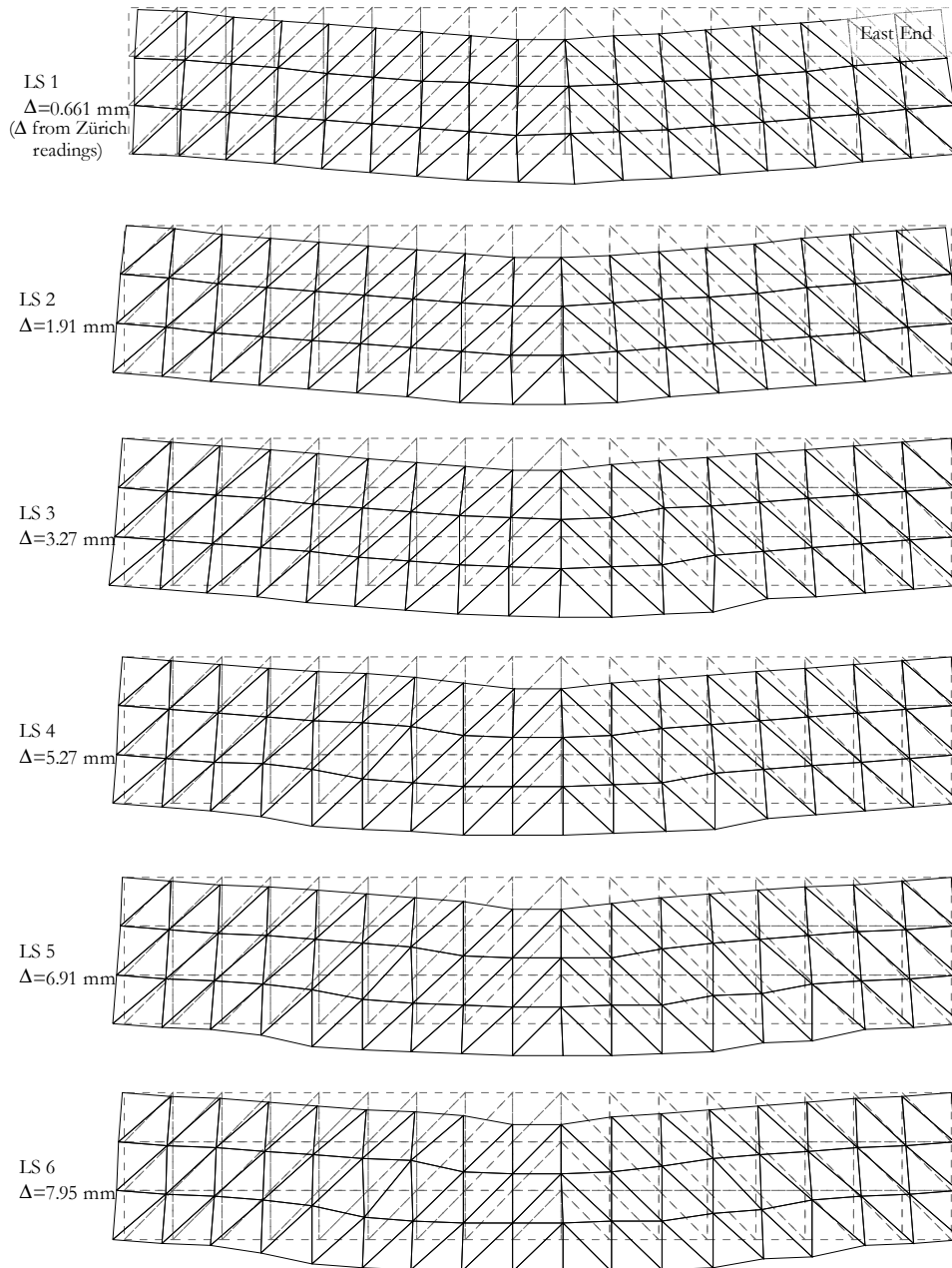


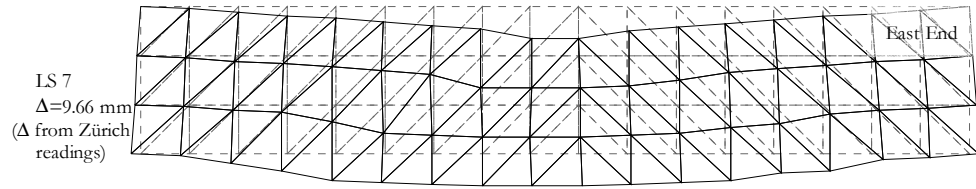
**Crack Diagrams, crack widths in (mm)**



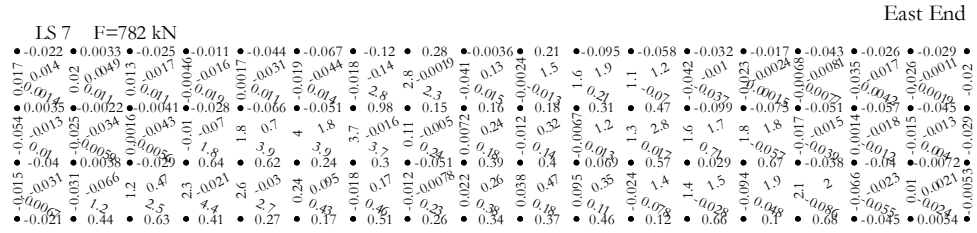




**Deformed shapes amplified to midspan displacement equivalent to 200 mm**







**B7. SPECIMEN L0C**

**Cast day:** May 30<sup>th</sup>, 2007

**Beam properties**

Cross section:  $b=1200$  mm,  $b=400$  mm

Effective depth: 1095 mm

Shear span: 2500 mm

Loading plates: 51/300/400 mm

Support plates: 51/150/400 mm

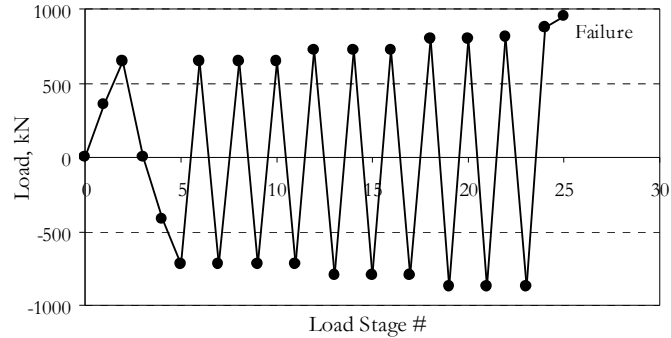
Longitudinal reinforcement:  $\rho_l=0.68\%$ ,  $f_y=650$  MPa

Transverse reinforcement:  $\rho_r=0\%$

Concrete:  $f_c' = 29.1$  MPa,  $\epsilon_c' = 1470 \mu\epsilon$ ,  $a_g = 20$  mm, *Modulus of rupture* = 3.7 MPa

Defects: no significant defects

**Test days:** October 23<sup>th</sup> – 25<sup>th</sup>, 2007

**Loading history****Test Remarks**

Maximum positive load: 953.0 kN

Maximum negative load: 868.7 kN

Displacement at failure: +11.1 mm

Failure mode:

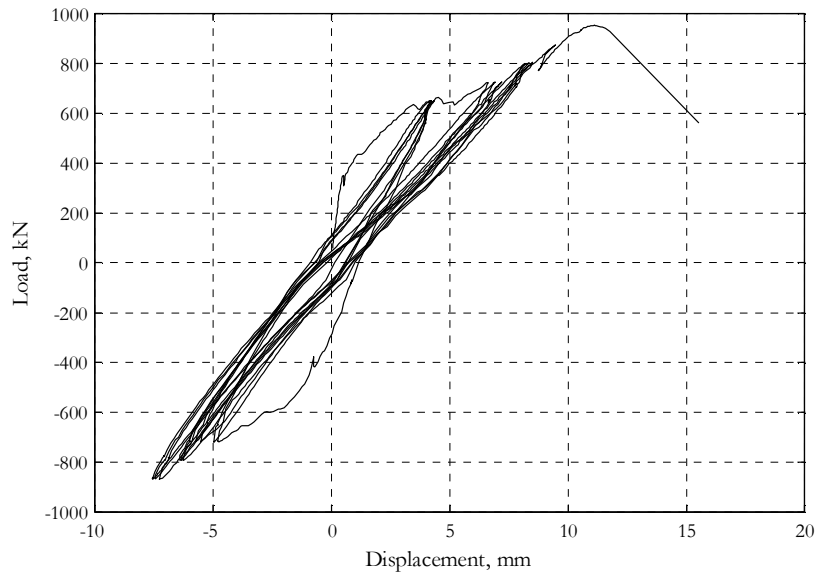
Other remarks: The beam failed with crushing above the most western diagonal crack near the edge of the top loading plate.

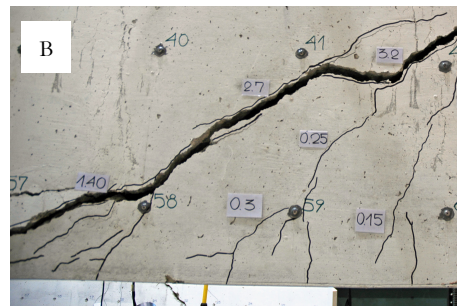
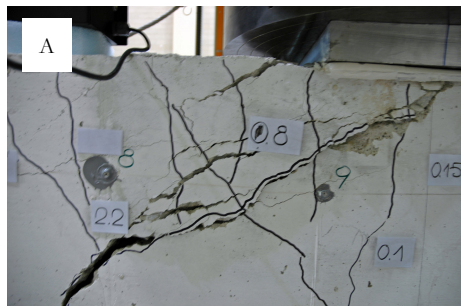
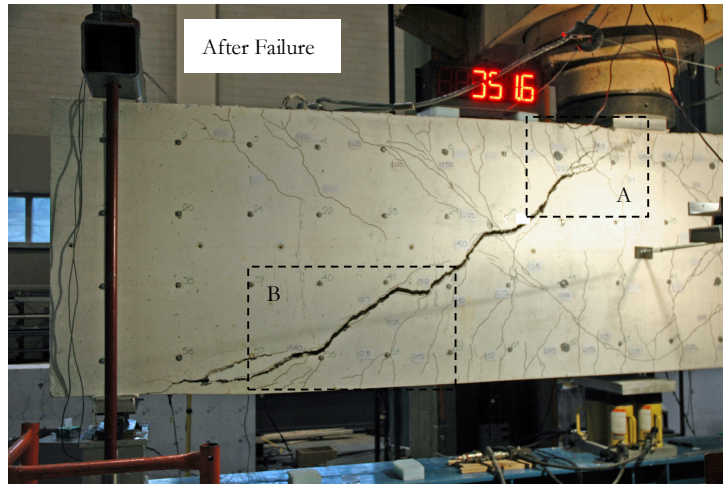
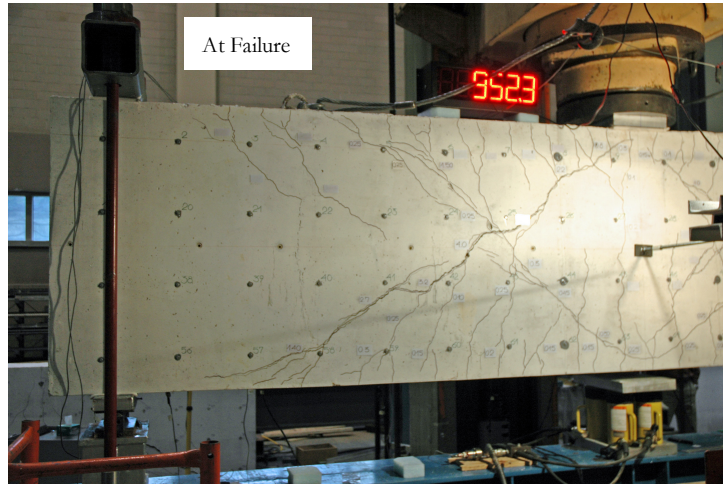
Other remarks:

- The formation and propagation of flexure-shear cracks was relatively quick.

- A series of short lines crossing the major “positive” diagonal cracks at angle of about  $90^\circ$  were drawn on the south face of the beam at Load Stage 4. Close examination of these lines under positive load revealed that the crack slip was significant only at the bottom part of the beam where the flexure-shear cracks were relatively steep.
- The specimen was recentered east-west prior to Load Stage 13.

Global response







## Data summary

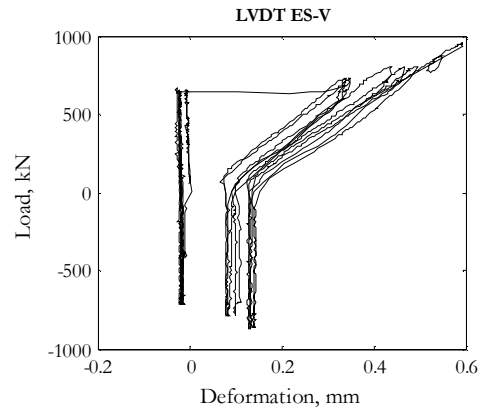
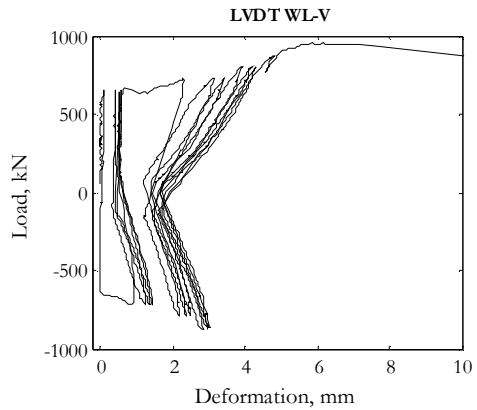
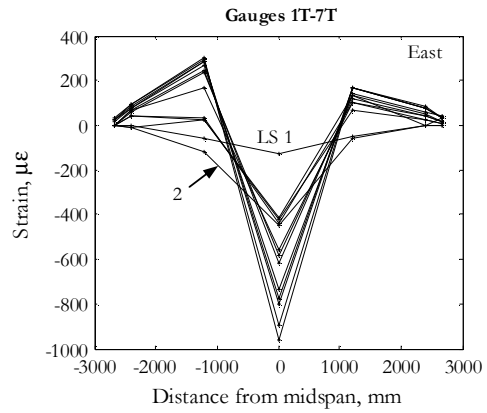
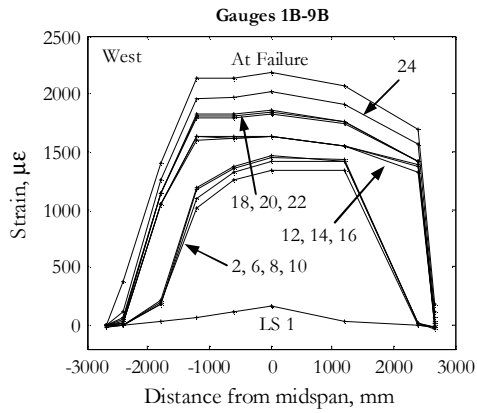
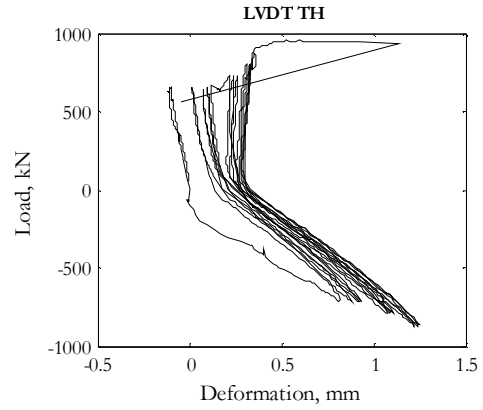
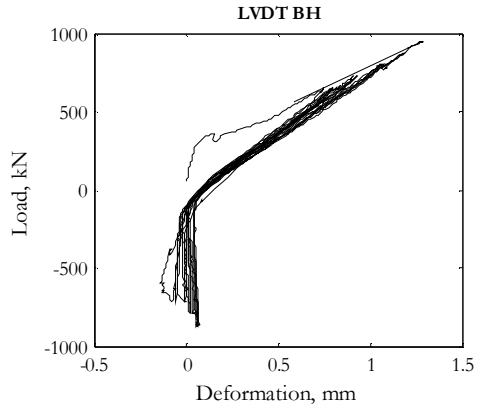
Load Stage	Data Set	Time elapsed	F	$\Delta=(BV+TV)/2$	BH	TH	ES-TE-BW	ES-V	ES-TW-BE	WS-TW-BE	WS-V	WS-TE-BW	EL-TE-BW	EL-V	EL-TW-BE	WL-TW-BE	WL-V	WL-TE-BW	Gauge 4B
(#)	(#)	(min)	(kN)	(mm)	(mm) $\times 10^{-3}$	(mm) $\times 10^{-3}$	(mm) $\times 10^{-3}$	(mm) $\times 10^{-3}$	(mm) $\times 10^{-3}$	(mm) $\times 10^{-3}$	(mm) $\times 10^{-3}$	(mm) $\times 10^{-3}$	(mm)	(mm)	(mm)	(mm)	(mm)	(mm)	( $\mu\epsilon$ )
-	9	14	57.4	0.0	3	-3	0	0	-4	-1	0	-2	0.01	0.00	0.00	0.00	0.00	-0.01	9
1	41	26	349.9	0.5	154	-56	11	-3	-15	0	-4	-5	0.02	0.02	-0.04	0.01	0.00	-0.02	64
2	107	76	651.1	4.2	753	-102	18	-7	-26	7	-7	-14	1.47	0.68	-0.03	0.48	0.08	-0.02	1015
3	139	118	7.6	1.2	157	0	-1	5	-2	-1	-3	-3	0.50	0.29	0.03	0.16	0.01	0.00	259
4	178	217	-418.5	-0.7	-85	406	-28	-10	-14	-34	-21	-16	0.18	0.14	0.07	-0.02	-0.03	-0.04	2
5	234	275	-718.2	-4.7	-76	823	-38	-12	-13	-44	-24	-15	0.02	0.56	1.72	-0.08	0.83	1.34	-12
-	263	311	-240.8	-2.6	-21	436	-30	-15	-21	-38	-24	-17	0.06	0.46	1.04	-0.04	0.73	0.96	91
-	278	316	116.3	0.0	188	119	-20	-18	-29	-31	-26	-25	0.34	0.32	0.41	0.07	0.45	0.46	333
6	330	321	651.7	4.1	798	20	-2	-21	-47	-20	-30	-39	1.86	1.20	0.21	0.49	0.40	0.21	1098
-	354	346	209.9	1.7	310	87	-15	-17	-33	-23	-26	-31	1.03	0.88	0.25	0.25	0.37	0.22	458
-	373	352	-140.8	-0.4	-9	267	-27	-16	-22	-31	-24	-25	0.52	0.66	0.40	0.01	0.33	0.32	104
7	416	359	-721.1	-5.0	-56	884	-38	-15	-13	-44	-25	-16	0.19	1.01	1.96	-0.08	1.22	1.66	10
-	440	386	-312.7	-2.9	-25	537	-30	-15	-19	-39	-24	-16	0.21	0.94	1.31	-0.04	0.94	1.14	68
-	473	1378	52.6	-0.3	115	196	-25	-18	-30	-33	-28	-31	0.32	0.70	0.57	0.04	0.59	0.58	319
8	544	1390	650.5	4.3	800	72	-3	-23	-57	-29	-36	-48	2.14	1.60	0.31	0.57	0.51	0.25	1176
-	584	1429	1.6	0.6	100	181	-30	-18	-32	-38	-32	-37	0.79	0.99	0.36	0.08	0.42	0.28	293
-	610	1438	-352.0	-2.4	-42	552	-40	-19	-27	-48	-33	-33	0.35	1.03	1.18	-0.04	0.82	0.94	135
9	638	1441	-717.8	-5.5	-8	919	-45	-19	-24	-57	-33	-29	0.17	2.14	2.80	-0.09	1.36	1.75	85
-	661	1479	-345.8	-3.5	3	601	-41	-19	-31	-50	-31	-25	0.22	1.82	1.98	-0.06	1.05	1.22	131
-	684	1494	53.9	-0.5	122	207	-32	-21	-36	-44	-35	-38	0.36	1.35	1.00	0.02	0.57	0.52	317
10	746	1503	651.1	4.2	821	100	-9	-24	-62	-34	-41	-53	2.27	2.13	0.61	0.60	0.56	0.27	1191

Load Stage	Data Set	Time elapsed	F	$\Delta=(BV+TV)/2$	BH	TH	ES-TE-BW	ES-V	ES-TW-BE	WS-TW-BE	WS-V	WS-TE-BW	EL-TE-BW	EL-V	EL-TW-BE	WL-TW-BE	WL-V	WL-TE-BW	Gauge-4B
-	782	1534	290.0	2.2	418	130	-20	-21	-49	-35	-37	-47	1.43	1.67	0.61	0.40	0.53	0.28	719
-	795	1543	-70.7	-0.2	32	256	-35	-21	-35	-45	-34	-39	0.59	1.32	0.71	0.03	0.43	0.31	209
11	847	1552	-718.7	-5.7	0	933	-49	-20	-28	-59	-35	-31	0.19	2.48	3.03	-0.09	1.43	1.80	89
-	867	1575	-343.0	-3.5	0	602	-44	-19	-31	-51	-32	-27	0.27	2.02	2.05	-0.06	1.08	1.22	131
-	889	1607	13.9	-0.6	89	232	-38	-21	-38	-42	-32	-32	0.42	1.42	0.95	0.01	0.60	0.55	281
-	923	1611	371.5	2.4	502	138	-26	-27	-54	-38	-37	-44	1.55	1.77	0.69	0.41	0.55	0.31	794
12	977	1620	723.6	6.6	915	216	1105	335	-95	-25	-38	-62	3.16	3.00	0.97	2.35	2.29	0.55	1602
-	998	1656	367.2	4.1	512	218	782	241	-72	-32	-37	-56	2.13	2.36	0.89	1.72	1.91	0.55	1002
-	1012	1663	3.3	1.0	87	277	350	99	-47	-45	-37	-44	0.98	1.75	0.81	0.89	1.37	0.57	414
-	1043	1670	-355.0	-2.5	-8	624	307	92	-40	-54	-37	-39	0.49	2.22	2.06	0.44	1.53	1.34	222
13	1077	1674	-792.8	-6.3	24	1078	274	85	-35	-63	-37	-33	0.31	3.19	3.69	0.25	2.19	2.46	151
-	1099	1700	-434.4	-4.1	18	764	274	81	-38	-55	-33	-29	0.36	2.70	2.71	0.28	1.84	1.89	182
-	1113	1701	-70.6	-1.2	29	352	281	81	-42	-47	-33	-32	0.46	1.93	1.46	0.35	1.33	1.11	246
-	1146	1714	288.2	2.6	408	206	568	146	-64	-39	-37	-46	1.64	2.08	0.94	1.29	1.74	0.66	782
14	1194	1719	726.1	6.9	938	241	1287	341	-99	-21	-38	-63	3.29	3.22	1.11	2.90	3.13	1.24	1627
-	1211	1738	345.5	4.0	500	231	848	227	-77	-21	-34	-50	2.08	2.41	0.98	1.98	2.42	0.92	918
-	1231	1742	-78.6	0.2	24	319	309	85	-41	-39	-35	-39	0.70	1.70	1.00	0.82	1.52	0.83	269
-	1260	1745	-439.3	-3.4	4	737	291	88	-38	-47	-36	-37	0.41	2.53	2.51	0.47	1.89	1.85	182
15	1287	1749	-791.7	-6.3	26	1094	275	81	-35	-56	-38	-34	0.31	3.29	3.78	0.36	2.38	2.70	142
-	1304	1762	-423.5	-4.1	14	761	281	80	-36	-50	-35	-32	0.36	2.72	2.75	0.38	2.01	2.07	171
-	1313	1762	0.0	-0.4	63	273	291	79	-44	-42	-36	-38	0.60	1.77	1.17	0.47	1.37	1.07	258
-	1344	1767	358.4	3.6	496	232	775	189	-75	-29	-39	-52	2.03	2.39	0.99	1.88	2.39	1.01	947
16	1392	1774	726.1	7.2	934	261	1383	345	-104	-11	-40	-65	3.46	3.46	1.20	3.11	3.41	1.54	1632
-	1419	1813	372.3	4.3	531	244	952	245	-82	-12	-36	-54	2.29	2.62	1.06	2.18	2.68	1.23	962
-	1461	2763	0.5	0.7	87	267	337	93	-40	-22	-31	-31	0.87	1.76	0.93	0.87	1.61	1.05	319

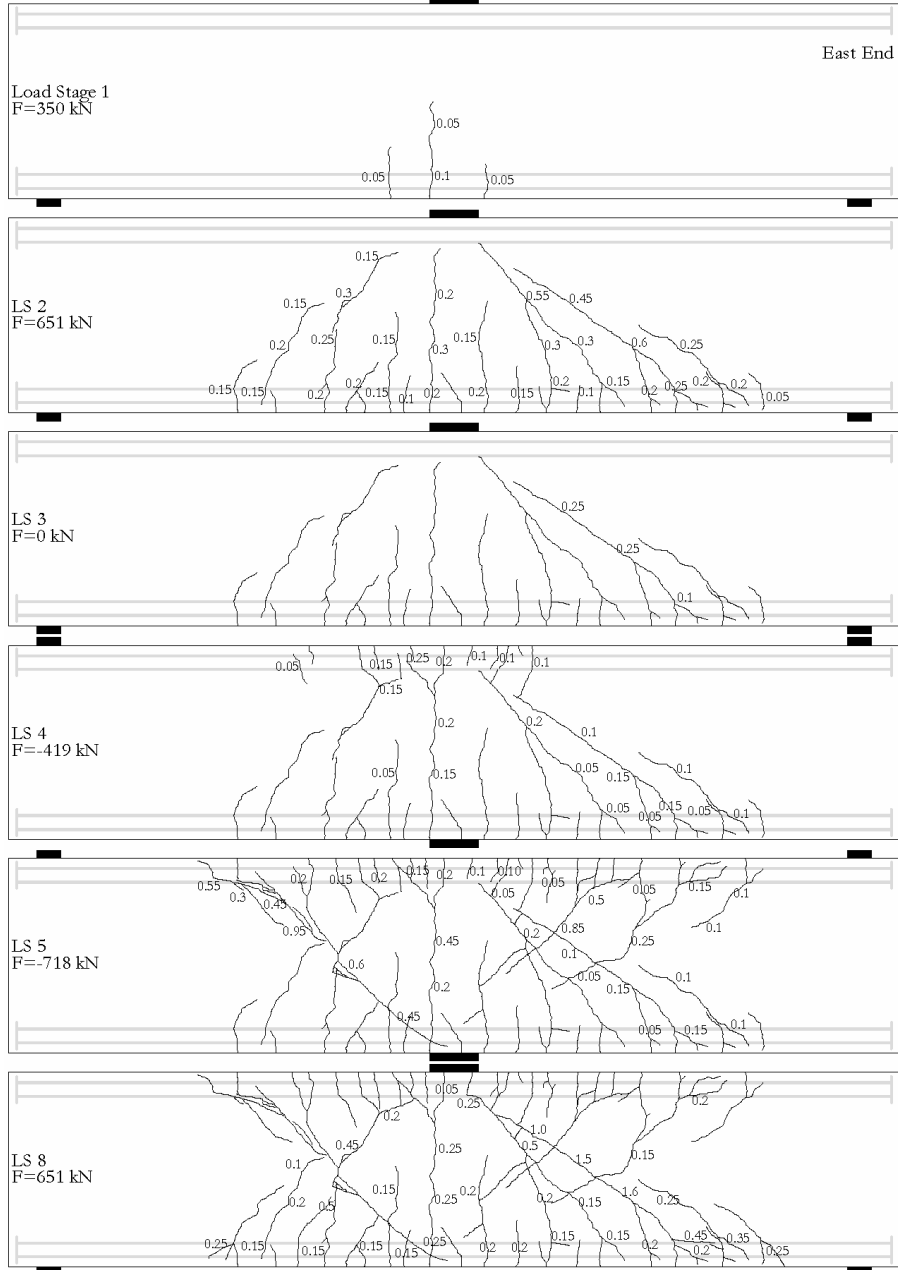
Load Stage	Data Set	Time elapsed	F	$\Delta=(BV+TV)/2$	BH	TH	ES-TE-BW	ES-V	ES-TW-BE	WS-TW-BE	WS-V	WS-TE-BW	EL-TE-BW	EL-V	EL-TW-BE	WL-TW-BE	WL-V	WL-TE-BW	Gauge 4B
-	1497	2793	-355.2	-2.7	20	662	312	102	-17	-22	-21	-19	0.47	2.42	2.29	0.55	1.84	1.89	203
17	1534	2799	-792.7	-6.4	44	1108	295	99	-13	-34	-27	-19	0.35	3.35	3.85	0.39	2.49	2.96	154
-	1561	2832	-436.8	-4.2	47	804	315	113	-1	-6	-5	2	0.43	2.85	2.90	0.49	2.16	2.39	182
-	1584	2849	-0.2	-0.2	96	294	320	101	-13	-5	-15	-16	0.66	1.80	1.22	0.58	1.44	1.24	269
-	1621	2858	350.0	3.7	511	266	845	214	-46	7	-15	-28	2.13	2.56	1.14	2.02	2.56	1.38	941
18	1674	2867	799.8	8.2	1068	309	1673	435	-83	41	-12	-41	3.95	3.93	1.43	3.61	3.91	2.02	1799
-	1706	2898	445.5	5.3	647	282	1214	324	-65	31	-20	-41	2.75	3.06	1.24	2.64	3.15	1.70	1132
-	1721	2900	80.5	1.7	188	282	539	152	-35	15	-20	-27	1.25	2.03	1.02	1.36	2.09	1.41	457
-	1757	2910	-270.0	-2.0	13	586	359	127	-8	6	-16	-16	0.51	2.28	2.04	0.67	1.84	1.95	219
19	1810	2920	-868.7	-7.3	61	1223	336	130	1	-1	-13	-2	0.35	3.70	4.30	0.48	2.82	3.52	139
-	1837	2957	-511.6	-5.0	54	907	345	130	2	12	-6	1	0.38	3.17	3.31	0.53	2.44	2.91	172
-	1858	2958	-149.7	-1.9	48	490	347	127	-1	20	-4	0	0.48	2.33	2.00	0.60	1.84	2.00	216
-	1895	2967	204.4	2.2	345	274	651	170	-30	28	-6	-14	1.60	2.33	1.20	1.62	2.35	1.58	659
20	1962	2978	803.0	8.4	1074	327	1769	467	-83	61	-10	-38	4.05	4.12	1.53	3.83	4.20	2.24	1809
-	1981	3000	427.3	5.1	623	301	1227	339	-60	51	-12	-31	2.68	3.12	1.32	2.71	3.32	1.93	1060
-	1991	3000	70.8	1.5	180	297	530	160	-26	33	-14	-19	1.19	2.05	1.08	1.33	2.14	1.58	391
-	2021	3009	-282.5	-2.3	16	614	356	133	-7	21	-15	-12	0.46	2.41	2.20	0.66	1.96	2.21	208
21	2073	3019	-868.0	-7.4	63	1240	344	133	3	16	-11	-2	0.34	3.80	4.38	0.52	2.93	3.74	140
-	2094	3034	-496.5	-5.0	53	899	350	135	1	24	-6	0	0.39	3.18	3.32	0.55	2.48	3.08	174
-	2113	3035	-141.9	-1.9	47	491	355	135	-1	32	-4	-1	0.47	2.32	1.99	0.61	1.87	2.13	214
-	2152	3061	210.9	2.4	363	287	707	186	-31	43	-8	-15	1.69	2.45	1.24	1.73	2.49	1.74	679
22	2226	3072	804.8	8.5	1095	334	1822	492	-83	76	-7	-37	4.13	4.21	1.61	3.91	4.33	2.39	1819
-	2261	3104	452.3	5.6	681	308	1325	368	-65	69	-10	-31	2.93	3.32	1.42	2.91	3.53	2.12	1159
-	2282	3117	84.7	1.6	209	303	581	176	-23	57	-5	-11	1.26	2.15	1.13	1.46	2.28	1.72	413

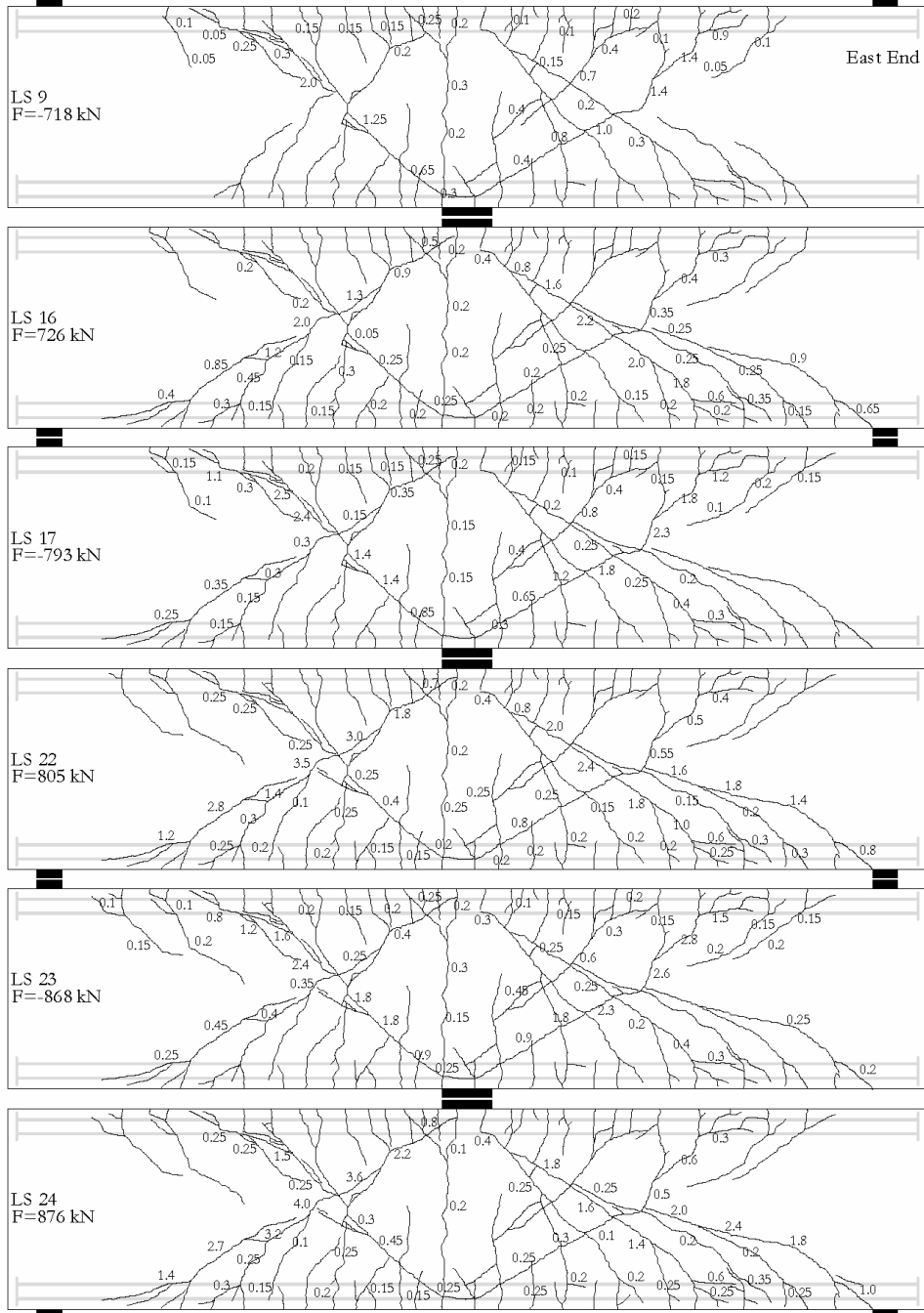
Load Stage	Data Set	Time elapsed	F	$\Delta=(BV+TV)/2$	BH	TH	ES-TE-BW	ES-V	ES-TW-BE	WS-TW-BE	WS-V	WS-TE-BW	EL-TE-BW	EL-V	EL-TW-BE	WL-TW-BE	WL-V	WL-TE-BW	Gauge-4B
-	2307	3122	-276.2	-2.3	26	616	370	145	-1	47	-5	-5	0.49	2.42	2.22	0.70	1.98	2.34	205
23	2372	3128	-867.5	-7.6	71	1247	351	141	5	32	-9	-2	0.32	3.88	4.47	0.55	3.00	3.86	139
-	2402	3159	-511.7	-5.2	57	919	355	141	3	37	-8	-2	0.36	3.30	3.44	0.57	2.57	3.20	171
-	2422	3160	-154.1	-2.1	51	509	363	142	0	43	-6	-4	0.45	2.41	2.09	0.63	1.95	2.28	213
-	2458	3176	199.6	2.3	344	289	707	189	-32	51	-10	-19	1.67	2.49	1.28	1.75	2.55	1.83	647
24	2535	3187	875.5	9.5	1191	357	2043	546	-94	106	-8	-43	4.54	4.60	1.73	4.36	4.78	2.56	1962
UL	2586	3238	953.0	11.1	1284	601	2299	593	-133	99	-34	-69	4.97	4.98	1.77	5.52	6.16	3.18	2140
-	2594	3239	560.5	15.5	592	-47	1374	370	-91	-428	-44	-35	2.80	3.36	1.41	16.87	24.03	16.42	1010

Note: The data from most of the strain gauges is not presented for the sake of brevity.

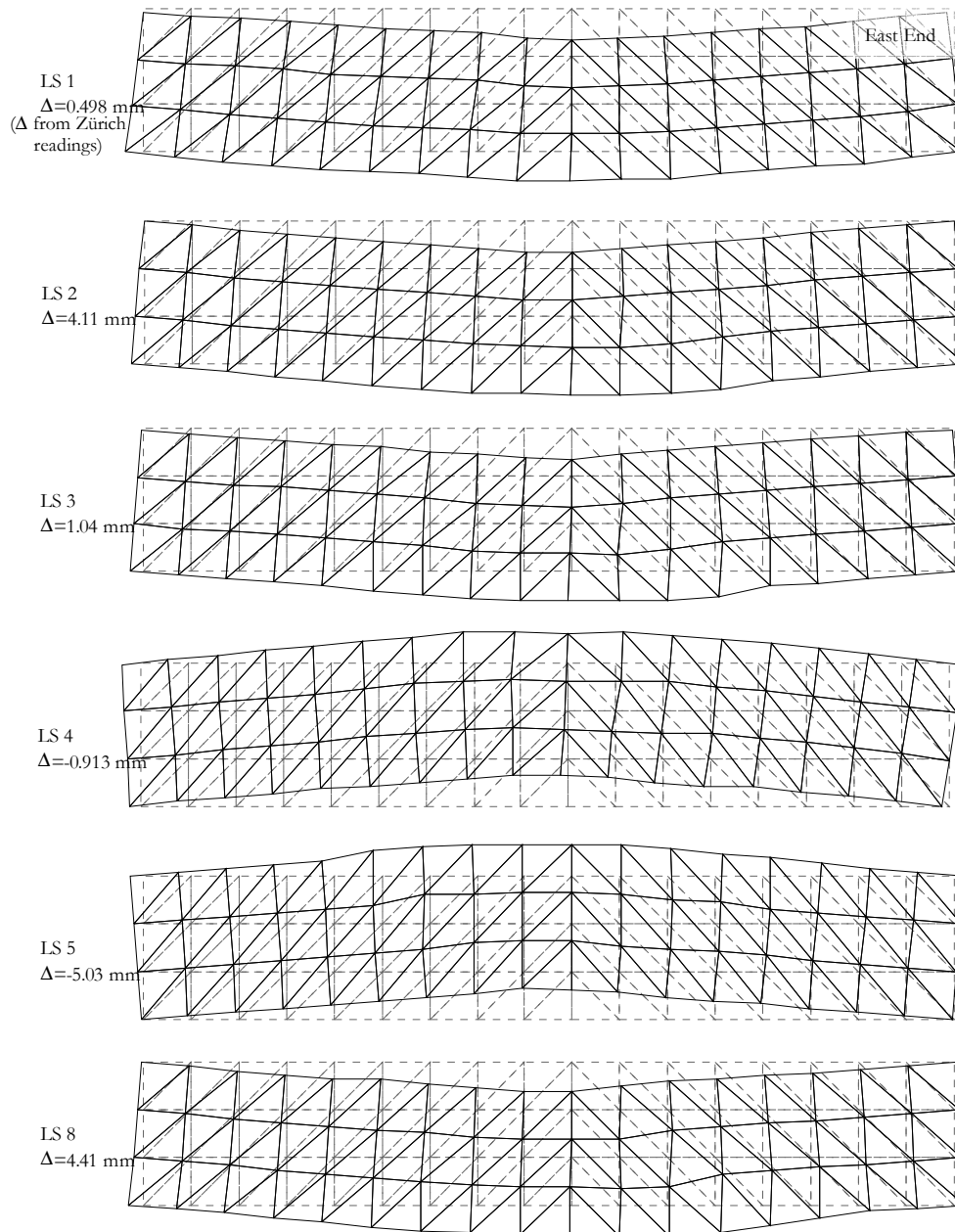


**Crack Diagrams, crack widths in (mm)**

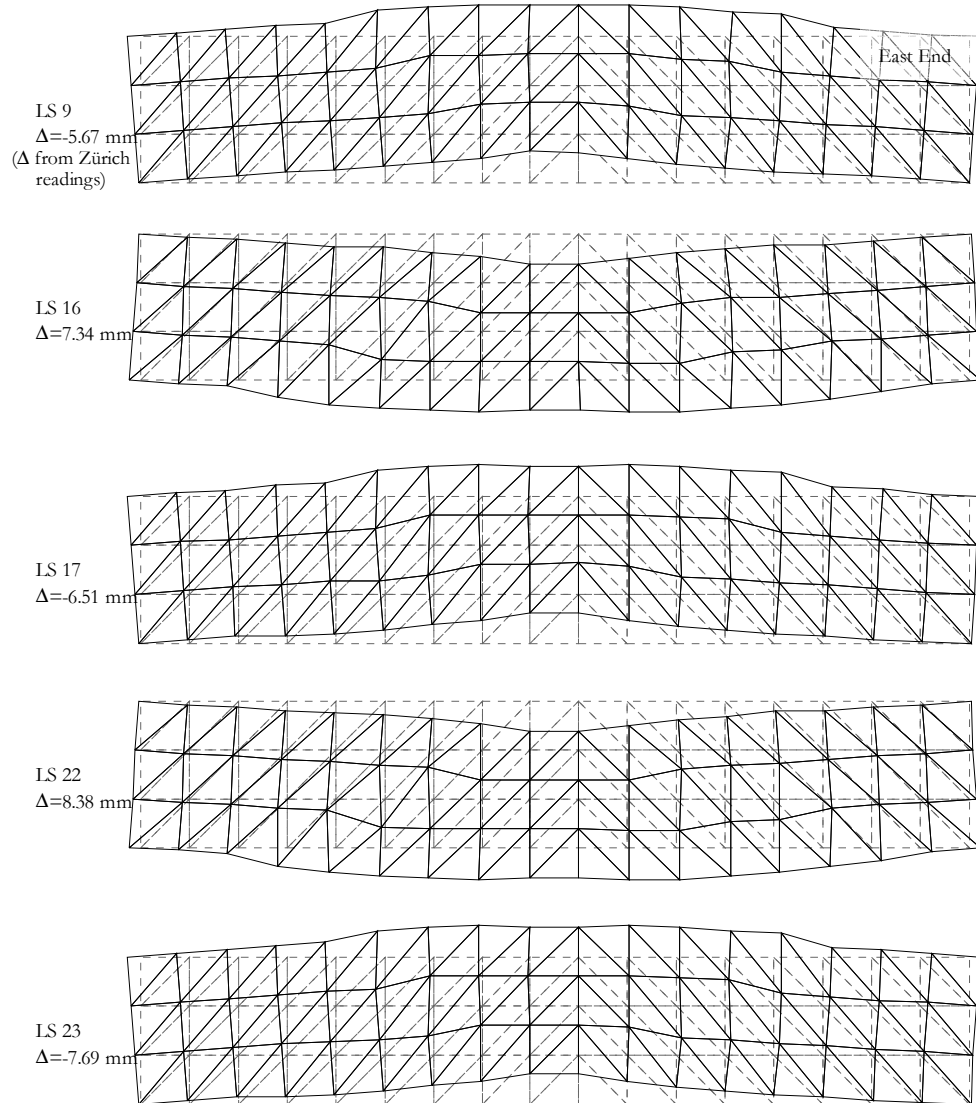




## Deformed shapes amplified to midspan displacement equivalent to 200 mm

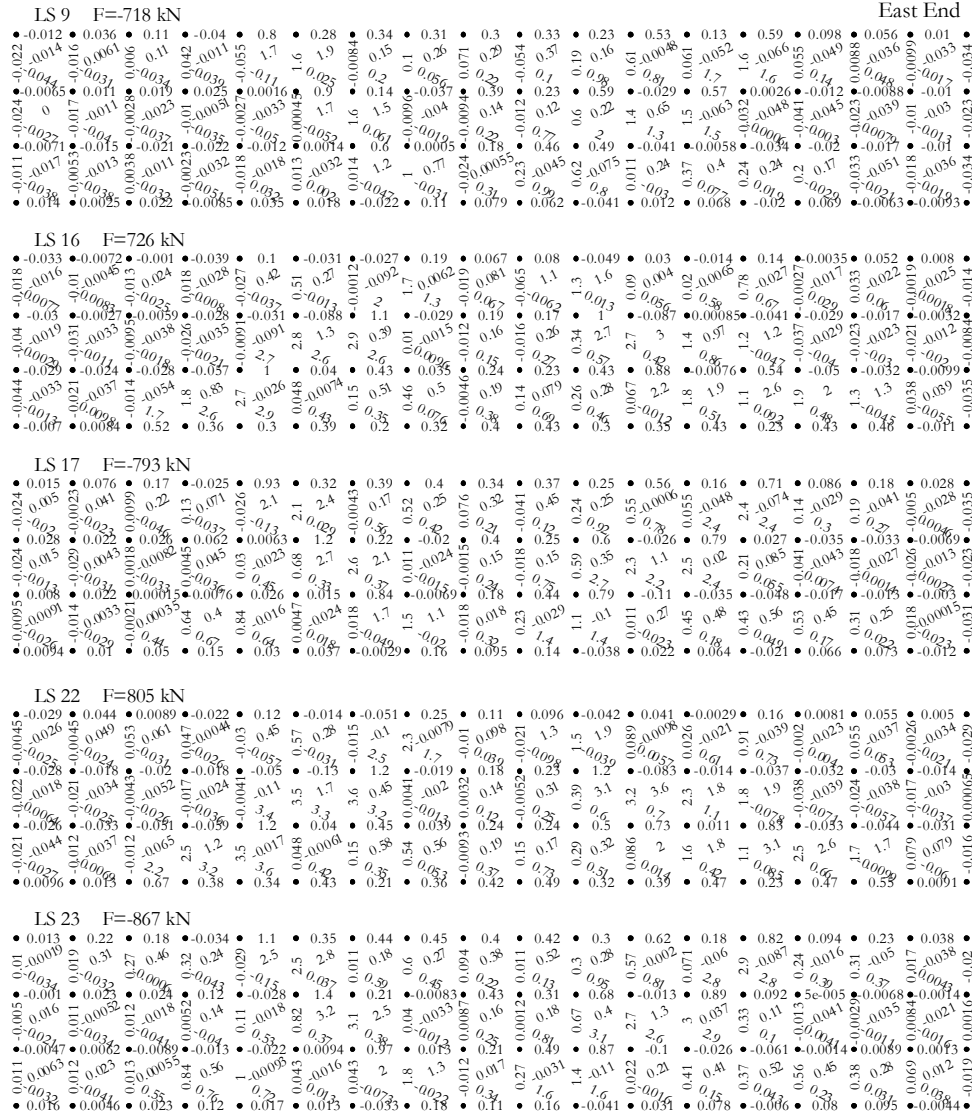






Zürich readings over 300/300 mm grid, deformations in (mm)





## B8. SPECIMEN L1M

Cast day: June 19<sup>th</sup>, 2007

### Beam properties

Cross section:  $b=1200$  mm,  $h=400$  mm

Effective depth: 1095 mm

Shear span: 2500 mm

Loading plates: 51/300/400 mm

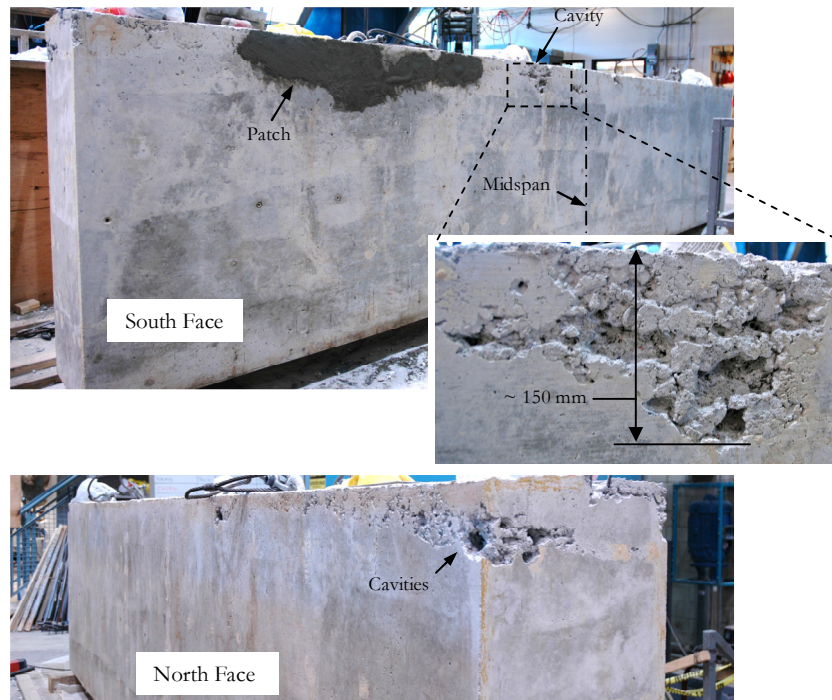
Support plates: 51/150/400 mm

Longitudinal reinforcement:  $\rho_l=0.68\%$ ,  $f_y=650$  MPa

Transverse reinforcement:  $\rho_t=0.1\%$ ,  $f_{yt}=490$  MPa

Concrete:  $f'_c = 37.8$  MPa,  $\epsilon_c=1770 \mu\epsilon$ ,  $a_g=20$  mm, *Modulus of rupture* = 3.7 MPa

Defects: The concrete mix for specimens L1M and L1C had relatively low workability (initial slump of 50 mm) which made the cast of the top layers of concrete difficult. As a result, specimen L1M had cavities in the side concrete cover of the top longitudinal bars (see the photographs below). The cavities were cleaned, watered, and patched with non-shrink grout on August 30<sup>th</sup>. The compressive strength of the grout was expected to develop as follows: 20 MPa after 24 hrs, 40 MPa after 7 days, and 55 MPa after 28 days.



**Test day:** November 2<sup>nd</sup>, 2007

**Test Remarks**

Maximum load: 1295.1 kN

Displacement at maximum load: 14.2 mm

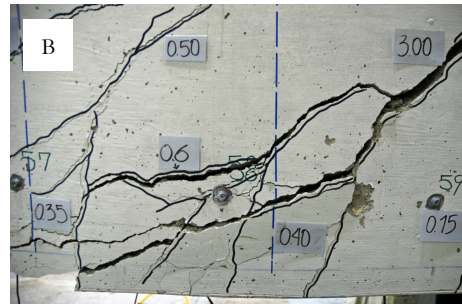
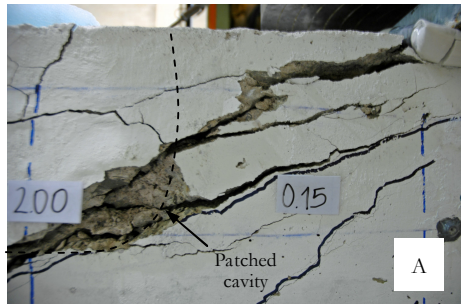
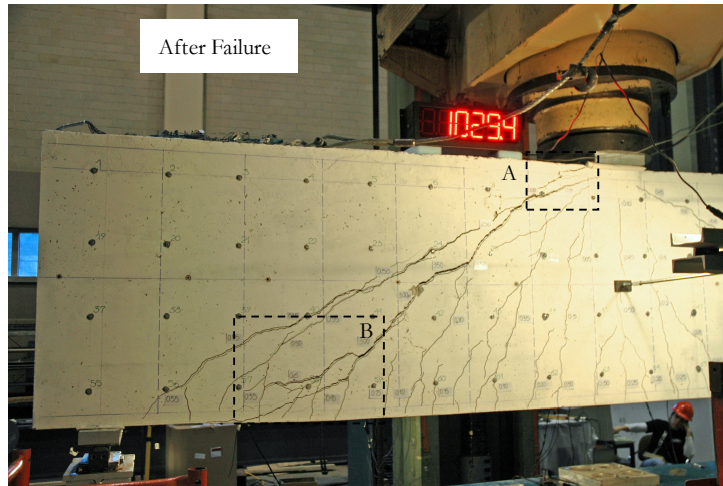
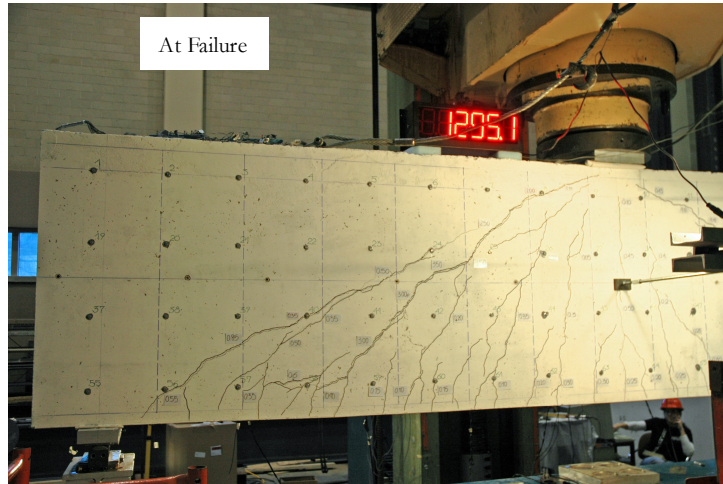
Failure mode: The beam failed in a relatively gradual manner with crushing above the most western diagonal crack near the edge of the top loading plate. Sounds indicating rupture of stirrups were heard after the load on the beam has started to decrease.

Other remarks:

- The formation and propagation of flexure-shear cracks was relatively gradual.
- No effects related to the patched cavities were observed.

**Global response**





## Data summary

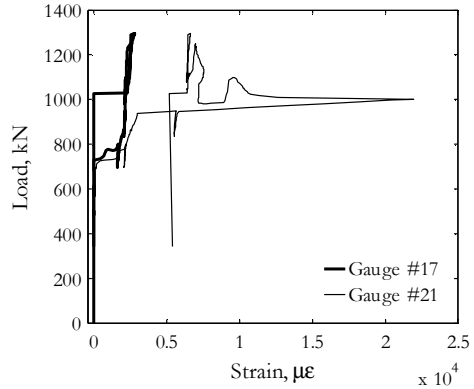
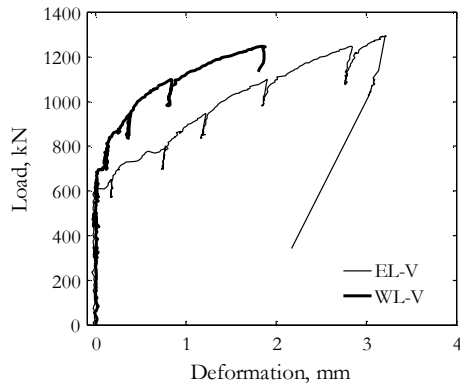
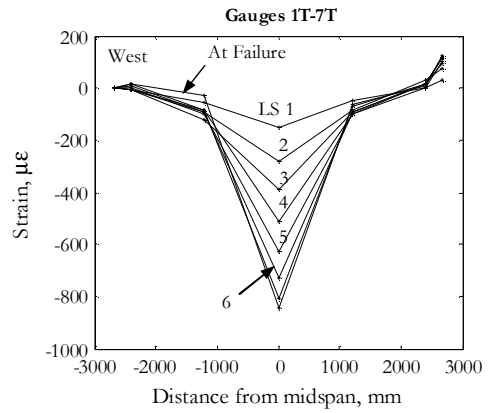
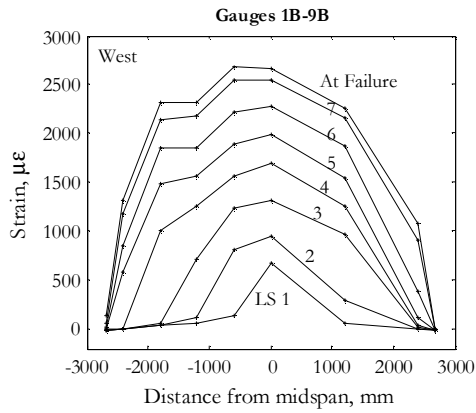
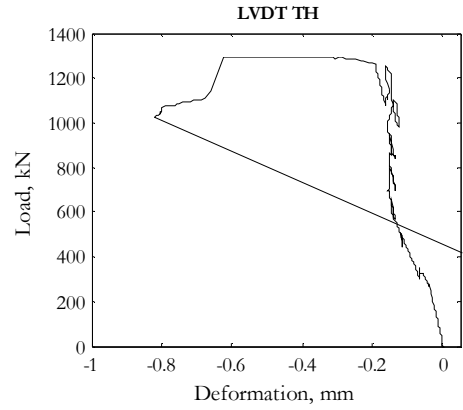
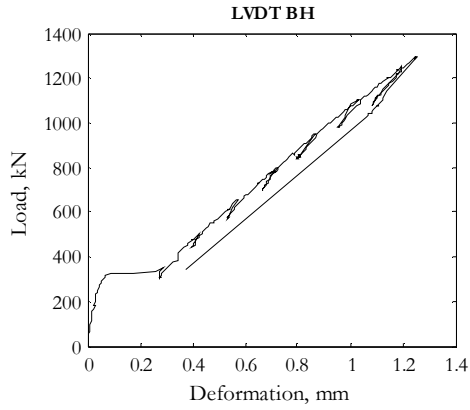
Load Stage	Data Set	Time elapsed	F	$\Delta=(BV+TV)/2$	BH	TH	ES-TE-BW	ES-V	ES-TW-BE	EL-TE-BW	EL-V	EL-TW-BE	WL-TW-BE	WL-V	WL-TE-BW	Gauge 4B	Gauge 17	Gauge 21
(#)	(#)	(min)	(kN)	(mm)	(mm) $\times 10^{-3}$	(mm) $\times 10^{-3}$	(mm) $\times 10^{-3}$	(mm) $\times 10^{-3}$	(mm) $\times 10^{-3}$	(mm)	(mm)	(mm)	(mm)	(mm)	(mm)	( $\mu\epsilon$ )	( $\mu\epsilon$ )	( $\mu\epsilon$ )
-	13	10	112.7	0.1	17	-13	-2	-1	-3	0.01	-0.02	-0.01	0.03	0.00	-0.01	16	1	-1
-	24	14	205.6	0.2	32	-28	0	-2	-5	0.03	-0.03	-0.02	0.03	0.00	-0.01	33	1	-1
-	31	15	275.8	0.3	46	-40	2	-1	-6	0.02	-0.02	-0.02	0.04	0.00	-0.01	45	1	-1
1	42	18	349.9	0.7	290	-67	3	-2	-8	0.04	-0.02	-0.03	0.03	0.01	-0.01	60	0	1
-	60	64	376.9	0.9	327	-81	2	-5	-10	0.02	-0.03	-0.05	0.03	0.00	-0.03	66	-5	2
-	64	65	406.3	1.1	344	-92	3	-5	-12	0.02	-0.03	-0.04	0.03	-0.01	-0.03	73	-5	2
-	67	66	434.4	1.3	362	-99	2	-7	-13	0.03	-0.03	-0.05	0.04	0.01	-0.03	75	-5	2
-	71	67	465.7	1.5	393	-108	2	-8	-15	0.04	-0.03	-0.05	0.06	0.00	-0.03	83	-6	2
2	77	68	503.2	1.9	425	-118	1	-9	-17	0.17	-0.04	-0.07	0.08	-0.01	-0.03	122	-6	5
-	97	101	528.8	2.1	453	-126	2	-9	-18	0.21	-0.03	-0.06	0.09	-0.01	-0.04	159	-8	7
-	100	102	555.7	2.3	480	-134	1	-10	-20	0.23	-0.03	-0.07	0.12	0.02	-0.03	208	-8	8
-	104	103	588.8	2.5	511	-142	1	-10	-21	0.26	-0.04	-0.05	0.25	-0.01	-0.05	336	-9	10
-	109	103	614.4	3.0	538	-147	2	-11	-22	0.58	0.11	-0.05	0.27	-0.02	-0.04	423	18	22
3	115	104	650.7	3.4	573	-147	2	-11	-23	0.69	0.16	-0.06	0.35	0.00	-0.04	708	19	24
-	139	153	678.8	3.7	603	-152	5	-10	-23	0.77	0.21	-0.07	0.45	0.02	-0.04	803	15	23
-	146	155	705.1	4.3	629	-153	9	-10	-25	0.89	0.25	-0.06	0.88	0.08	-0.07	1093	-5	190
-	150	156	731.9	4.7	652	-153	10	-10	-26	1.10	0.42	-0.07	0.99	0.09	-0.07	1143	232	1276
-	155	157	762.6	5.1	684	-152	11	-10	-28	1.29	0.54	-0.05	1.10	0.11	-0.06	1201	802	1772
4	162	159	800.1	5.7	721	-151	14	-10	-31	1.58	0.76	-0.02	1.22	0.13	-0.04	1261	1670	2194
-	193	207	831.3	6.1	755	-151	14	-14	-40	1.69	0.84	-0.01	1.37	0.15	-0.05	1326	1910	2365
-	199	209	862.6	6.5	782	-149	30	-7	-44	1.79	0.89	-0.01	1.60	0.19	-0.02	1390	2053	2529

Load Stage	Data Set	Time elapsed	F	$\Delta=(BV+TV)/2$	BH	TH	WS-TW-BE	WS-V	WS-TE-BW	EL-TE-BW	EL-V	EL-TW-BE	WL-TW-BE	WL-V	WL-TE-BW	Gauge 4B	Gauge 17	Gauge 21
-	206	211	888.8	7.1	809	-146	404	106	-57	1.92	1.01	0.02	1.98	0.28	0.02	1451	2120	2772
-	210	213	918.8	7.4	837	-146	442	114	-60	2.06	1.12	0.05	2.10	0.32	0.04	1508	2122	2937
5	215	215	948.2	7.8	867	-151	480	124	-63	2.20	1.22	0.07	2.27	0.38	0.05	1568	2162	5649
-	246	264	982.6	8.3	904	-154	517	135	-64	2.27	1.34	0.09	2.42	0.43	0.09	1631	2168	15768
-	250	265	1009.4	8.6	933	-154	549	143	-66	2.39	1.43	0.11	2.58	0.49	0.12	1686	2183	12649
-	254	266	1035.7	9.0	961	-149	592	154	-69	2.54	1.55	0.13	2.76	0.57	0.17	1743	2192	10524
-	262	269	1068.2	9.5	994	-143	648	168	-72	2.72	1.70	0.17	2.98	0.68	0.19	1816	2193	10074
6	268	271	1099.4	10.0	1030	-138	699	183	-74	2.93	1.90	0.25	3.23	0.84	0.27	1861	2212	9549
-	299	310	1128.2	10.6	1072	-144	762	206	-74	3.20	2.13	0.31	3.52	1.01	0.39	1931	2245	7574
-	304	312	1158.2	11.0	1098	-146	804	222	-77	3.35	2.26	0.35	3.74	1.18	0.49	1983	2270	7374
-	309	313	1187.6	11.5	1128	-147	850	249	-80	3.51	2.42	0.39	3.93	1.33	0.56	2041	2279	7199
-	315	314	1214.4	11.9	1158	-147	914	293	-83	3.68	2.59	0.44	4.19	1.55	0.65	2098	2300	7049
7	325	316	1249.4	12.6	1196	-162	998	336	-86	3.93	2.83	0.54	4.54	1.84	0.83	2173	2555	6974
UL	385	381	1295.1	14.2	1251	-353	1399	483	-104	4.28	3.22	0.69	5.88		1.50	2321	2792	6624
-	387	381	1140.1	15.3	1143	-662	1562	484	-98	4.05	3.13	0.71	8.09		3.32	2126	2475	6474
-	407	383	1038.8	17.7	1075	-807	1703	502	-95	3.92	3.04	0.74	11.96		5.65	1968	2295	6424
-	415	384	342.6	24.2	374	167	1403	415	-43	2.38	2.17	0.78	27.24		11.36	794	-7	5399

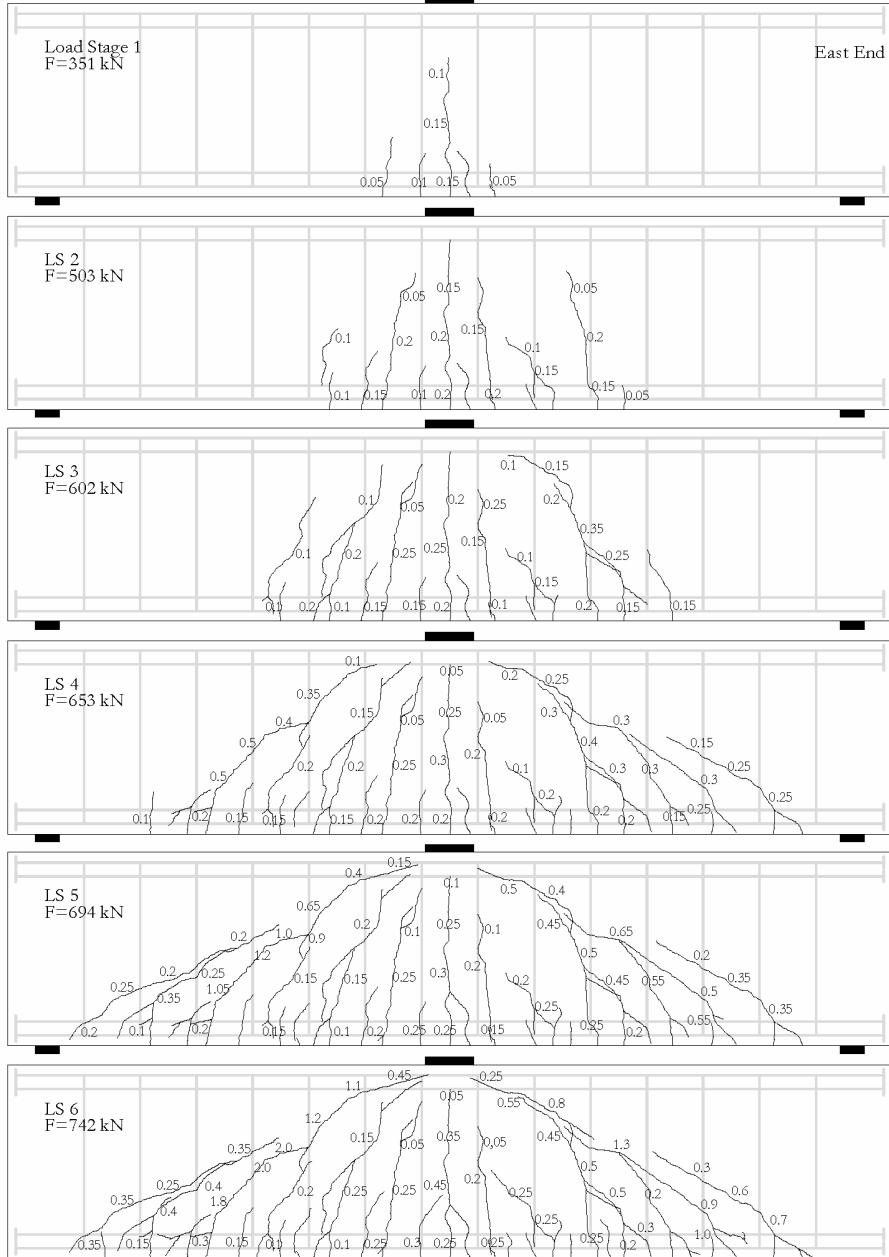
## Notes:

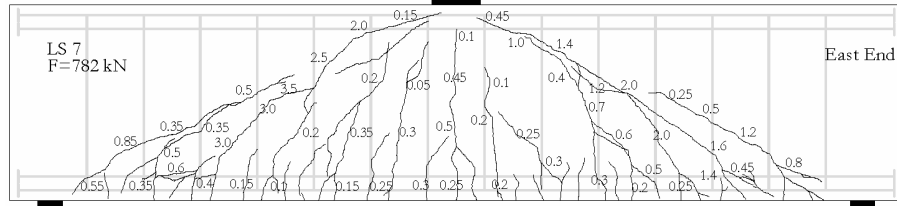
- 1) The data from LVDTs ES-TW-BE, ES-V, and ES-TE-BW as well as the data from most of the strain gauges is not presented for the sake of brevity.
- 2) LVDT WL-V did not work properly after Load Stage 7.

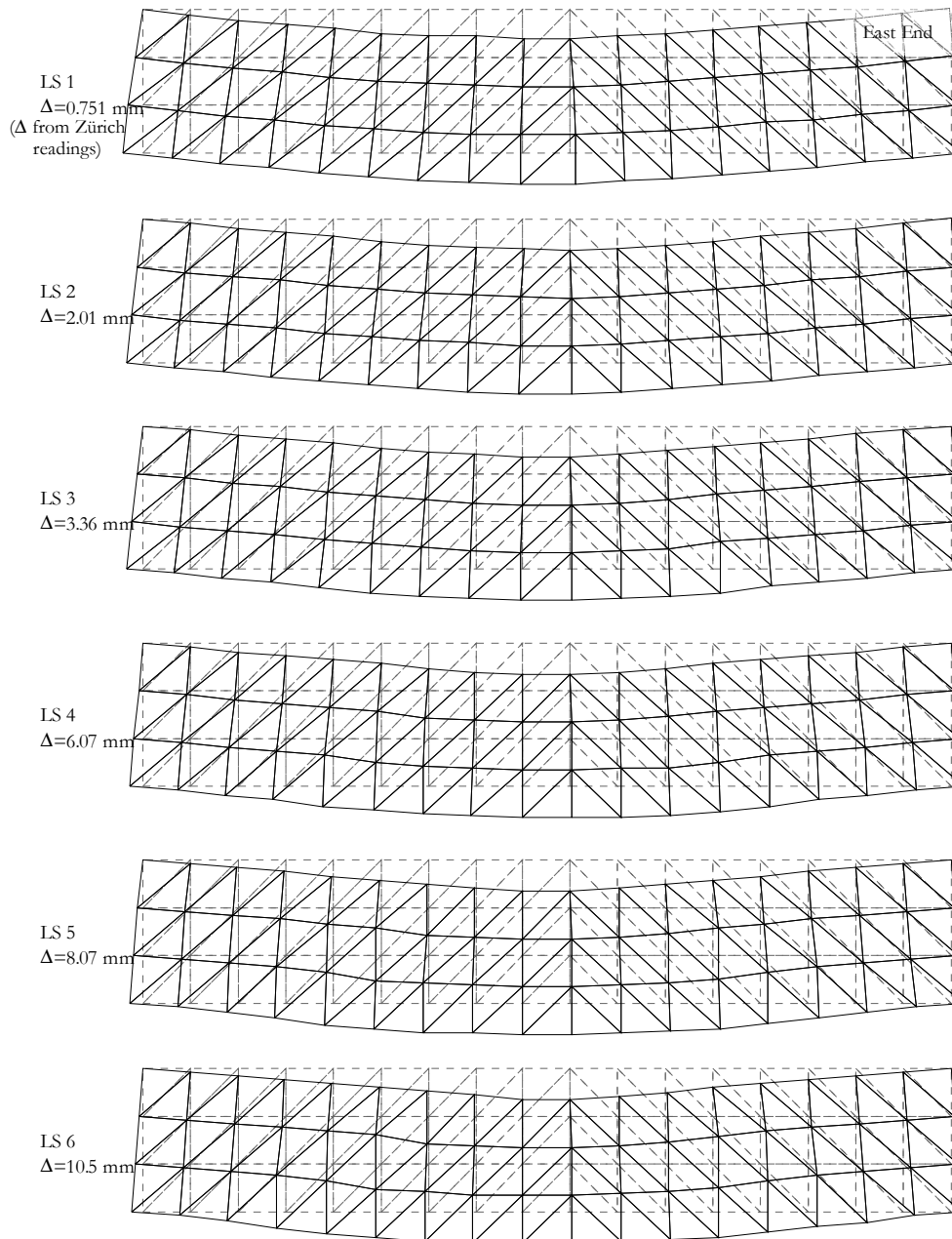


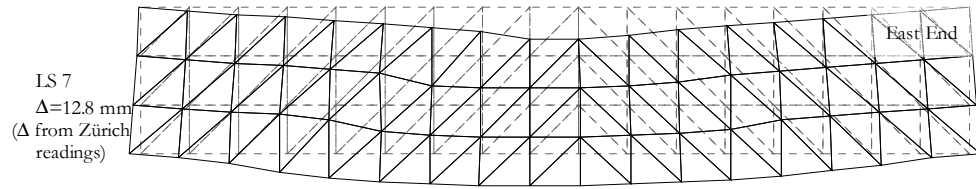


**Crack Diagrams, crack widths in (mm)**

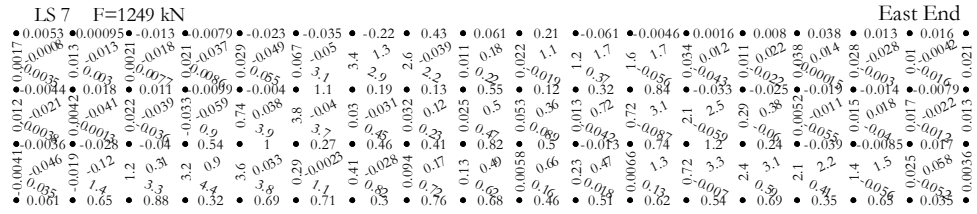




**Deformed shapes amplified to midspan displacement equivalent to 200 mm**







**B9. SPECIMEN L1C**

**Cast day:** June 19<sup>th</sup>, 2007

**Beam properties**

Cross section:  $b=1200$  mm,  $b=400$  mm

Effective depth: 1095 mm

Shear span: 2500 mm

Loading plates: 51/300/400 mm

Support plates: 51/150/400 mm

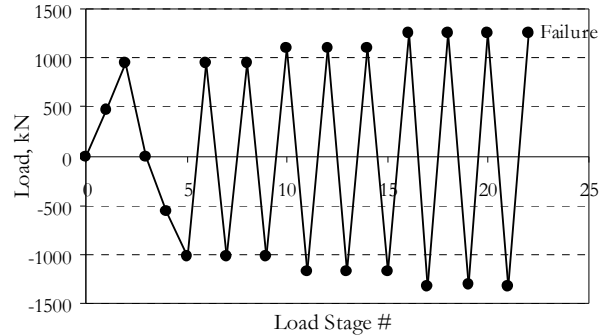
Longitudinal reinforcement:  $\rho_l=0.68\%$ ,  $f_y=650$  MPa

Transverse reinforcement:  $\rho_v=0.1\%$ ,  $f_{yv}=490$  MPa

Concrete:  $f'_c = 37.8$  MPa,  $\epsilon'_c=1770 \mu\epsilon$ ,  $a_g=20$  mm, *Modulus of rupture* = 3.7 MPa

Defects: no significant defects

**Test days:** November 12<sup>th</sup> – 14<sup>th</sup>, 2007

**Loading history****Test Remarks**

Maximum positive load: 1252.6 kN

Maximum negative load: 1330.7 kN

Displacement at failure: +13.7 mm

Failure mode: The beam failed in a relatively gradual manner with crushing above the most western diagonal crack near the edge of the top loading plate. Sounds indicating rupture of stirrups were heard after the load on the beam has started to decrease.

Other remarks:

- The formation and propagation of flexure-shear cracks was relatively gradual.



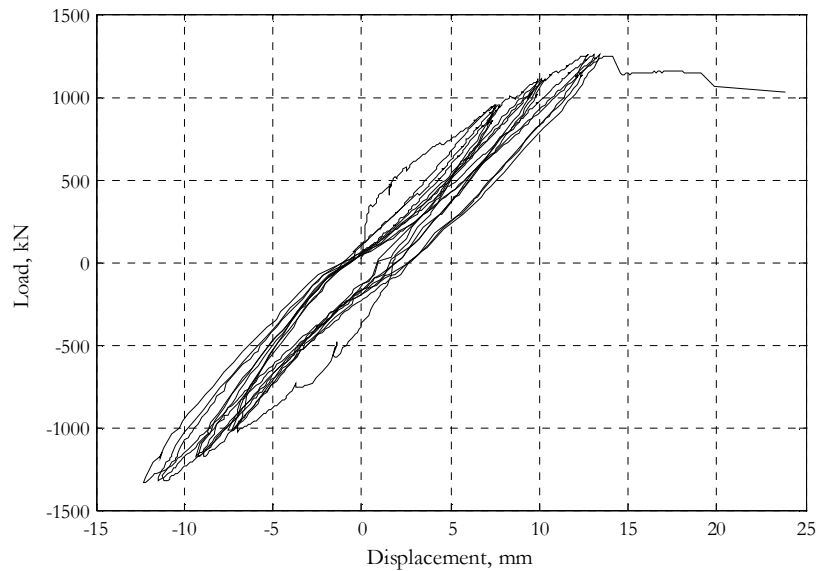
- A series of short lines crossing the major “positive” diagonal cracks at angle of about  $90^\circ$  were drawn on the south face of the beam at Load Stage 4. Close examination of these lines under positive load revealed that the crack slip was significant only at the bottom part of the beam where the flexure-shear cracks were relatively steep.

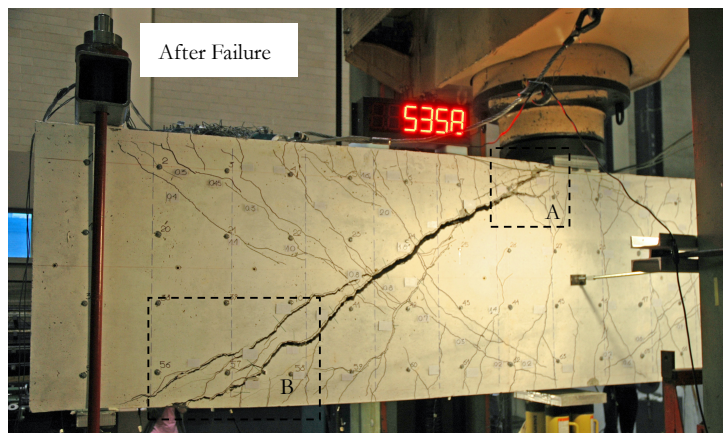
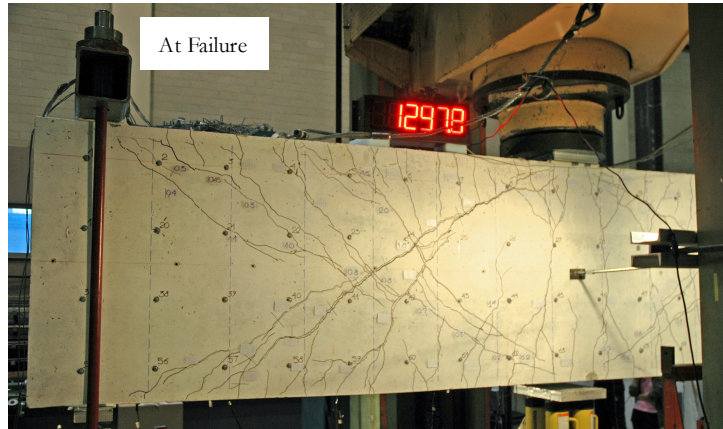
- The hydraulic pump providing oil for the four bottom jacks saturated at load of about -690 kN between load stages 4 and 5. In order to reset the pump, the specimen was partially unloaded.

- The readings from the four load cells which were used to measure the negative load indicated presence of small torsion on the beam while loading to LS 7.

- During the initial loading to LS 8 it was noticed that the pressure in the four bottom jacks was not completely dissipated.

### Global response





## Data summary

Load Stage	Data Set	Time elapsed	F	$\Delta=(BV+TV)/2$	BH	TH	WS-TW-BE	WS-V	WS-TE-BW	EL-TE-BW	EL-V	EL-TW-BE	WL-TW-BE	WL-TE-BW	Gauge 4B	Gauge 2	Gauge 22
(#)	(#)	(min)	(kN)	(mm)	(mm) $\times 10^{-3}$	(mm) $\times 10^{-3}$	(mm) $\times 10^{-3}$	(mm) $\times 10^{-3}$	(mm) $\times 10^{-3}$	(mm)	(mm)	(mm)	(mm)	(mm)	( $\mu\epsilon$ )	( $\mu\epsilon$ )	( $\mu\epsilon$ )
-	3	7	12.9	0.0	7	-2	0	0	-1	0.01	0.01	-0.01	0.00	0.00	3	0	0
1	53	24	477.0	1.6	478	-113	8	-3	-11	-0.01	0.00	-0.06	0.06	-0.03	70	1	1
2	142	84	953.9	7.5	1061	-152	-27	-9	-48	1.87	1.05	-0.04	1.91	-0.02	1833	11	11
3	191	155	1.3	1.8	147	49	-55	-2	-6	0.55	0.38	0.04	0.77	0.04	433	-6	-6
4	223	202	-573.1	-1.5	-55	605	-73	-5	3	0.28	0.23	0.16	0.37	0.16	-27	-15	-15
5	308	266	-1022.8	-7.0	-93	904	-77	-7	2	-0.02	1.07	2.11	0.18	1.98	-51	201	201
-	326	321	-165.0	-2.7	21	167	-18	-6	-4	0.04	0.73	1.23	0.24	1.02	121	177	177
-	388	1302	239.9	1.4	329	-169	-4	-1	-9	0.58	0.69	0.58	0.81	0.42	585	97	97
6	468	1315	951.4	7.5	1060	-314	-2	-4	-38	2.10	1.48	0.27	2.39	0.26	1860	80	80
-	496	1329	287.7	3.5	441	-211	-13	-2	-15	1.17	1.00	0.31	1.62	0.32	883	68	68
-	505	1332	-216.4	-0.6	66	62	-33	0	-1	0.35	0.72	0.67	0.83	0.64	199	110	110
7	543	1346	-1018.3	-7.3	-40	804	-67	-4	4	-0.02	1.40	2.48	0.34	2.37	1	601	601
-	561	1368	-305.0	-3.3	44	149	-3	-2	0	0.04	0.98	1.54	0.37	1.41	121	371	371
-	616	1381	415.7	3.2	542	-296	36	7	-8	1.08	1.06	0.53	1.43	0.45	898	113	113
8	683	1395	951.4	7.8	1076	-395	24	-5	-43	2.30	1.75	0.34	2.52	0.34	1870	101	101
-	718	1439	297.4	3.6	468	-296	13	-3	-20	1.34	1.24	0.42	1.72	0.39	883	89	89
-	731	1449	-166.4	-0.4	87	-48	-16	-2	-5	0.50	0.88	0.71	0.87	0.71	211	158	158
9	760	1463	-1021.8	-7.5	-11	724	-56	-7	-1	0.01	1.57	2.62	0.36	2.51	6	832	832
-	785	1510	-277.0	-3.2	65	79	-7	-3	-2	0.13	1.07	1.58	0.44	1.49	122	420	420
-	806	1516	130.1	0.9	276	-276	18	-2	-11	0.54	0.89	0.73	0.97	0.60	433	154	154
-	852	1523	570.7	4.9	724	-385	17	-5	-30	1.60	1.43	0.46	1.91	0.42	1213	121	121

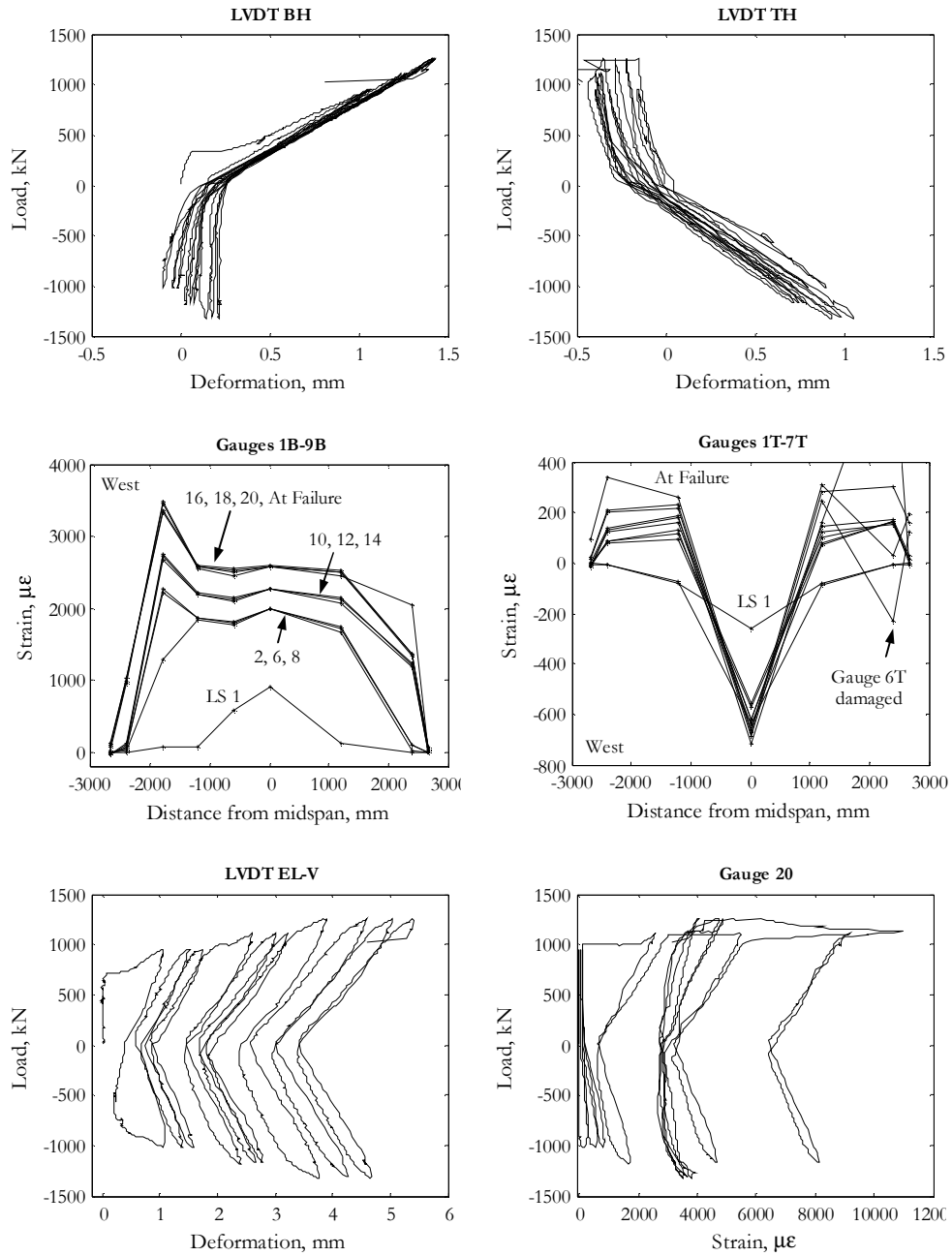
Load Stage	Data Set	Time elapsed	F	$\Delta=(BV+TV)/2$	BH	TH	WS-TW-BE	WS-V	WS-TE-BW	EL-TE-BW	EL-V	EL-TW-BE	WL-TW-BE	WL-TE-BW	Gauge 4B	Gauge 2	Gauge 22
10	916	1533	1103.9	9.9	1244	-394	8	-8	-54	3.27	2.60	0.55	3.24	0.47	2183	2579	2579
-	942	1564	458.9	5.6	653	-307	5	-1	-24	2.23	2.06	0.60	2.46	0.52	1180	1407	1407
-	957	1570	-101.1	1.3	179	-82	-5	1	-2	1.22	1.43	0.72	1.53	0.69	378	624	624
-	970	1571	-525.6	-3.3	64	249	-51	1	3	0.46	1.65	1.86	0.90	1.82	141	741	741
11	1010	1576	-1177.0	-8.9	31	794	-63	1	12	0.21	2.38	3.54	0.59	3.28	24	1672	1672
-	1038	1611	-473.1	-4.8	86	248	-40	-1	3	0.25	1.83	2.57	0.63	2.31	130	1089	1089
-	1053	1615	-1.1	-0.6	213	-167	-1	3	-1	0.54	1.46	1.54	0.97	1.22	300	649	649
-	1090	1641	403.9	3.8	590	-317	-3	-7	-28	1.78	1.96	0.92	1.95	0.73	953	1534	1534
12	1133	1646	1102.6	10.1	1260	-369	-5	-8	-55	3.55	3.01	0.77	3.58	0.60	2202	5416	5416
-	1159	1665	465.7	5.8	666	-309	-3	-1	-24	2.47	2.43	0.81	2.74	0.65	1213	4266	4266
-	1172	1669	-77.7	1.2	187	-145	-13	-1	-2	1.25	1.71	1.02	1.67	0.90	420	3241	3241
-	1198	1673	-485.1	-3.2	84	197	-57	-3	1	0.49	1.94	2.20	1.06	1.98	181	3566	3566
13	1249	1679	-1173.6	-9.2	56	746	-71	-6	5	0.22	2.64	3.85	0.72	3.66	59	4691	4691
-	1266	1705	-475.6	-5.0	108	249	-42	-2	4	0.30	2.09	2.78	0.79	2.67	168	3841	3841
-	1281	1713	1.7	-0.5	204	-196	-3	-1	-6	0.69	1.65	1.64	1.10	1.47	343	3229	3229
-	1302	1716	417.6	4.1	612	-305	2	-2	-20	2.02	2.24	1.02	2.21	0.92	993	4260	4260
14	1343	1720	1102.6	10.3	1268	-360	3	-2	-47	3.71	3.23	0.88	3.77	0.74	2215	9185	9185
-	1368	1763	499.5	6.1	687	-310	-2	1	-24	2.63	2.67	0.91	2.92	0.80	1248	7691	7691
-	1426	2736	-79.1	1.1	179	-170	-34	-7	-9	1.25	1.86	1.16	1.71	1.06	425	6416	6416
-	1450	2744	-491.3	-3.4	108	175	-64	-10	-9	0.53	2.10	2.42	1.19	2.22	220	6941	6941
15	1488	2749	-1171.5	-9.3	77	721	-81	-13	-5	0.26	2.79	4.01	0.87	3.89	97	8116	8116
-	1514	2794	-507.1	-5.3	116	246	-61	-12	-9	0.35	2.22	2.98	0.96	2.92	201	7191	7191
-	1528	2796	-3.3	-0.8	188	-204	-29	-10	-12	0.66	1.80	1.83	1.19	1.71	338	6466	6466
-	1559	2812	397.7	4.0	572	-330	-31	-12	-30	2.09	2.36	1.08	2.34	1.04	973	7366	7366

Load Stage	Data Set	Time elapsed	F	$\Delta=(BV+TV)/2$	BH	TH	WS-TW-BE	WS-V	WS-TE-BW	EL-TE-BW	EL-V	EL-TW-BE	WL-TW-BE	WL-TE-BW	Gauge 4B	Gauge 2	Gauge 22
-	1595	2816	850.1	8.1	1020	-377	-31	-11	-47	3.17	2.96	0.94	3.26	0.86	1770	8366	8366
16	1647	2824	1252.6	12.8	1419	-347	872	42	-88	4.43	3.89	1.06	5.16	1.06	2555	5191	5191
-	1680	2880	633.2	8.4	837	-284	664	44	-60	3.36	3.34	1.09	4.26	1.17	1590	3191	3191
-	1692	2881	180.6	4.0	350	-166	484	37	-33	2.18	2.63	1.19	3.26	1.33	733	2721	2721
-	1716	2892	-232.1	-0.1	132	46	393	29	-14	1.08	2.41	2.12	2.36	2.06	410	2949	2949
-	1748	2895	-634.1	-4.3	120	361	354	25	-13	0.61	2.70	3.22	1.87	3.25	285	3191	3191
17	1812	2903	-1326.6	-11.2	147	929	302	20	-7	0.48	3.76	5.35	1.50	5.37	160	3816	3816
-	1849	2947	-620.1	-6.7	179	396	332	24	-5	0.57	3.18	4.20	1.55	4.34	276	2919	2919
-	1863	2948	-116.0	-2.5	225	-15	381	27	-7	0.70	2.65	3.14	1.71	3.21	373	2846	2846
-	1902	2956	294.3	3.1	486	-221	512	27	-23	2.21	2.98	1.85	3.05	1.95	840	3241	3241
-	1938	2960	700.7	7.4	901	-260	702	36	-45	3.39	3.58	1.49	4.03	1.58	1558	3516	3516
18	2007	2970	1250.7	13.1	1437	-281	1144	71	-71	4.98	4.58	1.47	5.77	1.53	2570	4041	4041
-	2032	3007	661.4	8.7	854	-215	889	61	-51	3.85	4.01	1.48	4.79	1.62	1593	2969	2969
-	2041	3008	194.1	4.5	381	-115	696	52	-25	2.68	3.30	1.59	3.75	1.80	820	2749	2749
-	2059	3015	-208.5	-0.2	181	67	566	47	-8	1.39	3.00	2.65	2.59	2.76	461	2885	2885
-	2089	3018	-622.2	-4.7	176	391	521	45	-6	0.92	3.33	3.85	2.14	3.97	345	2871	2871
19	2145	3025	-1318.2	-11.4	180	980	449	41	-3	0.74	4.26	5.83	1.86	5.92	207	3666	3666
-	2163	3041	-685.5	-7.3	197	497	474	43	-4	0.80	3.71	4.76	1.90	4.94	305	2636	2636
-	2170	3041	-141.4	-2.8	229	46	532	47	-5	0.89	3.13	3.61	2.04	3.72	400	2776	2776
-	2194	3050	261.0	3.2	446	-145	652	42	-19	2.47	3.37	2.07	3.45	2.21	820	3291	3291
-	2210	3052	669.5	7.5	862	-181	857	51	-37	3.69	4.00	1.74	4.46	1.86	1525	3791	3791
20	2259	3063	1251.4	13.5	1431	-221	1226	75	-75	5.29	5.03	1.68	6.19	1.72	2578	4641	4641
-	2277	3083	691.4	9.2	878	-165	997	77	-38	4.24	4.49	1.72	5.23	1.87	1640	3066	3066
-	2286	3084	199.2	4.6	378	-60	784	69	-7	2.94	3.69	1.86	4.07	2.08	798	2871	2871

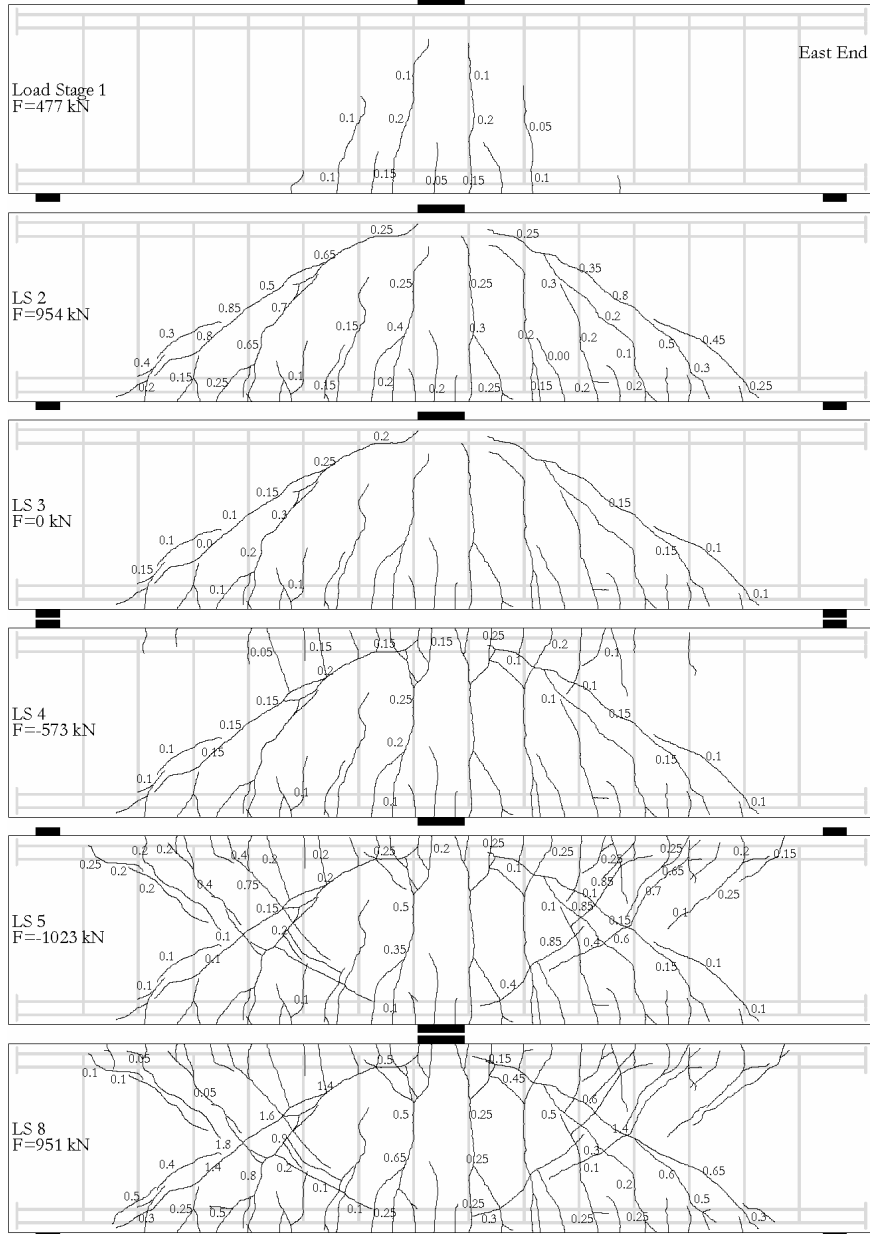
Load Stage	Data Set	Time elapsed	F	$\Delta=(BV+TV)/2$	BH	TH	WS-TW-BE	WS-V	WS-TE-BW	EL-TE-BW	EL-V	EL-TW-BE	WL-TW-BE	WL-TE-BW	Gauge 4B	Gauge 2	Gauge 22
-	2303	3089	-202.3	-0.4	212	105	639	70	10	1.56	3.42	3.04	2.79	3.22	463	2686	2686
-	2335	3092	-610.2	-4.9	209	436	592	68	11	1.13	3.77	4.27	2.39	4.41	363	2801	2801
21	2384	3098	-1330.7	-12.3	217	1061	543	71	12	0.93	4.68	6.30	2.31	6.88	228	3516	3516
-	2405	3121	-715.0	-8.0	220	566	570	71	7	0.97	4.12	5.19	2.30	5.80	325	2824	2824
-	2416	3122	-185.4	-3.5	236	140	629	75	7	1.04	3.58	4.06	2.38	4.57	418	2901	2901
-	2435	3133	248.2	3.0	415	-67	714	56	-7	2.69	3.74	2.28	3.78	2.72	793	3391	3391
-	2453	3135	650.1	7.4	810	-107	907	61	-29	3.91	4.35	1.94	4.88	2.21	1475	3791	3791
UL	2498	3141	1248.9	13.7	1426	-149	1276	94	-60	5.60	5.39	1.89	6.81	2.05	2593	4891	4891
-	2549	3147	1028.9	23.9	809	-467	5093	74	-20	4.09	4.58	1.96	26.47	24.034	1483	3141	3141

## Notes:

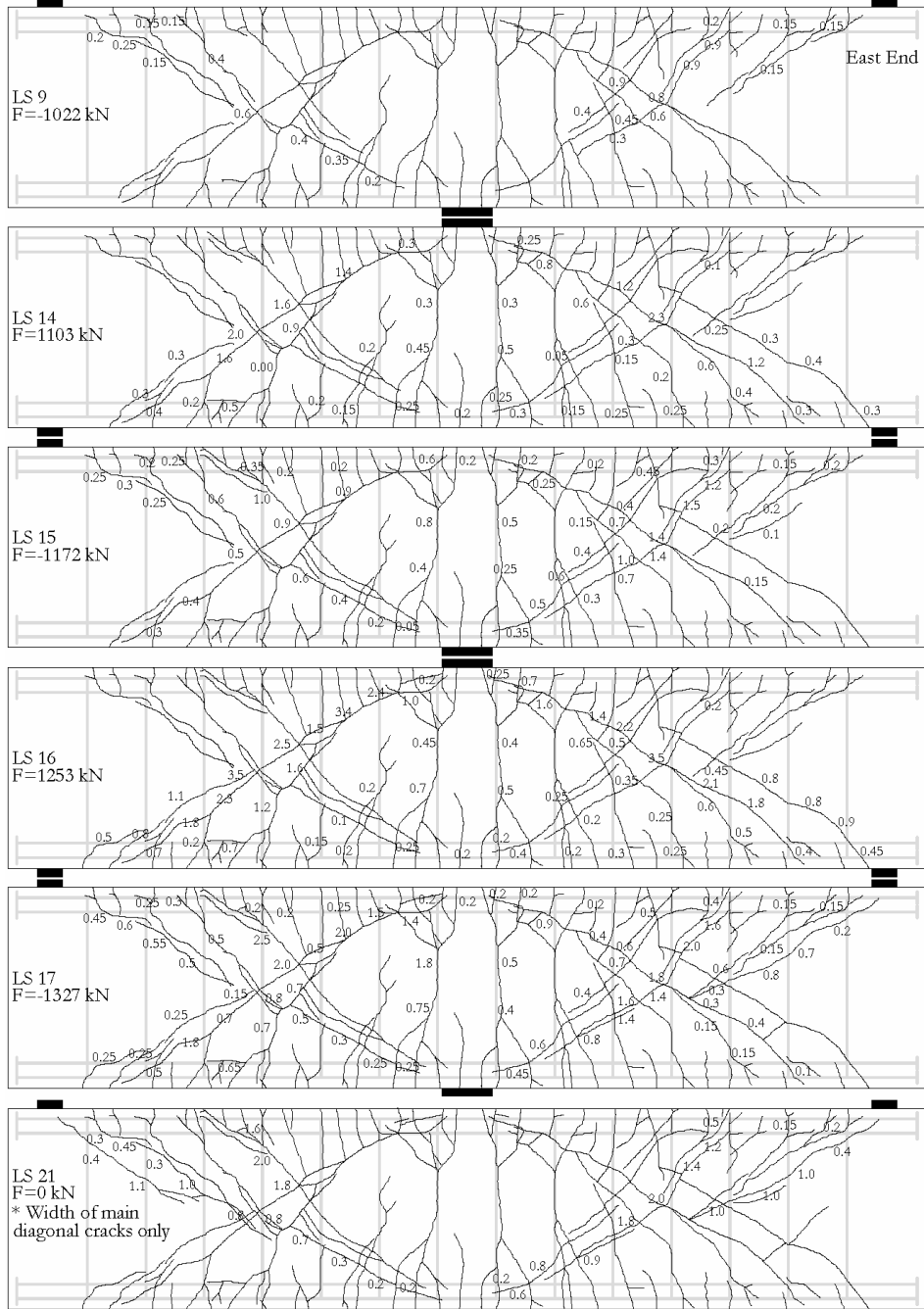
- 1) The data from LVDTs ES-TW-BE, ES-V, and ES-TE-BW as well as the data from most of the strain gauges is not presented for the sake of brevity.
- 2) The data from LVDT WL-V is not shown since the measuring device did not work properly.

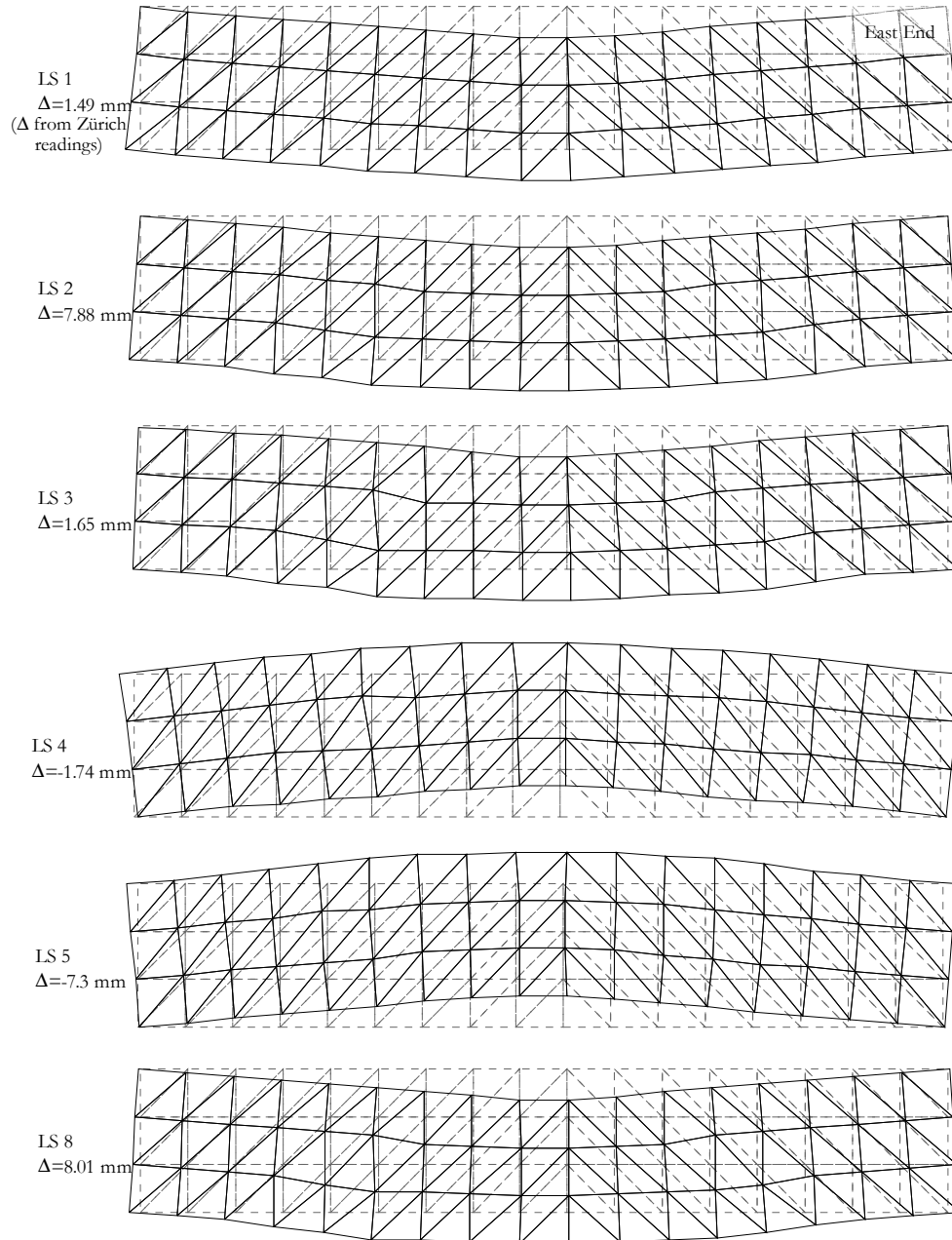


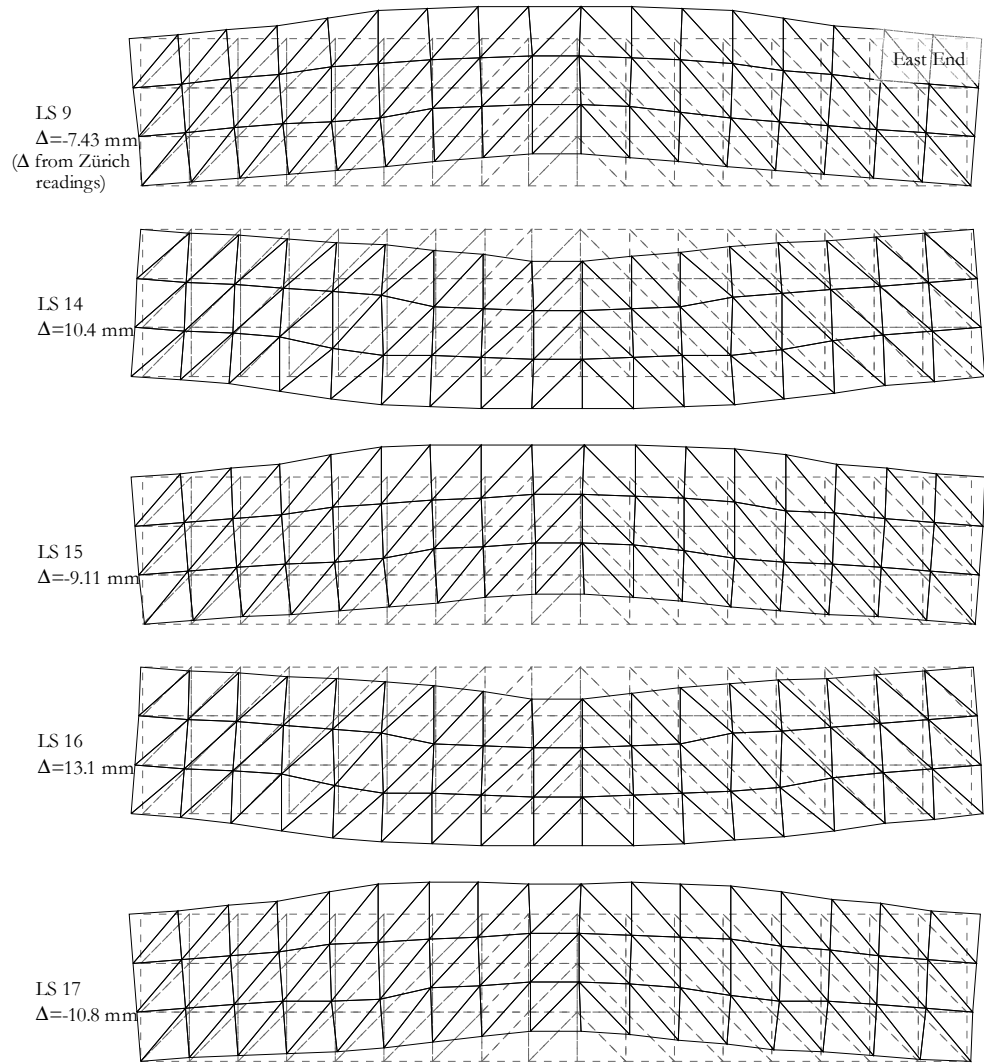
## Crack Diagrams, crack widths in (mm)







**Deformed shapes amplified to midspan displacement equivalent to 200 mm**



Zürich readings over 300/300 mm grid, deformations in (mm)

LS 1 F=477 kN East End

LS 2 F=954 kN

LS 3 F=0 kN

LS 4 F=-573 kN

LS 5 F=-1023 kN

LS 8 F=951 kN

The image contains six tables of numerical data, each representing a different load case (LS 1, LS 2, LS 3, LS 4, LS 5, LS 8) at an 'East End' location. Each table consists of a grid of values, where each value is a decimal number representing deformation in millimeters. The values are arranged in rows and columns, with some values rotated slightly for readability. The tables are separated by their respective load case labels and force values (e.g., F=477 kN, F=954 kN, F=0 kN, F=-573 kN, F=-1023 kN, F=951 kN). The data points are distributed across the grid, showing variations in deformation across the 300/300 mm grid.



**B10. SPECIMEN SB**

**Cast day:** May 16<sup>th</sup>, 2007

**Beam properties**

Cross section:  $b=1200$  mm,  $b=400$  mm

Effective depth: 1070 mm

Shear span: 1700 mm

Loading plates: 51/300/400 mm

Support plates: 51/150/400 mm

Longitudinal reinforcement:  $\rho_l=0.60\%$ ,  $f_y=650$  MPa

Transverse reinforcement:  $\rho_t=0\%$

Concrete:  $f'_c = 30.5$  MPa,  $\epsilon'_c=1460 \mu\epsilon$ ,  $a_g=20$  mm, *Modulus of rupture* = 3.6 MPa

Defects: no significant defects

**Test day:** November 22<sup>nd</sup>, 2007

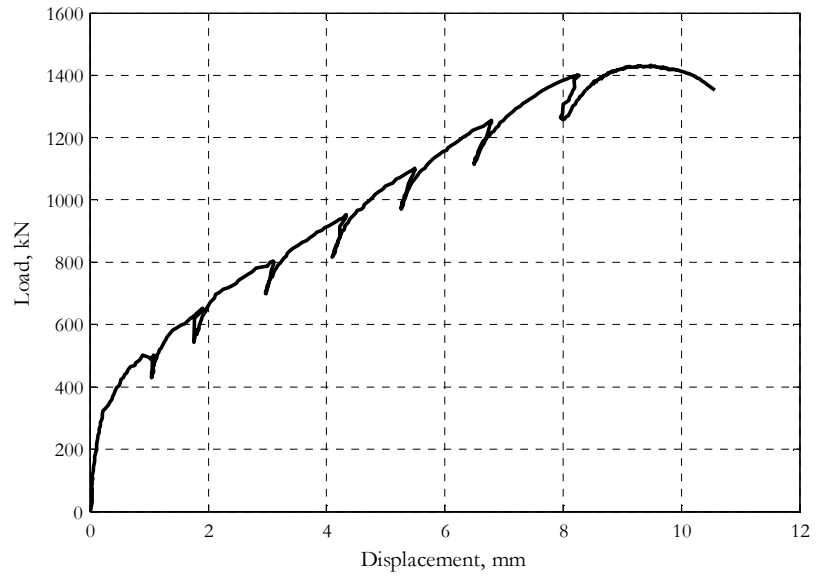
**Test Remarks**

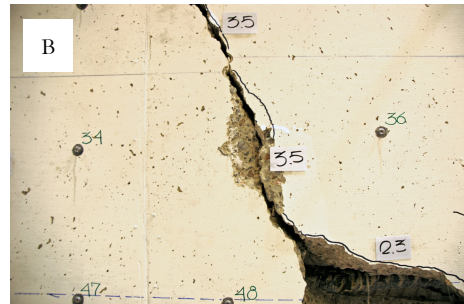
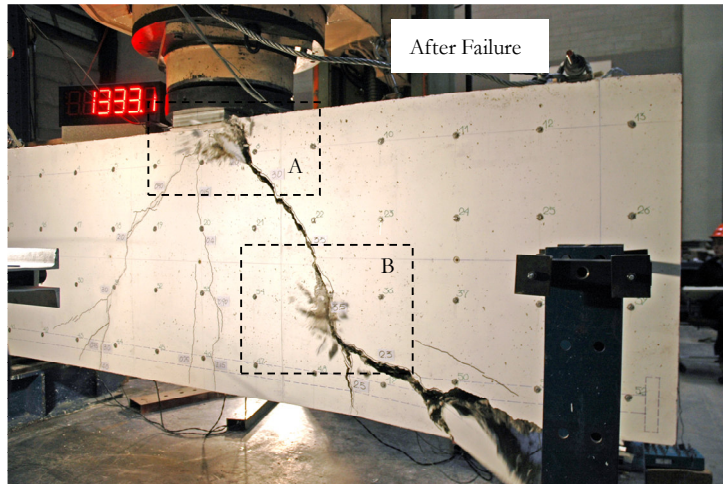
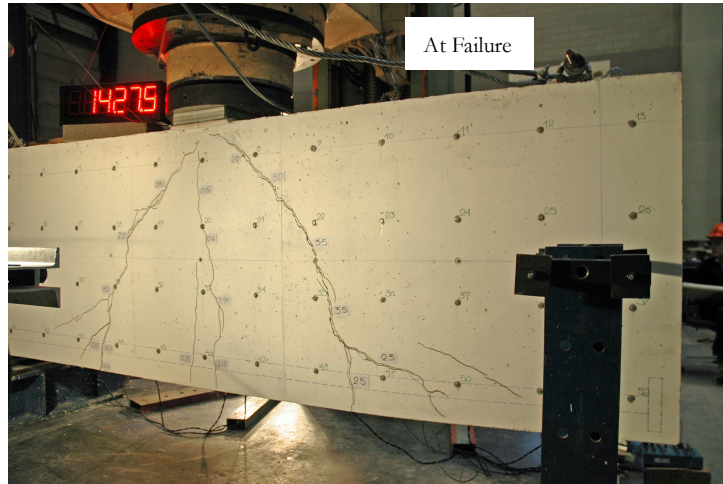
Maximum load: 1431.3 kN

Displacement at maximum load: 9.5 mm

Failure mode: The load on the beam had started to decrease when explosive crushing of concrete occurred at two locations: above the eastern diagonal crack near the edge of the loading plate, and at the eastern diagonal crack at the middle of the bottom half of the section. Big pieces of concrete separated from the bottom part of the specimen in the zone confined between the critical diagonal crack and the east support.

Global response





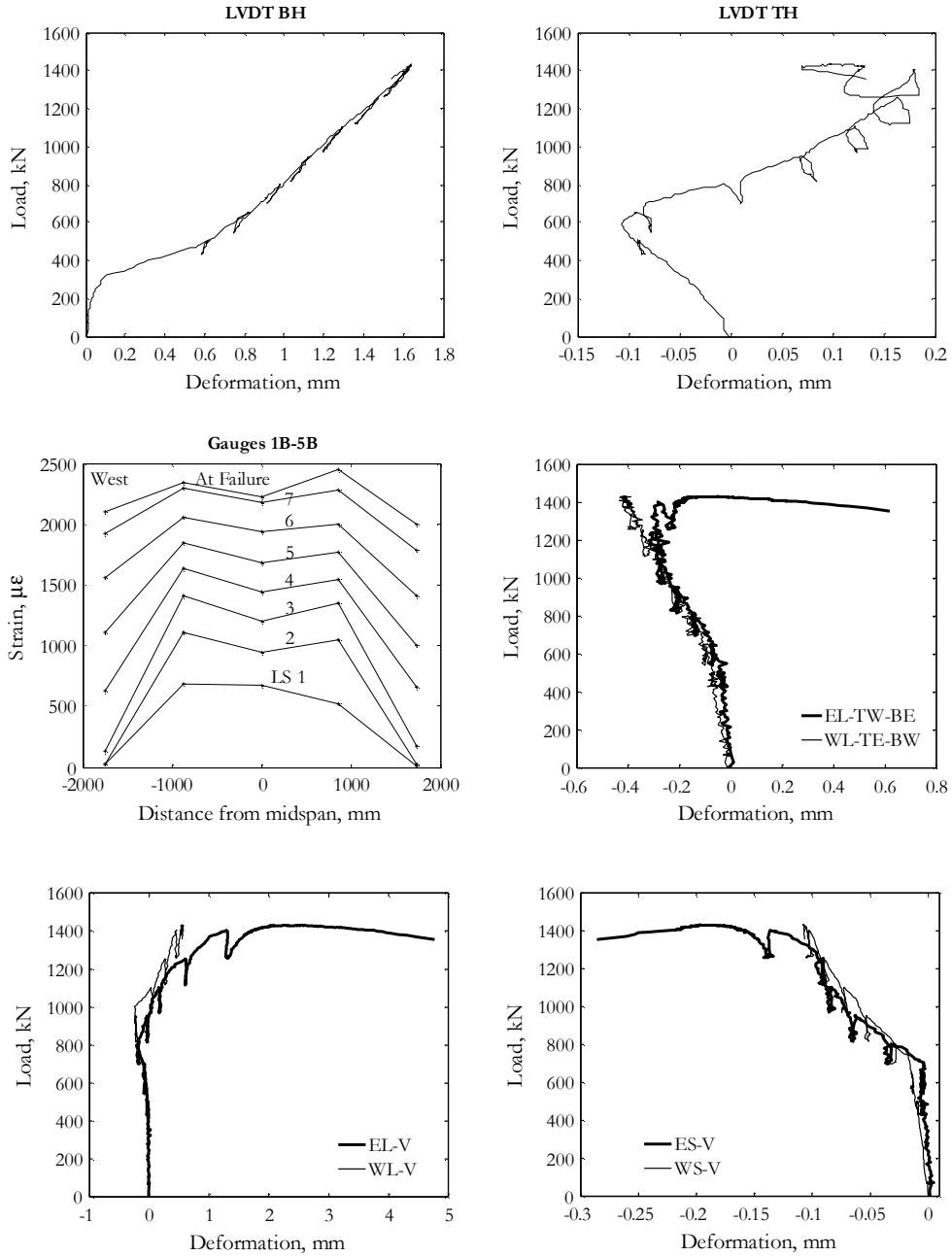


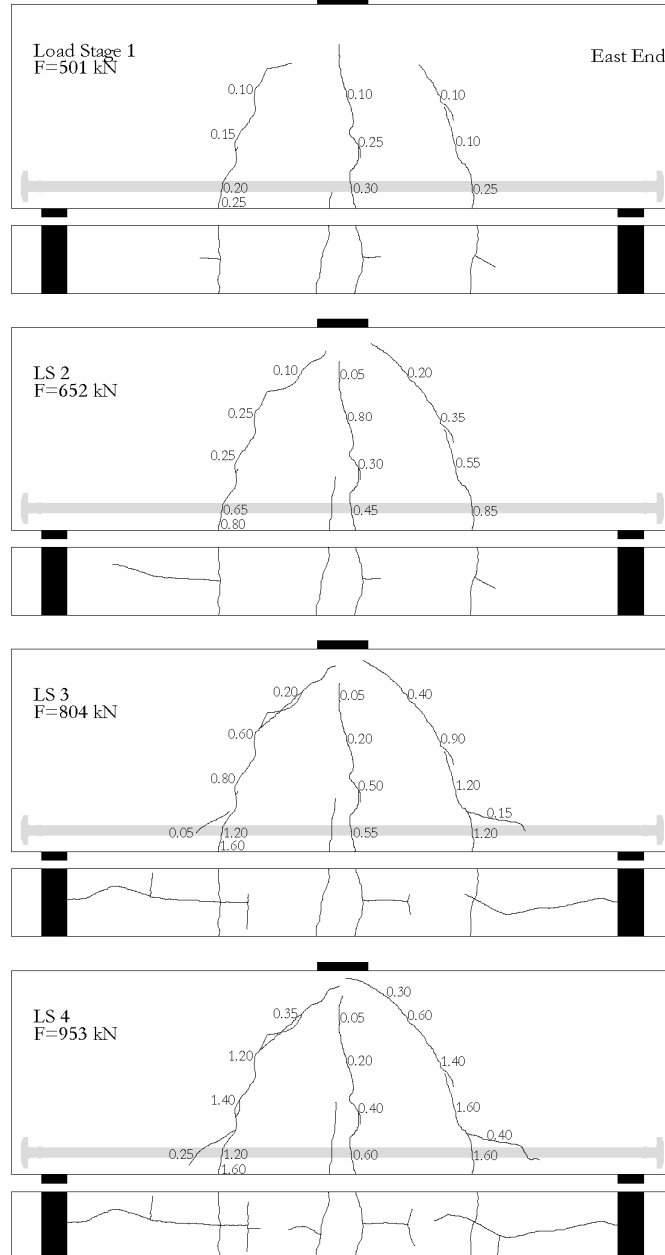
## Data summary

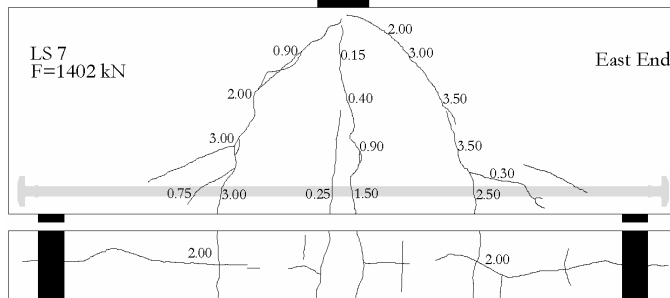
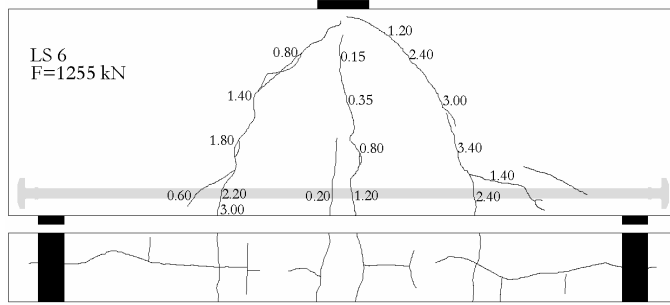
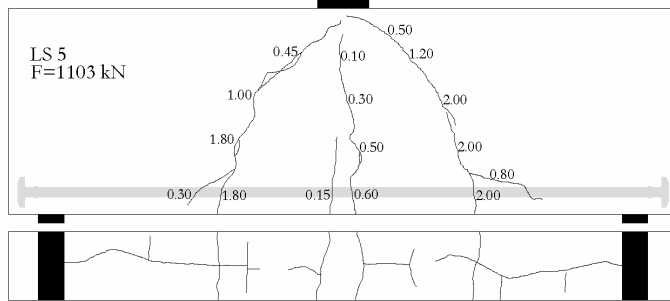
Load Stage	Data Set	Time elapsed	F	$\Delta=(BV+TV)/2$	BH	TH	ES-TF-BW	ES-V	ES-TW-BE	WS-TW-BE	WS-V	WS-TF-BW	EL-TF-BW	EL-V	EL-TW-BE	WL-TW-BE	WL-V	WL-TF-BW	Gauge 5B
(#)	(#)	(min)	(kN)	(mm)	(mm) $\times 10^{-3}$	(mm) $\times 10^{-3}$	(mm) $\times 10^{-3}$	(mm) $\times 10^{-3}$	(mm) $\times 10^{-3}$	(mm) $\times 10^{-3}$	(mm) $\times 10^{-3}$	(mm) $\times 10^{-3}$	(mm)	(mm)	(mm)	(mm)	(mm)	(mm)	( $\mu\epsilon$ )
-	25	42	193.7	0.1	34	-26	5	1	-3	2	-4	-10	0.00	-0.02	-0.01	-0.01	-0.01	-0.04	6
-	38	45	302.5	0.2	89	-43	5	-1	-7	3	-6	-16	0.02	-0.02	-0.02	-0.01	-0.02	-0.05	9
-	42	46	343.6	0.3	194	-54	6	0	-11	3	-7	-18	0.03	-0.01	-0.03	-0.01	-0.03	-0.06	10
-	47	47	386.1	0.4	294	-62	5	-3	-12	3	-8	-19	0.03	-0.02	-0.04	-0.02	-0.01	-0.06	11
-	52	47	430.7	0.6	429	-74	7	-3	-15	3	-8	-20	0.04	-0.01	-0.01	0.00	-0.02	-0.06	12
-	56	48	464.4	0.7	530	-81	6	-5	-16	2	-9	-21	0.09	-0.01	-0.03	-0.02	-0.02	-0.07	13
1	68	50	501.3	1.1	618	-91	7	-5	-20	4	-9	-25	0.19	-0.03	-0.03	0.20	-0.04	-0.08	15
-	93	93	533.2	1.2	662	-99	8	-6	-21	5	-12	-29	0.22	-0.03	-0.05	0.26	-0.05	-0.07	17
-	97	94	569.4	1.4	702	-105	12	-6	-24	5	-13	-31	0.27	-0.04	-0.05	0.32	-0.06	-0.09	18
-	100	94	597.6	1.5	750	-106	12	-6	-27	5	-13	-33	0.37	-0.05	-0.06	0.40	-0.06	-0.09	20
2	110	96	651.9	1.9	816	-92	8	-6	-34	0	-14	-37	0.58	-0.07	-0.08	0.59	-0.11	-0.09	25
-	134	119	680.1	2.1	858	-84	6	-4	-33	-3	-15	-38	0.66	-0.08	-0.08	0.68	-0.10	-0.12	27
-	138	120	712.6	2.3	894	-76	3	-8	-35	-4	-16	-41	0.75	-0.11	-0.09	0.78	-0.13	-0.10	32
-	142	122	743.2	2.5	923	-54	-14	-15	-38	-10	-17	-45	0.95	-0.15	-0.11	0.90	-0.14	-0.14	59
-	145	124	769.4	2.7	947	-40	-21	-18	-42	-18	-25	-47	1.10	-0.17	-0.12	1.03	-0.16	-0.15	79
3	150	126	803.8	3.1	982	-5	-36	-32	-47	-27	-31	-49	1.35	-0.20	-0.15	1.22	-0.18	-0.17	169
-	181	161	836.9	3.4	1026	13	-44	-39	-49	-29	-33	-46	1.52	-0.16	-0.17	1.37	-0.20	-0.17	262
-	184	163	863.2	3.6	1049	23	-48	-45	-54	-34	-38	-51	1.64	-0.13	-0.17	1.45	-0.21	-0.18	339
-	187	165	888.8	3.8	1075	36	-51	-48	-55	-38	-42	-54	1.76	-0.09	-0.18	1.55	-0.23	-0.20	419
-	191	167	916.9	4.0	1106	53	-56	-54	-57	-45	-48	-57	1.93	-0.07	-0.20	1.72	-0.24	-0.22	532
4	197	169	952.6	4.3	1136	70	-60	-63	-62	-50	-53	-62	2.12	-0.04	-0.22	1.87	-0.23	-0.24	649

Load Stage	Data Set	Time elapsed	F	$\Delta=(BV+TV)/2$	BH	TH	ES-TE-BW	ES-V	ES-TW-BE	WS-TW-BE	WS-V	WS-TE-BW	EL-TE-BW	EL-V	EL-TW-BE	WL-TW-BE	WL-V	WL-TE-BW	Gauge 5B
-	234	215	985.1	4.6	1169	79	-66	-71	-70	-54	-58	-65	2.27	0.03	-0.24	2.04	-0.24	-0.25	762
-	238	216	1018.2	4.8	1203	87	-66	-74	-73	-56	-60	-67	2.37	0.05	-0.23	2.14	-0.19	-0.25	789
-	242	217	1050.7	5.1	1239	102	-67	-78	-75	-57	-64	-71	2.48	0.07	-0.26	2.28	-0.09	-0.28	852
5	249	218	1102.6	5.5	1291	122	-66	-84	-80	-59	-72	-79	2.71	0.16	-0.27	2.54	0.03	-0.28	999
-	285	250	1129.4	5.8	1329	125	-61	-89	-86	-61	-77	-82	2.91	0.23	-0.29	2.67	0.11	-0.29	1092
-	288	251	1155.1	6.0	1359	134	-58	-93	-88	-62	-80	-85	3.02	0.27	-0.31	2.77	0.15	-0.31	1134
-	292	252	1181.9	6.2	1389	140	-52	-95	-90	-64	-84	-89	3.14	0.33	-0.31	2.87	0.15	-0.31	1202
-	296	254	1211.9	6.4	1428	150	-39	-97	-92	-65	-86	-92	3.27	0.42	-0.31	2.99	0.20	-0.33	1274
6	301	255	1255.1	6.8	1473	164	26	-90	-96	-65	-90	-94	3.51	0.61	-0.29	3.15	0.26	-0.34	1414
-	335	285	1285.1	7.2	1501	157	59	-96	-105	-65	-94	-96	3.76	0.75	-0.29	3.32	0.34	-0.37	1519
-	339	285	1315.7	7.4	1536	167	86	-103	-107	-69	-96	-99	3.90	0.85	-0.31	3.42	0.36	-0.37	1579
-	342	286	1341.3	7.6	1567	174	113	-111	-111	-70	-98	-100	4.01	0.93	-0.30	3.53	0.38	-0.38	1637
-	345	287	1369.4	7.8	1595	177	132	-118	-114	-72	-99	-102	4.21	1.01	-0.30	3.63	0.41	-0.39	1702
7	353	288	1401.9	8.2	1626	181	220	-136	-115	-73	-103	-106	4.47	1.29	-0.28	3.80	0.46	-0.40	1792
UL	471	335	1431.3	9.5	1641	99	665	-198	-119	-75	-108	-108	5.68	2.53	-0.05	4.07	0.55	-0.41	1992
-	516	338	1353.2	10.6	1537	132	1599	-286	-109	-75	-106	-107	7.32	4.77	0.62	3.96	0.55	-0.41	2109

Note: The data from gauges 1B to 4B is not presented for the sake of brevity.

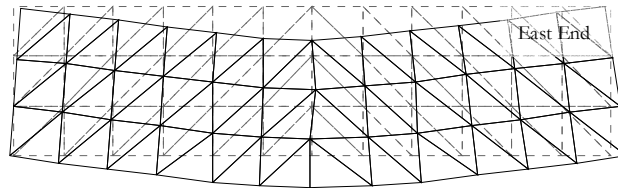


**Crack Diagrams, crack widths in (mm)**

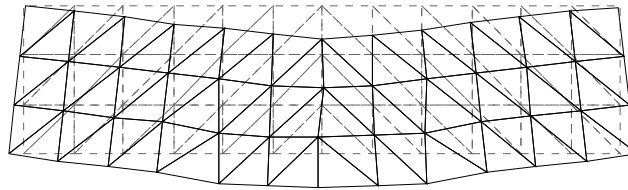


## Deformed shapes amplified to midspan displacement equivalent to 200 mm

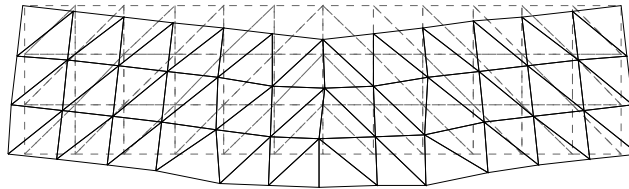
LS 1  
 $\Delta=1.36$  mm  
( $\Delta$  from Zürich  
readings)



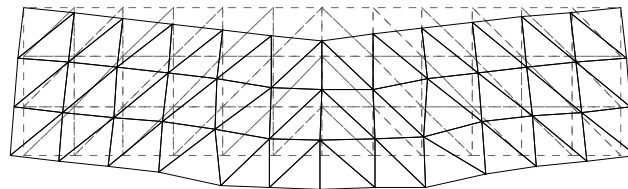
LS 2  
 $\Delta=2.11$  mm



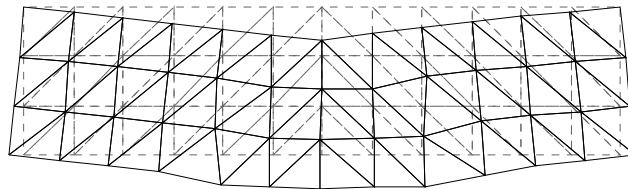
LS 3  
 $\Delta=3.21$  mm



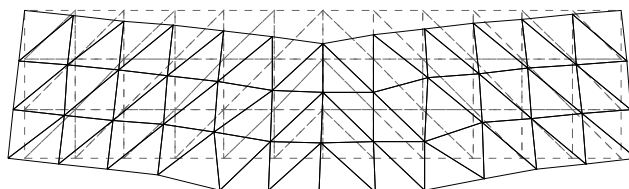
LS 4  
 $\Delta=4.59$  mm

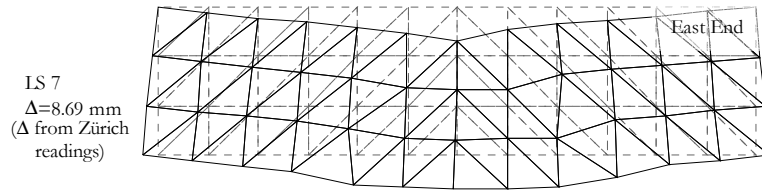


LS 5  
 $\Delta=5.92$  mm



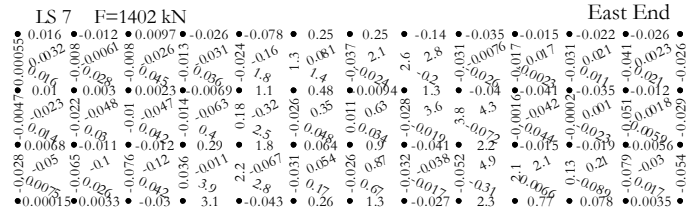
LS 6  
 $\Delta=7.1$  mm











**B11. SPECIMEN MB**

**Cast day:** May 16<sup>th</sup>, 2007

**Beam properties**

Cross section:  $b=1200$  mm,  $b=400$  mm

Effective depth: 1070 mm

Shear span: 1700 mm

Loading plates: 51/300/400 mm

Support plates: 51/150/400 mm

Longitudinal reinforcement:  $\rho_l=0.60\%$ ,  $f_y=650$  MPa

Transverse reinforcement:  $\rho_t=0\%$

Concrete:  $f_c' = 30.5$  MPa,  $\epsilon_c'=1460$   $\mu\epsilon$ ,  $a_g=20$  mm, *Modulus of rupture* = 3.6 MPa

Defects: no significant defects

**Test day:** November 28<sup>th</sup>, 2007

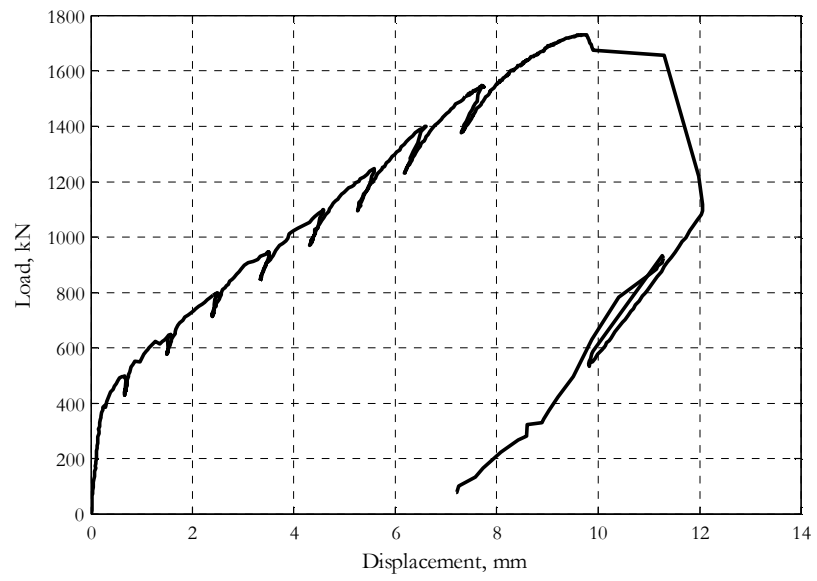
**Test Remarks**

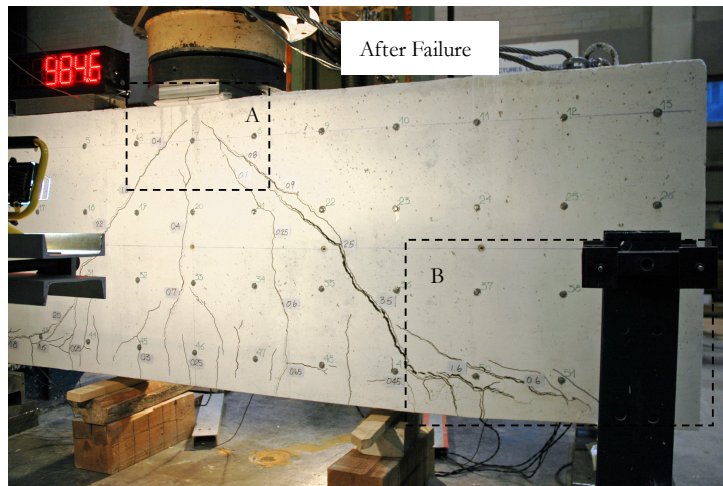
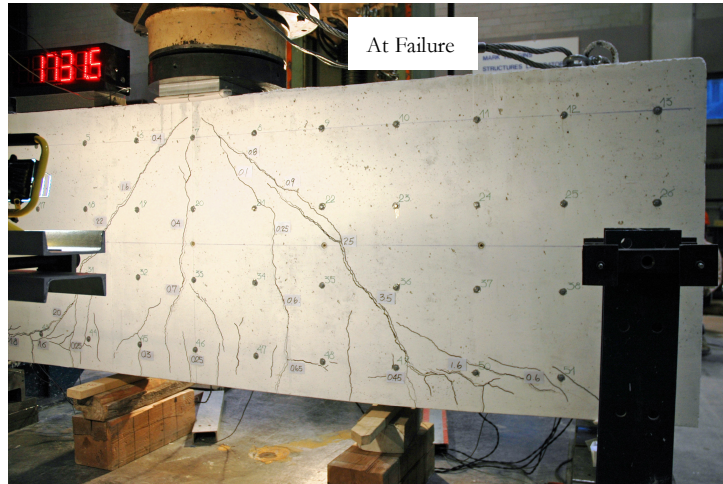
Maximum load: 1731.2 kN

Displacement at maximum load: 9.6 mm

Failure mode: The specimen failed with sudden widening of the most eastern diagonal crack and splitting along the lap splice between the straight bars and the anchor hooks.

Global response

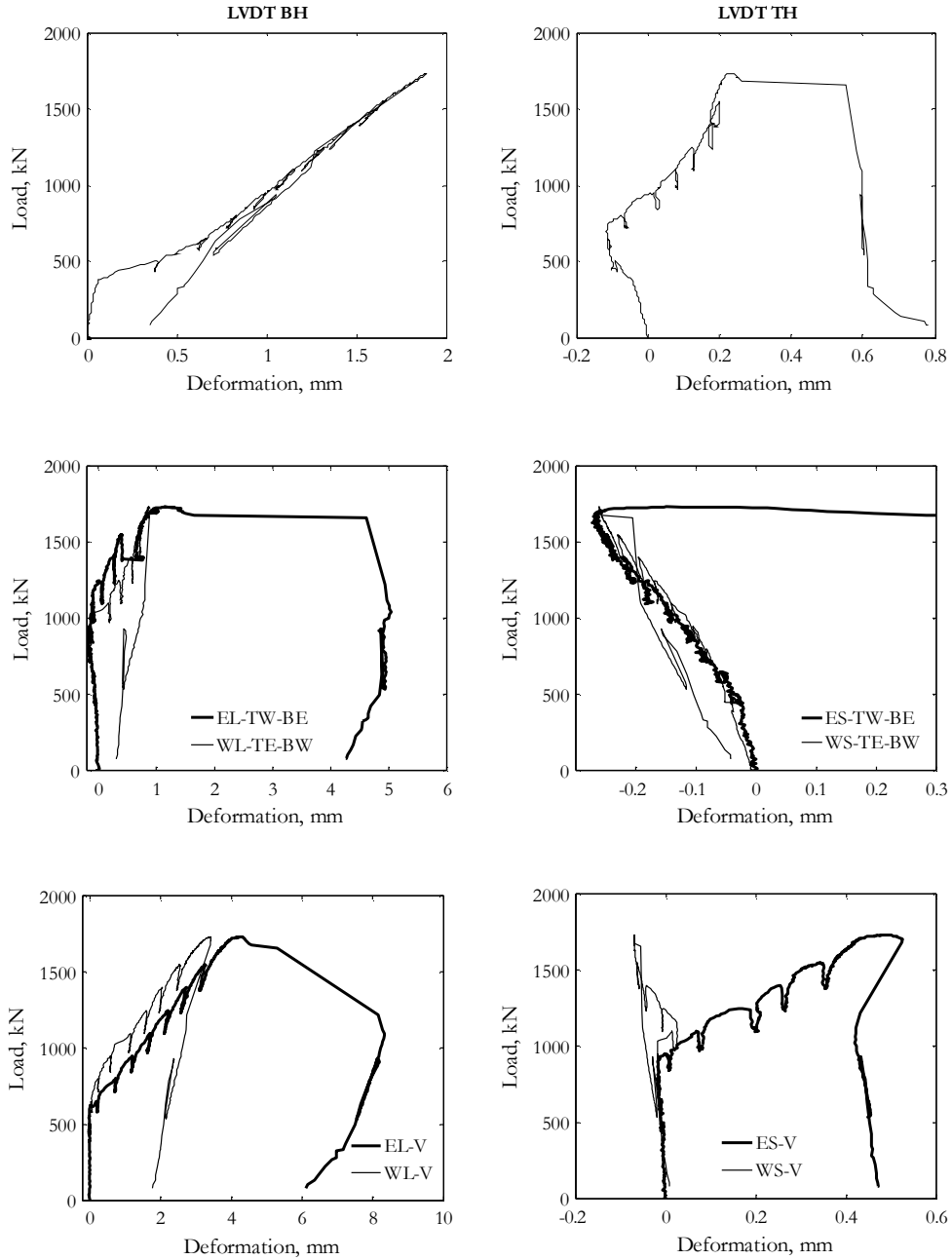


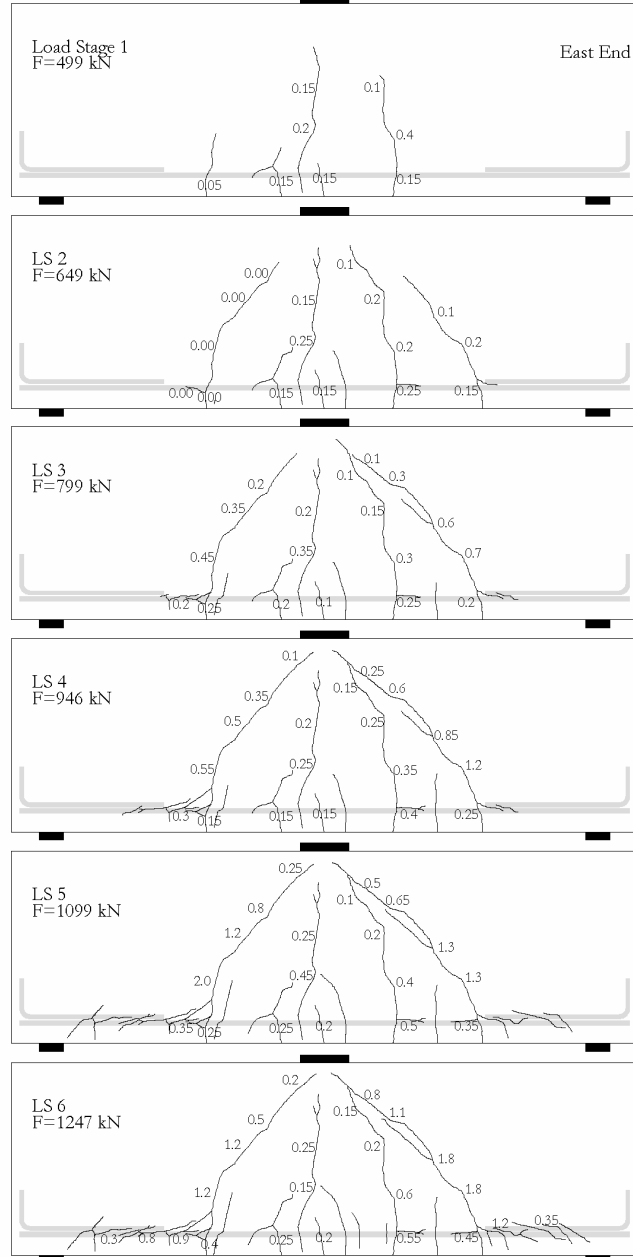


## Data summary

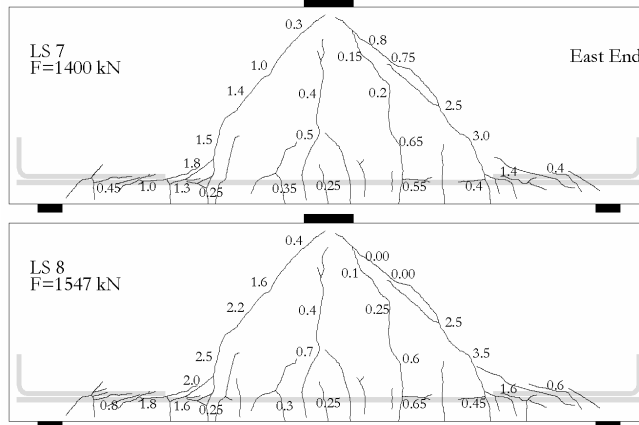
Load Stage	Data Set	Time elapsed	F	$\Delta=(BV+TV)/2$	BH	TH	ES-TE-BW	ES-V	ES-TW-BE	WS-TW-BE	WS-V	WS-TE-BW	EL-TE-BW	EL-V	EL-TW-BE	WL-TW-BE	WL-V	WL-TE-BW
(#)	(#)	(min)	(kN)	(mm)	(mm) $\times 10^{-3}$	(mm) $\times 10^{-3}$	(mm) $\times 10^{-3}$	(mm) $\times 10^{-3}$	(mm) $\times 10^{-3}$	(mm) $\times 10^{-3}$	(mm) $\times 10^{-3}$	(mm) $\times 10^{-3}$	(mm)	(mm)	(mm)	(mm)	(mm)	(mm)
-	53	51	376.8	0.2	71	-44	-1	-6	-12	7	-9	-20	0.02	-0.01	-0.04	0.03	-0.01	-0.05
1	69	89	498.7	0.7	395	-92	3	-8	-18	11	-8	-22	0.11	0.01	-0.06	0.08	-0.02	-0.05
-	98	125	558.7	1.0	507	-106	4	-6	-24	9	-11	-28	0.18	-0.01	-0.05	0.22	-0.01	-0.07
-	105	126	614.3	1.2	610	-111	3	-10	-24	11	-11	-31	0.22	0.02	-0.07	0.31	0.02	-0.07
2	113	127	648.7	1.6	663	-112	11	-10	-29	14	-11	-31	0.51	0.19	-0.10	0.38	0.06	-0.08
-	136	165	699.9	1.8	719	-113	10	-15	-38	14	-15	-35	0.65	0.30	-0.11	0.43	0.08	-0.10
-	141	168	742.4	2.1	770	-110	20	-16	-41	18	-16	-38	0.87	0.45	-0.14	0.52	0.13	-0.11
3	150	171	798.7	2.5	834	-73	60	-16	-47	22	-16	-41	1.18	0.73	-0.13	0.72	0.23	-0.13
-	180	208	841.2	2.7	879	-58	77	-16	-48	25	-18	-45	1.33	0.86	-0.16	0.84	0.30	-0.13
-	185	209	884.9	3.0	928	-42	95	-17	-53	29	-18	-48	1.44	0.97	-0.17	0.97	0.38	-0.14
-	188	210	913.1	3.2	956	-21	122	-15	-55	31	-18	-49	1.56	1.06	-0.16	1.13	0.47	-0.15
4	196	211	946.2	3.5	999	11	176	-2	-59	40	-18	-52	1.72	1.21	-0.15	1.35	0.59	-0.15
-	230	242	978.7	3.8	1035	29	235	17	-65	49	-18	-56	1.88	1.37	-0.13	1.48	0.66	-0.14
-	235	245	1024.3	4.0	1076	41	275	33	-70	56	-19	-59	2.03	1.49	-0.13	1.58	0.72	-0.12
-	239	246	1054.9	4.3	1110	62	317	53	-74	120	1	-66	2.14	1.60	-0.11	1.83	0.98	0.08
5	244	246	1098.7	4.6	1152	76	362	67	-77	167	13	-71	2.27	1.71	-0.11	1.99	1.16	0.18
-	285	277	1131.2	4.8	1195	85	407	89	-78	200	25	-73	2.42	1.84	-0.09	2.14	1.27	0.20
-	291	278	1176.8	5.1	1241	97	464	98	-85	239	19	-77	2.56	1.95	-0.09	2.28	1.39	0.24
-	296	279	1210.6	5.3	1280	109	552	122	-87	277	8	-80	2.69	2.08	-0.05	2.39	1.48	0.29
6	301	281	1246.8	5.6	1319	124	659	170	-91	334	-6	-84	2.86	2.21	0.02	2.54	1.61	0.34
-	338	314	1276.8	5.9	1362	145	787	201	-99	390	-14	-88	3.06	2.39	0.10	2.70	1.76	0.43

Load Stage	Data Set	Time elapsed	F	$\Delta=(BV+TV)/2$	BH	TH	ES-TE-BW	ES-V	ES-TW-BE	WS-TW-BE	WS-V	WS-TE-BW	EL-TE-BW	EL-V	EL-TW-BE	WL-TW-BE	WL-V	WL-TE-BW
-	344	315	1326.8	6.1	1409	156	862	212	-104	422	-21	-92	3.20	2.50	0.15	2.81	1.83	0.45
-	348	316	1366.8	6.3	1450	167	937	228	-107	471	-31	-95	3.32	2.60	0.18	2.93	1.93	0.51
7	353	316	1399.9	6.6	1490	180	1056	254	-110	535	-44	-98	3.46	2.74	0.26	3.07	2.05	0.58
-	390	346	1426.2	6.9	1521	177	1163	283	-119	590	-54	-105	3.62	2.89	0.29	3.22	2.20	0.61
-	396	347	1469.9	7.1	1569	185	1225	287	-123	621	-57	-109	3.75	2.99	0.32	3.35	2.30	0.63
-	401	348	1504.9	7.4	1603	191	1284	299	-125	653	-60	-111	3.87	3.09	0.34	3.47	2.39	0.65
8	429	349	1546.8	7.7	1653	201	1402	343	-126	710	-65	-115	4.06	3.27	0.39	3.66	2.54	0.69
-	494	384	1573.7	8.1	1685	188	1527	377	-131	767	-67	-122	4.24	3.46	0.70	3.86	2.74	0.76
-	515	385	1614.3	8.4	1739	196	1599	389	-134	798	-69	-125	4.40	3.58	0.74	4.00	2.85	0.75
-	538	386	1643.1	8.6	1775	200	1653	403	-134	824	-70	-127	4.52	3.69	0.78	4.12	2.96	0.79
-	554	387	1672.4	8.9	1817	206	1729	415	-132	859	-70	-129	4.67	3.80	0.85	4.27	3.09	0.82
-	570	388	1701.8	9.1	1851	212	1805	429	-129	893	-70	-130	4.79	3.93	1.03	4.40	3.18	0.84
UL	592	389	1731.2	9.6	1890	230	2149	476	-75	946	-70	-131	5.12	4.20	1.14	4.62	3.38	0.86
-	609	390	1117.4	12.1	1247	593	8783	421	1133	797	-52	-97	9.65	8.28	4.97	3.58	2.72	0.80
-	650	392	534.3	9.8	710	603	8468	448	1197	616	-20	-58	8.51	7.56	4.94	2.67	2.16	0.43
9	657	395	932.4	11.3	1056	595	8828	432	1138	642	-29	-79	9.34	8.14	4.86	3.12	2.37	0.44
-	680	421	77.7	7.2	349	783	7148	470	1131	501	8	-21	6.60	6.11	4.26	2.06	1.77	0.32

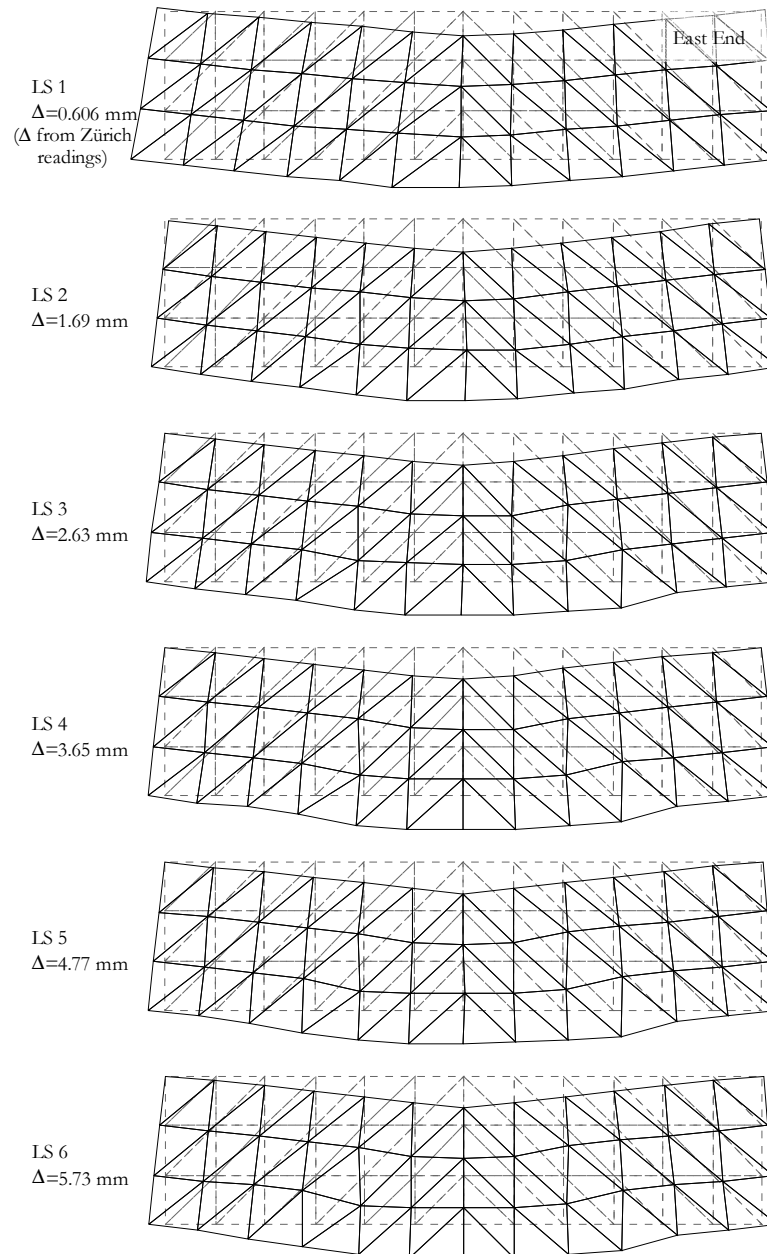


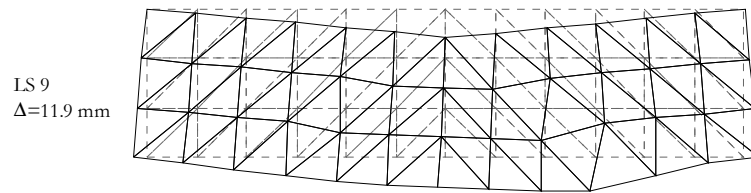
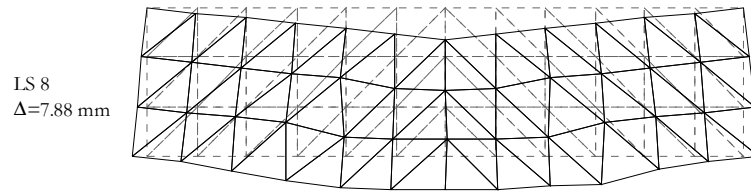
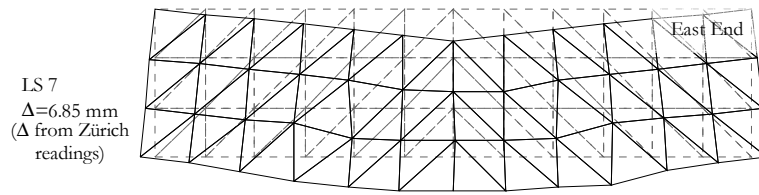
**Crack Diagrams, crack widths in (mm)**



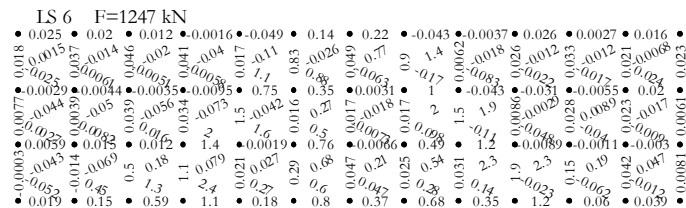
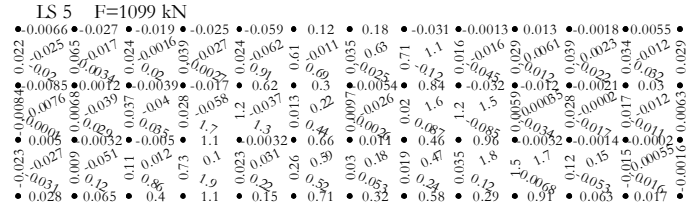
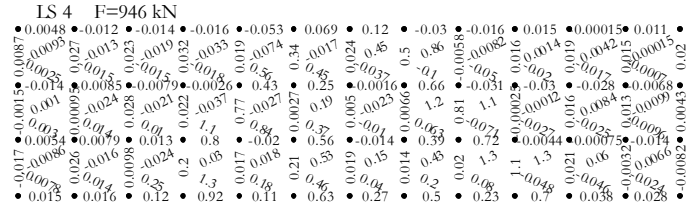
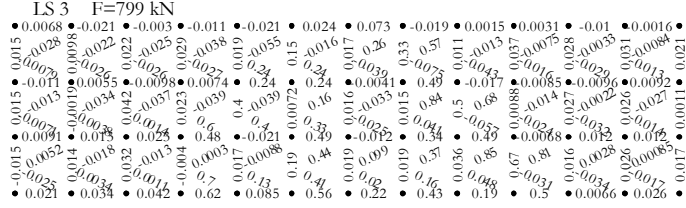
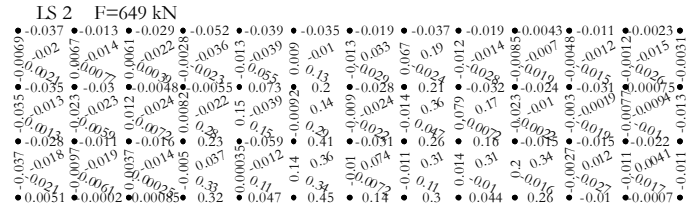
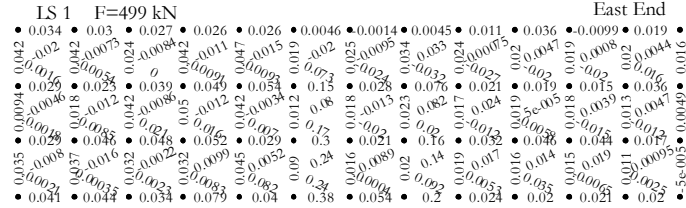


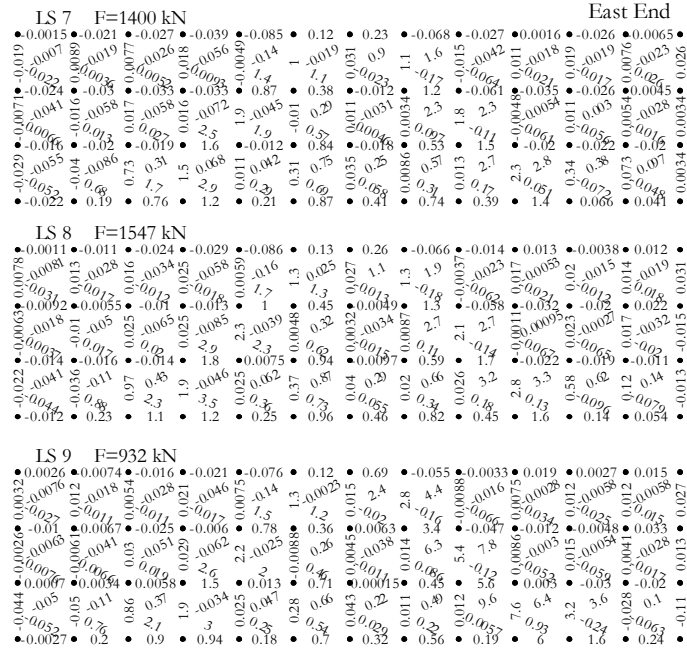
## Deformed shapes amplified to midspan displacement equivalent to 200 mm





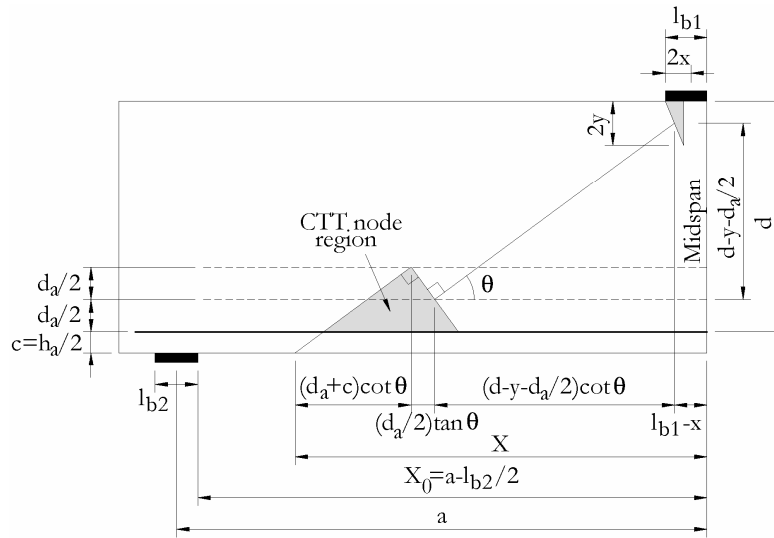
Zürich readings over 300/300 mm grid, deformations in (mm)







## APPENDIX C. CALCULATION OF ANGLE $\theta$



Angle  $\theta$  is calculated from the following geometrical condition:

$$X = (d_a/2 + c + d - y) \cot \theta + \frac{d_a}{2} \tan \theta + (l_{b1} - x) = X_0 = a - \frac{l_{b2}}{2}$$

This equation results in:

$$\tan \theta = \frac{-B - \sqrt{B^2 - 4AC}}{2A},$$

Where:

$$A = d_a/2,$$

$$B = l_{b1} - x - a + l_{b2}/2,$$

$$C = d_a / 2 + c + d - y.$$

If  $(B^2 - 4A.C) < 0$ , the above calculations should be repeated with reduced  $d_a$  obtained from condition  $B^2 = 4A.C$ :

$$d_{a,red} = -B_1 + \sqrt{B_1^2 + 4B},$$

Where:

$$B_1 = 2(c + d - y).$$

The reduced value of  $d_a$  should be used in all equations of the improved strut-and-tie model.



## APPENDIX D. VERIFICATION OF THE IMPROVED STRUT-AND-TIE MODEL

# *	a/d	d (mm)	$\rho_1$ (%)	$f_c'$ (MPa)	$V_{u,exp}$ (kN)	$V_{u,CSA}$ (kN)	$V_{u,ISTM}$ (kN)	$\frac{V_{u,exp}}{V_{u,CSA}}$	$\frac{V_{u,exp}}{V_{u,ISTM}}$
1	2	3	4	5	6	7	8	9	10
53	1.52	533	2.72	17.8	296.5	174.1	209.9	1.70	1.41
54	1.52	533	2.72	20.6	303.2	198.0	236.1	1.53	1.28
55	1.52	533	3.46	24.3	267.6	236.0	278.3	1.13	0.96
56	1.52	533	3.46	17.2	289.8	173.7	210.5	1.67	1.38
57	1.52	533	4.25	21.7	421.1	217.7	259.3	1.93	1.62
58	1.52	533	4.25	20.6	396.6	208.3	249.1	1.90	1.59
59	1.52	533	2.72	21.4	347.7	204.3	243.0	1.70	1.43
60	1.52	533	2.72	22.9	356.6	216.8	256.5	1.64	1.39
61	1.52	533	3.46	23.3	303.2	227.2	268.8	1.33	1.13
62	1.52	533	3.46	22.4	341.0	219.5	260.4	1.55	1.31
63	1.52	533	4.25	21.7	389.9	218.3	260.0	1.79	1.50
64	1.52	533	4.25	25.0	436.6	247.3	291.4	1.77	1.50
66	3.00	267	2.15	31.0	67.4	60.0	61.5	1.12	1.10
67	2.99	268	2.22	31.0	76.3	60.9	62.4	1.25	1.22
68	2.96	270	2.37	31.5	71.8	62.9	64.1	1.14	1.12
69	3.00	267	1.62	21.2	56.9	48.2	48.2	1.18	1.18
70	2.99	268	1.63	21.6	60.7	48.9	48.9	1.24	1.24
71	2.96	270	1.60	19.2	56.3	47.1	47.1	1.19	1.19
72	2.95	272	1.66	16.8	56.3	45.7	45.7	1.23	1.23
73	2.99	268	0.81	6.3	20.7	25.8	25.8	0.80	0.80
74	2.94	272	0.83	6.1	25.1	26.0	26.0	0.97	0.97
75	2.93	273	0.80	6.9	26.0	27.1	27.1	0.96	0.96
76	2.92	274	0.82	6.8	25.8	27.2	27.2	0.95	0.95
94	1.45	183	2.12	24.0	36.9	36.9	45.1	1.00	0.82
95	1.97	181	2.33	25.9	34.2	23.2	32.4	1.47	1.06
96	1.93	184	2.14	27.2	33.9	24.6	34.8	1.38	0.97
158	0.97	368	1.85	14.6	367.0	263.6	289.0	1.39	1.27
159	0.95	375	0.57	12.7	278.0	192.3	212.1	1.45	1.31
160	0.98	362	2.50	22.6	511.5	409.5	440.0	1.25	1.16
161	0.97	368	1.85	26.3	500.4	434.6	466.7	1.15	1.07

\* As specified by Collins, Bentz, and Sherwood, 2008

1	2	3	4	5	6	7	8	9	10
162	0.97	368	1.24	28.9	511.5	432.2	463.6	1.18	1.10
163	1.00	356	3.83	45.4	900.7	805.8	846.6	1.12	1.06
164	0.97	368	1.85	46.8	778.4	686.8	726.8	1.13	1.07
165	1.45	367	1.86	13.9	238.5	138.7	172.4	1.72	1.38
166	1.42	375	0.57	11.3	211.7	93.6	116.4	2.26	1.82
167	1.45	368	2.46	29.8	523.1	277.1	324.0	1.89	1.61
168	1.45	368	1.85	27.1	396.4	244.3	287.3	1.62	1.38
169	1.46	365	1.24	24.2	423.0	209.4	249.0	2.02	1.70
170	1.45	368	1.24	31.9	434.2	257.5	299.9	1.69	1.45
171	1.44	370	1.17	31.4	467.6	249.7	290.5	1.87	1.61
173	1.50	356	3.83	45.3	578.8	442.5	507.0	1.31	1.14
174	1.42	375	1.82	45.5	578.7	359.3	406.6	1.61	1.42
175	1.96	362	1.88	14.7	201.2	96.0	130.8	2.09	1.54
176	1.91	372	0.57	13.7	130.0	70.8	90.8	1.84	1.43
177	1.93	368	2.46	27.5	323.5	152.0	207.2	2.13	1.56
178	1.93	368	1.85	32.3	256.8	166.8	222.0	1.54	1.16
179	1.93	368	1.24	33.1	267.9	157.3	207.6	1.70	1.29
180	2.02	353	3.83	47.2	334.7	276.8	356.3	1.21	0.94
181	1.93	368	1.85	43.9	323.5	213.6	275.1	1.51	1.18
182	2.76	368	1.85	34.8	157.6	123.0	126.6	1.28	1.24
222	2.42	137	1.86	27.6	19.6	18.3	20.8	1.07	0.94
228	2.42	137	2.89	17.7	17.8	17.4	17.4	1.02	1.02
230	1.86	137	2.37	14.9	20.7	16.4	19.4	1.26	1.07
233	2.42	137	2.89	14.9	18.4	16.3	16.3	1.13	1.13
247	1.51	404	3.05	25.4	311.4	176.4	215.1	1.76	1.45
248	1.51	404	3.05	23.0	309.1	161.6	198.8	1.91	1.56
249	1.51	404	1.85	25.6	289.1	165.0	200.6	1.75	1.44
250	1.51	404	1.88	26.4	311.4	169.8	206.0	1.83	1.51
251	1.51	404	1.17	25.7	266.9	151.5	184.3	1.76	1.45
252	1.51	404	1.16	27.0	266.9	157.2	190.6	1.70	1.40
253	1.51	404	0.75	22.4	220.8	123.4	152.0	1.79	1.45
254	1.51	404	0.75	26.7	222.4	140.7	171.3	1.58	1.30
270	1.93	368	1.83	37.6	289.1	188.0	246.2	1.54	1.17
271	1.93	368	1.83	33.3	135.7	170.4	226.0	0.80	0.60
312	2.49	306	1.59	22.8	59.2	45.3	57.0	1.31	1.04
313	2.42	314	1.59	30.0	76.9	51.4	68.2	1.50	1.13
328	2.50	305	1.59	22.6	57.0	50.0	61.8	1.14	0.92
352	2.48	267	1.25	30.1	46.0	44.9	58.9	1.03	0.78
361	2.46	142	0.95	12.6	100.5	57.8	57.8	1.74	1.74
362	1.00	270	2.07	32.4	388.5	304.2	317.0	1.28	1.23
363	1.48	270	2.07	32.4	260.0	171.4	193.1	1.52	1.35
364	2.00	270	2.07	32.4	147.2	100.7	127.4	1.46	1.16
365	2.48	270	2.07	32.4	81.6	68.8	95.7	1.19	0.85
366	2.48	270	2.07	32.4	87.0	68.8	95.7	1.26	0.91

**Behaviour of Large Non-Slender RC Beams under Monotonic and Reversed Cyclic Load 339**

1	2	3	4	5	6	7	8	9	10
367	3.00	270	2.07	32.4	60.3	65.0	73.1	0.93	0.83
368	3.00	270	2.07	32.4	76.5	65.0	73.1	1.18	1.05
379	3.00	70	1.71	35.1	7.3	4.7	4.8	1.56	1.52
380	3.00	70	1.71	35.1	7.2	4.7	4.8	1.54	1.50
381	3.00	140	1.62	31.3	21.2	16.9	16.9	1.26	1.26
382	3.00	140	1.62	31.3	23.2	16.9	16.9	1.38	1.38
383	3.00	210	1.62	33.8	46.4	37.4	37.4	1.24	1.24
384	3.00	210	1.62	33.8	42.9	37.4	37.4	1.15	1.15
385	3.00	210	1.62	33.8	42.9	37.4	37.4	1.15	1.15
386	3.00	280	1.68	34.6	74.1	65.2	66.2	1.14	1.12
387	3.00	280	1.68	34.6	71.3	65.2	66.2	1.09	1.08
388	3.00	280	1.68	34.6	71.3	65.2	66.2	1.09	1.08
389	3.00	150	1.29	38.3	21.6	18.2	21.3	1.18	1.01
390	3.00	300	1.28	38.3	64.7	51.1	51.1	1.27	1.27
391	3.00	450	1.28	38.3	101.5	96.4	96.4	1.05	1.05
392	3.00	600	1.28	38.3	152.1	136.8	136.8	1.11	1.11
393	2.78	270	1.82	22.2	58.4	56.0	63.3	1.04	0.92
394	2.78	270	1.78	22.2	74.6	55.6	63.0	1.34	1.18
395	2.78	270	2.47	27.6	91.2	66.0	77.4	1.38	1.18
435	2.67	168	2.00	34.6	4.7	4.8	6.0	1.00	0.80
436	2.67	168	2.00	34.6	4.7	4.8	6.0	0.98	0.78
437	2.67	122	1.98	28.5	4.3	4.7	5.9	0.92	0.73
439	2.67	122	1.97	28.5	4.4	4.8	6.0	0.92	0.74
446	2.67	170	1.96	13.7	6.7	6.9	6.9	0.98	0.98
447	2.67	170	1.96	13.7	5.9	6.9	6.9	0.86	0.86
448	2.67	147	2.08	28.3	9.6	8.8	10.5	1.10	0.92
449	2.67	147	2.08	28.3	9.8	8.8	10.5	1.12	0.94
450	2.67	86	1.97	29.7	5.6	4.9	5.6	1.14	1.00
451	2.67	86	1.97	29.7	5.8	4.9	5.5	1.18	1.04
452	2.67	86	1.97	29.7	5.8	4.9	5.6	1.17	1.04
454	2.67	122	1.92	29.7	10.5	9.6	12.1	1.10	0.87
456	2.67	171	1.92	35.0	23.5	19.7	24.0	1.19	0.98
457	2.67	170	1.96	35.0	23.9	19.4	24.0	1.23	1.00
458	2.67	170	1.95	33.9	21.0	19.3	23.5	1.09	0.89
462	2.67	122	1.96	29.2	26.0	19.0	23.8	1.37	1.09
467	2.67	62	2.88	26.0	16.4	10.7	11.8	1.53	1.39
468	2.67	63	2.84	26.0	17.9	10.9	11.7	1.65	1.54
470	2.67	62	1.92	30.0	15.5	10.1	12.2	1.54	1.28
471	2.67	62	1.90	30.0	15.7	10.2	12.3	1.54	1.28
473	2.67	61	1.93	30.3	18.6	10.1	12.3	1.85	1.52
486	2.67	341	1.86	28.0	28.6	31.6	38.2	0.91	0.75
487	2.67	340	1.80	25.8	27.6	31.1	36.9	0.89	0.75
488	2.67	253	1.81	34.5	188.7	156.4	199.2	1.21	0.95
489	2.67	252	1.85	34.1	171.2	156.9	199.9	1.09	0.86

1	2	3	4	5	6	7	8	9	10
496	1.51	403	3.05	25.4	312.9	177.3	216.3	1.76	1.45
497	1.51	403	3.05	23.0	310.7	162.4	199.9	1.91	1.55
498	1.51	403	1.88	21.9	261.8	145.7	179.5	1.80	1.46
499	1.51	403	1.88	26.4	312.9	170.6	207.1	1.83	1.51
500	1.51	403	1.85	25.7	288.5	166.5	202.4	1.73	1.42
501	1.51	403	1.85	25.6	290.7	165.7	201.6	1.75	1.44
502	1.51	403	1.86	24.1	290.8	158.0	193.2	1.84	1.51
503	1.51	403	1.86	24.9	304.0	162.2	197.7	1.87	1.54
504	1.51	403	1.16	23.1	224.0	139.8	171.5	1.60	1.31
505	1.51	403	1.16	27.0	268.4	157.9	191.5	1.70	1.40
506	1.51	403	1.17	25.4	224.0	150.9	183.8	1.48	1.22
507	1.51	403	1.17	25.7	268.4	152.1	185.2	1.76	1.45
508	1.51	403	0.75	22.4	222.4	123.9	152.8	1.80	1.46
509	1.51	403	0.75	26.7	224.0	141.3	172.1	1.59	1.30
510	1.51	403	0.75	25.5	179.5	136.6	166.9	1.31	1.08
511	1.51	403	0.75	22.8	188.6	125.6	154.7	1.50	1.22
516	2.84	403	0.84	26.1	71.4	69.5	69.5	1.03	1.03
517	2.84	403	0.84	25.8	62.4	69.2	69.2	0.90	0.90
518	2.84	403	0.84	30.6	75.1	73.1	73.1	1.03	1.03
521	0.67	305	0.83	24.6	89.8	72.8	74.5	1.23	1.21
525	1.00	203	1.67	23.3	85.3	66.3	69.6	1.29	1.23
527	1.00	203	2.58	19.9	106.9	62.6	65.8	1.71	1.62
528	1.00	203	1.67	35.2	109.8	91.7	95.6	1.20	1.15
532	2.35	390	2.06	30.6	109.9	109.7	153.7	1.00	0.71
533	2.35	390	3.09	29.9	170.4	114.5	161.9	1.49	1.05
718	2.00	542	2.55	26.8	163.3	100.7	147.0	1.62	1.11
721	2.46	552	2.82	27.0	112.4	95.6	113.7	1.18	0.99
723	1.03	528	2.75	30.3	548.0	415.0	441.2	1.32	1.24
725	1.00	542	2.67	27.4	585.6	423.7	445.7	1.38	1.31
726	2.99	544	2.41	27.4	102.1	90.2	90.2	1.13	1.13
727	1.98	549	2.71	24.8	196.9	102.6	144.6	1.92	1.36
730	2.63	518	2.87	30.8	114.8	96.4	121.1	1.19	0.95
736	0.99	274	2.69	25.5	233.6	157.6	171.0	1.48	1.37
737	1.01	269	2.72	27.2	239.6	171.4	184.8	1.40	1.30
742	1.99	273	2.77	25.3	110.6	57.0	72.9	1.94	1.52
743	2.47	275	2.75	25.3	72.8	54.5	55.3	1.34	1.32
746	2.47	275	2.68	26.2	76.3	54.6	56.5	1.40	1.35
747	2.50	272	2.73	26.2	77.2	53.9	58.0	1.43	1.33
748	2.02	270	2.75	27.2	111.9	57.8	78.9	1.94	1.42
852	2.00	1097	2.72	26.9	326.2	240.8	324.9	1.35	1.00
853	2.50	1095	2.70	26.4	237.0	152.8	221.1	1.55	1.07
854	3.00	1092	2.71	27.0	165.1	147.8	147.8	1.12	1.12
876	3.00	600	1.26	29.6	119.5	132.8	132.8	0.90	0.90
877	3.00	900	1.26	27.5	166.8	175.6	175.6	0.95	0.95

**Behaviour of Large Non-Slender RC Beams under Monotonic and Reversed Cyclic Load 341**

1	2	3	4	5	6	7	8	9	10
878	3.00	1200	1.26	25.2	185.2	207.6	207.6	0.89	0.89
879	3.00	600	0.63	26.6	106.2	101.1	101.1	1.05	1.05
880	3.00	600	0.63	24.7	114.1	98.8	98.8	1.15	1.15
881	3.00	900	0.63	27.2	139.8	139.1	139.1	1.00	1.00
882	3.00	900	0.63	27.7	127.5	139.9	139.9	0.91	0.91
888	2.47	370	1.03	29.9	80.5	69.9	69.9	1.15	1.15
889	2.47	370	1.03	29.9	80.5	69.9	69.9	1.15	1.15
890	3.00	254	1.03	17.1	36.5	31.2	31.2	1.17	1.17
891	3.00	254	1.03	46.9	54.7	43.4	45.5	1.26	1.20
892	3.00	254	3.10	18.6	56.0	43.9	43.9	1.28	1.28
897	1.50	127	1.64	26.5	70.5	37.9	42.5	1.86	1.66
898	2.50	197	1.70	26.8	54.7	36.1	44.7	1.51	1.22
962	0.90	406	1.88	38.1	293.6	277.8	287.7	1.06	1.02
963	1.06	406	1.88	32.3	273.6	196.6	209.9	1.39	1.30
965	2.56	234	1.08	27.0	40.9	32.2	32.2	1.27	1.27
971	2.50	226	0.79	25.8	117.5	102.1	102.1	1.15	1.15
972	2.50	225	1.39	24.6	139.5	120.8	120.8	1.15	1.15
1172	1.00	270	0.70	17.5	98.6	79.5	88.8	1.24	1.11
1173	1.50	270	0.70	22.6	63.8	54.3	67.4	1.17	0.95
1174	2.00	270	0.70	23.2	46.6	36.4	48.2	1.28	0.97
1179	1.00	270	1.47	25.3	166.8	124.2	136.2	1.34	1.22
1180	1.50	270	1.47	25.3	122.6	69.4	85.2	1.77	1.44
1181	2.00	270	1.47	24.2	90.7	46.4	58.1	1.96	1.56
1182	2.50	270	1.47	28.7	68.7	46.1	49.2	1.49	1.39
1183	3.00	270	1.47	23.5	60.1	40.6	40.6	1.48	1.48
1186	1.00	270	1.91	34.4	166.8	167.5	181.6	1.00	0.92
1187	1.50	270	1.91	34.8	112.8	94.6	113.2	1.19	1.00
1188	2.00	270	1.91	34.3	93.2	56.6	77.7	1.65	1.20
1189	2.50	270	1.91	34.8	71.1	53.3	60.2	1.33	1.18
1190	3.00	270	1.91	38.6	58.7	52.2	52.2	1.12	1.12
1199	3.00	356	1.69	49.3	96.0	93.9	93.9	1.02	1.02
1200	3.00	356	1.69	49.3	97.1	93.9	93.9	1.03	1.03
1201	3.00	356	1.69	41.6	87.4	83.5	83.5	1.05	1.05
1202	3.00	356	1.69	41.6	94.4	83.5	83.5	1.13	1.13
1203	3.00	356	1.69	45.2	99.4	91.2	91.2	1.09	1.09
1204	3.00	356	1.69	45.2	96.4	91.2	91.2	1.06	1.06
1205	3.00	177	1.74	34.5	23.8	21.7	21.7	1.10	1.10
1206	3.00	177	1.74	34.5	23.9	21.7	21.7	1.10	1.10
1207	3.00	177	1.74	36.8	24.5	22.2	22.2	1.10	1.10
1208	3.00	177	1.74	36.8	25.5	22.2	22.2	1.15	1.15
1209	3.00	177	1.74	40.1	26.5	22.8	22.8	1.16	1.16
1210	3.00	177	1.74	40.1	23.2	22.8	22.8	1.02	1.02
1211	3.00	177	1.74	31.6	22.1	21.1	21.1	1.05	1.05
1212	3.00	177	1.74	32.4	23.4	21.2	21.2	1.10	1.10

1	2	3	4	5	6	7	8	9	10
1213	3.00	177	1.74	44.7	21.4	23.7	23.7	0.90	0.90
1247	2.99	255	0.19	37.2	28.9	20.7	20.7	1.39	1.39
1249	0.77	305	1.93	20.5	141.8	158.2	162.0	0.90	0.87
1250	0.77	305	1.93	20.9	136.1	161.1	164.9	0.84	0.83
1251	1.01	305	1.93	21.7	149.0	121.6	128.9	1.23	1.16
1252	1.34	305	1.93	20.7	115.6	78.2	88.8	1.48	1.30
1253	2.01	305	1.93	19.5	73.4	36.5	50.1	2.01	1.46
1275	2.48	298	3.34	21.1	77.8	53.3	56.6	1.46	1.37
1276	2.48	298	3.34	46.3	117.9	72.3	96.2	1.63	1.23
1277	2.48	298	3.34	81.3	111.3	96.6	133.4	1.15	0.83
1278	2.48	298	3.34	85.9	177.8	101.0	137.3	1.76	1.29
1279	2.48	298	3.34	71.2	205.8	86.6	124.5	2.38	1.65
1280	1.50	298	3.34	23.1	116.1	84.8	105.8	1.37	1.10
1281	1.50	298	3.34	41.8	311.5	142.3	168.7	2.19	1.85
1282	1.50	298	3.34	65.8	432.6	206.6	237.8	2.09	1.82
1283	1.50	298	3.34	79.5	275.7	240.2	273.6	1.15	1.01
1284	1.50	298	3.34	81.3	495.0	244.4	278.1	2.02	1.78
1296	2.00	268	1.19	69.0	85.3	96.8	124.7	0.88	0.68
1297	2.00	268	2.44	69.0	129.6	115.1	154.0	1.13	0.84
1300	2.50	200	0.56	19.8	26.5	21.4	21.4	1.24	1.24
1301	2.50	200	0.81	18.9	30.5	23.9	23.9	1.27	1.27
1302	2.50	200	1.10	18.9	43.0	26.5	26.8	1.62	1.61
1303	2.50	200	1.82	18.9	54.0	30.7	30.7	1.75	1.75
1304	2.50	200	1.10	20.1	40.4	27.1	27.8	1.49	1.45
1305	1.05	950	0.95	26.1	699.0	421.5	458.3	1.66	1.53
1306	1.05	950	0.95	26.4	600.0	425.3	462.3	1.41	1.30
1308	2.20	455	0.88	43.2	177.0	124.5	152.1	1.42	1.16
1309	2.50	250	1.55	47.1	97.1	82.2	110.3	1.18	0.88
1310	2.50	250	1.55	51.0	83.4	87.4	115.8	0.95	0.72
1314	3.00	250	2.57	45.5	93.2	75.4	92.3	1.24	1.01
1315	3.00	250	2.57	46.8	91.2	76.1	93.8	1.20	0.97
1316	3.00	250	3.18	49.1	86.3	82.3	103.4	1.05	0.83
1317	3.00	250	3.18	50.5	82.4	83.2	105.3	0.99	0.78
1323	2.00	200	1.34	24.2	60.0	34.9	40.5	1.72	1.48
1324	2.80	200	1.34	24.2	45.0	31.3	31.3	1.44	1.44
1334	3.00	208	1.77	60.8	48.9	38.9	46.5	1.26	1.05
1335	2.70	208	1.77	60.8	80.1	42.5	56.4	1.89	1.42
1336	2.30	208	1.77	60.8	82.3	57.6	74.6	1.43	1.10
1337	2.00	208	1.77	60.8	55.6	73.9	91.3	0.75	0.61
1338	1.00	208	1.77	60.8	222.4	192.7	202.7	1.15	1.10
1352	3.00	208	2.25	67.0	46.7	41.3	53.7	1.13	0.87
1353	2.70	208	2.25	67.0	80.1	48.4	65.0	1.66	1.23
1354	2.30	208	2.25	67.0	64.1	65.7	85.9	0.97	0.75
1355	2.00	208	2.25	67.0	122.3	84.4	103.2	1.45	1.18

1	2	3	4	5	6	7	8	9	10
1356	1.00	208	2.25	67.0	213.5	220.3	230.9	0.97	0.92
1370	2.70	207	3.26	64.3	45.4	51.6	73.0	0.88	0.62
1371	2.30	207	3.26	64.3	56.9	70.3	91.8	0.81	0.62
1372	2.00	207	3.26	64.3	106.8	90.5	110.3	1.18	0.97
1373	1.00	207	3.26	64.3	244.6	237.2	247.9	1.03	0.99
1380	3.00	2000	0.28	27.1	402.0	441.8	441.8	0.91	0.91
1381	3.00	2000	0.14	26.2	382.0	331.9	331.9	1.15	1.15
1382	3.00	1000	0.14	24.6	102.0	100.4	100.4	1.02	1.02
1385	0.50	930	0.66	16.8	849.0	825.6	837.0	1.03	1.01
1386	0.50	930	0.66	18.8	654.0	903.0	915.0	0.72	0.71
1387	0.50	930	0.66	15.8	642.0	785.8	796.9	0.82	0.81
1388	1.00	930	1.08	20.4	588.0	552.2	601.8	1.06	0.98
1389	1.00	930	1.08	15.4	430.0	438.1	482.6	0.98	0.89
1390	1.50	930	1.69	17.0	369.0	270.4	335.8	1.36	1.10
1391	1.50	930	1.69	16.9	387.0	269.0	334.3	1.44	1.16
1392	1.50	930	1.69	15.0	375.0	242.2	304.6	1.55	1.23
1393	0.50	160	0.85	19.9	221.0	239.8	241.0	0.92	0.92
1394	1.50	160	1.90	20.6	140.0	94.6	108.2	1.48	1.29
1445	3.00	221	1.82	54.0	58.1	47.8	47.8	1.22	1.22
1446	2.30	221	1.82	54.0	70.8	52.6	76.8	1.35	0.92
1448	3.00	207	3.24	54.0	82.6	54.9	67.5	1.50	1.22
1449	2.30	207	3.24	54.0	107.1	76.6	100.8	1.40	1.06
1450	3.00	221	1.82	77.8	67.9	48.4	56.5	1.40	1.20
1451	2.30	221	1.82	77.8	102.7	67.0	91.6	1.53	1.12
1453	3.00	207	3.24	77.8	82.6	55.5	78.9	1.49	1.05
1454	2.30	207	3.24	77.8	175.8	94.6	122.1	1.86	1.44
1456	3.00	207	3.24	86.4	107.2	60.4	83.2	1.78	1.29
1457	2.30	207	3.24	86.4	148.3	102.7	131.2	1.44	1.13
1458	3.00	221	1.82	97.7	56.2	52.2	62.9	1.08	0.89
1459	2.30	221	1.82	97.7	77.7	79.5	102.7	0.98	0.76
1461	3.00	207	3.24	97.7	77.7	66.5	88.7	1.17	0.88
1462	2.30	207	3.24	97.7	156.1	112.8	142.6	1.38	1.10
1463	3.00	442	1.82	77.8	179.8	161.7	203.3	1.11	0.88
1464	3.00	442	1.82	77.8	180.3	161.7	203.3	1.12	0.89
1465	2.30	442	1.82	77.8	438.7	253.8	330.9	1.73	1.33
1468	3.00	414	3.24	77.8	280.7	215.2	286.6	1.30	0.98
1469	2.30	414	3.24	77.8	576.3	364.6	461.8	1.58	1.25
1470	2.30	414	3.24	77.8	710.3	364.6	461.8	1.95	1.54
1471	3.00	41	1.62	46.2	2.9	2.3	2.5	1.30	1.17
1472	3.00	41	1.62	46.2	2.7	2.3	2.5	1.19	1.08
1473	3.00	41	1.62	46.2	3.2	2.3	2.5	1.41	1.27
1474	3.00	83	1.62	46.2	5.4	4.4	4.7	1.24	1.15
1475	3.00	83	1.62	46.2	5.0	4.4	4.7	1.16	1.07
1476	3.00	83	1.62	46.2	4.5	4.4	4.7	1.02	0.94

1	2	3	4	5	6	7	8	9	10
1477	3.00	165	1.62	46.2	7.3	8.1	8.9	0.90	0.82
1478	3.00	165	1.62	46.2	8.4	8.1	8.9	1.04	0.94
1479	3.00	165	1.62	46.2	8.3	8.1	8.9	1.02	0.92
1480	3.00	41	1.65	46.8	3.2	2.3	2.5	1.42	1.28
1481	3.00	41	1.65	46.8	3.0	2.3	2.5	1.29	1.16
1482	3.00	41	1.65	46.8	3.1	2.3	2.5	1.35	1.21
1483	3.00	83	1.65	46.8	5.5	4.4	4.8	1.25	1.15
1484	3.00	83	1.65	46.8	5.6	4.4	4.8	1.27	1.16
1485	3.00	83	1.65	46.8	5.2	4.4	4.8	1.18	1.08
1486	3.00	165	1.65	46.8	9.1	8.2	9.1	1.11	1.00
1487	3.00	165	1.65	46.8	9.8	8.2	9.1	1.19	1.08
1488	3.00	165	1.65	46.8	10.1	8.2	9.1	1.24	1.12
1493	1.50	350	0.34	55.0	159.0	136.2	152.9	1.17	1.04
1494	2.00	350	0.34	30.6	62.0	56.1	65.9	1.10	0.94
1495	1.00	216	2.07	47.0	155.7	153.9	164.1	1.01	0.95
1496	2.00	216	2.07	41.4	56.6	52.1	69.1	1.09	0.82
1497	3.00	216	2.07	39.7	36.7	37.6	38.0	0.98	0.96
1498	1.00	216	2.07	103.8	241.5	278.3	292.4	0.87	0.83
1499	2.00	216	2.07	103.4	101.6	104.7	128.2	0.97	0.79
1500	3.00	216	2.07	104.2	45.7	48.7	63.5	0.94	0.72
1501	3.00	125	0.83	22.9	31.5	21.9	21.9	1.44	1.44
1502	3.00	420	0.74	22.9	70.6	60.9	60.9	1.16	1.16
1503	3.00	720	0.79	23.2	100.8	94.8	94.8	1.06	1.06
1504	1.00	360	1.13	16.1	226.0	200.8	221.9	1.13	1.02
1505	1.00	360	1.13	21.8	322.0	256.8	280.6	1.25	1.15
1506	1.00	360	1.13	22.1	344.0	259.6	283.5	1.33	1.21
1507	1.00	360	1.13	24.3	425.0	279.8	304.7	1.52	1.39
1508	1.00	360	1.13	13.9	220.0	177.8	197.6	1.24	1.11
1509	1.00	360	1.13	20.1	347.0	240.6	263.7	1.44	1.32
1510	1.00	360	1.13	25.2	396.0	288.0	313.1	1.38	1.26
1511	1.00	360	1.13	20.0	323.0	239.7	262.7	1.35	1.23
1512	1.00	360	1.13	18.2	318.0	222.1	244.2	1.43	1.30
1513	1.00	360	1.13	19.8	246.0	237.7	260.6	1.03	0.94
1514	1.00	360	1.13	26.4	437.0	298.6	324.2	1.46	1.35
1515	1.00	160	1.52	18.1	165.0	143.0	150.6	1.15	1.10
1516	1.00	360	1.13	19.9	270.0	238.7	261.6	1.13	1.03
1517	1.00	560	1.12	19.8	350.0	322.5	351.3	1.09	1.00
1518	1.00	740	1.10	19.4	365.0	432.9	473.4	0.84	0.77
1519	1.00	930	1.08	20.0	505.0	544.4	593.6	0.93	0.85
1539	3.00	372	0.81	80.6	83.0	73.2	73.2	1.13	1.13
1540	3.00	362	1.94	96.8	121.0	103.2	113.1	1.17	1.07
1542	3.00	270	1.87	53.7	71.1	67.1	67.1	1.06	1.06
1543	3.00	270	1.87	53.7	71.6	67.1	67.1	1.07	1.07
1544	3.00	272	1.01	53.7	58.3	54.5	54.5	1.07	1.07



**Behaviour of Large Non-Slender RC Beams under Monotonic and Reversed Cyclic Load 345**

1	2	3	4	5	6	7	8	9	10
1545	3.00	272	1.01	53.7	56.4	54.5	54.5	1.04	1.04
1546	3.00	267	3.35	53.7	78.1	79.2	79.2	0.99	0.99
1547	3.00	267	3.35	53.7	78.5	79.2	79.2	0.99	0.99
1548	3.00	255	4.68	53.7	89.7	83.1	93.0	1.08	0.97
1549	3.00	255	4.68	53.7	95.4	83.1	93.0	1.15	1.03
1550	1.50	270	1.87	53.7	212.5	120.1	144.8	1.77	1.47
1551	1.50	270	1.87	53.7	215.3	120.1	144.8	1.79	1.49
1556	3.00	142	1.87	53.7	41.0	37.3	42.6	1.10	0.96
1557	3.00	142	1.87	53.7	39.3	37.3	42.6	1.05	0.92
1558	3.00	550	1.88	53.7	226.1	215.8	215.8	1.05	1.05
1559	3.00	550	1.88	53.7	214.5	215.8	215.8	0.99	0.99
1560	3.00	915	1.87	53.7	271.8	316.6	316.6	0.86	0.86
1561	3.00	915	1.87	53.7	332.1	316.6	316.6	1.05	1.05
1562	3.00	150	2.65	32.4	27.5	21.3	21.7	1.29	1.27
1563	3.00	150	2.65	32.4	31.9	21.3	21.7	1.49	1.47
1564	3.00	150	2.65	38.4	29.3	22.7	24.0	1.29	1.22
1565	3.00	150	2.65	38.4	30.7	22.7	24.0	1.35	1.28
1566	3.00	150	2.65	48.7	29.6	24.7	27.7	1.20	1.07
1567	3.00	150	2.65	48.7	32.3	24.7	27.7	1.31	1.16
1568	3.00	150	2.65	70.9	33.4	25.6	34.2	1.30	0.97
1569	3.00	150	2.65	70.9	33.9	25.6	34.2	1.32	0.99
1570	3.00	150	2.65	83.4	38.3	27.1	37.0	1.41	1.03
1571	3.00	150	2.65	83.4	42.5	27.1	37.0	1.57	1.15
1572	3.00	150	2.65	127.5	34.4	35.6	45.7	0.97	0.75
1573	3.00	150	2.65	127.5	48.1	35.6	45.7	1.35	1.05
1574	3.00	225	2.55	124.5	69.7	43.6	57.4	1.60	1.21
1575	3.00	225	2.55	124.5	42.5	43.6	57.4	0.98	0.74
1580	3.00	300	2.58	127.5	54.0	69.6	85.0	0.78	0.64
1581	3.00	300	2.58	127.5	83.1	69.6	85.0	1.19	0.98
1585	2.64	208	0.74	92.4	75.5	76.5	90.8	0.99	0.83
1586	2.61	211	1.05	91.3	103.5	89.2	113.1	1.16	0.92
1587	2.64	208	0.57	85.0	88.5	85.6	99.9	1.03	0.89
1588	0.85	443	2.58	79.5	500.0	579.6	595.9	0.86	0.84
1589	1.13	443	2.58	77.6	255.0	400.5	427.8	0.64	0.60
1590	1.69	443	2.58	77.6	185.0	212.0	247.7	0.87	0.75
1603	3.00	300	1.26	24.8	33.5	30.3	30.3	1.11	1.11
1604	3.00	300	1.26	24.8	29.5	30.3	30.3	0.97	0.97
1605	3.00	500	1.36	27.3	82.5	81.9	81.9	1.01	1.01
1606	3.00	500	1.36	27.3	101.5	81.9	81.9	1.24	1.24
1607	3.00	950	1.22	20.7	216.0	229.6	229.6	0.94	0.94
1608	3.00	950	1.22	20.6	237.5	229.2	229.2	1.04	1.04
1609	3.00	2000	1.20	22.2	610.5	667.1	668.2	0.92	0.91
1610	3.00	2000	1.20	23.1	560.0	676.9	684.1	0.83	0.82
1611	2.95	225	0.89	99.0	85.0	82.7	95.4	1.03	0.89

1	2	3	4	5	6	7	8	9	10
1612	2.92	450	0.81	99.0	131.9	172.9	194.7	0.76	0.68
1613	2.88	925	0.76	99.0	193.1	269.8	301.8	0.72	0.64
1614	2.96	110	0.91	37.0	40.1	34.8	34.8	1.15	1.15
1615	2.95	225	0.89	37.0	72.9	65.7	65.7	1.11	1.11
1616	2.92	450	0.81	37.0	131.6	112.8	112.8	1.17	1.17
1617	2.88	925	0.76	37.0	191.7	184.6	184.6	1.04	1.04
1618	2.86	1890	0.74	33.6	257.7	269.2	269.2	0.96	0.96
1620	2.50	313	1.20	34.2	157.9	139.5	171.4	1.13	0.92
1621	2.50	440	1.20	34.2	186.8	185.3	210.0	1.01	0.89
1622	2.50	889	1.20	34.2	360.2	314.9	323.2	1.14	1.11
1624	2.50	313	2.00	34.2	178.4	162.9	203.6	1.09	0.88
1625	2.50	440	2.00	34.2	214.6	215.6	248.6	1.00	0.86
1626	2.50	889	2.00	34.2	379.7	362.5	377.3	1.05	1.01
1628	2.50	313	1.20	58.6	157.1	174.7	224.0	0.90	0.70
1629	2.50	440	1.20	58.6	197.7	213.4	274.7	0.93	0.72
1630	2.50	889	1.20	58.6	310.4	340.9	425.4	0.91	0.73
1632	2.50	313	2.00	58.6	189.5	197.0	270.1	0.96	0.70
1633	2.50	440	2.00	58.6	198.2	243.2	328.3	0.81	0.60
1634	2.50	889	2.00	58.6	331.1	394.5	499.5	0.84	0.66
1663	1.50	215	3.77	52.0	112.9	101.9	119.1	1.11	0.95
1664	2.00	215	3.77	52.0	87.9	63.5	84.5	1.38	1.04
1665	2.50	215	3.77	52.0	56.4	49.4	65.2	1.14	0.87
1666	1.50	215	3.77	73.0	142.2	134.6	154.1	1.06	0.92
1667	2.00	215	3.77	73.0	99.4	84.2	107.9	1.18	0.92
1668	2.50	215	3.77	73.0	80.4	55.3	82.1	1.45	0.98
1669	0.56	444	2.57	49.1	850.0	799.7	805.3	1.06	1.06
1670	0.84	444	2.57	42.5	700.0	493.5	508.6	1.42	1.38
1671	1.13	444	2.57	37.4	570.0	309.1	334.4	1.84	1.70
1678	2.92	925	1.01	36.0	225.0	199.9	199.9	1.13	1.13
1679	2.92	925	1.01	36.0	249.0	199.9	199.9	1.25	1.25
1680	2.92	925	1.01	98.0	193.0	282.9	323.6	0.68	0.60
1681	2.92	925	1.01	39.0	204.0	205.4	205.4	0.99	0.99
1682	2.92	925	1.01	98.0	217.0	282.9	323.6	0.77	0.67
1683	2.92	925	1.01	39.0	223.0	205.5	205.5	1.09	1.09
1684	2.92	925	1.01	39.0	235.0	205.5	205.5	1.14	1.14
1685	2.92	925	0.51	94.0	163.0	223.2	245.0	0.73	0.67
1687	1.50	191	1.65	30.1	112.8	78.8	87.7	1.43	1.29
1688	2.00	191	1.65	30.1	70.1	47.2	58.2	1.49	1.20
1689	2.50	191	1.65	30.1	44.7	30.2	42.9	1.48	1.04
1690	3.00	191	1.65	37.7	29.4	30.1	35.1	0.97	0.84
1692	2.00	140	2.02	34.0	25.0	16.5	22.5	1.51	1.11
1694	2.00	140	2.02	63.0	31.0	25.9	34.3	1.20	0.90
1696	2.00	140	2.02	87.0	35.0	33.1	42.5	1.06	0.82
1698	2.33	1000	0.42	21.0	429.0	263.8	284.8	1.63	1.51

**Behaviour of Large Non-Slender RC Beams under Monotonic and Reversed Cyclic Load 347**

1	2	3	4	5	6	7	8	9	10
1699	2.33	1000	0.42	18.4	315.0	252.7	263.4	1.25	1.20
1700	2.33	1000	0.42	18.4	378.0	252.7	263.4	1.50	1.44
1701	2.33	1000	0.42	18.4	329.0	252.7	263.4	1.30	1.25
1702	2.33	1000	0.60	25.5	387.0	317.6	366.0	1.22	1.06
1703	2.41	996	0.66	25.5	381.0	323.1	361.5	1.18	1.05
1704	2.20	1000	0.98	21.0	771.0	351.4	446.4	2.19	1.73
1705	2.33	1000	0.98	20.6	435.0	343.1	381.4	1.27	1.14
1706	2.33	1000	0.98	22.4	531.0	353.6	401.3	1.50	1.32
1707	2.33	1000	0.98	22.4	579.0	353.6	401.3	1.64	1.44
1708	2.33	1000	0.98	31.7	532.0	399.7	495.7	1.33	1.07
1709	2.33	1000	0.98	31.7	524.0	399.7	495.7	1.31	1.06
1710	2.33	1000	0.98	31.7	605.0	399.7	495.7	1.51	1.22
1711	2.00	1000	0.84	19.5	330.0	168.5	229.6	1.96	1.44
1712	1.50	1000	0.84	19.5	723.0	268.8	341.3	2.69	2.12
1713	1.50	1000	0.84	20.3	550.0	277.7	351.3	1.98	1.57
1714	1.75	1000	0.84	19.5	409.0	205.7	284.6	1.99	1.44
1715	1.82	962	1.75	20.3	330.0	266.9	374.6	1.24	0.88
1716	1.43	1000	0.84	20.3	380.0	300.1	371.7	1.27	1.02
1717	2.92	925	1.01	21.0	179.0	165.6	165.6	1.08	1.08
1718	2.92	925	1.01	32.0	185.0	191.9	191.9	0.96	0.96
1719	2.92	925	1.01	38.0	180.0	203.6	203.6	0.88	0.88
1720	2.92	925	1.01	65.0	185.0	225.4	257.5	0.82	0.72
1721	2.92	925	1.01	80.0	172.0	243.6	288.4	0.71	0.60
1723	2.92	925	0.50	32.0	165.0	152.2	152.2	1.08	1.08
1724	2.81	1925	0.36	30.8	227.2	210.4	210.4	1.08	1.08
1725	2.93	1845	1.52	27.5	407.0	296.4	296.4	1.37	1.37
1726	0.85	500	1.56	23.7	265.2	241.9	255.7	1.10	1.04
1727	0.50	500	1.56	49.1	642.2	643.4	648.2	1.00	0.99
1728	0.85	500	1.56	49.1	401.1	430.1	448.6	0.93	0.89
1729	1.25	500	1.56	49.1	337.4	266.1	296.0	1.27	1.14
1730	2.00	500	1.56	49.1	112.5	120.7	159.7	0.93	0.70
1737	2.75	346	0.72	37.3	58.9	50.7	55.9	1.16	1.05
1738	2.75	346	0.72	37.3	63.3	50.7	55.9	1.25	1.13
1747	1.00	200	1.91	38.4	214.2	203.9	211.8	1.05	1.01
1748	1.00	400	1.69	35.5	285.3	284.9	305.0	1.00	0.94
1749	1.00	600	1.76	40.8	424.5	423.0	451.3	1.00	0.94
1750	0.56	355	1.01	31.4	447.0	398.0	402.1	1.12	1.11
1751	0.54	555	0.97	31.4	535.0	457.3	465.1	1.17	1.15
1752	0.54	555	0.97	31.4	479.0	457.3	465.1	1.05	1.03
1753	0.55	685	1.05	31.4	597.0	539.7	549.1	1.11	1.09
1754	0.53	935	0.90	31.4	582.0	562.0	563.3	1.04	1.03
1755	0.56	355	1.01	78.5	733.0	768.6	774.7	0.95	0.95
1756	0.54	555	0.97	78.5	823.0	910.1	921.9	0.90	0.89
1757	0.55	685	1.05	78.5	1010.0	1085.2	1099.8	0.93	0.92

1	2	3	4	5	6	7	8	9	10
1758	0.53	935	0.90	78.5	1029.0	1156.7	1177.5	0.89	0.87
1759	1.13	355	1.01	31.4	192.1	193.8	213.0	0.99	0.90
1760	1.13	355	1.01	31.4	311.6	193.8	213.0	1.61	1.46
1761	1.08	555	0.97	31.4	375.3	236.3	260.7	1.59	1.44
1762	1.09	685	1.05	31.4	271.5	290.7	324.0	0.93	0.84
1763	1.09	685	1.05	31.4	330.3	290.7	324.0	1.14	1.02
1764	1.07	935	0.90	31.4	543.9	316.7	353.6	1.72	1.54
1765	1.06	355	1.01	78.5	498.8	405.2	430.7	1.23	1.16
1766	1.06	355	1.01	78.5	385.1	405.2	430.7	0.95	0.89
1767	1.08	555	0.97	78.5	573.3	461.6	495.3	1.24	1.16
1768	1.09	685	1.05	78.5	338.1	570.9	617.4	0.59	0.55
1769	1.09	685	1.05	78.5	360.6	570.9	617.4	0.63	0.58
1770	1.07	935	0.90	78.5	769.3	627.2	678.5	1.23	1.13
1771	2.93	920	0.76	64.1	1272.1	1379.9	1610.1	0.92	0.79
1772	2.73	330	2.16	61.3	124.9	98.7	108.7	1.27	1.15
1773	2.95	305	3.89	61.9	169.9	106.6	137.8	1.59	1.23
1774	2.91	1151	0.74	31.8	243.8	262.6	262.6	0.93	0.93
1775	2.96	437	0.92	37.7	115.8	95.8	95.8	1.21	1.21
1776	2.94	440	0.90	38.5	113.3	96.8	96.8	1.17	1.17
1777	2.94	440	0.91	39.0	476.0	389.6	389.6	1.22	1.22
1778	2.96	437	0.91	37.9	444.8	383.3	383.3	1.16	1.16
1779	2.94	440	0.91	40.6	1295.3	1183.6	1183.6	1.09	1.09
1784	2.95	84	1.63	33.0	14.5	11.1	11.5	1.30	1.26
1785	2.95	84	1.62	33.0	18.5	11.2	11.5	1.66	1.60
1786	2.95	84	1.63	33.0	15.0	11.1	11.5	1.35	1.30
1787	2.95	168	1.60	30.0	28.8	20.5	20.7	1.40	1.39
1788	2.95	168	1.62	30.0	30.5	20.3	20.6	1.50	1.48
1789	2.98	166	1.62	30.0	29.7	20.3	20.6	1.47	1.44
1790	2.97	333	1.55	34.0	42.2	37.3	37.3	1.13	1.13
1791	2.97	333	1.61	34.0	40.6	36.3	36.3	1.12	1.12
1792	2.97	333	1.61	34.0	42.9	36.3	36.3	1.18	1.18
1803	3.00	434	0.33	40.7	85.0	65.5	65.5	1.30	1.30
1805	2.24	223	1.35	43.0	68.0	45.3	64.4	1.50	1.06
1806	1.12	223	1.35	42.2	135.5	142.0	155.2	0.95	0.87
1807	3.00	406	3.07	26.7	90.7	92.7	94.7	0.98	0.96
1808	1.50	406	3.07	26.8	285.1	235.9	269.9	1.21	1.06
1809	2.25	406	3.07	26.9	151.7	106.4	152.7	1.43	0.99
1823	2.16	925	0.76	33.8	249.2	224.5	282.9	1.11	0.88
1824	1.08	925	0.76	33.8	602.8	713.4	788.5	0.84	0.76
1825	2.89	1400	0.83	38.4	265.0	247.7	247.7	1.07	1.07
1826	2.89	1400	0.83	40.3	242.0	251.9	251.9	0.96	0.96
1827	2.89	1400	0.83	73.6	240.0	310.1	359.1	0.77	0.67
1828	2.89	1400	0.83	31.4	265.0	263.7	263.7	1.00	1.00
1829	2.89	1400	0.83	33.2	266.0	268.8	268.8	0.99	0.99

**Behaviour of Large Non-Slender RC Beams under Monotonic and Reversed Cyclic Load 349**

1	2	3	4	5	6	7	8	9	10
1830	2.89	1400	0.83	28.1	242.0	266.1	266.1	0.91	0.91
1831	2.89	1400	0.83	28.5	288.0	267.3	267.3	1.08	1.08
1832	2.89	1400	0.83	41.0	272.0	302.1	302.1	0.90	0.90
1833	2.89	1400	0.83	40.1	298.0	299.9	299.9	0.99	0.99
1834	2.89	1400	0.83	40.1	323.0	299.9	299.9	1.08	1.08
1835	2.89	280	0.83	41.9	36.6	33.0	34.4	1.11	1.06
1836	2.89	280	0.83	41.9	38.3	33.0	34.4	1.16	1.11
1837	2.89	280	0.83	77.3	37.7	41.9	48.8	0.90	0.77
1838	2.89	280	0.83	39.2	39.1	33.8	34.9	1.16	1.12
1839	2.89	280	0.83	38.1	38.2	33.5	34.3	1.14	1.11
1840	2.89	280	0.83	29.1	41.8	31.2	32.0	1.34	1.31
1841	2.89	280	0.83	29.1	34.9	31.2	32.0	1.12	1.09
1842	2.89	280	0.83	43.5	38.5	35.5	41.2	1.09	0.93
1843	2.89	280	0.83	43.5	40.6	35.5	41.2	1.15	0.99
1844	1.93	850	0.72	51.0	444.1	524.0	641.6	0.85	0.69
1845	1.93	850	0.44	51.0	788.6	452.2	530.2	1.74	1.49
1846	1.93	850	0.72	38.0	385.1	422.1	536.8	0.91	0.72
1847	1.93	850	0.44	38.0	690.6	368.8	445.8	1.87	1.55
1848	2.74	850	0.72	32.0	284.6	280.2	280.2	1.02	1.02
1849	2.74	850	0.44	32.0	327.6	234.8	234.8	1.40	1.40
Average								1.264	1.115
COV								0.250	0.222



## APPENDIX E. VecTor2 INPUT FILES

### D1. SPECIMEN S1C

Structure data: file S1C.s2r

```
* * * * *
*           V e c T o r 2           *
*   S T R U C T U R E   D A T A   *
* * * * *
```

STRUCTURAL PARAMETERS  
\*\*\*\*\*

```
Structure Title      (30 char. max.) : beam S1C
Structure File Name ( 8 char. max.) : S1C
No. of R.C. Material Types          : 2
No. of Steel Material Types         : 3
No. of Bond Material Types          : 0
No. of Rectangular Elements         : 448
No. of Quadrilateral Elements       : 0
No. of Triangular Elements          : 0
No. of Truss Bar Elements           : 127
No. of Linkage Elements              : 0
No. of Contact Elements              : 0
No. of Joints                     : 494
No. of Restraints                   : 19
```

MATERIAL SPECIFICATIONS  
\*\*\*\*\*

(A) REINFORCED CONCRETE  
-----

<NOTE:> TO BE USED IN RECTANGULAR AND TRIANGULAR ELEMENTS ONLY

CONCRETE  
-----

MAT TYP	Ns #	T mm	f'c MPa	[ f't MPa	Ec MPa	e0 me	Mu	Cc /C	Agg mm	Dens kg/m3	Kc mm2/s	[Sx Sy] mm mm
0.000	1	1	400.000	33.000	0.000	0.000		1.630		0.000	0.000	20.000
0.000	2	0	400.000	33.000	0.000	0.000		1.630		0.000	0.000	20.000

REINFORCEMENT COMPONENTS  
-----

MAT TYP	REF TYP	DIR deg	As %	Db mm	Fy MPa	Fu MPa	Es MPa	Esh MPa	esh me	Cs /C	Dep me	
1	1	90.000		0.101	9.500	490.000			600.000		200000.000	880.000
25.000		0.000		0.000								

(B) STEEL  
-----

<NOTE:> TO BE USED FOR TRUSS ELEMENTS ONLY

MAT	REF	AREA	Db	Fy	Fu	Es	Esh	esh	Cs	Dep
TYP	TYP	mm <sup>2</sup>	mm	MPa	MPa	MPa	MPa	me	/C	me
1	1	1530.000		25.000		652.000		862.000		2333.000
10.000		0.000	0.000							
2	1	7854.000		100.000		2000.000		4000.000		20000.000
10.000		0.000	0.000							
3	1	7854.000		100.000		2000.000		4000.000		20000.000
10.000		0.000	0.000							

## (C) BOND

<NOTE:> TO BE USED FOR EXTERIOR/INTERIOR BONDED ELEMENTS

MAT	REF	{ Ao	U1	U2	U3	S1	S2	S3	{ CPF	Cmin	No.	HOOK }
TYP	TYP	mm <sup>2</sup>	MPa	MPa	MPa	mm	mm	mm	0-1	mm	LYR	0/1
/												

ELEMENT INCIDENCES  
\*\*\*\*\*

## (A) RECTANGULAR ELEMENTS

<<<<< FORMAT >>>>>

ELMT	INC1	INC2	INC3	INC4	[#ELMT	d(ELMT)	d(INC)]	[#ELMT	d(ELMT)	d(INC)]/
1	29	24	17	35	1	1	1	1	1	/
2	24	29	36	19	1	1	1	1	1	/
3	36	33	21	19	1	1	1	1	1	/
4	11	15	14	12	1	1	1	1	1	/
5	52	50	69	71	1	1	1	1	1	/
6	13	21	33	28	1	1	1	1	1	/
7	64	40	45	55	1	1	1	1	1	/
.										/
.										/
441	455	456	439	438	1	1	1	1	1	/
442	460	459	476	477	1	1	1	1	1	/
443	475	492	493	476	1	1	1	1	1	/
444	456	473	474	457	1	1	1	1	1	/
445	491	492	475	474	1	1	1	1	1	/
446	490	473	472	489	1	1	1	1	1	/
447	493	494	477	476	1	1	1	1	1	/
448	474	473	490	491	1	1	1	1	1	/

## (B) QUADRILATERAL ELEMENTS

<<<<< FORMAT >>>>>

ELMT	INC1	INC2	INC3	INC4	[#ELMT	d(ELMT)	d(INC)]	[#ELMT	d(ELMT)	d(INC)]/
/										

## (C) TRIANGULAR ELEMENTS

<<<<< FORMAT >>>>>

ELMT	INC1	INC2	INC3	[ #ELMT	d(ELMT)	d(INC) ]	[ #ELMT	d(ELMT)	d(INC)] /
/									

## (D) TRUSS ELEMENTS

<<<<< FORMAT >>>>>

ELMT	INC1	INC2	[ #ELMT	d(ELMT)	d(INC)]	[#ELMT	d(ELMT)	d(INC)] /
449	24	29	1	1	1	1	1	/
450	29	45	1	1	1	1	1	/
451	45	55	1	1	1	1	1	/
452	55	73	1	1	1	1	1	/
453	73	92	1	1	1	1	1	/
454	92	104	1	1	1	1	1	/
.								/
.								/
569	148	149	1	1	1	1	1	/
570	149	150	1	1	1	1	1	/



```

571 150 151 1 1 1 1 1 1 /
572 151 152 1 1 1 1 1 1 /
573 152 153 1 1 1 1 1 1 /
574 153 154 1 1 1 1 1 1 /
575 117 97 1 1 1 1 1 1 /
/

```

(E) LINKAGE ELEMENTS

```

<<<<< FORMAT >>>>>
ELMT INC1 INC2 [ #ELMT d(ELMT) d(INC) ] [ #ELMT d(ELMT) d(INC) ]
/

```

(F) CONTACT ELEMENTS

```

<<<<< FORMAT >>>>>
ELMT INC1 INC2 INC3 INC4 [ #ELMT d(ELMT) d(INC) ] [ #ELMT d(ELMT) d(INC) ]
/

```

MATERIAL TYPE ASSIGNMENT  
\*\*\*\*\*

```

<<<<< FORMAT >>>>>
ELMT MAT ACT [ #ELMT d(ELMT) ] [ #ELMT d(ELMT) ] /
1 2 1 1 1 1 1 /
2 2 1 1 1 1 1 /
3 2 1 1 1 1 1 /
4 2 1 1 1 1 1 /
5 1 1 1 1 1 1 /
6 2 1 1 1 1 1 /
7 2 1 1 1 1 1 /
8 2 1 1 1 1 1 /
9 2 1 1 1 1 1 /
10 2 1 1 1 1 1 /
11 2 1 1 1 1 1 /
12 2 1 1 1 1 1 /
13 1 1 1 1 1 1 /
14 2 1 1 1 1 1 /
.
.
.

```

```

570 3 1 1 1 1 1 /
571 3 1 1 1 1 1 /
572 3 1 1 1 1 1 /
573 3 1 1 1 1 1 /
574 3 1 1 1 1 1 /
575 2 1 1 1 1 1 /
/

```

COORDINATES

\*\*\*\*\*

```

<NOTE:> UNITS: in OR mm
<<<<< FORMAT >>>>>
NODE X Y [ #NODES d(NODES) d(X) d(Y) ] [ #NODES d(NODES) d(X) d(Y) ] /
17 0.000 0.000 1 1 0.000 0.000 1 1 0.000
0.000 /
24 0.000 64.000 1 1 0.000 0.000 1 1 0.000
0.000 /
19 0.000 150.000 1 1 0.000 0.000 1 1 0.000
0.000 /
21 0.000 225.000 1 1 0.000 0.000 1 1 0.000
0.000 /
13 0.000 300.000 1 1 0.000 0.000 1 1 0.000
0.000 /
10 0.000 375.000 1 1 0.000 0.000 1 1 0.000
0.000 /
11 0.000 450.000 1 1 0.000 0.000 1 1 0.000
0.000 /
12 0.000 525.000 1 1 0.000 0.000 1 1 0.000
0.000 /
1 0.000 600.000 1 1 0.000 0.000 1 1 0.000
0.000 /

```

2	0.000	675.000	1	1	0.000	0.000	1	1	0.000
0.000	/								
3	0.000	750.000	1	1	0.000	0.000	1	1	0.000
0.000	/								
			:						
			:						
483	1925.000	375.000	1	1	0.000	0.000	1	1	0.000
0.000	/								
484	1925.000	450.000	1	1	0.000	0.000	1	1	0.000
0.000	/								
485	1925.000	525.000	1	1	0.000	0.000	1	1	0.000
0.000	/								
486	1925.000	600.000	1	1	0.000	0.000	1	1	0.000
0.000	/								
487	1925.000	675.000	1	1	0.000	0.000	1	1	0.000
0.000	/								
488	1925.000	750.000	1	1	0.000	0.000	1	1	0.000
0.000	/								
489	1925.000	825.000	1	1	0.000	0.000	1	1	0.000
0.000	/								
490	1925.000	900.000	1	1	0.000	0.000	1	1	0.000
0.000	/								
491	1925.000	975.000	1	1	0.000	0.000	1	1	0.000
0.000	/								
492	1925.000	1050.000	1	1	0.000	0.000	1	1	0.000
0.000	/								
493	1925.000	1136.000	1	1	0.000	0.000	1	1	0.000
0.000	/								
494	1925.000	1200.000	1	1	0.000	0.000	1	1	0.000
0.000	/								
117	250.000	-50.000	1	1	0.000	0.000	1	1	0.000
0.000	/								
	/								

SUPPORT RESTRAINTS  
\*\*\*\*\*

<NOTE:> CODE: '0' FOR NOT RESTRAINED NODES AND '1' FOR RESTRAINED ONES

<<<<< FORMAT >>>>>

NODE X-RST Y-RST [ #NODE d(NODE) ] /

97	0	1	1	1	/
478	1	0	1	1	/
479	1	0	1	1	/
480	1	0	1	1	/
481	1	0	1	1	/
482	1	0	1	1	/
483	1	0	1	1	/
484	1	0	1	1	/
485	1	0	1	1	/
486	1	0	1	1	/
487	1	0	1	1	/
488	1	0	1	1	/
489	1	0	1	1	/
490	1	0	1	1	/
491	1	0	1	1	/
492	1	0	1	1	/
493	1	0	1	1	/
494	1	0	1	1	/
117	1	0	1	1	/
	/				

<<< STRUCTURE FILE NOTES >>>

## Cyclic load, Step 1: files Vector.job, S1Cg.l2r, S1Cext.l2r

```

* * * * *
*   V E C T O R   *
*   J O B   D A T A *
* * * * *

```

```

Job Title      (30 char. max.)      : beam S1C
Job File Name  ( 8 char. max.)      : S1C
Date          (30 char. max.)      : 21/09/08

```

## STRUCTURE DATA

```

-----
Structure Type      : 2
File Name          ( 8 char. max.) : S1C

```

## LOADING DATA

```

-----
No. of Load Stages      : 21
Starting Load Stage No. : 1
Load Series ID   ( 5 char. max.) : LS

```

Load Case	File Name (8 char. max.)	Initial	Final	Factors LS-Inc	Type	Reps	C-Inc
1	S1Cg	1.000000	1.000000	0.000000	1	1	0.000000
2	S1Cext	0.000000	1.000000	0.100000	2	1	0.000000
3	NULL	0.000000	0.000000	0.000000	1	1	0.000000
4	NULL	0.000000	0.000000	0.000000	1	1	0.000000
5	NULL	0.000000	0.000000	0.000000	1	1	0.000000

## ANALYSIS PARAMETERS

```

-----
Analysis Mode          (1-2) : 1
Seed File Name        (8 char. max.) : LS_00
Convergence Limit     (>1.0) : 1.000010
Averaging Factor      (<1.0) : 0.500
Maximum No. of Iterations : 200
Convergence Criteria  (1-5) : 2
Results Files         (1-4) : 2
Output Format          (1-3) : 1

```

## MATERIAL BEHAVIOUR MODELS

```

-----
Concrete Compression Base Curve      (0-3) : 2
Concrete Compression Post-Peak       (0-3) : 1
Concrete Compression Softening       (0-8) : 1
Concrete Tension Stiffening           (0-6) : 1
Concrete Tension Softening            (0-3) : 1
Concrete Tension Splitting            (0-1) : 0
Concrete Confined Strength             (0-2) : 1
Concrete Dilation                      (0-1) : 1
Concrete Cracking Criterion            (0-4) : 1
Concrete Crack Slip Check              (0-2) : 1
Concrete Crack Width Check            (0-2) : 1
Concrete Bond or Adhesion              (0-3) : 1
Concrete Creep and Relaxation          (0-1) : 1
Concrete Hysteresis                    (0-2) : 3
Reinforcement Hysteresis               (0-2) : 1
Reinforcement Dowel Action             (0-1) : 1
Reinforcement Buckling                 (0-1) : 1
Element Strain Histories                (0-1) : 1
Element Slip Distortions                (0-4) : 1
Strain Rate Effects                     (0-1) : 1
Structural Damping                     (0-1) : 1
Geometric Nonlinearity                 (0-1) : 1

```

Crack Allocation Process (0-1) : 1

<<< JOB FILE NOTES>>>

\* \* \* \* \*  
\* V e c T o r 2 \*  
\* L O A D D A T A \*  
\* \* \* \* \*

LOAD CASE PARAMETERS  
\*\*\*\*\*

Structure Title (30 char. max.) : beam S1C  
Load Case Title (30 char. max.) : S1Cg  
Load Case File Name (8 char. max.) : S1Cg  
No. of Loaded Joints : 3  
No. of Prescribed Support Displacements : 0  
No. of Elements with Gravity Loads : 448  
No. of Elements with Temperature Loads : 0  
No. of Elements with Concrete Prestrain : 0  
No. of Elements with Ingress Pressure : 0  
No. of Element Surfaces w/ Thermal Load : 0  
No. of Nodes with Lumped Masses : 0  
No. of Nodes with Impulse Forces : 0  
Ground Acceleration Record (0-1) : 0

JOINT LOADS  
\*\*\*\*\*

<NOTE:> UNITS: KIPS OR KN  
<<<<< FORMAT >>>>>  
NODE FX Fy [ #NODE d(NODE) d(Fx) d(Fy) ] /  
63 0.000 3.732 1 1 0.000 0.000/  
79 0.000 7.463 1 1 0.000 0.000/  
109 0.000 3.732 1 1 0.000 0.000/  
/

SUPPORT DISPLACEMENTS  
\*\*\*\*\*

<NOTE:> UNITS: MM OR IN  
<<<<< FORMAT >>>>>  
JNT DOF DISPL [ #JNT d(JNT) ] /  
/

GRAVITY LOADS  
\*\*\*\*\*

<NOTE:> UNITS: KG/M3  
<<<<< FORMAT >>>>>  
ELMT DENS GX GY [ #ELMT d(ELMT) ] [ #ELMT d(ELMT) ] /  
1 2470.000 0.000 -1.000 1 1 1 1/  
2 2470.000 0.000 -1.000 1 1 1 1/  
:  
:  
447 2470.000 0.000 -1.000 1 1 1 1/  
448 2470.000 0.000 -1.000 1 1 1 1/  
/

TEMPERATURE LOADS  
\*\*\*\*\*

<NOTE:> UNITS: F OR C  
<<<<< FORMAT >>>>>  
ELMT TEMP [ #ELMT d(ELMT) d(TEMP) ] [ #ELMT d(ELMT) d(TEMP) ] /  
/

CONCRETE PRESTRAINS  
\*\*\*\*\*

<NOTE:> UNITS: me  
<<<<< FORMAT >>>>>

```

ELMT STRAIN [ #ELMT d(ELMT) d(STRAIN) ] [ #ELMT d(ELMT) d(STRAIN) ] /
/
                                INGRESS PRESSURES
                                *****

<NOTE:> UNITS: MPa
<<<<< FORMAT >>>>>
ELMT PRESSURE [ #ELMT d(ELMT) d(PRS) ] [ #ELMT d(ELMT) d(PRS) ] /
/
                                SURFACE THERMAL LOADS
                                *****

<NOTE:> UNITS: Sec, Degrees C
<<<<< FORMAT >>>>>
NODE1 NODE2 Tm1 Tp1 Tm2 Tp2 Tm3 Tp3 [#SURF d(NODE)] [#SURF d(NODE)] /
/
                                LUMPED MASSES
                                *****

<NOTE:> UNITS: kg, m/s
<<<<< FORMAT >>>>>
NODE DOF-X DOF-Y MASS GF-X GF-Y Vo-X Vo-Y [ #NODE d(NODE) ] /
/
                                IMPULSE FORCES
                                *****

<NOTE:> UNITS: Sec, kN
<<<<< FORMAT >>>>>
NODE DOF T1 F1 T2 F2 T3 F3 T4 F4 [ #NODE d(NODE) ] /
/
                                GROUND ACCELERATION
                                *****

<NOTE:> UNITS: Sec, G
<<<<< FORMAT >>>>>
TIME ACC-X ACC-Y
/

<<<< LOAD FILE NOTES >>>>

* * * * *
*   V e c T o r 2   *
*   L O A D   D A T A   *
* * * * *

                                LOAD CASE PARAMETERS
                                *****

Structure Title      (30 char. max.) : beam S1C
Load Case Title     (30 char. max.) : S1Cext
Load Case File Name (8 char. max.)  : S1Cext
No. of Loaded Joints : 7
No. of Prescribed Support Displacements : 0
No. of Elements with Gravity Loads : 0
No. of Elements with Temperature Loads : 0
No. of Elements with Concrete Prestrain : 0
No. of Elements with Ingress Pressure : 0
No. of Element Surfaces w/ Thermal Load : 0
No. of Nodes with Lumped Masses : 0
No. of Nodes with Impulse Forces : 0
Ground Acceleration Record (0-1) : 0

                                JOINT LOADS
                                *****

<NOTE:> UNITS: KIPS OR KN
<<<<< FORMAT >>>>>
NODE Fx Fy [ #NODE d(NODE) d(Fx) d(Fy) ] /
63 0.000 155.3 1 1 0.000 0.000/
79 0.000 310.7 1 1 0.000 0.000/
109 0.000 155.3 1 1 0.000 0.000/
443 0.000 -155.3 1 1 0.000 0.000/

```

```

460 0.000 -310.7 1 1 0.000 0.000/
477 0.000 -310.7 1 1 0.000 0.000/
494 0.000 -155.3 1 1 0.000 0.000/
/
SUPPORT DISPLACEMENTS
*****
<NOTE:> UNITS: MM OR IN
<<<<< FORMAT >>>>>
JNT DOF DISPL [ #JNT d(JNT) ] /
/
GRAVITY LOADS
*****
<NOTE:> UNITS: KG/M3
<<<<< FORMAT >>>>>
ELMT DENS GX GY [ #ELMT d(ELMT) ] [ #ELMT d(ELMT) ] /
/
TEMPERATURE LOADS
*****
<NOTE:> UNITS: F OR C
<<<<< FORMAT >>>>>
ELMT TEMP [ #ELMT d(ELMT) d(TEMP) ] [ #ELMT d(ELMT) d(TEMP) ] /
/
CONCRETE PRESTRAINS
*****
<NOTE:> UNITS: me
<<<<< FORMAT >>>>>
ELMT STRAIN [ #ELMT d(ELMT) d(STRAIN) ] [ #ELMT d(ELMT) d(STRAIN) ] /
/
INGRESS PRESSURES
*****
<NOTE:> UNITS: MPa
<<<<< FORMAT >>>>>
ELMT PRESSURE [ #ELMT d(ELMT) d(PRS) ] [ #ELMT d(ELMT) d(PRS) ] /
/
SURFACE THERMAL LOADS
*****
<NOTE:> UNITS: Sec, Degrees C
<<<<< FORMAT >>>>>
NODE1 NODE2 Tm1 Tp1 Tm2 Tp2 Tm3 Tp3 [ #SURF d(NODE) ] [ #SURF d(NODE) ] /
/
LUMPED MASSES
*****
<NOTE:> UNITS: kg, m/s
<<<<< FORMAT >>>>>
NODE DOF-X DOF-Y MASS GF-X GF-Y Vo-X Vo-Y [ #NODE d(NODE) ] /
/
IMPULSE FORCES
*****
<NOTE:> UNITS: Sec, kN
<<<<< FORMAT >>>>>
NODE DOF T1 F1 T2 F2 T3 F3 T4 F4 [ #NODE d(NODE) ] /
/
GROUND ACCELERATION
*****
<NOTE:> UNITS: Sec, G
<<<<< FORMAT >>>>>
TIME ACC-X ACC-Y
/

<<< LOAD FILE NOTES >>>

```

## Cyclic load, Step 2: files Vector.job, S1Cg.l2r, S1Cext1.l2r, S1Cext1.l2r

```

* * * * *
*   V E C T O R   *
*   J O B   D A T A   *
* * * * *

```

```

Job Title      (30 char. max.)      : beam S1C
Job File Name  ( 8 char. max.)      : S1C
Date           (30 char. max.)      : 21/09/08

```

## STRUCTURE DATA

```

-----
Structure Type      : 2
File Name          ( 8 char. max.) : S1C

```

## LOADING DATA

```

-----
No. of Load Stages      : 3
Starting Load Stage No. : 22
Load Series ID ( 5 char. max.) : LS

```

Load Case	File Name (8 char. max.)	Initial	Final	Factors LS-Inc	Type	Reps	C-Inc
1	S1Cg	1.000000	1.000000	0.000000	1	1	0.000000
2	S1Cext1	0.000000	1.000000	0.500000	1	1	0.000000
3	S1Cext2	-1.000000	0.000000	0.500000	1	1	0.000000
4	NULL	0.000000	0.000000	0.000000	1	1	0.000000
5	NULL	0.000000	0.000000	0.000000	1	1	0.000000

## ANALYSIS PARAMETERS

```

-----
Analysis Mode      (1-2) : 1
Seed File Name    (8 char. max.) : LS_00
Convergence Limit (>1.0) : 1.000010
Averaging Factor (<1.0) : 0.500
Maximum No. of Iterations : 200
Convergence Criteria (1-5) : 2
Results Files     (1-4) : 2
Output Format      (1-3) : 1

```

## MATERIAL BEHAVIOUR MODELS

```

-----
Concrete Compression Base Curve (0-3) : 2
Concrete Compression Post-Peak (0-3) : 1
Concrete Compression Softening (0-8) : 1
Concrete Tension Stiffening (0-6) : 1
Concrete Tension Softening (0-3) : 1
Concrete Tension Splitting (0-1) : 0
Concrete Confined Strength (0-2) : 1
Concrete Dilation (0-1) : 1
Concrete Cracking Criterion (0-4) : 1
Concrete Crack Slip Check (0-2) : 1
Concrete Crack Width Check (0-2) : 1
Concrete Bond or Adhesion (0-3) : 1
Concrete Creep and Relaxation (0-1) : 1
Concrete Hysteresis (0-2) : 3
Reinforcement Hysteresis (0-2) : 1
Reinforcement Dowel Action (0-1) : 1
Reinforcement Buckling (0-1) : 1
Element Strain Histories (0-1) : 1
Element Slip Distortions (0-4) : 1
Strain Rate Effects (0-1) : 1
Structural Damping (0-1) : 1

```

Geometric Nonlinearity (0-1) : 1  
 Crack Allocation Process (0-1) : 1

<<< JOB FILE NOTES>>>

\* \* \* \* \*  
 \* V e c T o r 2 \*  
 \* L O A D D A T A \*  
 \* \* \* \* \*

LOAD CASE PARAMETERS  
 \*\*\*\*\*

Structure Title (30 char. max.) : beam S1C  
 Load Case Title (30 char. max.) : S1Cg  
 Load Case File Name (8 char. max.) : S1Cg  
 No. of Loaded Joints : 0  
 No. of Prescribed Support Displacements : 0  
 No. of Elements with Gravity Loads : 448  
 No. of Elements with Temperature Loads : 0  
 No. of Elements with Concrete Prestrain : 0  
 No. of Elements with Ingress Pressure : 0  
 No. of Element Surfaces w/ Thermal Load : 0  
 No. of Nodes with Lumped Masses : 0  
 No. of Nodes with Impulse Forces : 0  
 Ground Acceleration Record (0-1) : 0

JOINT LOADS  
 \*\*\*\*\*

<NOTE:> UNITS: KIPS OR KN  
 <<<<< FORMAT >>>>>  
 NODE FX Fy [ #NODE d(NODE) d(Fx) d(Fy) ] /  
 /

SUPPORT DISPLACEMENTS  
 \*\*\*\*\*

<NOTE:> UNITS: MM OR IN  
 <<<<< FORMAT >>>>>  
 JNT DOF DISPL [ #JNT d(JNT) ] /  
 /

GRAVITY LOADS  
 \*\*\*\*\*

<NOTE:> UNITS: KG/M3  
 <<<<< FORMAT >>>>>  
 ELMT DENS GX GY [#ELMT d(ELMT)] [ #ELMT d(ELMT)] /  
 1 2470.000 0.000 -1.000 1 1 1 1/  
 2 2470.000 0.000 -1.000 1 1 1 1/  
 .  
 .  
 447 2470.000 0.000 -1.000 1 1 1 1/  
 448 2470.000 0.000 -1.000 1 1 1 1/  
 /

TEMPERATURE LOADS  
 \*\*\*\*\*

<NOTE:> UNITS: F OR C  
 <<<<< FORMAT >>>>>  
 ELMT TEMP [ #ELMT d(ELMT) d(TEMP) ] [ #ELMT d(ELMT) d(TEMP) ] /  
 /

CONCRETE PRESTRAINS  
 \*\*\*\*\*

<NOTE:> UNITS: me  
 <<<<< FORMAT >>>>>  
 ELMT STRAIN [ #ELMT d(ELMT) d(STRAIN) ] [ #ELMT d(ELMT) d(STRAIN) ] /  
 /

INGRESS PRESSURES



```

*****
<NOTE:> UNITS: MPa
<<<<< FORMAT >>>>>
ELMT PRESSURE [ #ELMT d(ELMT) d(PRS) ] [ #ELMT d(ELMT) d(PRS) ] /
/
SURFACE THERMAL LOADS
*****
<NOTE:> UNITS: Sec, Degrees C
<<<<< FORMAT >>>>>
NODE1 NODE2 Tm1 Tp1 Tm2 Tp2 Tm3 Tp3 [#SURF d(NODE)] [#SURF d(NODE)] /
/
LUMPED MASSES
*****
<NOTE:> UNITS: kg, m/s
<<<<< FORMAT >>>>>
NODE DOF-X DOF-Y MASS GF-X GF-Y Vo-X Vo-Y [ #NODE d(NODE) ] /
/
IMPULSE FORCES
*****
<NOTE:> UNITS: Sec, kN
<<<<< FORMAT >>>>>
NODE DOF T1 F1 T2 F2 T3 F3 T4 F4 [ #NODE d(NODE) ] /
/
GROUND ACCELERATION
*****
<NOTE:> UNITS: Sec, G
<<<<< FORMAT >>>>>
TIME ACC-X ACC-Y
/

```

<<< LOAD FILE NOTES >>>

```

* * * * *
*   V e c t o r 2   *
*   L O A D   D A T A   *
* * * * *

```

LOAD CASE PARAMETERS  
\*\*\*\*\*

```

Structure Title      (30 char. max.) : beam S1C
Load Case Title     (30 char. max.) : S1Cext1
Load Case File Name (8 char. max.)  : S1Cext1
No. of Loaded Joints : 4
No. of Prescribed Support Displacements : 0
No. of Elements with Gravity Loads : 0
No. of Elements with Temperature Loads : 0
No. of Elements with Concrete Prestrain : 0
No. of Elements with Ingress Pressure : 0
No. of Element Surfaces w/ Thermal Load : 0
No. of Nodes with Lumped Masses : 0
No. of Nodes with Impulse Forces : 0
Ground Acceleration Record (0-1) : 0

```

JOINT LOADS  
\*\*\*\*\*

```

<NOTE:> UNITS: KIPS OR KN
<<<<< FORMAT >>>>>
NODE   FX   Fy   [ #NODE d(NODE) d(Fx) d(Fy) ] /
  427  0.000  3.732  1  1  0.000  0.000/
  444  0.000  7.463  1  1  0.000  0.000/
  461  0.000  7.463  1  1  0.000  0.000/
  478  0.000  3.732  1  1  0.000  0.000/
/

```

SUPPORT DISPLACEMENTS

```

*****
<NOTE:> UNITS: MM OR IN
<<<<< FORMAT >>>>>
JNT DOF DISPL [ #JNT d(JNT) ] /
/
GRAVITY LOADS
*****
<NOTE:> UNITS: KG/M3
<<<<< FORMAT >>>>>
ELMT DENS GX GY [ #ELMT d(ELMT) ] [ #ELMT d(ELMT) ] /
/
TEMPERATURE LOADS
*****
<NOTE:> UNITS: F OR C
<<<<< FORMAT >>>>>
ELMT TEMP [ #ELMT d(ELMT) d(TEMP) ] [ #ELMT d(ELMT) d(TEMP) ] /
/
CONCRETE PRESTRAINS
*****
<NOTE:> UNITS: me
<<<<< FORMAT >>>>>
ELMT STRAIN [ #ELMT d(ELMT) d(STRAIN) ] [ #ELMT d(ELMT) d(STRAIN) ] /
/
INGRESS PRESSURES
*****
<NOTE:> UNITS: MPa
<<<<< FORMAT >>>>>
ELMT PRESSURE [ #ELMT d(ELMT) d(PRS) ] [ #ELMT d(ELMT) d(PRS) ] /
/
SURFACE THERMAL LOADS
*****
<NOTE:> UNITS: Sec, Degrees C
<<<<< FORMAT >>>>>
NODE1 NODE2 Tm1 Tp1 Tm2 Tp2 Tm3 Tp3 [ #SURF d(NODE) ] [ #SURF d(NODE) ] /
/
LUMPED MASSES
*****
<NOTE:> UNITS: kg, m/s
<<<<< FORMAT >>>>>
NODE DOF-X DOF-Y MASS GF-X GF-Y Vo-X Vo-Y [ #NODE d(NODE) ] /
/
IMPULSE FORCES
*****
<NOTE:> UNITS: Sec, kN
<<<<< FORMAT >>>>>
NODE DOF T1 F1 T2 F2 T3 F3 T4 F4 [ #NODE d(NODE) ] /
/
GROUND ACCELERATION
*****
<NOTE:> UNITS: Sec, G
<<<<< FORMAT >>>>>
TIME ACC-X ACC-Y
/

```

<<< LOAD FILE NOTES >>>

```

* * * * *
*   V e c t o r 2   *
*   L O A D   D A T A   *
* * * * *

```

```

LOAD CASE PARAMETERS
*****

```

Structure Title (30 char. max.) : beam S1C

```

Load Case Title      (30 char. max.) : S1Cext2
Load Case File Name (8 char. max.)  : S1Cext2
No. of Loaded Joints : 3
No. of Prescribed Support Displacements : 0
No. of Elements with Gravity Loads   : 0
No. of Elements with Temperature Loads : 0
No. of Elements with Concrete Prestrain : 0
No. of Elements with Ingress Pressure : 0
No. of Element Surfaces w/ Thermal Load : 0
No. of Nodes with Lumped Masses      : 0
No. of Nodes with Impulse Forces     : 0
Ground Acceleration Record (0-1)    : 0
    
```

JOINT LOADS  
\*\*\*\*\*

```

<NOTE:> UNITS: KIPS OR KN
<<<<< FORMAT >>>>>
NODE  Fx  Fy  [ #NODE d(NODE) d(Fx) d(Fy) ] /
  63  0.000 -3.732 1 1 0.000 0.000/
  79  0.000 -7.463 1 1 0.000 0.000/
 109  0.000 -3.732 1 1 0.000 0.000/
/
    
```

SUPPORT DISPLACEMENTS  
\*\*\*\*\*

```

<NOTE:> UNITS: MM OR IN
<<<<< FORMAT >>>>>
JNT  DOF  DISPL  [ #JNT d(JNT) ] /
/
    
```

GRAVITY LOADS  
\*\*\*\*\*

```

<NOTE:> UNITS: KG/M3
<<<<< FORMAT >>>>>
ELMT  DENS  GX  GY  [#ELMT d(ELMT)] [ #ELMT d(ELMT)] /
/
    
```

TEMPERATURE LOADS  
\*\*\*\*\*

```

<NOTE:> UNITS: F OR C
<<<<< FORMAT >>>>>
ELMT  TEMP  [ #ELMT d(ELMT) d(TEMP) ] [ #ELMT d(ELMT) d(TEMP) ] /
/
    
```

CONCRETE PRESTRAINS  
\*\*\*\*\*

```

<NOTE:> UNITS: me
<<<<< FORMAT >>>>>
ELMT  STRAIN  [ #ELMT d(ELMT) d(STRAIN) ] [ #ELMT d(ELMT) d(STRAIN) ] /
/
    
```

INGRESS PRESSURES  
\*\*\*\*\*

```

<NOTE:> UNITS: MPa
<<<<< FORMAT >>>>>
ELMT  PRESSURE  [ #ELMT d(ELMT) d(PRS) ] [ #ELMT d(ELMT) d(PRS) ] /
/
    
```

SURFACE THERMAL LOADS  
\*\*\*\*\*

```

<NOTE:> UNITS: Sec, Degrees C
<<<<< FORMAT >>>>>
NODE1  NODE2  Tm1  Tp1  Tm2  Tp2  Tm3  Tp3  [#SURF d(NODE)] [#SURF d(NODE)] /
/
    
```

LUMPED MASSES  
\*\*\*\*\*

```

<NOTE:> UNITS: kg, m/s
<<<<< FORMAT >>>>>
NODE  DOF-X  DOF-Y  MASS  GF-X  GF-Y  Vo-X  Vo-Y  [ #NODE d(NODE) ] /
/
    
```

IMPULSE FORCES  
\*\*\*\*\*

```

<NOTE:> UNITS: Sec, kN
    
```

```

<<<<< FORMAT >>>>>
NODE DOF T1 F1 T2 F2 T3 F3 T4 F4 [ #NODE d(NODE) ] /
/
GROUND ACCELERATION
*****
<NOTE:> UNITS: Sec, G
<<<<< FORMAT >>>>>
TIME ACC-X ACC-Y
/

<<< LOAD FILE NOTES >>>

```

### Cyclic load, Step 3: files Vector.job, S1Cg.l2r, S1Cext.l2r

```

* * * * *
*   V E C T O R   *
*   J O B   D A T A   *
* * * * *

```

```

Job Title      (30 char. max.)      : beam S1C
Job File Name  ( 8 char. max.)      : S1C
Date           (30 char. max.)      : 21/09/08

```

#### STRUCTURE DATA

```

-----
Structure Type      : 2
File Name           ( 8 char. max.) : S1C

```

#### LOADING DATA

```

-----
No. of Load Stages      : 21
Starting Load Stage No. : 25
Load Series ID ( 5 char. max.) : LS

```

Load Case	File Name (8 char. max.)	Initial	Final	Factors LS-Inc	Type	Reps	C-Inc
1	S1Cg	1.000000	1.000000	0.000000	1	1	0.000000
2	S1Cext	0.000000	1.000000	0.100000	2	1	0.000000
3	NULL	0.000000	0.000000	0.000000	1	1	0.000000
4	NULL	0.000000	0.000000	0.000000	1	1	0.000000
5	NULL	0.000000	0.000000	0.000000	1	1	0.000000

#### ANALYSIS PARAMETERS

```

-----
Analysis Mode      (1-2) : 1
Seed File Name     (8 char. max.) : LS_00
Convergence Limit  (>1.0) : 1.000010
Averaging Factor   (<1.0) : 0.500
Maximum No. of Iterations : 200
Convergence Criteria (1-5) : 2
Results Files      (1-4) : 2
Output Format       (1-3) : 1

```

#### MATERIAL BEHAVIOUR MODELS

```

-----
Concrete Compression Base Curve (0-3) : 2
Concrete Compression Post-Peak (0-3) : 1
Concrete Compression Softening (0-8) : 1
Concrete Tension Stiffening (0-6) : 1
Concrete Tension Softening (0-3) : 1
Concrete Tension Splitting (0-1) : 0
Concrete Confined Strength (0-2) : 1

```

```

Concrete Dilation (0-1) : 1
Concrete Cracking Criterion (0-4) : 1
Concrete Crack Slip Check (0-2) : 1
Concrete Crack width Check (0-2) : 1
Concrete Bond or Adhesion (0-3) : 1
Concrete Creep and Relaxation (0-1) : 1
Concrete Hysteresis (0-2) : 3
Reinforcement Hysteresis (0-2) : 1
Reinforcement Dowel Action (0-1) : 1
Reinforcement Buckling (0-1) : 1
Element Strain Histories (0-1) : 1
Element Slip Distortions (0-4) : 1
Strain Rate Effects (0-1) : 1
Structural Damping (0-1) : 1
Geometric Nonlinearity (0-1) : 1
Crack Allocation Process (0-1) : 1
    
```

<<< JOB FILE NOTES>>>

```

* * * * *
*   V e c t o r 2   *
*   L O A D   D A T A   *
* * * * *
    
```

LOAD CASE PARAMETERS  
\*\*\*\*\*

```

Structure Title (30 char. max.) : beam S1C
Load Case Title (30 char. max.) : S1Cg
Load Case File Name (8 char. max.) : S1Cg
No. of Loaded Joints : 4
No. of Prescribed Support Displacements : 0
No. of Elements with Gravity Loads : 448
No. of Elements with Temperature Loads : 0
No. of Elements with Concrete Prestrain : 0
No. of Elements with Ingress Pressure : 0
No. of Element Surfaces w/ Thermal Load : 0
No. of Nodes with Lumped Masses : 0
No. of Nodes with Impulse Forces : 0
Ground Acceleration Record (0-1) : 0
    
```

JOINT LOADS  
\*\*\*\*\*

```

<NOTE:> UNITS: KIPS OR KN
<<<<< FORMAT >>>>>
NODE   FX   Fy   [ #NODE d(NODE) d(Fx) d(Fy) ] /
  427  0.000  3.732  1  1  0.000  0.000/
  444  0.000  7.463  1  1  0.000  0.000/
  461  0.000  7.463  1  1  0.000  0.000/
  478  0.000  3.732  1  1  0.000  0.000/
/
    
```

SUPPORT DISPLACEMENTS  
\*\*\*\*\*

```

<NOTE:> UNITS: MM OR IN
<<<<< FORMAT >>>>>
JNT  DOF  DISPL [ #JNT d(JNT) ] /
/
    
```

GRAVITY LOADS  
\*\*\*\*\*

```

<NOTE:> UNITS: KG/M3
<<<<< FORMAT >>>>>
ELMT  DENS  GX  GY  [#ELMT d(ELMT)] [ #ELMT d(ELMT)] /
  1    2470.000  0.000  -1.000  1  1  1  1/
  2    2470.000  0.000  -1.000  1  1  1  1/
    
```

```

      .
      .
      .
447 2470.000 0.000 -1.000 1 1 1 1/
448 2470.000 0.000 -1.000 1 1 1 1/
/
      TEMPERATURE LOADS
      *****

<NOTE:> UNITS: F OR C
<<<<< FORMAT >>>>>
ELMT TEMP [ #ELMT d(ELMT) d(TEMP) ] [ #ELMT d(ELMT) d(TEMP) ] /
/
      CONCRETE PRESTRAINS
      *****

<NOTE:> UNITS: me
<<<<< FORMAT >>>>>
ELMT STRAIN [ #ELMT d(ELMT) d(STRAIN) ] [ #ELMT d(ELMT) d(STRAIN) ] /
/
      INGRESS PRESSURES
      *****

<NOTE:> UNITS: MPa
<<<<< FORMAT >>>>>
ELMT PRESSURE [ #ELMT d(ELMT) d(PRS) ] [ #ELMT d(ELMT) d(PRS) ] /
/
      SURFACE THERMAL LOADS
      *****

<NOTE:> UNITS: Sec, Degrees C
<<<<< FORMAT >>>>>
NODE1 NODE2 Tm1 Tp1 Tm2 Tp2 Tm3 Tp3 [#SURF d(NODE)] [#SURF d(NODE)] /
/
      LUMPED MASSES
      *****

<NOTE:> UNITS: kg, m/s
<<<<< FORMAT >>>>>
NODE DOF-X DOF-Y MASS GF-X GF-Y Vo-X Vo-Y [ #NODE d(NODE) ] /
/
      IMPULSE FORCES
      *****

<NOTE:> UNITS: Sec, kN
<<<<< FORMAT >>>>>
NODE DOF T1 F1 T2 F2 T3 F3 T4 F4 [ #NODE d(NODE) ] /
/
      GROUND ACCELERATION
      *****

<NOTE:> UNITS: Sec, G
<<<<< FORMAT >>>>>
TIME ACC-X ACC-Y
/

```

<<< LOAD FILE NOTES >>>

```

* * * * *
*   V e c t o r 2   *
*   L O A D   D A T A   *
* * * * *

```

LOAD CASE PARAMETERS  
\*\*\*\*\*

```

Structure Title (30 char. max.) : beam S1C
Load Case Title (30 char. max.) : S1Cext
Load Case File Name (8 char. max.) : S1Cext
No. of Loaded Joints : 9
No. of Prescribed Support Displacements : 0
No. of Elements with Gravity Loads : 0

```

No. of Elements with Temperature Loads : 0  
 No. of Elements with Concrete Prestrain : 0  
 No. of Elements with Ingress Pressure : 0  
 No. of Element Surfaces w/ Thermal Load : 0  
 No. of Nodes with Lumped Masses : 0  
 No. of Nodes with Impulse Forces : 0  
 Ground Acceleration Record (0-1) : 0

JOINT LOADS  
 \*\*\*\*\*

<NOTE:> UNITS: KIPS OR KN  
 <<<< FORMAT >>>>  
 NODE FX Fy [ #NODE d(NODE) d(Fx) d(Fy) ] /  
 68 0.000 -146.8 1 1 0.000 0.000/  
 85 0.000 -293.5 1 1 0.000 0.000/  
 102 0.000 -293.5 1 1 0.000 0.000/  
 120 0.000 -146.8 1 1 0.000 0.000/  
 427 0.000 146.8 1 1 0.000 0.000/  
 444 0.000 293.5 1 1 0.000 0.000/  
 461 0.000 293.5 1 1 0.000 0.000/  
 478 0.000 146.8 1 1 0.000 0.000/  
 117 0.000 293.5 1 1 0.000 0.000/  
 /

SUPPORT DISPLACEMENTS  
 \*\*\*\*\*

<NOTE:> UNITS: MM OR IN  
 <<<< FORMAT >>>>  
 JNT DOF DISPL [ #JNT d(JNT) ] /  
 /

GRAVITY LOADS  
 \*\*\*\*\*

<NOTE:> UNITS: KG/M3  
 <<<< FORMAT >>>>  
 ELMT DENS GX GY [ #ELMT d(ELMT) ] [ #ELMT d(ELMT) ] /  
 /

TEMPERATURE LOADS  
 \*\*\*\*\*

<NOTE:> UNITS: F OR C  
 <<<< FORMAT >>>>  
 ELMT TEMP [ #ELMT d(ELMT) d(TEMP) ] [ #ELMT d(ELMT) d(TEMP) ] /  
 /

CONCRETE PRESTRAINS  
 \*\*\*\*\*

<NOTE:> UNITS: me  
 <<<< FORMAT >>>>  
 ELMT STRAIN [ #ELMT d(ELMT) d(STRAIN) ] [ #ELMT d(ELMT) d(STRAIN) ] /  
 /

INGRESS PRESSURES  
 \*\*\*\*\*

<NOTE:> UNITS: MPa  
 <<<< FORMAT >>>>  
 ELMT PRESSURE [ #ELMT d(ELMT) d(PRS) ] [ #ELMT d(ELMT) d(PRS) ] /  
 /

SURFACE THERMAL LOADS  
 \*\*\*\*\*

<NOTE:> UNITS: Sec, Degrees C  
 <<<< FORMAT >>>>  
 NODE1 NODE2 Tm1 Tp1 Tm2 Tp2 Tm3 Tp3 [ #SURF d(NODE) ] [ #SURF d(NODE) ] /  
 /

LUMPED MASSES  
 \*\*\*\*\*

<NOTE:> UNITS: kg, m/s  
 <<<< FORMAT >>>>  
 NODE DOF-X DOF-Y MASS GF-X GF-Y Vo-X Vo-Y [ #NODE d(NODE) ] /  
 /

IMPULSE FORCES  
 \*\*\*\*\*

```

<NOTE:> UNITS: Sec, kN
<<<<< FORMAT >>>>>
NODE DOF T1 F1 T2 F2 T3 F3 T4 F4 [ #NODE d(NODE) ] /
/

```

```

GROUND ACCELERATION
*****

```

```

<NOTE:> UNITS: Sec, G
<<<<< FORMAT >>>>>
TIME ACC-X ACC-Y
/

```

```

<<< LOAD FILE NOTES >>>

```

#### Cyclic load, Step 4: files Vector.job, S1Cg.l2r, S1Cext1.l2r, S1Cext2.l2r

```

* * * * *
*   V E C T O R   *
*   J O B   D A T A   *
* * * * *

```

```

Job Title      (30 char. max.)      : beam S1C
Job File Name  ( 8 char. max.)      : S1C
Date           (30 char. max.)      : 21/09/08

```

#### STRUCTURE DATA

```

-----
Structure Type          : 2
File Name              ( 8 char. max.) : S1C

```

#### LOADING DATA

```

-----
No. of Load Stages          : 3
Starting Load Stage No.     : 46
Load Series ID ( 5 char. max.) : LS

```

Load Case	File Name (8 char. max.)	Initial	Final	Factors LS-Inc	Type	Reps	C-Inc
1	S1Cg	1.000000	1.000000	0.000000	1	1	0.000000
2	S1Cext1	-1.000000	0.000000	0.500000	1	1	0.000000
3	S1Cext2	0.000000	1.000000	0.500000	1	1	0.000000
4	NULL	0.000000	0.000000	0.000000	1	1	0.000000
5	NULL	0.000000	0.000000	0.000000	1	1	0.000000

#### ANALYSIS PARAMETERS

```

-----
Analysis Mode          (1-2) : 1
Seed File Name        (8 char. max.) : LS_00
Convergence Limit     (>1.0) : 1.000010
Averaging Factor      (<1.0) : 0.500
Maximum No. of Iterations : 200
Convergence Criteria  (1-5) : 2
Results Files         (1-4) : 2
Output Format          (1-3) : 1

```

#### MATERIAL BEHAVIOUR MODELS

```

-----
Concrete Compression Base Curve (0-3) : 2
Concrete Compression Post-Peak (0-3) : 1
Concrete Compression Softening (0-8) : 1
Concrete Tension Stiffening (0-6) : 1
Concrete Tension Softening (0-3) : 1
Concrete Tension Splitting (0-1) : 0

```



```

Concrete Confined Strength      (0-2) : 1
Concrete Dilation              (0-1) : 1
Concrete Cracking Criterion    (0-4) : 1
Concrete Crack Slip Check     (0-2) : 1
Concrete Crack Width Check    (0-2) : 1
Concrete Bond or Adhesion     (0-3) : 1
Concrete Creep and Relaxation (0-1) : 1
Concrete Hysteresis           (0-2) : 3
Reinforcement Hysteresis     (0-2) : 1
Reinforcement Dowel Action    (0-1) : 1
Reinforcement Buckling       (0-1) : 1
Element Strain Histories      (0-1) : 1
Element Slip Distortions     (0-4) : 1
Strain Rate Effects           (0-1) : 1
Structural Damping            (0-1) : 1
Geometric Nonlinearity       (0-1) : 1
Crack Allocation Process      (0-1) : 1
    
```

<<< JOB FILE NOTES>>>

```

* * * * *
*   V e c T o r 2   *
*   L O A D   D A T A   *
* * * * *
    
```

LOAD CASE PARAMETERS  
\*\*\*\*\*

```

Structure Title      (30 char. max.) : beam S1C
Load Case Title     (30 char. max.) : S1Cg
Load Case File Name (8 char. max.)  : S1Cg
No. of Loaded Joints : 0
No. of Prescribed Support Displacements : 0
No. of Elements with Gravity Loads : 448
No. of Elements with Temperature Loads : 0
No. of Elements with Concrete Prestrain : 0
No. of Elements with Ingress Pressure : 0
No. of Element Surfaces w/ Thermal Load : 0
No. of Nodes with Lumped Masses : 0
No. of Nodes with Impulse Forces : 0
Ground Acceleration Record (0-1) : 0
    
```

JOINT LOADS  
\*\*\*\*\*

```

<NOTE:> UNITS: KIPS OR KN
<<<<< FORMAT >>>>>
NODE  FX  Fy  [ #NODE d(NODE) d(Fx) d(Fy) ] /
/
    
```

SUPPORT DISPLACEMENTS  
\*\*\*\*\*

```

<NOTE:> UNITS: MM OR IN
<<<<< FORMAT >>>>>
JNT  DOF  DISPL [ #JNT d(JNT) ] /
/
    
```

GRAVITY LOADS  
\*\*\*\*\*

```

<NOTE:> UNITS: KG/M3
<<<<< FORMAT >>>>>
ELMT  DENS  GX  GY  [#ELMT d(ELMT)] [ #ELMT d(ELMT)] /
  1  2470.000  0.000  -1.000  1  1  1  1/
  2  2470.000  0.000  -1.000  1  1  1  1/
  .
  .
  .
    
```

```

447 2470.000 0.000 -1.000 1 1 1 1/
448 2470.000 0.000 -1.000 1 1 1 1/
/
      TEMPERATURE LOADS
      *****
<NOTE:> UNITS: F OR C
<<<<< FORMAT >>>>>
ELMT TEMP [ #ELMT d(ELMT) d(TEMP) ] [ #ELMT d(ELMT) d(TEMP) ] /
/
      CONCRETE PRESTRAINS
      *****
<NOTE:> UNITS: me
<<<<< FORMAT >>>>>
ELMT STRAIN [ #ELMT d(ELMT) d(STRAIN) ] [ #ELMT d(ELMT) d(STRAIN) ] /
/
      INGRESS PRESSURES
      *****
<NOTE:> UNITS: MPa
<<<<< FORMAT >>>>>
ELMT PRESSURE [ #ELMT d(ELMT) d(PRS) ] [ #ELMT d(ELMT) d(PRS) ] /
/
      SURFACE THERMAL LOADS
      *****
<NOTE:> UNITS: Sec, Degrees C
<<<<< FORMAT >>>>>
NODE1 NODE2 Tm1 Tp1 Tm2 Tp2 Tm3 Tp3 [#SURF d(NODE)] [#SURF d(NODE)] /
/
      LUMPED MASSES
      *****
<NOTE:> UNITS: kg, m/s
<<<<< FORMAT >>>>>
NODE DOF-X DOF-Y MASS GF-X GF-Y Vo-X Vo-Y [ #NODE d(NODE) ] /
/
      IMPULSE FORCES
      *****
<NOTE:> UNITS: Sec, kN
<<<<< FORMAT >>>>>
NODE DOF T1 F1 T2 F2 T3 F3 T4 F4 [ #NODE d(NODE) ] /
/
      GROUND ACCELERATION
      *****
<NOTE:> UNITS: Sec, G
<<<<< FORMAT >>>>>
TIME ACC-X ACC-Y
/

```

<<< LOAD FILE NOTES >>>

```

* * * * *
*   V e c t o r 2   *
*   L O A D   D A T A   *
* * * * *

```

LOAD CASE PARAMETERS  
\*\*\*\*\*

```

Structure Title (30 char. max.) : beam S1C
Load Case Title (30 char. max.) : S1Cext1
Load Case File Name (8 char. max.) : S1Cext1
No. of Loaded Joints : 4
No. of Prescribed Support Displacements : 0
No. of Elements with Gravity Loads : 0
No. of Elements with Temperature Loads : 0
No. of Elements with Concrete Prestrain : 0
No. of Elements with Ingress Pressure : 0

```

No. of Element Surfaces w/ Thermal Load : 0  
 No. of Nodes with Lumped Masses : 0  
 No. of Nodes with Impulse Forces : 0  
 Ground Acceleration Record (0-1) : 0

JOINT LOADS  
 \*\*\*\*\*

<NOTE:> UNITS: KIPS OR KN  
 <<<<< FORMAT >>>>>  
 NODE Fx Fy [ #NODE d(NODE) d(Fx) d(Fy) ] /  
 427 0.000 -3.732 1 1 0.000 0.000/  
 444 0.000 -7.463 1 1 0.000 0.000/  
 461 0.000 -7.463 1 1 0.000 0.000/  
 478 0.000 -3.732 1 1 0.000 0.000/  
 /

SUPPORT DISPLACEMENTS  
 \*\*\*\*\*

<NOTE:> UNITS: MM OR IN  
 <<<<< FORMAT >>>>>  
 JNT DOF DISPL [ #JNT d(JNT) ] /  
 /

GRAVITY LOADS  
 \*\*\*\*\*

<NOTE:> UNITS: KG/M3  
 <<<<< FORMAT >>>>>  
 ELMT DENS GX GY [ #ELMT d(ELMT) ] [ #ELMT d(ELMT) ] /  
 /

TEMPERATURE LOADS  
 \*\*\*\*\*

<NOTE:> UNITS: F OR C  
 <<<<< FORMAT >>>>>  
 ELMT TEMP [ #ELMT d(ELMT) d(TEMP) ] [ #ELMT d(ELMT) d(TEMP) ] /  
 /

CONCRETE PRESTRAINS  
 \*\*\*\*\*

<NOTE:> UNITS: me  
 <<<<< FORMAT >>>>>  
 ELMT STRAIN [ #ELMT d(ELMT) d(STRAIN) ] [ #ELMT d(ELMT) d(STRAIN) ] /  
 /

INGRESS PRESSURES  
 \*\*\*\*\*

<NOTE:> UNITS: MPa  
 <<<<< FORMAT >>>>>  
 ELMT PRESSURE [ #ELMT d(ELMT) d(PRS) ] [ #ELMT d(ELMT) d(PRS) ] /  
 /

SURFACE THERMAL LOADS  
 \*\*\*\*\*

<NOTE:> UNITS: Sec, Degrees C  
 <<<<< FORMAT >>>>>  
 NODE1 NODE2 Tm1 Tp1 Tm2 Tp2 Tm3 Tp3 [ #SURF d(NODE) ] [ #SURF d(NODE) ] /  
 /

LUMPED MASSES  
 \*\*\*\*\*

<NOTE:> UNITS: kg, m/s  
 <<<<< FORMAT >>>>>  
 NODE DOF-X DOF-Y MASS GF-X GF-Y Vo-X Vo-Y [ #NODE d(NODE) ] /  
 /

IMPULSE FORCES  
 \*\*\*\*\*

<NOTE:> UNITS: Sec, kN  
 <<<<< FORMAT >>>>>  
 NODE DOF T1 F1 T2 F2 T3 F3 T4 F4 [ #NODE d(NODE) ] /  
 /

GROUND ACCELERATION  
 \*\*\*\*\*

<NOTE:> UNITS: Sec, G  
 <<<<< FORMAT >>>>>

TIME ACC-X ACC-Y  
/

<<< LOAD FILE NOTES >>>

\* \* \* \* \*  
\* V e c T o r 2 \*  
\* L O A D D A T A \*  
\* \* \* \* \*

LOAD CASE PARAMETERS  
\*\*\*\*\*

Structure Title (30 char. max.) : beam S1C  
Load Case Title (30 char. max.) : S1Cext2  
Load Case File Name (8 char. max.) : S1Cext2  
No. of Loaded Joints : 3  
No. of Prescribed Support Displacements : 0  
No. of Elements with Gravity Loads : 0  
No. of Elements with Temperature Loads : 0  
No. of Elements with Concrete Prestrain : 0  
No. of Elements with Ingress Pressure : 0  
No. of Element Surfaces w/ Thermal Load : 0  
No. of Nodes with Lumped Masses : 0  
No. of Nodes with Impulse Forces : 0  
Ground Acceleration Record (0-1) : 0

JOINT LOADS  
\*\*\*\*\*

<NOTE:> UNITS: KIPS OR KN  
<<<<< FORMAT >>>>>  
NODE FX Fy [ #NODE d(NODE) d(Fx) d(Fy) ] /  
63 0.000 3.732 1 1 0.000 0.000/  
79 0.000 7.463 1 1 0.000 0.000/  
109 0.000 3.732 1 1 0.000 0.000/  
/

SUPPORT DISPLACEMENTS  
\*\*\*\*\*

<NOTE:> UNITS: MM OR IN  
<<<<< FORMAT >>>>>  
JNT DOF DISPL [ #JNT d(JNT) ] /  
/

GRAVITY LOADS  
\*\*\*\*\*

<NOTE:> UNITS: KG/M3  
<<<<< FORMAT >>>>>  
ELMT DENS GX GY [ #ELMT d(ELMT) ] [ #ELMT d(ELMT) ] /  
/

TEMPERATURE LOADS  
\*\*\*\*\*

<NOTE:> UNITS: F OR C  
<<<<< FORMAT >>>>>  
ELMT TEMP [ #ELMT d(ELMT) d(TEMP) ] [ #ELMT d(ELMT) d(TEMP) ] /  
/

CONCRETE PRESTRAINS  
\*\*\*\*\*

<NOTE:> UNITS: me  
<<<<< FORMAT >>>>>  
ELMT STRAIN [ #ELMT d(ELMT) d(STRAIN) ] [ #ELMT d(ELMT) d(STRAIN) ] /  
/

INGRESS PRESSURES  
\*\*\*\*\*

<NOTE:> UNITS: MPa  
<<<<< FORMAT >>>>>  
ELMT PRESSURE [ #ELMT d(ELMT) d(PRS) ] [ #ELMT d(ELMT) d(PRS) ] /

```

/
                                SURFACE THERMAL LOADS
                                *****
<NOTE:> UNITS:  Sec, Degrees C
<<<<< FORMAT >>>>>
NODE1 NODE2  Tm1 Tp1  Tm2 Tp2  Tm3 Tp3  [#SURF d(NODE)] [#SURF d(NODE)] /
/
                                LUMPED MASSES
                                *****
<NOTE:> UNITS:  kg, m/s
<<<<< FORMAT >>>>>
NODE DOF-X DOF-Y MASS  GF-X GF-Y Vo-X Vo-Y [ #NODE d(NODE) ] /
/
                                IMPULSE FORCES
                                *****
<NOTE:> UNITS:  Sec, kN
<<<<< FORMAT >>>>>
NODE DOF T1  F1  T2  F2  T3  F3  T4  F4 [ #NODE d(NODE) ] /
/
                                GROUND ACCELERATION
                                *****
<NOTE:> UNITS:  Sec, G
<<<<< FORMAT >>>>>
TIME ACC-X ACC-Y
/

<<< LOAD FILE NOTES >>>

```

**D2. SPECIMEN L0M**

**Job data: file Vector.job**

```

* * * * *
*   V E C T O R   *
*   J O B   D A T A   *
* * * * *

```

```

Job Title      (30 char. max.)      : beam L0M
Job File Name  ( 8 char. max.)      : L0M
Date           (30 char. max.)      : 15/09/08

```

STRUCTURE DATA

```

-----
Structure Type ( 8 char. max.)      : 2
File Name      ( 8 char. max.)      : L0M

```

LOADING DATA

```

-----
No. of Load Stages                : 101
Starting Load Stage No.            : 1
Load Series ID ( 5 char. max.)     : LS

```

Load Case	File Name (8 char. max.)	Initial	Final	LS-Inc	Type	Reps	C-Inc
1	L0M g	1.000000	1.000000	0.000000	1	1	0.000000
2	L0M ext	0.000000	1.000000	0.010000	1	1	0.000000
3	NULL	0.000000	0.000000	0.000000	1	1	0.000000
4	NULL	0.000000	0.000000	0.000000	1	1	0.000000
5	NULL	0.000000	0.000000	0.000000	1	1	0.000000

ANALYSIS PARAMETERS

-----

```

Analysis Mode          (1-2) : 1
Seed File Name        (8 char. max.) : NULL
Convergence Limit     (>1.0) : 1.000010
Averaging Factor      (<1.0) : 0.500
Maximum No. of Iterations : 60
Convergence Criteria  (1-5) : 2
Results Files         (1-4) : 2
Output Format          (1-3) : 1

```

MATERIAL BEHAVIOUR MODELS

```

-----
Concrete Compression Base Curve      (0-3) : 2
Concrete Compression Post-Peak       (0-3) : 1
Concrete Compression Softening       (0-8) : 1
Concrete Tension Stiffening          (0-6) : 1
Concrete Tension Softening           (0-3) : 1
Concrete Tension Splitting           (0-1) : 0
Concrete Confined Strength           (0-2) : 1
Concrete Dilation                    (0-1) : 1
Concrete Cracking Criterion           (0-4) : 1
Concrete Crack Slip Check            (0-2) : 1
Concrete Crack Width Check           (0-2) : 1
Concrete Bond or Adhesion            (0-3) : 1
Concrete Creep and Relaxation         (0-1) : 1
Concrete Hysteresis                  (0-2) : 3
Reinforcement Hysteresis             (0-2) : 1
Reinforcement Dowel Action           (0-1) : 1
Reinforcement Buckling               (0-1) : 1
Element Strain Histories              (0-1) : 1
Element Slip Distortions             (0-4) : 1
Strain Rate Effects                  (0-1) : 1
Structural Damping                   (0-1) : 1
Geometric Nonlinearity               (0-1) : 1
Crack Allocation Process              (0-1) : 1

```

<<< JOB FILE NOTES>>>

Structure data: file L0M.s2r

```

* * * * *
*           V e c t o r 2           *
*   S T R U C T U R E   D A T A   *
* * * * *

```

STRUCTURAL PARAMETERS

\*\*\*\*\*

```

Structure Title      (30 char. max.) : beam L0M
Structure File Name  ( 8 char. max.) : L0M
No. of R.C. Material Types : 2
No. of Steel Material Types : 3
No. of Bond Material Types : 0
No. of Rectangular Elements : 608
No. of Quadrilateral Elements : 0
No. of Triangular Elements : 0
No. of Truss Bar Elements : 167
No. of Linkage Elements : 0
No. of Contact Elements : 0
No. of Joints : 664
No. of Restraints : 19

```

MATERIAL SPECIFICATIONS

\*\*\*\*\*

(A) REINFORCED CONCRETE

<NOTE:> TO BE USED IN RECTANGULAR AND TRIANGULAR ELEMENTS ONLY

CONCRETE

MAT TYP	Ns #	T mm	f'c MPa	[ f't MPa	Ec MPa	e0 me	Mu	Cc /C	Agg mm	Dens kg/m3	Kc mm2/s	[Sx Sy] mm mm
1	0	400.000	29.100	0.000	0.000	0.000	1.470	0.000	0.000	0.000	20.000	
2	0	400.000	29.100	0.000	0.000	0.000	1.470	0.000	0.000	0.000	20.000	

REINFORCEMENT COMPONENTS

MAT TYP	REF TYP	DIR deg	As %	Db mm	Fy MPa	Fu MPa	Es MPa	Esh MPa	esh me	Cs /C	Dep me
/											

(B) STEEL

<NOTE:> TO BE USED FOR TRUSS ELEMENTS ONLY

MAT TYP	REF TYP	AREA mm2	Db mm	Fy MPa	Fu MPa	Es MPa	Esh MPa	esh me	Cs /C	Dep me
1	1	1530.000	25.000	652.000	862.000	200000.000	2333.000			
2	1	7854.000	100.000	2000.000	4000.000	200000.000	20000.000			
3	1	400.000	15.000	490.000	600.000	200000.000	880.000	25.000		

(C) BOND

<NOTE:> TO BE USED FOR EXTERIOR/INTERIOR BONDED ELEMENTS

MAT TYP	REF TYP	{ Ao mm^2	U1 MPa	U2 MPa	U3 MPa	S1 mm	S2 mm	S3 mm	CPF 0-1	Cmin mm	No. LYR	HOOK 0/1
/												

ELEMENT INCIDENCES

\*\*\*\*\*

(A) RECTANGULAR ELEMENTS

<<<<< FORMAT >>>>>

ELMT	INC1	INC2	INC3	INC4	[#ELMT	d(ELMT)	d(INC)]	[#ELMT	d(ELMT)	d(INC)]/
1	27	4	14	35	1	1	1	1	1	/
2	4	27	23	15	1	1	1	1	1	/
:										
607	663	664	647	646	1	1	1	1	1	/
608	644	643	660	661	1	1	1	1	1	/

(B) QUADRILATERAL ELEMENTS

<<<<< FORMAT >>>>>

ELMT	INC1	INC2	INC3	INC4	[#ELMT	d(ELMT)	d(INC)]	[#ELMT	d(ELMT)	d(INC)]/
/										

(C) TRIANGULAR ELEMENTS

<<<<< FORMAT >>>>>

ELMT	INC1	INC2	INC3	[ #ELMT	d(ELMT)	d(INC) ]	[ #ELMT	d(ELMT)	d(INC) ] /
/									

(D) TRUSS ELEMENTS

<<<<< FORMAT >>>>>

ELMT	INC1	INC2	[ #ELMT	d(ELMT)	d(INC)]	[#ELMT	d(ELMT)	d(INC) ]/
609	4	27	1	1	1	1	1	/
610	27	48	1	1	1	1	1	/

```

      .
      .
774 288 289 1 1 1 1 1 1 /
775 289 290 1 1 1 1 1 1 /
/
      (E) LINKAGE ELEMENTS
      -----
<<<<< FORMAT >>>>>
ELMT INC1 INC2 [ #ELMT d(ELMT) d(INC) ] [ #ELMT d(ELMT) d(INC) ]
/
      (F) CONTACT ELEMENTS
      -----
<<<<< FORMAT >>>>>
ELMT INC1 INC2 INC3 INC4 [ #ELMT d(ELMT) d(INC) ] [ #ELMT d(ELMT) d(INC) ]
/
      MATERIAL TYPE ASSIGNMENT
      *****
<<<<< FORMAT >>>>>
ELMT MAT ACT [ #ELMT d(ELMT)] [ #ELMT d(ELMT) ] /
1 2 1 1 1 1 1 /
2 2 1 1 1 1 1 /
      .
      .
774 3 1 1 1 1 1 /
775 3 1 1 1 1 1 /
/
      COORDINATES
      *****
<NOTE:> UNITS: in OR mm
<<<<< FORMAT >>>>>
NODE X Y [ #NODES d(NODES) d(X) d(Y) ] [ #NODES d(NODES) d(X) d(Y) ] /
14 0.000 0.000 1 1 0.000 0.000 1 1 0.000 0.000 /
35 50.000 0.000 1 1 0.000 0.000 1 1 0.000 0.000 /
664 2725.000 1200.000 1 1 0.000 0.000 1 1 0.000 0.000 /
136 250.000 -50.000 1 1 0.000 0.000 1 1 0.000 0.000 /
/
      SUPPORT RESTRAINTS
      *****
<NOTE:> CODE: '0' FOR NOT RESTRAINED NODES AND '1' FOR RESTRAINED ONES
<<<<< FORMAT >>>>>
NODE X-RST Y-RST [ #NODE d(NODE) ] /
112 0 1 1 1 /
648 1 0 1 1 /
649 1 0 1 1 /
650 1 0 1 1 /
651 1 0 1 1 /
652 1 0 1 1 /
653 1 0 1 1 /
654 1 0 1 1 /
655 1 0 1 1 /
656 1 0 1 1 /
657 1 0 1 1 /
658 1 0 1 1 /
659 1 0 1 1 /
660 1 0 1 1 /
661 1 0 1 1 /
662 1 0 1 1 /
663 1 0 1 1 /
664 1 0 1 1 /
136 1 0 1 1 /
/

<<<< STRUCTURE FILE NOTES >>>>>

```



Monotonic load: files L0Mg.l2r, L0Mext.l2r

\* \* \* \* \*  
 \* V e c T o r 2 \*  
 \* L O A D D A T A \*  
 \* \* \* \* \*

LOAD CASE PARAMETERS  
 \*\*\*\*\*

Structure Title (30 char. max.) : beam LOM  
 Load Case Title (30 char. max.) : LOM g  
 Load Case File Name (8 char. max.) : LOM g  
 No. of Loaded Joints : 3  
 No. of Prescribed Support Displacements : 0  
 No. of Elements with Gravity Loads : 608  
 No. of Elements with Temperature Loads : 0  
 No. of Elements with Concrete Prestrain : 0  
 No. of Elements with Ingress Pressure : 0  
 No. of Element Surfaces w/ Thermal Load : 0  
 No. of Nodes with Lumped Masses : 0  
 No. of Nodes with Impulse Forces : 0  
 Ground Acceleration Record (0-1) : 0

JOINT LOADS  
 \*\*\*\*\*

<NOTE:> UNITS: KIPS OR KN  
 <<<< FORMAT >>>>  
 NODE Fx Fy [ #NODE d(NODE) d(Fx) d(Fy) ] /  
 66 0.000 5.283 1 1 0.000 0.000/  
 89 0.000 10.567 1 1 0.000 0.000/  
 116 0.000 5.283 1 1 0.000 0.000/  
 /

SUPPORT DISPLACEMENTS  
 \*\*\*\*\*

<NOTE:> UNITS: MM OR IN  
 <<<< FORMAT >>>>  
 JNT DOF DISPL [ #JNT d(JNT) ] /  
 /

GRAVITY LOADS  
 \*\*\*\*\*

<NOTE:> UNITS: KG/M3  
 <<<< FORMAT >>>>  
 ELMT DENS GX GY [ #ELMT d(ELMT) ] [ #ELMT d(ELMT) ] /  
 1 2470.000 0.000 -1.000 1 1 1 1/  
 2 2470.000 0.000 -1.000 1 1 1 1/  
 .  
 .  
 607 2470.000 0.000 -1.000 1 1 1 1/  
 608 2470.000 0.000 -1.000 1 1 1 1/  
 /

TEMPERATURE LOADS  
 \*\*\*\*\*

<NOTE:> UNITS: F OR C  
 <<<< FORMAT >>>>  
 ELMT TEMP [ #ELMT d(ELMT) d(TEMP) ] [ #ELMT d(ELMT) d(TEMP) ] /  
 /

CONCRETE PRESTRAINS  
 \*\*\*\*\*

<NOTE:> UNITS: me  
 <<<< FORMAT >>>>  
 ELMT STRAIN [ #ELMT d(ELMT) d(STRAIN) ] [ #ELMT d(ELMT) d(STRAIN) ] /  
 /

INGRESS PRESSURES

```

*****
<NOTE:> UNITS: MPa
<<<<< FORMAT >>>>>
ELMT PRESSURE [ #ELMT d(ELMT) d(PRS) ] [ #ELMT d(ELMT) d(PRS) ] /
/
      SURFACE THERMAL LOADS
*****
<NOTE:> UNITS: Sec, Degrees C
<<<<< FORMAT >>>>>
NODE1 NODE2 Tm1 Tp1 Tm2 Tp2 Tm3 Tp3 [#SURF d(NODE)] [#SURF d(NODE)] /
/
      LUMPED MASSES
*****
<NOTE:> UNITS: kg, m/s
<<<<< FORMAT >>>>>
NODE DOF-X DOF-Y MASS GF-X GF-Y Vo-X Vo-Y [ #NODE d(NODE) ] /
/
      IMPULSE FORCES
*****
<NOTE:> UNITS: Sec, kN
<<<<< FORMAT >>>>>
NODE DOF T1 F1 T2 F2 T3 F3 T4 F4 [ #NODE d(NODE) ] /
/
      GROUND ACCELERATION
*****
<NOTE:> UNITS: Sec, G
<<<<< FORMAT >>>>>
TIME ACC-X ACC-Y
/

```

<<< LOAD FILE NOTES >>>

```

* * * * *
*   V e c t o r 2   *
*   L O A D   D A T A   *
* * * * *

```

```

LOAD CASE PARAMETERS
*****

```

```

Structure Title      (30 char. max.) : beam LOM
Load Case Title      (30 char. max.) : LOM ext
Load Case File Name  (8 char. max.)  : LOM ext
No. of Loaded Joints : 7
No. of Prescribed Support Displacements : 0
No. of Elements with Gravity Loads : 0
No. of Elements with Temperature Loads : 0
No. of Elements with Concrete Prestrain : 0
No. of Elements with Ingress Pressure : 0
No. of Element surfaces w/ Thermal Load : 0
No. of Nodes with Lumped Masses : 0
No. of Nodes with Impulse Forces : 0
Ground Acceleration Record (0-1) : 0

```

```

JOINT LOADS
*****

```

```

<NOTE:> UNITS: KIPS OR KN
<<<<< FORMAT >>>>>
NODE Fx Fy [ #NODE d(NODE) d(Fx) d(Fy) ] /
66 0.000 80 1 1 0.000 0.000/
89 0.000 160 1 1 0.000 0.000/
116 0.000 80 1 1 0.000 0.000/
613 0.000 -80 1 1 0.000 0.000/
630 0.000 -160 1 1 0.000 0.000/
647 0.000 -160 1 1 0.000 0.000/

```

```

/ 664 0.000 -80 1 1 0.000 0.000/
/
SUPPORT DISPLACEMENTS
*****

<NOTE:> UNITS: MM OR IN
<<<<< FORMAT >>>>>
JNT DOF DISPL [ #JNT d(JNT) ] /
/
GRAVITY LOADS
*****

<NOTE:> UNITS: KG/M3
<<<<< FORMAT >>>>>
ELMT DENS GX GY [ #ELMT d(ELMT) ] [ #ELMT d(ELMT) ] /
/
TEMPERATURE LOADS
*****

<NOTE:> UNITS: F OR C
<<<<< FORMAT >>>>>
ELMT TEMP [ #ELMT d(ELMT) d(TEMP) ] [ #ELMT d(ELMT) d(TEMP) ] /
/
CONCRETE PRESTRAINS
*****

<NOTE:> UNITS: me
<<<<< FORMAT >>>>>
ELMT STRAIN [ #ELMT d(ELMT) d(STRAIN) ] [ #ELMT d(ELMT) d(STRAIN) ] /
/
INGRESS PRESSURES
*****

<NOTE:> UNITS: MPa
<<<<< FORMAT >>>>>
ELMT PRESSURE [ #ELMT d(ELMT) d(PRS) ] [ #ELMT d(ELMT) d(PRS) ] /
/
SURFACE THERMAL LOADS
*****

<NOTE:> UNITS: Sec, Degrees C
<<<<< FORMAT >>>>>
NODE1 NODE2 Tm1 Tp1 Tm2 Tp2 Tm3 Tp3 [ #SURF d(NODE) ] [ #SURF d(NODE) ] /
/
LUMPED MASSES
*****

<NOTE:> UNITS: kg, m/s
<<<<< FORMAT >>>>>
NODE DOF-X DOF-Y MASS GF-X GF-Y Vo-X Vo-Y [ #NODE d(NODE) ] /
/
IMPULSE FORCES
*****

<NOTE:> UNITS: Sec, kN
<<<<< FORMAT >>>>>
NODE DOF T1 F1 T2 F2 T3 F3 T4 F4 [ #NODE d(NODE) ] /
/
GROUND ACCELERATION
*****

<NOTE:> UNITS: Sec, G
<<<<< FORMAT >>>>>
TIME ACC-X ACC-Y
/

<<<< LOAD FILE NOTES >>>>

```